V D U B RACOSYS 99

INTERNATIONAL CONFERENCE ON ~~BUILD UP~~ RECENT DEVELOPMENTS IN DURABILITY ANALYSIS OF COMPOSITE SYSTEMS

BOOKLET OF ABSTRACTS

Brussels
11-14 July, 1999

20000619 032

AD NUMBER	DATE	DTIC

1. REPORT IDENTIFYING INFORMATION

A. ORIGINATING AGENCY

FREE UNIVERSITY OF BROSSELS, BELGIUM

B. REPORT TITLE AND/OR NUMBER INT'L CONFERENCE ON RECENT DEVELOPMENTS IN DURABILITY ANALYSIS OF COMPOSITE SYSTEMS

C. MONITOR REPORT NUMBER

R+D 8646-AN-02

D. PREPARED UNDER CONTRACT NUMBER

N68171-99-H-5598.

2. DISTRIBUTION STATEMENT

APPROVED FOR PUBLIC RELEASE

DISTRIBUTION UNLIMITED

PROCEEDINGS

DURACOSYS 99

V
D U RACOSYS 99
B

BOOKLET OF ABSTRACTS

Brussels
11-14 July, 1999

V D U B RACOSYS 99

FINAL PROGRAMME

11-14 July, 1999

Last moment changes can still occur.
Those changes will be communicated during the sessions
and indicated on the daily programme on the general
information board.

International Scientific Board

R. ADAMS (Bristol, United Kingdom)
S. AIVAZZADEH (Nevers, France)
L. BERGLUND (Lulea, Sweden)
O. BERGSMA (Delft, The Netherlands)
T. BLASZCZYNSKI (Poznan, Poland)
H. BRINSON (Houston, USA)
O. BRÜLLER (Munich, Germany)
I. EMRI (Ljubljana, Slovenia)
P. GUDMUNDSON (Stockholm, Sweden)
Z. HASHIN (Tel Aviv, Israel)
N. HIMMEL (Kaiserslautern, Germany)
P. HOGG (London, United Kingdom)
S. JOHNSON (Georgia Tech, USA)
W. KNAUSS (Caltech, Pasadena, USA)
P. LAGACE (MIT, Cambridge, USA)
J.A. MANSON (EPFL, Lausanne, Switzerland)
TIANGXIANG MAO (Bejing, China)
A. MIRAVETE (Zaragoza, Spain)
Y. MIYANO (Kanazawa, Japan)
G. PAPANICOLAOU (Patras, Greece)
T. PEIJS (Eindhoven, The Netherlands)
D. PERREUX (Besançon, France)
R. PYRZ (Aalborg, Denmark)
E. SANCAKTAR (Akron, USA)
K. SCHULTE (Hamburg-Harburg, Germany)
R. TALREJA (Georgia Tech, Atlanta, USA)
V. TAMUSZ (Riga, Latvia)
A. VAUTRIN (St.Etienne, France)
I. VERPOEST (KULeuven, Belgium)
J. WEITSMAN (Knoxville, USA)

Belgian Host Committee

A. CARDON (V.U.Brussels)
R. BOURGOIS (Royal Military School, Brussels)
J. DEGRIECK (Univ. Ghent)
P. HALLEUX (U.L.Brussels)
R. KEUNINGS (U.C.Louvain-La-Neuve)
I. VERPOEST (KULeuven)

Local Organizing Committee

A. CARDON
M. BOURLAU, A. VANAEKEN
P. BOUQUET, K. HOES, Chr. VAN VOSSOLE, S. HAROU-KOUKA
A. VRIJDAG, F. BOULPAEP, R. HEREMANS, D. DEBONDT, G. VAN DEN NEST

	Monday July 12, 1999		Tuesday July 13, 1999		Wednesday July 14, 1999
8.30	Opening	8.30	Session 5 (2GL)	8.30	Session 9 (2GL)
8.45	Session 1 (2GL)				
10.15-10.45	Break	10.00-10.30	Break	10.00-10.30	Break
10.45	Session 2 (1GL + 2P)	10.30	Session 6 (SOP)	10.30	Session 10 (5P)
12.15-13.30	Lunch	12.45-13.45	Lunch	12.30-13.45	Lunch
13.45	Session 3 (2SL + 3P)	14.00	Session 7 (1GL + 1SL + 1P)	14.00	Session 11 (7P)
15.35-16.05	Break	15.30-16.00	Break	15.40-16.10	Break
16.05	Session 4 (SOP)	16.00	Session 8 (4P)	16.50	General discussion
18.15-18.45	General discussion	17.45	Optional excursion with		Conclusions – Closure
			dinner	19.30	Conference dinner

GL   :   General Invited Lecture (45 minutes : questions, answers and discussion included)

SL   :   Special Invited Lecture (25 minutes : questions, answers and discussion included)

P   :   Oral Presentation (20 minutes : questions, answers and discussion included)

SOP   :   Short Oral Presentation (10 minutes : questions, answers and discussions around the posters on exhibit from Monday at noon till

           Wednesday afternoon break)

Members of our staff will be at the Dôme Hotel at 7.30 a.m. and will guide you, starting at 7.45 a.m., through the Metro to the conference location (University Campus).
Starting at 7.30 a.m. the registration will be open at the conference location till 4.00 p.m.

<div align="center">

*

*   *

</div>

8.30   Opening and Introduction

Session 1 : Fatigue and Damage
Chair : Zvi HASHIN - Israel

8.45   "Fatigue in Composite Laminates - A qualitative link from micromechanics to fatigue life performance"
K. Gamstedt (RISØ National Laboratory, Denmark)

9.30   "Modelling and computation until final fracture of composite laminates"
P. Ladevèze (ENS-LMT Cachan, France)

10.15-10.45 : Break

Session 2 : Moisture - Fatigue - Ageing
Chair : Jack WEITSMAN - USA

10.45   "Ageing and long term behaviour of composite tubes"
P. Davies, R. Boizau, D. Choqueuse (IFREMER Brest, France),
L. Salmon, F.D. Jagnat (EDT - Moret sur Loing, France)

11.30   "Interactions between moisture and fatigue damage in unidirectional glass-epoxy composites subjected to flexural loading"
A. Chateauminois (Ecole Central de Lyon, France)

11.50   "Contribution to the durability analysis of a thick composite structure under complex mechanical and hygroscopic loads"
Y. Poirette, F. Pierron, A. Vautrin (Ecole des Mines St. Etienne, France)

12.15-13.30 : Lunch

Session 3 :   Damage – Damping – Ageing
Chair : Hal BRINSON – USA

13.45   "Durability of polymer matrix composites : some remarks by the
AMAC Committee on Durability"
D. Perreux (AMAC-LMARC Besançon, France)

14.10   "Effects of moisture on damage evolution, strain inhomogeneity and
fracture in a particulate composite"
C.T. Liu (Air Force Research Lab., Edwards AFB, CA, USA)

14.35   "The damping and dynamic moduli of fibre reinforced polymer
composites after exposure to hot-wet conditioning"
R.D. Adams, M.M. Singh, University Bristol, United Kingdom)

14.55   "Modelling of composite interfaces subjected to thermal and
physical aging"
D.A. Mendels, Y. Leterrier, J.A. Manson (EPFL, Lausanne,
Switzerland)

15.15   "Accelerated evaluation of environmental ageing monitored by
fatigue crack growth experiments"
V. Altstädt, S. Keiter (Univ. Hamburg-Harburg, Germany)

15.35-16.05 : Break

16.05 Session 4 : Short Oral Presentations   (Serie 1)
Chair : Shahram Aivazzadeh, France

Short oral presentations (10 minutes) with poster support (serie 1),
questions, answers and discussions will be possible in the general
discussion and around the posters.

4.1.   "Damage/weight loss relationship for bismaleimide matrix under
isothermal oxidative ageing"
X. Colin, C. Marais, J. Verdu, L. Audoin (ONERA Chatillon-ENSAM
Paris, France)

4.2   "Interphasial stress and strain fields in multi-phase particulates:
influence of moisture content"
N.K. Anifantis, P.A. Kakavas, G. Papanicolaou (Univ. Patras,
Greece)

4.3   "Chemical resistance of pultruded E-glass polyester composits"
K. Van de Velde, P. Kiekens (University Ghent, Belgium)

4.4 "Performance of pultruded FRP reinforcement with embedded fiber optic sensors"
A.L. Kalamkarov (Dalhousie University, Canada)

4.5 "Monitoring and modeling the durability of polymers used for composite offshore oil transport"
D. Kranbuehl et al. (College of William and Mary, Williamsburg, USA)

4.6 "Modeling of hygrothermal effects in composites and polymer adhesive systems"
S. Roy, Weiqun Xu (University of Missouri-Rolla, USA)

4.7 "Influence of fiber-matrix adhesion on the fatigue behaviour of cross-ply glass-fiber epoxy composites"
J. Gassan (University Kassel, Germany)

4.8 "Assessment of time-temperature superposition principle as a basis for long term behaviour prediction of CFRP under bending loads"
R.Miranda-Guedes (University of Porto, INEGI, Portugal)

4.9 "Viscoelastic contact problems of fiber reinforced polymers"
T. Neff, O. Brüller (Technical University of Münich, Germany)

4.10 "Creep and stress relaxation of composite cylinders"
J.T. Tzeng (US Army Research Lab., USA)

4.11 "AE Measurement in Acid Corrosion"
M. Maeda, H.Hamada, Y. Fujii (Kyoto Instite of Technology, Japan)

4.12 "Modelling of the buckling of plastic containers"
J.L. Spoormaker, I.D. Skrypnyk, T.O. Vasyljkevych (Delft University of Technology, The Netherlands)

4.13 "Tensile and Fatigue Damage in Woven Ceramic Matrix Composites"
A. Haque, M. Rahman, S. Jeelani, Tuskegee University, USA

18.15-18.18.40 : General discussion

Posters will be on exhibit from Monday at noon till the Wednesday afternoon break.

Evening free

Session 5 : Strength criteria - Long term predictions
Chair : Ken REIFSNIDER - USA

8.30   "3D strength criteria derived from the so-called failure mode
        concept - Verification for concrete, FRP and foam"
        R. Cuntze (MAN Technology, Germany)

9.15   "Long term prediction of fatigue life of unidirectional CFRP"
        Y. Miyano (Kanazawa Institute of Technology, Japan)

10.00-10.30 : Break

10.30 Session 6 : Short oral presentations (serie 2)
Chair : Georges VERCHERY - France

6.1   "Experimental Characterisation and analytical prediction of
        microscopic deformation in interlaminartoughened laminates with
        transverse cracks"
        N. Takeda, L.N. McCartney, S. Ogihara (University of Tokyo, Japan)

6.2   "Method for identification of elastic and damage properties of
        laminates composites based on experiment design"
        R. Rikards (Riga Technical University, Latvia)

6.3   "Durability estimation of carbon/polytetrafluoroethylene
        composites for hydraulic downhole motor"
        K. Kemmochi, H. Takayanagi, T. Hamada (Nat. Inst. Materials &
        Chemical Research, Japan)

6.4   "Durability of fiber reinforced plastic (FRP) pipes : increasing
        the quality of the bonds"
        P.M. Oude Weme, C.A.M. Van den Ende (N.V. KEMA, The Netherlands)

6.5   "Comparison of warp knitted and stitched non-crimp fabrics"
        H. Pattyn, I. Verpoest, J. Ivens (Catholic University Leuven,
        Belgium)

6.6   "Predicting the durability of PMR-15 composites at elevated
        temperatures"
        K.J. Bowles (NASA Lewis Research Center, USA)

6.7   "Durability of adhesive joints subjected to elevated temperature
        aging"
        D.R. Veazie, J. Qu, J. Lindsay (Clark Atlanta University, USA)

6.8   "On the use of acoustic emission and scanning electron microscopy
        to investigate fatigue damage in plain-woven fabric composites"
        S.D. Pandita, G. Huysmans, M. Wevers, I. Verpoest (Catholic
        University Leuven, Belgium)

6.9   "Study of the effect of fiber orientation on the nonlinear viscoelastic behaviour of continuous fiber polymer composites"
S.P. Zaoutsos, G.C. Papanicolaou (University of Patras, Greece)

6.10   "Damage modelling of composite structures viscoelastic effects"
M. Chafra, Y. Chevalier (Inst. Supérieur des Matériaux et de la Construction Mécanique (ISMCM) Saint-Ouen, France)

6.11   "Ultimate bearing capacity of cement composite sections under long term physico-chemical exposure"
T.Blaszczynski (Technical University of Poznan, Poland)

6.12   "Damage identificatin of composite material during stress rupture using acoustic emission technique"
A. Rotem (Technion IIT, Israel)

12.35-13.45 : Lunch

Session 7 : Moisture – Infrastructure applications
Chair : Wolfgang KNAUSS – USA

14.00   "The influence of moisture on the physical aging response of epoxy: experimental results and modeling considerations
G. McKenna (NIST, Gaithersburg, USA)

14.45   "Hybrid composites with nonlinear behaviour for reinforcing of concrete"
V.Tamuzs, R. Tepfers (Institute of Polymer Mechanics, Riga, Latvia)

15.10   "Free-thaw durability of polymer matrix composites in infrastructure"
J. Haramis, N. Verghese, J.J. Lesko (Virginia Tech, USA)

15.30-16.00 : Break

Session 8 : Infrastructure applications – Fatigue – Failure
Chair : Bob ADAMS – United Kingdom

16.00   "Durability of fiber reinforced composites in civil instrastructures. Issues, results and implications"
V.M. Karbhari, J. Zhang (University of California, San Diego, USA)

16.20   "Durability of reinforced concrete beams repaired by composites under creep and fatigue loading"
E. Ferrier, G. Lagarde, P. Hamelin (Université Claude Bernard, Lyon, France)

16.40 "Application of dielectric measurements for the assessment of durability in composite systems"
P. Boinard, F Dumoulin, D. Hayward, W.M. Banks, A. Pethrick (University of Strathclyde, Scotland)

17.00 "Failure of laminated composites at thickness discontinuities under complex loading"
S. Lee, W.G. Knauss (Caltech, California, USA)

Evening free or, with departure from the conference location at 17h45, optional excursion to the old university city of Leuven (visit of the Town Hall, the City, the Begijnhof and dinner in the Faculty Club), with return in Brussels around 23.00.

<u>Wednesday July 14, 1999</u>

Session 9 : Aerospace applications
Chair : Peter GUDMUNDSON - Sweden

8.30   "Durability Assessment of Polymeric Composites for High Speed
        Civil Transport"
        T. Gates (NASA Langley, USA)

9.15   "Durability through in-flight evaluation of honeycomb composite
        structures"
        J. Seferis (University of Washington, Seattle, USA)

10.00-10.30 : Break

Session 10 : Ageing - Temperature - Hybrids
Chair : Alain VAUTRIN - France

10.30   "Investigation of the hygrothermal ageing of composites by means
        of Raman spectroscopy"
        A. Cervenka, R.J. Young, D.J. Bannister (University of Manchester
        and Umist, United Kingdom)

10.50   "Failure mechanics of thin coatings under multiaxial loading"
        Y. Leterrier, D. Pellaton, J. Andersons, J.A. Manson (EPFL,
        Lausanne, Switzerland).

11.10   "Effect of temperature and strain rate on the performance of
        polymeric composites"
        K. Reifsnider, C. Mahieu, B. Waltzer, F. Sun (Virginia Tech, USA)

11.30   "Evolution of matrix cracking in cross-ply CFRP laminates :
        differences between mechanical and thermal loadings"
        C. Henaff-Gardin, I. Goupillard, M.C. Lafarie-Frenot (ENSMA,
        Futuroscope, France)

11.50   "Durability of Titanium-graphite hybrid laminates"
        D.A. Burianek, S.M. Spearing (MIT, Cambridge, USA)

12.30-13.45 : Lunch

Session 11 : Experimental aspects – Fatigue
Chair : Norbert HIMMEL – Germany

14.00 "Initiation versus growth criteria for transverse cracks"
P. Gudmundson (Royal Institute of Technology, Stockholm, Sweden)

14.20 "X-ray microtomography : a new technique for analysis of composite materials"
R. Pyrz (Aalborg University, Denmark)

14.40 "In-situ investigation of time-dependent behaviour of polymeric composite subjected to shear loads"
SUN Yong-Qi (Northwest Institute of Textile Science & Technology, Chian, China)

15.00 "Influence of quasi lifetime treatments on the static and fatigue durability of continuous glass fibre reinforced polypropylene"
J.F. Neft, P. Scharzer, (Volkswagen AG, Wolfsburg, Germany), K. Schulte (University Hamburg-Harburg, Germany)

15.20 "A model on thermal degradation of fatigue strength and its application in fatigue life prediction of polymer composites with hysteretic heating"
X. Xiao, I.Al-Hmouz (Concordia University, Canada)

15.40-16.10 : Break

16.10 "Long term prediction of fatigue life for FRP joint system"
M. Nakada, Y. Miyano, S.W. Tsai (Kanazawa Inst. of Technology, Japan)

16.30 "Fatigue behaviour of composite joints"
Y. Dzenis (University of Nebraska-Lincoln, USA)

16.50-17.20 : General discussion and conclusions

19.45 : Conference dinner.

POSTERS

(From Monday July 12 at noon till Wednesday July 14 at the afternoon break)

4.1 - 4.11   Short oral presentations - Serie 1
6.1 - 6.13   Short oral presentations - Serie 2

P.1   "Experimental characterisation of damage progress in high temperature CFRP laminates"
S. Ogihara, N.Takeda (Science University of Tokyo, Japan)

P.2   "Influence of the Shape of a stricker on the mechanical responses of composite beams"
L. Gauillaumat (LAHEFIP-ENSAM Talance, France)

P.3   "Curing conditions and sample preparations for the analysis of the transverse creep behaviour of unidirectional graphite-epoxy composites"
Chr. Van Vossole, P. Bouquet, A. Cardon (Free University Brussels (V.U.B.), Belgium

P.4   "Durability of stressed E-glass fibre in alkaline medium"
G. Swit (University of Technology, Kielce, Poland)

P.5   "Effect of Marine Exposure on Wheaterability of FRP Laminates"
H. Takayanagi, K. Kenmochi, I. Kimpara (National Institute of Materials & Chemical Research, Japan)

P.6   "Accelerated marine ageing of composites and metal/composite joints"
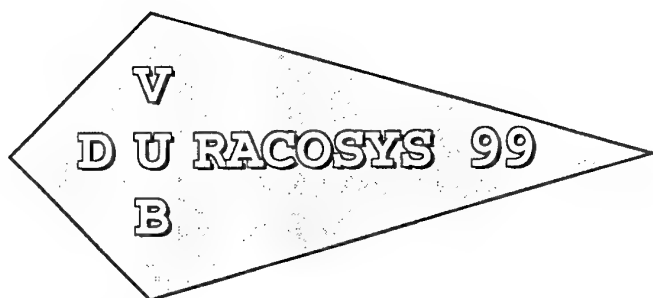P. Davies, A. Roy (IFREMER Brest, France)

P.7   "Reliability of continuous fiber-reinforced ceramic composites under stress-rupture conditions in oxidizing environments
E. Lara-Curzio (Oak Ridge National Laboratory, USA)

P.8   Thermal aging on G_{II} interlaminar fracture mode response of multiaxial 2D composites
F.Segovia-Lopez, C.Bloem (Polytechnical University of Valencia, Spain and Escuela de Igenieria Mecanica, Mérida, Venezuela)

V
D U RACOSYS 99
B

Brussels, July 11-14, 1999

LIST OF PARTICIPANTS

ADAMS Robert D.
UNIVERSITY OF BRISTOL
Dept. of Mechanical Engineering
Queen's Building, University Walk
BRISTOL BS8 1TR
United Kingdom

AIVAZZADEH Shahram
Inst. Sup. de l'Automobile et des Transports
ISAT Nevers
49, rue Mademoiselle-Bourgeois - BP 31
F-58000 NEVERS
France

ALTSTÄDT, Volker
TU Hamburg-Harburg
Dept. Polymers & Composites (AB 5-09,)
Denickestrasse 15
D-21073 HAMBURG
Germany

BANKS W.A.
University of Strathclyde
Div. Mechanics of Materials/Dept. Mech. Eng.
75 Montrose street - James Weir Building
GLASGOW G1 1XJ
Scotland

BLASZCZYNSKI Tomasz
Technical University Poznan
Institute of Structural Engineering
Ul. Piotrowo 5
60-965 POZNAN
Poland

BLOEM Carlos
Escuela de Ingenieria Mecànica y Materiales
Facultad de Ingenieria
Av. Tulio Febres Cordero
5101 Mérida, Edo. Mérida
Venezuela

BOINARD Pascal
Dept. of Pure and Applied Chemistry
Lab. of Phys. Chem. - C302
Thmas Graham Build., 295 Cathedral street
GLASGOW G1 1XL
Scotland

BOUQUET Pascal
FREE UNIVERSITY BRUSSELS (V.U.B.)
Dept. MEMC - Fac. TW
Pleinlaan, 2
1050 Brussels
Belgium

BOWLES, Kenneth J.
NASA Lewis Research Center

21000 Brookpark Road
CLEVELAND, OHIO 44135
USA

BRINSON Hal F.
University of Houston
Mechanical Engineering Department
4800 Calhoun
HOUSTON, TX 77204-0900
U.S.A.

CARDON Albert
FREE UNIVERSITY BRUSSELS (V.U.B.)
Dept. MEMC - Fac. TW
Pleinlaan, 2
1050 Brussels
Belgium

CERVENKA Tony
University of Manchester and Umist
Manchester Material Science Centre
Grosvenor Street
MANCHESTER, M1 7HS
United Kingdom

CHATEAUMINOIS Antoine
Ecole Centrale de Lyon
Dépt. Matériaux-Mécanique Physique

F-69131 ECULLY Cedex
France

CHEVALIER Yvon
ISMCM-CESTI ,
LISMMA - Groupe Rhéologie et Structures
3, rue Fernand Hainaut
F-93407 SAINT OUEN CEDEX
France

COLIN Xavier
ONERA
Dépt. des Matériaux et Systèmes Composites
Avenue de la Division Leclerc, 29
F-92322 Chatillon
France

CUNTZE, R.G.
MAN Technologie AG
Division of Spacecraft
Liebigstrasse, 5A
D-85757 Karlsfeld/Münich
Germany

DAVIES Peter
IFREMER - Centre de Brest
Lab. Matériaux Marins - DITI/GO/MM
B.P. 70
F-29280 PLOUZANE
France

DONG Wei
Medicine Department
Room 303, Jia-58, Peng Zhuang
Chongwen District, Yongwai
Beijing 100045
P.R.China

DZENIS Yris A.
University of Nebraska Lincol
Dept. of Engineering Mechanics
221 Bancroft Hall
LINCOLN, NE 65588 0347
USA

FERRIER Emannuel
Université Claude Bernard
L2M - IUT A Génie Civil
43, bd. du 11 Novembre
F-69622 VILLEURBANNE
France

FUKUDA Hiroshi
Science University of Tokyo
Dept. Materials Science & Technology
2641 YAMAZAKI
Noda, Chiba 278-8510
JAPAN

GAMSTEDT Kristofer
RISO National Laboratory
Materials Research Dept.
P.O. Box 49
DK-4000 ROSKILDE
Denmark

GASSAN J.
Universität Gesamthochschule Kassel
Institut für Werkstoffechimie
Mnchebergstrasse 3
D-34109 KASSEL
GERMANY

GATES Tom
NASA Langley Research Center

Mail Stop 188E
HAMPTON, VA 23681
USA

GAUVIN Raymond
Ecole Polytechnique Montréal
Dépt. de Génie Mécanique
2900, Edouard-Montpetit, C.P. 6079
MONTREAL H3C 3A7
Canada

GUDMUNDSON Peter
Royal Institute of Technology
Dept. of Solid Mechanics

S-10044 Stockholm
Sweden

GUILLAUMAT Laurent
L.A.M.E.F.-E.N.S.A.M.
Esplanade des Arts et Métiers

F-33405 Tallence Cedex
France

HAMADA Taishi
Science University of Tokyo
Graduate School Student
2641 Yamazaki
Noda, Chiba, 278-8510
Japan

HAQUE Anwar
Tuskegee University
TU Center for Advanced Materials
Mechanical Engineering Dept.
TUSKEGEE, AL 36088
USA

HASHIN Zvi
Tel-Aviv University
Dept. of Solid Mechanics, Materials & Struct.
Ramat-Aviv
Tel Aviv, 69978
Israel

HENAFF-GARDIN Catherine
LMPM
ENSMA - Teleport 2 - BP109
Chasseneuil du Poitou
F-86960 FUTUROSCOPE
FRANCE

HIMMEL Norbert
University of Kaiserslautern
Institute for Composite Materials
B.O. Box 3049
D-67663 KAISERSLAUTERN
Germany

KAKAVAS P.A.
University of Patras
Mechanical Engineering Department
Composite Materials Group
265 00 PATRAS
GREECE

KALAMKAROV A.L.
Dalhousie University
Daltech/ Faculty of Engineering
P.O. Box 1000
HALIFAX, NS B3J 2X4
Canada

KARBHARI Vistasp M.
University of California, San Diego
Division of Structural Engineering
9500 Gilman Drive
LA JOLLA, CA 92093-0085
USA

KNAUSS Wolfgang G.
CALTECH
Dept. of Aeronautics and Applied Mechanics
Mail Code : 105-50
PASADENA, CALIFORNIA 91125
USA

KRANBUEHL David
The College of William and Mary
Chemistry Department

Williamsburg, VA 23187
USA

LADEVEZE P.
ENS-Cachan
Dépt. Mécanique et Technologie
Avenue du Président Wilson, 61
F-94235 CACHAN CEDEX
France

LARA-CURZIO Edgar
Oak Ridge National Lab. (High Temp.Mat.Lab
Metals & Ceramics Division, Building 4515
Mail Stop-6069, P.O. Box 2008
OAK RIDGE, TN 37831-6069
USA

LESKO J.J.
Virginia Tech
Dept. of Engineering Science & Mechanics
120 Patton Hall
Blacksburg, VA 24061-0219
U.S.A.

LETERRIER Yves
Ecole Polytechnique Fédérale de Lausanne
Laboratoire de Technologie des Composites
et Polymères - DMX
CH-1015 LAUSANNE
Switzerland

LIU Chi Tsieh
OL-AC Airfore Res. Laboratory/PRSM

10 E. Saturn Blvd.
Edwards AFB, CA 93524-7680
USA

MAEDA Machiko
Kyoto Institute of Technology
Matsugasaki, SAK40

KYOTO, 606 8585
Japan

McKENNA Greg, Dr.
NIST - Structure and Mechanics Group
Polymers Division
100 Bureau Drive, Stop 8544
Gaithersburg, MD 20899
USA

MENDELS D.-A.
Ecole Polytechnique Fédérale de Lausanne
Laboratoire de Technologie des Composites
et Polymères - DMX
CH-1015 LAUSANNE
Switzerland

MIRANDA GUEDES Rui
INEGI
Instituto de Engenharia Mecanica e Gestao Industrial -
Ruo dos Bragas
4000 PORTO
PORTUGAL

MIYANO Yasushi
Kanazawa Institute of Technology
Materials System Research Laboratory
7-1 Ohgigaoka Nonoichi
ISHIKAWA 921
JAPAN

MORTAIGNE Bruno
DGA/DCE/CTA/MSA/site d'Arceuil Nord
Dépt. "Matériaux pour strucgtures allégées"
16bis, avenue prieur de la côte d'or
F-94114 ARCEUIL
France

NAKADA Masayuki
Kanazawa Institute of Technology
Materials System Research Laboratory
3-1 Yatsukaho, Matto
ISHIKAWA 924-0838
JAPAN

NEFF Thomas
Technical University of München
Dept. of Mechanics and Material Testiong
Boltzmannstrasse, 15
D-85747 MUNICH
Germany

NEFT, Johannes
VOLKSWAGEN AG
Zentrallabor - K-GQ-31
P.O.Box 1437-1
D-38436 WOLFSBURG
Germany

OGIHARA Shinji
SCience University of Tokyo
Dept. of Mechanical Engineering
2641 Yamasaki, Noda
Chiba 278-8510
Japan

OUDE WEME Petra
N.V. KEMA
KST-MAT
P.O. BOX 9035
NL-6800 ET ARNHEM
NETHERLANDS

PANDITA Surya D.
K.U.LEUVEN
Dept. Metaalkunde en Toegepaste Materiaalkunde
De Croylaan 2
3001 LEUVEN
Belgie

PAPANICOLAOU G.C.
University of Patras
Dept. of Mechanical Engineering
Composite Materials Group
PATRAS-RION 26500
GREECE

PATTYN Henk
K.U.LEUVEN
Dept. Metaalkunde en Toegepaste Materiaalkunde
De Croylaan 2
3001 LEUVEN
Belgie

PAUCHARD Vincent
Ecole Centrale de Lyon
Département IFoS - MMP
36, avenue Guy de Collongue/ B.P. 163
F-69139 ECULLY
France

PERREUX D.
Université de Franche Comte
Lab. de Mécanique Appliquée Besançon
24 rue de L'Epilaphe
F-25000 Besançon
France

POIRETTE Yann
Ecole des Mines de St. Etienne
Dept. of Materials and Mech. Engineering
Cours Fauriel, 158
F-42023 St. Etienne Cedex 2
France

PYRZ Ryszard
Aalborg University
Institute of Mechanical Engineering
Pontoppidanstraede 101
DK-9220 AALBORG 0
DENMARK

JER Ken
Tech
of Engineering Science & Mechanics
rials Response Group
.cksburg, VA 24061-0219
J.S.A.

RIKARDS Rolands
Riga Technical University (Faculty Civ. Eng.)
Inst. of Computer Analysis of Structures
Kalku Street 1
LV-1658 RIGA
LATVIA

ROTEM A.
Technion
Faculty of Mechanical Engineering

HAIFA, 32000
ISRAEL

ROY Samit
University of Missouri-Rolla
Center for Rock Mechanics

ROLLA, MO 65401 0000
USA

SALMON Laurent
Electricité de France (EDF)
EMA/EDF - Site de Renardières
Route de Sens
F-77818Moret-sur-Loing
France

SCHMIDTKE Klaus
DaimlerChrysler
Forschung und Technik (FT4/WF)
Postfach 80 04 65
D-81663 MÜNCHEN
GERMANY

SEFERIS James C.
University of Washington
Dept. Chem. Engineering BF-10

SEATTLE, WASHINGTON 98195
U.S.A.

SHOHAM Zvi
RAFAEL
P.O. Box 2250
CODE M1
HAIFA 31021
ISRAEL

SPEARING Mark
MIT - Dept. Aeronautics & Astronautics
Technology Lab. for Advances Composites
77 Massachusetts Avenue, Room 33-315
CAMBRIDGE, MA 02139
USA

SPOORMAKER Jan
Delft University of Technology
Faculty of Design, Engineering & Production
Jaffalaan, 9
2628 BX DELFT
The Netherlands

SUN YONG-QI
Research Center of Composite Materials
Lab for Nonlinear Mechanics of Cont. Media
Northwest Institute of Textile Sci & Tech
710048 CHIAN
China

SWIT Grzegorz
Kielce University of Technology

Al. 1000 - Lecia P.P. 3
25-314 KIELCE
Poland

TAKAYANAGI Hiroshi
National Institute of Materials and Chem. Res.
Dept. of Composite Materials
1-1 Higashi
Tsukuba, Ibaraki 305-0046
Japan

TAKEDA Nobuo
The University of Tokyo
Dept. of Aeronautics and Astronautics
7-3-1 Hongo, Bunkyo-ku
Tokyo 113-8656
Japan

TAMUZS Vitauts
Institute of Polymer Mechanics
Latvian SSR Academy of Sciences
23, Aizkraukles street
RIGA, LV-1006
LATVIA

TZENG Jerome T.
US Army Research Laboratory
Weapons & Materials Research Doctorate
Attn. AMSRL-WM-MB
Aberdeen Proving Ground, MD 21005-5066
USA

VALOT Emannuel
I.S.A.T.

49, rue Mademoiselle Boirgeois - BP 31
F-58027 NEVERS
France

VAN DE VELDE Kathleen
Universiteit Gent

Technologiepark 9
9052 Zwijnaarde
België

VAN VOSSOLE Chr.
FREE UNIVERSITY BRUSSELS (V.U.B.)
Dept. MEMC - Fac. TW
Pleinlaan, 2
1050 Brussels
Belgium

VAUTRIN Alain
Ecole des Mines de St. Etienne
Dept. of Materials and Mech. Engineering
Cours Fauriel, 158
F-42023 St. Etienne Cedex 2
France

VEAZIE David R.
Clark Atlanta University
Dept. of Engineering
223 James P. Brawley Dr., S.W.
ATLANTA, GEORGIA 30314-4391
USA

VERCHERY George
Inst. Sup. de l'Automobile et des Transports
ISAT Nevers
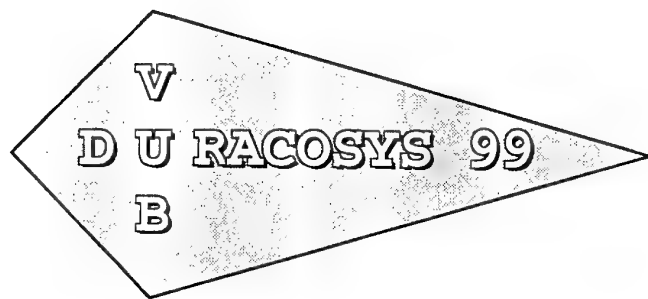49, rue Mademoiselle-Bourgeois - BP 31
F-58000 NEVERS
France

WEITSMAN Jack
University of Tennessee
Dept. of Mechanics & Aerospace Eng.
307, Perkins Hall
KNOXVILLE, TN 37996-2030
USA

XINRAN Xiao
Concordia University
Dept. of Mechanical Engineering
1455 de Maissonneuve Blvd. W. # H549
Montreal, Quebec H3G 1M8
Canada

YERYOMIN Konstantin

Metallurgov avenue, 6-66
MAGNITOGORSK
RUSSIA

ZHENG Xianmei
Medicine Department
Room 303, Jia-58, Peng Zhuang
Chongwen District, Yongwai
Beijing 100045
P.R.China

V DUB RACOSYS 99

FINAL PROGRAMME

11-14 July, 1999

Last moment changes can still occur.
Those changes will be communicated during the sessions
and indicated on the daily programme on the general
information board.

International Scientific Board

R. ADAMS (Bristol, United Kingdom)
S. AIVAZZADEH (Nevers, France)
L. BERGLUND (Lulea, Sweden)
O. BERGSMA (Delft, The Netherlands)
T. BLASZCZYNSKI (Poznan, Poland)
H. BRINSON (Houston, USA)
O. BRÜLLER (Munich, Germany)
I. EMRI (Ljubljana, Slovenia)
P. GUDMUNDSON (Stockholm, Sweden)
Z. HASHIN (Tel Aviv, Israel)
N. HIMMEL (Kaiserslautern, Germany)
P. HOGG (London, United Kingdom)
S. JOHNSON (Georgia Tech, USA)
W. KNAUSS (Caltech, Pasadena, USA)
P. LAGACE (MIT, Cambridge, USA)
J.A. MANSON (EPFL, Lausanne, Switzerland)
TIANGXIANG MAO (Bejing, China)
A. MIRAVETE (Zaragoza, Spain)
Y. MIYANO (Kanazawa, Japan)
G. PAPANICOLAOU (Patras, Greece)
T. PEIJS (Eindhoven, The Netherlands)
D. PERREUX (Besançon, France)
R. PYRZ (Aalborg, Denmark)
E. SANCAKTAR (Akron, USA)
K. SCHULTE (Hamburg-Harburg, Germany)
R. TALREJA (Georgia Tech, Atlanta, USA)
V. TAMUSZ (Riga, Latvia)
A. VAUTRIN (St.Etienne, France)
I. VERPOEST (KULeuven, Belgium)
J. WEITSMAN (Knoxville, USA)

Belgian Host Committee

A. CARDON (V.U.Brussels)
R. BOURGOIS (Royal Military School, Brussels)
J. DEGRIECK (Univ. Ghent)
P. HALLEUX (U.L.Brussels)
R. KEUNINGS (U.C.Louvain-La-Neuve)
I. VERPOEST (KULeuven)

Local Organizing Committee

A. CARDON
M. BOURLAU, A. VANAEKEN
P. BOUQUET, K. HOES, Chr. VAN VOSSOLE, S. HAROU-KOUKA
A. VRIJDAG, F. BOULPAEP, R. HEREMANS, D. DEBONDT, G. VAN DEN NEST

Monday July 12, 1999

Time	Event
8.30	Opening
8.45	Session 1 (2GL)
10.15-10.45	Break
10.45	Session 2 (1GL + 2P)
12.15-13.30	Lunch
13.45	Session 3 (2SL + 3P)
15.35-16.05	Break
16.05	Session 4 (SOP)
18.15-18.45	General discussion

Tuesday July 13, 1999

Time	Event
8.30	Session 5 (2GL)
10.00-10.30	Break
10.30	Session 6 (SOP)
12.45-13.45	Lunch
14.00	Session 7 (1GL + 1SL + 1P)
15.30-16.00	Break
16.00	Session 8 (4P)
17.45	Optional excursion with dinner

Wednesday July 14, 1999

Time	Event
8.30	Session 9 (2GL)
10.00-10.30	Break
10.30	Session 10 (5P)
12.30-13.45	Lunch
14.00	Session 11 (7P)
15.40-16.10	Break
16.50	General discussion
	Conclusions – Closure
19.30	Conference dinner

GL   : General Invited Lecture (45 minutes : questions, answers and discussion included)

SL   : Special Invited Lecture (25 minutes : questions, answers and discussion included)

P   : Oral Presentation (20 minutes : questions, answers and discussion included)

SOP : Short Oral Presentation (10 minutes : questions, answers and discussions around the posters on exhibit from Monday at noon till Wednesday afternoon break)

<u>Monday July 12, 1999</u>

Members of our staff will be at the Dôme Hotel at 7.30 a.m. and will guide you, starting at 7.45 a.m., through the Metro to the conference location (University Campus).
Starting at 7.30 a.m. the registration will be open at the conference location till 4.00 p.m.

<div align="center">

*

*   *

</div>

8.30   Opening and Introduction

Session 1 : Fatigue and Damage
Chair : Zvi HASHIN - Israel

8.45   "Fatigue in Composite Laminates - A qualitative link from micromechanics to fatigue life performance"
K. Gamstedt (RISØ National Laboratory, Denmark)

9.30   "Modelling and computation until final fracture of composite laminates"
P. Ladevèze (ENS-LMT Cachan, France)

10.15-10.45 : Break

Session 2 : Moisture - Fatigue - Ageing
Chair : Jack WEITSMAN - USA

10.45   "Ageing and long term behaviour of composite tubes"
P. Davies, R. Boizau, D. Choqueuse (IFREMER Brest, France),
L. Salmon, F.D. Jagnat (EDT - Moret sur Loing, France)

11.30   "Interactions between moisture and fatigue damage in unidirectional glass-epoxy composites subjected to flexural loading"
A. Chateauminois (Ecole Central de Lyon, France)

11.50   "Contribution to the durability analysis of a thick composite structure under complex mechanical and hygroscopic loads"
Y. Poirette, F. Pierron, A. Vautrin (Ecole des Mines St. Etienne, France)

12.15-13.30 : Lunch

Session 3 :   Damage – Damping – Ageing
Chair : Hal BRINSON – USA

13.45   "Durability of polymer matrix composites : some remarks by the AMAC Committee on Durability"
D. Perreux (AMAC-LMARC Besançon, France)

14.10   "Effects of moisture on damage evolution, strain inhomogeneity and fracture in a particulate composite"
C.T. Liu (Air Force Research Lab., Edwards AFB, CA, USA)

14.35   "The damping and dynamic moduli of fibre reinforced polymer composites after exposure to hot-wet conditioning"
R.D. Adams, M.M. Singh, University Bristol, United Kingdom)

14.55   "Modelling of composite interfaces subjected to thermal and physical aging"
D.A. Mendels, Y. Leterrier, J.A. Manson (EPFL, Lausanne, Switzerland)

15.15   "Accelerated evaluation of environmental ageing monitored by fatigue crack growth experiments"
V. Altstädt, S. Keiter (Univ. Hamburg-Harburg, Germany)

15.35-16.05 : Break

16.05 Session 4 : Short Oral Presentations   (Serie 1)
Chair : Shahram Aivazzadeh,   France

Short oral presentations (10 minutes) with poster support (serie 1), questions, answers and discussions will be possible in the general discussion and around the posters.

4.1.   "Damage/weight loss relationship for bismaleimide matrix under isothermal oxidative ageing"
X. Colin, C. Marais, J. Verdu, L. Audoin (ONERA Chatillon-ENSAM Paris, France)

4.2   "Interphasial stress and strain fields in multi-phase particulates: influence of moisture content"
N.K. Anifantis, P.A. Kakavas, G. Papanicolaou (Univ. Patras, Greece)

4.3   "Chemical resistance of pultruded E-glass polyester composits"
K. Van de Velde, P. Kiekens (University Ghent, Belgium)

4.4 "Performance of pultruded FRP reinforcement with embedded fiber optic sensors"
A.L. Kalamkarov (Dalhousie University, Canada)

4.5 "Monitoring and modeling the durability of polymers used for composite offshore oil transport"
D. Kranbuehl et al. (College of William and Mary, Williamsburg, USA)

4.6 "Modeling of hygrothermal effects in composites and polymer adhesive systems"
S. Roy, Weiqun Xu (University of Missouri-Rolla, USA)

4.7 "Influence of fiber-matrix adhesion on the fatigue behaviour of cross-ply glass-fiber epoxy composites"
J. Gassan (University Kassel, Germany)

4.8 "Assessment of time-temperature superposition principle as a basis for long term behaviour prediction of CFRP under bending loads"
R.Miranda-Guedes (University of Porto, INEGI, Portugal)

4.9 "Viscoelastic contact problems of fiber reinforced polymers"
T. Neff, O. Brüller (Technical University of Münich, Germany)

4.10 "Creep and stress relaxation of composite cylinders"
J.T. Tzeng (US Army Research Lab., USA)

4.11 "AE Measurement in Acid Corrosion"
M. Maeda, H.Hamada, Y. Fujii (Kyoto Instite of Technology, Japan)

4.12 "Modelling of the buckling of plastic containers"
J.L. Spoormaker, I.D. Skrypnyk, T.O. Vasyljkevych (Delft University of Technology, The Netherlands)

4.13 "Tensile and Fatigue Damage in Woven Ceramic Matrix Composites"
A. Haque, M. Rahman, S. Jeelani, Tuskegee University, USA

18.15-18.18.40 : General discussion

Posters will be on exhibit from Monday at noon till the Wednesday afternoon break.

Evening free

Session 5 : Strength criteria - Long term predictions
Chair : Ken REIFSNIDER - USA

8.30   "3D strength criteria derived from the so-called failure mode concept - Verification for concrete, FRP and foam"
        R. Cuntze (MAN Technology, Germany)

9.15   "Long term prediction of fatigue life of unidirectional CFRP"
        Y. Miyano (Kanazawa Institute of Technology, Japan)

10.00-10.30 : Break

10.30 Session 6 : Short oral presentations (serie 2)
Chair : Georges VERCHERY - France

6.1   "Experimental Characterisation and analytical prediction of microscopic deformation in interlaminartoughened laminates with transverse cracks"
        N. Takeda, L.N. McCartney, S. Ogihara (University of Tokyo, Japan)

6.2   "Method for identification of elastic and damage properties of laminates composites based on experiment design"
        R. Rikards (Riga Technical University, Latvia)

6.3   "Durability estimation of carbon/polytetrafluoroethylene composites for hydraulic downhole motor"
        K. Kemmochi, H. Takayanagi, T. Hamada (Nat. Inst. Materials & Chemical Research, Japan)

6.4   "Durability of fiber reinforced plastic (FRP) pipes : increasing the quality of the bonds"
        P.M. Oude Weme, C.A.M. Van den Ende (N.V. KEMA, The Netherlands)

6.5   "Comparison of warp knitted and stitched non-crimp fabrics"
        H. Pattyn, I. Verpoest, J. Ivens (Catholic University Leuven, Belgium)

6.6   "Predicting the durability of PMR-15 composites at elevated temperatures"
        K.J. Bowles (NASA Lewis Research Center, USA)

6.7   "Durability of adhesive joints subjected to elevated temperature aging"
        D.R. Veazie, J. Qu, J. Lindsay (Clark Atlanta University, USA)

6.8   "On the use of acoustic emission and scanning electron microscopy to investigate fatigue damage in plain-woven fabric composites"
        S.D. Pandita, G. Huysmans, M. Wevers, I. Verpoest (Catholic University Leuven, Belgium)

6.9 "Study of the effect of fiber orientation on the nonlinear viscoelastic behaviour of continuous fiber polymer composites"
S.P. Zaoutsos, G.C. Papanicolaou (University of Patras, Greece)

6.10 "Damage modelling of composite structures viscoelastic effects"
M. Chafra, Y. Chevalier (Inst. Supérieur des Matériaux et de la Construction Mécanique (ISMCM) Saint-Ouen, France)

6.11 "Ultimate bearing capacity of cement composite sections under long term physico-chemical exposure"
T.Blaszczynski (Technical University of Poznan, Poland)

6.12 "Damage identificatin of composite material during stress rupture using acoustic emission technique"
A. Rotem (Technion IIT, Israel)

12.35-13.45 : Lunch

Session 7 : Moisture – Infrastructure applications
Chair : Wolfgang KNAUSS – USA

14.00 "The influence of moisture on the physical aging response of epoxy: experimental results and modeling considerations
G. McKenna (NIST, Gaithersburg, USA)

14.45 "Hybrid composites with nonlinear behaviour for reinforcing of concrete"
V.Tamuzs, R. Tepfers (Institute of Polymer Mechanics, Riga, Latvia)

15.10 "Free-thaw durability of polymer matrix composites in infrastructure"
J. Haramis, N. Verghese, J.J. Lesko (Virginia Tech, USA)

15.30-16.00 : Break

Session 8 : Infrastructure applications – Fatigue – Failure
Chair : Bob ADAMS – United Kingdom

16.00 "Durability of fiber reinforced composites in civil instrastructures. Issues, results and implications"
V.M. Karbhari, J. Zhang (University of California, San Diego, USA)

16.20 "Durability of reinforced concrete beams repaired by composites under creep and fatigue loading"
E. Ferrier, G. Lagarde, P. Hamelin (Université Claude Bernard, Lyon, France)

16.40 "Application of dielectric measurements for the assessment of durability in composite systems"
P. Boinard, F Dumoulin, D. Hayward, W.M. Banks, A. Pethrick (University of Strathclyde, Scotland)

17.00 "Failure of laminated composites at thickness discontinuities under complex loading"
S. Lee, W.G. Knauss (Caltech, California, USA)

Evening free or, with departure from the conference location at 17h45, optional excursion to the old university city of Leuven (visit of the Town Hall, the City, the Begijnhof and dinner in the Faculty Club), with return in Brussels around 23.00.

Session 9 : Aerospace applications
Chair : Peter GUDMUNDSON – Sweden

8.30   "Durability Assessment of Polymeric Composites for High Speed
        Civil Transport"
        T. Gates (NASA Langley, USA)

9.15   "Durability through in-flight evaluation of honeycomb composite
        structures"
        J. Seferis (University of Washington, Seattle, USA)

10.00-10.30 : Break

Session 10 : Ageing – Temperature – Hybrids
Chair : Alain VAUTRIN – France

10.30   "Investigation of the hygrothermal ageing of composites by means
        of Raman spectroscopy"
        A. Cervenka, R.J. Young, D.J. Bannister (University of Manchester
        and Umist, United Kingdom)

10.50   "Failure mechanics of thin coatings under multiaxial loading"
        Y. Leterrier, D. Pellaton, J. Andersons, J.A. Manson (EPFL,
        Lausanne, Switzerland).

11.10   "Effect of temperature and strain rate on the performance of
        polymeric composites"
        K. Reifsnider, C. Mahieu, B. Waltzer, F. Sun (Virginia Tech, USA)

11.30   "Evolution of matrix cracking in cross-ply CFRP laminates :
        differences between mechanical and thermal loadings"
        C. Henaff-Gardin, I. Goupillard, M.C. Lafarie-Frenot (ENSMA,
        Futuroscope, France)

11.50   "Durability of Titanium-graphite hybrid laminates"
        D.A. Burianek, S.M. Spearing (MIT, Cambridge, USA)

12.30-13.45 : Lunch

Session 11 : Experimental aspects - Fatigue
Chair : Norbert HIMMEL - Germany

14.00 "Initiation versus growth criteria for transverse cracks"
P. Gudmundson (Royal Institute of Technology, Stockholm, Sweden)

14.20 "X-ray microtomography : a new technique for analysis of composite materials"
R. Pyrz (Aalborg University, Denmark)

14.40 "In-situ investigation of time-dependent behaviour of polymeric composite subjected to shear loads"
SUN Yong-Qi (Northwest Institute of Textile Science & Technology, Chian, China)

15.00 "Influence of quasi lifetime treatments on the static and fatigue durability of continuous glass fibre reinforced polypropylene"
J.F. Neft, P. Scharzer, (Volkswagen AG, Wolfsburg, Germany), K. Schulte (University Hamburg-Harburg, Germany)

15.20 "A model on thermal degradation of fatigue strength and its application in fatigue life prediction of polymer composites with hysteretic heating"
X. Xiao, I.Al-Hmouz (Concordia University, Canada)

15.40-16.10 : Break

16.10 "Long term prediction of fatigue life for FRP joint system"
M. Nakada, Y. Miyano, S.W. Tsai (Kanazawa Inst. of Technology, Japan)

16.30 "Fatigue behaviour of composite joints"
Y. Dzenis (University of Nebraska-Lincoln, USA)

16.50-17.20 : General discussion and conclusions

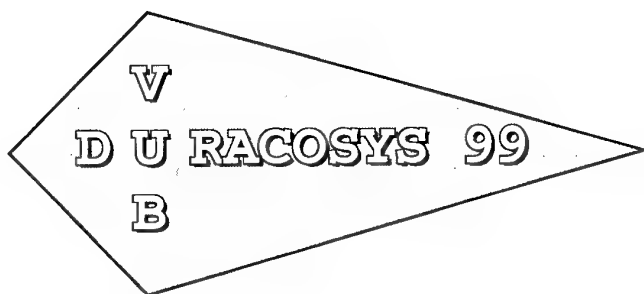19.45   : Conference dinner.

POSTERS

(From Monday July 12 at noon till Wednesday July 14 at the afternoon break)

4.1 - 4.11   Short oral presentations - Serie 1
6.1 - 6.13   Short oral presentations - Serie 2

P.1   "Experimental characterisation of damage progress in high temperature CFRP laminates"
       S. Ogighara, N.Takeda (Science University of Tokyo, Japan)

P.2   "Influence of the Shape of a stricker on the mechanical responses of composite beams"
       L. Gauillaumat (LAHEFIP-ENSAM Talance, France)

P.3   "Curing conditions and sample preparations for the analysis of the transverse creep behaviour of unidirectional graphite-epoxy composites"
       Chr. Van Vossole, P. Bouguet, A. Cardon (Free University Brussels (V.U.B.), Belgium

P.4   "Durability of stressed E-glass fibre in alkaline medium"
       G. Swit (University of Technology, Kielce, Poland)

P.5   "Effect of Marine Exposure on Wheaterability of FRP Laminates"
       H. Takayanagi, K. Kenmochi, I. Kimpara (National Institute of Materials & Chemical Research, Japan)

P.6   "Accelerated marine ageing of composites and metal/composite joints"
       P. Davies, A. Roy (IFREMER Brest, France)

P.7   "Reliability of continuous fiber-reinforced ceramic composites under stress-rupture conditions in oxidizing environments
       E. Lara-Curzio (Oak Ridge National Laboratory, USA)

P.8   Thermal aging on G_{II} interlaminar fracture mode response of multiaxial 2D composites
       F.Segovia-Lopez, C.Bloem (Polytechnical University of Valencia, Spain and Escuela de Igenieria Mecanica, Mérida, Venezuela)

V
D U RACOSYS 99
B

Brussels, July 11-14, 1999

<div style="border">
LIST OF PARTICIPANTS
</div>

ADAMS Robert D.
UNIVERSITY OF BRISTOL
Dept. of Mechanical Engineering
Queen's Building, University Walk
BRISTOL BS8 1TR
United Kingdom

AIVAZZADEH Shahram
Inst. Sup. de l'Automobile et des Transports
ISAT Nevers
49, rue Mademoiselle-Bourgeois - BP 31
F-58000 NEVERS
France

ALTSTÄDT, Volker
TU Hamburg-Harburg
Dept. Polymers & Composites (AB 5-09,)
Denickestrasse 15
D-21073 HAMBURG
Germany

BANKS W.A.
University of Strathclyde
Div. Mechanics of Materials/Dept. Mech. Eng.
75 Montrose street - James Weir Building
GLASGOW G1 1XJ
Scotland

BLASZCZYNSKI Tomasz
Technical University Poznan
Institute of Structural Engineering
Ul. Piotrowo 5
60-965 POZNAN
Poland

BLOEM Carlos
Escuela de Ingenieria Mecànica y Materiales
Facultad de Ingenieria
Av. Tulio Febres Cordero
5101 Mérida, Edo. Mérida
Venezuela

BOINARD Pascal
Dept. of Pure and Applied Chemistry
Lab. of Phys. Chem. - C302
Thmas Graham Build., 295 Cathedral street
GLASGOW G1 1XL
Scotland

BOUQUET Pascal
FREE UNIVERSITY BRUSSELS (V.U.B.)
Dept. MEMC - Fac. TW
Pleinlaan, 2
1050 Brussels
Belgium

BOWLES, Kenneth J.
NASA Lewis Research Center

21000 Brookpark Road
CLEVELAND, OHIO 44135
USA

BRINSON Hal F.
University of Houston
Mechanical Engineering Department
4800 Calhoun
HOUSTON, TX 77204-0900
U.S.A.

CARDON Albert
FREE UNIVERSITY BRUSSELS (V.U.B.)
Dept. MEMC - Fac. TW
Pleinlaan, 2
1050 Brussels
Belgium

CERVENKA Tony
University of Manchester and Umist
Manchester Material Science Centre
Grosvenor Street
MANCHESTER, M1 7HS
United Kingdom

CHATEAUMINOIS Antoine
Ecole Centrale de Lyon
Dépt. Matériaux-Mécanique Physique

F-69131 ECULLY Cedex
France

COLIN Xavier
ONERA
Dépt. des Matériaux et Systèmes Composites
Avenue de la Division Leclerc, 29
F-92322 Chatillon
France

DAVIES Peter
IFREMER - Centre de Brest
Lab. Matériaux Marins - DITI/GO/MM
B.P. 70
F-29280 PLOUZANE
France

DZENIS Yris A.
University of Nebraska Lincol
Dept. of Engineering Mechanics
221 Bancroft Hall
LINCOLN, NE 65588 0347
USA

FUKUDA Hiroshi
Science University of Tokyo
Dept. Materials Science & Technology
2641 YAMAZAKI
Noda, Chiba 278-8510
JAPAN

GASSAN J.
Universität Gesamthochschule Kassel
Institut für Werkstoffechimie
Mnchebergstrasse 3
D-34109 KASSEL
GERMANY

CHEVALIER Yvon
ISMCM-CESTI ,
LISMMA - Groupe Rhéologie et Structures
3, rue Fernand Hainaut
F-93407 SAINT OUEN CEDEX
France

CUNTZE, R.G.
MAN Technologie AG
Division of Spacecraft
Liebigstrasse, 5A
D-85757 Karlsfeld/Münich
Germany

DONG Wei
Medicine Department
Room 303, Jia-58, Peng Zhuang
Chongwen District, Yongwai
Beijing 100045
P.R.China

FERRIER Emannuel
Université Claude Bernard
L2M - IUT A Génie Civil
43, bd. du 11 Novembre
F-69622 VILLEURBANNE
France

GAMSTEDT Kristofer
RISO National Laboratory
Materials Research Dept.
P.O. Box 49
DK-4000 ROSKILDE
Denmark

GATES Tom
NASA Langley Research Center

Mail Stop 188E
HAMPTON, VA 23681
USA

GAUVIN Raymond
Ecole Polytechnique Montréal
Dépt. de Génie Mécanique
2900, Edouard-Montpetit, C.P. 6079
MONTREAL H3C 3A7
Canada

GUDMUNDSON Peter
Royal Institute of Technology
Dept. of Solid Mechanics

S-10044 Stockholm
Sweden

GUILLAUMAT Laurent
L.A.M.E.F.-E.N.S.A.M.
Esplanade des Arts et Métiers

F-33405 Tallence Cedex
France

HAMADA Taishi
Science University of Tokyo
Graduate School Student
2641 Yamazaki
Noda, Chiba, 278-8510
Japan

HAQUE Anwar
Tuskegee University
TU Center for Advanced Materials
Mechanical Engineering Dept.
TUSKEGEE, AL 36088
USA

HASHIN Zvi
Tel-Aviv University
Dept. of Solid Mechanics, Materials & Struct.
Ramat-Aviv
Tel Aviv, 69978
Israel

HENAFF-GARDIN Catherine
LMPM
ENSMA - Teleport 2 - BP109
Chasseneuil du Poitou
F-86960 FUTUROSCOPE
FRANCE

HIMMEL Norbert
University of Kaiserslautern
Institute for Composite Materials
B.O. Box 3049
D-67663 KAISERSLAUTERN
Germany

KAKAVAS P.A.
University of Patras
Mechanical Engineering Department
Composite Materials Group
265 00 PATRAS
GREECE

KALAMKAROV A.L.
Dalhousie University
Daltech/ Faculty of Engineering
P.O. Box 1000
HALIFAX, NS B3J 2X4
Canada

KARBHARI Vistasp M.
University of California, San Diego
Division of Structural Engineering
9500 Gilman Drive
LA JOLLA, CA 92093-0085
USA

KNAUSS Wolfgang G.
CALTECH
Dept. of Aeronautics and Applied Mechanics
Mail Code : 105-50
PASADENA, CALIFORNIA 91125
USA

KRANBUEHL David
The College of William and Mary
Chemistry Department

Williamsburg, VA 23187
USA

LARA-CURZIO Edgar
Oak Ridge National Lab. (High Temp.Mat.Lab
Metals & Ceramics Division, Building 4515
Mail Stop-6069, P.O. Box 2008
OAK RIDGE, TN 37831-6069
USA

LETERRIER Yves
Ecole Polytechnique Fédérale de Lausanne
Laboratoire de Technologie des Composites
et Polymères - DMX
CH-1015 LAUSANNE
Switzerland

MAEDA Machiko
Kyoto Institute of Technology
Matsugasaki, SAK40

KYOTO, 606 8585
Japan

MENDELS D.-A.
Ecole Polytechnique Fédérale de Lausanne
Laboratoire de Technologie des Composites
et Polymères - DMX
CH-1015 LAUSANNE
Switzerland

MIYANO Yasushi
Kanazawa Institute of Technology
Materials System Research Laboratory
7-1 Ohgigaoka Nonoichi
ISHIKAWA 921
JAPAN

LADEVEZE P.
ENS-Cachan
Dépt. Mécanique et Technologie
Avenue du Président Wilson, 61
F-94235 CACHAN CEDEX
France

LESKO J.J.
Virginia Tech
Dept. of Engineering Science & Mechanics
120 Patton Hall
Blacksburg, VA 24061-0219
U.S.A.

LIU Chi Tsieh
OL-AC Airfore Res. Laboratory/PRSM

10 E. Saturn Blvd.
Edwards AFB, CA 93524-7680
USA

McKENNA Greg, Dr.
NIST - Structure and Mechanics Group
Polymers Division
100 Bureau Drive, Stop 8544
Gaithersburg, MD 20899
USA

MIRANDA GUEDES Rui
INEGI
Instituto de Engenharia Mecanica e Gestao Industrial -
Ruo dos Bragas
4000 PORTO
PORTUGAL

MORTAIGNE Bruno
DGA/DCE/CTA/MSA/site d'Arceuil Nord
Dépt. "Matériaux pour strucgtures allégées"
16bis, avenue prieur de la côte d'or
F-94114 ARCEUIL
France

NAKADA Masayuki
Kanazawa Institute of Technology
Materials System Research Laboratory
3-1 Yatsukaho, Matto
ISHIKAWA 924-0838
JAPAN

NEFF Thomas
Technical University of Münich
Dept. of Mechanics and Material Testiong
Boltzmannstrasse, 15
D-85747 MUNICH
Germany

NEFT, Johannes
VOLKSWAGEN AG
Zentrallabor - K-GQ-31
P.O.Box 1437-1
D-38436 WOLFSBURG
Germany

OGIHARA Shinji
SCience University of Tokyo
Dept. of Mechanical Engineering
2641 Yamasaki, Noda
Chiba 278-8510
Japan

OUDE WEME Petra
N.V. KEMA
KST-MAT
P.O. BOX 9035
NL-6800 ET ARNHEM
NETHERLANDS

PANDITA Surya D.
K.U.LEUVEN
Dept. Metaalkunde en Toegepaste Materiaalkunde
De Croylaan 2
3001 LEUVEN
Belgie

PAPANICOLAOU G.C.
University of Patras
Dept. of Mechanical Engineering
Composite Materials Group
PATRAS-RION 26500
GREECE

PATTYN Henk
K.U.LEUVEN
Dept. Metaalkunde en Toegepaste Materiaalkunde
De Croylaan 2
3001 LEUVEN
Belgie

PAUCHARD Vincent
Ecole Centrale de Lyon
Département IFoS - MMP
36, avenue Guy de Collongue/ B.P. 163
F-69139 ECULLY
France

PERREUX D.
Université de Franche Comte
Lab. de Mécanique Appliquée Besançon
24 rue de L'Epilaphe
F-25000 Besançon
France

POIRETTE Yann
Ecole des Mines de St. Etienne
Dept. of Materials and Mech. Engineering
Cours Fauriel, 158
F-42023 St. Etienne Cedex 2
France

PYRZ Ryszard
Aalborg University
Institute of Mechanical Engineering
Pontoppidanstraede 101
DK-9220 AALBORG 0
DENMARK

REIFSNIDER Ken
Virginia Tech
Dept. of Engineering Science & Mechanics
Materials Response Group
Blacksburg, VA 24061-0219
U.S.A.

RIKARDS Rolands
Riga Technical University (Faculty Civ. Eng.)
Inst. of Computer Analysis of Structures
Kalku Street 1
LV-1658 RIGA
LATVIA

ROTEM A.
Technion
Faculty of Mechanical Engineering

HAIFA, 32000
ISRAEL

ROY Samit
University of Missouri-Rolla
Center for Rock Mechanics

ROLLA, MO 65401 0000
USA

SALMON Laurent
Electricité de France (EDF)
EMA/EDF - Site de Renardières
Route de Sens
F-77818Moret-sur-Loing
France

SCHMIDTKE Klaus
DaimlerChrysler
Forschung und Technik (FT4/WF)
Postfach 80 04 65
D-81663 MÜNCHEN
GERMANY

SEFERIS James C.
University of Washington
Dept. Chem. Engineering BF-10

SEATTLE, WASHINGTON 98195
U.S.A.

SHOHAM Zvi
RAFAEL
P.O. Box 2250
CODE M1
HAIFA 31021
ISRAEL

SPEARING Mark
MIT - Dept. Aeronautics & Astronautics
Technology Lab. for Advances Composites
77 Massachusetts Avenue, Room 33-315
CAMBRIDGE, MA 02139
USA

SPOORMAKER Jan
Delft University of Technology
Faculty of Design, Engineering & Production
Jaffalaan, 9
2628 BX DELFT
The Netherlands

SUN YONG-QI
Research Center of Composite Materials
Lab for Nonlinear Mechanics of Cont. Media
Northwest Institute of Textile Sci & Tech
710048 CHIAN
China

SWIT Grzegorz
Kielce University of Technology

Al. 1000 - Lecia P.P. 3
25-314 KIELCE
Poland

TAKAYANAGI Hiroshi
National Institute of Materials and Chem. Res.
Dept. of Composite Materials
1-1 Higashi
Tsukuba, Ibaraki 305-0046
Japan

TAKEDA Nobuo
The University of Tokyo
Dept. of Aeronautics and Astronautics
7-3-1 Hongo, Bunkyo-ku
Tokyo 113-8656
Japan

TAMUZS Vitauts
Institute of Polymer Mechanics
Latvian SSR Academy of Sciences
23, Aizkraukles street
RIGA, LV-1006
LATVIA

TZENG Jerome T.
US Army Research Laboratory
Weapons & Materials Research Doctorate
Attn. AMSRL-WM-MB
Aberdeen Proving Ground, MD 21005-5066
USA

VALOT Emannuel
I.S.A.T.

49, rue Mademoiselle Boirgeois - BP 31
F-58027 NEVERS
France

VAN DE VELDE Kathleen
Universiteit Gent

Technologiepark 9
9052 Zwijnaarde
België

VAN VOSSOLE Chr.
FREE UNIVERSITY BRUSSELS (V.U.B.)
Dept. MEMC - Fac. TW
Pleinlaan, 2
1050 Brussels
Belgium

VAUTRIN Alain
Ecole des Mines de St. Etienne
Dept. of Materials and Mech. Engineering
Cours Fauriel, 158
F-42023 St. Etienne Cedex 2
France

VEAZIE David R.
Clark Atlanta University
Dept. of Engineering
223 James P. Brawley Dr., S.W.
ATLANTA, GEORGIA 30314-4391
USA

VERCHERY George
Inst. Sup. de l'Automobile et des Transports
ISAT Nevers
49, rue Mademoiselle-Bourgeois - BP 31
F-58000 NEVERS
France

WEITSMAN Jack
University of Tennessee
Dept. of Mechanics & Aerospace Eng.
307, Perkins Hall
KNOXVILLE, TN 37996-2030
USA

XINRAN Xiao
Concordia University
Dept. of Mechanical Engineering
1455 de Maissonneuve Blvd. W. # H549
Montreal, Quebec H3G 1M8
Canada

YERYOMIN Konstantin

Metallurgov avenue, 6-66
MAGNITOGORSK
RUSSIA

ZHENG Xianmei
Medicine Department
Room 303, Jia-58, Peng Zhuang
Chongwen District, Yongwai
Beijing 100045
P.R.China

Fatigue in Composite Laminates – A Qualitative Link from Micromechanisms to Fatigue Life Performance

Kristofer Gamstedt
Materials Research Department
Risø National Laboratory
P.O. Box 49, DK-4000 Roskilde
Denmark

Fatigue is an increasingly important issue for load-carrying applications made of polymer-matrix composites. One way to deal with the fatigue problem is from a macroscopic and structural viewpoint, in which fatigue design criteria are sought. This would allow for more slender and lighter designs, resulting in e.g. lower fuel consumption for aerospace and automotive applications. Another aspect of fatigue concerns the microlevel and the composite material itself. By choosing a suitable type of fibre, interfacial treatment and matrix, one could improve the fatigue resistance of the material. Between the microstructural level of the composite material and the macroscopic level of the composite structure lies a spectrum of interacting complex mechanisms. To establish a direct quantitative link between these levels is an immense task, which would require computer power and experimental techniques that are yet to be invented. A first step would be to find a *qualitative link* between the microstructure and global fatigue life performance by an experimental investigation of the underlying mechanisms. In this manner, the influence of a weak interface and a concomitant high debond rate on the fatigue life properties could be found. The variability of fibre strength is another important parameter, which is associated with the mechanism of fibre rupture. The fibre breaks can then act as initiation sites for further damage growth. In the present study, micromechanisms of these kinds have been investigated in a number of carbon and glass fibre reinforced plastics with long continuous fibres, and analysed together with the resulting macroscopic fatigue behaviour. The aim is to shed light on the relation between the micromechanisms and fatigue performance for these polymer matrix materials, and thereby indicate how the material can be improved to suppress the detrimental mechanisms.

Due to the complexity that arise from the influence of applied loading mode and laminate lay-up on the mechanisms, some simplifications are required in order to narrow down the problem and to identify the dominating and critical microstructural properties. If all possible parameters are taken into consideration, e.g. a general laminate lay-up subjected to variable multiaxial loading in service environment, the micromechanical scenario becomes too complicated to be analysed in a more exact non-empirical way. We would then be forced and compelled to a macroscopic approach, which does not allow for any extrapolative predictions or indicate how the material can be improved. The simplifications should be made judiciously to maintain relevance in view of applications. If we consider the stacking sequence of a general multidirectional laminate, it is the longitudinal ply that is the critical element since it is generally the main load-carrying constituent and the last ply to fail. Previous investigations have also shown that the longitudinal plies control the fatigue life of multidirectional laminates when interpreted in terms of global applied strain. Focus is therefore placed on unidirectional composites with the fibres in the 0° direction. Concerning the loading mode, only tensile fatigue with a stress ratio of $R = \sigma_{min}/\sigma_{max} = 0.1$ is used at this stage. The simple loading modes must be clarified first before moving on to more complex loading.

The tested materials were carbon-fibre reinforced epoxy (AS4/8552 from Hexcel) and carbon-fibre reinforced PEEK (APC-2 from ICI). Both materials had the same kind of AS4 fibres, and were processed according to the manufacturer's recommendation. The chosen stacking sequence was $[0_4]_T$ with dimensions accordance with recognised standards. Specimens of the same dimensions made of glass-fibre reinforced plastics were also analysed. These were made of polypropylene with and without a maleic anhydride modification reinforced by E-glass fibres. The purpose of the matrix modification was to improve the interfacial adhesion.

During the course of fatigue testing at 10 Hz and $R = 0.1$, the tensile machine was intermittently stopped, and replications were made on the surface of the composite specimens. These were later studied under optical microscope in chronological order to form a sequence of micrographs that show how the fatigue damage propagates. The replicas were made by applying pressure with a polymer film onto the specimen surface. The film was made malleable with acetone and let harden on the specimen to give a negative of the surface topology.

30 μm

Figure 1. Fibre-bridged crack in fatigue of carbon fibre/epoxy at $\varepsilon_{max} = 1.1\%$ and 10^3 cycles

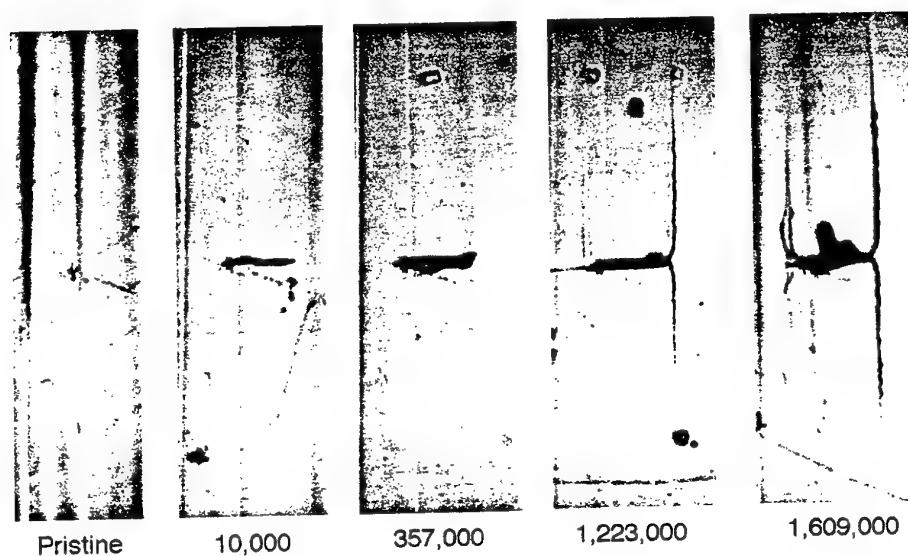| Pristine | 10,000 | 357,000 | 1,223,000 | 1,609,000 |

Figure 2. Debond growth with increasing cycles in carbon fibre/epoxy at $\varepsilon_{max} = 0.9$ % (⊢———⊣ 20 μm)

In Figure 1, a fibre-bridged crack in the carbon fibre/epoxy material with superficial fibres is shown. This material showed strong interfaces, and matrix cracks were initiated from individual fibre breaks, and grew in the transverse direction. As the crack grew around and past adjacent fibres, the crack became bridged by the fibres. The progressive mechanism was matrix crack growth in the transverse direction. Final failure occurs when the bridging fibres are broken and the crack propagates catastrophically.

At low strain amplitudes close to the fatigue limit, another scenario presented itself in the carbon fibre/epoxy material. A sequence of replicas is presented in Figure 2. The transverse bridged cracks were then effectively arrested by fibre-matrix debonding. These debonds grew to a limited extent, and then stopped, after which no further development of damage was detected. In this case, the debonding acts as an arrest mechanism to the progressive matrix cracking mechanism. The role of debonding for this material is schematically presented in Figure 3.
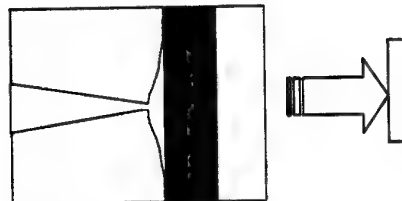

Progressive region

Propagation of fibre bridged crack
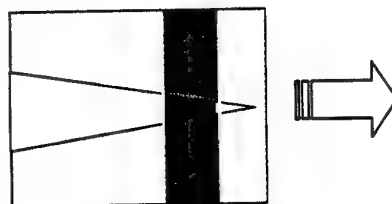
Fatigue limit

Termination of crack growth by debonding

Figure 3. Illustration of the role of limited debonding in fatigue of carbon fibre/epoxy

In the carbon fibre/PEEK material, debonding was also present, but played an entirely different role. Single-fiber fragmentation tests have shown that carbon fibre/PEEK possesses a weaker interface than that of carbon fibre/epoxy under quasi-static conditions. This was also the case under fatigue conditions. The debonding was pronounced at all amplitudes, and grew to large extents. The debonds seemed to initiate from the distributed fibre breaks, and propagated along the entire specimen. As the debonds grow, the stress profiles in the neighbouring fibres continually change. Some segments will be over-stressed, and because of the strength distribution along the fibres, weak parts will fail. This will in turn give rise to further debonding, etc. Eventually, the entire specimen will break. The described sequence of damage development is schematically portrayed in Figure 4. This type of damage evolution is spatially distributed, and results in a global and uniform degradation of the material, whereas the more brittle behaviour of carbon fibre/epoxy with its strong interface gives rise to localised damage where the most severe crack is the sole cause of failure. The stronger interface showed brittle-like planar fracture surfaces, where as the weak-interface material exhibited brush-like failures with protruding fibres.

A similar study on two kinds of glass fibre/polypropylene has shown identical behaviour compared to the carbon fibre materials, both in terms of mechanisms and fatigue-life behaviour. Despite the difference both in fibres and matrix types, the similarity to the

observed trends for carbon-fibre reinforced plastics was striking. By a maleic anhydride modification of the polypropylene matrix, the interface was strengthened, and small localised cracks grew in the transverse direction. Without the modification, the adhesion between the non-polar thermoplastic matrix and the glass fibres was poor, which gave rise to abundant debonding. The debonds grew to large extents and caused breaks in nearby fibres, which eventually led to ultimate failure. Macroscopically, this led to fatigue lives that were approximately a decade shorter than the strong-interface composite.
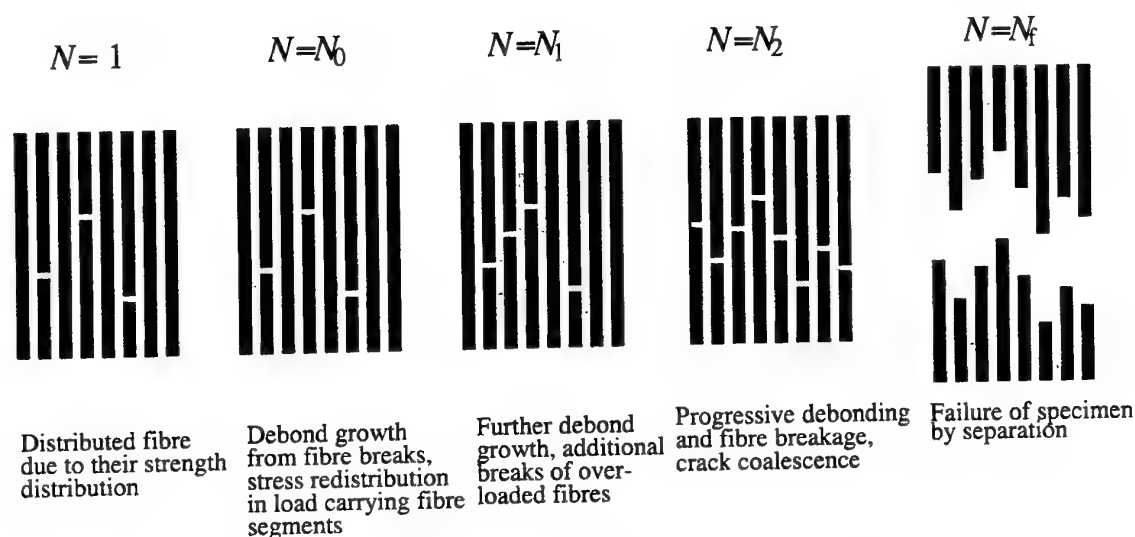

$N = 1$	$N = N_0$	$N = N_1$	$N = N_2$	$N = N_f$
Distributed fibre due to their strength distribution	Debond growth from fibre breaks, stress redistribution in load carrying fibre segments	Further debond growth, additional breaks of over-loaded fibres	Progressive debonding and fibre breakage, crack coalescence	Failure of specimen by separation

Figure 4. Schematic illustration of fatigue damage accumulation by enhanced debonding

The fatigue behaviour of unidirectional composite can be interpreted with fatigue-life diagrams (cf. Figure 5) as conceived by Talreja. In a fatigue life diagram, the applied peak strain is plotted with respect to lifetime. Three different scatter bands are partitioned off based on distinct operative fatigue mechanisms. Failure in Region I derives from rupture of fibres, such as under quasi-static loading conditions. In the sloping scatter band, Region II, progressive mechanisms have to be active. The present study has identified fibre-bridged cracking or long-range debonding in this region. For the two types of composites reinforced by either carbon or glass fibres, there was a shift leftwards in the fatigue-life diagram with pronounced debonding. For the materials with fatigue resistant interfaces, the localised damage growth in the transverse direction resulted in relatively longer fatigue lives. At the fatigue limit in Region III, the driving force for damage propagation is below its threshold, and no substantial damage will form under reasonable testing time. Alternatively, the propagation of damage is effectively stopped by an arrest mechanism such as local debonding.

As mentioned previously, the longitudinal ply is typically the critical element in a general lay-up. Damage and failure occur in the off-axis plies at an earlier stage compared with the longitudinal plies. If the adjacent off-axis plies have an influence in the fatigue life of the laminate, their influence can be taken into account by analysing the variation in stress in the critical longitudinal plies caused by the developing damage in the off-axis plies. The longitudinal plies are then effectively subjected to variable amplitude loading. In this scenario, the results from the fatigue-life diagram can still be used, although the local ply strain must be considered instead of the global applied strain.

The disparate nature of mechanisms at different strain amplitudes can also explain the influence of sequential variable amplitude loading in qualitative terms. A common behaviour

for composite materials is that a high-low sequence of block amplitude loading results in relatively shorter lifetimes compared with a corresponding low-high order. The present study has shown that at high amplitudes the initiatory mechanism of fibre breakage prevails, whereas progressive debonding predominates at lower amplitudes where it is given sufficient time to propagate to large extents. These debonds tend to originate from fibre breaks. In a high-low sequence, an abundance of fibre breaks will form during the high amplitude interval, from which a multitude of debonds will propagate and cause new fibre breaks during the low amplitude interval. On the other hand, if the low amplitude interval precedes the one with high amplitude, the debonds will have fewer fibre breaks from which they could propagate, and hence the accumulation of damage will be more moderate. This type of interaction of different fatigue mechanisms can explain the observed loading history dependencies and shortcomings of Palmgren-Miner's rule for composite materials.
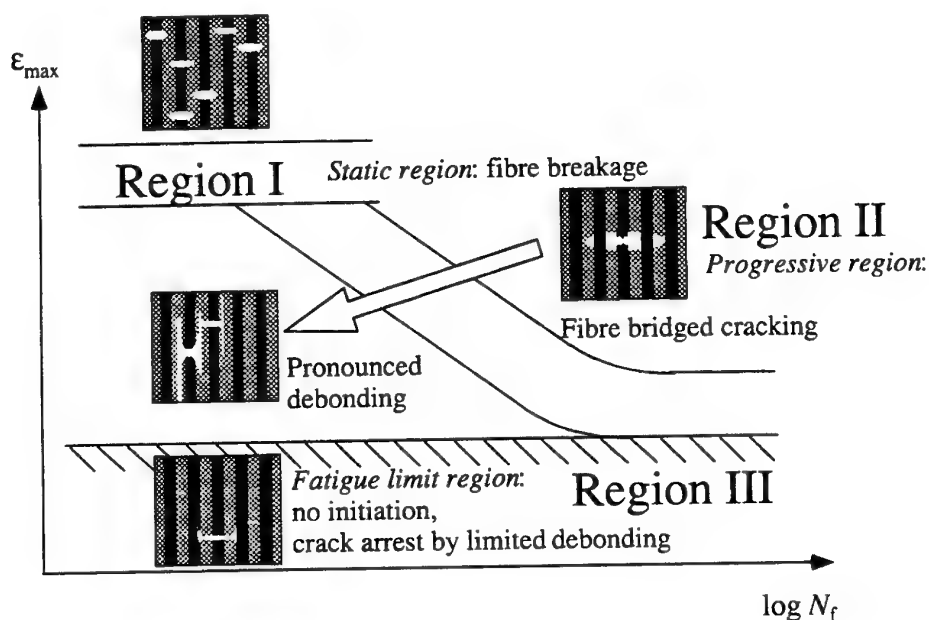

Figure 5. Fatigue life diagram with underlying mechanisms

In view of the observed micromechanisms and accompanying fatigue life behaviour, it can be summarised that pronounced debond growth has a detrimental effect on the global fatigue properties. If this mechanism can be suppressed by a stronger and more resistant interface, longer fatigue lives of the material are expected. However, limited debonding can have beneficial effect if it acts as a crack-arresting mechanism, which prevents further damage propagation. In this respect, an optimum in fatigue resistance is expected in terms of propensity to debond propagation. For improvement of the fatigue resistance, it can been recommended to monitor the development of fatigue damage microscopically, and then take measures to modify the composite composition to repress the deleterious mechanisms responsible for fatigue degradation and eventual failure. Micromechanism monitoring by surface replication can be recommended since it has proved to be straightforward and easy to use. Much further experimental characterisation and modelling work is needed to conceive a quantitative predictive model from the micromechanisms to fatigue life performance.

MODELLING AND COMPUTATIONS UNTIL FINAL FRACTURE OF LAMINATE COMPOSITES

Ladevèze Pierre
LMT-Cachan (ENS Cachan / CNRS / Univ. Paris 6)
61, avenue du Président Wilson - 94235 CACHAN Cedex - FRANCE
E-mail: ladeveze@lmt.ens-cachan.fr

Abstract

One main challenge in composite design is to compute the damage state of a composite structure subjected to complex loading at any point and at any time until final fracture. Damage refers to the more or less gradual developments of microcracks which lead to macrocracks and then to rupture ; macrocracks are simulated as completely damage zones.
Our solution for composites and especially laminate composites is based on what we call a damage mesomodel. It is a semi-discrete modelling for which the damage state is locally uniform within the mesoconstituents. For laminates, it is uniform throughout the thickness of each single layer ; as a complement, continuum damage models with delay effects are introduced. Attention is focused herein on damage computation and in particular on the localization phenomena description. Last comparison between simulations and tests for delamination tests are shown for quasi-static and dynamic loadings.

1. INTRODUCTION

An initial step, which has been achieved in other studies, is to define what we call a laminate mesomodel. At the mesoscale, characterized by the thickness of the ply, the laminates structure is described as a stacking sequence of homogeneous layers throughout the thickness and interlaminar interfaces [13]. The main damage mechanisms are described as: fiber breaking, matrix micro-cracking and adjacent layers debonding. The single-layer model includes both damage and inelasticity [15] [5] [6]. The interlaminar interface is defined as a two-dimensional mechanical model which ensures traction and displacement transfer from on ply to another. Its mechanical behavior depends on the angle between the fibers of two adjacent layers [4] [17]. Other approaches are [2] [8] [19] [20].

It is well-known that fracture simulation using a continuum damage model leads to severe theoretical and numerical difficulties. A second step which has also been achieved, is to overcome theses difficulties [7]. For laminates and, more generally, for composites, we propose the concept of the mesomodel: the state of damage is uniform within each meso-constituent. For laminates, it is uniform throughout the thickness of each single layer; as a complement, continuum damage models with delay effects are introduced [14] [16].

Two models have to be identified: the single layer model and the interface model. The appropriate tests used consist of: tension, bending, delamination. Each composite specimen, which contains several layers and interfaces, is computed in order to derive the material quantities intrinsic to the single layer or to the interlaminar interface. The proposed procedure is rather simple and has been applied to various materials. Various comparisons with experimental results have been performed to show the possibilities and the limits of our proposed computational damage mechanics approach for laminates.

2. MESOMODELLING OF LAMINATES

In our pragmatic approach, the characteristic length is the thickness of the plies. The meso-model is defined by means of two meso-constituents:
  • the single layer,
  • the interface, which is a mechanical surface connecting two adjacent layers and depending on the relative orientation of their fibres (Fig. 2).
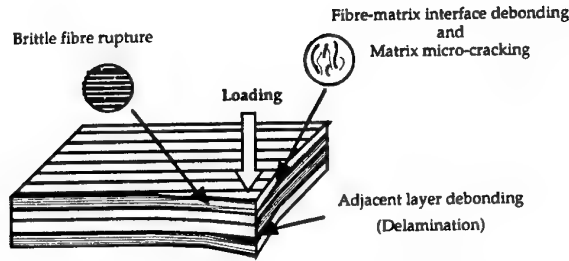
Fig. 1. Damage and failure mechanisms

The damage mechanisms are taken into account by means of internal damage variables. A meso-model is then defined by adding another property: a uniform damage state is prescribed throughout the thickness of the elementary ply. This point plays a major role when trying to simulate a crack with a damage model. As a complement, delayed damage models are introduced.
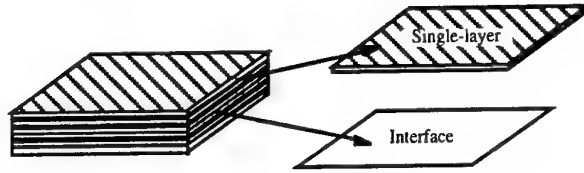

Fig. 2. Laminate modelling

One limitation of the proposed meso-model is that the fracture of the material is described by means of only two types of macrocracks:
  • delamination cracks within the interfaces,
  • cracks, orthogonal to the laminate mid-plane, with each cracked layer being completely cracked throughout its thickness.
Another limitation is that very severe dynamic loading cannot be studied; the dynamic wavelength must be larger than the thickness of the plies.
The single-layer model is briefly given here. A similar model is used for the interface.

2.1. Damage kinematics of the single-layer model

The composite materials (e.g.: carbon-fibre/epoxy-resin) under consideration in this study has only one reinforced direction. In what follows, the subscripts 1, 2 and 3 designate respectively the fibre direction, the transverse direction inside the layer and the normal direction. The energy of the damaged material defines the damage kinematics. Using common notations, this energy is:

$$
E_D \equiv \frac{1}{2(1-d_F)} \left| \frac{\langle\sigma_{11}\rangle^2}{E_1^0} + \frac{\emptyset(\langle-\sigma_{11}\rangle)}{E_1^0} - \left(\frac{v_{21}^0}{E_2^0} + \frac{v_{12}^0}{E_1^0}\right)\sigma_{11}\,\sigma_{22} - \left(\frac{v_{31}^0}{E_3^0} + \frac{v_{13}^0}{E_1^0}\right)\sigma_{11}\,\sigma_{33} - \left(\frac{v_{32}^0}{E_3^0} + \frac{v_{23}^0}{E_2^0}\right)\sigma_{22}\,\sigma_{33} \right|
$$

$$
+ \frac{\langle-\sigma_{22}\rangle^2}{E_2^0} + \frac{\langle-\sigma_{33}\rangle^2}{E_3^0} + \frac{1}{2}\left| \frac{1}{(1-d')}\left(\frac{\langle\sigma_{22}\rangle^2}{E_2^0} + \frac{\langle\sigma_{33}\rangle^2}{E_3^0}\right) + \frac{1}{(1-d)}\left(\frac{\sigma_{12}^2}{G_{12}^0} + \frac{\sigma_{23}^2}{G_{23}^0} + \frac{\sigma_{31}^2}{G_{31}^0}\right) \right|
$$

$\emptyset$ is a material function which takes into account the non-linear response in compression. d_F, d and d' are three scalar internal variables which remain constant within the thickness of each single-layer and serve to describe the damage mechanisms inside. The unilateral aspect of microcracking is taken into account by splitting the energy into a "tension" energy and a "compression" energy; $\langle.\rangle$ denotes the positive part. The thermodynamic forces associated with the mechanical dissipation are:

$$Y_d \equiv \frac{\partial}{\partial d}\langle\!\langle E_D \rangle\!\rangle\big|_{\sigma\,:\,cst} = \frac{1}{2(1-d)^2}\langle\!\langle \frac{\sigma_{12}^2}{G_{12}^0} + \frac{\sigma_{23}^2}{G_{23}^0} + \frac{\sigma_{31}^2}{G_{31}^0} \rangle\!\rangle$$

$$Y_{d'} \equiv \frac{\partial}{\partial d'}\langle\!\langle E_D \rangle\!\rangle\big|_{\sigma\,:\,cst} = \frac{1}{2(1-d')^2}\langle\!\langle \frac{\langle\sigma_{22}\rangle^2}{E_2^0} + \frac{\langle\sigma_{33}\rangle^2}{E_3^0} \rangle\!\rangle$$

$$Y_F \equiv \frac{\partial}{\partial d_F}\langle\!\langle E_D \rangle\!\rangle\big|_{\sigma\,:\,cst} = \frac{1}{2(1-d_F)^2}$$

$$\langle\!\langle \frac{\langle\sigma_{11}\rangle^2}{E_1^0} + \frac{\varnothing\left(\langle-\sigma_{11}\rangle\right)}{E_1^0} - \left(\frac{v_{12}^0}{E_1^0} + \frac{v_{21}^0}{E_2^0}\right)\sigma_{11}\,\sigma_{22} - \left(\frac{v_{13}^0}{E_1^0} + \frac{v_{31}^0}{E_3^0}\right)\sigma_{11}\,\sigma_{33} - \left(\frac{v_{32}^0}{E_3^0} + \frac{v_{23}^0}{E_2^0}\right)\sigma_{22}\,\sigma_{33} \rangle\!\rangle$$

$\langle\!\langle . \rangle\!\rangle$ denotes the mean value within the thickness.

Remark : Damage/plasticity (or viscoplasticity) coupling of the single-layer has been introduced in [13] [15].

2.2. *Damage evolution law*

From experimental results, it follows that the governing forces of damage evolution are:
$$Y = \left[Y_d + bY_{d'}\right]\ ,\ Y' = \left[Y_{d'} + b'Y_d\right]\ ,\ Y_F$$
where b and b' are material constants which balance the transverse energy's influence and the shear energy's influence. For small damage rates, we get :

$$d = f_d\left(\underline{Y}^{1/2}\right) \text{ for } d \leq 1$$

$$d' = f_{d'}\left(\underline{Y'}^{1/2}\right) \text{ for } d' \leq 1$$

$$d_F = f_F\left(\underline{Y}_F^{1/2}\right) \text{ for } d_F \leq 1$$

where:

$$\underline{r}_{|t} = \sup_{\tau \leq t} r_{|\tau}$$

f_d, $f_{d'}$ and f_F are material functions ; both progressive and brittle damage evolutions are present. For large damage rates, we have introduced a damage model with delay effects:

$$\dot{d} = \frac{1}{\tau_c}\left[1 - \exp\left(-a\left\langle f_d\left(Y^{1/2}\right) - d\right\rangle\right)\right] \text{ if } d < 1\ ,\ d = 1 \text{ otherwise}$$

$$\dot{d}' = \frac{1}{\tau_c}\left[1 - \exp\left(-a\left\langle f_{d'}\left(Y'^{1/2}\right) - d'\right\rangle\right)\right] \text{ if } d' < 1\ ,\ d' = 1 \text{ otherwise}$$

$$\dot{d}_F = \frac{1}{\tau_c}\left[1 - \exp\left(-a\left\langle f_F\left(Y_F^{1/2}\right) - d_F\right\rangle\right)\right] \text{ if } d_F < 1\ ,\ d_F = 1 \text{ otherwise}$$

The same material constants, τ_c and a, are taken for the three damage evolution laws. For this damage model with delay effects, the variations of the forces Y, Y' and Y_F do not lead to instantaneous variations of the damage variables d, d' and d_F. There is a certain delay, defined by the characteristic time τ_c. Moreover, a maximum damage rate, which is $1/\tau_c$, does exist. Let us also note herein that a clear distinction can be made between this damage model with delay effects and viscoelastic or viscoplastic models: the characteristic time introduced in the damage model with delay effects is of several orders of magnitude less than in the viscous case. This characteristic time is, in fact, related to the fracture process.

3. IDENTIFICATION

Our used references for testing are [1] [9] [10] [11] [12] [18] [21]. The single-layer model and the interface model have been identified for various materials. Figure 3 gives the main damage material function for the M55J/M18 material.
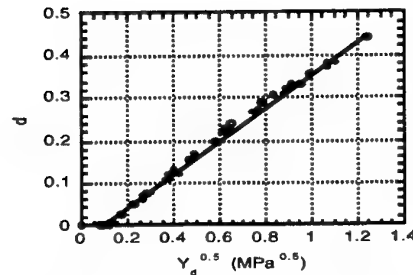

Fig. 3. Shear damage material function $Y_d^{1/2} \rightarrow f_d\left(Y_d^{1/2}\right)$ of the single-layer for the M55J/M18 material

Concerning the interface model, $\pm \theta$ interfaces have been studied. Figure 4 shows the corrected critical energy release rate obtained for classical delamination tests and for different staking sequences. Theses values which do not depend on θ (excepted for $0°/0°$ interface) are used for identifying the interface model.
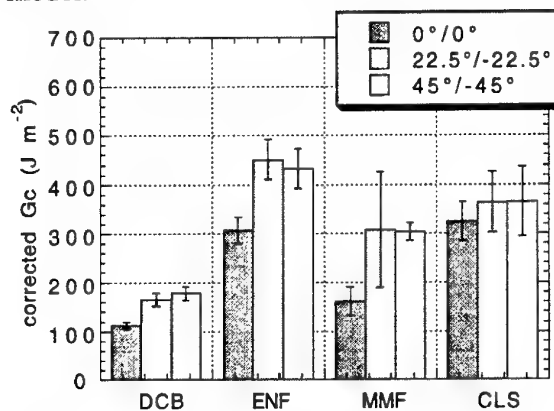
Fig. 4 : Critical energy release rates at propagation

4. QUALITATIVE ANALYSIS OF THE DAMAGE MODEL WITH DELAY EFFECTS

One considers the following one-dimensional bar problem where the bar can be damaged
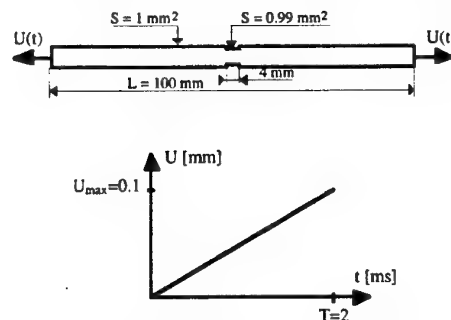
Fig. 5. One-dimensional bar problem

The results obtained for different meshes are plotted in figure 6. It can be seen that the numerical results do not depend on the mesh size. All of these results demonstrate that fracture phenomena are well described by a damage model with delay effects. Figure 7 shows that even for quasi-static loadings, fracture is locally a dynamic phenomenon.
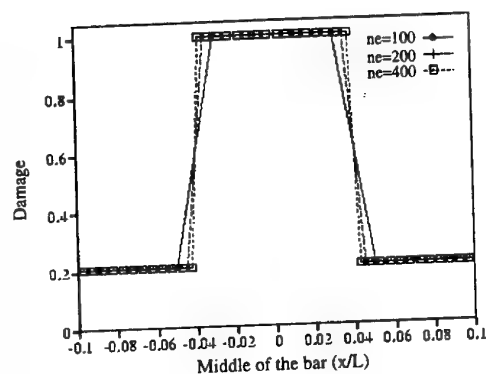

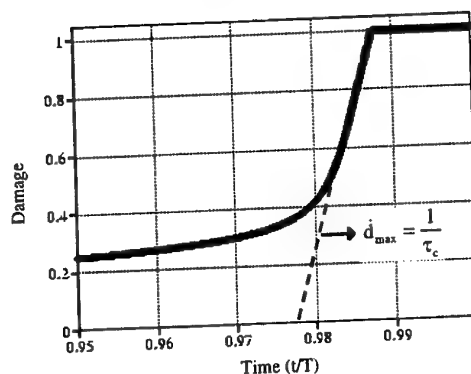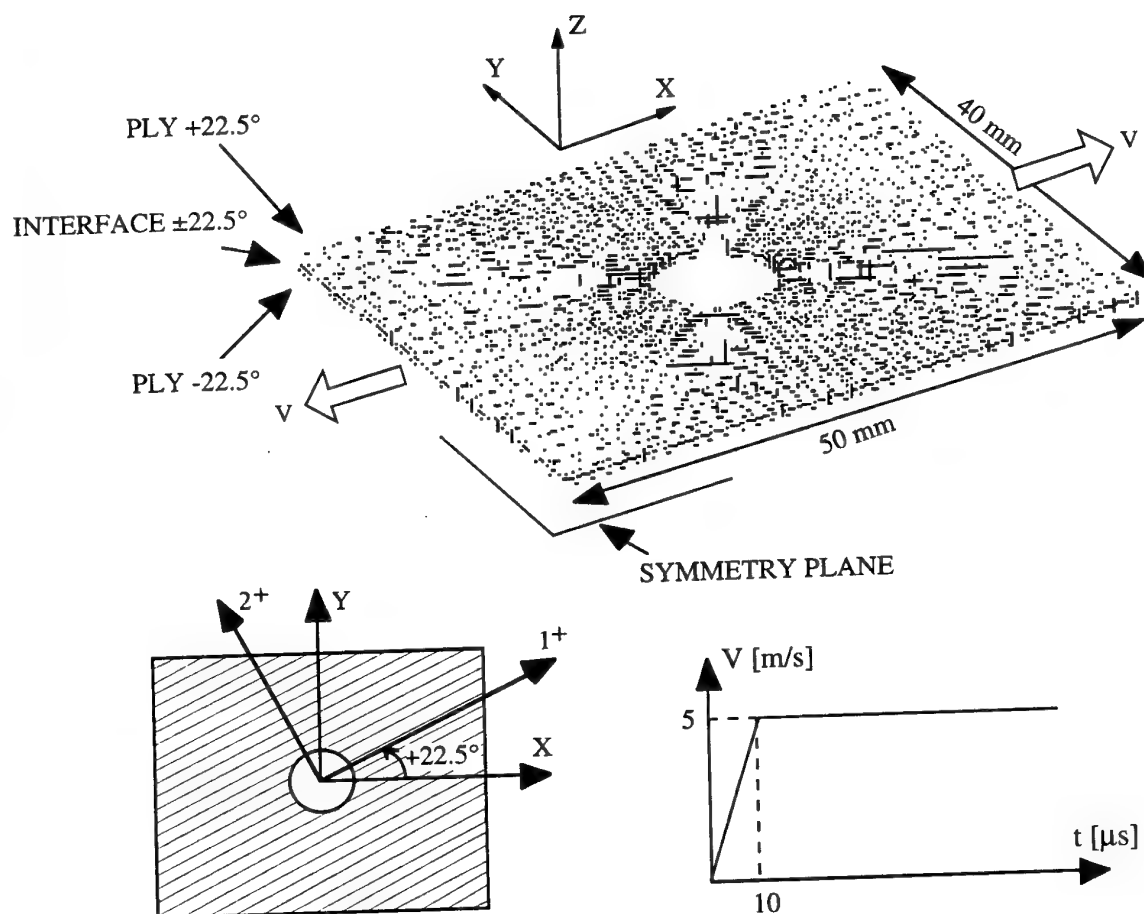Fig. 6. Zoom of the bar damage state of the central zone at time 2ms

Fig. 7. Zoom of the damage-time evolution at the bar's centre

5. EXAMPLES OF LAMINATED STRUCTURES COMPUTATIONS

Essentially, various delamination calculations will be shown, in particular in dynamics. One is partially shown herein.
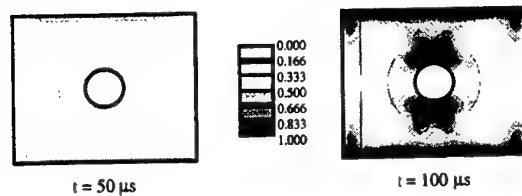
Fig. 9 . Interface damage map at several time

REFERENCES

[1] H.J. Albertsen, J. Ivens, P. Peters, M. Wevers & I. Verpoest, Interlaminar fracture toughness of CFRP influenced by fibre surface treatment: Part 1: Experimental results, Composite Science and Technology 54 (1995) 133-145.

[2] D.H. Allen, Damage evolution in laminates, in: R. Talreja ed., Damage Mechanics of Composites Materials (Elsevier, Amsterdam, 1994) 79-114.

[3] O. Allix and J.F. Deü, Delay-damage modeling for fracture prediction of laminated composites under dynamic loading, Engineering Transactions 45 (1997) 29-46.

[4] O. Allix and P. Ladevèze, Interlaminar interface modelling for the prediction of laminate delamination, Composite Structures 22 (1992) 235-242.

[5] O. Allix, N. Bahlouli, C. Cluzel and L. Perret, Modelling and identification of temperature-dependent mechanical behaviour of the elementary ply in carbon/epoxy laminates, Composites Science and Technology 56 (1996) 883-888.

[6] O. Allix, P. Ladevèze and E. Vitecoq, Modelling and identification of the mechanical behaviour of composite laminates in compression, Composite Science and Technology 51 (1994) 35-42.

[7] Z.P. Bazant, Z. Bittnar and M. Jirasek, Fracture and Damage in Quasibrittle Structures (eds.) (Elsevier, Amsterdam, 1994).

[8] J.L. Chaboche, O. Lesné and T. Pottier, Continuum Damage Mechanics of Composites: Towards a Unified Approach, in: G.Z. Voyiadjis, J.W. Wu and J.L. Chaboche eds., Damage Mechanics in Engineering Materials (Elsevier, Amsterdam, 1998) 3-26.

[9] P. Davis, Measurement of GIc and GIIc in Carbon/Epoxy composites, Composite Science and Technology 39 (1990) 193-205.

[10] C.T. Herakovich, Mechanics of fibrous composites (J. Wiley, 1998).

[11] A. Highsmith and K.L. Reifsnider, Stiffness reduction mechanism in composite material, in: ASTM-STP 775, Damage in Composite Materials (1982) 103-107.

[12] R.Y. Kim, Experimental observations of free-edge delamination, in: N.J. Pagano ed., Interlaminar response of composite materials (1989) 111-160.

[13] P. Ladevèze, Sur la mécanique de l'endommagement des composites, in: C. Bathias & D. Menkès eds., Comptes-Rendus des JNC5, Pluralis Publication, Paris (1986) 667-683.

[14] P. Ladevèze, A damage computational approach for composites: Basic aspects and micromechanical relations, Computational Mechanics 17 (1995) 142-150.

[15] P. Ladevèze and E. Le Dantec, Damage modeling of the elementary ply for laminated composites, Composite Science and Technology 43-3 (1992) 257-267.

[16] P. Ladevèze, O. Allix, J.F. Deu and D. Lévèque, A mesomodel for localisation and damage computation in laminates, Comput. Meth. Appl. Mech. Engng (to appear 1999)

[17] P. Ladevèze, O. Allix, L. Gornet, D. Lévêque and L. Perret, A computational damage mechanics approach for laminates: Identification and comparison with experimental results, in: G.Z. Voyiadjis, J.W. Wu & J.L. Chaboche eds., Damage Mechanics in Engineering

[18] P. Robinson and D.Q. Song, A modified DCB specimen for mode I testing of multidirectional laminates, Composite Science and technology 26 (1992) 1554-1577.

[19] R. Talreja, Transverse cracking and stiffness reduction in composite laminates, Journal of Composite Materials 19 (1985) 355-375.

[20] G.Z. Voyiadjis, J.W. Wu and J.L. Chaboche, Damage Mechanics in Engineering Materials (Elsevier, Amsterdam, 1998).

[21] J.M. Whithney, Experimental characterization of delamination fracture, in: N.J. Pagano ed., Interlaminar response of composite materials, Comp. Mat. Series 5 (1989) 111-239.

Aging and long term behaviour of composite tubes

P. Davies, R. Baizeau, D. Choqueuse (IFREMER, Brest)

L. Salmon, F. Nagot (EDF Les Renardières, Moret-sur-Loing)

Abstract This paper will discuss results from studies undertaken by IFREMER and EDF over the last ten years. The aim of these studies has been to examine the aging and long term behaviour of glass fibre reinforced epoxy composite tubes for cooling water applications. First, aging of resins and composites in water is discussed. Results from tests to establish the kinetics of resin hydrolysis are used to predict composite degradation with time, based on panels immersed for 8 years at 20, 40 and 60°C. Then results from creep tests on tubes under internal pressure with closed ends, lasting up to 18 months are given. Creep strains are shown to be much lower than those measured in similar tubes with free ends reported previously. Damaged and assembled tubes have been tested. Finally current research activities are discussed.

Introduction:

Thin wall filament wound glass fibre reinforced composite tubes are being used extensively today, but these structures have been available for over 40 years. Early applications were mostly military, such as missiles and rocket casings (e.g. Kies 1962), but they can now be found in chemical engineering plants (Mallison 1988), fishing boats (Croquette 1992), offshore platforms (Gibson 1993), and many other industrial cooling systems. In oil and gas production the main use is small diameter low pressure pipe for water flood systems. Williams (1999) reports that Shell now has over 2250 kilometres of FRP (fibre reinforced plastic) piping materials in service round the world. Much of the development work for these applications was performed in the 1960's and 1970's (e.g. Bax 1970, Spencer 1978).

The main incentive for using FRP pipe systems to replace steel is their good resistance to corrosion, and failure rates in sea water in service have been shown to be significantly lower for FRP (de Bruijn 1996). It was mainly for this reason that in 1991 EDF (Electricité de France) decided to introduce composite circuits in their new nuclear power station at Civaux near Poitiers. The circuits involved bring river water to cooling and fire systems and the stringent safety requirements for such applications required extensive full scale testing at EDF and the CEA (French Atomic Energy Authority). Several collaborative research projects were also run. The present paper presents an overview of results from one such project, with IFREMER, but results from other studies on glass/epoxy tubes with the Applied Mechanics Laboratory, (LMARC) in Besançon (Maire 1992, Thiebaud 1994, Perreux 1995, Suri 1995), Ecole Centrale in Paris (Bai 1996), and on glass/polyester tubes at LMT Cachan (Ghorbel 1996) are also available.

The collaboration between IFREMER and EDF focused on long term behaviour and aging. At the IFREMER Brest Centre glass/epoxy pipework has been used successfully for over 20 years in a sea water distribution system, but for the power station application the safety authorities required guarantees concerning the long term behaviour. A programme of aging and creep tests was therefore initiated and results from the first phase were presented at DURACOSYS in 1995 (Baizeau 1995).

In the first part of the present paper the aging of resin and composite samples will be discussed. In 1995 results from 3 year immersion aging of composites was described. Results after 8 years will now be presented, and the basis for a simple lifetime prediction method based on resin behaviour will be shown. The second part of the paper concentrates on the behaviour of tubes under internal pressure, including creep behaviour of undamaged and damaged tubes. Finally current research areas and future requirements are discussed.

I. Aging of epoxy resin and glass/epoxy composites in water.

The degradation of composites in water may result from many different mechanisms, involving the fibre, fibre-matrix interface and matrix. In order to treat aging practically simplifying assumptions are therefore necessary. One approach is to determine, for each mechanism, a characteristic time before which the mechanism can be ignored but beyond which it plays a significant role in the durability of the material. This approach will be illustrated below for the case of wet aging of glass reinforced anhydride cured epoxy, by considering the hydrolysis of the matrix.

a) Resin properties
Anhydride cured epoxies contain esters which are susceptible to hydrolysis. The chemical reaction is: $RCOOR' + H_2O \rightarrow RCOOH + R'OH$. The hydrolysis of the polymer leads to molecular chain breakage and water molecules can fix to the material. It leads to an increase in sample weight of 18 g/mole of broken chains. The resin weight change will therefore be a monotone function of the number of breakages. A simple weight measurement should therefore enable quantitative information on the kinetics of hydrolysis to be obtained. This assumes that weight gain due to water diffusion into the polymer can be separated from the overall weight change, (and that other damage does not occur simultaneously) which can be ensured by using very thin specimens. Figure 1 shows this schematically. Samples of epoxy resin (diglicidyl ether of bisphenol A, DGEBA) with methyl tetra hydrophthalic anhydride (MTHPA) were immersed at three temperatures, 60, 70 and 80°C. A kinetic model was used based on the following assumptions: the reaction is homogeneous throughout the material, the kinetics are of second order (one with respect to the ester functions concentration, one with respect to water concentration), and solubility of water varies little with temperature. This has allowed the time to reach a given degree of advancement to be calculated for all temperatures. The determination of a critical level of hydrolysis leading to mechanical failure is next required in order to be able to predict the lifetime of the component.

By measuring the failure stress and strain as a function of water absorbed on samples of resin aged in water at 60°C, a critical value of percentage weight gain (and hence of hydrolysis) corresponding to a drop in mechanical properties was determined, Figure 2. For the epoxy/anhydride system studied here that value is around 4%. By introducing this critical value (4% water absorbed in the resin) in the kinetic model a lifetime can be determined for the matrix. This varies from several centuries at 20°C to less than one year at 80°C.

b) Composite panel weight gain
Figure 3 shows the results from 8 year immersion in distilled water at different temperatures (20, 40 and 60°C) of 3 mm thick composite panels, filament wound at ±55°. The curve for immersion at 60°C shows a similar form to those in Figure 1, with an increase in weight gain after about 3 years. Tg measurements were made periodically by DSC, then after 7 years specimens at each temperature were removed and dynamic mechanical analysis was performed in 3 point flexure (temperature increased at 2°C/minute). Results are shown below, Table 1, indicating that the glass transition temperature of 60°C aged samples has dropped significantly.

Table 2. Glass transition temperatures (DSC & DMA), aged composite panels

Aging temperature	Initial	10 m	22 m	35 m	7 years (DMA)
20°C	129	130	129	131	116°C
40°C	129	130	129	132	119°C
60°C	124	123	119	115	86°C

Scanning electron microscopy was performed on polished regions and fracture surfaces of regions on the exterior and centre of specimens at all three temperatures. Specimens aged at 20°C showed no evidence of interfacial debonding after 7 years. Those aged at 40°C show some signs of interface debonding on the surface but not in the centre, while those aged at 60°C show at the surface there clear interfacial degradation but again at the centre of the specimens there is no debonding. Given these results it may be possible to assume that the bulk of the specimen is degrading in a homogeneous manner and to apply the kinetic model of resin hydrolysis to predict an order of magnitude of the state of hydrolysis in the composite panels. In order to do this the criterion used to indicate this state was taken to be the glass transition temperature. A reasonable correlation between predictions and measurements was obtained.

c) Correlation with behaviour of tubes
Samples taken from tubes fully immersed for 5.8 years at 60°C were also examined and the same degradation mechanism was observed, some interfacial debonding near the surface but none in the centre of the tube wall. This suggests that the simplified approach based on resin hydrolysis kinetics, combined with regular checks on glass transition temperature, may provide a useful tool in determination of the service life of these tubes. When tubes are only exposed to water on the inside wall there may need to be an adjustment to the weight gain kinetics however, as previous results (Baizeau 1995) indicated that weight increases were much lower than expected based on plate or fully immersed tube results. Some additional tests involving machining of inner and outer layers were performed (Suri 1995) to try to explain this phenomenon but did not clarify the reasons. As far as the degradation mechanisms are concerned this effect should be positive in reducing the degradation rate. Another aspect which can affect the correlation is the presence of voids, high levels of which can be introduced during filament winding. Chiou (1996) has also reported anomalies in long term behaviour of tubes which were attributed to the presence of voids.

d) Mechanical property changes after aging
A small number of flexure and short beam shear tests were performed on samples taken from the panels aged at 60°C after 3 years. Two panels were tested, one which had shown a rapid increase in weight gain (to 3%), while the other had only gained 1% weight, Figure 4. These wouild therefore correspond to panels above and below the knee in the resin property plot. In flexure there is a clear drop in strength, Table 3, but this property is governed by the surface degradation (interface debonds). In interlaminar shear however, governed by shear of the resin in the centre of the sample, the loss in strength is only marked for the sample with high weight gain.

Panel	Flex strength, MPa		ILSS, MPa	
	35°	55°	35°	55°
Reference (unaged)	410	127	44	19.5
Panel 1 (3%)	231	87	30	13
Panel 2 (1%)	302	120	43	18.5

Table 3. Results from tests on composite panels after 3 years at 60°C

A further project is now underway at IFREMER in which samples of the same epoxy with three hardeners, (anhydride, aliphatic and aromatic amines) are being aged.

e) Accelerating tests with pressure

While raising temperature is often a convenient way to accelerate aging tests, increasing hydrostatic pressure may also be used. This is also more appropriate for applications such as underwater pipelines, and some tests have been run to look at how pressure affects diffusion kinetics in these materials. Examples of results for the same epoxy resin with three different fibre types, for specimens cut from filament wound tubes wound at ±55°, aged at 60°C, will be shown.

II. Creep of tubes and tube assemblies under internal pressure loading

Two series of tests have been performed to investigate the long term behaviour under internal pressure. A total of 24 tubes, each 1 to 1.4 metres long, has been tested, Table 2. The internal diameter is 150 mm, wall thickness is nominally 5 mm. The first phase of the project, a series of 12 creep tests on tubes without internal liner and loaded with free ends ($\sigma_z = 0$) at different temperatures and pressures, was described at DURACOSYS 95. A description of the second phase, which involved tests on tubes with internal liners, will be presented at this conference. The aims of these tests were to establish the influence of creep on stiffness, to compare the free end and fixed end loading conditions, to examine how damage affects subsequent creep behaviour and to see how bonded and mechanical joints behaved.

Table 2. Summary of creep tests performed.

Series	Pressure MPa (σ_q)	Temperature, °C (Number)	Duration Creep/Recovery	Details
1.	2.7 (38)	25, 40, 55	12m/1m	All type A
No liner	4.0 (56)	25, 40, 55	9m/1m	
Free ends $\sigma_z=0$	2.7 (38)	25, 40 (2), 55	6m/2.5m	
	5.4 (76)	55 (2)	6m/2.5m	
2.	0.8 (11)	20 (3)	17m/1m	A,B,C
With liner	1.7 (24)	40 (5)	17m/1m	A, B, D1-3
Fixed ends,	3.8 (53)	40	10m/1m	B
$\sigma_z=\sigma_q/2$	3.8 (53)	60 (3)	10m/1m	A (2), C

A: Straight tube, B: Mechanical joint at centre, C: Tulip adhesive joint at centre, D: Damaged
Hoop stresses applied to damage: D1 35 MPa, D2: 67 MPa, D3: 130 MPa

In addition to following the strain response by strain gauges throughout the creep and recovery cycle (over 100 strain, temperature and pressure channels were recorded), mechanical tests were also performed on the tubes before and after this cycle. These involved subjecting tubes to low pressure cycles with two loading conditions, fixed and free ends (i.e. with and without axial stress), and allowed the influence of the creep cycle on residual stiffness to be assessed.

a) Creep results

There is only space here to show examples of the creep behaviour, more details will be presented in the full paper. Figure 5 shows strains measured at the start and end of creep and recovery cycles for two conditions. It is apparent that the creep strains are very low, and much lower than creep under free end loading conditions reported for Phase 1 of the project.

b) Influence of damage

Different levels of damage were introduced into three tubes by loading under internal pressure. These tubes were then loaded in creep at 40°C and 17 bars for an 18 month cycle, including 17

months of creep and 1 month's recovery. The presence of this damage affected the creep behaviour and also resulted in reduced stiffness of these tubes after creep.

c) The bonded and mechanically joined assemblies behaved in a satisfactory way throughout the tests, and no leaks were noted.

III. Current and future research
The presentation will be concluded by a view of current research work at IFREMER and EDF, including the influence of hardeners on long term behaviour, studies of tolerance to tubes to delaminations and impact damage, influence of defects in bonded joints, and the development of improved regulations for dimensionning tubes.

References

Bai J et al., 'Mechanical behaviour of ±55° filament wound glass fibre /epoxy tubes, Parts I-IV, Comp. Sci & Tech., 1996.

Baizeau R, Davies P, Choqueuse D, LeBras J, 'Evaluation of the integrity of composite tubes', DURACOSYS95, ed Cardon, Fukuda & Reifsnider, Balkena 1996, p225.

Bax J, 'Deformation behaviour and failure of glass fibre reinforced resin material', Plastics & Polymers, 1970, Feb. p27.

Chiou P-L, Bradley WL 'Moisture-induced degradation of glass/epoxy filament wound composite tubes', J. Thermopl. Comp., 9, April 1996, p118.

Croquette J,'Parquic JC, Forestier JM, Dufour X, Proc. IFREMER conf., Composite materials for Marine Applications, 1992, p412.

de Bruijn JCM, van den Ende CAM, 'GRP pipes are safer than steel ones', Reinforced plastics Feb. 1996 , p40.

Ghorbel I, Spiteri P, 'Durability of closed end pressurized GRP pipes under hygrothermal conditions', Parts I & II, J. Comp. Mats., 30, 14, 1996, p1562 & p1581.

Gibson AG, Chapter 11 in 'Composite materials in marine structures', ed Shenoi & Wellicome, Cambridge Ocean Technology, 1993.

Spencer B, Hull D, 'Effect of winding angle on the failure of filament wound pipe', Composites 9, 1978, p263.

Kies JA, Bernstein H, 'Recent advances in glass fiber reinforced plastic rocket motors', Proc 17th Annu conf. Reinf. Plastics, 1962 6-B.

Maire J-F, 1992, PhD Université de Franche Comté

Mallison JH, 'Corrosion resistant plastic composites in chemical plant design', Dekker 1988.

Perreux D, Varchon D, LeBras J, 'The mechanical and hygrothermal behaviour of composite pipes', Proc. ENERCOMP 95, Montréal, p819.

Suri C, 1995, PhD Université de Franche Comté

Thiebaud F, 1994, PhD Université de Franche Comté

Williams JG, Silverman SA, 'Composites Technology used onshore with synergy to offshore applications', OTC Paper 11062, 1999.

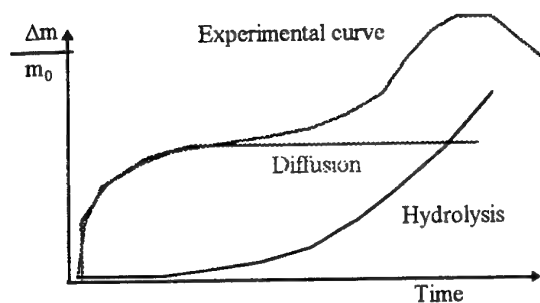Figure 1 Resin weight change during immersion

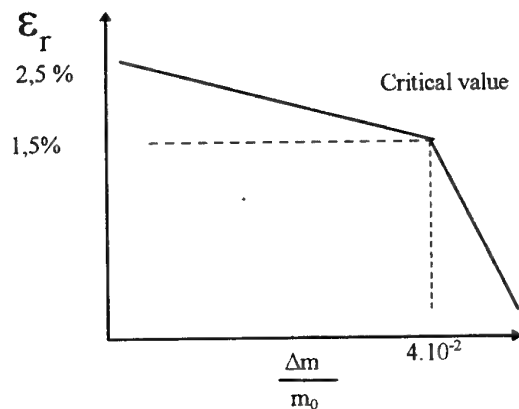Figure 2. Failure strain versus percentage of water absorbed.

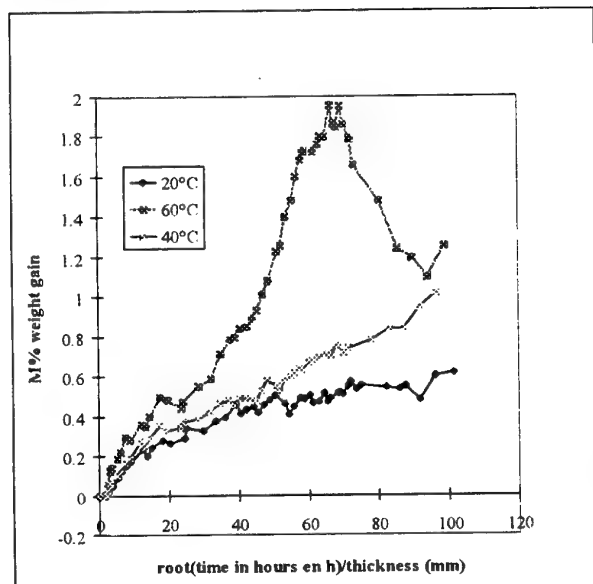Figure 3. Weight gain during eight year aging of ±55° composite panels in water

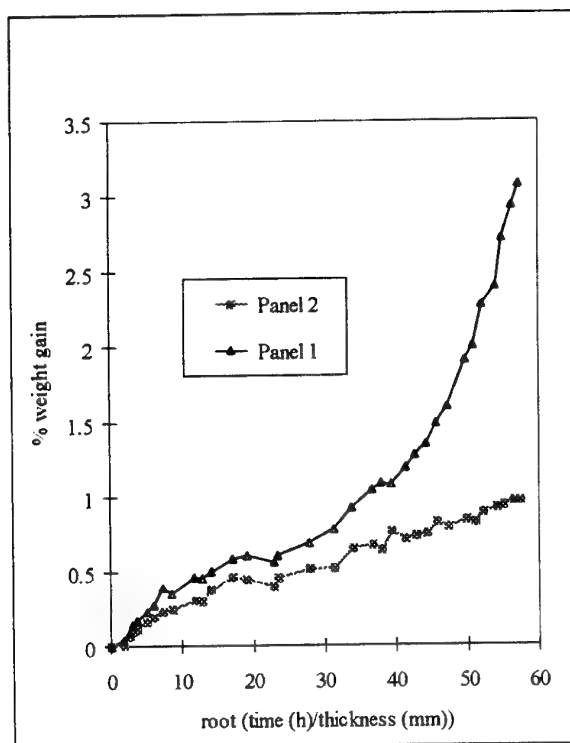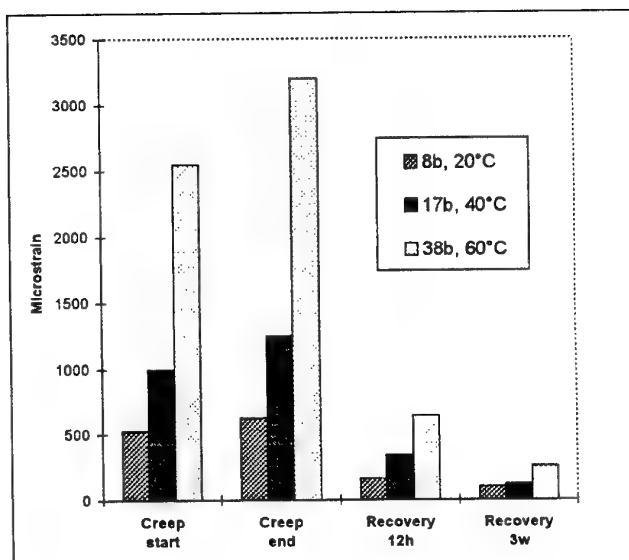Figure 4. Weight gains of pecimens aged at 60°C removed for testing after 3 years.

Figure 5. Creep (10 months 38 b, 17 months 8&17 b) and recovery (1 month) strains.

INTERACTIONS BETWEEN MOISTURE AND FATIGUE DAMAGE IN UNIDIRECTIONNAL GLASS/EPOXY COMPOSITES SUBJECTED TO FLEXURAL LOADING

Antoine Chateauminois

Département Sciences et Techniques des Matériaux et Surfaces, UMR IFoS 5621
Ecole Centrale de Lyon, BP 163 - 69131 Ecully Cedex, France
E-Mail: antoine.chateauminois@ec-lyon.fr

It is widely established that the durability of polymer matrix composites in hot/wet environments involves several physico-chemical and mechanical damage processes occurring at very different time and length scales [1]. From matrix plasticization or hydrolysis at the macromolecular level up to crack propagation at the macroscopic scale, the characteristic length scales can vary by several orders of magnitude. In a similar way, the kinetics of the individual chemical or mechanical degradation processes are ranging from minutes to years. Moreover, each of these strongly coupled mechanisms involve different activation energies, which makes the development of accelerated ageing procedures a highly complex task. The development of relevant testing methodologies and predictive models can therefore only be envisaged if the main degradation mechanisms and their interrelations are identified through a multidisciplinary analysis of the material degradation under combined environmental and mechanical loading.

The development of such an approach will be considered in the specific context of the flexural fatigue behaviour of unidirectional glass/epoxy composites in moist environments. In such a configuration, the fatigue damage is mainly driven by the delayed failure of the glass fibres, which are substantially weakened in moist environments. On the basis of different investigations carried out in our laboratory over the past few years, some of the mean features of the relationship between fatigue damage and hygrothermal ageing will be reviewed herein.

Endurance properties of aged unidirectional glass/epoxy composites

At the macroscopic scale, the overall loss of fatigue properties resulting from water exposure can be quantified by reporting the lifetimes in conventional S-N diagrams. For a wide range of composites systems, ageing conditions and strain ratios, hygrothermal ageing was often found to be associated with a significant shift of the endurance curves to low strains (Fig.1). Two main trends have been established [2,3,4]:

(i) Even when the water uptakes M_t are similar, properties losses are systematically much more pronounced after immersion in water than after exposure to relative humidity.

(ii) After immersion, the residual fatigue properties for a given value of M_t are strongly dependent upon the conditioning treatment used to obtain this water content. As illustrated in Fig. 1, the fatigue properties depend in fact in a complex manner on the ageing time and temperature.

These two features demonstrate that the relative weight gain M_t of the specimens can not be considered as a relevant parameter to quantify the extent of the hygrothermally induced damage. In that sense, the classical water sorption curves by their own are of no use for the prediction of lifetimes reduction. This complex behaviour can be explained by considering the strong interrelations between the fibre strength and the phyisco-chemical processes occurring in the matrix during water sorption.
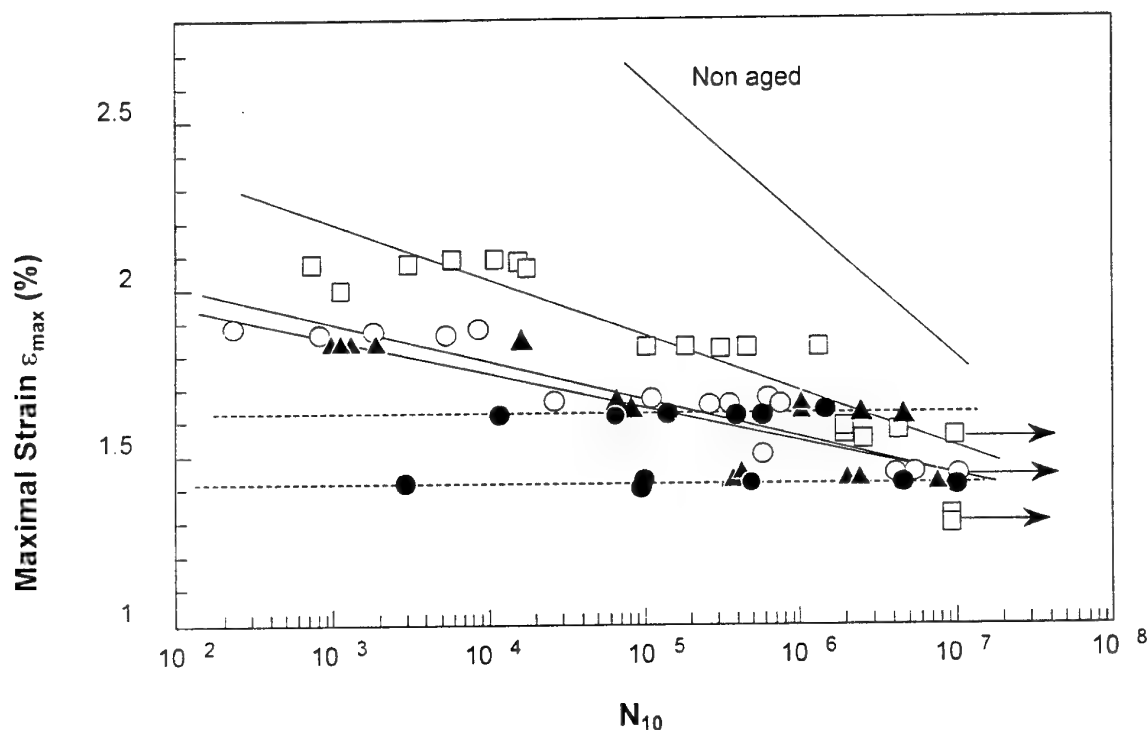
Fig.1 : *Three point bending S-N curves after water immersion (M$_t$ ● 1.5 %)*
N$_{10}$ is the number of cycles to 10% stiffness loss.
Aged (✗) 180 days at 50°C. (✦)77 days at 60°C. (▲)51 days at 70°C and (▦) 10 days at 90°C

Relationships between the fibre mechanical properties and the chemical degradation of the matrix

Water sorption in epoxy networks results in both reversible plasticization and irreversible hydrolytic degradation. The occurrence of both processes can be conveniently checked by Dynamic Mechanical Thermal Analysis (DMTA) of the aged specimens before and after drying (Fig.2). as long as the chemical degradation is associated with a decrease in the cross-link density[5]. Except for some high Tg matrix[6]. extensive hydrolysis was found to occur in most of the conventional epoxy systems studied. These processes have two main implications regarding material degradation:

(i) As water sorption through the thickness of the material involves very long transient steps, the resulting chemical degradation of the material is highly heterogeneous, even if a saturated state is considered. This was demonstrated by the dependence of the water sorption kinetics upon the specimen geometry. This heterogeneous nature of the water-induced damage strongly questions the validity of the extrapolation of fatigue tests on aged specimens to various loading configurations.

(ii) The chemical degradation of the epoxy network and the interface often results in the leaching of low molecular weight species, which can strongly affect the physico-chemical environment (especially the pH) of the fibre at the interface. For example, it was observed that the hydrolysis of residual amount of some amine-based hardeners results in the leaching of ammoniac, which in turn induces a significant increase in the pH of the ageing media. The main consequence of these physico-chemical changes is to affect the subcritical crack growth processes in the glass fibres. As a result, a strong coupling can be established between the network hydrolysis (molecular level), the stress corrosion cracking of the individual fibres (micro-mechanical level) and the resulting fatigue properties (macroscopic scale).
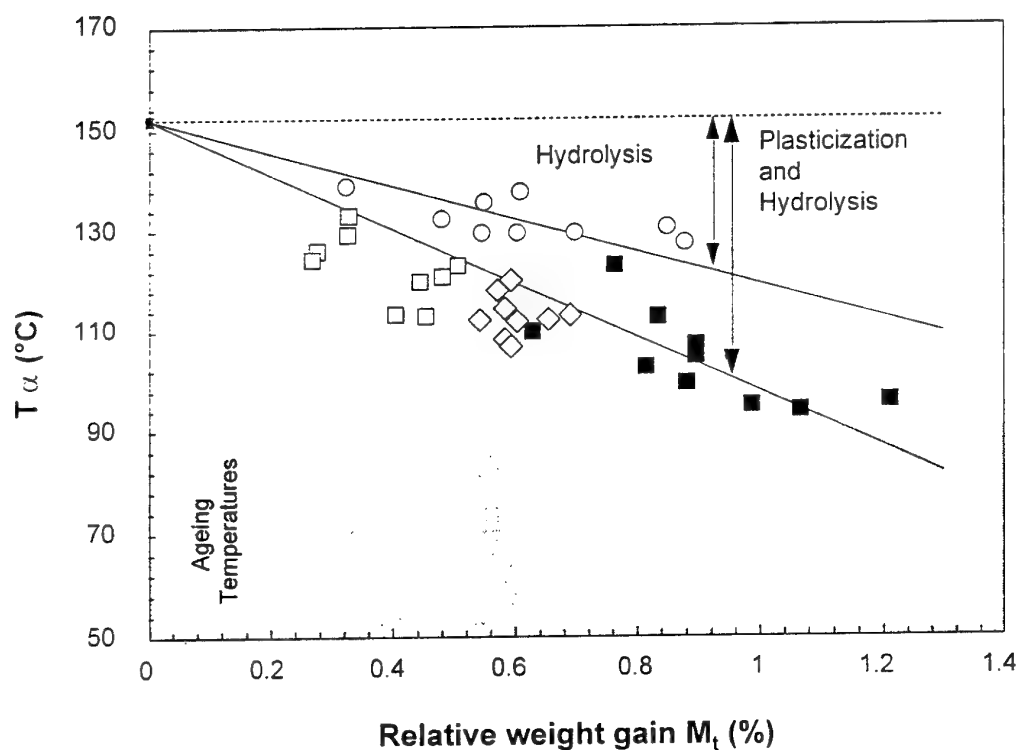

Fig.2 : *Thermo-mechanical analysis of water aged composites before and after drying (D.M.T.A., 1Hz)*

Aged at ( ) 50% R.H., ( ) 80% R.H., ( ) immersion; ( ) aged composite after drying

These coupling effects between chemical and mechanical damage were investigated by in-situ micro-mechanical investigations. Under flexural loading, the damage presents the advantage to be localised over a restricted area on the tensile side of the specimen, where the fibre failures can be detected and quantified using optical microscope observations. Using this technique, it was therefore possible to quantify on a statistical basis the residual strength

properties of the fibre in the real physico-chemical environment encountered during the ageing process. These investigations have been focused on the early stages of fibre failure, i.e. before the appearance of macroscopic cracking. Such an approach is justified by the fact that the fatigue resistance of the composite is largely governed by the tolerance of the composite to the accumulation of broken fibres during the early stages of the fatigue test[7].

Using this methodology, semi-quantitative relationships have been established between the changes in the statistical distribution of in-situ fibre strength upon ageing and the decreases in the fatigue properties, as they can be described within the frame of a Wöhler relationship[4,8]. These observations accounted for the observed differences between water immersion and exposure to relative humidity, the network chemical degradation being much more effective in liquid environment.

Accordingly, it may now be envisaged to predict - on a quantitative basis - the fatigue resistance of the aged composite by modelling the stress corrosion cracking processes of the fibre under the combined influence of time, temperature, water concentration and applied stress. This approach is currently developed using the potential of the in-situ statistical analysis of fibre breaking.

References

1   Schutte. C. (1994). " Environmental durability of glass-fiber composites." *Materials Science and Engineering R-Reports* **13**(7): 265-323.

2   Chateauminois. A.. Chabert. B.. Soulier. J. P. and Vincent. L. (1993). "Hygrothermal ageing effects on the static fatigue of glass/epoxy composites." *Composites* **24**(7): 547-555.

3   Vauthier. E.. Chateauminois. A. and Bailliez. T. (1996). "Fatigue damage nucleation and growth in a unidirectional glass/epoxy composite subjected to hygrothermal ageing." *Polymer and Polymer Composites* **4**(5): 343-351.

4   Vauthier. E.. Abry. J. C.. Bailliez. T. and Chateauminois. A. (1998). "Interactions between hygrothermal ageing and fatigue damage in unidirectionnal glass/epoxy composites." *Composites Science and Technology* **58**: 687-692.

5   Chateauminois. A., Chabert. B.. Soulier. J. P. and Vincent. L. (1995). "Dynamic mechanical analysis of epoxy composites plasticized by water: artifacts and reality." *Polymer Composites* **16**(4): 288-296.

6   Chateauminois. A.. Chabert. B.. Souliert. J. P. and Vincent. L. (1994). "Interfacial degradation during hygothermal ageing. Investigations by sorption/desorption experiments and viscoelastic analysis." *Polymer* **35**(22): 4765-4774.

7   Reifsnider. K. L. (1994). "Modeling of the interphase in polymer matrix composite material systems." *Composites* **25**(7): 461-496.

8   Vauthier. E.. Abry. J. C.. Baillez, T. and Chateauminois. A. (1997). "Influence of hygrothermal ageing on the fatigue behaviour of a unidirectionnal glass/epoxy composite". *International Conference on Fatigue of Composites*. Paris. Société Française de Métallurgie et des Matériaux (SF2M). 323-330.

Contribution to the durability analysis of a thick composite structure under complex mechanical and hygroscopic loads.

Y. POIRETTE, F. PIERRON, A. VAUTRIN

Département Mécanique et Matériaux
Ecole Nationale Supérieure des Mines de Saint Etienne
158, cours Fauriel
42023 Saint-Etienne Cedex 02, France

The use of composite materials to design structural components subjected to complex hygro-thermo-mechanical loadings requires careful analysis of the long-term behaviour of these materials under service loads. In particular, hygrothermal time dependent gradients can occur and lead to serious modifications of the behaviour of the total structure. Good understanding of these phenomena and developments of specific approaches allowing numerical simulations of the structure in service are necessary to check the effectiveness of the composite solutions and set up guide routes to support the use of composites as structural materials.

The present work is part of an important study dealing with the design and development of a novel power transmission for locomotives. The elastic design has been carried out in the framework of a feasability study (Cerisier et al.,[1996]). The proposed solution is a composite shaft with varying section (Fig. 1) that performs the torque transmission with maximum stiffness and allows a vertical shift of its ends with a minimum stiffness (Cardan effect). The selected material is a glass/epoxy woven composite with 45° orientation with respect to the shaft axis. The present approach deals with the durability of the overall composite structure under long-term service life. The paper addresses the particular methodology that has been adopted to reach the target in due time.
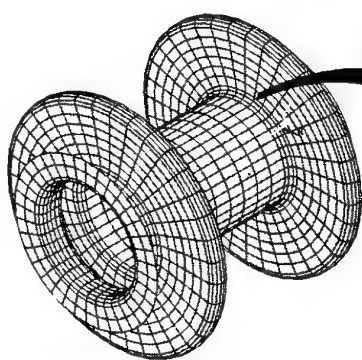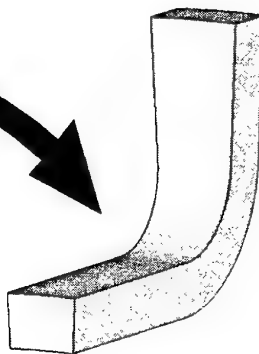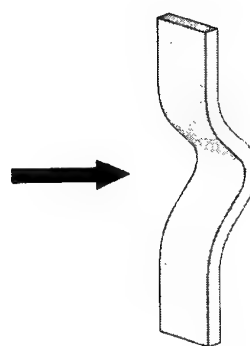
| *Fig 1 :* | *Fig 2 :* | *Fig 3 :* |
| the transmission | the area of interest | the curved beam |

The areas that are subjected to high stresses have been first determined by using a 2D FE analysis of the complete structure (Fig. 1). This analysis has been carried out with the ANSYS 5.4 package. It showed that the most critical areas are the joining zones between the cylinder and the flanges where the curvature radius is similar to the thickness of the

component. So, it became essential to look at the three-dimensional aspect of the problem. A 3D sub-model was defined (Fig. 2) to compute the full 3D stress state. This second analysis showed that a complex mechanical stress field exists which is mainly a combination of through-thickness shear, through-thickness tension and in-plane shear in the material axes. Results of the 3D analysis led to the design of a testing specimen. That should be able to simulate the behaviour of this critical area. Moreover, the geometry of this coupon must be such that the specimens can be conditioned for the study of the effects of the moisture on the mechanical properties. Therefore, a curved beam specimen (Fig. 3) loaded in tension has been designed.

The curved beam dimensions have been adjusted by computation to get stress fields similar to the fields inside the area of interest in the component. Taking into account symmetries of the specimen, only a quarter of the curved beam was modeled (Fig. 4).

First manufactured specimens had the followed nominal dimensions : thickness = 10 mm, height = 32 mm, average radius = 20 mm and width = 40 mm.
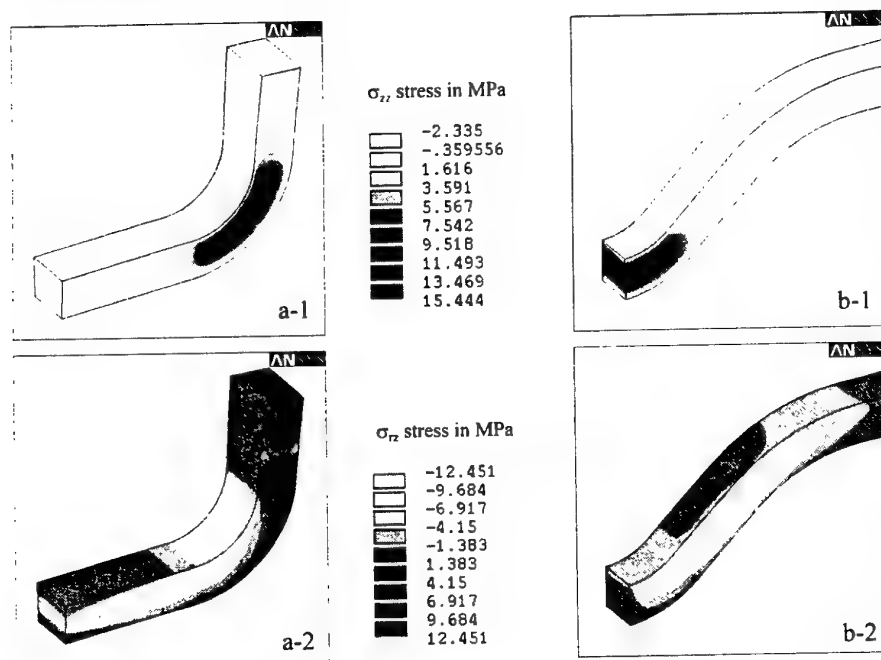
Fig 4 : Comparison between stress fields of through-thickness tension (1) and shear (2) in transmission (a) under flexural load and curved beam (b) in tension.

The paper will discuss in details the curved beams used to simulate the effect of a gradient of moisture throughout the component. To do so it has been necessary to experimentally obtain some of the 3D material properties under a uniform concentration of moisture.

As a first step, the moisture coefficients of the composite material have been measured. Thin samples have been cut out from 1 mm and 18 mm thick plates to determine the diffusion coefficients in the directions parallel and normal to the fibres. Additional samples have been cut out from a 5 mm plate for full 3D diffusion. All have been conditioned in various temperature and moisture environments : 60%, 80% and 96% relative humidity (R.H.) at 60°C, 96% R.H. at 40°C and 25°C. These conditions were obtained using saturated solutions of several salts. Prior to conditioning, each sample has been dried out in an oven at 40°C. During the conditioning, the water uptake has been monitored by weighing the samples, using

a refined procedure to take surface evaporation into account. Finally, the use of 3D Fick's law has led to the 3D diffusion coefficients and the moisture contents at saturation for different sets of temperature and relative humidity.

These results have been used to introduce a moisture gradient in the numerical model (Fig. 5) to take into account the specimen behaviour under hygroscopic load.
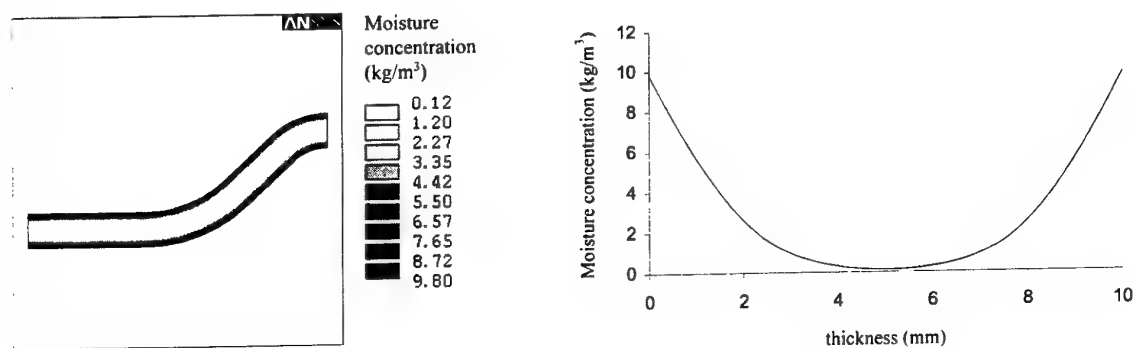

Fig 5 : Example of moisture concentration profile (kg/m³) along the specimen thickness after a 3000 hours conditioning.

As a second step, particular tests to characterize the mechanical properties have been conducted at different saturation levels. In particular, V-notched beams have been cut in the 2 and 18 mm thick plates to perform Iosipescu in-plane and through-thickness tests. Furthermore, curved beams with 0° fabric orientation were manufactured as well. The thickness of these specimens was adapted to make absorption of water possible in due time before experimental tests.

All specimens were instrumented by strain gauges and conditioned at 60°C in different wet environments (60%, 80% and 96% R.H.). The weighing of reference samples allows to determine the maximum moisture content for each conditioning. The tests carried out on the samples at saturation finally led to the change of the relevant mechanical properties as a function of moisture to perform numerical simulation : in-plane and out-of-plane shear moduli, through-thickness tensile behaviour versus various moisture contents.

Dry specimens have been tested for reference. Figure 6 shows the global behaviour of a 0° curved beam under tensile load. Finite element analysis and the failure mode observed in through-thickness tension allow to evaluate the interlaminar tensile strength.

Lastly, other curved specimens with 45° fabric orientation from their axis have been manufactured. They have been conditioned to be mechanically tested in tension before moisture saturation has been reached. The purpose of these experiments is to understand the influence of a moisture gradient on the structure behaviour. Indeed, the transmission will never be saturated during usual service life, but will be subjected to moisture gradients. So, experimental results and numerical simulations should lead to assessment of the behaviour of the component and the effect of moisture content on stress field or failure mode.

Again, dry specimens have been tested.

Data obtained on saturated specimens would be available to simulate the stiffness and strength properties of the curved specimens subjected to moisture gradients and complex

stress states. Finally, the future comparison of the numerical simulations to the experimental data, derived from the direct testing of curved specimens, would give offer a first glimpse of the reliability of this simple approach and would lead to a first assessment of the true effect of moisture gradients when complex stress states are dominating.
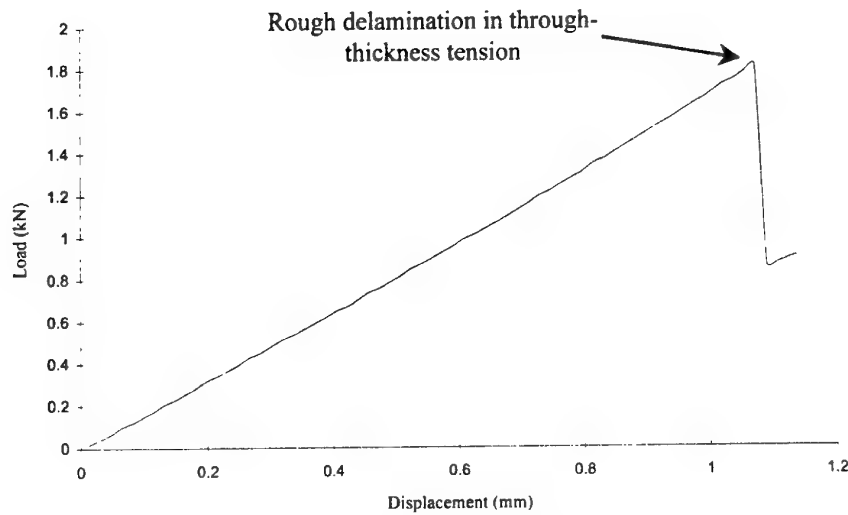
Fig 6 : Tension test of 0° curved beam specimen.

REFERENCE

Cerisier, F., Grédiac, M., Pierron, F., Vautrin, A., "Design of a locomotive transmission in composite materials", 3rd biennial joint conference on Engineering Systems Design and Analysis, 1996.

DURABILITY OF POLYMER MATRIX COMPOSITES : SOME REMARKS BY THE AMAC COMMITTEE ON DURABILITY

D. PERREUX[1,2]

[1]Commission durabilité de l'AMAC
[2]Laboratoire de Mécanique Appliquée. R.C
24 rue de l'Epitaphe - 25000 Besançon FRANCE.

ABSTRACT :

The French composite materials association (AMAC) has members from both the industrial and academic sectors. For many years, AMAC has been aware of the potential economic impact of the durability of composites, and especially on the development of the use of polymer matrix composites. To try to improve the situation, AMAC created a committee on durability in 1995, whose tasks were to study the problem and to propose ways to increase the publics knowledge of polymer matrix composites. In May 1998, the committee organised a meeting in Arcueil (France), which focused on the industrial concerns for polymer matrix composites durability.

This paper summarises the various problems discussed during this meeting. This paper does not present solutions to problems ; rather it reports the ideas expressed at the meeting which were aimed at the improving knowledge in the field of durability.

The durability problems discussed during the meeting were mainly centred on physico-chemical and mechanical aspects. In this paper, some of these aspects will be discussed, before presenting some problems which arise when both phenomena are coupled.

Effects of Microstructure on Damage Evolution, Strain Inhomogeneity, and fracture in a particulate Composite

C.T. Liu
Air force Research Laboratory
Ol-AC AFRL/PRSM
10 E. Saturn Blvd.
Edwards AFB CA 93524-7680, U.S.A

It is well known that a highly filled particulate composite material, on the microscopic scale, can be considered a nonhomogeneous material. Depending upon the degree of crosslink of the matrix material, filler particle size and distribution, and the bond strength at the interface of the particle and the matrix, the local stress and strength will vary in a random fashion. Therefore, when the material is strained, damage may develop in the material. The damage developed in the material may be in the form of microcracks or microvoids in the matrix or in the form of dewetting between the particle and the matrix. The damage will not be confined to a specific location; rather, it will diffuse into a relatively large area or zone. The growth of the damage in the material may take place by tearing of the material or by successive nucleation and coalescence of the microvoids. These damage processes are time-dependent processes, and they are mainly responsible for the time-sensitivity of the constitutive and crack growth behavior in these materials. Therefore, in order to gain an advanced understanding of the failure process in these materials, a detailed knowledge of deformation process, damage initiation and evolution mechanisms, and crack-damage interaction are required.

In this study, the strain fields within a 2 mm region near the crack tip in a particulate composite, containing hard particles embedded in a rubbery matrix, were determined using a digital image correlation technique. The specimen (Fig. 1) was subjected to a constant strain rate loading condition at room temperature. During the test, digital images were obtained at a given time interval, and they were analyzed, using a digital image correlation program, to determine the strain fields near the crack tip.

A plot of the iso- intensity principal strain contours is shown in Fig. 2 . The data is presented as maximum principal strain (MPS) rather than the usual components of the strain, because the crack opening and void formation depend on the local principal strains. In Fig. 2 , the crack is shown as the horizontal line with the crack tip at a location of x=0.4 mm and y = 1.25 mm (or 0.4mm, 1.25mm). The gray area surrounding the crack is the noise region in which the data can not be analyzed. This is because the digital image correlation program doesn't converge in places where new geometrical features appear. The cases of crack propagation and void formation are examples in which new features appear in the image and the digital image correlation program doesn't recognize the relationship between the features in the undeformed and the deformed images. Referring back to Fig. 2, it is seen that , starting at the crack tip, there is a broken thin

line that goes toward the right of figure, representing the future crack propagation path. Also, it is seen that the strain fields are highly nonhomogeneous and high strain regions are localized in the neighborhood of the crack tip. For example, the largest MPS, greater than 20%, is reached about 0.2 mm from the crack tip. In addition, there are several other high strain regions located near the crack tip. The average size of these high strain regions has a diameter of 400 microns. It is interesting to point out that the high strain region located at (1.4 mm and 1.3 mm) is the location where a void will develop as the applied far field strain (FFS) is increased.

A plot of the MPS concentration factor, defined as a ratio of MPS to FFS, along the crack plane as a function of the FFS is shown in Fig.3. From Fig. 3, the curves representing FFS of 1% to 4% fall very close to each other indicating that the distribution of MPS is fairly linear with the FFS . However, when the FFS level increases to 5% , a significant increase in MPS concentration factor occurs in a region between $x = 0.7$ mm and $x = 1.8$ mm. This phenomenon is probably due to the separation of the particle and the binder, resulting in a significant increase in MPS. When the FFS is continuously increased, eventually, a void is formed in this high strain region, and the crack advances by the coalescence of the crack tip with the void.

In the above paragraphs, we discussed the effect of microstructure on the strain distributions near the crack tip. In the following paragraphs, the damage mechanisms and the local fracture behavior in the immediate neighborhood of the crack tip are discussed.

When crack occurs, the high stress at the crack tip will induce high damage near the crack tip region. The high damage zone at the crack tip is defined as the failure process zone, which is a key parameter in viscoelastic fracture mechanics. Experimental data reveal that when the local strain reaches a critical value, small voids are generated in the failure process zone. Due to the random nature of the microstructure, the first void is not necessarily formed in the immediate neighborhood of the crack tip. The formation of the voids is not restricted to the surface of the specimen where the maximum normal strain occurs. Since the tendency of the filler particle to separate from the binder under a triaxial loading condition is high, it is expected that voids, or damage zones, will also be generated in the specimen's interior. Consequently, there are a large number of strands, which separate the voids and are essentially made of the binder material, that form inside the failure process zone. Under this condition, the transverse constraint is minimized. As the applied strain increases with time, material fracture would occur at the blunted end of the crack tip. The failure of the material between the void and the crack tip leads the crack to grow a short distance. In other words, the coalescence of the void and the crack tip leads the crack to grow into the failure process zone. This kind of crack growth mechanism continues until the main crack tip reaches the failure process zone tip. When this occur, the crack tip resharpens temporarily.

In this study, the damage field near the crack tip in a cracked sheet specimen subjected to a constant strain rate of 1.0 min^{-1} was investigated using the real-time x-ray technique. The specimen was made of the same particulate composite material as used in the crack propagation test. Prior to testing, a 23 mm crack was cut at the center of the specimen with a razor blade. During the test, Lockheed-Martin Research Laboratory's high-energy real-time x-ray system (HERTS) was used to investigate the characteristics of the damage field near the crack tip.

The recorded x-ray data were processed to create a visual indication of the energy absorbed in the material. A region of high absorption (i.e. a low damage area) will be shown as a dark area, whereas a region of low absorption will produce a light or white area, with 254 shades of gray in between. Also, the x-ray image at a given applied strain level can be plotted in the from of iso-intensity contours of the transmitted x-ray energy to enhance the resolution of the damaged field.

Figure 4 shows the contours of transmitted x-ray energy near the tip of a propagating crack under the constant strain rate condition. In this figure, the number between two contour lines is the minimum intensity level of a range of I_t between the minimum intensity level and the next intensity level. A small number indicates that the intensity of the transmitted x-ray energy is high or that the damage is high. These contour plots show the details of the size and shape of the damage zone as well as the damage intensity inside the damage zone.

In conclusion, the heterogeneity of the microstructure plays a key role for local damage and strain distributions near the crack tip. Experimental results indicate that the high strain field is localized within 1 mm of the crack tip. Also, the real-time x-ray technique is a promising technique to monitor damage initiation and evolution processes.
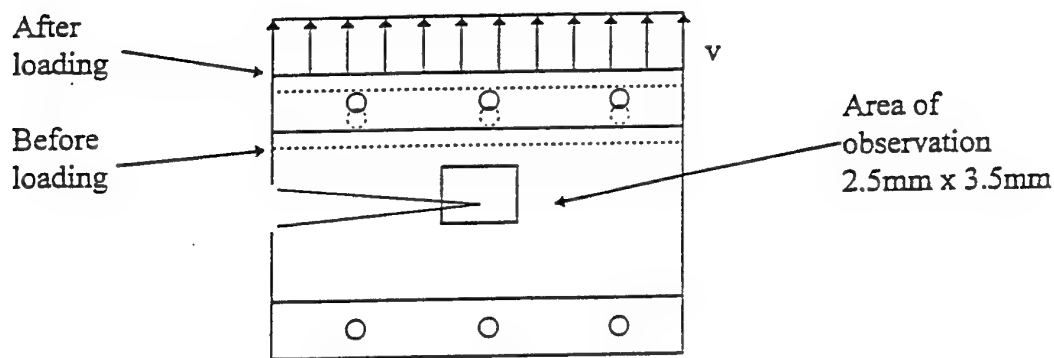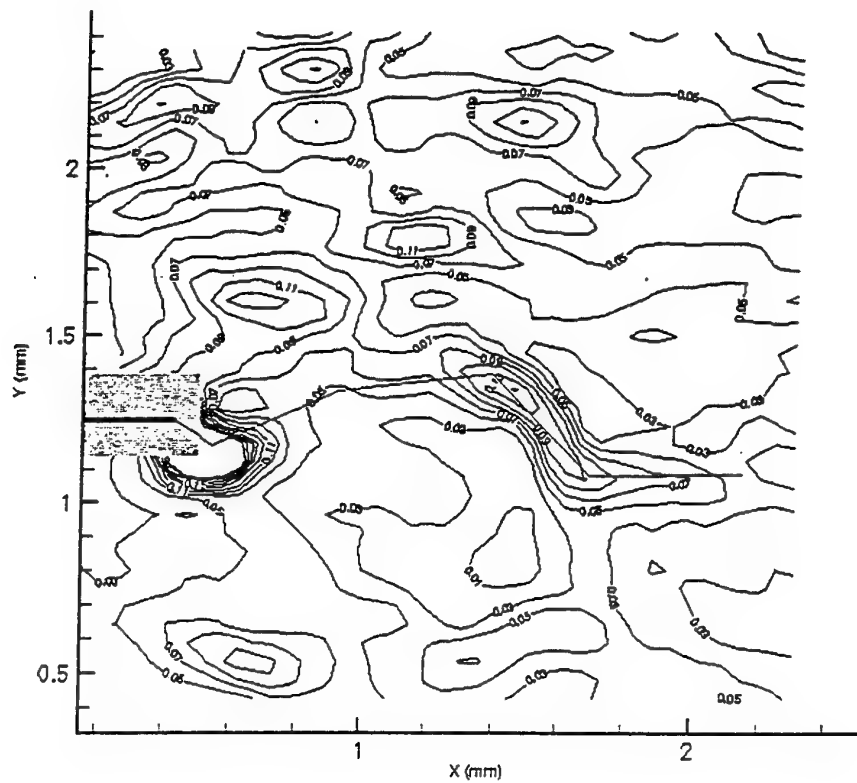
Fig. 1   Specimen geometry.

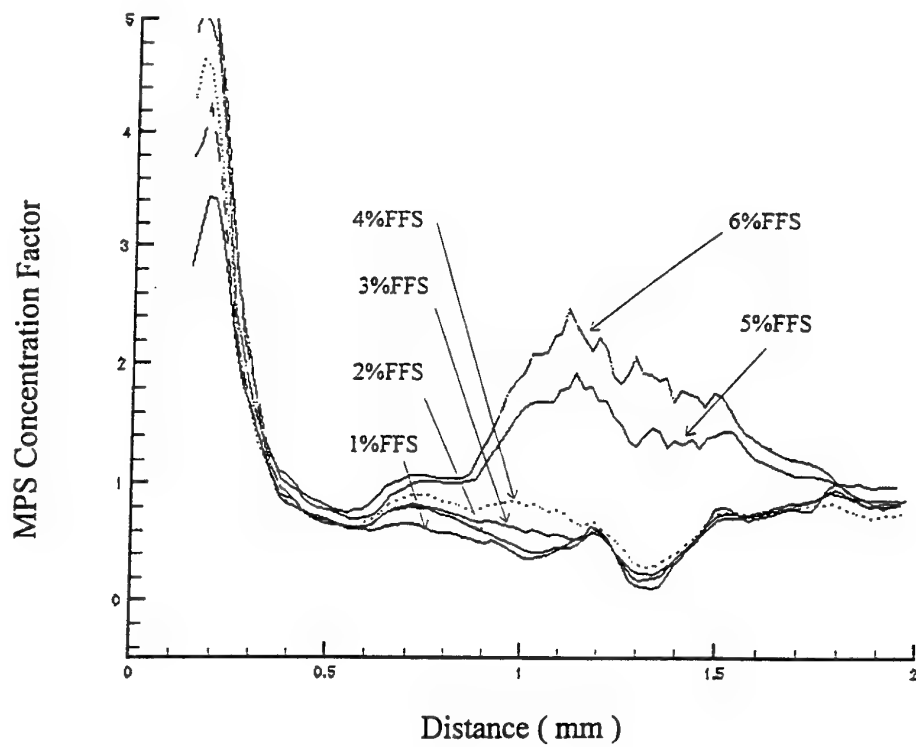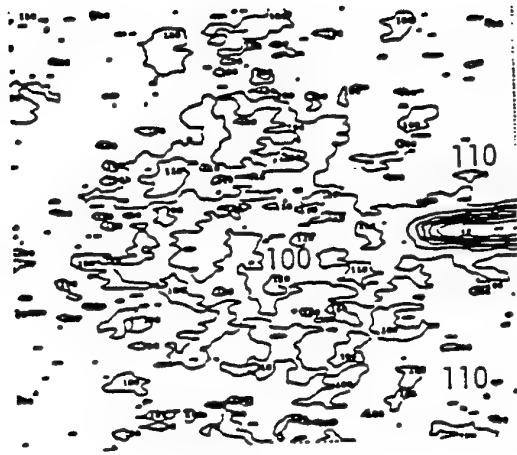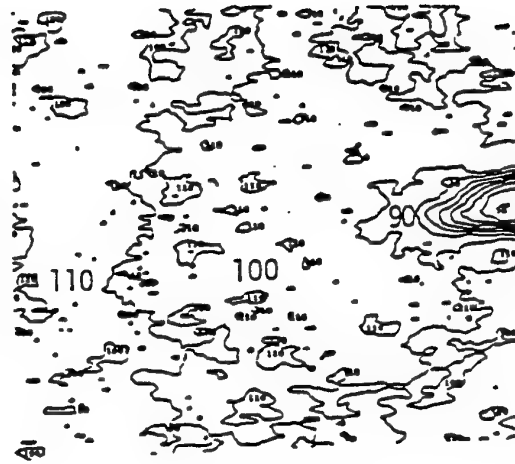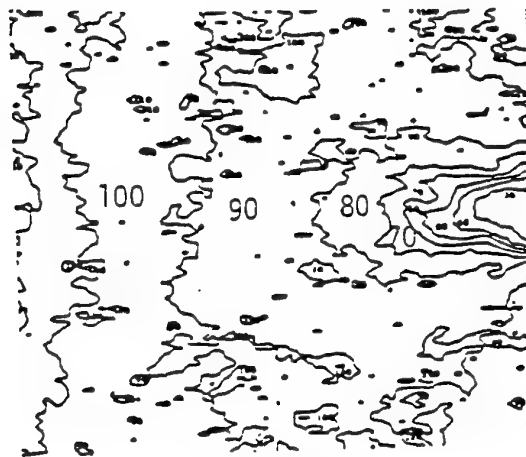Fig. 2   Maximun principal strain at 6% applied strain

Fig. 3   Maximum principal strain concentration factor
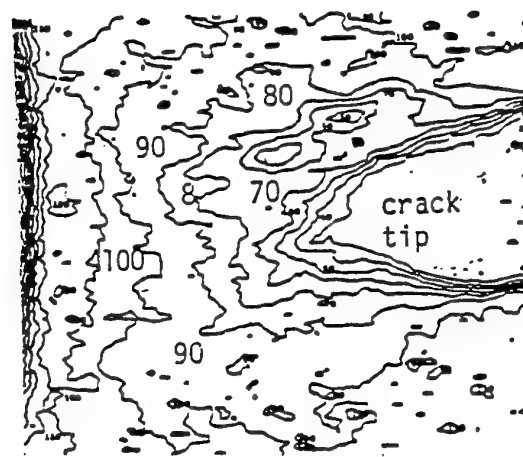along the crack plane.

(a) $\epsilon = 3\%$

(b) $\epsilon = 6\%$

(c) $\epsilon = 9\%$

(d) $\epsilon = 12\%$

Fig. 4   Iso-intensity contour plots of I_t near the crack tip.

The damping and dynamic moduli of fibre reinforced polymer composites after exposure to hot, wet conditioning

R.D. Adams
Department of Mechanical Engineering, University of Bristol, Bristol, BS8 1TR

M.M. Singh
Department of Engineering Materials, University of Southampton, Southampton, SO17 1BJ

ABSTRACT: Several polymer matrix composites were exposed to steam at 100°C to provide accelerated ageing. Moisture uptake, shear modulus, damping and interlaminar shear strength were correlated to provide a means of nondestructively evaluating the moisture-induced degradation.

INTRODUCTION

Fibre-reinforced polymer composites are widely used in aerospace applications, and are increasingly finding a place in the automotive and sports industries. Among their attractions are their resistance to corrosion, and their inherently good vibration damping properties, which can be designed into a composite structure, avoiding the use of 'add-on' damping treatments. In wet of humid conditions, however, these materials absorb water which has a plasticising effect on the matrix and causes a loss in the mechanical performance. The extent of this loss depends on the nature of the polymer, as well as on the hygrothermal loading history. To assess the durability of polymer composite components, lengthy experiments are required; if accelerated testing is used, the validity of extrapolating the results to in-serve conditions is always questionable. A means of assessing the integrity of a composite component nondestructively, while in service, so that it can be replaced before failure, is highly desirable, and would allow designers to turn to composites with greater confidence. Since damage and degradation of fibre-reinforced polymers are often not clearly manifest on the surface, visual inspection is usually insufficient and more sophisticated methods are required.

Measurements of modulus and damping capacity derived from vibration tests have been used as a nondestructive evaluation tool. One of the objectives of this work was to investigate the usefulness of such measurements for the nondestructive assessment of moisture-induced degradation of the mechanical performance of fibre-reinforced polymers. Further, changes in the macroscopic mechanical properties reflect changes to the microstructure, and insight into the mechanisms of moisture uptake in composites can be gained from studying the effects of moisture and temperature on the overall dynamic response of relatively large specimens.

MATERIALS

A number of polymer composites was studied: these were three different carbon-fibre-reinforced epoxy resins, a glass-fibre-reinforced epoxy, and carbon-fibre-reinforced PEEK (poly(ether ether ketone)). The epoxy resins were thermosetting, brittle resins, such as are now common as matrix materials in composites used in the aircraft industry. PEEK, however, is an aromatic thermoplastic resin, which has recently gained popularity because of its stability in hot, wet environments, its relative ease of component manufacture, and the potential for recycling and reusing the material.

ENVIRONMENTAL CONDITIONING

Steam was chosen as a suitably aggressive environment for this work. At higher temperatures and high humidity, some fibre-reinforced polymers exhibit non-Fickian diffusion, which may be ascribed either to structural damage in the form of micro-cracks, or to hydrogen bonding of the water
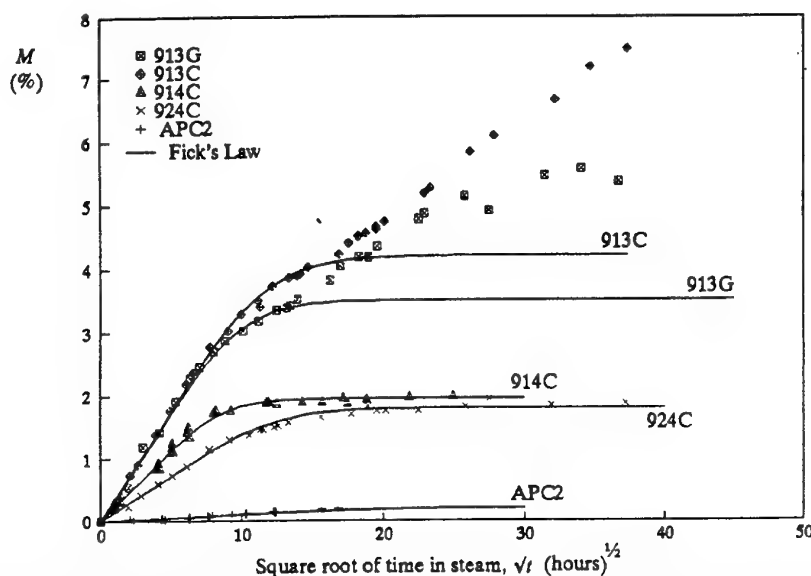
1

Fig. 1. Percentage mass increase for the five composite materials as a function of the square root of time in steam.

molecules to the polymer. The combination of temperature and relative humidity at which non-Fickian behaviour occurs depends on the resin system. Because one aim of this study was to explore the possibilities of using changes in the dynamic properties as the basis of nondestructive evaluation of mechanical degradation, it was of interest to attempt to damage some of the specimens. Although, because of their known response to such environments, fibre-reinforced composite components are unlikely, in practice, ever to be subjected to steam, 100% relative humidity at 100°C provides the worst possible conditions at atmospheric pressure. The high temperature and humidity also ensured a relatively short time to reach equilibrium moisture levels. Steam was chosen in preference to boiling water, to avoid uncertainties arising from leaching of constituents into the water.

EXPERIMENTAL METHODS

The dynamic shear properties of all the materials were determined at intervals during conditioning of the specimens in steam, in hot air and during recovery. To find the longitudinal shear modulus and the corresponding loss factor, a torsion pendulum was used.

RESULTS AND DISCUSSION

Moisture absorption

The percentage mass increase for the five composite materials is shown as a function of the square root of time in steam in Fig. 1. The lines on Fig. 1 represent the curves for Fickian diffusion that most nearly fit the experimental data.

The diffusion parameters, D and M_∞ were determined by an iterative method and are presented in Table 1.

Collings[1] derived empirical relationships to predict the values of D and M_∞ for the carbon-fibre-reinforced composites 913C, 914C and 924C, under varying conditions of relative humidity and temperature. The predictions for these materials at 100°C and 100% relative humidity are also given in Table 1.

It is clear that the diffusion parameters of the 914C and 924C materials are reasonably well predicted. From Fig. 1, it can be seen that the 914C, 924C and APC2 materials exhibited essentially Fickian behaviour, even under these extreme conditions. It is, perhaps, worth noting that conditions of 70°C and 85% relative humidity are now chosen as the standard for conditioning aerospace materials.

Collings' empirical relationships for these conditions would predict a saturation moisture content of 1.47% for 914C and 1.14% for 924C, somewhat lower than observed at 100°C and 100% relative humidity.
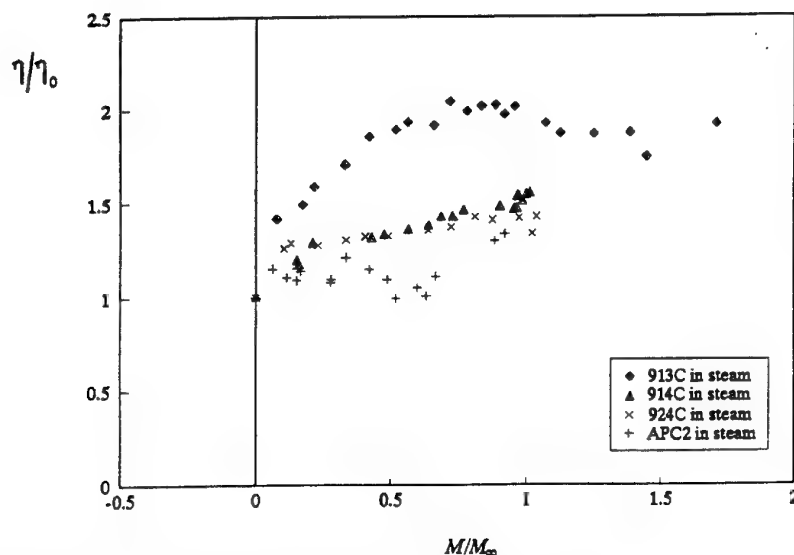
2

R.D. Adams, M.M. Singh

Fig. 2. Change in the longitudinal shear loss factor, η, as a function of M/M∞

Table 1. Measured diffusion parameters of fibre-reinforced composites and unreinforced matrix resins exposed to steam. 1R = RAE predictions.

Material	M_∞ (%)	D_c (mm^2 s^{-1})
913G, 0°	3.45	1.90 x 10^{-6}
913C, 0°	4.20	1.16 x 10^{-6}
913C^{1R}	2.26	2.2 x 10^{-6}
914C, 0°	1.95	1.77 x 10^{-6}
914C^{1R}	1.95	1.5 x 10^{-6}
924C, 0°	1.80	0.80 x 10^{-6}
924C^{1R}	1.52	0.98 x 10^{-6}
APC, 0°	0.21	0.34 x 10^{-6}
913 unreinforced	8.54	2.15 x 10^{-6}

Effect on loss factor

To compare more directly the behaviour of the 5 different composites and the unreinforced resin, the change in the longitudinal shear loss factor, η, of all the materials has been plotted as function of M/M_∞, which is a measure of how close the moisture content is to the saturation level (Fig. 2). The change in loss factor is defined by η/η_0 where η_0 is the value of the dry material before moisture conditioning. Each point represents the average of the values obtained. Initially, three specimens were tested each time, then two, when the first specimen was removed for drying, and finally, only one specimen, in the last stages of conditioning when the second specimen had been removed for drying.

The extent of the influence of the matrix on the shear loss factor is illustrated by the difference between the loss factors of the reinforced epoxies and that of the carbon-fibre-reinforced thermoplastic, APC2. Whereas all the fibre-reinforced epoxies had an initial loss factor in the region of 0.013, that of the APC2 was only one third of this, about 0.004. Even the APC2, however, showed a slight increase in loss factor with absorbed moisture, although the quantity of water was only about 10% of that absorbed by the epoxies (see Table 1). The observed scatter in the results for the APC2 is due to the fact that the loss factor is so small, so that small changes due to experimental error cause relatively large fluctuations in the ratio η/η_0.

All the epoxy composites experienced an initial sharp increase in loss factor, followed by a more gradual increase with rising moisture content, as shown in Fig. 2. The carbon-fibre-reinforced 914 and 924 resins behaved in an almost identical manner, but the 924C demonstrated a sharper initial increase in loss factor than the 914C. The 913 composites experienced a greater increase in loss factor than the other composites. A stage was reached, however, when the loss factor became almost constant as the moisture level approached the saturation level, and then was reduced again as the moisture content increased further, when it can be assumed that the moisture uptake was no longer predominantly by diffusion. The glass transition temperatures, T_g, of the 913, 914 and 924 resins are given by Ciba-Geigy as 131, 180 and 190°C, respectively. Absorbed moisture in polymers is known to lower the glass transition temperature[2, 3] and the larger increase in loss factor of the 913 composites may be due to the reduction of the matrix T_g, even though all measurements were made at 20°C, well below the dry T_g of all the materials.
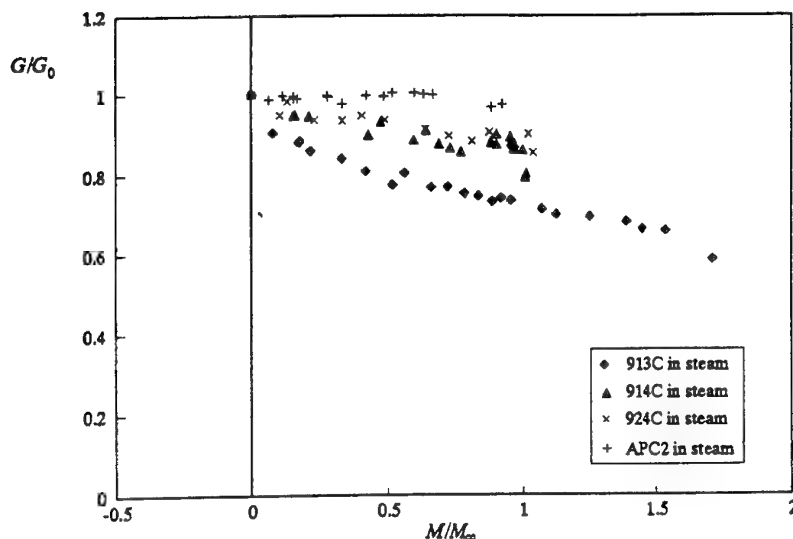
3

Fig. 3. Change in shear modulus, G/G_0, during moisture uptake as a function of M/M_∞
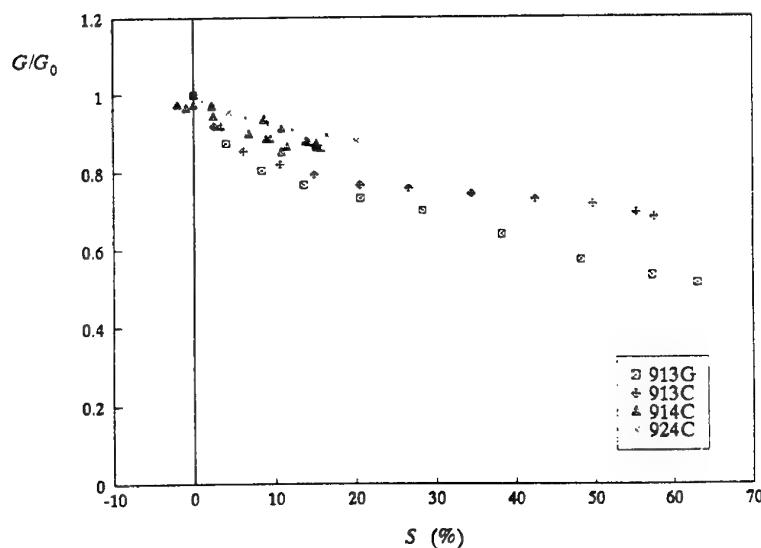

Fig. 4. Changes in the shear modulus of the epoxy composites as a function of the loss in ILSS, S.

Effect on longitudinal shear modulus

The change in shear modulus G/G_0, of the six materials during moisture uptake is shown as a function of M/M_∞ in Fig. 3. Once again the order of degradation was the same: the APC2 was least affected, the 914C and 924C materials (which had a similar response), the unreinforced, carbon-fibre-reinforced and glass-fibre-reinforced 913 followed in that order. The greater loss of modulus of the 913 composites than of the plain resin could be due to the gross damage in the form of delamination and due to

changes in the interface or interphase between the fibres and the matrix that cannot occur in the unreinforced polymer.

Correlation of dynamic shear properties with the loss of ILSS

In Figs 4 and 5, the changes in the shear modulus and in the loss factor, respectively, of the epoxy composites are shown as a function of the loss in ILSS, S, expressed as a percentage of the initial preconditioning strength.
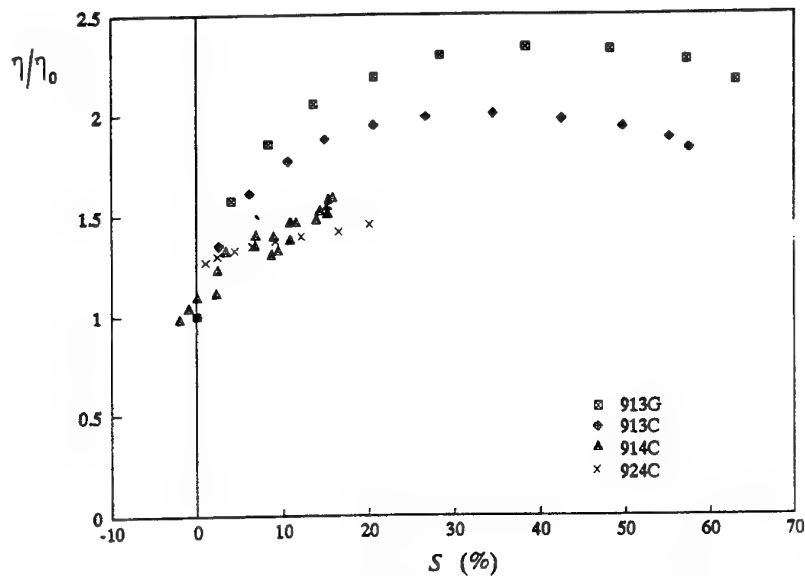
4

R.D. Adams, M.M. Singh

Fig. 5. Changes in the loss factor of the epoxy composites as a function of the loss in ILSS, S.

Thus S is given by:

$$S = \frac{ILSS_0 - ILSS_M}{ILSS_0} \times 100\% \quad (1)$$

where $ILSS_0$ and $ILSS_M$ are the interlaminar strength initially and at a moisture content M, respectively. Figure 4 shows that, for all these composites, there was a strong correlation between the dynamic shear modulus and the loss in interlaminar shear strength, the larger was the reduction in shear strength, the greater was the fall in shear modulus. The loss factor was more sensitive to the loss in strength (Fig. 5), but for the 913C and 913G materials, which continued to experience a fall in shear strength with prolonged exposure to steam, the loss factor levelled out at high moisture contents. This means that, for these materials, the loss factor was a less useful gauge of the strength of the material. For the 914C and 924C materials, both the loss factor and the longitudinal shear modulus were indicators of the material strength. Modulus measurements are, therefore, better as a nondestructive indication of the interlaminar shear strength of a hydrophilic composite material than are loss factor measurements.

CONCLUSIONS

Samples of several fibre-reinforced epoxies and fibre-reinforced PEEK were exposed to steam. The moisture absorption characteristics, longitudinal shear modulus and loss factor, and the interlaminar shear strength were monitored, with a view to assessing the feasibility of the use of dynamic measurements as a nondestructive tool for determining the structural integrity of polymer composites degraded by moisture. The degree of damage inflicted by steam depended on the type of polymer matrix. Epoxy resin reinforced with glass fibre was more degraded than when reinforced with carbon fibre, suggesting that the interphase plays a role in the response to moisture conditioning. The longitudinal shear modulus was found to be a reliable indicator of the interlaminar shear strength of polymer composites. Changes in the shear loss factor were more sensitive to the loss of interlaminar shear strength, but were less useful for extremely hydrophilic materials.

REFERENCES

1. Collings, T.A., *Environmental Structural Testing*, Royal Aerospace Establishment, Technical Report TR 880683 (CRAG Report), 1988.

2. Carter, H.G. & Kibler, K.G., Langmuir-type model for anomalous moisture diffusion in composite resins. *J. Comp. Mater.*, **12**, pp. 118-131, 1978.

3. McKague, L., Environmental synergism and simulation in resin matrix composites. *Advanced Composite Materials – Environmental Effects*, ASTM STP 658, ed. J.R. Vinson, pp. 193-204, 1978.

5

R.D. Adams, M.M. Singh

MODELLING OF COMPOSITE INTERFACES SUBJECT TO THERMAL STRESSES AND PHYSICAL AGING

D.-A. Mendels, Y. Leterrier, and J.-A. E. Månson[*]

Laboratoire de Technologie des Composites et Polymères (LTC)
Ecole Polytechnique Fédérale de Lausanne (EPFL)
CH-1015 Lausanne, Switzerland

*: to whom correspondence should be addressed.

INTRODUCTION

On cooling from above to below the glass transition temperature, which is the case in most processing operations, amorphous polymers depart from thermodynamic equilibrium. The subsequent slow evolution of the polymer towards equilibrium has been shown to significantly affect its mechanical properties, by a process known as physical aging (Struik, 1978). This mechanism is also active in polymer matrices used in fibre reinforced structural composites. However, in the composite, the homogeneous stress state usually found in the neat polymer is radically modified by the internal stress state of the matrix, as well as by additional stress resulting from loading of the composite structure (Mendels et al., 1999). The influence of local stress concentrations at the fibre/matrix interface on the structural recovery and aging of the polymer is still unclear, although it has been assessed that structural recovery profoundly changes the viscoelastic response of the polymer (McKenna et al., 1995). Such phenomenon hampers the analysis of the failure of composites, controlled to a large extent by the interface strength. The present work investigates how interfacial properties are modified upon physical aging. First, the micro-mechanics of the interface and their evolution upon aging are studied through the microbond test. Second, this theory is coupled to that of the energy release rate and their equivalence is assessed by experimental investigation.

MODELLING OF THE INTERFACIAL SHEAR STRENGTH FOR THE MICROBOND TEST

The microbond test has been extensively used to assess the shear strength of polymer/fibre interfaces. In this test, the interfacial shear strength is determined from the force required to debond a droplet of cured resin on an individual fibre. In a recent work, the classical analysis of the test has been modified from a novel elastic stress transfer model (Mendels et al., 1999), using two different approaches: by introducing the exact droplet profile into the analysis, or by using a cylinder of equivalent length and volume to the droplet. The former requires numerical integration, and provides an insight into the commonly observed cone of debonding phenomenon, whereas the equivalent cylinder model results in an analytical formulation. These two approaches were shown to be equivalent and result in the determination of the same interfacial shear stress (Figure 1).

The analytical expression of the experimental interfacial shear strength τ_{exp} is used in the present study to compare interfacial regions subjected to different levels of internal stresses, such as those resulting from physical aging (Chambers et al., 1989):

$$\tau_{exp} = \tau_0 \frac{\tanh(\beta L)}{\beta L} - K \frac{\tanh(\beta L/2)\tanh(\beta L)}{\beta L}, \text{ with } \beta = \left[\kappa\left(a^2 E_f + \left(b^2 - a^2\right)E_m\right)\Big/ aE_f\left(1 + \nu_m\right)\right]^{1/2} \quad (1)$$

$$\text{and } \kappa = \frac{12.\left(2(b-a) + \xi\left(b^2 - a^2\right)\right)}{a\left\{24a\left(b^2 - a^2\right) - 16\left(b^3 - a^3\right) - 3\xi\left(a^2 - b^2\right)^2 + 6b(2 + \xi b)\left[2b^2 \ln\left(b/a\right) - \left(b^2 - a^2\right)\right]\right\}} \quad (2)$$

The parameter β is determined from the elastic properties of the system (fibre and matrix moduli E_f and E_m) and from its geometry (fibre and matrix radii a and b)(Mendels et al., 1999), τ_0 is the intrinsic shear strength, and K the internal stress parameter as detailed in the following section.

EFFECT OF AGING ON INTERFACIAL STRENGTH

A DGEBA epoxy resin (Dow Chemicals DER332) was cured 24 hours at 100°C with a diamine (Jeffamine D400) in a stoechiometric amount, with a resulting glass transition temperature T_g of 42.1°C, as measured by Differential Scanning Calorimetry (heating rate 20°C/min). Casted coupons were first annealed 2 hours at 70°C, then quenched to the aging temperature (37.0°C), aged isothermally, and finally tested at room temperature in relaxation under a constant tensile strain of 1%. The relaxation modulus of the epoxy network is shown in Figure 2 as a function of aging time, and described by a KWW type model (Lee et al., 1989). This type of representation is used to obtain the time – aging time shift factor a_{te}, as well as the aging rate (Struik, 1978).

E-glass fibres with a γ-APS (OSI Specialties aminosilane 1100) surface treatment, and Young modulus of 70 GPa were used. Epoxy droplets were cured on fibres, and aged according to the above procedure. The microbond test was performed on both quenched droplets and droplets aged 4320 min at 37°C.

A marked increase of 40% in τ_{exp} is found upon aging, which is attributed to the presence of internal stresses and the densification of the matrix. To clarify this considerable increase, internal stresses were calculated according to:

$$K = K_\infty + \left(K_0 - K_\infty\right)\exp\left(-(t/\tau)^\lambda\right), \text{ with } \tau = \tau_r a_T a_{te}(\sigma) \text{ and } K_0 = a\alpha E_f\left(\alpha_m - \alpha_f\right)\Delta T/2 \qquad (3)$$

where K_0 is the thermo-elastic stress, K_∞ the relaxed stress, a_T the time-temperature shift factor, a_{te} the time-aging time shift factor introduced earlier, τ_r the reference relaxation time, t_e the aging time, and σ involves the stress dependence of the aging process (Lee et al., 1989). The exponent λ accounts for the width of the distribution of relaxation times in a classical KWW stretched exponential formalism, and was found to be equal to 0.33±0.04 from the relaxation tests depicted in Figure 2. The resulting simulation shown in Figure 3 compares well with the experiment, and allows the determination of an unique τ_0 value, independent of aging time, and equal to 22.1±0.2 MPa.

This interesting finding, which indicates that physical aging does not change the intrinsic properties of the interfacial region, needs to be further investigated. To this end, the energy release rate approach is used as an alternative and detailed in the following section.

ENERGY RELEASE RATE FORMULATION

The energy release rate at the interface is derived from Equations (1) & (2), combined with the analysis introduced by Liu & Nairn (1999), who devised the limiting energy release rate G_∞ as a function of the droplet length L, taken as crack length. To do so, the equivalent cylinder is taken as infinite to get free of the singularity existing when the crack length equals the embedded length (Figure 4). One obtains:

$$G_\infty(L) = \frac{a}{2}\left[C_{33s}\left(\sigma_d - kL\right)^2 + D_{3s}\left(2\sigma_d - k\left(2L - \frac{1}{\beta}\right)\right)\Delta T + \left(\frac{D_3^2}{C_{33}} + \frac{v_m\left(\alpha_T - \alpha_m\right)^2}{v_f A_0}\right)\Delta T^2\right] \qquad (4)$$

where σ_d is the debond axial stress, obtained from the peak force in the force displacement plot, k is the frictional stress transfer rate parameter detailed later, α_T and α_m are the respective coefficients of thermal expansion (CTE) for fibre and matrix, and ΔT is the difference between glass transition (freshly cured samples) or aging (aged samples) temperature and the

ambient. The factor β in this analysis is taken from the previous model (Eq. (1) & (2)), and therefore corresponds to the equivalent cylinder stress transfer parameter, v_m and v_f are respectively the matrix and fibre volume. The other coefficients are obtained using the following equations, in which subscripts A, T stand for axial and transverse directions:

$$A_0 = \frac{v_m(1-v_T)}{v_f E_T} + \frac{1-v_m}{E_m} + \frac{1+v_m}{v_f E_f}; \quad A_3 = -\left(\frac{v_A}{E_A} + \frac{v_f v_m}{v_m E_m}\right) \tag{5}$$

$$C_{33} = \frac{1}{2}\left(\frac{1}{E_A} + \frac{v_f}{v_m E_m}\right) - \frac{v_m A_3^2}{v_f A_0}; \quad C_{33s} = \frac{1}{2}\left(\frac{1}{E_A} + \frac{v_f}{v_m E_m}\right) \tag{6}$$

$$D_3 = -\frac{v_m A_3}{v_f A_0}(\alpha_T - \alpha_m) + \frac{1}{2}(\alpha_A - \alpha_m); \quad D_{3s} = \frac{1}{2}(\alpha_A - \alpha_m) \tag{7}$$

By expressing the frictional stress as coulombian we let the frictional parameter k does account for lateral shrinkage upon cure and further shrinkage during cooling to the test temperature, and during aging. To do so, the radial shrinkage is introduced following the two concentric cylinders approach, and assuming that Poisson's effect are negligible (see for example Timoshenko and Goodier, 1970).

In the present section, the previous experimental results analysed through the interfacial shear strength criterion are used. Interestingly, it was found that the average friction estimated from the experimental data after debonding closely match that determined using least squares with minimising the standard deviation on G_∞. Under these conditions the energy release rate is determined following several stress levels, as shown in Figure 5. These stress levels were calculated for the thermo-elastic case or including their relaxation upon aging, using an expression similar to Equation (3).

Due to the high CTE of the epoxy matrix, important internal stresses are developed. Neglecting the relaxation of these stresses would lead to large overestimation of G_∞. Similarly, one would also determine a considerable decrease in G_∞ upon aging, which would contradict the previous strength analysis. This paradox is resolved by introducing the relaxation of internal stresses into the analysis, leading to a close match, with $G_\infty = 262 \pm 14$ J/m^2 (unaged), versus $G_\infty = 266 \pm 10$ J/m^2 (aged). This analysis therefore yields the same results as the preliminary one, which is that physical aging does not modify the intrinsic properties of the interface, rather, it modifies the relaxation rate of process-induced internal stresses.

Although this study only considered mode II failure of the interface, the results should be of a broad significance also for other failure modes, and therefore relevant for composite laminates.

CONCLUSIONS

Two methods for analysing the microbond test were presented, namely the interfacial shear strength and the energy release rate analyses. These methods were tested in the case of freshly cured and aged epoxy droplets on glass fibres, and were shown to yield similar results. In the peculiar case of the model system chosen, no changes of the intrinsic mechanical properties of the interface are found upon structural recovery of the polymer. This result is obtained providing that the relaxation of internal stresses, and the shift of relaxation times of the matrix when it is physically aged is accounted for. This coupling between structural recovery and stress relaxation appears to be critical in describing the behaviour of the model composite system considered, when both analyses are carried out.

REFERENCES

Chambers, R.S., F.P. Gerstle, S.L. Monroe, J. Am. Cream. Soc., 1989, **72**, p. 929-932.

Lee, A. and G.B. McKenna, Polymer, 1989. **31**: p. 423-430.

Liu, C.-H. and J. A. Nairn, Int. J. Adh. Adhes., 1999, **19**: p. 59-70.

McKenna, G.B., Y. Leterrier, C.R. Schultheisz, Polym. Eng. Sci., 1995, **35**, 403-410.

Mendels, D.-A., Y. Leterrier, and J.-A.E. Månson, in press in J. Compos. Mater., 1999.

Struik, L.C.E., *Physical Ageing in Amorphous Polymers and Other Materials*. 1978, Elsevier.

Timoshenko, S.P., Goodier, J.N., *Theory of Elasticity*, 1970, McGraw-Hill.
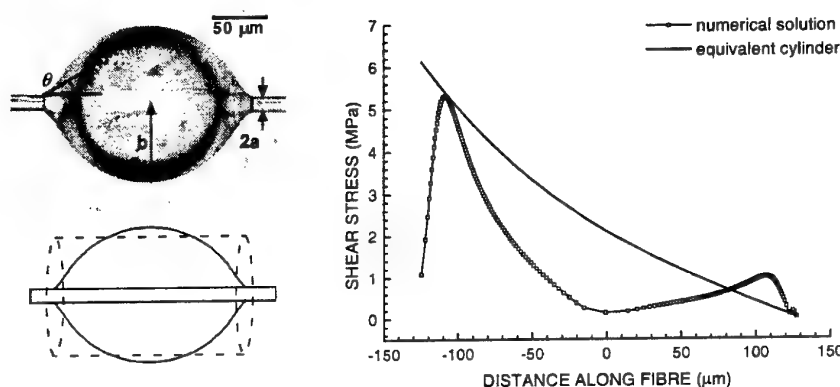
Figure 1: droplet and its simulated profile, and shear stress along droplet interface
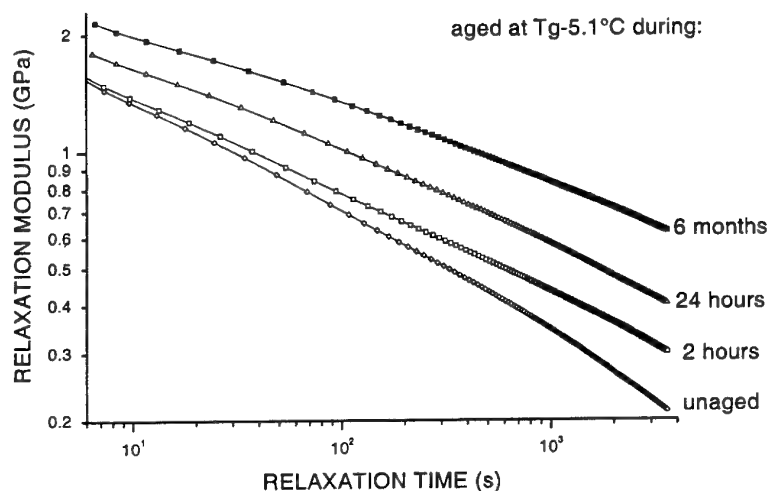
Figure 2: relaxation modulus of the epoxy network at 20°C after aging at Tg-5.1°C up to 6 months
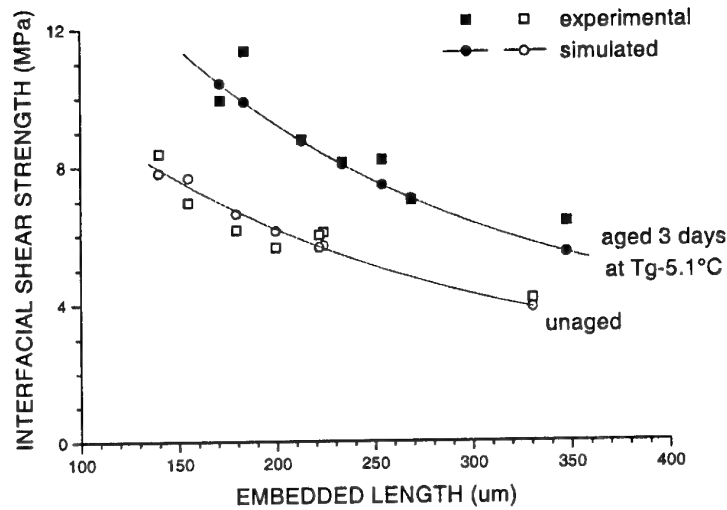
Figure 3: comparison between experimental and simulated IFSS vs. embedded length
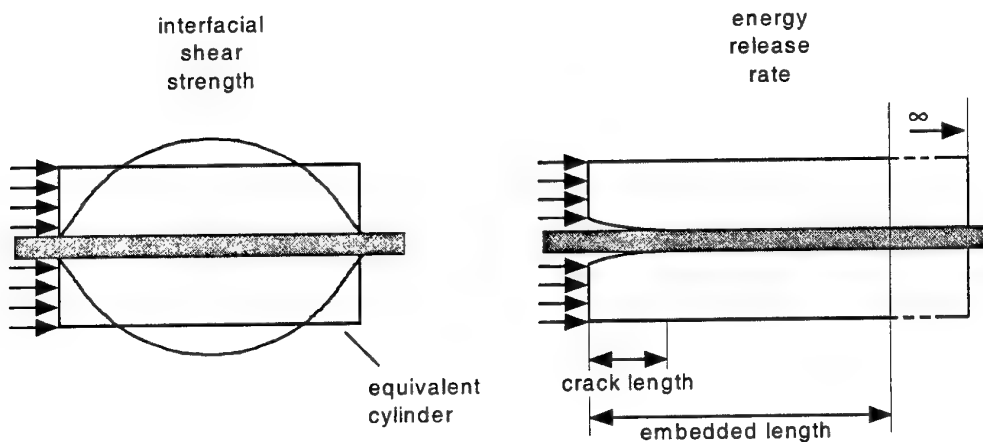

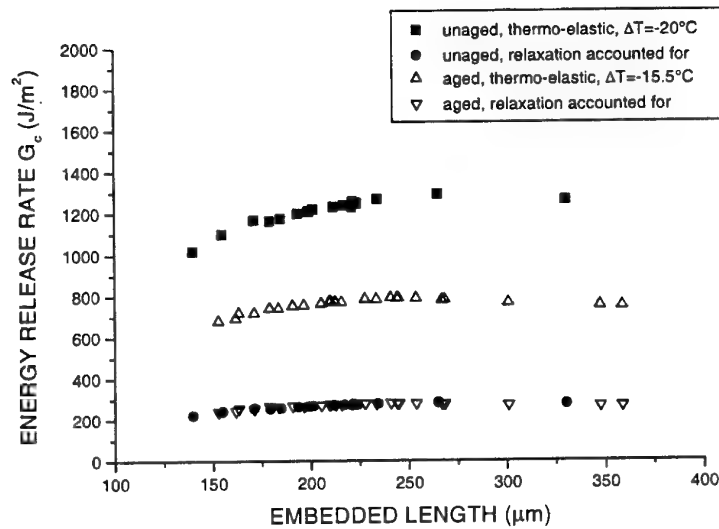*Figure 4: interfacial shear strength vs. energy release rate approach*

Figure 5: Effect of internal stress level on R-curves (Coulombian friction is accounted for)

Accelerated evaluation of environmental ageing monitored by fatigue crack growth experiments

Volker Altstädt, Sven Keiter, Michael Renner
Technical University Hamburg-Harburg, Polymer Engineering, Hamburg, Germany

Alois Schlarb
Braun Medical AG, Escholzmatt, Switzerland

ABSTRACT: This article describes fatigue crack growth experiments to investigate the degradation of the durability of polymers due to fluid environments. The degradating effect of media causing stress cracking can be observed on the fracture surfaces of tested samples by scanning electron microscopy. Strategies to improve environmental stress cracking like changes in molecular weight, orientation, toughening with rubber particles of different sizes are discussed. Fatigue crack growth experiments can be employed as a very fast and effective screening method.

1 INTRODUCTION

Fatigue crack propagation (FCP) experiments can be employed as a fast and effective screening method for determining long-term mechanical properties of polymers. Advantages of this method, like the need for a very small quantity of test material (<10 g), the broad range of fatigue crack propagation rates (from 10^{-2} mm/cycle to 10^{-7} mm/cycle) measured within one specimen and a well defined stress state at the crack tip favor the use of FCP experiments instead of traditional S-N curves (Altstädt & Loth & Schlarb 1995). These experiments can also be conducted in the presence of a specific environment and are able to provide valuable information about environmental effects on crack propagation.

If the FCP experiment is carried out in the presence of a critical fluid environment, a more or less progressive degradation of mechanical properties (embrittlement) depending on the polymer can be observed. This degradation is caused by enhanced disentanglement and chain scission of the molecules affected by a solving liquid. The process is called environmental stress cracking (ESC). ESC is defined as the simultaneous action of stress and contact with specific fluids. Approximately 15% of all failures of polymer components are due to ESC. Since prediction in many cases is exceedingly difficult, assessment through suitable laboratory tests becomes important (Kambour 1973). Standard tests for environmental stress cracking of polymers are the *Ball or Impression Method* (ISO 4600), the *Bent Strip Method* (ISO 4599) and the *Constant Tensile Stress Method* (ISO 6252).

In these standards either a constant static load or a constant deformation is applied. In the case of the bent strip method and the impression method the residual strength is quantified through a succeeding impact or tensile test. This, however, does not imply that the stress state at the crack tip in the moment of failure is well defined. Moreover, the common standardized test methods do not consider a well defined stress state within the test specimen. This could be achieved by applying the principles of linear elastic fracture mechanics to ESC test procedures in combination with a Compact Tension (CT) specimen. In contrast to tensile or impact tests, the stress state at the crack tip of a CT-specimen is well defined. A specific fluid is able to penetrate to the front of the crack tip. Under cyclic loading the propagation of a fatigue crack through the bulk material of the CT-specimen is affected by the presence of the fluid. From the dynamics of crack propagation an information about the interaction between the crack tip, designated as a microscopically small probe, the fluid environment and the ESC sensitivity of a specific polymer, polymer blend or polymer composite can be achieved.
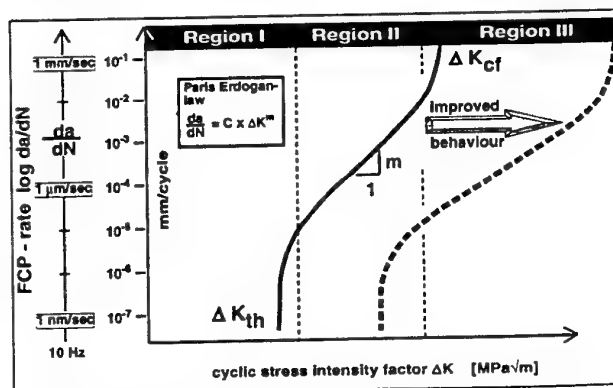

Figure 1. Scheme of a fatigue crack propagation diagram

1.1 Fatigue crack growth

All fatigue failures in polymers or polymer composites involve one phase in which a defect zone such as a craze or microcrack initiates, followed by a propagation phase to final fracture. Based on the assumption, that the fatigue lifetime is determined by the propagation phase, a preexisting flaw is assumed. The stress state at the tip of the crack is defined by the stress intensity factor range ΔK. For the case of fatigue, Paris (1964) showed, that a linear relationship predicted by a simple power law for a double logarithmic scale exists between the FCP rate da/dN and the applied ΔK (Figure 1).

The linear dependence is frequently observed only over an intermediate range of growth rates. When investigating a wide range of da/dN, deviations from this linear behavior may be observed, as illustrated schematically in Figure 1. That is, FCP-rates decrease rapidly to vanishingly small values as ΔK approaches the threshold value ΔK_{th}. This ΔK level defines a design criterion that is analogous to the fatigue limit determined from traditional S-N curves (Hertzberg 1980, Janzen 1991). FCP rates increase markedly as ΔK approaches K_{cf}, at which unstable fracture occurs within one loading cycle. From the standpoint of evaluating a materials fatigue resistance, any decrease in FCP rates at a given value of ΔK or, alternately, any increase in ΔK to drive a crack at a given speed is, of course, beneficial.

As shown in Figure 2, the experiments can be conducted also under constant ΔK conditions. In this case, specific influences of a medium could be detected by a change in the crack propagation rate as a function of exposure time. For metallic materials fatigue crack growth experiments under environment are described in ASTM E 647, for polymers no standard procedure exists until now.

Environmental stress cracking (ESC) of polymers is a phenomenon which has been researched over a period of more than 40 years. The phenomenon involves so many influential variables that the behavior cannot be predicted with sufficient accuracy. The only alternative is testing. For this any advances in test methods are important to make research more efficient and effective.
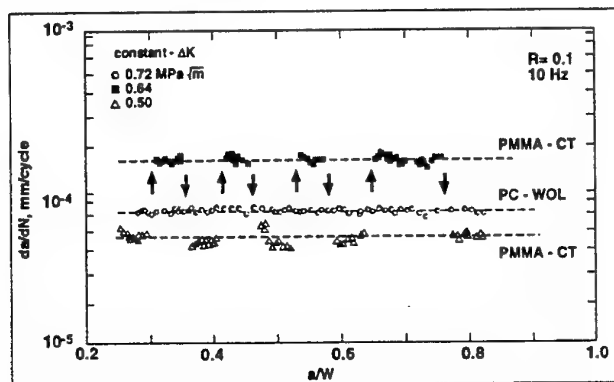

Figure 2. Experiments under constant ΔK (Lang 1984).

material	property
PS 148H®	polystyrene - M_w 238,000 g/mol
PS 168N®	polystyrene - M_w 354,000 g/mol
PS 486M®	polystyrene impact modified by small PB particles
PS 2710®	polystyrene impact modified by large PB particles

Table 1. Investigated materials.
®Trademark of BASF AG, Germany

2 EXPERIMENTAL

2.1 Materials

Amorphous thermoplastics are sensitive to ESC. Particular Polystyrene (PS) is well known to be sensitive against fluid permeation causing crazing (Kambour 1973). To study the effect of molecular weight and various types of rubber modification on the ESC behavior under fatigue crack growth conditions, commercial PS polymers were selected for this investigation. The materials were kindly supplied by BASF AG, Ludwigshafen, Germany and are listed in Table 1.

All polymers were processed by injection molding under standard conditions and tested considering the injection molding direction.

2.2 Test Methods

Compact-type (CT) specimens were cut from rectangular injection molded plates with 4 mm nominal thickness and precracked by a razor blade. All fatigue crack growth tests were run on a Schenck PSA® servohydraulic test system at a frequency of 10 Hz under sinusoidal loading in tension-tension with a minimum to maximum load ratio (R) of 0.1 at room temperature. The tests were run under ΔK control with a software designed by Fracture Technology Associates, Inc.. A ΔK-decreasing portion and a ΔK-increasing portion were measured separately with two different specimens of the same material and combined to one FCP-diagram. The crack length was monitored by a compliance technique, as published by Saxena & Hudak (1978).

The tests under environment were carried out by applying vegetable oil through a soaked sponge, which was fixed on both sides of the specimen as an unlimited source. By this the crack was always covered with the soaked sponge. The vegetable oil was a commercial sunflower oil (tradename Livio®). In this investigation all tests were run within load amplitude limits under ΔK control. The fatigue behavior would be expected to deteriorate because under the softening effect of a liquid medium, the samples would be strained more extensively for each loading cycle.
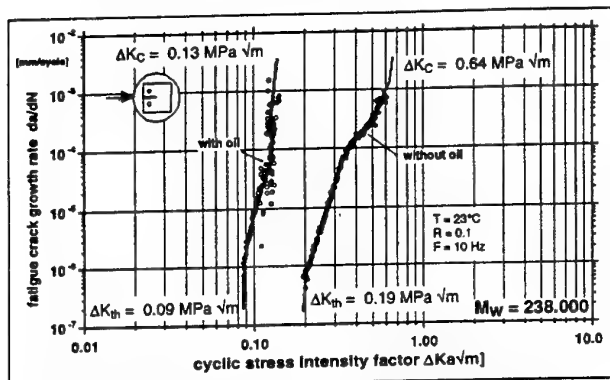
Figure 3. *FCP with and without a stress cracking media - PS 148H.*

Figure 5. Molecule orientation effects on crack propagation *- PS 148H.*

2.2 Fractography

Fracture surfaces were studied with a field emission electron microscope LEO 32 . The microscope was operated at an accelerating voltage of 0.5-1 kV. Because of the low accelerating voltage no gold coating of the specimen was necessary and the specimens could be investigated directly after fracture of the specimen in the fatigue experiment.

3 RESULTS AND DISCUSSION

3.1 Effect of molecular weight

Physical properties of polymers are strongly dependent on the average molecular weight M_W and sequence distribution M_W/M_N, because the presence of molecular entanglements can significantly affect the mechanical behavior. As previously shown by Altstädt (1997) for different commercial PS systems prepared by free radical polymerization and by anionic polymerization the number average M_N of the molecular weight corresponds well to an increase of the fatigue crack growth behavior. Further experiments were conducted in this study to explore the effect environmental ageing.

The effect of molecular weight on the ESC behavior was investigated for two different PS systems.
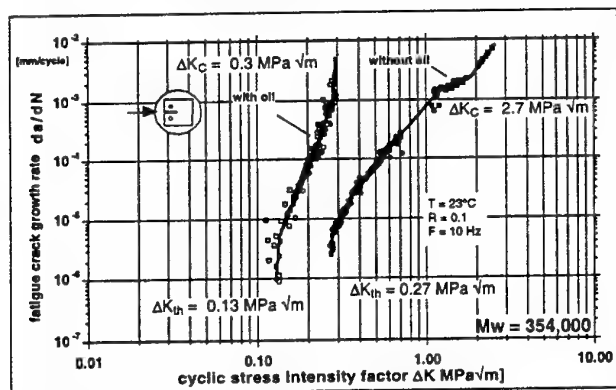

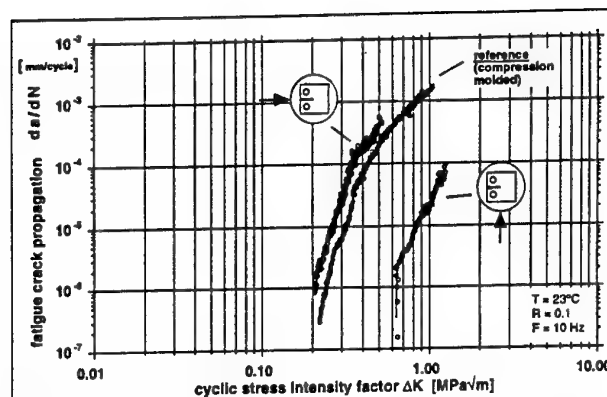Figure 4. *FCP with and without a stress cracking media - PS 168N.*

These were tested with and without oil environment. As shown in Figure 3 - 4 both PS systems exhibit a severe decrease in fatigue crack growth resistance when tested under oil environment. In both cases, ΔK for a given fatigue crack growth rate is significantly reduced and the slope of the curve is increased, simultaneously a decrease in ΔK_{th} is observed.

The comparison of both PS systems clearly shows an improved ESC resistance under fatigue loading of the PS with the higher molecular weight. This is reflected in a smaller slope of the linear portion of the FCP-diagram and a higher ΔK_C and ΔK_{th} for PS 168N.

3.2 Effect of orientations

To investigate possible orientations of the molecules due to the injection moulding process on the ESC resistance under fatigue loading conditions, samples of polystyrene were tested parallel and perpendicular to the injection molding direction. A specimen prepared from granules by compression molding, which should have a minimum of orientation, was included in the investigation as a reference. To minimize the effect of a plastic deformation possibly induced by precracking with the razor blade, the precrack was extended for a minimum 2 mm by fatigue loading before starting the experiment. In some cases it was difficult to carry out the test, because the crack grew parallel to the injection direction or an additional crack was initiated on the fixing holes of the samples.

As shown in Figure 5 the FCP-diagram of the specimens tested perpendicular to the injection moulding direction is shifted significantly to higher ΔK values compared to the specimens tested parallel. While the reference specimens processed by compression molding behave similar to those with parallel orientation. Obviously it is easier for the fatigue crack to propagate in the direction of the oriented entanglement network. This can be explained by the fact, that crack propagation in PS is accompanied by crazing. Molecules which are already stretched in one direction are losing the ability to fibrillate in the other direction. By this the probability for chain scission is
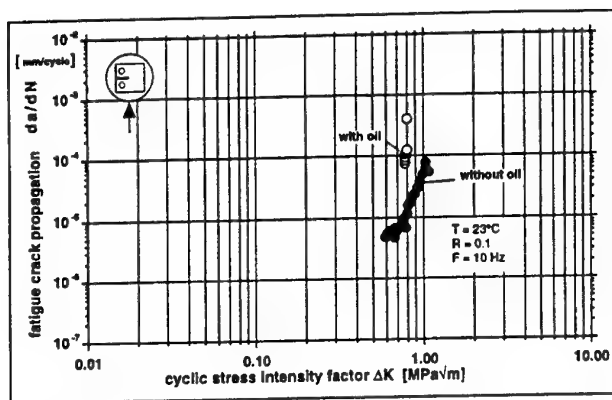
Figure 6. Injection molded samples tested perpendicular to the injection direction — *PS 168N*.

Figure 7. Effect of small styrene–butadiene rubber particles incorporated in PS — PS 486M.

increasing and the breakdown of the material drawn into the process zone occurs at lower ΔK values.

If polystyrene is tested perpendicular to the injection molding direction and a stress cracking media is present at the same time, an additional embrittlement can be observed by the steep increase in the FCP-curve which makes it almost impossible to measure the dynamic of crack propagation in a broad range of crack propagation rates as usual (Figure 6).

3.3 Toughness modification by rubber particles

A common strategy to improve the mechanical behavior of thermoplastics is to incorporate uniformly distributed rubber particles in the polystyrene matrix. In the case of HIPS (high impact polystyrene) styrene-butadiene block copolymers are used. This strategy is also applied to improve the environmental stress crack resistance of polystyrene.

For this investigation two commercial PS grades with different average diameter of the rubber particles were selected (PS 486M: $\varnothing \approx 2$ µm, PS 2710: $\varnothing \approx 5$ µm). The systems were tested with and without exposure to vegetable oil. The corresponding FCP-diagrams are shown in Figure 7 - 8.

The FCP behavior of the two rubber modified polystyrenes is comparable in the threshold region and in region III (Figure 1) at high propagation rates. A significant difference is visible in region II of intermediate crack propagation rates 10^{-5} to 10^{-4} mm/cycle. Particular PS with larger rubber particles is more effective in decreasing the slope of the crack growth curve.

Compared to the unmodified PS 148H and PS 168N (Figure 3 - 4) the observed ranking in terms of FCP behavior is PS 148H < PS 486M = PS 2710 < PS 168N. This ranking is changed completely if the tests are conducted in the presence of vegetable oil: PS 148H << PS 168N < PS 486M < PS 2710. Obviously rubber toughening is more efficient for the improvement of the ESC resistance under fatigue crack growth conditions as the increase in molecular weight corre-
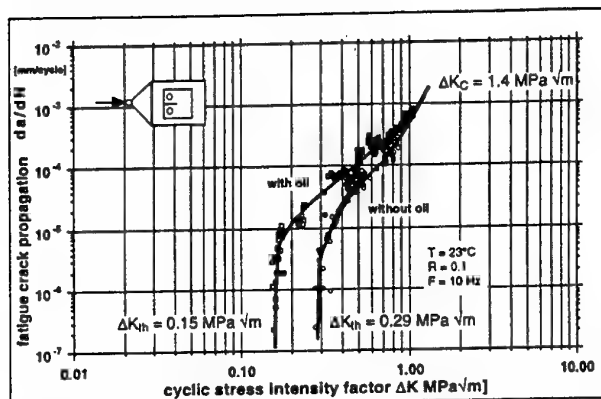
sponding to PS 148H and PS 168N. A remarkable difference between the two rubber modified systems is visible in the threshold region. The ΔK_{th} value of PS 2710 is not affected by the presence of the medium while ΔK_{th} of PS 486M is reduced by a factor of two.

The observation of the fracture surfaces in Figures 9 - 12 reveals the different size of the rubber particle of the two PS systems (Figure 9 - 11). Tested in air, in both cases the crack propagates through the rubber particles which is only possible in the case of good interfacial bonding. Tested in vegetable oil, the fracture surface appears to be very smooth. In the case of PS 486M some marks from the underlying morphology are visible.

It is generally accepted that rubber particles act as stress concentrators, initiate crazes as well as participate in their termination. The contribution of toughness depends on the concentration of the rubber, the particle size and the interfacial bonding. In the case of fatigue crack growth small particles are more efficient at low crack propagation rates because the plastic zone size is smaller, while larger particles are more efficient at higher propagation rates and the corresponding larger plastic zone diameter.

Under the influence of a stress cracking medium it seems that in the case of large rubber particles small crazes may easily develop. As a consequence the diffusion rate of oil is reduced, because of the increased
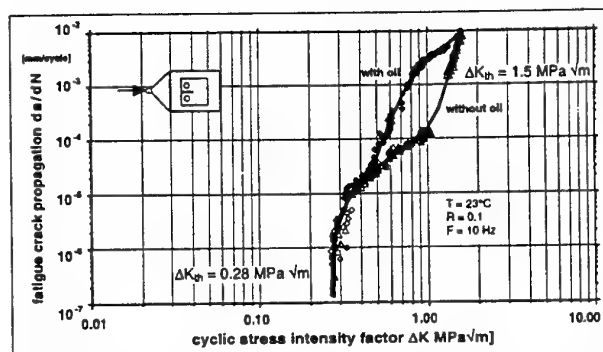

Figure 8. Effect of large styrene–butadiene rubber particles incorporated in PS — PS 2710.
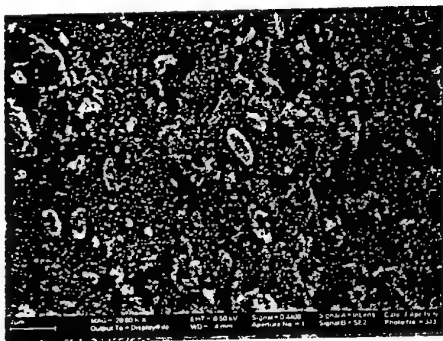
Figure 9. FCP fracture surface of PS 486M tested under air environment.
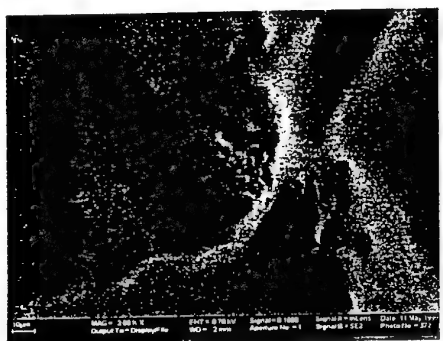

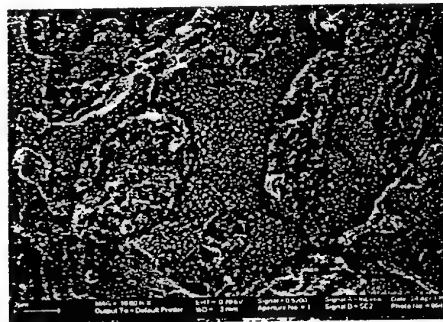Figure 10. FCP fracture surface of PS 486M tested under oil environment.

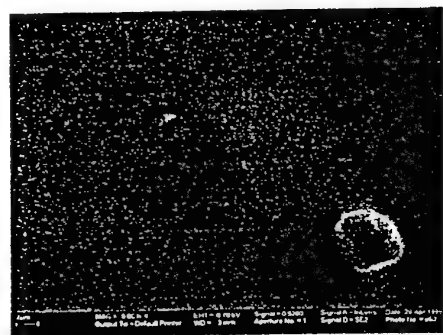Figure 11. FCP fracture surface of PS 2710 tested under air environment.

Figure 12. FCP fracture surface of PS 2710 tested under oil environment.

fibril density. Small rubber particles show less intensive crazing and the crazes are easier overloaded because of a higher effective opening of the crack tip. In the latter case the oil can penetrate easier through the crazes . This effect is stronger in region I of the FCP curve as compared to region II (Figure 1). At high crack propagation rates, it seems to be possible, that the oil is not able to penetrate fast enough to the crack tip which explains the same ΔK_c values of the two rubber modified systems.

4 CONCLUSIONS

Fatigue crack propagation (FCP) experiments can be employed as a fast and effective screening method for the evaluation of environmental. As shown for PS, molecular weight, molecular orientation and rubber toughening are playing an important role on the ESC behavior.

ACKNOWLEDGMENT

REFERENCES

Altstädt V. & Loth W. & Schlarb A. 1995, *Comparison of Fatigue Test Methods for Research and Development of Polymers and Polymer Composites*; Proceeding of the International Conference on Progress in Durability of Composite Systems. Brussels, Belgium, 16-21.7.1995.

Altstädt V. 1997, *Fatigue Crack Propagation in Homopolymers and Blends with High and Low Interphase* Strength; Proceedings "European Conference on Macromolecular Physics - Surfaces and Interfaces in Polymers and Composites", Lausanne, June 1st-6th 1997.

Bubeck 1981, Polym. Eng. Sci. 21, p 624.

Hertzberg R.W. & Manson J.A. 1990, *Fatigue of Engineering Plastics* New York: Academic Press.

Janzen, W. & G.W. Ehrenstein 1991. *Bemessungsgrenzen von glasfaserverstärktem PBT bei schwingender Beanspruchung.* Kunststoffe 81-3, p. 231.

Kambour, R.P. & Gruner C.L. & Romagosa E.E. 1973, J. Polymer. Sci., Polym. Phys., Vol.11, p.1879.

Lang, R.W. 1984, *Applicability of Linear Elastic Fracture Mechanics to Fatigue in Polymer and Short - Fiber Composites;* Ph.D. Dissertation Lehigh University, Bethlehem, PA, USA.

Paris, P. C. 1964, Proceedings of the 10th. Sagamore Conference. Syracuse Univ. Press, NY, p. 107.

Saxena A. & Hudak S.J. & Donald J. K. & Schmidt D.W. 1978, J. Test Eval. 6 p 167.

DAMAGE/WEIGHT LOSS RELATIONSHIP
FOR BISMALEIMIDE MATRIX
UNDER ISOTHERMAL OXIDATIVE AGEING

X. Colin [1], C. Marais[1], J.L. Cochon [1], J. Verdu [2]

[1] ONERA, Département des Matériaux et Systèmes Composites,
29, avenue de la Division Leclerc, 92322 Châtillon, France

[2] ENSAM, Laboratoire de Tranformation et de Vieillissement des Plastiques
151, boulevard de l'Hôpital, 75013 Paris, France

Carbon/polymer composites are likely to be used as structural materials for next generation supersonic aircraft and thus will have to face severe service conditions. Previous studies [1,2] showed up a gradual structural modification of the organic matrix of composite laminates during accelerated thermal ageing. Damage is a combination both of oxidation and thermally induced micro-cracking of the matrix. Suitable sampling and testing as well as adequate modelling are required to predict the long-term behaviour of the composite materials.
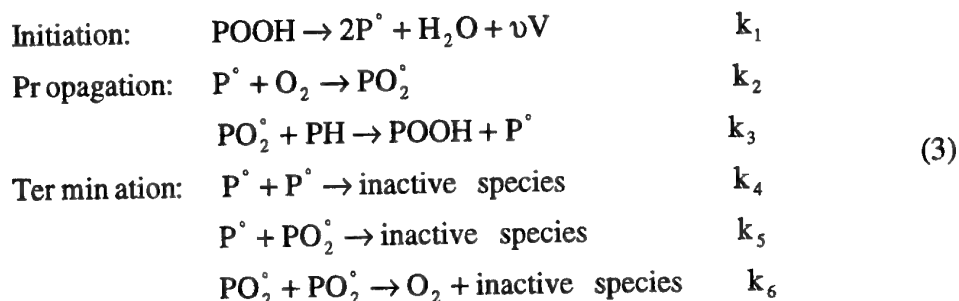
The present paper focus on matrix oxidation after isothermal ageing. Since carbon fibres are thermally stable over a temperature range from 150°C to 240°C, the study will be restricted to the bismaleimide polymer used as a matrix for a T800H/F655-2 composite system supplied by Hexcel-Genin. Besides, since the microscopic analysis [3] displays an heterogeneous oxidation of the polymer such as an ageing-induced « skin-core » structure representative of the oxidation process controlled by oxygen diffusion, the methodology set for classical linear polymers [4] will be applied on the bismaleimide thermoset resin. This methodology is summarized in figure 1.

First, an one-dimensional kinetic model relevant to the degradation of polymers is adjusted for the bismaleimide polymer. This model predicts both oxygen concentration and reaction product within the thickness of the sample by coupling an oxygen diffusion law to the chemical reaction kinetics. The oxygen diffusion is modelled by the classical Fick's second law whereas analytical expressions of the local oxygen chemical consumption rate $R(C)$ and local weight loss are proposed. Afterwards, the model is compared to experimental data. With this intention, thermogravimetric measurements on very thin polymer films subjected to various oxygen partial pressures were carried out. Moroever, optical microscopic examinations on cross sections of polymer thick plates were also carried out after ageing in air for several thousands hours. As a result, the validity range of the model is discussed. Finally, consequences on the mechanical behaviour of the polymer matrix are considered.
It must be highlighted that the oxidized skin contributes to a surface embrittlement which leads to a micro-cracking on the long-term.

Figure 1 : Methodology followed for studying the polymer oxidation.

KINETIC EQUATIONS

Most of the authors looks upon oxygen diffusion throughout a bulk polymer obeys to the Fick's second law. Now, the kinetic models only differ from one to another by selecting of an analytical expression of the local oxygen consumption rate R(C) :

$$\frac{\partial C}{\partial t} = D\frac{\partial^2 C}{\partial x^2} - R(C) \qquad (1)$$

where, C is the oxygen concentration, unknown parameter in the equation; t is the ageing time; x is the depth of oxygen penetration coming from reactive species; and D is the oxygen diffusion coefficient of the polymer, assumed independent of all three, depth, ageing time and oxygen concentration. This coefficient is determined by classical permeation tests.

In the steady-state, this equation becomes :

$$D\frac{\partial^2 C}{\partial x^2} - R(C) = 0 \qquad (2)$$

The selected analytical expression for R(C) took place from an investigation performed on the standard oxidation scheme proposed by Bolland & Gee [5]. This scheme composed of three main stages can be presented as following:

$$
\begin{aligned}
\text{Initiation:} \quad & POOH \rightarrow 2P^\circ + H_2O + \upsilon V & k_1 \\
\text{Propagation:} \quad & P^\circ + O_2 \rightarrow PO_2^\circ & k_2 \\
& PO_2^\circ + PH \rightarrow POOH + P^\circ & k_3 \\
\text{Termination:} \quad & P^\circ + P^\circ \rightarrow \text{inactive species} & k_4 \\
& P^\circ + PO_2^\circ \rightarrow \text{inactive species} & k_5 \\
& PO_2^\circ + PO_2^\circ \rightarrow O_2 + \text{inactive species} & k_6
\end{aligned} \tag{3}
$$

where, $k_{i=1,...,6}$ are rate constants; and V are volatil molecules, formed with a yield υ, and separated from H_2O molecules coming from OH° radicals.

After putting $\psi = 4\dfrac{k_4 k_6}{k_5^2}$ and $\beta = \dfrac{k_2 k_6}{2k_5 k_3[PH]}$, and achieving some simplifications (which will be detailed in the final paper), it may be expressed the oxygen consumption rate. On the basis of the steady-state and $\beta C > 2\psi$ and after suitable transformation, the expression takes the form :

$$
R(C) = 2\frac{k_3^2[PH]^2}{k_6}\frac{\beta C}{1+\beta C}\left(1 - \frac{\beta C}{2(1+\beta C)}\right) \tag{4}
$$

From this equation, the relationship between the weight loss and oxygen consumption can be expressed thus :

$$
\frac{\left(\dfrac{dM}{M_0}\right)}{dt} = \frac{k_3^2[PH]^2}{\rho k_6}\frac{\beta C}{1+\beta C}\left((46 - \upsilon M_V) - 32\frac{\beta C}{1+\beta C}\right) \tag{5}
$$

where, M_0 is the initial polymer weight; M is the polymer weight for thermal ageing; M_v is the molar weight of volatil species V; and ρ is the initial polymer density.

EXPERIMENTAL VALIDATION

The validation of the kinetic model (2) was divided in two steps. In a first stage, to validate analytical expressions (4) and (5), thermogravimetric measurements were performed on very thin polymer films, in order to avoid any diffusion-controlled effect on kinetics, subjected to various oxygen partial pressures. For each oxygen partial pressure, the rate of weight loss was determined in the steady-state. As an example, data obtained at 240°C are given in Figure 2 where it can seen that the analytical expression (5) shows a good agreement for most of oxygen partial pressures. Below 0.2 bars, a slight divergence is observed but it remains reasonably low in a first approximation.
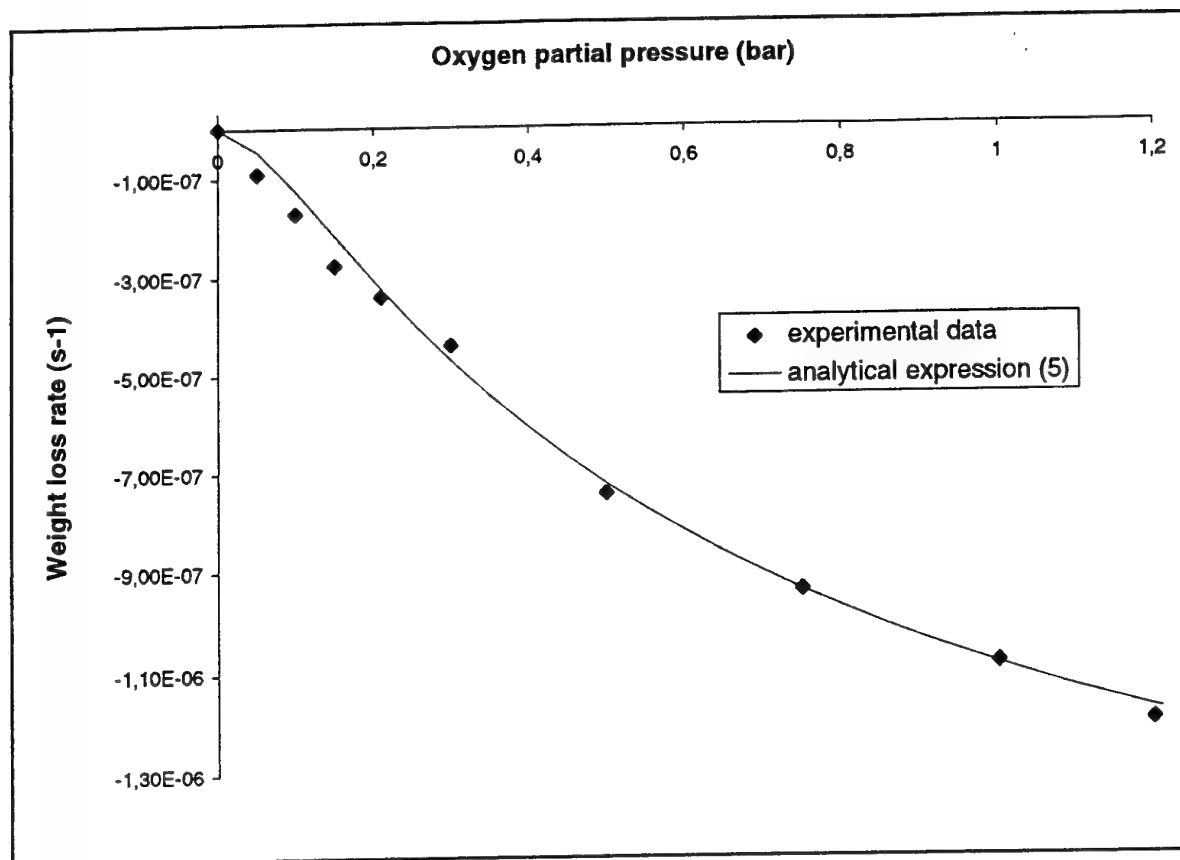
Figure 2 : Weight loss rate measured, in the steady-state, on polymer films of 50 μm thick exposed to different oxygen partial pressures at 240°C. Comparison with the theoretical rates calculated with the analytical expression (5).

In a second stage, the global model (2) was tried. Oxygen concentration and reaction product profiles were computed and a theoretical oxidized layer thickness was determined. Since the calculated value is the same order of magnitude than the oxidized skin thickness observed by optical microscopy [3], the model appears to be built on solid basis.

REFERENCES

[1] J.-P. Favre, H. Levadoux, T. Ochin & J. Cinquin. «Ageing of organic matrix composites at moderate temperatures - A first assessment», 10th Nat. Conf. on Comp. Mat. (JNC-10), edited by D. Baptiste & A. Vautrin, Vol. 1, 205-214, (AMAC, Paris, 1996).

[2] J.D. Nam & J.C. Seferis. «Anisotropic thermo-oxidative stability of carbon fiber reinforced polymeric composites», SAMPE Quaterly 24, 1 (1992) 10.

[3] X. Colin, C. Marais, J.P. Favre. «Damage/weight loss relationship of polymer composites under thermal ageing», presented at ICCM-12 and published on the ICCM-12 Proceedings (Paris, July 5th-7th 1999).

[4] L. Audouin, V. Langlois, J. Verdu & JCM de Bruijn. «Role of oxygen diffusion in polymer ageing: kinetic and mechanical aspects», J. of Material Science 29 (1994) 569.

[5] Bolland J.L. & Gee G. Trans. Far. Soc., 42 (1946) 236-244.

INTERPHASIAL STRESS AND STRAIN FIELDS
IN MULTI-PHASE PARTICULATES:
INFLUENCE OF MOISTURE CONTENT

N.K. Anifantis, P.A. Kakavas and G.C. Papanicolàou

Composite Materials Group

Department of Mechanical and Aeronautical Engineering

University of Patras, 26500 Patras, Greece

Email: Gpapan@meibm.mech.upatras.gr

In polymeric matrix composites the environmental conditions may cause severe changes at their overall properties due mainly to physical or chemical degradation of the polymeric matrix. These changes are associated to the temperature variations, moisture absorption and volumetric expansion, thus producing reduction in material moduli, loss of adhesion, debonding even corrosion cracking. The increased sensitivity of such materials to environmental degradation is closely related to the complex material structure based on the existence and cooperation of different materials within the same unit cell, and accordingly, the presence of step inhomogeneities. Water absorption by the epoxy resin leads to a softening of the resin with a loss of stiffness and strength. Composites having high filler contents absorb little moisture and show negligible change in modulus, although composites having matrix-dominated behavior exhibit the most moisture pickup and the greatest reduction in modulus[1]. The applied stress also has an effect on moisture absorption in polymers and polymer composites. Thus, the presence of residual stresses may cause increased moisture absorption[2].

In composites consisted from two dominant material phases, secondary phases exist known as interphases. They are developed along the boundaries between the dominant phases of the material due to mechanical or chemical material interactions and manufacturing procedures. These are very thin material layers characterized by the existence of strong inhomogeneities, impurities and flaws, and thus operate as low reliability and failure initialization regions. Among various models proposed to describe their behavior, the most reliable and simple are those considering exponential variation of properties in the direction of thickness[3].

Assuming particles of spherical shape, a unit cell may be considered which presents the representative volume element to study the effect of moisture absorption in the development of stress and strain fields in particulate composites. This unit cell consists of three separate subregions properly bonded to construct the composite, which are the filler, the interphase and the matrix. Filler and matrix are considered homogeneous, the interphase being inhomogeneous in the radial only direction. Under these assumptions, the modulus of elasticity of interphase E_i may be written in the following form

$$E_i = E_m(M) + [\alpha E_f - E_m(M)]R(\rho)$$

where E_f is the modulus of elasticity of the filler, and α express the adhesion efficiency. Function $R(\rho)$ describes the radial variation of modulus

$$R(\rho) = \frac{1 - \rho\, e^{1-\rho}}{1 - \rho_f\, e^{1-\rho_f}}$$

where $\rho = r / r_i$ and $\rho_f = r_f / r_i$. In the above equations, $E_m(M)$ is the modulus of elasticity of the matrix, and M the moisture content. The degradation of matrix modulus is illustrated in Figure 1 for the Epikote 828LV epoxy. The values of $E_m(M)$ are normalized in this Figure with respect to matrix modulus, in the dry condition E_{mo}.

Parameter α is a measure of the adhesion efficiency between the matrix and the filler. It may be defined as the magnitude of the discontinuity of material moduli between the filler and the interphase, at the position $r = r_f$. In the present work the effect of the modulus of elasticity is considered only, so that the parameter α is defined as a ratio of elastic moduli

$$\alpha = \frac{E_{io}}{E_f}$$

where $E_{io} = E_i(r_f)$. The value $\alpha = 1$ corresponds to full adhesion conditions, whereas lower values of α assign imperfect adhesion conditions. Furthermore, when $\alpha = 0$, a two phase model is obtained in which no interphase is present. The interphase thickness $\Delta r = r_i - r_f$ is also a function of absorbed moisture as shown in Figure 2 for the same epoxy resin as it was considered above. The dependence of the interphase zone on the moisture absorption was discussed in reference[4], and the experimental results have shown that the interphasial region is a function of the filler volume fraction too. As the filler volume fraction increases, the thickness of the interphase increases too. For values of moisture content around 0.55% a minimum value of the thickness is observed. In the case of moisture absorption, the action of moisture results in partial disruption of the bonds between filler and matrix by the formation of additional cavities which would be filled with water. It has been established that the water enters at the interphase at a rate of approximately four hundred and fifty times more rapidly than in the bulk matrix itself, and consequently any absorbed moisture is concentrated preferentially in the interphase.

Let us consider that the representative volume element of the problem is discretized in n subdomains with the shape of a spherical shell. Then a particular subdomain e, for e = 1, 2, ..., n, is defined between the radii r_e and r_{e+1}, and the material properties within it are constant in average sense, but different from adjacent ones, depending on the inhomogenuity presented by the constituent phases. The first and the last shell represent the filler and the matrix respectively. In order to study the stress state inside the representative volume element, a pressure p is applied to the its external surface. Due to spherical symmetry, the stresses and strains depend only on the radial ordinate. Then the displacement field $u_e = u_e(r)$, in each subdomain e, is given by[5]

$$u_e = \frac{A_e}{r^2} + B_e\,r, \qquad e = 1, 2, ..., n$$

where A_e, B_e are unknown constants to be determined. Sequential application of interfacial compatibility and equilibrium conditions between subdomain boundaries yields a linear algebraic system of equations for constants A_e, B_e, $e = 1, 2, ..., n$. Numerical solution of this system produces the general solution for whole the structure under consideration, and thus strain and stress data. Results obtained in this way, depend on global design variables, i.e. filler radius and volume fraction, material properties, moisture absorption and adhesion efficiency. Hence, a general method has been developed to describe residual stress and strains with moisture absorption, developed in any particulate with perfect or imperfect adhesion between phases.
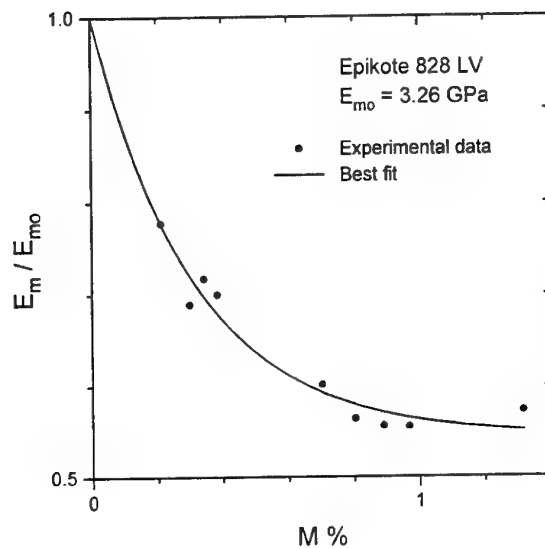
Figure 1 Degradation modulus of elasticity with moisture absorption for Epikote
828LV epoxy resin

Figure 3 illustrates the distribution inside the interphase of the tangential strain which is the most sensitive to moisture absorption distribution. Considering various volume filler fractions, the variation of radial and tangential stresses is shown in Figure 4. Both stress components present upper and lower bounds at the ends of the interphase, in a reverse manner, the radial component of stress being slowly higher. The moisture content seems to have negligible effect on stress fields. On the other hand, the softening effect of imperfect adhesion illustrated in this Figure, produces a step change of both stress components near the surface of the filler. Present results show that the moisture absorption from particulate composites has a negligible effect on stresses and a moderate effect on strains. Reduction in matrix stiffness due to moisture absorption has a negligible effect on stress and moderate to strain due to stiffness reduction in matrix, a reduction in stiffness of interphase occurs also resulting step stress gradient and reduced strength of the particulate composite. In other words, moisture absorption is accompanied by an increase of stress gradient and negligible change in stress inside the interphase. This interaction

is shown to be more sensitive to adhesion efficiency between matrix and filler. Most important on the elastic behavior of the model is the presence of imperfections on adhesion. Results show that imperfect adhesion soften the material structure and produce step gradients in stresses without increasing the stress concentration. Numerical results show development of a step stress gradient and differential strains in the region of interphase imperfect adhesion. Presence of such conditions may cause severe failures in this region.
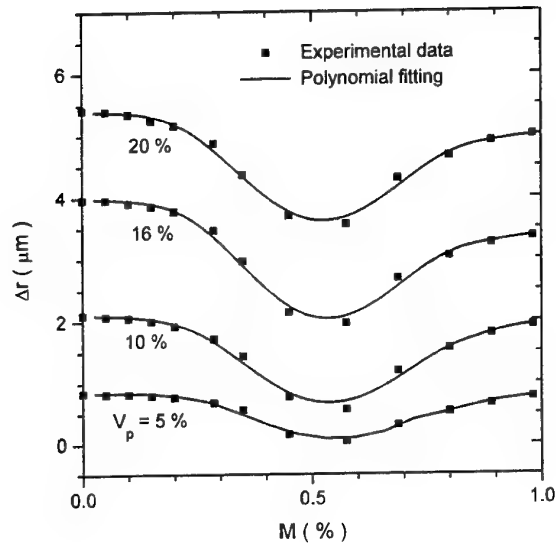
Figure 2 Interphase thickness with moisture content
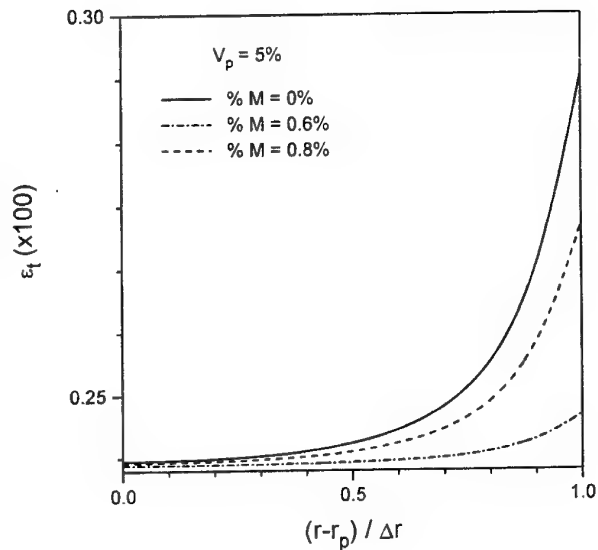
Figure 3 Variation of tangential component of strain with moisture content
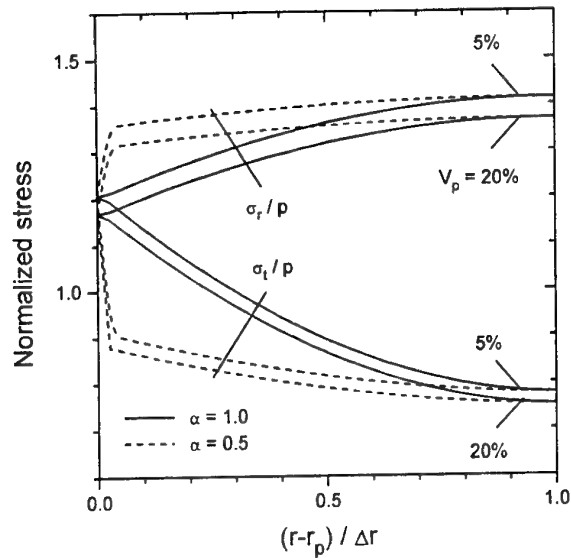
Figure 4 Distribution of stresses within the interphase

[1] Shen, C. & G.S. Springer, Moisture absorption and desorption of composite materials, *Journal of Composite Materials*, **10**, 2-20, 1976.

[2] Marom, G, & L.J. Broutman, Moisture penetration into composites under external stress, *Polymer Composites*, **2**, 132-136, 1981.

[3] Kakavas, P.A., N.K. Anifantis, K. Bexevanakis, D.E. Katsareas & G.C. Papanicolaou, The effect of interphasial imperfections on the micromechanical stress and strain distribution in fiber reinforced composites, *Journal of Materials Science*, **30**, 4541-4548, 1995.

[4] Theocharis, P.S, G.C. Papanicolaou & E.A Contou, Interrelation between moisture absorption, mechanical behavior and extent of the boundary interphase in particulate composites, *Journal of Applied Polymer Science*, **28**, 345-3153, 1983.

[5] Chamis, C.C., Simplified composite micromechanics equations for mechanical, thermal and moisture-related properties, in J.W. Weeton et al. (eds), *Engineers' Guide to Composite Materials*, 3-8-3-24, ASM International, Materials Park, OH, 1987.

Chemical resistance of pultruded E-glass reinforced polyester composites

K. Van de Velde, P. Kiekens

Universiteit Gent, Department of Textiles, Belgium

Introduction

Glass fibre reinforced composite profiles offer an alternative solution to wood and metals where structural performance and corrosion resistance are key factors. Such profiles are produced via the pultrusion technique. Present applications include ladders, handrails, grid floors, construction profiles for the chemical, water treatment, offshore and related markets.

A good understanding of the corrosion behaviour of the pultruded composites is necessary in order to guarantee the lifetime and the safety of the structural components in service.[1-4]

In this work, the chemical resistance of pultruded E-glass fibre reinforced polyesters with different filler types is studied. The mechanical, physical, optical and structural properties of the pultruded flat profiles before and after immersion in sea water, demineralised water, sodium hydroxide (5%) and sulphuric acid (10%) are analysed.

Experimental

Materials

Flat profiles of E-glass reinforced isophtalic polyester with different kind of fillers were pultruded. The glass fibre reinforced plastics are covered with a polyethylene terephtalate veil.

An overview of the test samples can be given as follows:

UP50z: isophtalic polyester, 50% E-glass, no filler
UP50c: isophtalic polyester, 50% E-glass, calcium carbonate as filler
UP50k: isophtalic polyester, 50% E-glass, kaolin clay as filler
UP60z: isophtalic polyester, 60% E-glass, no filler
UP60c: isophtalic polyester, 60% E-glass, calcium carbonate as filler
UP60k: isophtalic polyester, 60% E-glass, kaolin clay as filler

Exposure environments

Strips of the pultruded composites were immersed in sea water, demineralised water, sodium hydroxide (5%) and sulphuric acid (10%) at ambient temperature.

Experimental procedure

Weight changes and dimensions of the samples before and after immersion are measured.

The visual defects are classified according to ASTM D4385-84a.

The flexural properties are measured with a Monsanto T10 tensile testing machine according to ASTM D790-86. The support span to depth ratio is 32 (L/d=32/1).

The tensile properties are measured with a Zwick 1485 tensile testing machine according to ASTM D638-89.

Barcol hardness is measured with a Barcol-Colman impressor according to ASTM D2583-87.

The structure of the composite and the fracture surfaces are analysed with a scanning electron microscope (SEM) Philips 501. The samples were glued on a sample holder and coated with a gold layer of approximately 150 Å. The accelerating voltage of the instrument is 30 kV.

The failure mode is also analysed with optical microscopy (OM).

Results and discussion

Weight changes and dimensions
In general, the weights of the pultruded composites increase after immersion due to absorption of the fluid. Variations in the dimensions of the samples are recorded.

Flexural tests
The maximum load (F_m), the maximum stress (S_m), the strain at maximum stress (r_m), and the modulus of elasticity in bending (E_b) are measured with 3-point loading test.

The flexural strength (maximum stress in outer fibre at moment of break) against the test periods for the various samples and per type of chemical is given in figure 1 .

As expected the mechanical properties of the pultruded composites with the highest reinforcement level are the best. Considering the fillers, the composites containing clay or calcium carbonate are stronger than the unfilled composites.

A deterioration of the mechanical properties of the pultruded composites in flexure after exposure is observed. The reduction in strength and moduli is most obvious after one month exposure. Thereafter, considering the standard deviations, the mechanical properties are roughly maintained except for sodium hydroxide

Tensile tests
The maximum load, tensile strength, elongation at break and modulus of elasticity were measured.

Exposure of the different pultruded composites to sea water, demineralised water, sulphuric acid (10%) and sodiumhydroxide (5%) results in a diminution of the tensile strength. This is most obvious for the alkaline environment.

Variations in the elastic moduli are also mostly expressed for the samples exposed to sulphuric acid and sodium hydroxide.

Barcol Hardness
The Barcol hardness of the pultruded composites before and after exposure is measured.

The Barcol hardness against the test periods for the various samples and per type of chemical is given in figure 2. A global reduction of the Barcol hardness after exposure to the different environments is seen. The highest decreases are seen after one month of exposure.

After longer times of exposure, increases of hardness of the composites can be seen. They are due to the higher expression and visibility of the glass mats on the surface and the erosion of the polymers.

Visual observations
The visual defects are in agreement with the other techniques.

After exposure of the composites to sea water, demineralised water, sodium hydroxide and sulphuric acid, extra voids in the cross sections and a higher expression of the glass fibres on the surface are seen. Other visual effects are seen dependant on the chemical environment.

Scanning electron microscopy
With the electron microscope little cracks on the surface and the cross sections of the composites are seen. Those cracks are the results of crimp and insufficient impregnation during the pultrusion process. In these weak points a migration of the exposure fluid can take place.

After exposure and depending on the type of environment, more cracks on the surface just beside a glass fibre and deeper cracks in the cross section as a result of dissolution, degradation or stress-cracking due to solution sorption of matrix material and debonding between the glass fibres and the matrix material were seen.

The results of SEM are in agreement with the mechanical observations.

Conclusions

Pultruded composites can be used as structural materials in various chemical environments due to the good strength-to-weight ratio and the resistance to chemical attack. Although, a good understanding of the chemical properties is necessary in order to guarantee the lifetime and the safety of the structural components in service. In this work, the chemical resistance against sea water, demineralised water, sodium hydroxide and sulphuric acid of pultruded E-glass fibre reinforced isopolyesters with different filler types is studied. Composites filled with calciumcarbonate and kaolin clay and unfilled composites containing 50% and 60% glass are analysed on their mechanical, physical, optical and structural properties.
The results point out that sodium hydroxide is the most corrosive environment, followed by sulphuric acid. Sea water is less corrosive than demineralised water.

References

1   Sonawala, S.P., Spontak, R.J., Degradation Kinetics of Glass Reinforced Polyesters in Chemical Environment I. Aqueous Solutions, *J. Mater. Sci.*, **31**, pp.4745-4756, 1996.
2   Sonawala, S.P., Spontak, R.J., Degradation Kinetics of Glass Reinforced Polyesters in Chemical Environment II. Organic solvents, *J. Mater. Sci.*, **31**, pp.4757-4765, 1996.
3   Harris, S.J., Nobel, B. , Owen, M.J., Metallographic Investigation of the Damage Caused to GRP by the Combined Action of Electrical, Mechanical and Chemical Environments, *J. Mater. Sci.*, **19**, pp.1596, 1984.
4   Haarsma, J.C., Evaluation of Resin-Glass Fibre Interface under Environmental Stress, *33rd Annual Technical Conference, Reinforced Plastics/Composites Institute,* The Society of the Plastics Industry, Section 22-E, p.3, 1978.
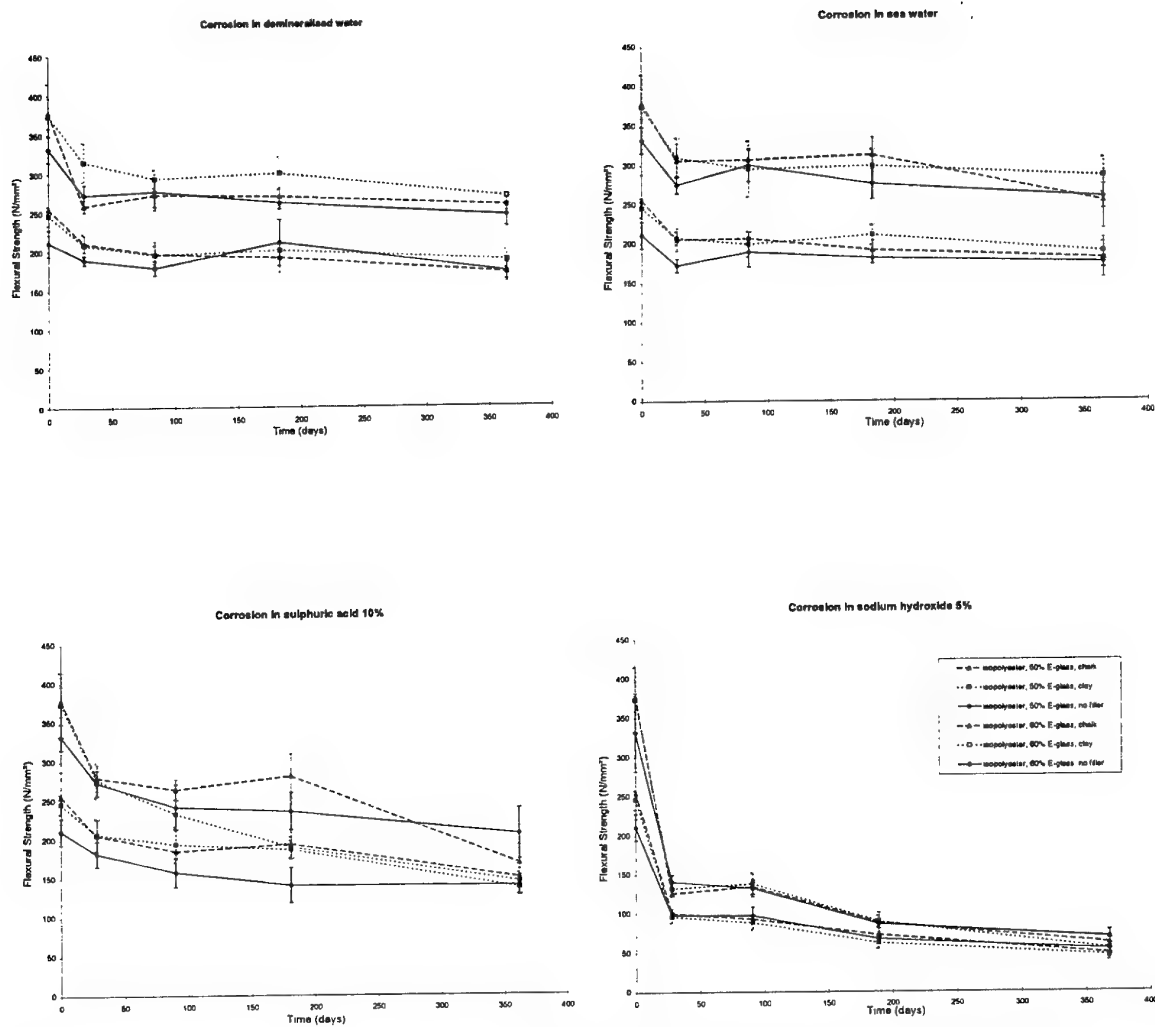
Figure 1: Flexural strength versus time of pultruded composites exposed to demineralised water, sea water, sodium hydroxide, sulphuric acid
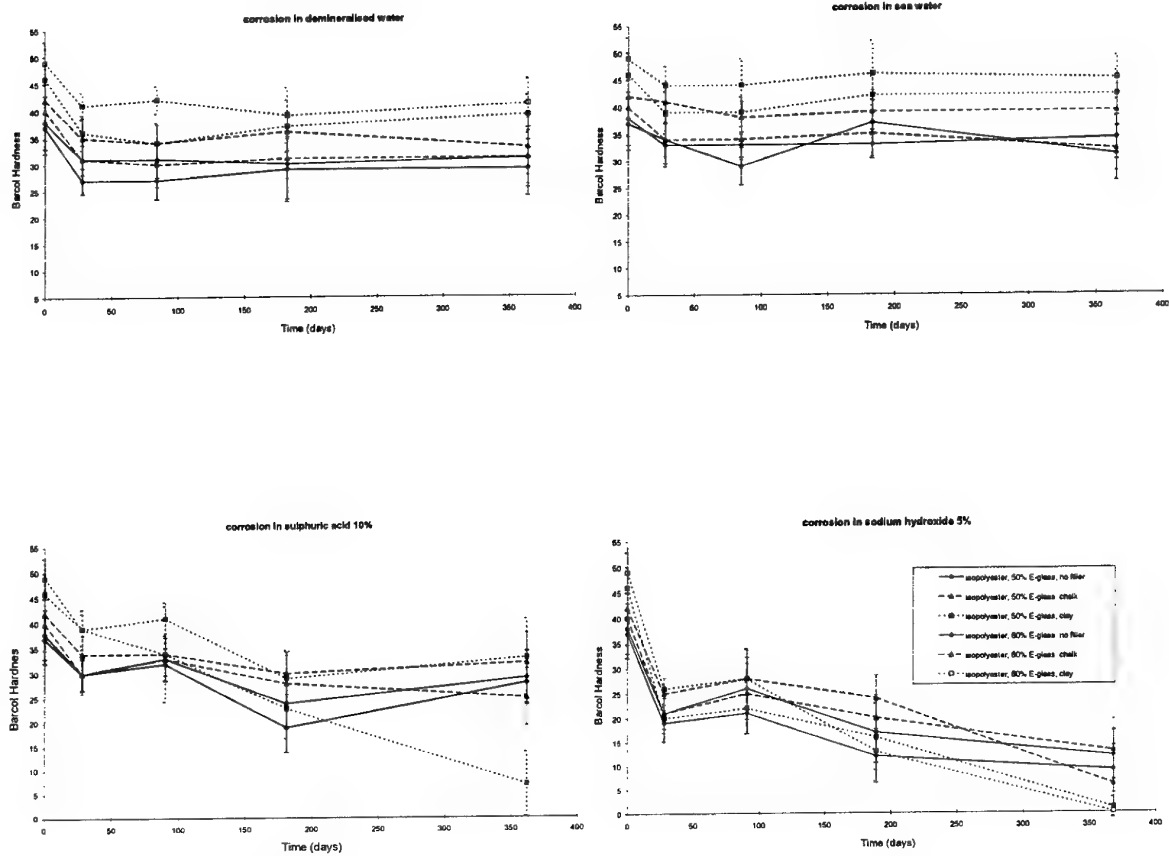
Figure 2: Barcol hardness versus time of pultruded composites exposed to demineralised water, sea water, sodium hydroxide, sulphuric acid

PERFORMANCE OF PULTRUDED FRP REINFORCEMENTS WITH EMBEDDED FIBER OPTIC SENSORS

A.L. Kalamkarov, D.O. MacDonald, S.B. Fitzgerald, and A.V. Georgiades

Department of Mechanical Engineering, Dalhousie University
P.O. Box 1000, Halifax, Nova Scotia
Canada B3J 2X4

The potential for the use of composite materials in the fields of civil engineering, transportation and marine engineering is very promising. High strength-to-weight ratios and inherent corrosion resistance are among the properties that make composites attractive for these applications. The introduction of composite materials in these areas has been slowed by the high cost of most composites and a lack of reliable long-term data as compared to more traditional materials such as steel and concrete. One method of compensating for the lack of long-term data is to monitor the health of the structure using so-called smart composite materials.

The current study is concerned with the pultrusion of smart FRP materials in which the fiber optic sensing element and accompanying lead are embedded inside the composite material during its processing [1, 2]. The embedded sensor is thus well protected from harsh environments as well as from rough handling during the construction phases of large projects. This research involves the pultrusion of glass and carbon fiber composite tendons which contain embedded fiber optic sensors. Two types of optical sensors are used; Fabry Perot and Bragg Grating sensors. It is found to be necessary to pre-reinforce Fabry Perot sensors prior to pultrusion [3]. The Bragg Grating sensors show a greater survivability in the pultrusion process than the Fabry Perot sensors and do not require pre-reinforcement.
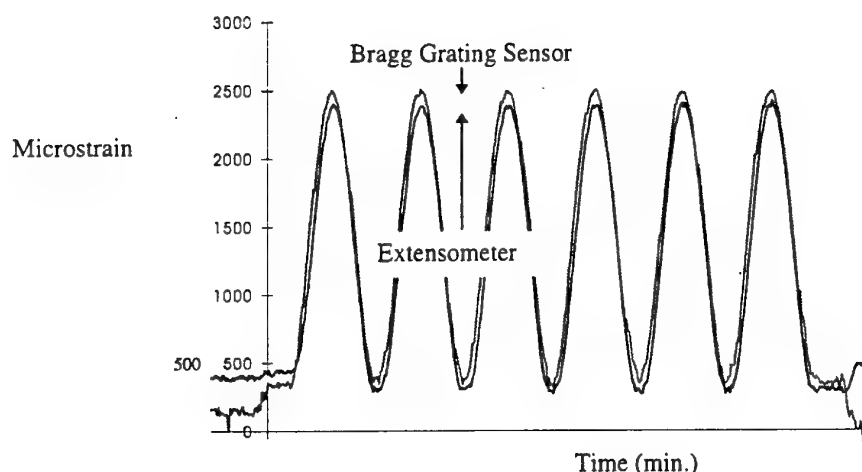

Fig. 1: Strain vs. Time Plot from Extensometer and an Embedded Bragg Grating Sensor in a Pultruded Glass FRP Tendon Subjected to a Sinusoidal Load at Room Temperature.

While fiber optic sensors and smart composite materials have shown promise in replacing or strategically complimenting traditional materials and strain gages, there is not a great deal of data available which reflect upon their long term behaviour which, as is the case with all materials, is significantly affected by the surrounding environment. For civil applications, the composite materials and associated fiber optic sensors will encounter, in addition to mechanical stress, external conditions of high and low temperature, humidity, and chemical ion exposure.

Appropriately, one of the primary objectives of the research was the study of the performance of embedded fiber optic sensors under conditions of static and dynamic loading at room temperature [4], as well as when exposed to both low and high temperature extremes. The experiments entailed subjecting the GFRP and CFRP tendons to sinusoidal and trapezoidal load waveforms of about 11 KN magnitude inside a temperature chamber. The temperature in the chamber was varied from -40°C to +60°C in increments of 20°C. The strain output from the embedded sensors was compared to that from externally mounted extensometers as well as to theoretical strain values. The experiments indicated that the performance of the fiber optic sensors was not affected by ambient temperatures falling within the range of -40°C to +60°C and the sensor readings conformed very well with the corresponding extensometer and theoretical readings. Typical graphs are shown in Figures 1-3.
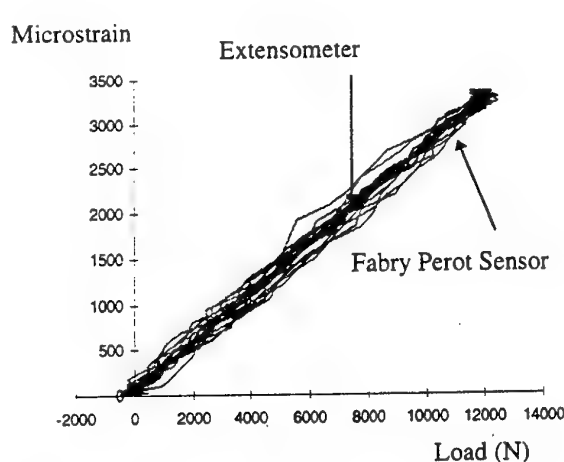

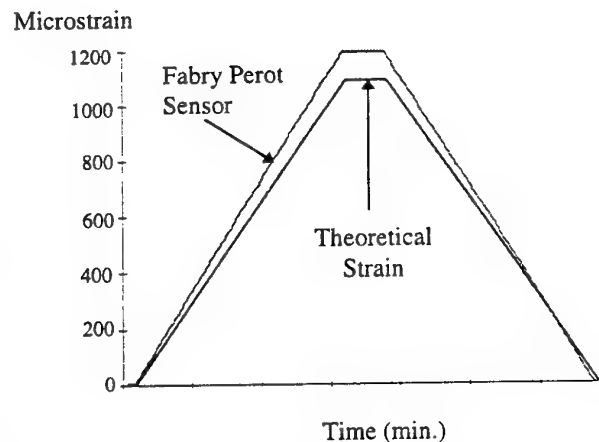Figure 2. Strain From Extensometer and Embedded Fabry Perot Sensor in a Glass FRP Tendon Subjected to a Sinusoidal Load at 60°C.

Figure 3. Strain From Extensometer and Embedded Fabry Perot Sensor in a Carbon FRP Tendon Subjected to a Trapezoidal Load at -20°C.

Another important objective of the research was to study the fatigue behaviour of the fiber optic sensors by examining the performance of FRP reinforcements with the embedded sensors under conditions of cyclic loading. It will be of interest to determine if the sensors still perform adequately and provide a strain readout after enduring a large number of stress cycles, and if the sensors retain their accuracy and repeatability. To this end, glass and carbon FRP tendons with embedded Fabry Perot and Bragg Grating sensors were subjected to a sinusoidal load waveform of 1 Hz frequency and ranging in magnitude from 6.5 KN to 11 KN (stress ratio of 0.6). Testing was carried out for a duration of 140000 to 350000 cycles. The strain values from the embedded sensor were compared to those obtained from an externally mounted extensometer (Figures 4, 5, and 6). It can be seen that the sensors embedded in the carbon tendons are unaffected by the

fatigue load, and their strain output is repeatable and accurate after a large number of load cycles. The same conclusions were reached for the case of the glass tendons.

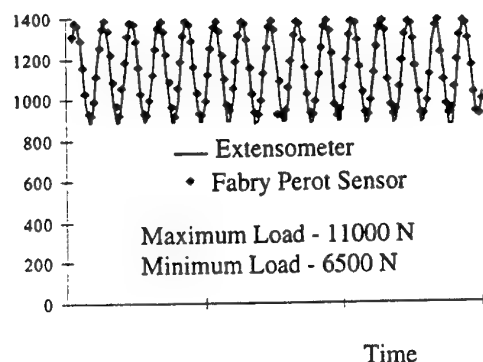Figure 4. Strain From Extensometer and Embedded Fabry Perot Sensor in a CFRP Tendon Subjected to Tension-Tension Fatigue for 70000 cycles.
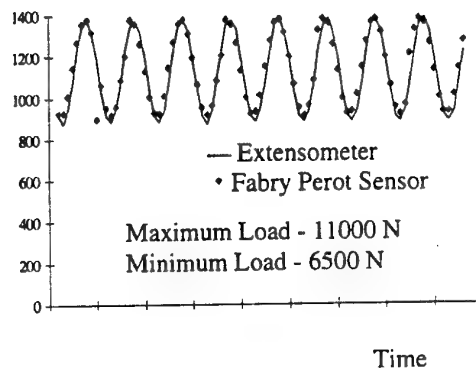
Figure 5. Strain From Extensometer and Embedded Fabry Perot Sensor in a CFRP Tendon Subjected to Tension-Tension Fatigue for 140000 cycles.

It is known that creep deformations may cause unacceptable dimensional changes or distortion and ultimately final failure if they are of significant magnitude. Both composites and more traditional materials such as steel can exhibit creep behaviour although it is more often related to elevated service temperatures. Appropriately, another objective of the current research is to characterize the long term creep behaviour of the embedded fiber optic sensors and assess their suitability for monitoring long term service conditions. The goal is not to characterize the composite tendons themselves, but rather to characterize the interaction of the tendon and the embedded sensor under conditions of sustained constant load levels.
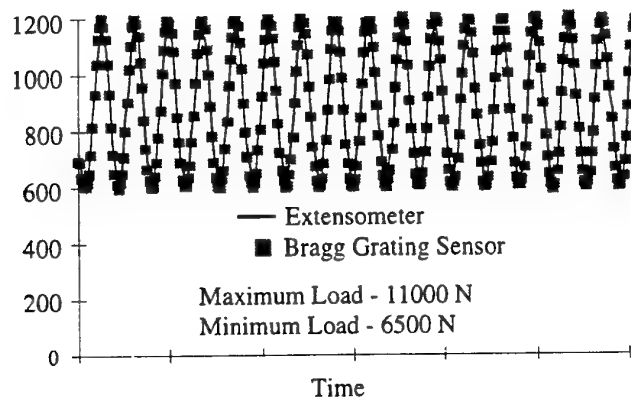

Figure 6. Strain From Extensometer and Embedded Bragg Grating Sensor in a CFRP Tendon Subjected to Tension-Tension Fatigue for 350000 cycles.

Both carbon and glass reinforced smart tendons were chosen for short term creep testing. Both tendons contained an embedded Fabry Perot fiber optic sensor. The applied load was 9 KN (for a period of 140 hours) for the case of the glass tendon, and 13.5 KN (for a period of 350 hours) for the case of the carbon tendon. The results of these tests are shown in Figures 7 and 8. It can be seen that output from the Fabry Perot sensors is practically constant over the entire duration of the tests, and thus it may be concluded that they do not exhibit short term creep behavior at the given experimental conditions. They have the potential for significant benefit in the long term monitoring of strain levels in composite prestressing cables. A similar testing program involving Bragg Grating sensors embedded in glass and carbon FRP tendons and subjected to constant loads will be conducted in the near future.
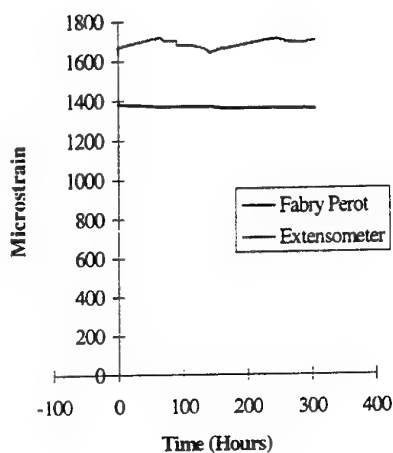

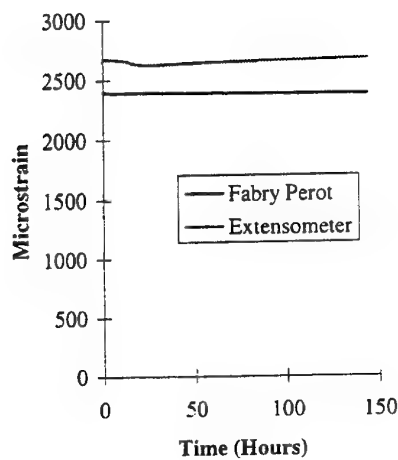Figure 7. Glass FRP Tendon at 9 KN for 140 Hours.

Figure 8. Carbon FRP Tendon at 11.5 KN for 350 hours.

It has thus been shown that embedded fiber optic sensors can successfully endure high and low temperature extremes, as well as repeated and sustained loading. More long term testing is planned in the range of 1500 test hours which will provide a more detailed look into the long term behaviour of the tendons and the sensors. This long term testing will also be conducted in more severe environments (e.g. alkaline solutions) which may simulate conditions encountered in concrete structures wherein the composite rods may be used as prestressing tendons and rebars.

ACKNOWLEDGMENT

REFERENCES

1. Kalamkarov, A.L., Liu, H.Q., and D.O. MacDonald, Experimental and Analytical Studies of Smart Composite Reinforcement, *Composites Part B: Engineering, International Journal*, **Vol. 29B(1)** (1998) 21-30.

2. Kalamkarov, A.L., MacDonald, D.O., and P. Westhaver, On Pultrusion of Smart FRP Composites, *Smart Sensing, Processing, and Instrumentation, Proc. SPIE* **3042** (1997) 400-409.

3. Kalamkarov, A.L., Fitzgerald, S.B., and D.O. MacDonald, The Use of Fabry Perot Fiber Optic Sensors to Monitor Residual Strains During Pultrusion of FRP Composites, *Composites Part B: Engineering, International Journal*, **Vol. B 30(2)** (1999) 167-175.

4. Kalamkarov, A.L., Fitzgerald, S.B., MacDonald, D.O., and A.V. Georgiades, Smart Pultruded Composite Reinforcements Incorporating Fiber Optic Sensors, *Proc. SPIE* **3400** (1998) 94-105.

MONITORING AND MODELING THE DURABILITY OF POLYMERS USED FOR COMPOSITE OFFSHORE OIL TRANSPORT

D. Kranbuehl, D. Hood, J. Rogozinski, A. Meyer, E. Powell, C. Higgins, C. Davis, C. Ambler, C. Elko, N. Olukcu

Department of Chemistry and Applied Science, College of William and Mary, PO Box 8795, Williamsburg, Virginia 23185-8795

KEYWORDS: aging, degradation, sensing, durability, dielectric properties, mechanical properties, in situ

ABSTRACT

This report focuses on the use of frequency dependent dielectric sensors (FDEMS) to monitor continuously, and in sit during use the changing state of a polymeric composite pipe in the use environment. This report focuses on using FDEMS to monitor both the changes in state-health of the polyphenyl sulfide (PPS) graphite tape used for the axial armour and the polyamide PA-11 used for the composite pipes oil-gas inner lining barrier. Current life monitoring work focuses on characterizing the chemical and physical processes occurring during aging, using FDEMS and laboratory measurements of mechanical and thermodynamic properties to monitor the aging rate and state of the polymer, and then integrating the sensor output with a model for predicting the remaining service life and state of the structure. The model predictions are periodically updated through the in situ online sensing measurements. This report will also discuss work on understanding of the relationship of the sensor measurement o the ionic and dipolar mobility to the macroscopic properties of polymeric materials.

INTRODUCTION

The use of polymeric materials in extended use structures such as airplanes, bridges and pipelines, where the expected lifetimes are 20 to 40 years and where failure can be catastrophic, is rapidly expanding. As such, there is a clear need to develop in situ health monitoring capabilities. This paper describes the progress toward the development of a frequency dependent dielectric measurement sensor (FDEMS) which is capable of detecting the change in the physical and chemical state of a polymeric material in situ during use in the field environment and during process-fabrication.

Health monitoring involves monitoring the degradation of a polymeric material's performance properties. In one sense, health monitoring is the reversal of cure monitoring during fabrication.

FDEMS provide a sensitive, automated, in situ sensing technique for monitoring changes in the state and properties of polymers during use as well as during intelligent processing. FDEMS in situ sensing can be designed and calibrated to monitor changes in mechanical service life properties of polymer materials during use in the field environment as well as in processing properties. The FDEMS sensor output already has been shown and used to monitor changes in viscosity, degree of cure and T_g during cure.[1-14] With the proper understanding of the type of polymer and the use environment, the FDEMS can be used to monitor modulus, maximum load and elongation at break during use. Monitoring degradation in these performance properties is the reversal of monitoring cure during which there is a buildup in mechanical properties. The FDEMS technique has advantages over other monitoring techniques in that it is: nondestructive, accurate/reproducible, sensitive, in situ, remote and automated.

This paper will discuss recent work on the use of FDEMS to monitor aging during off shore use of flexible composite pipe designed to transport oil-gas in an offshore oil-sea environment. Current durability monitoring work focuses on characterizing the chemical and physical processes occurring during aging, determining the state of the polymer, using FDEMS sensing to monitor the aging rate, mechanical and chemical analyses, and predicting the remaining service life and health of the structure. This report will discuss work on developing a fundamental understanding of the relationship of the sensor measurement of the ionic and dipolar mobility to the macroscopic mechanical performance properties of polymeric materials. The report will describe recent work on the use of FDEMS, and differential scanning calorimetry along with tensile and torsional mechanical measurements to monitor aging in thermoplastics during use in salt water, oil and acidic environments. The polymers being studied are polyphenyl PPS, graphite tape, sulfide and polyamide-11 which are used for flexible composite pipe to transport oil-gas in an offshore environment. The PPS graphite tape is used for axial windings to withstand the 100 bar plus internal pressures and the polyamide-11. PA-11 is used as is the inner lining barrier to contain the acidic, oil, water flow from the ocean floor to the offshore platform. These results can be incorporated into an aging-durability model. The sensor output provides in situ online data continuously updating the current state of the polymer. Thus the model can make continuously updated predictions of the remaining service life and projected replacement date of the polymer.

BACKGROUND

Frequency dependent dielectric measurements, made over many decades of frequency, Hz-MHZ, have already been shown to be a sensitive, convenient automated means for characterizing the processing properties of thermosets and thermoplastics.[1-14] Using a planar wafer thin sensor, measurements can be made in situ in almost any environment. Through the frequency dependence of the impedance, this sensing technique is able to monitor changes in the molecular mobility of ions and dipoles. These changes in molecular mobility are then related to chemical and physical changes which occur during use or during processing. The FDEMS techniques have the advantage that measurements can be made both in the laboratory, in situ in the fabrication tool and in situ during use. Few laboratory measurement techniques have the advantage of being able to make measurements in a processing tool and in the field in a composite, in an adhesive bond line, of a thin film or a coating. It can be used at temperatures exceeding 400 $^\circ$C and at pressures of 60 atm, with

an accuracy of 0.1% and a range in magnitude of over 10 decades. It is difficult for most other in the field techniques to attain this level of sensitivity in harsh processing environments.

At the heart of dielectric sensing is the ability to measure the changes at the molecular level in the translational mobility of ions and charge in terms of the conductivity and in the rotational mobility of dipoles in terms of a rotational time τ in the presence of a force created by an electric field. Mechanical properties reflect the response in displacement on a macroscopic level due to a mechanical force acting on the whole sample. The reason why dielectric sensing is quite sensitive is rooted in the fact that changes on the macroscopic level originate from changes in force displacement relationships on a molecular level. Indeed, it is these molecular changes in force-displacement relationships which dielectric sensing measures as the resin cures and ages. They are the origin of the resin's macroscopic changes in mechanical performance properties, during use and processing properties during fabrication.

MODELING OF HYGROTHERMAL EFFECTS IN COMPOSITES AND POLYMER ADHESIVE SYSTEMS

Samit Roy[*] and Weiqun Xu[**]

Asst. Professor[*] & Ph.D. Candidate[**], Department of Mechanical Engineering
University of Missouri-Rolla, Rolla, MO 65401

Introduction

It is now widely recognized that cyclic moisture absorption and desorption plays a significant role in influencing the mechanical behavior, and therefore, long-term durability of polymers and PMC. Numerous diffusion models have been proposed over the years for modeling hygrothermal effects in PMC. The one most frequently used by researchers is the one-dimensional Fickian model. Unfortunately, this model tends to overestimate the moisture absorption in panels for short diffusion time [1]. Some researchers have suggested that the deviation can be explained by a two-stage Fickian process [2,3]. Others claim that the diffusion process in a PMC is really non-Fickian [4,5]. In reality, the nature of the diffusion process depends on the material and on the environmental conditions that the material is exposed to. For example, if the rate of viscoelastic relaxation in a polymer is comparable to the rate of moisture diffusion, then the diffusion is likely to be non-Fickian. In addition, the presence of strong temperature and stress gradients has been known to engender non-Fickian driving forces. The presence of damage in the form of matrix cracks could also lead to anomalous diffusion. Employing a rigorous thermodynamic approach, Weitsman[6] developed a model for coupled damage and moisture transport in a transversely isotropic, fiber reinforced polymer composite. The damage entity was represented as a skew-symmetric tensor and was included in the model as an internal state variable. However, the model was mathematically complex and was not amenable to a simple closed-form solution.

In this paper, theory of irreversible thermodynamics is applied within the framework of continuum mechanics to derive governing equations for diffusion in a PMC from first principles. A special form for Gibbs potential is formulated for an orthotropic material using stress, temperature, damage and moisture concentration as independent state variables. The resulting governing equations are capable of modeling the effect of interactions between complex stress, temperature, damage and moisture concentration on the diffusion process within an orthotropic material. The primary focus of this work is to model diffusion in the presence of a pre-existing state of damage; consequently damage evolution is not included in the present analysis for tractability. Because the mathematically complex nature of the governing equations precludes a closed-form solution, a variational formulation is used to derive the weak form of the nonlinear governing equations that are then solved using the finite element method. This approach provides a significant improvement over solution methods reported in the literature for this type of problems. For model validation, the model predictions are compared with experimental data for the special case of isothermal diffusion in an unstressed 5-harness satin weave graphite/epoxy [0/90/0/90]$_s$ laminate with distributed matrix micro-cracks.

1

Model Development

The Gibbs potential for an orthotropic material subjected to applied stress and internal damage must be expressed in a polynomial form that remains invariant to coordinate transformations. Such a polynomial can be mathematically expressed as a combination of invariant terms obtained from the so-called irreducible integrity bases [7,8]. The irreducible integrity bases for an orthotropic material are,

$$\overline{\sigma}_{11}, \overline{\sigma}_{22}, \overline{\sigma}_{33}, d_{11}, d_{22}, d_{33}, \overline{\sigma}_{23}^{2}, \overline{\sigma}_{13}^{2}, \overline{\sigma}_{12}^{2}, \overline{\sigma}_{23}\overline{\sigma}_{13}\overline{\sigma}_{12}, d_{23}^{2}, d_{13}^{2}, d_{12}^{2}, d_{23}d_{13}d_{12},$$

$$\overline{\sigma}_{23}d_{23}, \overline{\sigma}_{13}d_{13}, \overline{\sigma}_{12}d_{12}, d_{23}\overline{\sigma}_{13}\overline{\sigma}_{12}, d_{13}\overline{\sigma}_{12}\overline{\sigma}_{23}, d_{12}\overline{\sigma}_{23}\overline{\sigma}_{13}, \overline{\sigma}_{23}d_{13}d_{12}, \overline{\sigma}_{13}d_{12}d_{23}, \overline{\sigma}_{12}d_{23}d_{13} \tag{1}$$

where, the normalized stress

$$\overline{\sigma}_{ij} = \frac{\sigma_{ij}}{\sigma_f},$$

where σ_f is the ultimate stress in a material principal direction, the damage tensor d_{ij} is a symmetric tensor of the 2nd rank, and ρ_s is the mass density of the composite laminate.

The chemical potential of moisture in the polymer is given by,

$$\mu = \rho_s \frac{\partial \phi}{\partial m} \tag{2}$$

where, ϕ is Gibbs potential, ρ_s is the mass density of the polymeric solid, and m is the moisture concentration. Conservation of diffusing mass within a unit volume of the polymer requires,

$$\frac{\partial m}{\partial t} = -\frac{\partial f_i}{\partial X_i} \quad , \quad i = 1,3 \tag{3}$$

where, in the absence of temperature, stress and damage gradients, moisture flux f_i for orthotropic symmetry is assumed to be of the form,

$$f_i = -D_i \frac{\partial \mu}{\partial X_i} \tag{4}$$

Combining equations (2), (3), and (4), gives the governing equation for diffusion,

$$\frac{\partial m}{\partial t} = \frac{\partial}{\partial X_i}\left(D_i \frac{\partial \mu}{\partial X_i}\right) \quad i = 1,3 \tag{5}$$

Consider a laminate with intralaminar cracks oriented perpendicular to the X_1 axis, subjected to inplane uniaxial loading in the X_1 direction under isothermal conditions as schematically shown in Figure 1. For the special case of uniaxial loading, the state of stress and damage reduce to,

$$\overline{\sigma}_{22} = \overline{\sigma}_{33} = \overline{\sigma}_{13} = \overline{\sigma}_{23} = \overline{\sigma}_{12} = 0$$

and, $\qquad d_{22} = d_{33} = d_{13} = d_{23} = d_{12} = 0$

Based on a definition of damage originally proposed by Talreja [8], it can be shown that the non-zero damage component d_{11} is given by,

$$d_{11} = \frac{\kappa(m,T)t_c^{2}\delta_1}{t} \tag{6}$$

2

In equation (6) $\kappa(m,T)$ is an experimentally determined influence parameter that incorporates the constraining influence of moisture concentration (m), temperature (T), ply-orientation, and fiber architecture on crack opening displacement; t_c is the crack size, t is the total thickness of the laminate, and δ_1 is the crack density in the X_1 direction as depicted in Figure 1.

Using the irreducible integrity bases from equation (1) and retaining terms up to second order in uniaxial stress and damage, the Gibbs potential becomes,

$$\rho_s\phi = \hat{C}_0 + \hat{C}_1\overline{\sigma}_{11} + \hat{C}_2 d_{11} + \hat{C}_3\overline{\sigma}_{11}^2 + \hat{C}_4\overline{\sigma}_{11}d_{11} + \hat{C}_5 d_{11}^2 + \hat{C}_6\sigma_{11}^2 d_{11} + \hat{C}_7\sigma_{11}d_{11}^2 \tag{7}$$

The chemical potential of moisture in the polymer for this special case is,

$$\mu = \rho_s\frac{\partial\phi}{\partial m}$$

$$= \rho_s\left[\frac{\partial\hat{C}_0}{\partial m} + \frac{\partial\hat{C}_1}{\partial m}\overline{\sigma}_{11} + \hat{C}_1\frac{\partial\overline{\sigma}_{11}}{\partial m} + \frac{\partial\hat{C}_2}{\partial m}d_{11} + \hat{C}_2\frac{\partial d_{11}}{\partial m}\right.$$

$$+ \frac{\partial\hat{C}_3}{\partial m}\overline{\sigma}_{11}^2 + 2\hat{C}_3\overline{\sigma}_{11}\frac{\partial\overline{\sigma}_{11}}{\partial m} + \frac{\partial\hat{C}_4}{\partial m}\overline{\sigma}_{11}d_{11} + \hat{C}_4 d_{11}\frac{\partial\overline{\sigma}_{11}}{\partial m} + \hat{C}_4\overline{\sigma}_{11}\frac{\partial d_{11}}{\partial m} \tag{8}$$

$$+ \frac{\partial\hat{C}_5}{\partial m}d_{11}^2 + 2\hat{C}_5 d_{11}\frac{\partial d_{11}}{\partial m} + \frac{\partial\hat{C}_6}{\partial m}\overline{\sigma}_{11}^2 d_{11} + 2\hat{C}_6\overline{\sigma}_{11}d_{11}\frac{\partial\overline{\sigma}_{11}}{\partial m} + \hat{C}_6\overline{\sigma}_{11}^2\frac{\partial d_{11}}{\partial m}$$

$$\left.+ \frac{\partial\hat{C}_7}{\partial m}\overline{\sigma}_{11}d_{11}^2 + \hat{C}_7 d_{11}^2\frac{\partial\overline{\sigma}_{11}}{\partial m} + 2\hat{C}_7\overline{\sigma}_{11}d_{11}\frac{\partial d_{11}}{\partial m} \right]$$

For the special case of uniform stress (i.e. $\overline{\sigma}_{11} = 0$), uniform damage, and uniform temperature distributions only the moisture gradient term is dominant and the governing equation (5) can be written as,

$$\frac{\partial m}{\partial t} = \frac{\partial}{\partial X_i}\left[\left(C_0 + C_1\delta_1 + C_2\delta_1^2\right)\frac{\partial m}{\partial X_i}\right] \tag{9}$$

The coefficients C_0, C_1, C_2, may depend on moisture concentration and temperature and are characterized from absorption experiments on pre-cracked laminate specimens.

Model Verifications

In order to verify the model predictions, moisture weight gain data for graphite/epoxy 5-harness satin $[0/90/0/90]_s$ laminate with different micro-crack densities were obtained from hygrothermal tests performed elsewhere[9]. Specifically, test specimens were mechanically pre-cracked by uniaxial fatigue as well as static loading and then exposed to 75% relative humidity at 40°C. The crack densities reported for the specimens were 6.142 cracks/ply/cm for the static load case and 11.142 cracks/ply/cm for the fatigue load case respectively. An un-cracked specimen was also included in the test matrix as the control specimen. The specimens were not subjected to any applied mechanical stress during absorption. The effective diffusivity for each test specimen was extracted from weight gain data using standard analytical procedure [1].

3

A quadratic least-squares curve-fit to the diffusivity data is shown by the solid line in Figure 2. The values of the damage coefficients defined in equation (9) were obtained using this procedure for this case and are given as $C_0 = 3.184 \times 10^{-09}$, $C_1 = -1.036 \times 10^{-10}$, and $C_2 = 1.184 \times 10^{-10}$. The corresponding equation for through-thickness diffusivity as a function of crack density is given by,

$$D_3 = 3.184 \times 10^{-09} - 1.036 \times 10^{-10} \delta_1 + 1.184 \times 10^{-10} \delta_1^2 \quad cm^2/sec \tag{10}$$

Moisture weight gain curves predicted by the model using the quadratic diffusivity-damage relation given by equation (10) and its comparison with test data are shown in Figures 3, 4, and 5. The results shown in Figure 3 correspond to an undamaged specimen. The moisture data shown in Figure 4 correspond to a micro-crack density of 6.142 cracks/ply/cm, and those in Figure 5 correspond to a micro-crack density of 11.142 cracks/ply/cm. Reasonable agreement between model predictions and test data is observed for all three cases for the duration of the tests.

References

1. Shen, C. H. and G.S. Springer, 1981, "Effects of Moisture and Temperature on the Tensile Strength of Composite Materials," in *Environmental Effects on Composite Materials*, G. S. Springer, ed., Lancaster, PA: Technomic Publishing Co., Inc., pp. 79-93.
2. Gurtin. M.E., and Yatomi, C. "On a model for Two Phase Diffusion in Composite Materials," *Journal of Composite Materials*, Vol. 13, (April 1979), pp. 126-130.
3. Carter. H.G., and Kibler, K.G. "Langmuir-Type Model for Anomalous Diffusion in Composite Resins," *Journal of Composite Materials*, Vol. 12, (April 1978), pp. 118-130.
4. Shirrell. C. D., Leisler, W. H. and F. A. Sandow. 1979. "Moisture-Induced Surface Damage in T300/5208 Graphite/Epoxy Laminates," *in Nondestructive Evaluation and Flaw Criticality for Composite Materials*, ASTM STP 696, R. B. Pipes, ed., American Society for Testing and Materials, pp. 209-222.
5. Weitsman, Y. 1991. "Moisture in Composites: Sorption and Damage," in *Fatigue of Composite Materials*. K. L. Reifsnider, ed., Elsevier Science Publishers B.V., pp. 385-429.
6. Weitsman. Y. 1987. "Coupled Damage and Moisture Transport in Fiber- Reinforced, Polymeric Composites," *International Journal of Solids and Structures*, 23(7):1003-1025.
7. Adkins, J.E.,1959. "Symmetry Relations for Orthotropic and Transversely Isotropic Materials." Arch. Rational Mech. Anal., Vol 4, pp. 193-213.
8. Talreja, R.. 1994. "Damage Characterization by Internal Variables," Damage Mechanics of Composite Materials, Edited by R. Talreja, Elsevier Science, pp. 53-78.
9. Private Communications, Pratt & Whitney Aircraft , West Palm Beach. Florida.
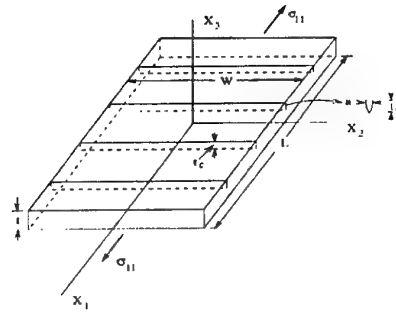
Figure 1. Schematic of a Micro-Cracked Laminate under Uniaxial Stress State
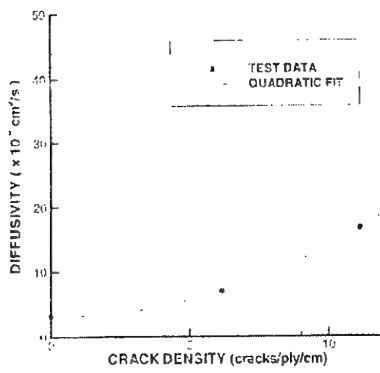

Figure 2. Change in Diffusivity with Micro-crack Density
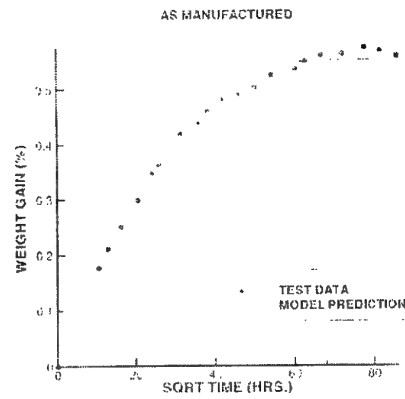

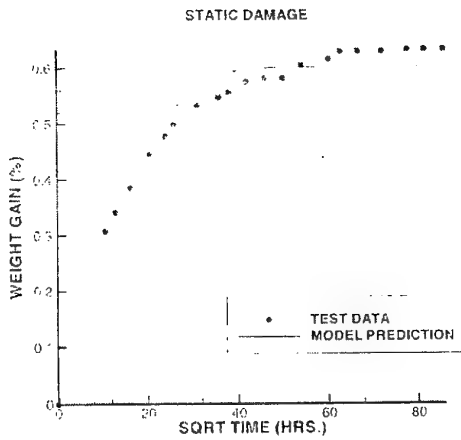Figure 3. Predicted vs. Measured Weight Gain for $\delta_1 = 0$ cracks/ply/cm

Figure 4. Predicted vs. Measured Weight Gain for $\delta_1 = 6.142$ cracks/ply/cm
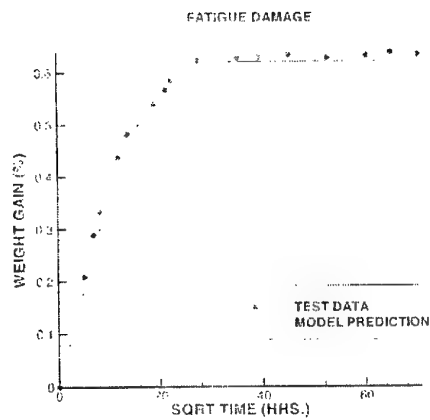

Figure 5. Predicted vs. Measured Weight Gain for $\delta_1 = 11.142$ cracks/ply/cm

5

Influence of Fiber-Matrix Adhesion on the Fatigue Behavior of Cross-Ply Glass-Fiber Epoxy Composites

Jochen Gassan

University of Kassel, Institut für Werkstofftechnik
Mönchebergstraße 3, 34109 Kassel (Germany)
Tel. (+49) 561-804-3673; Fax. (+49) 561-804-3692
e-mail: Gassan@hrz.uni-kassel.de

1. Introduction

The fatigue behavior of composite materials has been a subject of active research in recent years. The damage process in laminated composites subjected to fatigue loading is significantly different from that observed in conventional materials. Four main damage modes have been observed in laminate composites under fatigue loading: matrix cracking, fiber-matrix debonding, delaminations, and fiber fracture. Typically, matrix cracking and delamination occur early in the life, while fiber-matrix debonds and fiber fractures initiate during the beginning of the life and accumulate rapidly towards the end, leading to final failure. It has been observed that the stiffness of the laminate reduces during the process of damage accumulation in laminated composites by using stiffness change as non-destructive fatigue damage parameter [1]. Crack propagation (crack bridging or debonding) plays an essential role in fatigue behavior of composites. When interface bonding is relatively weak, debonding and frictional sliding occur readily upon crack extension, allowing fibers to remain intact and bridge the crack. Upon cyclic loading of the composite, the frictional sliding at the interface changes interface properties such as roughness. When the fibers are frictionally bonded to the matrix, the interfacial sliding can be fully characterized by the interfacial sliding shear stress, τ. Interfacial sliding shear stress has found to be not constant, the changes in τ have been attributed to fiber surface abrasion, asperity wear, and matrix plasticity. A strong interface would inhibit interface sliding and lead to fiber fracture instead of crack bridging by intact fibers [2-4].

More practically oriented papers [5,6] summarized the influence of interface on the fatigue behavior of carbon fiber/epoxy cross ply composites. It was found that the fatigue performance is improved by increases interface strength. It has also been reported that fatigue performance is reduced by increasing interface strength in the case of brittle epoxies because these matrices have been shown to initiate matrix cracks.

Little information is available regarding interface effects on the fatigue performance of glass fiber composites. For instance, Keusch et al. [6] looked into the fatigue performance of cross-ply epoxy based laminates [0/90/90/0] under tension-tension loading with different fiber-matrix adhesion in the 0° and 90° plies. The fatigue strength of these laminates was measured to be in order: good adhesion in the 0° and 90° plies, good adhesion in the 0° plies and a reduced one in the 90° plies, reduced adhesion in the 0° plies and a good one in the 90° plies, and at least, reduced adhesion in both, the 0° and 90° plies. Van den Oever et al. [7] showed for unidirectional glass-fiber polypropylene composites by 10° off-axis fatigue tests that the interface has a large influence on damage development at a normalized lifetime n/N > 10 %, while below both types of composites showed the same stiffness.

2. Materials, Composite Preparation and Test Procedure

In this study continuous E-glass fibers with a specially developed epoxy compatible sizing

(EP-Sizing) for a strong fiber matrix adhesion and with a polyethylene sizing to generate a weak fiber-matrix interaction (PE-Sizing) were used and embedded in an epoxy resin (LY556/HY917/DY070 from Ciba Geigy GmbH). The EP sizing bases on an uncured bisphenol A epoxy binder which contains γ-aminopropyltriethoxy silane, while the PE sizing is pure high moleculare weight polyethylene (Hordamer PE 03 from Hoechst AG). The laminantes were manufactured by using a two step process: unidirectional prepreg tapes were produced by filament winding technology and hot pressed under vacuum and 80°C to cross-ply composites.

Finally, the composites were additionally cured by 1 h at 100°C and 8 h at 140°C. The fiber volume fraction in each of the cured panels was determined using DIN EN 60. The average fiber volume fraction in the 'EP-sized' and 'PE-sized' panels were 0.4. The 150 mm long, 16 mm wide, and 2 mm thick specimens were cut from the cross-ply laminates. Cross-ply end tapes were bonded to the coupons.

All of the fatigue tests were performed on a servohydraulic MTS test machine under load controlled mode. A 25 mm extensometer was used to monitore strain continuously during the fatigue test. Tension-tension fatigue tests in load increasing mode with different stress-ratios 'R' and frequencies 'f' were done for the different material systems. Damage was monitored by recording the dynamic stress-strain curves continuously during the test. Further, different dynamic modulus characteristics and the loss energy, both defined according to Figure 1, were calculated.
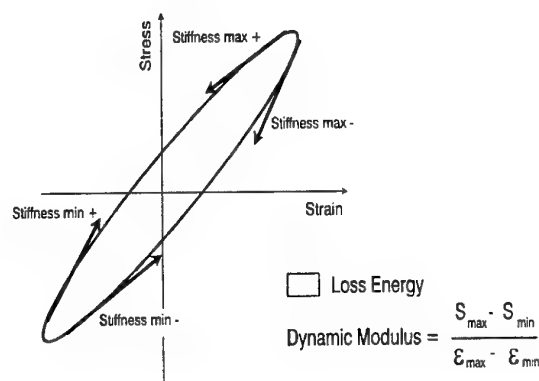

Figure 1:
Dynamic Stress-Strain curve and definition of the characteristic values used according to Lazan [8]

$$Dynamic\ Modulus = \frac{S_{max} - S_{min}}{\varepsilon_{max} - \varepsilon_{min}}$$

3. Results and Discussion

It is obvious that in fibrous composite materials energy is dissipated, loss-energy, during crack initation and propagation by a multiplicity of microfracture events occuring at the crack tip including fiber fracture, matrix cracking, interfacial breakdown, fiber 'relaxation', and fiber pull-out [9]. Because of the fact that each of these different microfracture events is related to a defined amount of dissipated energy the loss energy seems to be an effective and sensitive tool for measuring damages directly in materials as was shown and discussed previously [10,11].

From Figure 2A one can see that the critical load for damage initiation/propagation is lower for the 'PE-sized' as for the 'EP-sized' glass-fiber reinforced epoxies, followed by a more significant period of continuous damage propagation for the 'EP-sized' composites. As a result of both, the load at failure was measured to be 230 MPa and 310 MPa for the composites containing 'PE-sized' and 'EP-sized' fibers, respectively. Increasing stress ratio in tension-tension mode from 0.01 to 0.1 lead to a slight increase in fracture load, while fracture load seems to be independent from frequencies used (5 and 10 Hz).
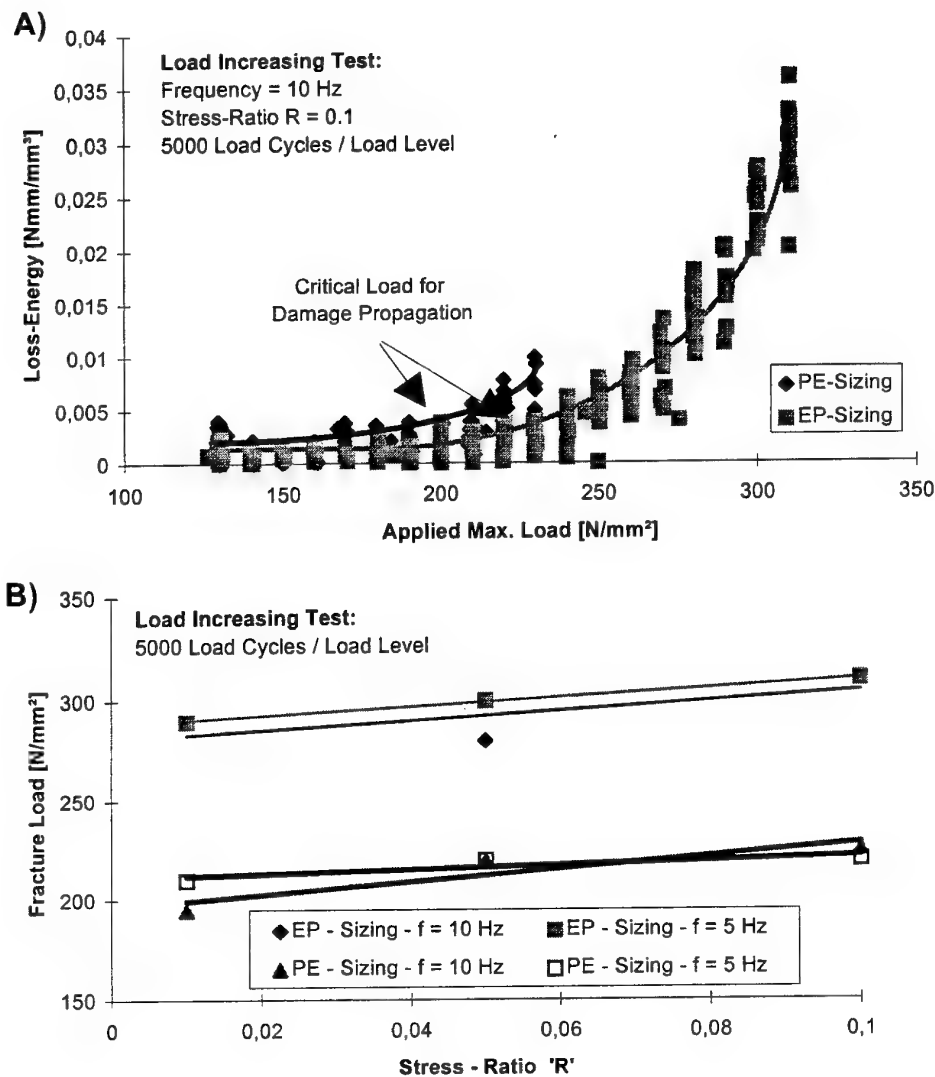
Figure 2: Influence of fiber-matrix adhesion on (A) on loss-energy vs. applied max. load (B) test conditions on fracture load of glass-fiber epoxy composites

Dynamic modulus vs. load cycles and applied max. load, respectively, for both types of composites is shown in Figure 3. One can see, that the dynamic modulus is in general lower and CDS is reached at lower max. applied loads in the case of composites containing PE-sized fibers. Further because of damages, hysteresis stress-strain loops are characterized by changing area and decreasing main slope. A theoretical loop is given in Figure 1, careful stress and strain measurements allow to determaine the changes in some stiffness characteristics (tangent modulus) of the loop, viz. 'Stiffness min +' at the start of loading and 'Stiffness max +' at the end of loading with typical changes in these stiffnesses for composites with PE- and EP-sized fibers. Both composites tested possess a strong non-linearity in the loading part of the stress-strain hysteresis loop (ratio 'stiffness max +' to 'stiffness min+') which is more significant for the PE-sized composites. Reasons for this non-linearity could be a result of fiber matrix sliding (dependent on interfacial adhesion and applied load) in the 0° plies as well as the possibility of crack closure arising from frictional

effects, consequently these cracks will not open unless a certain stress is applied [12] and in consequence also the crack density. A similar discussion is published by Walls et al. [13] for MMC's, where the reduction in modulus is connected with matrix cracking, while the non-linearity in the stress-strain response was more a result of the interface sliding. Both of these structural mechanisms lead to a more significant non-linearity of the PE-sized composites during the whole test and independent from applied max. load.
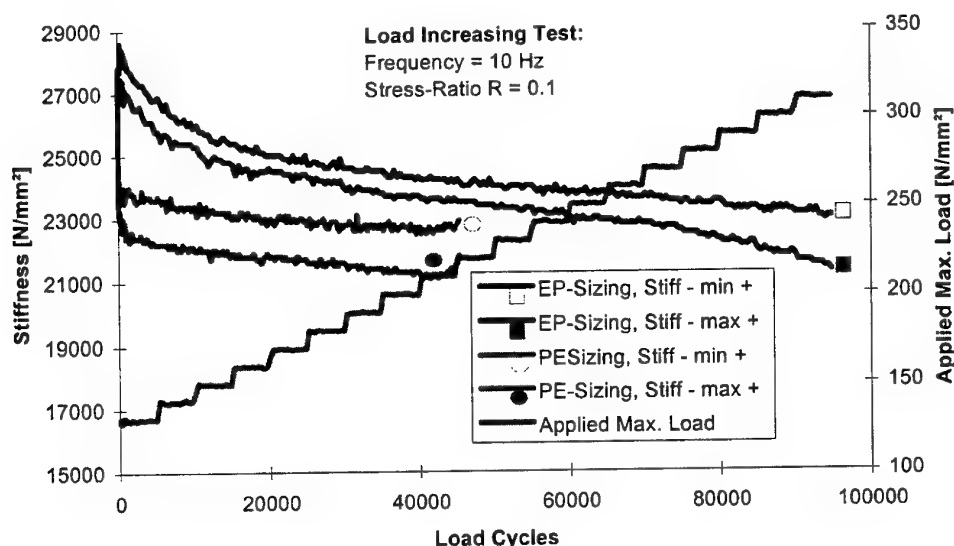
Figure 3.   Influence of fiber-matrix adhesion on the stiffness of glass-fiber epoxy composites

4.   Conclusion
The effect of glass-fiber epoxy interface in cross-ply reinforced composites on the fatigue behavior (load increasing test) was studied by using differently sized glass-fibers. The composites only differed in the interface, all other conditions being kept constant. To generate a weak interphase a 'PE' sizing was used, while a 'EP' sizing led to a strong adhesion.
It was shown that the loss energy is a sensitive tool to characterize the nature of fiber matrix adhesion. The critical load for damage initiation/propagation, defined by the loss energy vs. applied max. load curve, for composites with poor adhesion between fiber and matrix was significantly lower (approx. 190 MPa) than for those composites containing well-bonded fibers (approx. 230 MPa). Further, rate of damage propergation for each load cycle was reduced in the second case. Test conditons such as stress-ratio (between 0.01 and 0.1) and frequency (5 and 10 Hz) are only on less significance regarding fracture load.
Further, the damage, as measured by stiffness reduction, was more significant for the composites with 'PE' sized fibers as was found for 'EP' sized ones. Further, the degree of non-linearity of the stress-strain hysteresis loop (ratio 'Stiffness max +' to 'Stiffness min +') was much lower for composites with 'EP' sized glass fibers as for that with the 'PE' sized ones.

5.   Acknowledgement

for the cession of the 'PE' and 'EP' sized fibers.

6.   References

1.   S. Subramanian, K.L. Reifsnider and W.W. Stinchcomb, *Intern. J. Fatigue* **17**, 343-351, (1995).

2.   B.N. Cox and D.B. Marshall, *Fatigue and Fracture of Engineering Materials and Structures* **14**, 847-861 (1991).

3.   V. Ramakrishnan and N. N.Jayaraman, *J. Mater. Sci.* **28**, 5592-5602 (1993).

4.   G. Bao and Y. Song, *Journal of Mechanics and Physics of Solids* **41**, 1425-1444 (1993).

5.   S. Subramanian, J.S. Elmore, W.W. Stinchcomb and K.L. Reifsnider, Influence of Fiber-Matrix Interphase on the Long-Therm Behavior of Graphit/Epoxy Composites, in: *Composite Materials: Testing and Design (Vol.12)*, R.B. Deo and C.R. Saff (Eds.), ASTM STP 1274, pp. 69-87.

6.   S. Keusch, H. Queck and K. Gliesche, *Composites Part A* **29A**, 701-705 (1998).

7.   M. van den Oever and T. Peijs, *Composites Part A* **29A**, 227-239 (1998).

8.   B.J. Lazan, Damping of Materials and Members in Structural Mechanics, Pergamon Press Inc., Oxford 1968

9.   P.W.R. Beaumont, *J. Adhesion* **6**, 107-137 (1974).

10.   A.K. Bledzki, J. Gassan and K. Kurek, *Experimental Mechanics* **37**, 324-327 (1997).

11.   A.K. Bledzki and J. Gassan, *JTEVA* **26**, 467-471 (1998).

12.   A.W. Pryce and P.A. Smith, *J. Mater. Sci.* **27**, 2695-2704 (1992).

13.   D.P. Walls, J.C. McNulty and F.W. Zok, *Metallurgica and Materials Transactions* **27A**, 1899-1907 (1996).

Assessment of Time-Temperature Superposition Principle as a Basis for a Long Term Behaviour Prediction of CFRP under Bending Load

Rui Miranda Guedes

Department of Mechanical Engineering and Industrial Management (DEMEGI)
Faculty of Engineering of University of Porto (FEUP)
Rua dos Bragas, 4050-123 PORTO, PORTUGAL

Introduction

Simple bending creep tests using cantilever beams are used in order to assess the potential application of Time-Temperature Superposition Principle (TTSP) as a basis for a long-term behaviour prediction. The TTSP is usually applied for the acceleration of creep tests and it as been proved to be well suited to characterise the influence of temperature over the mechanical properties. Unfortunately there is no experimental demonstration of a real equivalence between the behaviour at higher temperatures for a short period of time and the long-term behaviour under a lower temperatures. Much effort shall be done to reduce the time and experimental work to describe creep behaviour. Some existing European standards test methods for prediction of long-term behaviour of GFRP pipes, for example, imply test data acquisition up to 10000 hours, more than one year. The future of FRP applications depend on a reliable short term creep characterisation, i.e. of a few weeks, for a confident extrapolation over a long period of time, i.e. 10 to 50 years.

This research was done at the INEGI (Institute of Engineering and Industrial Management) in the context of the characterisation of advanced composite materials to build support structures of particle detectors. These structures should present a high dimensional stability, small deviations from the initial position will lead to large errors in signal detection of the beam. The detectors will make part of the new particle accelerator called LHC (Large Hadron Collider). This is a big project of the European Laboratory for Particle Physics (CERN) with new challenges in many engineer fields, especially in the application of new materials.

Two types of extrapolation were tested at the linear viscoelastic domain. The first one use the experimental data obtained at 50°C for a minimum period of time fitted to a Findley model (Simple Power Law). Another approach applied the TTSP to obtain the creep master curve. The curves were obtained from dynamic experimental data at frequencies from 0.01Hz up to 100Hz and at different temperatures from 23°C up to 135°C.

The creep extensions were measured, close to the section of maximum moment, using electric strain gauges, one on the top surface (tension) and other on the bottom surface (compression). The signal from an unloaded specimen was used to compensate temperature effects. The loads were selected in order to ensure a maximum stress level lower than 10% of the rupture stress σ_r.

The linear viscoelastic behaviour is usually observed at relatively low stress levels, hence the proposed maximum stress level lower than 10% of σ_r is expected to maintain the behaviour in the linear domain.

Material

A brief presentation of the experimental test specimens and test apparatus is given. A set of 50x200mm^2 specimens was sectioned from composite plates fabricated at INEGI using the unidirectional UC125 RNA and the twill woven CC194 RNA with the same resin system (RNA).

The stacking sequence of the laminates and the geometry of test specimens were imposed by the CERN.

For the carbon fibre composites the time dependency exhibited by the fibre dominated mechanical properties E_{11}, ν_{12} is negligibly small, when compared to the highly time dependent matrix dominated properties. Analysing the staking sequences used in this work, no significant creep should be expected due to the existence of fibres in the loading direction. So if the deformations are constant then an internal stress transfer should occur, i.e., the non-0° plies should exhibit stress relaxation

Static bending properties of the test specimens

The 3 point bending flexural tests were used to determine the flexural modulus (E_b) and the flexural stress strength (σ_r). The geometry of the tests follows the ASTM D790M standard except for the rate definition. In these tests it was used a rate of 5mm/min instead of 12mm/min as recommended by the standard. The measured properties are as follows:

Table 1: Flexural properties of the test specimens UC125 RNA [0°/45°/90°/-45°]$_{2s}$

Specimen	A1	A2	A3	Average
E_b (GPa)	38.84	38.57	39.07	38.83 +/- 0.25
σ_r (MPa)	653	649	624	642 +/- 16

Table 2: Flexural properties of the test specimens UC125 RNA [0°/90°]$_{4s}$

Specimen	B1	B2	B3	Average
E_b (GPa)	46.76	46.72	48.72	47.40 +/- 1.15
σ_r (MPa)	846	848	854	849 +/- 4

Table 3: Flexural properties of the test specimens CC194 RNA [0°]$_{4s}$

Specimen	C1	C2	C3	Average	Supplier
E_b (GPa)	41.94	42.5	42.16	42.20 +/- 0.28	50
σ_r (MPa)	717	727	731	725 +/- 7	900

Dynamic-Mechanical-Thermal-Analyser (DMTA) test results

The characterisation of the mechanical properties of polymeric materials on a DMTA analyser gives the complex compliance (S^*) as a function of angular frequency ω. In order to characterise the viscoelastic material behaviour in a very broad range of frequencies (or times), it is necessary to combine measurements at several temperatures applying the time-temperature superposition principle (TTSP). According to this principle, a given property measured for short times must be identical with one measured for longer times at a lower temperature, except that the curves are shifted parallel to the horizontal axis, matching to form a master curve.

The dynamic test specimens were cutted out from the plates with the three different stacking sequences. The dynamic tests were carried out in a beam cantilever apparatus, as shown in Figure 1. The specimens had a thickness of 2.2mm, width of 10.0mm and the distance between the support and the load application of 22.0mm.

For each temperature level, the frequencies varied from 0.1Hz to 100Hz. The maximum imposed deflection was 64μm and the temperature levels were within the range of 20°C to 135°C. After the frequency-time transformation; the short-term compliance curves in time domain were obtained. Then the data is shifted for each temperature to a reference temperature, T_{ref}, using the time-

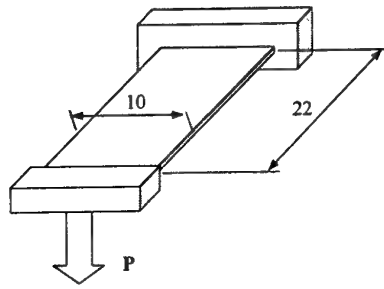temperature superposition principle (TTSP) to build up the master creep compliance curve, as shown in Figure 2.

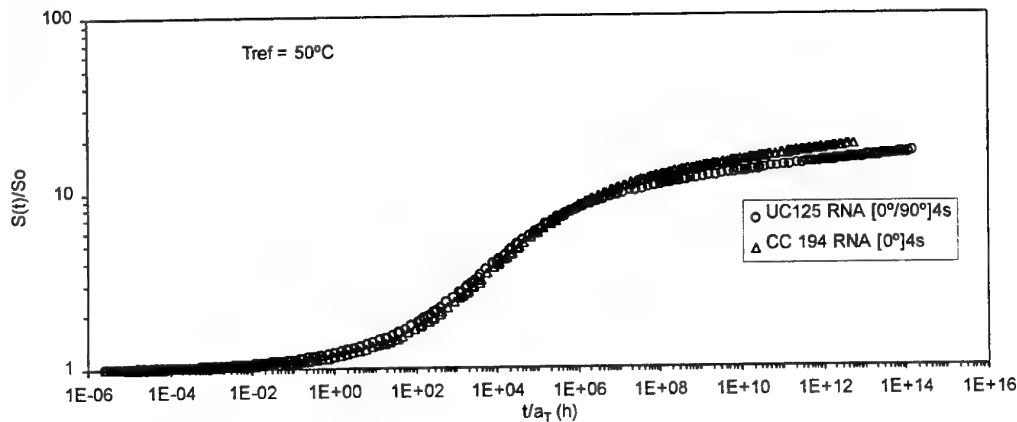Figure 1: Geometry of DMTA test specimens.

Figure 2: Creep compliance master curves.

Experimental results for the creep tests

Due to limitations on temperature control device inside the laboratory, an environmental chamber was used. Inside the chamber the temperature and the relative humidity was maintained steady: 23°C+/-1°C and Hr. 50%+/-2% for the first test and 50°C+/-1°C and Hr. 50%+/-2% for the second test, which is still going on.

In Figure 3 the test apparatus is shown inside the environmental chamber. The maximum applied stresses are lower than 10% of the rupture stress. A close view of test apparatus with the respective geometry is shown in the same figure.
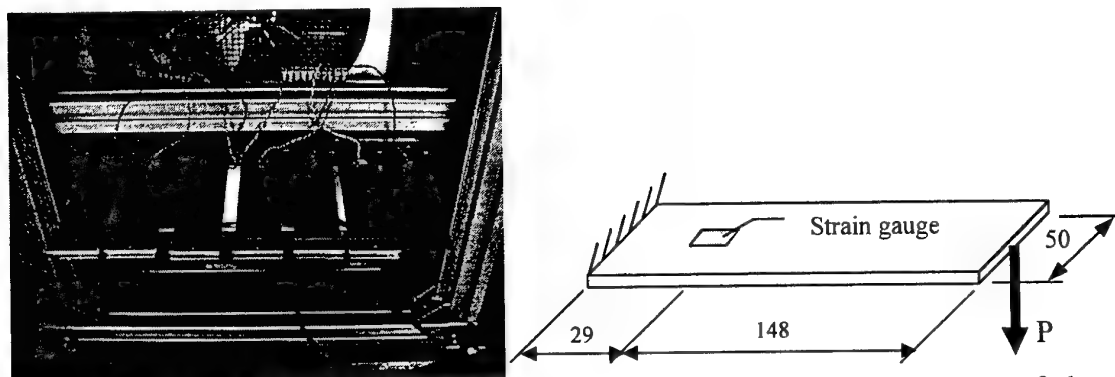
Figure 3: Test apparatus inside the environmental chamber and the geometry of the test apparatus.

The creep extensions are measured using strain gauges. For the bending tests, the tensile and compression extensions were recorded close to the section of maximum bending moment, as shown in Figure 3.

The creep compliance is defined as:

$$S(t) = \frac{\varepsilon(t)}{\sigma_0} \tag{1}$$

For a better comparison of all test specimens the relative creep compliance was used instead. The relative creep compliance is defined as:

$$S_R = \frac{S(t)}{S_0} \tag{2}$$

After almost 1800 hours of bending creep test of specimens made of UC125 RNA at 23°C and 50%Hr, no significant creep strains was detected within the strain gauges accuracy, i.e. ±20με.

These results motivated the decision to increase the temperature to 50°C instead of increasing the loading stress, with two purposes: accelerate the viscoelastic behaviour and avoid the non-linear behaviour.

The results of the second tests, after almost 2000 hours, revealed an increase of the creep compliance around 6.7% in average for the CC194 and around 2.5% in average for the UC125. Surprisingly the creep tests pointed that the CC194 has a larger increase of the creep compliance. In Figures 4 and 5 the creep test results are plotted with the simple power law predictions (Findley) along with master creep compliance curve (DMTA) and the predictions for an latter approach (Model) developed latter. All experimental results are in tension except the B2(C) and C5(C) that are in compression. The Findley or the simple power law was defined as it follows:

$$S(t) = S_0 + S_1 \left(\frac{t}{\tau_0} \right)^n \tag{3}$$

where, $S(t)$ is the creep compliance, t the time, n a material constant, S_0 the time independent initial compliance, S_1 the coefficient of the time dependent compliance and τ_0 is a unit reference time.

The latter approach was developed after a careful analysis of the DMTA test apparatus. It was not difficult to conclude that the beam cantilever should be considered a short beam. So it become obvious that the DMTA results depend on the shear compliance of the matrix rather than the on creep compliance of the laminate. Therefore the viscoelastic properties of the matrix could be determined approximately (Horoschenkoff, 1990). A nonlinear viscoelastic analysis of the carbon fibre matrix interphase was already presented by another researcher (Sancaktar, 1990). The present approach considers that the interface between each ply of the laminate, with a thickness to be determined, is viscoelastic, i.e., a rich resin interlayer zone with the same properties of the resin. Introducing this data into the LAMFLU program (Guedes & Marques, 1998), it was possible to make predictions that compared reasonably with the experimental results.

Conclusions

One simple explanation for CC194 behaviour can be found on the reinforcement tissue itself. The overlap of the transverse and longitudinal fibres (twill woven) produces plies with fibres not stretched. The stretching of the fibres is the promoted by the tensile stresses and the viscoelastic matrix. This phenomenon should not happen in unidirectional reinforcements. Nevertheless this paradigm did not seem satisfactory to explain the experimental results.

The creep master curves obtained from the dynamic mechanical and thermal analysis (DMTA) were very similar for both laminates UC125 RNA [0°/90°]$_{4s}$ and CC194 RNA [0°]$_{4s}$.

The master curves shown an increase of the creep compliance (limit value?) between 16 and 19 times of the initial value. Further the master curves indicate, as shown in Figure 2, that it takes an absurd time to reach this limit at 50°C (1 millions of years).

One the other hand the comparison of the creep master curves and the creep test results have shown a large discrepancy. A re-interpretation of the DMTA results was necessary with the introduction of a viscoelastic interface between each ply into the laminate model. This resulted into a new approach that explain the experimental results and permit a long-term prediction, of the creep bending response of the UC125 RNA [0°/90°]$_{4s}$ and CC194 RNA [0°]$_{4s}$ laminates based on Time-Temperature-Superposition-Principle master curves.
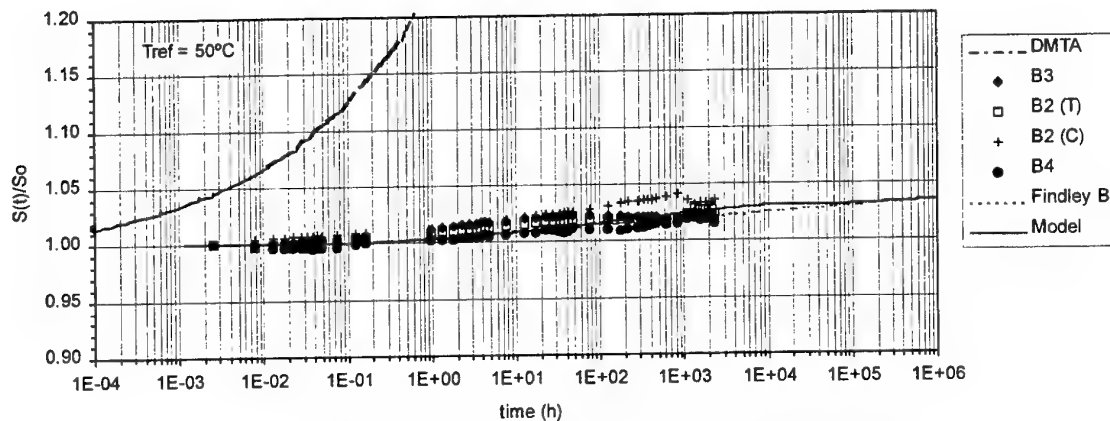
Figure 4: Relative creep compliance for the UC125 RNA [0°/90°]$_{4s}$ test specimens.
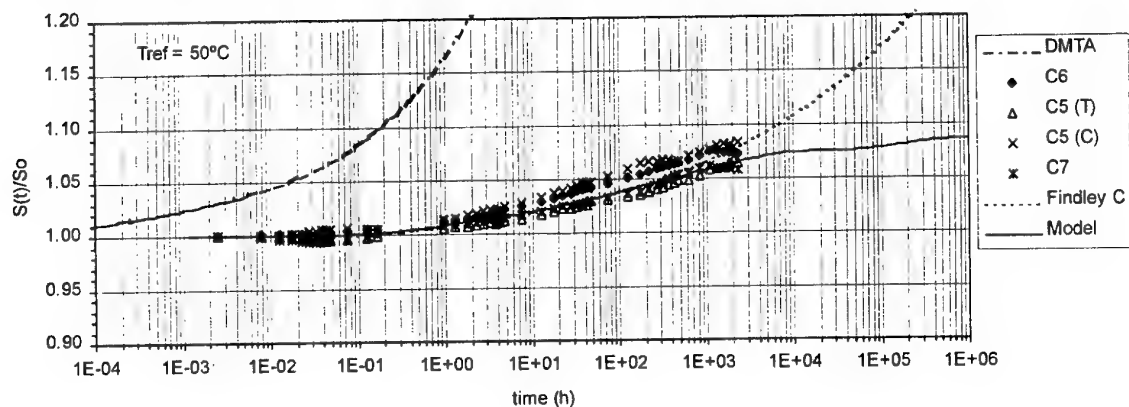
Figure 5: Relative creep compliance for the CC194 RNA [0°]$_{4s}$ test specimens.

References

A. Horoschenkoff, 1990, *Characterization of the Creep Compliances J_{22} and J_{66} of the Orthotropic Composites with PEEK and Epoxy Matrices Using the Nonlinear Viscoelastic Response of the Neat Resins*, Journal of Composite Materials, 24, pp. 879-891.

Rui Miranda Guedes, António Torres Marques, Albert Cardon, 1998, *Analytical and Experimental Evaluation of Nonlinear Viscoelastic-Viscoplastic Composite Laminates under Creep, Creep-Recovery, Relaxation and Ramp Loading*, Mechanics of Time-Dependent Materials, 2, pp. 113-128.

Rui Miranda Guedes, António Torres Marques, Albert Cardon, 1999, *Creep/Creep-Recovery Response of Fibredux 920C-TS-5-42 Composite under Flexural Loading*, Applied Composite Materials, 6, pp. 71-86.

Jhumur Lahiri, G. Rohini Devi, S. V. Subrahmanyam and K. Balakrishna, 1988, *Establishing the criteria for selecting suitable interlayer material for double-layered filament-wound CFRP structures*, Composites, 19 (5), pp. 376-382.

E. Sancaktar, P. Zhang, 1990, *Nonlinear Viscoelastic Modelling of the Fiber-Matrix Interphase in Composite Materials*, Journal of Mechanical Design, 112, pp. 605-619.

Brian Cox, Gerry Flanagan, 1997, *Handbook of Analytical Methods for Textile Composites*, NASA Contractor Report 4750.

Viscoelastic Contact Problems of Fiber Reinforced Polymers

Thomas Neff
Department of Mechanics and Material Testing, Technical University of Munich, Germany

Otto Brüller
Department of Mechanics and Material Testing, Technical University of Munich, Germany

ABSTRACT

The relative new class of materials – the fiber reinforced polymers (FRP) – exhibits a couple of outstanding properties. These materials have a low density and high strength and they can be designed to have different moduli and strength in different directions. Nevertheless, problems occur if structural parts made of metal connected by screws or pins should be substituted by parts made of FRP. Because of economical reasons, in most cases, especially in the case of series production, the original fixtures should be maintained. To fix a given component using screws or pins, one has to drill holes into the material. With fiber reinforced materials, as expected, the fibers will be cut and the strength of the component decreases considerably. The aim of the present work is to describe the behavior of the contact metal pin – fiber reinforced material under mechanical loading.

1. THEORETICAL CONSIDERATIONS

The well known correspondence principle in viscoelasticity can be applied only if there are no changes of the contact surfaces between the almost rigid pin and the viscoelastic fiber reinforced plastic. In such cases the possibility exists to reduce a viscoelastic (time-dependent) contact problem to an elastic (time-independent) one. In the present case the correspondence principle can be used if the contact area does not change with time. This restriction can only be fulfilled when the diameter of the pin and that of the hole in the FRP do not differ and remain constant. In practice the situation is different: pins may be smaller than the hole and this new situation demands a new theoretical development to be done in the next future.

2. EXPERIMENTAL

The used material were 16 layer (0°, 90°, ±45°) carbon fiber composites. The matrix was an epoxy resin (Martens Plus EP). The rectangular specimens (thickness: 2.4 mm) were loaded by a pin of ¼" (6.35 mm) which was inserted in a hole of the specimens having the same nominal diameter. Both diameters, of the pin and of the hole, are within a tolerance of 1μm. Fig. 1 shows the schematical arrangement of the testing setup. The strain of the specimen was measured using self made strain gauge based extensometers (Fig. 2).
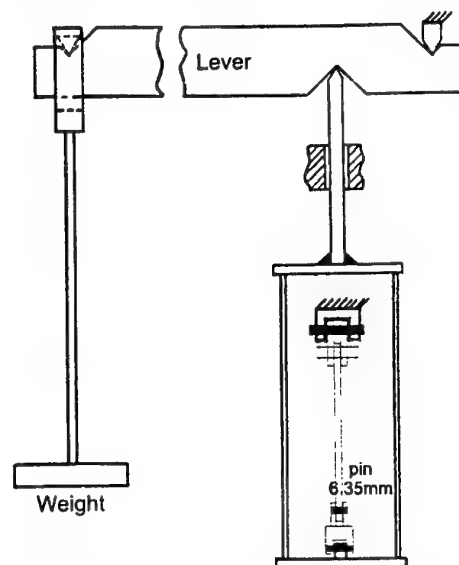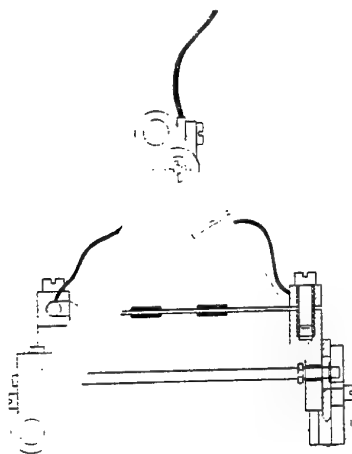

Figure 1: The experimental setup

Figure 2: Extensometer

Figure 4: Creep curves of pin loaded non-reinforced polymer specimens

3. RESULTS

As a first step, the creep behavior of the pure resin has been investigated. Figs. 3, 4, and 5 show the results. Fig. 3 presents the result of standard creep tests conducted on shoulder specimens of rectangular cross-section. In Fig. 4 the results of creep tests carried out on specimens made of the same non-reinforced polymer loaded via a pin–hole connection are shown. One can see that the creep strain of the shoulder specimens at the end of the measurement (after 100 h) is higher than that of the pin-loaded specimens. This unexpected behaviour points to a size-effect. So in a second step rectangular specimens in the same size as the holed ones were usually loaded. Fig. 5 shows the results of the rectangular specimens.

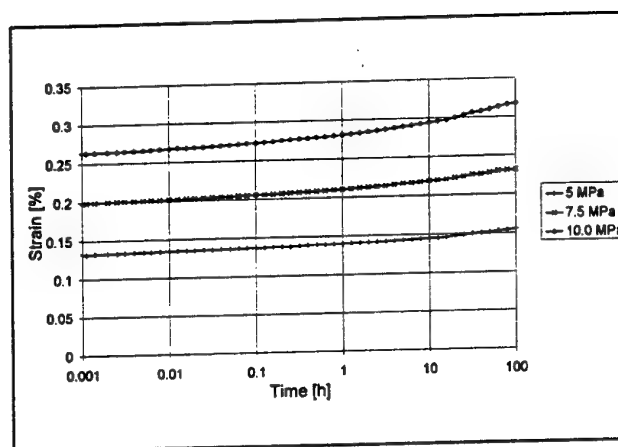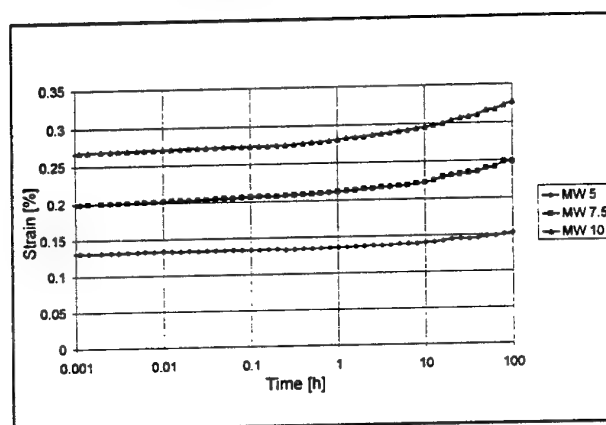

Figure 5: Creep curves of the non reinforced polymer (rectangular specimens)

It is seen that the influence of pin loading is very small as compared with conventional loading. The deformation of the hole itself is as small as it can be neglected in relation to the creep strain of the polymer. In the case of pin loaded tests, the working stress was choosen as the load necessary to produce stresses of 20, 30, and 40 MPa on the projected area of the hole. The working stresses in the remainder of the cross-section were about 5, 7.5, and 10 MPa respectively. The tests conducted on FRP specimen have shown that in this case the creep strain is about one decade lower. Because of this fact the loading of the reinforced specimens was increased in additional test series to 20 and 30 MPa. Although theoretically the influence of the contact area of the pin–specimen was supposed to be substantial, the results show practically no influence. These creep curves are shown in Fig. 6 and 7.
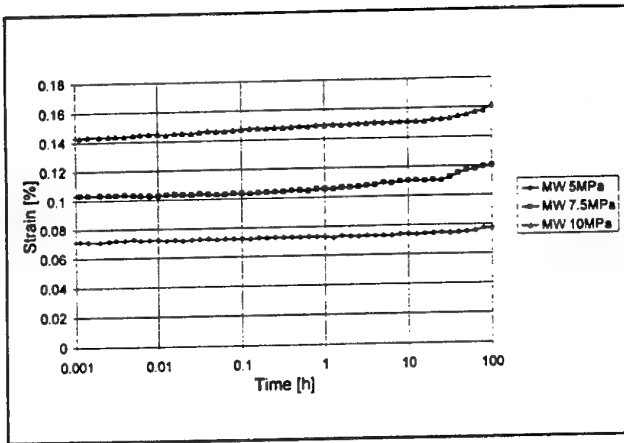

Figure 3: Creep curves of non reinforced polymer (shoulder specimens)

Figure 6: Creep curves of pin loaded FRP specimens at 5, 7.5, and 10 MPa
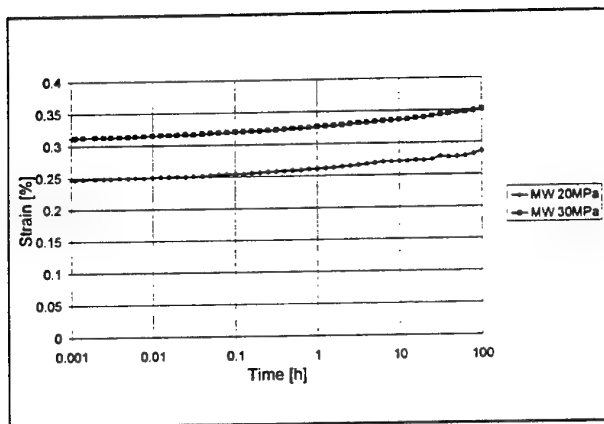
Figure 7: Creep curves of pin loaded FRP specimens at 20 and 30 MPa

CONCLUSIONS

The behavior of a metal pin – FRP plate connection depends primarily on the matrix of the material. Using a duroplastic matrix, the loading type, i.e. with or without pin, has no influence on the behavior of the material. In a next step the behavior of thermoplastic polymers will be tested using the same procedure. In addition, different types of layer combinations have to be tested at different temperatures and loads.

LITERATURE

Johnson, K.L., (1985), *Contact Mechanics*, Cambridge University Press, Cambridge, UK

Kloiber, R., (1997), *Kleinflächige Lasteinleitung bei kohlefaserverstärktem Epoxydharz*, Student Project, Technical University of Munich

Götz, M., (1999), *Kriechverhalten von Epoxydharz*, Student Project, Technical University of Munich

Creep and Stress Relaxation of Composite Cylinders

Jerome T. Tzeng
US Army Research Laboratory
Weapons and Materials Research Directorate
Attn: AMSRL-WM-MB
Aberdeen Proving Ground, MD 21005-5066

Composite materials are currently used for lightweight pressure vessels and highly efficient rotors for energy storage. For both applications, pre-stresses are built in during fabrication of the cylinders through a "press-fit" procedure to enhance the mechanical performance. Composite overwrap pressure vessels are prestressed; therefore, the liner is in a state of hoop compression and the composite overwrap is in tension. For the other application, the rotors are subjected to a radial compression prior to operation. Accordingly, centrifugal force resulting from the rotation of the rotors generates tensile stresses in the radial and circumferential directions. Since the composite rotors are mainly reinforced in circumference (filament wound cylinders), the radial tensile stress is critical to the ultimate performance of the rotors. Accordingly, it is essential to design and build the rotors with radial pre-compression. However, polymer matrix composites generally creep over a long period of time, especially at an elevated temperature. The associated stress relaxation in the composite will result in the loss of the pre-stresses and potentially rotor. The objective of this investigation is to develop an analytical method to study the viscoelastic behavior of thick-walled composite cylinders. The analysis can be applied to the design of flywheel machinery and overwrapped composite pressure vessels.

In this study, the linear quasi-static viscoelastic behavior of a thick laminated composite cylinder with an elevated temperature change is investigated. The analysis accounts for ply-by-ply variation of properties, temperature changes, and fiber orientations. The thick cylinder is assumed to be in the absence of thermomechanical coupling and to be in the state of generalized plane strain such that all the stress and strain components are independent of the axial coordinate. Moreover, due to the nature of axisymmetry, all the stress and strain components are also independent of the circumferential coordinate. The mechanical responses of this thick composite cylinder will, therefore, only have to satisfy the governing equation in the radial direction. Invoking the Boltzmann superposition integral for the complete spectrum of increments of anisotropic material constants with respect to time, the thermoviscoelastic constitutive relations of the anisotropic composite cylinder can be derived in integral forms. Since the thick composite cylinder is subjected to a constant elevated temperature, and boundary conditions are all independent of time, formulations of the linear thermal viscoelastic problem can have forms identical to those of the corresponding linear thermoelastic problem by taking advantage of the elastic-viscoelastic correspondence principle. In other words, all of these integral constitutive equations reduce to the algebraic relations, which are very similar to those developed for thermoelastic media when they are Laplace-transformed by means of the rule for convolution integrals. The thermoelastic analysis can thus be used to derive the transformed thermal viscoelastic

solutions in the frequency domain.

MATHEMATICAL FORMULATION

Consider a filament-wound axisymmetric thick composite cylinder consisting of N layers with the axial coordinate z, the radial coordinate r, and the circumferential coordinate θ. The composite cylinder has the inner radius a, the outer radius b, and the length L. Accordingly, there is a corresponding thermoelastic problem with the transformed displacement components $\bar{u}$, $\bar{v}$, and $\bar{w}$ in the axial direction, the circumferential direction, and the radial direction, respectively, in each layer. The axisymmetric character of the thick composite cylinder along with the assumption of the state of generalized plane strain leads to a simplified displacement field, which reflects the circumferential independence and only radial dependence of $\bar{w}$,

$$\bar{u}(r,\theta,z) = \bar{u}(r,z), \quad \bar{v}(r,\theta,z) = \bar{v}(r,z), \quad and \quad \bar{w}(r,\theta,z) = \bar{w}(r).$$

(1)

The transformed displacement field gives the transformed strain components in cylindrical coordinates as follows:

$$\bar{\varepsilon}_{rr} = \frac{d\bar{w}(r)}{dr}, \quad \bar{\varepsilon}_{\theta\theta} = \frac{\bar{w}(r)}{r}, \quad \bar{\varepsilon}_{zz} = \frac{d\bar{u}}{dz} = \bar{\varepsilon}^0, and$$

(2)

$$\bar{\varepsilon}_{\theta r} = \bar{\varepsilon}_{zr} = \bar{\varepsilon}_z = 0.$$

The unabridged form of the constitutive relation for each layer in cylindrical coordinates with the radial coordinate r normal to the plane of symmetry is expressed as

$$
\begin{Bmatrix} \bar{\sigma}_{zz} \\ \bar{\sigma}_{\theta\theta} \\ \bar{\sigma}_{rr} \\ \bar{\sigma}_{\theta r} \\ \bar{\sigma}_{zr} \\ \bar{\sigma}_{z\theta} \end{Bmatrix}
=
\begin{bmatrix}
\tilde{C}_{11} & \tilde{C}_{12} & \tilde{C}_{13} & 0 & 0 & \tilde{C}_{16} \\
\tilde{C}_{12} & \tilde{C}_{22} & \tilde{C}_{23} & 0 & 0 & \tilde{C}_{26} \\
\tilde{C}_{13} & \tilde{C}_{23} & \tilde{C}_{33} & 0 & 0 & \tilde{C}_{36} \\
0 & 0 & 0 & \tilde{C}_{44} & \tilde{C}_{45} & 0 \\
0 & 0 & 0 & \tilde{C}_{45} & \tilde{C}_{55} & 0 \\
\tilde{C}_{16} & \tilde{C}_{26} & \tilde{C}_{36} & 0 & 0 & \tilde{C}_{66}
\end{bmatrix}
\begin{Bmatrix} \bar{\varepsilon}_{zz} \\ \bar{\varepsilon}_{\theta\theta} \\ \bar{\varepsilon}_{rr} \\ \bar{\varepsilon}_{\theta r} \\ \bar{\varepsilon}_{zr} \\ \bar{\varepsilon}_{z\theta} \end{Bmatrix}
- \frac{\Delta T}{s}
\begin{Bmatrix} \tilde{B}_{zz} \\ \tilde{B}_{\theta\theta} \\ \tilde{B}_{rr} \\ 0 \\ 0 \\ \tilde{B}_{z\theta} \end{Bmatrix}.
$$

(3)

Furthermore, from the previous discussions, it can be shown that two of the three equilibrium equations are satisfied automatically. The only nontrivial equilibrium equation is the one in the radial direction:

$$\frac{\partial \bar{\sigma}_{rr}}{\partial r} + \frac{\bar{\sigma}_{rr} - \bar{\sigma}_{\theta\theta}}{r} = 0.$$

(4)

Substituting (1), (2), and (3) into (4), the transformed stress components $\overline{\sigma}_{rr}$ and $\overline{\sigma}_{\theta\theta}$ are obtained in terms of the transformed radial displacement $\overline{w}$. Incorporating the resulting $\overline{\sigma}_{rr}$ and $\overline{\sigma}_{\theta\theta}$ functions gives a non-homogeneous Euler differential equation of $\overline{w}$ for a layer in Laplace domain

$$r^2 \frac{d^2\overline{w}}{dr^2} + r\frac{d\overline{w}}{dr} - \overline{\lambda}^2\overline{w} = \frac{r}{\tilde{C}_{33}} \left[\frac{\Delta T}{s} (\tilde{B}_{rr} - \tilde{B}_{\theta\theta}) - (\tilde{C}_{13} - \tilde{C}_{12})\overline{\varepsilon}^{\,o} \right], \tag{5}$$

where

$$\overline{\lambda}^2 = \frac{\tilde{C}_{22}}{\tilde{C}_{33}}. \tag{6}$$

Solving (11) for $\overline{w}$ yields homogeneous and particular solutions as follows:

$$\overline{w} = \overline{A}_1 r^{\lambda-} + \overline{A}_2 r^{-\lambda-} + \tilde{w}_p, \tag{7}$$

Finally, it is understood that the initial condition of the original thermoviscoelastic problem is displacement-free state of rest. The boundary condition is of free traction and, hence, of free transformed traction on both inner and outer circular surfaces:

$$\overline{\sigma}_{rr} = \overline{\sigma}_{\theta r} = \overline{\sigma}_{zr} = 0 \quad \text{at } r = a, b. \tag{8}$$

On both end surfaces, stress resultants are zero:

$$\sum_{k=1}^{N} \int_{r_i}^{r_o} \overline{\sigma}_{zz} r\, dr = \overline{\sigma}_{zr} = \overline{\sigma}_{z\theta} = 0 \quad \text{at } z = 0, L, \tag{9}$$

The r_i and r_o are inner and outer radii, respectively, of the kth layer. The continuity conditions at each interface between two adjacent layers require continuous radial traction and continuous radial displacement at any instant as shown in Figure 2. Thus, when written in the transformed form, they become

$$\overline{\sigma}_{rr,o}^{(k)} - \overline{\sigma}_{rr,i}^{(k+1)} = 0 \quad and \quad \overline{w}_{,o}^{(k)} = \overline{w}_{,i}^{(k+1)}, \tag{10}$$

Where $k = 1,...,N - 1$; and subscripts i and o denote inner and outer surfaces, respectively. Accordingly, the formulation accounts for ply-by-ply variations of material properties and temperature change. The matrix form numerical solution procedure with parallel computing techniques resolved the complexity and time-consuming calculation procedures in Laplace transform of a multi-layered composite cylinder.

RELAXATION OF THERMAL AND MECHANICAL STRESSES

The time-dependent thermal viscoelastic behavior of a 100-layer AS-4/3502 (graphite/ epoxy) composite cylinder subjected to a temperature increase $\Delta T = 150°$ C is examined. Accordingly, initial residual stress built up in the cylinder due to the ΔT. The composite cylinder has an inner radius $a = 3.5$ in, an outer radius $b = 4.1$ in, and a thickness of

each layer $h = 6.0 \times 10^{-3}$ in. Stacking sequence is given as $[0/30/60/90]_{2s}$ from inside out with the 0° direction coinciding with the axis of the cylinder. The creep properties of an AS-4/ 3502 graphite/ epoxy composite with a fiber volume fraction of 0.67 were measured and least-squares curve fitted in power law forms as follows:

$$S_{22}(t) = \left[1.7051 \, (t)^{0.1954} + 1\right] S_{22}^0 \qquad (11)$$

and

$$S_{66}(t) = \left[11.3076 \, (t)^{0.2771} + 1\right] S_{66}^0 , \qquad (12)$$

where

$$S_{22}^0 = 7.5328 \times 10^{-7} / \text{psi} \quad and \quad S_{66}^0 = 1.3834 \times 10^{-6} / \text{psi} .$$

The compliance in the fiber direction, $S_{11} = 5.9 \times 10^{-8} / \text{psi}$, and Poisson's ratios, $\nu_{12} = \nu_{13} = 0.3, \ \nu_{23} = 0.36$, are assumed to be time-independent. Thermal expansion coefficients of the composite in three principal directions are $\alpha_{11} = -0.5 \times 10^{-6} /°C$ and $\alpha_{22} = \alpha_{33} = 40.0 \times 10^{-6} /°C$, where the negative value indicates shrinkage with temperature increase.

Figures 1 shows relaxation of thermal stresses across the thickness of the cylinder at three instants, instantaneous (initial stress), two years, and infinite time. The "saw" shaped radial stress distribution is the result of variation of fiber orientations through the thickness of cylinder. Relaxation of radial stress is clearly illustrated, which approaches to a constant over a period time. Figure 2 illustrates the relaxation of radial stresses through the thickness at three instants. The radial stress at the inner radius is 1000 psi, equivalent to the pressure applied. The radial stress is zero at the outer surface of the cylinder since it is traction free. The curve is constructed by connecting the stress value at all the interfaces of layers. Significant relaxation occurs over a period of time as shown in the radial stress profiles.

CONCLUSIONS

An analysis has been developed for viscoelastic behavior of laminated composite cylinders with ply-by-ply variation of anisotropic viscoelastic properties, which cannot be studied using an isotropic model. Stress relaxation and creep are properly determined in a cylinder subjected to a thermal and mechanical loads. The anisotropic viscoelastic behavior of the composite causes interesting characteristics in cylinders, which are critical for the durability of the structure. Creep and stress relaxation could exist in the fiber direction even though the fiber dominant properties are elastic. This is mainly due to the contribution of the Poisson's effects of viscoelastic transverse and shear properties. Viscoelastic characteristics are critical to the service life cycle of applications such as pressure vessels and composite rotors designed with built-in pre-stress to achieve desired mechanical performance.

REFERENCES

1. Tzeng, J. T., and L. S. Chien, "A Thermal/Mechanical Model of Axially Loaded Thick-Walled Composite Cylinders." J. of Composites Engineering, vol. 4, no. 2, 1994.
2. Chien, L. S., and J. T. Tzeng, "A Thermal Viscoelastic Analysis for Thick-walled Composite Cylinders." J. of Composite Materials, vol. 29, no. 4, 1995.
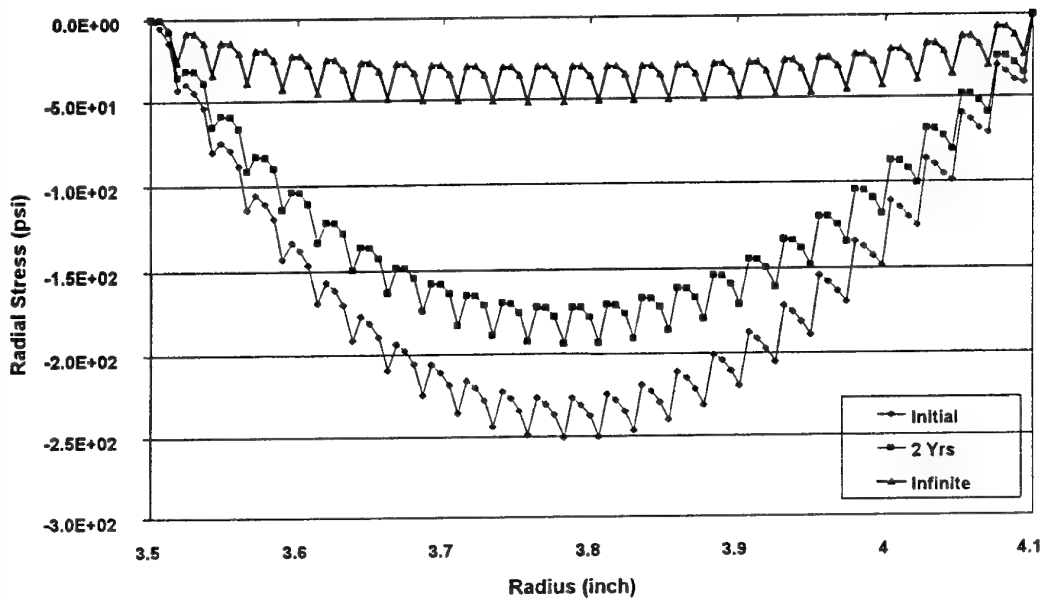
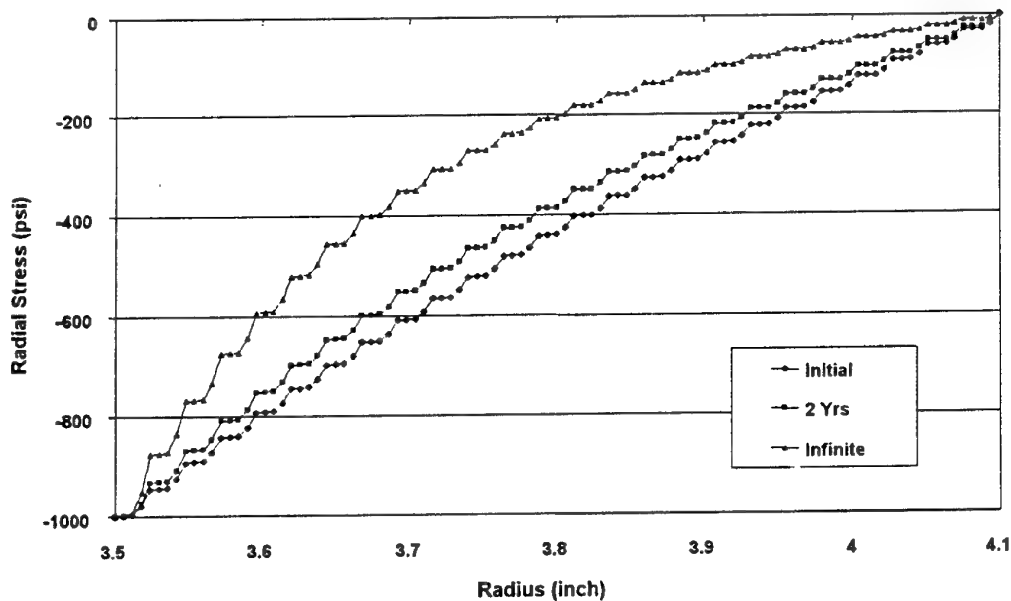Figure 1: Radial stress profiles in a cylinder subjected to thermal

Figure 2: Radial stress profiles in a cylinder subjected to internal

AE MEASUREMENT IN ACID CORROSION

Machiko MAEDA*, Hiroyuki HAMADA*, Yoshimichi FUJII**

*Kyoto Institute of Technology
Matsugasaki, Sakyo, 606-8585, Kyoto, JAPAN
**Seikow Chemical Engineering & Machinery, Ltd.
3-1-16 Shioe, Amagasaki, 661-0976 Hyogo, JAPAN

INTRODUCTION

Glass fiber reinforced plastics (GFRP) are widely used as an anti-corrosive material in the chemical process industry for application such as pipe work, reaction vessel, storage tanks, pumps, fans, scrubbers, etc. However, serious accident occasionally happens when it is used under loads for long period [1] and a few cases have been reported. For example, L.S. Norwood and P.J. Hogg[2] reported a case study of GFRP tanks damaged by acid. Furthermore, A.Trevett[3] reported some cases caused by acid stress corrosion even in much lower level than the standard. To prevent from such severe accidents, it is determined to design tanks less than about 10% of the tensile strength. The acid stress corrosion of GFRP is related to the corrosion of the glass fiber as reinforcement. It has been considered that matrix resin works as resistance in composites and prevents from that the glass fiber is attacked by acid. However, once the acid reaches to the glass fiber, for example through cracks, it could be damaged. E glass normally used in GFRP is easily damaged by acid, and it is well known that C glass resists in acid condition. It is suggested that types of glass fiber greatly related to durability of GFRP laminates. However, no result on GFRP using C glass was reported. Moreover, durability of GFRP is normally evaluated by long term testing. It is considered that the damage propagation in early period of testing greatly affects the lifetime. To estimate their lifetime by short term testing should become a useful method in industry. In this study, creep test with acoustic emission (AE) monitoring was performed to determine the fracture mechanism of E and C glass reinforced plastics and relationship between fracture behavior in early period and lifetime was considered.

MATERIALS AND EXPERIMENTALS

Glass fiber reinforced vinyl ester laminates used in this study were fabricated by a hand lay-up method. Vinylester resin (R806; Showa high polymer Co. Ltd.) was used as matrix. The glass fiber reinforced vinylester laminates used in this study were fabricated by a hand lay-up method. Four types of GFRP were used in this study. E and ECR types chopped strand mat reinforced composites were made of 3 plies, 3mm thick and E and C types woven cloth reinforced composites were made of 12 plies, 3mm thick.

For a specified creep stress each specimen was initially creep tested in air for 2hrs and then tested in acid environment (5% nitric acid) until the specimen ruptured. Several specimens were tested at different creep stress levels. AE
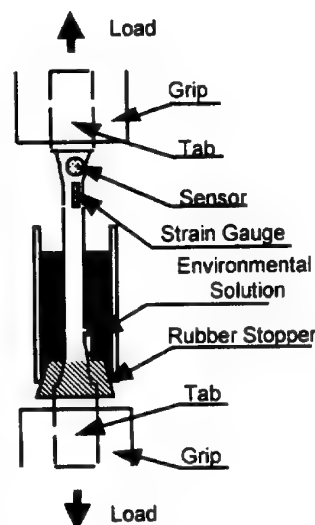

Fig. 1 Illustration of environmental creep test

signals were detected using a piezoelectric transducer with a resonant frequency of 150KHz throughout creep testing. The sensor was mounted on the specimen as shown in Fig. 1. Only the ring down counts were measured and recorded using an X-T recorder. All specimens were tested at room temperature. The fracture surfaces were observed by scanning electron microscopy (SEM). In this study, creep strain generally measured during the test was not monitored. Acid stress corrosion is due to the micro fracture occurred specific parts in the specimen, so that it was very difficult to consider the fracture behavior from the strain of whole specimen.

RESULTS AND DISCUSSION

Fig. 2 shows the result of AE monitoring for E glass cloth specimens. AE rate increased drastically after acid solution added. The AE rates in early period increased with increasing and the lifetimes indicated in the figure decreased with increasing the load level. Fig. 3 shows the result of AE monitoring for C glass cloth specimen. AE rate did not change with adding acid solution. Furthermore, the AE rate became less. It was cleared that the acid solution attacked only E glass fiber, which is easily attacked by acid. On the other hand, AE activity did not increase for a short period, when the reinforcement was not damaged. The AE counts detected on C glass specimen at low stress level would be caused by interfacial damage. From SEM observation, flat fracture surface, which was one proof of the acid stress corrosion, was observed in E glass specimens. It was suggested that AE rate sensitively detected the propagation of the acid stress corrosion. On the other hand, the fiber-pull-out fracture was observed in C glass specimens from SEM observation. From this point, it was also clear that the resources of AE counts in C glass specimen would be damages in interface. The AE rate increased and the lifetimes decreased with increasing the load level as well as E glass specimen as shown in Fig. 4. The fracture mechanisms were different in E and C glass specimens and it should have caused that C glass specimens had longer lifetime compared with E glass specimen at same stress level. A same manner was observed also in mat specimens. Relationship between AE rate in early period and lifetime is shown in Fig. 5. Correlation between AE rate and lifetime was clearly found and the lifetime could be predicted from this figure. It means the possibility to predict lifetime of specimen by AE monitoring.
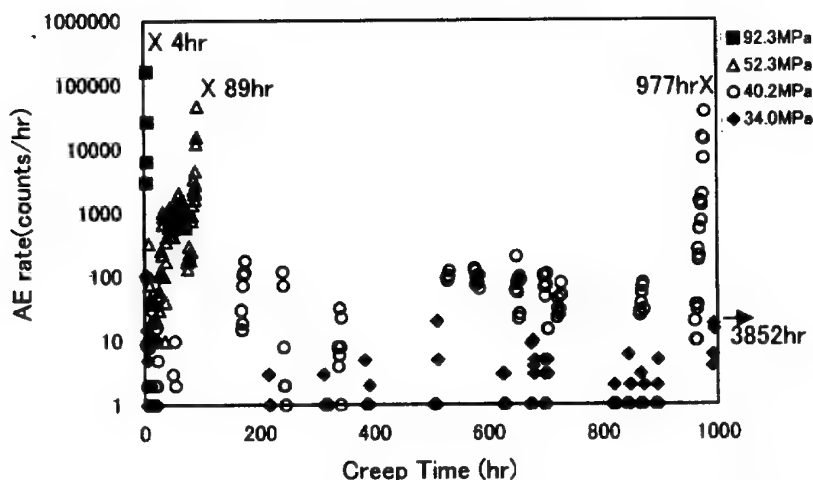

Fig.2　AE rate and failure time in creep in acid solution (E glass cloth FRP)
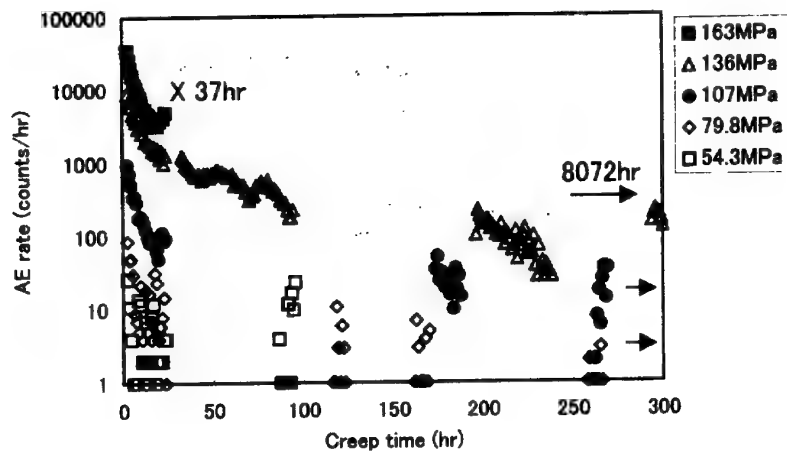
Fig.3　AE rate and failure time in creep in acid solution (C glass cloth FRP)

CONCLUSION

AE monitoring sensitively detected the damage propagation of glass fiber in composite. The difference of fracture mechanism between E and C glass reinforced plastics were clearly indicated from SEM observation. It was shown from AE monitoring that the damage propagating speeds of E and C glass specimen were different and the speed of C glass specimen was slower than E glass one. Furthermore, the possibility of lifetime prediction was shown in this study.

References

1. F.R. Jones, J.W. Rock and A.R. Wheatley, *Composites*, **14**,1983, 262
2. L.S. Norwood and P.J. Hogg, *Composite Structures* **2**,1984, pp.1-22
3. A. Trevett, *Chem. Eng. (GBR)***620** (1996) pp.27-30
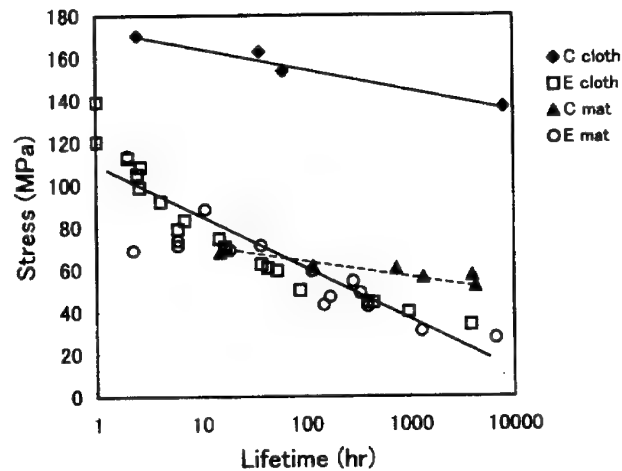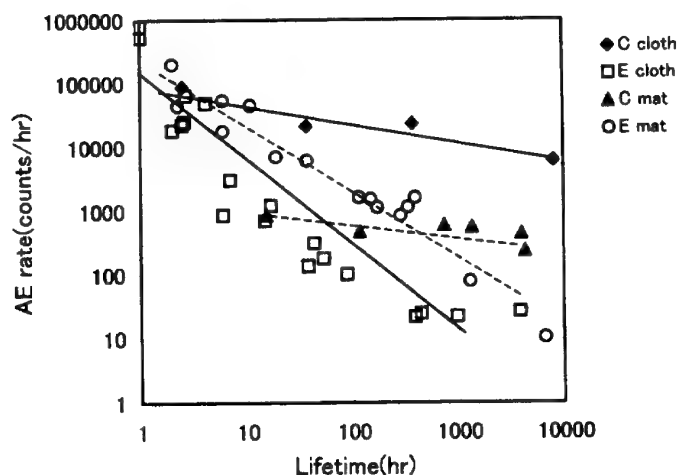
Fig. 4　Relationship between stress and lifetime

Fig. 5　Relationship between AE rate and lifetime

MODELLING OF THE BUCKLING OF PLASTIC CONTAINERS

J.L. Spoormaker[1], I.D. Skrypnyk[2], T.O. Vasyljkevych[2]

[1] Faculty of Design, Engineering and Production, Delft University of Technology
9, Jaffalaan, 2628BX, Delft, the Netherlands
[2] Karpenko Physico-Mechanical Institute of National Academy of Sciences of Ukraine
5, Naukova st., Lviv, 290601, Ukraine

Abstract

Plastic containers are required to be as light as possible in order to lower material and transportation costs, but the reliability of the containers is required to be very high. It is possible to satisfy these requirements due to improved grades of thermoplastics and optimisation of the design of plastic containers. Because of the improved toughness of new grades of thermoplastics, the failure mechanism: *crack initiation and propagation* is less dominant for many plastic containers. Instead *buckling* is becoming more important due to the decreased thickness of these products. Hence, although containers will not lose their structural integrity, their required load carrying capacity might decrease.

Our *research project* is aimed at developing methods for the optimisation of the design of plastic containers accounting for the *non-linear time dependent behaviour of High Density Polyethylene* (HDPE).

As a practical example, which has to be analysed (accomplished) within this investigation, the study of the stability of a HDPE crate for beer bottles has been chosen. The crates, with (filled) bottles, are required to be stored on pallets, from several days to even months. The pallets are stacked one on top the other, resulting in a very high load on the bottom crate. The loads might cause buckling of the corner stiffening ribs of crates. This causes the drop of a whole pallet and a loss the beer bottles and containers, but moreover the possibility of injuring people.

An important feature of these incidents is their delay with time: the drop of a pallet can even happen after an extended period of time. Obviously, the buckling of a crate's corner occurs after the material creeps under compressive loading. The objective of the research is to predict, using Finite Element Method (FEM), the onset of buckling of plastic bottle crates under compressive loading.

During the first stage of the investigation, the buckling behaviour of simple HDPE test specimens (strips and U-profiles) has been studied, experimentally as well as numerically, in order to obtain better understanding of creep assisted buckling. The experiments and simulations with visco-elastic strips allowed us to study creep assisted buckling in comparison to traditional Euler's buckling of elastic materials. The U-profile specimens have been chosen, to investigate buckling behaviour of simple elements with stiffening ribs.

The proposed [1] generalisation of the Schapery model is used, to enable Finite Element simulations of the buckling behaviour. This model enables a simple representation of experimental creep and recovery data, using a series of non-linear Voigt-Kelvin elements. It enables a fast estimation of material parameters as a result of minimisation of the total error between experimental data and model prediction. The experimental data for creep and recovery tests have been modelled with an accuracy 1...3%. The model of non-linear visco-elasticity has been implemented into the FEM package MARC [2], using Henriksen discretisation scheme [3] for the convolution integral with a Prony-series type kernel. The results of the experiments with a compressive ramp loading on HDPE strips and the corresponding numerical simulation are presented on Fig. 1. The tests have been performed for strips with a cross-section of 3×10 mm^2 and of six different lengths. The deformation rate in these experiments was 5% per minute.

The buckling behaviour of a HDPE U-profile under compressive loading has been modelled (Fig.2.). The U-profile, consisting of a plate ($270 \times 85 \times 3$ mm) and two symmetrical side wings ($270 \times 35 \times 3$ mm), was modelled using 256 shell elements. The lower edge of the U-profile was clamped and the upper edge was prevented to rotate and loaded by a ramp compressive load (displacement rate = 0.24 mm/s).
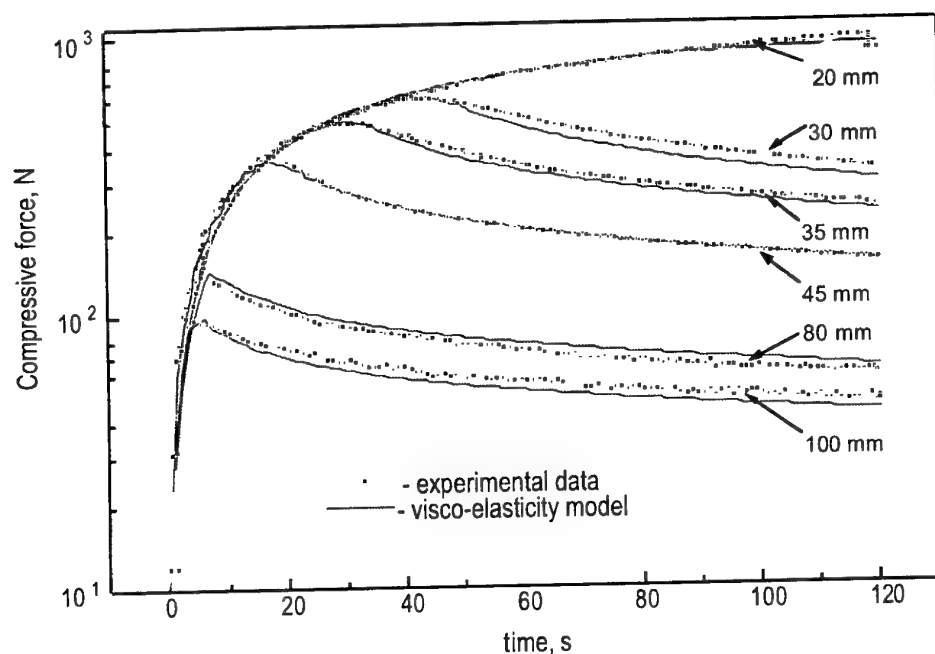
Fig. 1. *Finite Element simulation of buckling behaviour of clamped HDPE strips (the length of the strips is marked near the corresponding curve).*
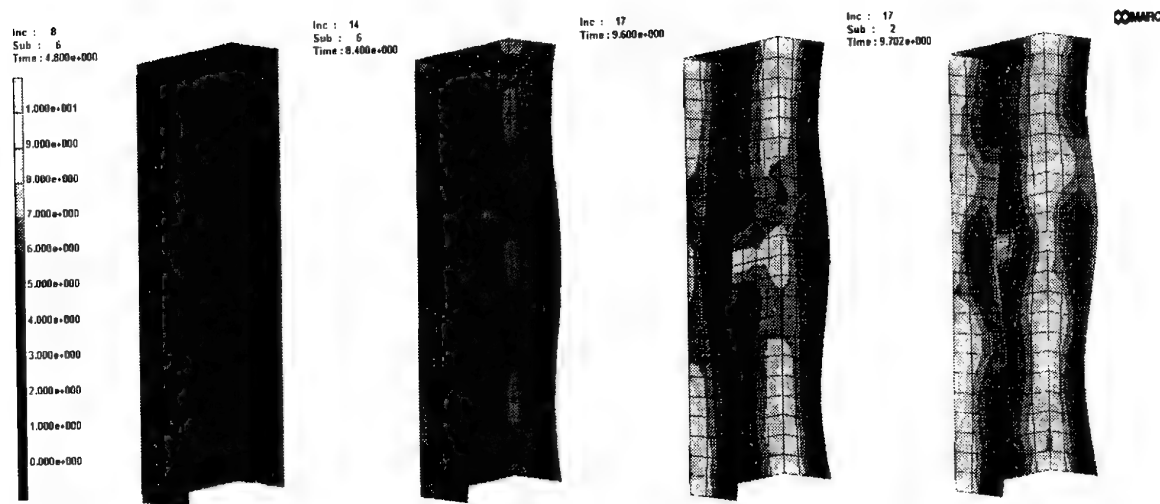
Figure 2. *Development of the buckling in time in an U-profile under compressive loading. The stresses on the scale are given in MPa. Time is given in seconds. "Inc" denotes load increment, while "Sub" is a number of sub-increments for calculation of the creep within an increment.*

It was also possible to reach a good agreement with the experimental data (Fig. 3). Because of the stiffening ribs in the U-profile, buckling occurs in two steps. First, the side wings buckle (second frame on Fig. 2). This leads to further buckling of the stiffening ribs (frames 3 and 4 on Fig. 4). It is worthwhile to notice, that the loading capacity of the U-profiled specimens is decreasing already after the side-wings have buckled (Fig. 3). Moreover the ability of a U-profile to carry the load depends on the buckling mode. If the side-wings buckle outside the U-profile, the second mode will occur (Fig. 3). However, if the side-wings bend inside the U-profile, they come in contact with the main plane of the U-profile and stiffen it. If the first buckling mode will develop this causes also a further slow decrease in the load carrying capacity.

It can be concluded that the developed generalised representation of the Schapery model and its implementation in MARC FEM software, is an adequate tool for investigating numerically creep induced buckling of plastic containers. It can also be used in computer aided design optimisation of plastic containers.
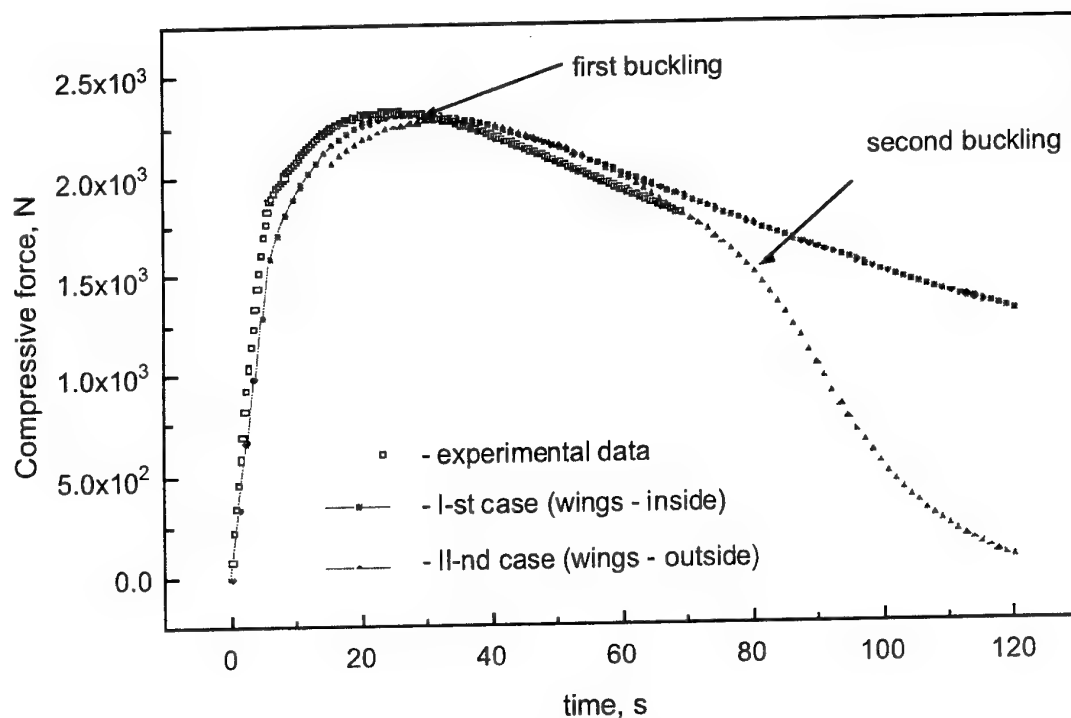
Figure 3. *Changing of loading carrying capacity of a HDPE U-profile in time during the compressive ramp loading experiment.*

References

1. **Skrypnyk, I.D., and Zweers, E.W.G.,** *Non-linear visco-elastic models for polymers materials (Creep and recovery behavior).* Report K345 of Faculty of Industrial Design Eng., TU Delft, 1996, Delft, the Netherlands, 40 p.

2. **Skrypnyk, I.D., and Spoormaker, J.L.,** *Non-linear visco-elastic models for polymers materials (Part II: Implementation into FEM).* Report K355 of The Faculty of Industrial Design Eng., TU Delft, 1996, Delft, the Netherlands, – 48 p.

3. **Henriksen, M.,** Computers & Structures, **18,** 1984, – p.133.

Fatigue Damage in Woven Ceramic Matrix Composites

A. Haque, M. Rahman, and S. Jeelani
Center for Advanced Materials
Tuskegee University, Tuskegee, AL-36088, USA

ABSTRACT

This paper investigates the behavior of SiC/SiNC woven composites under tensile and cyclic loading both at room and elevated temperatures. The ultimate strength, failure strain, proportional limit and modulus data at a temperature range of 23°C-1380°C are generated. The tensile strength and the modulus of SiC/SiNC woven composites have been observed to decrease insignificantly with increased temperatures beyond the linear portion of the stress/strain plot. The stress/strain plot shows a pseudo-yield point at 25% of the failure strain (ε_f) which indicates damage initiation in the form of matrix cracking. The evolution of damage beyond $0.25 \, \varepsilon_f$ both at room and elevated temperature comprises of multiple matrix cracking, interfacial debonding and fiber pullout. Although the nature of the stress/strain plot shows damage-tolerant behavior under static loading both at room and elevated temperature, the life expectancy of SiC/SiNC composites degrades significantly under cyclic loading at elevated temperature. This is mostly due to the interactions of fatigue damage caused by the mechanically induced plastic strain and the damage developed by the creep strain. The in situ damage evolutions are monitored by acoustic events parameters, ultrasonic C-scan and stiffness degradation.

INTRODUCTION

Ceramic matrix composites (CMCs) are considered to be attractive candidates for various gas turbine, heat engine and airframe structural components due to their high strength, high modulus, low thermal conductivity and good thermal shock resistance [1]. The ability of CMCs to sustain load degrades overtimes as the damage initiates and develops due to external loading conditions and presence of various environments. Understanding the physical mechanisms of damage development and determining the relevant properties over long period under expected service conditions are very important in order to use CMCs for various applications. The important information that need to be identified in the overall damage development process are the mechanisms that initiates the damage, then the damage growth rate and finally the failure state. All these factors eventually determine the life expectancy of the CMCs. Although some works are performed in the past relating to damage mechanics and durability of whisker, particulate and continuous fiber reinforced ceramic matrix composites [2-5], the demand for textile or woven ceramic matrix composites are increasing significantly in recent years due to their enhanced multidirectional and out-of-plane properties. The type that has been most commonly used in producing ceramic composites is the "satin weave". In most cases, the satin weaves are expected to provide superior properties than the plain weave because of larger section of unbent fiber. As a result this paper focuses the damage development and material responses of SiC/SiNC woven composites under monotonic tensile and tension-tension cyclic loading at room and elevated temperatures. The damage initiation and growth rate are monitored by acoustic emission, ultrasonic C-scans and modulus degradation measurements and both the tensile strength and fatigue life are correlated with the developed damage parameters.

EXPERIMENTAL WORK

Materials Specification

The ceramic matrix composite was composed of Nicalon silicon carbide woven fabric and Silicon Nitrogen Carbon (SiNC) matrix. The Nicalon[TM] ceramic fiber was basically beta-SiC crystallites and an amorphous mixtures of silicon, carbon and oxygen. The diameter of the fiber was approximately 15 microns with an average density of 2.55 gm/cm^3. The CMC was manufactured through polymer impregnation and pyrolysis process. The matrix precursor was first impregnated into the eight-harness satin weave quasi-isotropic $[0/\pm45/90]_s$ fabric lay-up, then cured by low temperature processing. The composite was then pyrolized to convert the pre-ceramic matrix polymer into a ceramic.

Specimen Design

An edge-loaded specimen geometry shown in Fig. 1 was used for all the tests at room and elevated temperatures. This specimen geometry eliminates the mounting of external tabbing materials and/or holes to accommodate the specimens in the grip of the test machine. The design of the specimen was initially proposed by Holmes and has been used to generate reliable tensile and fatigue test results without any slippage[6].

Test Environment

Tensile and fatigue testing of the CMC was performed using Instron-8502 servohydraulic frame equipped with a self-aligning supergrip. A two zone short furnace equipped with Kanthal super ·33 heating elements (molybdenum disilicate elements) was used to perform the elevated temperature tests. The length of the furnace hot zone was 101.6 mm. The edge-loaded specimen geometry and the self-aligning grips provided accurate and reproducible alignment.

All dimensions are in millimeters

Figure 1.   An edge-loaded tensile specimen.

RESULTS AND DISCUSSIONS

Tensile Responses

The stress-strain plot for SiC/SiNC composites under monotonic tensile loading at room, 700°C and 1380°C temperatures are shown in Fig. 2. The results show very negligible degradation in failure strength and rather slightly improved failure strain at the elevated temperatures. This minimal change in both failure stresses and modulus are due to sustained interfacial bonding between the SiC fiber and SiNC matrix at elevated temperature. This is due to the fact that the
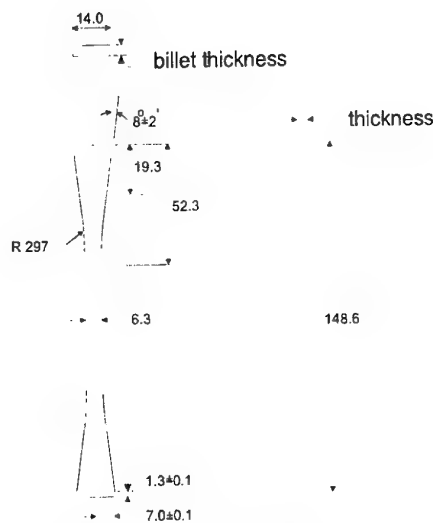
oxidation resistance of the SiNC matrix is shown to be very good up to 1400°C. The oxidation resistance of SiNC matrix depends on the formation of SiO_2 – protection layer. Usually porous non- oxide materials show mass changes greater than 2.5 % due to the oxidation of the pore walls. The oxidation behavior of pyrolyzed SiNC-ceramic is different and the complete mass gain is shown to be less than 0.7% at 1400°C after 24 hours, with higher oxidation temperature yielding increasing mass gains [7]. A proprietary coating in Nicalon fiber by Dow Corning protects the oxidation of the fiber in the SiC/SiNC composite at elevated temperatures in the range 1200 – 1250°C.
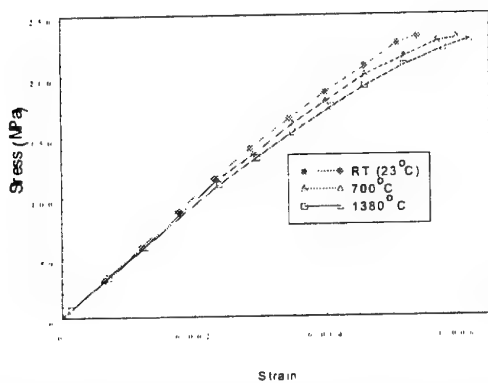
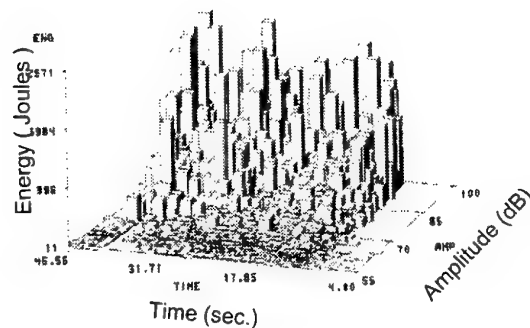Figure 2.   Stress vs. strain plot at room temperature(23°C), 700°C and 1380°C.

Figure 3.   Amplitude, energy and time plot of acoustic emission data under tensile loading.

The stress-strain curves both at room and elevated temperature showed extreme linearity at the initial stage confirming that the load is carried out by both the matrix and the fiber. This stage continued up to 0.12% strain. Beyond 0.12% strain the stress-strain plots continued to deviate from the linearity due to crack initiation and growth until the final failure occurred at approximately 0.55% strain. No major activity was also observed in the energy, time and amplitude plots of the acoustic emission data shown in Fig. 3 during the period when load was carried by both the matrix and the fiber. This data in Fig. 3 was acquired during room temperature tensile test. The time period at which the nonlinearity begins in the stress/strain plot coincides with the time span in the acoustic emission plot shown in Fig. 3. Figure 3 shows no major activity up to 25% of the total time period and consequently, Fig. 3 shows extreme linearity up to approximately 25% of the total failure strain. Since the load was applied at constant displacement rate, 25% of the failure strain obviously occurred at 25% of the total loading period. Some of the microcracks are even shown to occur at a very earlier stage before the transition point. These microcracks are identified by low amplitude acoustic events in the range of 55-70 dB shown in Fig. 3. The crack initiation mostly proceeds with matrix crack in the transverse fiber bundles of 0 and 90° weave and then eventually proceeds to + 45 and –45° weaves. Crack growth and propagation basically started at the beginning of the transition point and this stage is also identified with the acoustic events data in the amplitude range of 70-95 dB. During the crack propagation stage, the fibers in the fill direction of +45° and -45° fabrics are fractured which are shown by some high energy and amplitude level peaks in Fig. 3. Low

amplitude fracture (55-70 dB) with matrix crack also continued during crack growth until the final failure occurred. The acoustic events with high amplitude (95-100 dB) and high energy contents (above 2970 Joules) indicate excessive fiber breakage (0° orientation) prior to final failure.

Figures 4-5 show the micrographs of the fractured surface of SiC/SiNC composites under tensile loading at room and elevated temperatures. The failure modes in the form of matrix microcrack, interfacial debonding, fiber pull out and fiber fracture were observed in Figs. 4-5. The interfacial debonding and fiber pull out occurred almost at the same rate both at room and elevated temperatures. Figure 5 shows cracked matrix particles on the fiber surface indicating strong interfacial bonding between the fiber and matrix at elevated temperature. The fractured surface morphology of the fiber at room temperature is shown to be comparatively rough and coarse than the morphology at elevated temperature. This possibly allowed little decrease in strength at elevated temperatures.
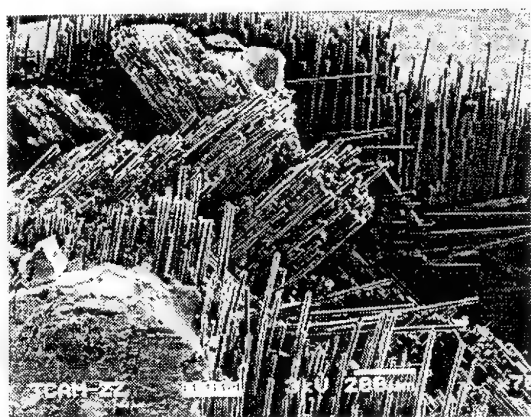

Figure 4. SEM micrograph of fractured surface under tensile loading at room temperature showing matrix crack, fiber pull out, interfacial debonding and fiber fracture (×70).
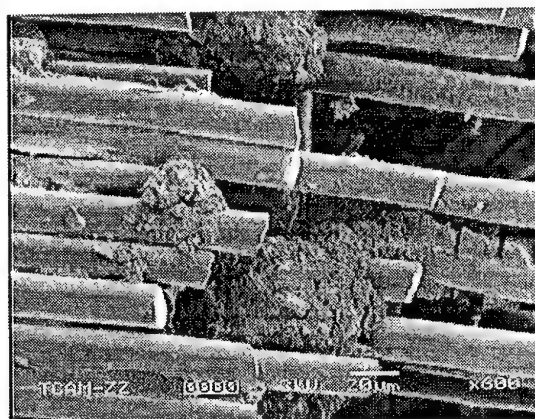
Figure 5. SEM micrograph of fractured surface under tensile loading at 1380°C showing matrix crack, fiber pull out and fiber breakage (×600).

Fatigue Responses

The fatigue tests were performed at room and elevated temperature levels (23°C and 700°C) under load control at a frequency of 5 Hz and stress ratio ($R = \sigma_{min}/\sigma_{max}$) of 0.1. A comparison of S-N plots at room and 700°C are shown in Figure 6. The results show that elevated temperature (700°C) has a tremendous effect on the fatigue life of SiC/SiNC composites. All the stress levels at room temperature were above the proportional limit, defined by onset of non-linear behavior in the stress-strain curve. At room temperature, the endurance limit is considerably high (approx. 80% of σ_{ult}). But at 700°C, the endurance limit is expected to be much lower (45% of σ_{ult}) which is still under investigation. The data that has been generated at 700°C shows that the the specimen fails after 0.15×10^6 cycles at $0.60 \ \sigma_{ult}$. The elevated

temperature tests are still continuing to determine the endurance limit at different temperatures (700°C, 900°C, 1200°C). Figure 7 shows the micrograph of fractured surface under fatigue loading at room temperature. A comparison of Figs 4 & 7 indicates an extended fractured surface with more matrix cracks and delamination for fatigue specimens than the tensile specimens. This shows that the extent of fatigue damage are more severe than the static damage. It is also observed that the extent of fractured surface increases as the stress level decreases providing a slow crack growth rate with higher fatigue life. Figure 8 shows the micrograph of the fractured specimen subjected to fatigue loading at 700°C. The micrograph of the fiber surface at room temperature is shown to be different than that at 700°C. At room temperature a coarse fiber texture with more matrix bonding are observed which indicates higher interfacial bond strength. But at 700°C, the fiber surfaces are shown to be more smooth and clear with some localized matrix accumulation.

Figure 6.　S-N diagram for fatigue test at room and elevated temperature.

This means that the bonding between fiber and matrix became weaker at this temperature and the fiber pulled out took place under less force allowing poor fatigue strength at 700°C. The morphology of the accumulated matrix also shows some chemical change of SiNC matrix with more pores at 700°C.
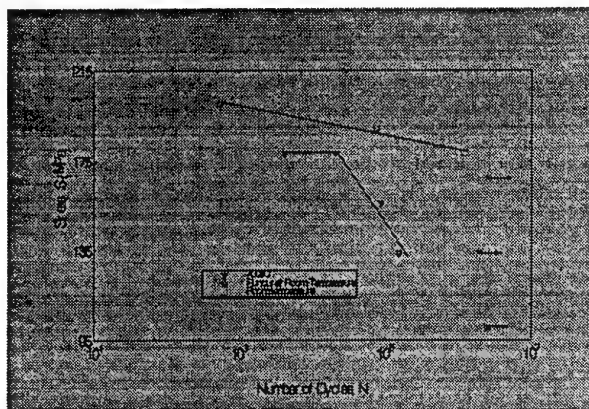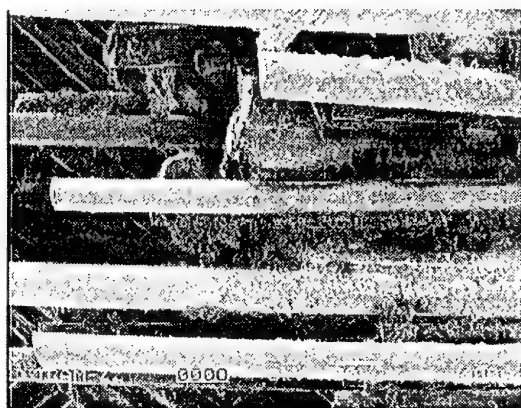

Figure 7. SEM micrograph of the fractured specimen subjected to fatigue loading at room temperature and at 90% of σ_{ult} showing matrix crack, fiber pull out and fiber breakage (×600).
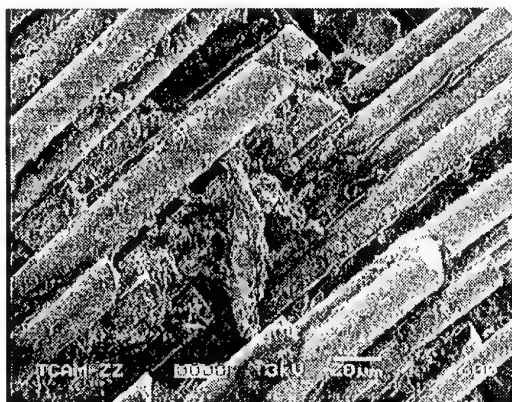

Figure 8. SEM micrograph of the fractured surface under fatigue loading at 700°C and at 80% of σ_{ult} showing matrix crack, fiber pull out and fiber breakage (×600).

CONCLUSSIONS

The tensile strength and modulus of SiC/SiNC woven composites have been observed to decrease negligibly with increased temperature beyond the linear portion of the stress/strain plot. Such linearity in the stress/strain plot is continued up to 25% of the failure strain (ε_f). The failure process initiates and propagates beyond 0.25 ε_f both at room and elevated temperature with matrix cracking, debonding and fiber pullout. The failure strain, ε_f is observed to increase with elevated temperature. The acoustic emission data is shown to monitor the activity of various failure modes during tensile loading. Fatigue strength at room temperature is found to be considerably high (80% of σ_{ult}). But elevated temperature has a remarkable effect on the fatigue strength. At 700°C, the fatigue strength is considered to be approximately 50% of σ_{ult} which is still under investigation. The work is on progress to study the modulus degradation and crack density during fatigue cycling. A fatigue damage evaluation model suitable for ceramic woven composites will be developed after completion of all the tests. The results will be discussed and presented at the conference.

REFERENCES

1. Levine, S.R., "Flight-Vehicle Materials, Structures, and Dynamics – Assessment and Future Directions", Vol. 3, ASME 1992, pp. 1-17
2. Yen, C.F. and Jones, M.L., "Material Modeling for Cross-Ply Ceramic Matrix Laminates with Progressive Damages and Environmental Degradation", MD-Vol.80, Composites and Functionally graded Materials, ASME 1997, pp. 189-202
3. Talreja, R., "Fatigue of Fiber-Reinforced Ceramics", Structural Ceramics- Processing, Microstructure and Properties, Proceedings of the 11th Rise International Symposium on Metallurgy and Materials Science, pp. 145-159
4. Pastor, M.S., Case, S.W. and Reifsnider, K.L., "Durability of Ceramic Matrix Composites", AD-Vol.56, Recent Advances in Mechanics and Aerospace Structures and Materials – 1998, ASME 1998, pp. 61-66.
5. Burr, A., Hild, F. and Leckie, F.A., "Damage, Fatigue, and Failure of Ceramic-Matrix Composites", Applications of Continuum Damage Mechanics to Fatigue and Fracture, ASTM STP 1315, D. L. McDowell, Ed., American Society for Testing and Materials, pp. 83-96
6. Holmes, J. W., J. of Materials Science, 26, pp. 1808-1814
7. Weibelzahl, W., Mutz, G., Suttor, D. and Ziegler, G., "Corrosion Stability and Mechanical Properties of Polysilazane – Derived SiCN – Ceramics", Key Engineering Materials, Vols 161 – 163, 1999, pp. 111-114

Progressive Failure of 3D-stressed Laminates:
Multiple Nonlinearity treated by the Failure Mode Concept (FMC)

R.G. Cuntze *

ABSTRACT

1 General about Progressive Failure

Progressive failure analysis of laminates or the prediction of laminate behaviour up to fracture was the focus of the 'Olympic Games (called *Failure Exercise*) on Yield Functions/Strength Criteria' arranged by M.Hinton and P. Soden (published in [Sod98]). The results of this competition were 'surprising' with respect to the large scatter.
The author therefore hopes to add a lamina stress-based *engineering approach* that will improve the quality of predicting *'Progressive failure of laminates subjected to 2D/3D-states of stress'*.
The basis is the Failure Mode Concept (FMC) and ply-by-ply macromechanical analysis.

Keywords: Laminates, progressive failure analysis, fibre reinforced plastics, static strength criteria

2 Main Features of the FMC

With respect to brief information, the features of the FMC are summarised in table 1.

Table 1: Main features of the FMC

- Each *mode* respresents one failure mechanism and one piece of the complete *failure surface* (surface of the failure body or *limit surface*)
- Each failure *mechanism* is represented by one failure *condition*. One failure mechanism is governed by one basic strength and therefore has a clearly defined equivalent stress
- Curve-fitting of the course of test data is only permitted in each pure failure mode regime
- Different, however, similar behaving materials obey the *same function* as failure condition but have *different curve parameters*
- Rounding-off in *mode interaction* (transition) zones is performed probabilistics-based, leading again to a continuous failure curve/surface
- An invariant formulation of a failure condition (scalar potential) considering the material's symmetries is possible
- Each term of the failure function is related to a physical mechanism observed in the stressed material element, e.g., I_2 marks a volume change and I_3 a shape change

- Additional parameters representing friction or fracture mechanics of defects in the material control the *shape* of the partial failure surface
- Equivalent stresses are used for the progressive damage description
- * Proof of Design, *Strength* analysis:
  - For each *mode* the equiv. stress is to be determined displaying where the design key has to be turned
  - At the end of the nonlinear analysis the *load*-related *reserve factor* has to be computed or the *margin of safety* $MS = f_{Res}^{(res)} - 1$, respectively .

3 Basics

- State of stress: For a UD material element fig. 1 depicts the prevailing 3D-state of stress. Additionally, with respect to the symmetries of this transversally-isotropic material the 5 basic strengths R and 5 elasticities are given in fig. 1 ($v_{\perp\perp}$ for 3D). Fig. 2 adds the information needed in order to apply Classical Laminate Theory (CLT, see literature)
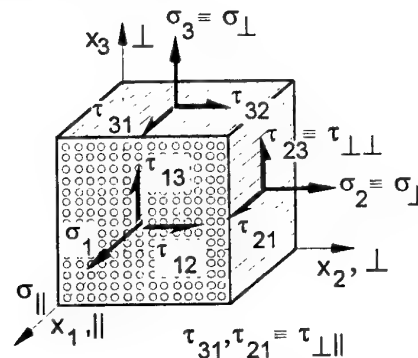
$$R_\parallel^t, R_\parallel^c, R_{\perp\parallel}, R_\perp^t, R_\perp^c \; ; E_\parallel, E_\perp, G_{\perp\parallel}, v_{\perp\parallel}, v_{\perp\perp}$$

Fig. 1: Material element of a UD lamina , 3D case (R: = strengths, t: = tension, c: = compression)

- *Invariants:* Strength criteria may be formulated by UD-stress-based invariants (v_f: = fibre volume fraction, E_f: = fibre modulus):

$$I_{1f} = v_f \cdot \sigma_{1f} \quad \text{with} \quad \sigma_{1f} = \varepsilon_1 \cdot E_f \; , E_f = E_\parallel / v_f;$$
$$I_2 = \sigma_2 + \sigma_3 \; ; I_4 = (\sigma_2 - \sigma_3)^2 + 4\tau_{23}^2;$$
$$I_3 = \tau_{31}^2 + \tau_{21}^2 \; ; I_1 = \sigma_1; \quad [Boe85]$$
$$I_5 = (\sigma_2 - \sigma_3)(\tau_{31}^2 - \tau_{21}^2) - 4\tau_{23}\tau_{31}\tau_{21}.$$

*Prof. Dr.-Ing. habil. R.G. Cuntze, Head of Main Department "Analysis" at MAN Technologie AG, Liebigstraße 5a, D-85757 Karlsfeld/Munich, Germany; Tel.: 0049 8131 89-1783, Fax: -1939, E-mail: Ralf_Cuntze@mt.man.de
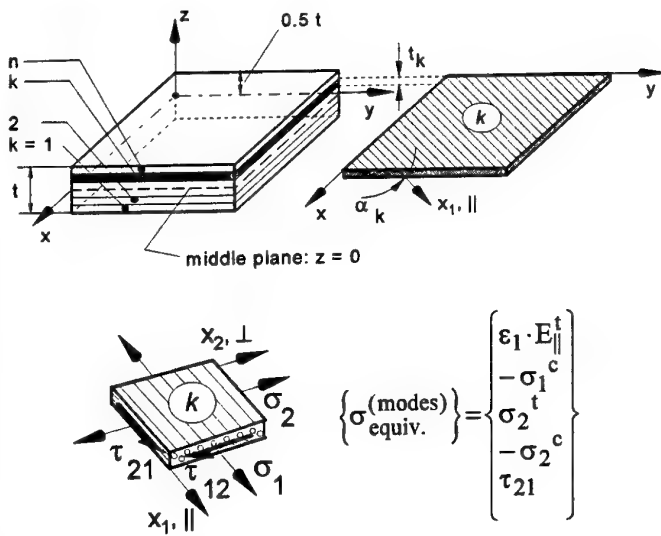
m:\gabler\cuntze\EAduracosys99.doc/14.06.99 / 13:12

Fig. 2: Laminate and k' th UD lamina subjected to a plane state of stress (midplane z = 0). 2D case , CLT
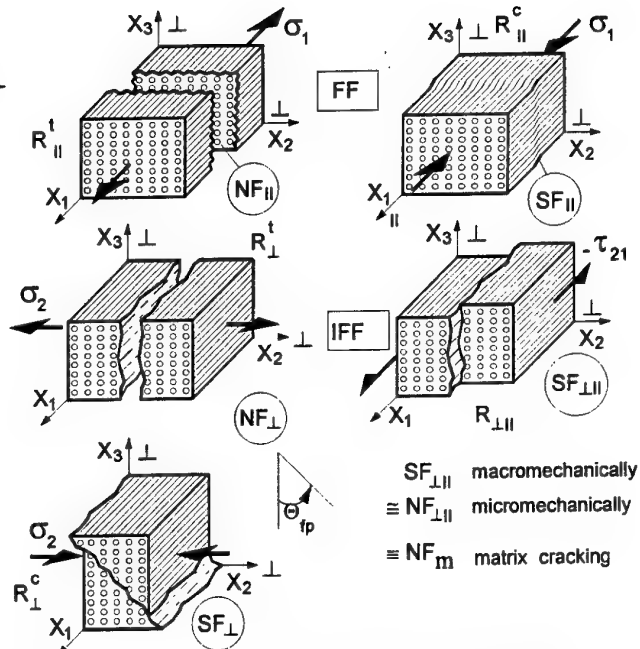

Fig. 3: Fracture types (≡ failure modes) of brittle transversally-isotropic material (UD).
(The physical fracture "planes" are pointed out in the figure [Cun98] Θ_{fp}: = fracture angle)

- *Rounding-off in the Mode Interaction Zones:* Of further interest is the rounding-off of the failure curve in the mixed failure domain (MiFD) or interaction or transition zone of adjacent failure modes, respectively. This will be accomplished by a simple formula - the 'Series Spring Model' - as an *engineering approach,* which also provides with the resultant reserve factor or the resultant effort.

- *Failure Modes or Types (fig 3):* A designer has to dimension a laminate versus Inter-Fibre-Fracture (IFF) and Fibre-Fracture (FF). IFF normally indicates the *onset of failure* whereas the appearance of FF in a single unidirectional (UD) lamina of the laminate usually marks *final failure.* In the case of brittle behaving FRP the failure is fracture.
Further, the 'explosive' effect of a so-called *wedge shape* failure $SF_\perp$ (a $\sigma_2{}^c$-caused IFF) of an embedded lamina of the laminate may lead to local delaminations and to buckling of the adjacent laminae.
Fig. 3 informs about the *types of fracture* which are recognised in case of *dense transversally-isotropic (ideal) materials.*

4 Strength Criteria Generated

Beltrami, Schleicher et al. assume that at initiation of yield the strain energy density in a cubic element of a material will consist of two portions:

$$W = \int \{\sigma\} \{\varepsilon\} \, d\{\varepsilon\} = W_{Vol} + W_{shape} .$$

Including Hooke's law in case of a transversally-isotropic body the expression will take the form

$$W = \frac{I_1^2}{2E_\parallel} + \frac{I_2(1-\nu_{\perp\perp})}{4E_\perp} - \frac{\nu_{\parallel\parallel}(I_1 I_2)}{E_\parallel} + \frac{I_3}{2G_{\parallel\parallel}} + \frac{(1+\nu_{\perp\perp})I_4}{4E_\perp} .$$

volume   volume   volume   shape   shape

Some of the invariant terms describe the volume change of the cube and others the change of the shape. Therefore, it appears mandatory which term has to be used in the formulation of a failure condition: it depends on the deformation of the material element.

Mainly based on this idea the following failure or strength conditions, which consider the *stress interaction,* have been derived ($\overline{R}$ marks the mean value)

- $F_\parallel^\sigma = \dfrac{I_{1f}}{\overline{R}_\parallel^t} = 1, \quad F_\parallel^\tau = \dfrac{-I_1}{\overline{R}_\parallel^c} = 1$ .... FF

- $F_{\perp\parallel} = \dfrac{I_3}{\overline{R}_{\perp\parallel}^2} + b_{\perp\parallel}\dfrac{I_2 I_3 - I_5}{\overline{R}_{\perp\parallel}^3} = 1, \, F_\perp^\sigma = \dfrac{I_2 + \sqrt{I_4}}{2\overline{R}_\perp^t} = 1$

$$F_\perp^\tau = (b_\perp^\tau - 1)\frac{I_2}{\overline{R}_\perp^c} + b_\perp^\tau \frac{I_4}{\overline{R}_\perp^{c2}} = 1 \qquad .... \text{ IFF}$$

with just two free curve parameters ($b_{\perp\parallel}, b_\perp^\tau$) remaining. They are to be determined from multiaxial test data. The invariant I_5 regards the difference of $\tau_{21}(\sigma_2)$ to $\tau_{31}(\sigma_2)$ (F = 1 is condition, F = 1 is criterion).

5 Nonlinearity: Hardening and Degradation

For reasons of clarity, material hardening is defined until the stress reaches its strength value R_m and thereby an initial failure level of IFF type. From that level on, that means for the *progressive failure* or damage regime, the term degradation is used. Of-course damaging still begins with material hardening.

Hardening: The degree of nonlinearity mainly depends on the nonlinearly behaving matrix material which greatly affects $E_\perp$ and $G_{\perp\|}$.

For the nonlinear stress analysis the relevant nonlinear stress-strain curves are to be provided. Data for the secant moduli of $E_\perp$, $G_{\perp\|}$ may be derived from Ramberg/Osgood mapping of the course of test data:

$$\varepsilon = \sigma / E_{(o)} + 0.002 \, (\sigma / R_{p0.2})^n$$

with the Ramberg/Osgood exponent

$$n = \ell n\left[\varepsilon(R_m)\right] / \ell n\left[R_m / R_{p0.2}\right]$$

estimated from the strength point $\left(R_m, \varepsilon(R_m)\right)$.

The alteration of Poisson's ratio $\nu_{\perp\|}$ is linked to the associated failure mode. E.g. in case of shear failure under compressive lateral stresses the value for $\nu_{\perp\|}$ will be higher (almost constant) than under tensile lateral stresses. Respecting the low effect Poisson's ratios have if using FRP with stiff fibres the following estimation should be a good approach:

- $F_\perp^\sigma$: $\nu_{\perp\|} = \nu_{\perp\|}(0) \cdot E_{\perp(sec)} / E_{\perp(0)}$.

Remark for modelling: In composite structures composed of stiff fibres and well-designed by netting theory the fibre net controls the strain behaviour.

Degradation: Above the *Initial Failure* level an appropriate progressive failure analysis method has to be employed (a *Successive Degradation Model* for the description of post initial failure) by using a failure mode criterion that indicates failure type and damage size.
Final Failure occurs after the structure has degraded to a level where it is no longer capable of carrying additional load.

Fig. 4 depicts the differences of the degradation course measured for a) an isolated e.g. tensile coupon specimen in the usual load controlled test, b) in a strain controlled test (this is possible at the institute BAM, Berlin, which has a very high frame stiffness). The curve b) is assumed here.
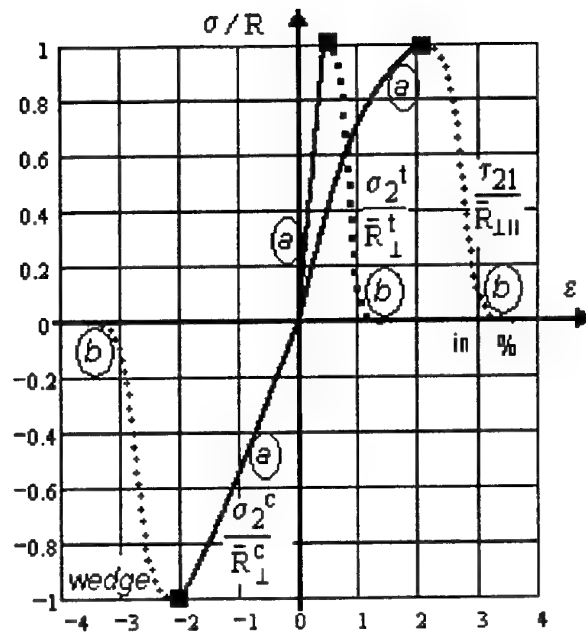

Fig. 4: Normalized stress-strain curves

Modelling of *Post Initial Failure* behaviour of a laminate requires that assumptions have to be made regarding the decaying properties of the actually degraded lamina or laminae. A simple function was used to map this degradation. It generally reads (the suffix d denotes degradation)

$$\sigma_d = R_m / (1 + \exp[(\bar{a} + \varepsilon) / \bar{b}])$$

with two curve parameters $\bar{a}$, $\bar{b}$ to be estimated by the data of two calibration points, e.g.

$(R_m \cdot 0.99, \varepsilon(R_m))$ and $(R_m \cdot 0.1, \varepsilon(R_m \cdot 0.1))$.

This function not has to model the stress-strain curves of a tested isolated lamina but that of a lamina embedded in a laminate, and thus regarding the altering microcrack density up to the critical damage state (CDS).
If applying test data from tensile coupons to embedded laminae, one has to consider that tensile coupon tests deliver test results of *weakest link type* (series model). An embedded or even only one-sided constraint lamina, however, is belonging to the class of *redundant types*.
Therefore, besides being strain-controlled also all the material flaws in a *thin* lamina cannot grow freely up to microcrack size in thickness direction because the neighbouring laminae will act as microcrack-stoppers (fracture mechanics problem, energy release).
In comparison to fig. 4, fig 5 further includes the curve for the embedded lamina. This curve is an integral and effective curve.

In the nonlinear analysis mean values are regarded in order to perform stress analysis that corresponds to an average structural behaviour.
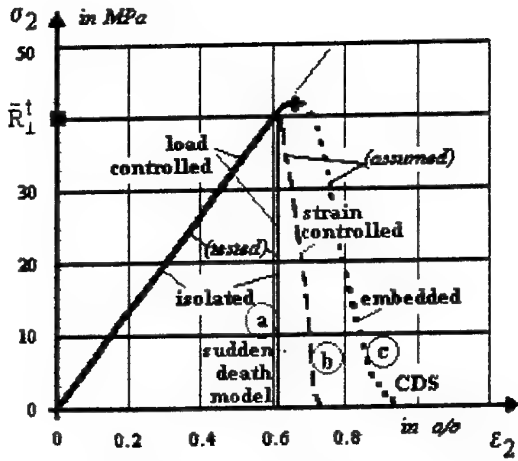
Fig. 5: The differences in the effective stress-strain behaviour of isolated and embedded UD-laminae

Therefore, when executing a nonlinear stress analysis the secant moduli to be utilized are mean values, too (in the strength analysis within the *Proof of Design* 'A' or 'B' values have to be taken).

6 Equivalent Stresses and Stress Effort

In the nonlinear stress analysis one needs besides CLT and stress-strain curves the failure conditions in order to model the *stress interaction* and to compute the equivalent stresses of each mode, which the increasing values in the hardening regime and decreasing values in the degradation regime. Further, the *mode interaction* (rounding-off) in the modes' transition zones has to be performed. This affords the computation of the resultant common stress Effort (stress effort: = equivalent stress/strength). In the case of linear behaviour and zero residual stresses it is related to the load-based reserve factor by $\overset{(res)}{Effort}=1/f_{Res}^{(res)}$.

Two computation steps now have to be regarded

- The determination of the modes' equivalent stress vector (positive values as with strengths; see fig. 2 and 3) from the failure conditions

$$\left\{\sigma_{equiv.}^{(modes)}\right\}=\left(\sigma_{eq}^{\sigma\|},\sigma_{eq}^{\tau\|},\sigma_{eq}^{\sigma\perp};\sigma_{eq}^{\tau\perp};\sigma_{eq}^{\perp\|}\right)^{T},$$

the terms of which now include the nonlinearly load dependent *load stresses* $\{\sigma\}_{(L)}$ and the also nonlinearity-dependent *residual* (curing) *stresses* $\{\sigma\}_{(R)}$.

- The determination of the resultant Effort, by applying the series spring model in order to consider the *mode interaction,* from the equation

$$\overset{(res)}{Effort}^{\dot{m}}=\left(\sigma_{eq}^{\sigma\|}/\overline{R}_{\|}^{t}\right)^{\dot{m}}+\left(\sigma_{eq}^{\tau\|}/\overline{R}_{\|}^{c}\right)^{\dot{m}}+\left(\sigma_{eq}^{\sigma\perp}/R_{\perp}^{t}\right)^{\dot{m}}+$$
$$+\left(\sigma_{eq}^{\tau\perp}/R_{\perp}^{c}\right)^{\dot{m}}+\left(\sigma_{eq}^{\perp\|}/\overline{R}_{\perp\|}\right)^{\dot{m}}.$$

The exponent $\dot{m}$ herein is assumed to be about 3 and shall be the same for each interaction zone.

As *triggering approach* (not optimized) the following is recommended

- $\overset{>(mode)}{\sigma_{eq}}=\sigma_{eq}^{(mode)}\cdot\overset{(res)}{Eff.}/\overset{(mode)}{max\,Eff.}\cdots\Delta\sigma>0$
  being an influence increase at *hardening*

- $\overset{<(mode)}{\sigma_{eq}}=\sigma_{eq}^{(mode)}\cdot\overset{(mode)}{max\,Eff.}/\overset{(res)}{Eff.}\cdots\Delta\sigma<0$
  being an influence decrease at *degradation*.

Neglecting the advantageous bulge of the (σ_2, τ_{21})-curve leads to the simple equivalent stress vector given in fig. 2, which was applied in fig. 7.

7 Calculation Procedure

Fig. 6 presents a flow chart of the nonlinear calculation. The solution procedure of the nonlinear analysis is to establish static equilibrium on each load step after material properties have been degraded.

Input:
- Geometry, load, boundary conditions
- Ramberg/Osgood-based property formulations

Load step 1:
- Initial mechanical properties, increment 1
- $\{\sigma\}_1,\{\epsilon\}_1\rightarrow\left\{\sigma_{equiv}^{(modes)}\right\}_1$,
- determination of degraded moduli
- iterations of static equilibrium $\uparrow$

Load step 2:
- secant moduli from load step 1
- determination of associated Poisson's ratios
- $\{\sigma\}_2,\{\epsilon\}_2\rightarrow\left\{\sigma_{equiv}^{(modes)}\right\}_2$,
- determination of degraded moduli
- iterations of static equilibrium $\uparrow$

Load step 3: and so further

Fig. 6: Nonlinear calculation scheme

If there are no new failures indicated by the failure criterion, then the load increment will be added. Dependent on the convergence rate, the laminate's stiffness matrix [K] has to be reassembled. For each iteration the procedure is repeated until convergence or failure is reached.

8 Application to a Laminate

In table 1 the properties for a CFRP laminate are outlined. Fig. 7 provides with the initial and final failure envelope of this case study ($[0/+45/-45/90]_s$)

Table 1: Mechanical and thermal properties [Sod98]

Fibre type		AS4
Matrix		3501-6 epoxy
Specification		Prepeg type
Manufacturer		Hercules
Fibre volume fraction,	V_f	0.60
Longitudinal modulus, [GPa]	$E_{\parallel}$	126
Transverse modulus, [GPa]	$E_{\perp}$	11
In-plane shear modulus, [GPa]	$G_{\parallel\perp}$	6.6
Major Poisson's ratio	$\nu_{\perp\parallel}$	0.28
Through thickness Poisson's ratio	$\nu_{\perp\perp}$	0.4
Longitudinal tensile strength [MPa]	$R_{\parallel}^t$	1950
Longitudinal compressive strength, [MPa]	$R_{\parallel}^c$	1480
Transverse tensile strength, [MPa]	$R_{\perp}^t$	48
Transverse compressive strength, [MPa]	$R_{\perp}^c$	200
In-plane shear strength, [MPa]	$R_{\perp\parallel}$	79[b]
Longitudinal tensile failure strain, [%]	$e_{\parallel}^t$	1.38
Longitudinal compressive failure strain [%]	$e_{\parallel}^c$	1.175
Transverse tensile failure strain [%]	$e_{\perp}^t$	0.436
Transverse compressive failure strain [%]	$e_{\perp}^c$	2.0
In-plane shear failure strain [%]	$\gamma_{\perp\parallel}$	2
Strain energy release rate, [Jm^{-2}]	G_{IC}	220
Longitudinal thermal coefficient, [10^{-6}/°C]	$\alpha_{\parallel}$	-1
Transverse thermal coefficient, [10^{-6}/°C]	$\alpha_{\perp}$	26
Curing: Stress free temperature [°C]		177
effective temperature difference [°C] ^{e} -177 + RT + 30 (moisture effect)		-125[e]

Fig. 7: Initial and final biaxial failure envelope.

9 Some Conclusions

- The solution procedure worked, both, in the failure exercise code [Mathcad] and in the FEM implementation Marc/Mentat]
- Convergency was still satisfying
- Degradation modelling looks promising, however, research has to verify degradation curves for embedded laminae. Appropriate test specimens and test evaluation have to be discussed
- The resulting curves to be generated for the 'failure exercise' are similar to Puck's curves.
- *Probabilistic* tools should be applied in order to improve the *deterministic* procedures and to smooth the sharp corners of a *laminate's* failure envelope.

10 Literature

[Cun93] *Cuntze, R.G.:* Deterministic and Probabilistic Prediction of the Distribution of Inter-Fibre Failure Test Data of Prestrained CFRP Tubes composed of Thin Layers and loaded by radial pressure. Wollongong. Advanced Composites '93, 579-585. The Minerals, Metals & Materials Society, 1993

[Cun98] *Cuntze, R.G. and Sukarie, G.:* Effective Dimensioning of 3D-stressed UD-laminae on Basis of Fracture-type Strength Criteria. Int. conf. on Mechanics of Composite Materials. Riga, April 20-23, 1998. Conference handbook, Presentation

[Cun99] *Cuntze, R.G.:* The Failure Mode Concept - A new comprehensive 3D-strength Analysis Concept for Any Brittle and Ductile behaving Material. Europ. Conf. on Spacecraft Structures, Materials and Mechanical Testing. ESA-CNES-DGLR-DLR; Braunschweig, Nov. 1998, ESA SP-428, 269-287

[Puck98] *Puck, A. and Schürmann, H.:* Failure Analysis of FRP Laminates by Means of Physically based Phenomenological Models. Special issue of "Composite Science and Technology" 58 (1998),

[Sod98a] *Soden, P.D., Hinton, M.J. and Kaddour, A.S.:* Lamina Properties, Lay-up Configurations and Loading Conditions for a Range of Fibre-reinforced Composite Laminates. Special Issue, Composite Science and Technology 58 (1998), 1011-1022

[Sod98b] *Soden, P.D., Hinton, M.J. and Kaddour, A.S.:* A Comparison of the Predictive Capabilities of Current Failure Theories for Composite Laminates. Special Issue, Composites Science and Technology 58 (1998), 1225-1254
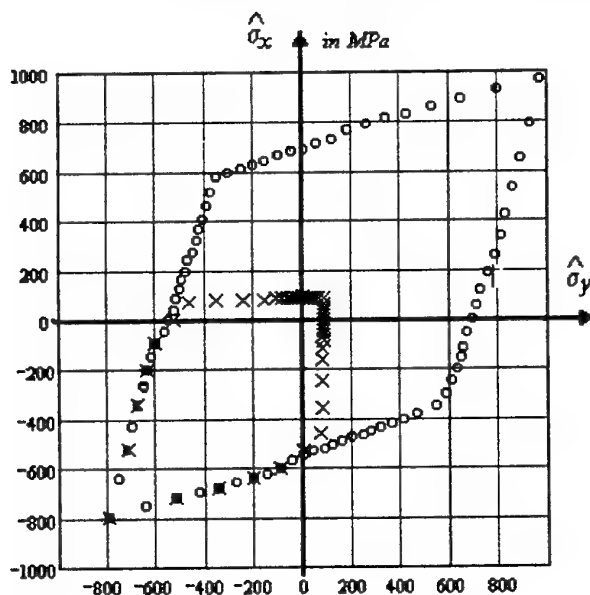
Long Term Prediction of Fatigue Life of Unidirectional CFRP

Yasushi MIYANO

Materials System Research Laboratory, Kanazawa Institute of Technology
3-1 Yatsukaho, Matto, Ishikawa 924-0838, Japan

INTRODUCTION

The mechanical behavior of polymer resins exhibits time and temperature dependence, called viscoelastic behavior, not only above the glass-transition temperature T_g but also below T_g. Thus, it can be presumed that the mechanical behavior of FRP using polymer resins as matrices also depends on time and temperature even below T_g which is within the normal operating-temperature range.

The time-temperature dependence of the flexural strength for satin-woven CFRP laminates under constant strain-rate (CSR) and fatigue loadings has been studied in our previous paper. It was observed that the fracture modes are almost identical under two types of loading over a wide range of time and temperature, and the same time-temperature superposition principle holds for CSR and fatigue strengths. Therefore, the master curve of fatigue strength can be obtained from the CSR strengths under various CSRs and temperatures and the fatigue strengths at a single frequency under various temperatures.

In this paper, the tensile test for resin impregnated carbon fiber strand employed as unidirectional CFRP and the flexural tests for longitudinal and transverse directions of unidirectional CFRP laminates by fatigue loading as well as CSR loading are carried out under various loading-rates and temperatures. The dependence of these fatigue strengths upon temperature and loading-rate as well as number of cycles to failure are discussed from the master curves of these fatigue strengths.

EXPERIMENTAL PROCEDURE

Preparation of Specimen

Epoxy resin impregnated carbon fiber strand (CF/Ep strand) was employed as the tensile test specimen for the longitudinal direction of unidirectional CFRP, which consists of high strength carbon fibers TORAYCA® T400-3K (TORAY) and a general purpose epoxy resin EPIKOTE® 828 (YUKA SHELL EPOXY). The glass-transition temperature T_g of the epoxy resin is 112°C.

Unidirectional CFRP laminate was employed as the flexural test specimen for the longitudinal and

transverse directions, which consists of high strength carbon fiber TORAYCA® T300-3K (TORAY) and a general purpose epoxy resin #2500 (TORAY). The glass transition temperature T_g of 2500 is 130°C. The fiber volume fraction of this CFRP laminate was approximately 55%.

Test Procedures

The tensile CSR tests for CF/Ep strand were carried out under various constant temperatures by using an Instron type testing machine with a small constant temperature chamber. Loading rates (crosshead speeds) were 0.01, 1, and 100mm/min. The fatigue tests were carried out under several constant temperatures at 2 loading frequencies f=2 and 0.02Hz by using an electro-hydraulic servo testing machine with a small constant temperature chamber. Stress ratio R (minimum stress/maximum stress) was 0.1. The tensile CSR and fatigue strengths σ of CF/Ep strand are defined by

$$\sigma = P_{max} \frac{\rho}{t_e} \qquad (1)$$

Where, P_{max} is the maximum load [N] of CF/Ep strand, ρ is the density of fiber [g/cm³], t_e is the tex of fiber strand [(g/1000m)*10⁻³]. Therefore, these strengths are calculated by using the cross-sectional area of carbon fiber strand.

Three point bending CSR tests for longitudinal and transverse directions of unidirectional CFRP laminates were carried out by using an Instron type testing machine with a constant temperature chamber. The nominal dimensions of the test specimens were 80, 10, and 3 mm (length, width, thickness) for the longitudinal direction and were 65, 15, and 3 mm for the transverse direction. The span of the test fixture was 60 mm for the longitudinal direction and was 50 mm for the transverse direction. The tests were carried out under various constant temperatures at three loading-rates V=0.02, 2, 200 mm/min. Specimens with the same dimensions were used for three point bending fatigue tests. The fatigue tests were carried out under several constant temperatures at f=2 and 0.02Hz by using an electro-hydraulic servo testing machine with a constant temperature chamber. Stress ratio R was 0.05. The flexural CSR and fatigue strengths σ of CFRP laminate are defined by

$$\sigma = \frac{3 \cdot P_{max} \cdot L}{2 \cdot b \cdot h^2} \qquad (2)$$

Where, P_{max} is the maximum load [N], L is the span [mm], b and h are width and thickness of specimen, respectively.

RESULTS AND DISCUSSION

Master Curve of CSR Strength

The left side of Fig.1 shows the tensile CSR strength σ_s for CF/Ep strand versus time to failure t_s at various temperatures. Where t_s is the time period from initial loading to maximum load in CSR tests. The master curve of σ_s was constructed by shifting σ_s at constant temperatures along the log

scale of t_s so that they overlapped each other as shown in the right side of Fig.1. Since the smooth master curve can be obtained, the time-temperature superposition principle is applicable for σ_s.
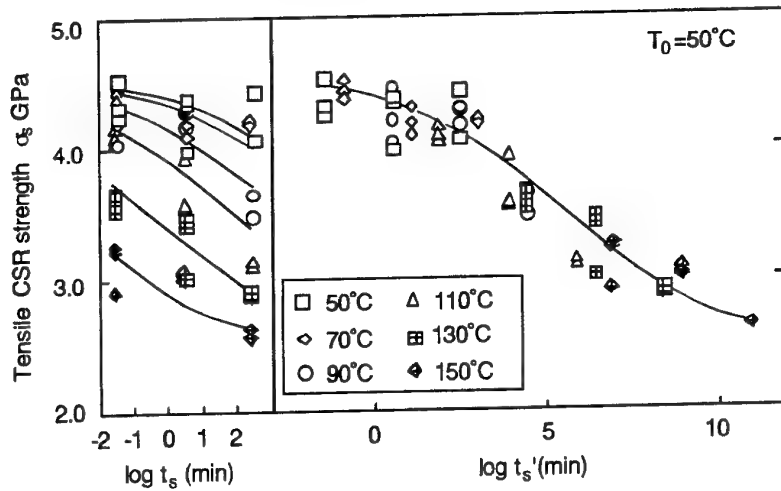

Fig.1 Master curves of tensile CSR strength for CF/Ep strand

The time-temperature shift factor $a_{To}(T)$ for σ_s are plotted in Fig.2. The hollow symbols in this figure show that for the creep compliance of matrix epoxy resin. The $a_{To}(T)$ for σ_s agrees well with that for the creep compliance of matrix resin, which are described by two Arrhenius' equations with different activation energies ΔH. Therefore, the time-temperature dependence of σ_s is controlled by the viscoelastic behavior of matrix resin.
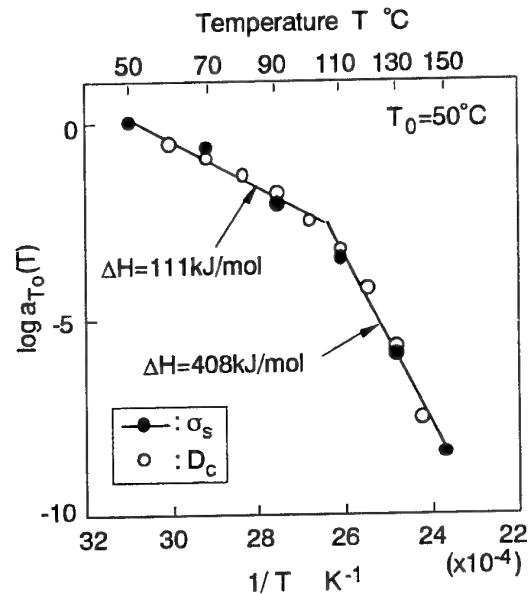

Fig.2 Time-temperature shift factors for CSR strength

Master Curve of Fatigue Strength

Figure 3 displays the tensile fatigue strength for CF/Ep strand versus the number of cycles to failure N_f (S-N curve) at a frequency f=2Hz together with the CSR strength at $t_s=1/(2f)$ which is regarded

as the fatigue strength at $N_f=1/2$. The upper side of Fig.4 shows σ_f versus reduced time to failure t_f', where the t_f' is obtained based on the time-temperature superposition principle which holds for the CSR strength. Each point on these master curves of constant reduced frequency f' represents a number of cycles to failure. Connecting the points of the same N_f with these curves, the master curves of σ_f for constant N_f are constructed as shown in the lower side of Fig.4.
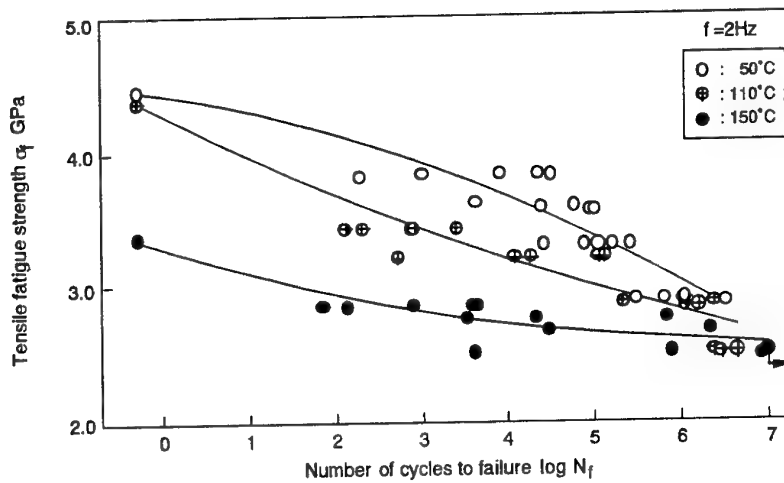

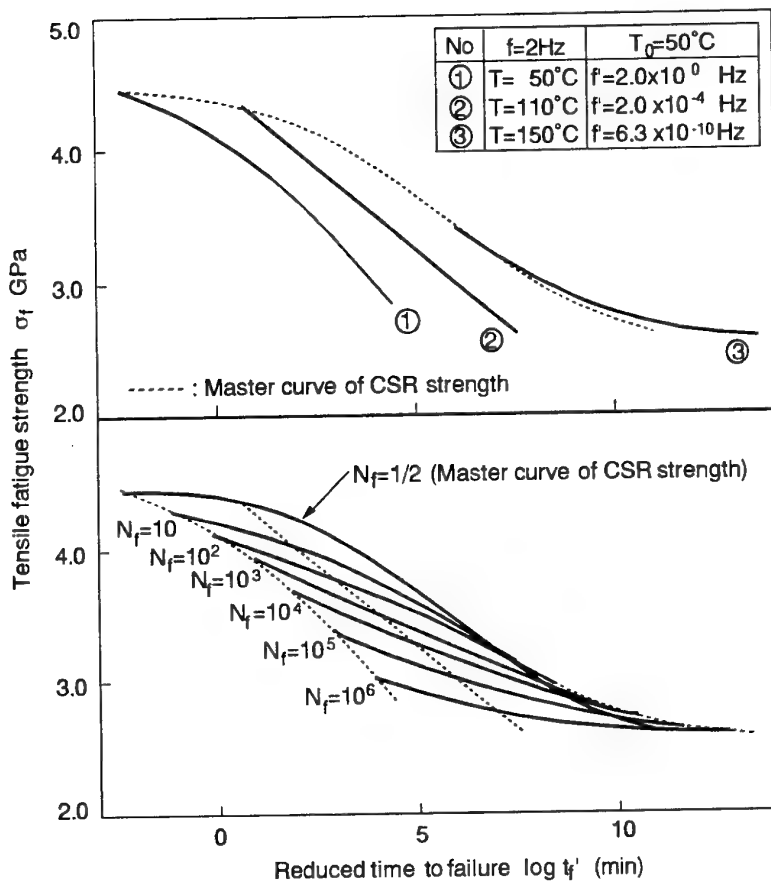Fig.3   S-N curves at frequency f=2Hz for tensile fatigue strength of CF/Ep strand

Fig.4   Master curves for tensile fatigue strength for CF/Ep strand

The predicted S-N curves at f=0.02Hz are displayed in Fig.5 together with test data. These curves are constructed from the master curves in Fig.4. Since the predicted S-N curves capture test data satisfactorily, the time-temperature superposition principle for CSR strength also holds for fatigue strength. Therefore, the validity for the construction of master curves of fatigue strength by using the time-temperature shift factor for CSR strength is confirmed.
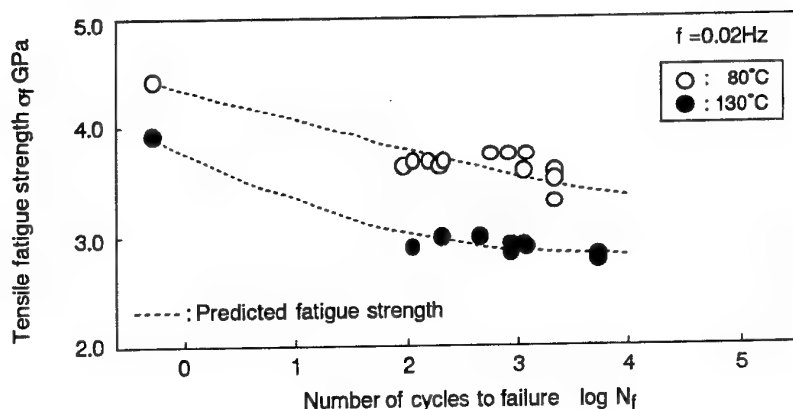

Fig.5   Predicted S-N curves at frequency f=0.02Hz for tensile fatigue strength of CF/Ep strand

Characterization of Three Kinds of Fatigue Strength

The master curves of the flexural fatigue strength for the longitudinal and transverse directions as well as the master curve of longitudinal tensile strength were obtained as shown in Fig.6 by the same procedure for CF/Ep strands.

The tensile fatigue fracture mode for the tensile test of CF/Ep strand is tensile in all ranges of time to failure, temperature, and number of cycles to failure N_f. The flexural fatigue fracture mode for the flexural test of longitudinal direction of unidirectional CFRP laminate is the compressive fracture on the compression side of specimen triggered by the microbuckling of fiber in all ranges of time to failure, temperature, and N_f. On the other hand, the flexural fracture mode for the flexural test of transverse direction of unidirectional CFRP laminate is the tensile fracture on the tension side of specimen in all ranges of time to failure, temperature, and N_f.

The remarkable time-temperature dependence is observed on the tensile fatigue strength for CF/Ep strand on which the viscoelastic behavior of matrix resin is presumed to be slightly influenced, not to mention that the flexural strength for the transverse direction on which the viscoelastic behavior of matrix resin is directly influenced as shown in Fig.6. The tensile fatigue strength decreases remarkably with N_f in the range of short time to failure and low temperature. On the other hand, the tensile fatigue strength decreases scarcely with N_f in the range of long time to failure and high temperature in the vicinity of glass transition temperature. The flexural fatigue strength for the longitudinal direction decreases remarkably with time to failure and temperature, however depends scarcely on N_f in all ranges of time to failure and temperature. The flexural fatigue strength for the transverse direction decreases remarkably with time to failure, temperature, and N_f in all ranges of time to failure and temperature.
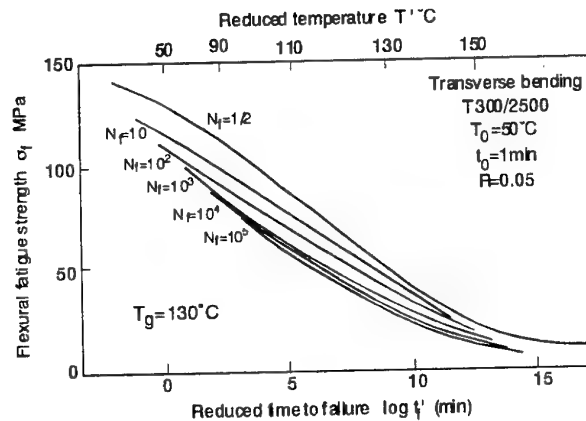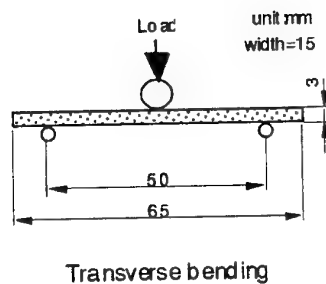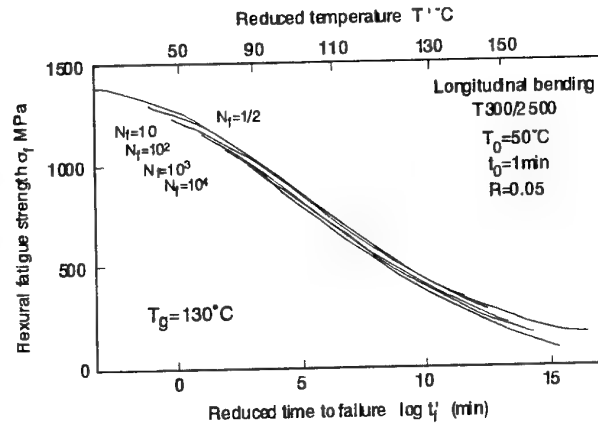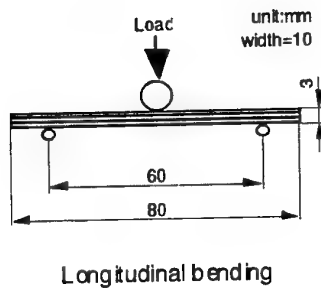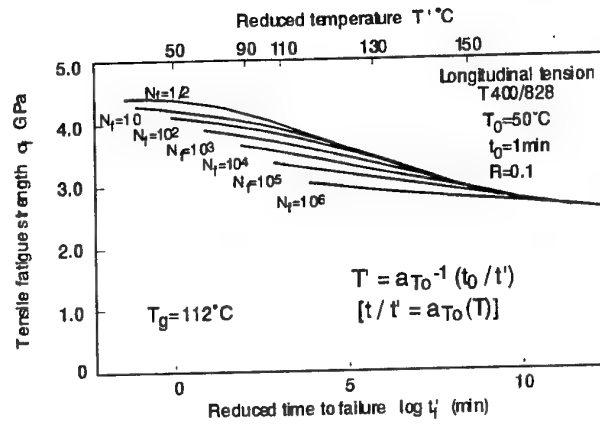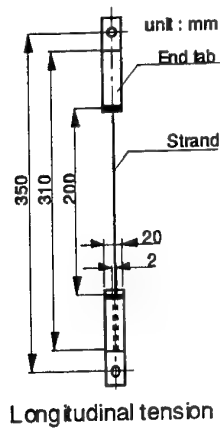
Fig.6   Master curves of fatigue strength under three types of loading

CONCLUSION

Tensile test for resin impregnated carbon fiber strand (CF/Ep strand) and the flexural tests for longitudinal and transverse directions of unidirectional CFRP laminates by fatigue loading as well as constant strain-rate (CSR) loading were carried out under various loading-rates and temperatures. The time-temperature superposition principle holds for all fatigue strengths as well as CSR strengths, therefore the master curves for all fatigue strengths can be obtained.   The dependence of these fatigue strengths upon number of cycles to failure as well as temperature and loading-rate can be characterized from these master curves.

Experimental Characterization and Analytical Prediction of Microscopic Deformation in Intelaminar-Toughened Laminates with Transverse Cracks

Nobuo Takeda*, L.Neil McCartney** and Shinji Ogihara***

* Department of Aeronautics and Astronautics, The University of Tokyo, 7-3-1 Hongo, Bunkyo-ku, Tokyo 113-8656, Japan
** Center for Materials Measurement and Technology, National Physical Laboratory, Teddington, Middlesex, TW11 0LW, United Kingdom
*** Department of Mechanical Engineering, Science University of Tokyo, 2641 Yamasaki, Noda, Chiba 278-8510, Japan

Introduction

The prediction of the initiation and multiplication of matrix cracks in composite laminates has received a great deal of attention [1-9]. In particular, transverse cracking in the 90° ply of cross-ply laminates has been extensively studied and many models have been proposed to predict transverse cracking. Shear-lag analyses [1-7] and variational mechanics [8, 9] were used for the prediction without checking the accuracy of stress field and the corresponding displacement field.

McCartney analyzed stress transfer between 0° and 90° plies in cracked cross-ply laminates [10]. The solutions were determined to satisfy the stress-strain-temperature relations either exactly or in an average sense. The advantage of this analysis is that the corresponding displacement field can be derived, whose accuracy can be checked by some experimental techniques. In this analysis, the variation of in-plane normal stress in through-thickness direction was neglected.

Recently, McCartney developed a new stress transfer model for predicting the stress and displacement distributions in a multiple-ply cross-ply laminate having a uniform distribution of cracks in some or all the 90° plies [11]. By making use of the ply refinement technique, where each ply of the laminate is subdivided into layers, through-thickness variations of the stress and displacement components can be predicted.

In the present study, a comparison is performed between this new model and the experimental results of the measurement of displacement fields in interlaminar-toughened CFRP cross-ply laminate in order to check the validity of the analytical method. The transverse crack opening displacement and the shear deformation along the ply interfaces near the transverse crack tips are measured using the micro-line/grid methods. Once the accuracy of the analysis is assured, it can be used with confidence to predict the evolution of transverse cracking.

Experiment

Two material systems were supplied by Toray Inc. One was interleaved CFRP, T800H/3631-FM300, with epoxy resin (FM300) layers about 100μm thick between 0° and 90° plies. The other was toughness-improved CFRP, T800H/3900-2, with selectively toughened interlaminar layers about 30μm thick at all the ply interfaces. The interlaminar layers have tough and fine thermoplastic resin (polyamide) particles dispersed in the base epoxy resin.

T800H is a high strength carbon fiber. The 3631 is a modified epoxy system with improved toughness compared with a conventional TGDDM/DDS epoxy system. The fiber volume fraction was about 45% for T800H/3631-FM300 and about 55% for T800H/3900-2. The low fiber volume fraction for T800H/3631-FM300 is due to the insertion of the thick FM300 resin films. The cross-ply laminate configuration was (0/90$_4$/0).

The micro-lines or micro-grids were printed using the photo-lithography technique on specimen edge surfaces [12-16]. First, the surface of the specimen was polished, then coated by the photo-resist, or photo-chemical reactive resin. The specimen was heated to cure the resist, and the surface was exposed to the light through the photo-mask, or the glass plate with micro-lines or grids. The exposed part of the resist was then removed in the developer, and vacuum-evaporated metal was deposited on the surface. Finally, the remaining resist was removed in the solvent to prepare the micro-lines or grids on the specimen surface.

Tensile load is applied on a specimen in an SEM (scanning electron microscope) with a servo-hydraulic loading machine and a specimen heating unit. The specimen was loaded at 20°C until the transverse crack interval became uniform, and both the images of local area near the crack tip and a complete view of the crack were photographed. The temperature was then raised to 80°C and the crack was photographed again. This procedure was repeated at 120°C and 160°C. The load was kept constant to investigate the effect of the temperature, that is, the effect of thermal residual stress on microscopic deformation. The crack opening displacement (COD) of the transverse cracks and the interlaminar shear deformation near the transverse crack tip were measured from these photographs.

Figure 1 (a) shows a schematic illustration of deformation around a transverse crack in the 90° ply of a cross-ply laminate. Rectangular (x and y) coordinates were selected as shown in Fig.1, and u and v denote displacements in x and y directions respectively. For example, if the micro-lines are printed parallel to the x axis, they deform, as shown in Fig.1, after transverse cracking. In this case, v can be measured as a function of x and y.

In the present study, the COD of a transverse crack was measured as a function of x. In addition, to evaluate the shear deformation, $\partial v / \partial x$ was measured as a function of y near the transverse crack tip. The quantity $\partial v / \partial x$, averaged in the interlaminar resin layer (IRL), and at the 90°/IRL interface on the 90° ply side, were measured. Detail of the definition of the shear deformation used in the present study is shown in Fig.1(b).

Analysis [11]

The problem under consideration concerns the in-plane deformation of a symmetric multilayered laminate constructed of 2N+2 perfectly bonded layers which can have any combination of orientations provided that laminate symmetry is preserved. The y-direction defines the longitudinal or axial direction, the z-direction defines the transverse direction and the x-direction defines the through-thickness direction. Transverse cracks in some or all the 90° plies are assumed to form only on the planes $y = \pm L$ resulting in a crack spacing $2L$, and to span entirely through the thickness and across the width of the ply.

Two fundamental assumptions were made in the analysis. One was that generalized plane strain conditions prevail in the laminate. The other was that the shear-stress components σ_{xy} and σ_{xz} are linear functions of x in each ply element. By making the above two fundamental assumptions, it is possible to derive an analytical representation for the stress and displacement fields, for any symmetric multiple-ply cross-ply laminate containing uniform distributions of cracks in the 90° plies, that satisfy exactly the equilibrium equations, the compatibility equations, three stress-strain relations, and the interface continuity conditions. By satisfying the remaining stress-strain relation on averaging it through thickness of each ply, the stress transfer problem is reduced to solving a system of ordinary differential equations that can be solved numerically.

One advantage of the present analysis is that the ply refinement techniques can be used where each ply of the laminate is subdivided into layers having the same properties in order that through-thickness variations of the stress and displacement components can be taken into account. Such through-thickness variations are of importance in the neighborhoods of transverse cracks where the ply refinement enables the effect of the stress singularity to be modeled accurately.

Resuls and Discussion

Figure 2 shows the comparison between the analytical predictions and the experimental results for the crack opening displacement (COD) in T800H/3631-FM300 (0/90$_4$/0) at various temperatures. Experimental results show that the temperature dependence of COD is very small. This can be explained qualitatively as follows. As temperature increases, the tensile thermal residual stress decreases which results in smaller COD. At higher temperature, the shear modulus of FM300 becomes lower, which may result in larger COD. The small temperature dependence of COD is expected to be a result of these two effects.

In Fig.2, analytical predictions are shown for case 1 (20°C, 80°C, 120°C and 160°C), case 2 (20°C) and case 3 (20°C). In case 1, the transverse crack tip is assumed to stop at the 90°/FM300 interface. In case 2, the transverse crack penetrates into the FM300 layer at the depth of 20μm which was observed in the experiment. In case 3, the transverse crack fully penetrates into the FM300 layer and the tip stops at the FM300/0° interface. Unfortunately, the

agreement is not very good. Two main reasons are considered. One is the temperature-dependent material properties are not well known especially for FM300. The other is that, in practice, the crack tip penetrates into FM300 layer at some depth. For more quantitative evaluation, these problems have to be considered.

Figure 3 shows the comparison between the analytical predictions of the new model with ply refinement techniques and the experimental results for the COD in T800H/3900-2 (0/90$_4$/0) laminate. The agreement is rather good compared with T800H/3631-FM300 laminate (Fig.2). The analytical predictions show larger temperature dependence, that is, smaller COD at higher temperature and larger COD at lower temperature. This may be due to the inaccuracy of temperature-dependent properties of polyamide particle-dispersed layer. The properties were assumed because they cannot be measured experimentally. Another explanation for the discrepancy is plastic deformation in the polyamide particle-dispersed layer, especially at higher temperature. Because the analysis is linear elastic, the non-linear behavior of the material is not considered. However, the agreement is good at lower temperature (at 20°C and 80°C) where the material can be assumed to be linear elastic, which implies the validity of the analysis.

Figure 4 shows a comparison between predictions by the analysis and the experimental results for the shear deformation, $\partial v/\partial x$, in T800H/3631-FM300 (0/90$_4$/0). Both the average shear deformation in the FM300 layer and the shear deformation at the 90°/FM300 interface in 90° ply side are shown as functions of the distance form the transverse crack tip. The shear deformation at 90°/FM300 interface is well predicted by the analysis. The agreement of average shear deformation in the FM300 layer is not very good especially at higher temperature which may be due to the inaccuracy of the temperature-dependent properties of FM300 and the possible effect of plastic deformation.

Figure 5 shows the comparison between the prediction of the new analysis and the experimental results for the shear deformation, $\partial v/\partial x$, in T800H/3900-2 (0/90$_4$/0). Again, both average shear deformation in the polyamide particle-dispersed layer and shear deformation at the 90°/polyamide particle-dispersed layer interface in 90° ply side are shown as functions of the distance form the transverse crack tip. The shear deformation at the 90°/polyamide particle-dispersed layer interface are well predicted by the analysis. The agreement of average shear deformation in polyamide particle-dispersed layer is not very good especially at higher temperature which may be due to the inaccuracy of the temperature-dependent properties of polyamide particle-dispersed layer and the possible effect of plastic deformation. For more quantitative evaluation of the microscopic deformation, it will be necessary to establish temperature-dependent material properties of the interlaminar resin and the consideration of non-linear material behavior such as plastic deformation.

References
1. Bailey, J.E., Curtis, P.T., and Parvizi, A., Proc. R. Soc. Lond., A., 366, 1979, 599-623
2. Laws, N. and Dvorak, G.J., J. Comp. Mat., 22, 1988, 900-916
3. Han, Y.M., Hahn, H.T. and Croman, R.B., Comp. Sci. Tech., 31, 1988, 165-177
4. Lim, S.G. and Hong, C.S., J. Comp. Mat., 23, 1989, 695-713
5. Lee, J.W. and Daniel, I.M., J. Comp. Mat., 24, 1990, 1225-1243
6. Takeda, N. and Ogihara, S., Comp. Sci. Tech., 52, 1994, 183-195
7. Takeda, N. and Ogihara, S., Comp. Sci. Tech., 52, 1994, 309-318
8. Hashin, Z., Mechanics of Materials, 4, 1985, 121-136
9. Nairn, J.A., J. Comp. Mat., 23, 1989, 1106-1129
10. McCartney, L.N., J. Mech. Phys. Solids, 40, 1992, 27-68
11. McCartney, L.N., NPL Report DMM(A)150, 1995
12. Takeda, N. and Ogihara, S., Composites Part A., 29, 1998, 1545-1552
13. Takeda, N., Niizuma, H., Ogihara, S. and Kobayashi, A., Exp. Mech., 37, 1997, 182-187
14. Takeda, N., Ogihara, S., Suzuki, S. and Kobayashi, A., J. Comp. Mat., 32, 1998, 83-100
15. Takeda, N, Ogihara, S., Nakata, K. and Kobayashi, A., Composite Interfaces, 5, 1998, 305-321
16. Takeda, N., Niizuma, H., Ogihara, S. and Kobayashi, A., Materials System, 16, 1995, 73-78 (in Japanese)

(a)

$$\text{average } \partial v / \partial x = \frac{\Delta v_1}{\Delta x_1} = \frac{\Delta v_1}{\text{thickness of interlaminar resin layer}}$$

$$\partial v / \partial x \text{ at } 90° / \text{IRL interface} = \frac{\Delta v_2}{\Delta x_2} = \frac{\Delta v_2}{30 \, \mu m}$$
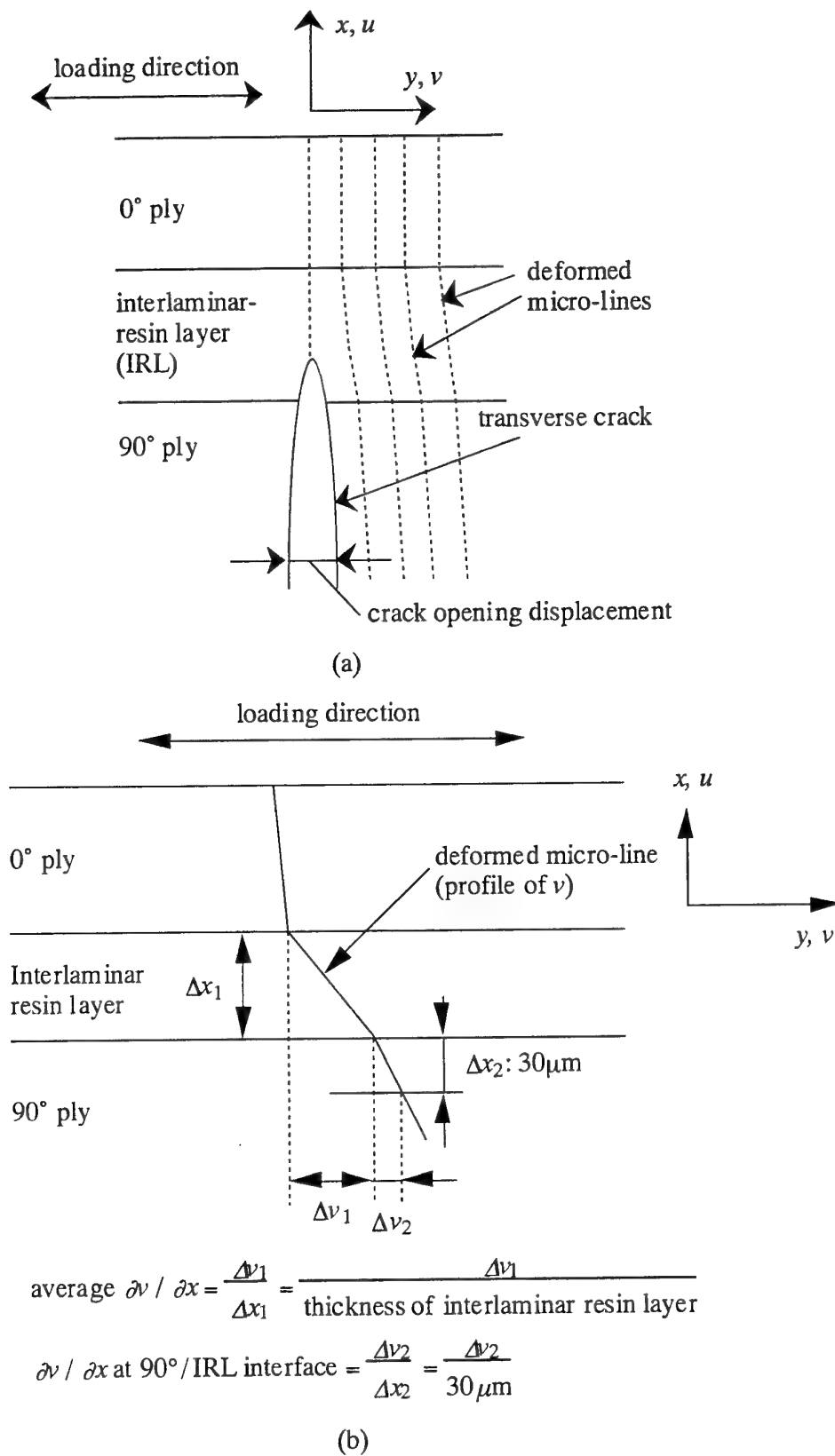
(b)

Figure 1.   Schematic illustration of microscopic deformation around the transverse crack.   (a) Schematic of deformed micro-line.   (b) Definition of shear deformation.
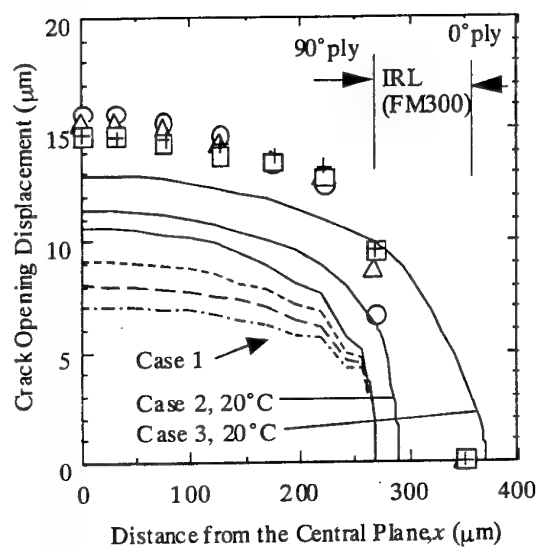
Figure 2. Crack opening displacement in T800H/3631-FM300 (0/90₄/0). Comparison between experimental results and analysis with the ply refinement techniques. (σ=216MPa, 2L=1.70 mm)

Figure 3. Crack opening displacement in T800H/3900-2 (0/90₄/0). Comparison between experimental results and analysis with the ply refinement techniques. (σ=160MPa, 2L=2.10 mm)

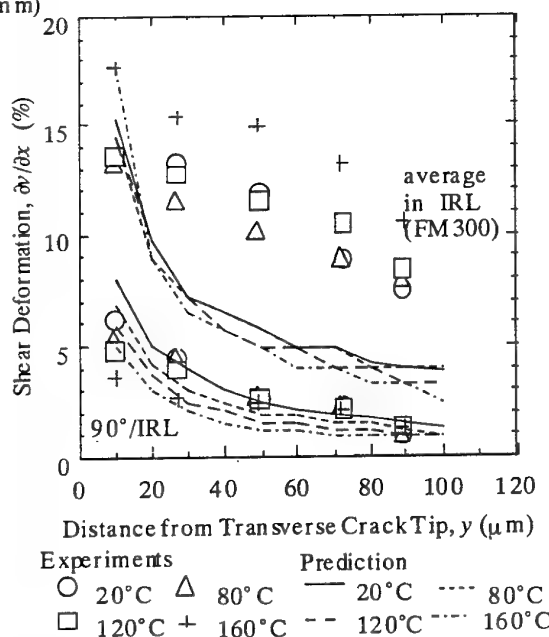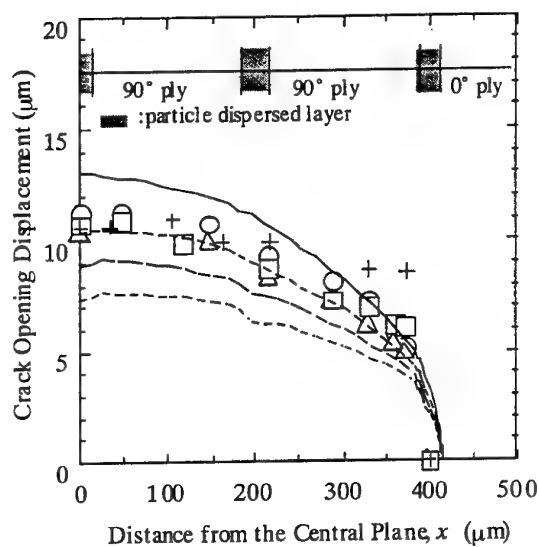Figure 4. Shear deformation as a function of the distance from the crack tip along longitudinal direction in T800H/3631-FM300 (0/90₄/0). Comparison between experimental results and analysis with the ply refinement techniques. (σ=216 MPa, 2L=1.70mm)
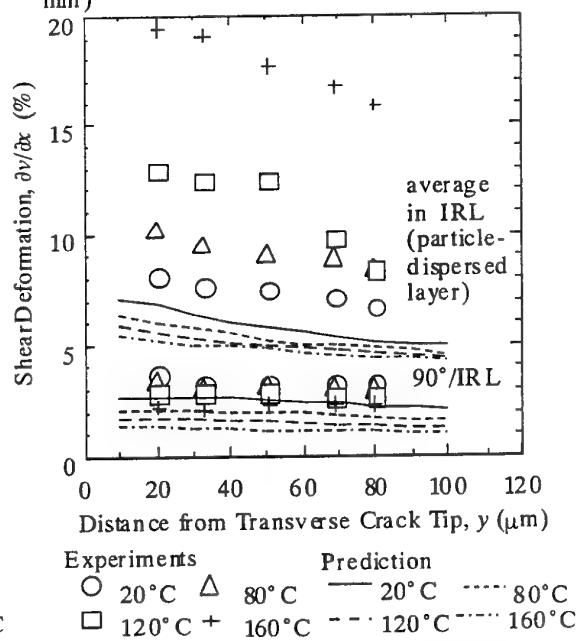

Figure 5. Shear deformation as a function of the distance from the crack tip along longitudinal direction in T800H/3900-2 (0/90₄/0). Comparison between experimental results and analysis with the ply refinement techniques. (σ=160MPa, 2L=2.10 mm)

5

METHOD FOR IDENTIFICATION OF ELASTIC AND DAMAGE PROPERTIES OF LAMINATED COMPOSITES BASED ON EXPERIMENT DESIGN

R. Rikards

Institute of Computer Analysis of Structures
Riga Technical university
Riga, LV-1658, Latvia
Email: rikards@latnet.lv

1. Introduction

A numerical-experimental method for the identification of mechanical properties of laminated composites from the experimental results is developed. It is proposed to use the experiment design to solve the identification (inverse) problems. The basic idea of the proposed approach is that simple mathematical models (response surfaces) are determined only by using the finite element solutions in the reference points of the experiment design. The difference between conventional [1] and present approach is that instead of direct minimization of identification functional the experiment design is used, by which response surfaces of the functional to be minimized are obtained. The response surface approximations are obtained by using the information on the behavior of a structure in the reference points of the experiment design. The finite element modeling of the structure is performed only in the reference points. Therefore, a significant reduction (about 50-100 times) in calculations of the identification functional can be achieved in comparison with the conventional methods of minimization. The functional to be minimized describes the difference between the measured and numerically calculated parameters of the response of structure. By minimizing the functional the identification parameters were obtained. The method was employed to identify the elastic and damage properties of the laminates from the measured eigenfrequencies of the plates. Previously the method of experiment design was used for solution of the optimum design problems [2]. Some identification problems previously were solved in [3, 4].

2. Parameters of identification and criterion

The numerical-experimental method proposed in the present investigation consists of the following stages. In the first stage the physical experiments have been performed. Also the parameters to be identified, the domain of search and criterion containing experimental data have been selected. In the second stage the finite element method has been used in order to model the frequency response of the structure. The results of the finite element solution of the eigenvalue problem have been employed as numerical experimental data. The finite element calculations have been performed in the reference points of the variables to be identified. The reference points have been determined by using the method of planning of experiments. In the third stage the numerical data obtained by the finite element solution in the reference points have been used in order to determine a simple functions for calculation of the

eigenfrequencies. In the fourth stage on the basis of the simple models and experimental data of the measured eigenfrequencies the identification of the material properties is performed. For this the corresponding functional is minimized by using a random search method.

The proposed numerical-experimental approach is used for identification of the elastic properties of laminated composite plates. For this the experimental data of the measured eigenfrequencies have been used. It is assumed that the plate dimensions (see Fig. 1), plate mass and the layer stacking sequence is to be known. The parameters to be identified are the elastic constants of a single layer in the laminated composite plate [1]. These five parameters of a transverse isotropic layer are

$E_1, E_2 = E_3$ - the two Young's moduli,
$G_{12} = G_{13}$ - the shear moduli,
$v_{12} = v_{13}$ - the Poisson's ratio,
G_{23} - the shear modulus in the plane of isotropy.

The plate is composed of transverse isotropic layers with principle material directions 1-2-3, where 1 is the fiber direction and 2,3 are the directions transverse to the fiber direction. In general the ith layer of the laminated plate is oriented at an arbitrary angle β_i. The angles of the layers are assumed to be fixed.
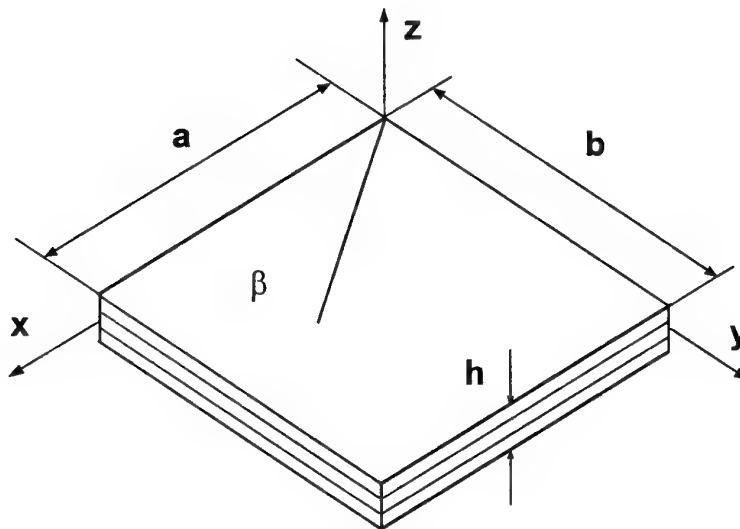

Fig. 1. Laminated composite plate.

The functional to be minimized (criterion) is the deviations between the measured and numerically calculated frequencies [1]

$$\Phi(\mathbf{x}) = \sum_{i=2}^{l} \frac{\left(\overline{\omega}_i^2 - C\widetilde{\omega}_i^2\right)^2}{\overline{\omega}_i^4} \tag{1}$$

It is seen that criterion (1) is a non-linear function of the parameters of identification $\mathbf{x}$. The identification of the material properties $\mathbf{x}$ is performed on the basis of information obtained by

the measurements of the I lowest frequencies. The identification problem is formulated as follows

$$\text{Minimize}_{\textbf{x}} \Phi(\textbf{x}) \qquad (2)$$

subject to constraints which characterize conditions that the elasticity matrix must be positive defined.

The functional [1] is minimized by using the finite element method, the method of experiment design and the response surface approach. Details of this procedure were described in [3, 4].

3. Examples

Method of experiment design was applied in order to solve different identification problems of composite laminates. The simplest case is determination of elastic properties since the functional (1) is convex. Convexity of the eigenvalue problem was proofed in [9]. Comparison with the reference solutions for identification of elastic constants of laminated plates is shown in Table 1. Dimensions for the plates SP1-SP3 were given in [1].

Table 1   Mechanical properties obtained by identification

Plates	Method	E_1, GPa	E_2, GPa	G_{12}, GPa	G_{23}, GPa	v_{12}
SP1	Present	71.3	68.8	24.5	-	0.32
	Mota Soares [1]	68.7	68.1	24.6	26.9	0.34
	Pedersen [5]	69.5	67.8	24.5	-	0.34
SP2	Present	44.2	17.7	7.2	4.9	0.195
	Araújo [6]	43.6	17.0	7.3	2.0	0.350
	Sol [8]	45.6	16.9	6.9	-	0.220
	Frederiksen [7]	45.4	17.3	7.3		0.255
SP3	Present	56.5	20.8	11.8	29.83	0.349
	Mota Soares [1]	57.2	21.4	11.3	11.8	0.300
	Pedersen [5]	61.3	21.4	9.8	-	0.280

A good agreement of the results obtained by the different methods is observed. Exception is the transverse shear modulus G_{23}. The reason of the differences is that the functional (1) in the case of relatively thin plates is rather insensitive to the transverse shear modulus. This parameter can be safely determined only from the experiments on the thick plates.

4. Conclusions

The present method of identification based on experiment design and response surface approach can predict the major elastic properties of the laminated composite plate specimens. The main advantage of the method of identification proposed in the present paper is significant reduction of the computational efforts in order to calculate the numerical frequencies, which are presented in the functional to be minimized. Estimated reduction of these calculations is about 100 times.

References

1. Mota Soares, C. M., Moreira de Freitas, M. and Araújo, A. L., Identification of Material Properties of Composite Plate Specimens. *Composite Structures*, **25** (1993) 277-285.

2. Rikards , R., Chate, A., Optimal Design of Sandwich and Laminated Composite Plates Based on Planing of Experiments, *Structural Optimization*, **10**, (1) (1995) 46-53.

3. Rikards, R. and Chate A., Identification of elastic properties of composites by method of planning of experiments, *Composite Structures*, **42** (3), 1998, 257-263.

4. Rikards, R., Chate, A., Steinchen, W., Kessler, A. and Bledzki, A. K. Method for identification of elastic properties of laminates based on experiment design, *Composites. Part B*, **30**, 1999, 279-289.

5. Pedersen, P., In: *Optimization Method Applied to Identification of Material Parameters. Discretization Methods and Structural Optimization - Procedures and applications*, eds. H. A. Eschenauer and G. Thierauf, Springer Verlag, Berlin, 1989, pp. 277-283.

6. Araújo, A. L. Método Numérico/Experimental para Carazterização Mecânica de Materiais Compósitos. M.Sc. Theses, Technical University of Lisabon, Mech. Eng. Dept., IST, April 1995 (in Portuguese).

7. Frederiksen, P. S. Identification of Material Parameters in Anisotropic Plates - A Combined Numerical-Experimental Method, PhD Theses, Department of Solid Mechanics, The Technical University of Denmark, 1992.

8. Sol, H., Identification of anisotropic plate rigidities using free vibration data, PhD Thesis, Free University of Brussels, 1986.

9. Rikards, R. B., Convexity of some classes of optimization problems for multilayer shells under conditions of stability and vibration. *Mechanics of Solids* (translation from Mekhanika Tverdogo Tela, translated from Russian by Allerton Press Inc.), **15** (1), 1980, 130-137.

Durability Estimation of Carbon/Polytetrafluoroethylene Composites for Hydraulic Downhole Motor

Kiyoshi KEMMOCHI[*1], Hiroshi TAKAYANAGI[*1], Taishi HAMADA[*2], Chouhachiro NAGASAWA[*3]
Jun TAKAHASHI[*1], Hiroshi TSUDA[*1], Hideki NAGAI[*1], and Hiroshi FUKUDA[*4]

*1   National Insutitute of Materials and Chemical Research, AIST, MITI
      1-1 Higashi, Tsukuba, Ibaraki 305-8565, JAPAN
*2   Science University of Tokyo, Graduate School
      2641 Yamazaki, Noda, Chiba 278-8510, JAPAN
*3   Kumamoto Industrial Research Institute
      3-11-38 Higashi, kumamoto, kumamoto 862-0901, JAPAN
*4   Science University of Tokyo
      2641 Yamazaki, Noda, Chiba 278-8510, JAPAN

Abstract :

Japan is one of the major volcanic countries, favored with abundant geothermal energy resources. It is estimated that approximately 10 percent of the world's geothermal energy exists in Japan. As geothermal energy is one of the nation's purely indigenous energy sources, its development has been widely favored. This domestic geothermal energy is not only clean and inexpensive but also is expected to be beneficial to the local society through multipurpose utilization. Furthermore, the geothermal energy is regarded as the most promising oil-alternative energy.

To practically use this geothermal energy, it is necesarry to dig geothermal wells to near the magma located about 3,000m to 4,000m below the surface. Therefore deep-seated geothermal power generation can efficiently obtain geothermal energy than a shallow-seated geothermal power generation. The excavators for the geothermal wells are called Downhole Motor (DHM). Although elastomers such as natural rubber are used as sealing materials and stators of DHM, the life time of these conventional elastomers is too short bacause various factors, such as high temperature over 200°C, complicated external forces, drilling mud and so on, operate on materials under deep-seated geothermal environment. The development of polymer compsites with heat resistance and durability is required to raise drilling-effiency. It is also expected to establish estimation methods to predict appropriately the life time of materials.

In this study, a testing equipment which can simulate effects of external forces, high temperature and the drilling mud was first designed and constructed (see Fig.1). This equipment enables to apply combined loading; compressive and torsion load. Then creep tests combined compressive and torsion load were performed on CF/PTFE for 100 hours at room and elevated temperatures (23, 40, 60, 80 and 100°C).

Fig.2 is an example of data. From these experimental data, master curves were obtained using the time-temperature superposition principle. The shift factors of these curves were also determined.

Then the validity of the estimation method based on shift factors was discussed using chemical kinetics. The result was satisfactly and due to its high accuracy, the possibility of applying the present method for the prediction of long term mechanical properties of materials in service was demonstrated.

Fig.1　Testing equipment for simulating geothermal environment.
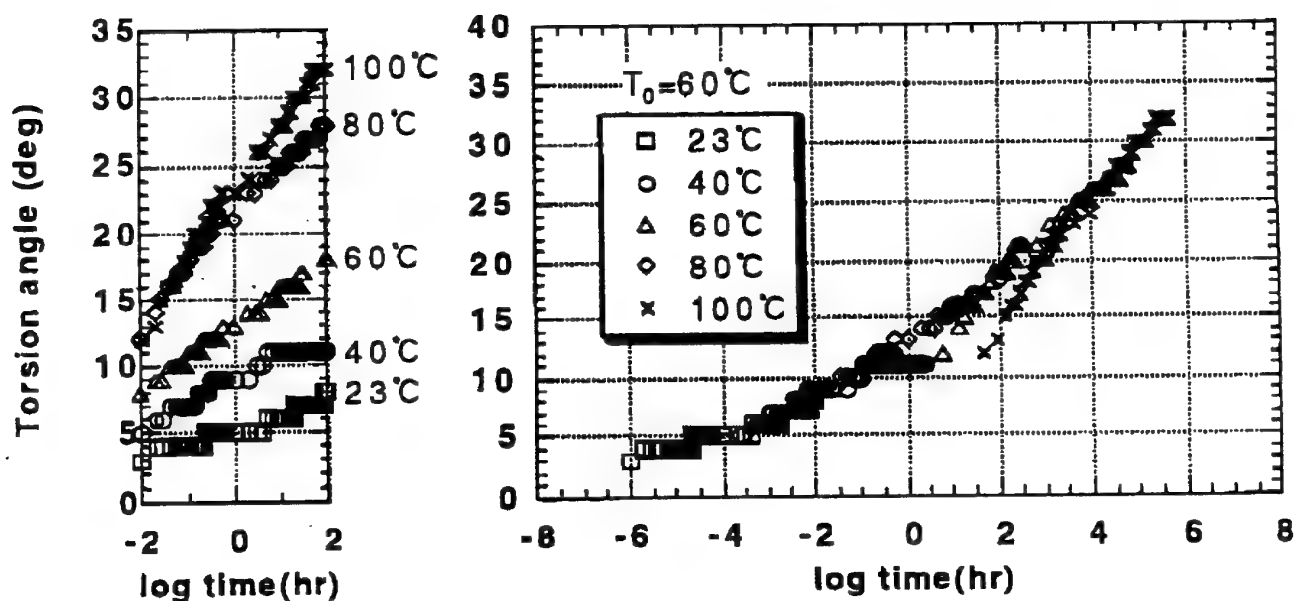
(a) Creep curves for CF/PTFE at room and elevated temperatures.

(b) Master curve of torsion angle for CF/PTFE at T_0=60℃, based on the test data from (a).

Fig.2　An example of an experimental results of the creep tests and master curve for CF/PTFE.

Quality assurance of adhesively bonded joints in GRP piping-systems

C.A.M. van den Ende, P.M. Oude Weme
KEMA, Materials Research, P.O. Box 6800, ET Arnhem, The Netherlands

Key words
GRP pipes / adhesively bonded joints / good workmanship / lack of adhesive / adhesive defects / curing / non destructive testing / ultrasonic method / radiography / cyclic fatigue testing / internal pressure and bending / internal pressure and axial testing / colorindicators for curing / fatigue testing / quality

Background
GRP pipes have several advantages compared to steel and lined steel pipes, e.g. corrosion resistance, light weight and costs. The physical limitations of the current generation of GRP pipes are pressure (< 100 bar) and temperature (< 140 °C). However, the psychological barriers are larger. Compared to welds in steel pipes the quality assurance for bonding GRP pipes is still underdeveloped. For steel a certification system, non destructive inspection methods and acceptance criteria for defects in the weld, are available. For the joining of GRP pipes adhesively bonded joints are most often used. No certification system exits.

The quality strongly depends on good workmanship. The low quality status of the joint decreases the wide acceptance of GRP pipes. In the first phase of this project ('92 –'95) practical guidelines have been set up for adhesive and laminated joints. For non-destructive testing (NDT) of the lack of adhesive in the joint, the ultrasonic through transmission method has been developed and the limits of radiography established. For curing the Differential Scanning Calometry (DSC) has been validated.

Further a first attempt to set up acceptance criteria for defects in the joints has been undertaken. These acceptance criteria were limited to the conditions of simple pressure testing and type and size of joints studied. The unexpected good performance in the tests of improperly cured joints were not taken into consideration.

Objective
The objective of the project is to increase the acceptance of GRP pipes by:
- Establishing acceptance criteria for defects based on long term failure behaviour of joints under practical conditions in relation to common occurring defects in the joints
- Field demonstration of developed non destructive inspection methods for adhesively bonded joints
- Developing methods for monitoring of the cure of the adhesive.

Approach
Good workmanship criteria to be required from trained, (certified) personnel which describe the minimal quality of the joint, have been set up together with pipe manufacturers.

The four most important loading conditions for GRP pipes in service have been identified. Representive, accelerated tests have been developed for these conditions. Joints made according to the minimal required good workmanship criteria have been subjected to these tests followed by detailed failure analyses.

A comparison of three different FEM apporoaches calculating the effect of a defect in the bond has been made with special attention for other than the tested 200 mm diameter.

The ultrasonic reflection method has been improved for this application. Both laboratory and field test are performed to ethablish the possibilities of ultrasonic and radiographic NDT methods.

A literature survey was performed followed by scouting tests and some development of the most promising methods to monitor the cure of the adhesive.

Results
According to the participating pipe manufacturers, minimal requirements can be expected for an adhesively bonded joint made by qualified personnel following the "practical guidelines". Minimal requirements for this Good Workmanship are set up only for the detectable defects by NDT, i.a. voids/lack of adhesive:
- the joint has less than 12,5% defects of the total surface; if the percentage is below 12,5% than also the next two criteria should be fulfilled:
  - locally the residual axial adhesive length should be at least 60%.
  - a defect with an opening at the inside and the outside of the joints should be less than 10 mm and 20% of the axial length.

As most critical conditions in service were identified:
- a combination of internal pressure and bending
- a combination of internal pressure and axial loading
- a combination of internal pressure and radial or axial shocks
- fatigue by a cyclic variation of internal pressure.

All the good workmanship test samples performed better than the pipe itself in this four test condition guaranteed structural integrity of a piping system.

These good workmanship criteria are restricted to room temperature, water as medium and to a diameter of 200 mm. FEM studies also indicated the validity for larger diameters and smaller diameters down to 70 mm. Application of GRP to even lower diameters is not recommended.

The original acceptance criteria for the curing of the adhesive passed the above mentioned tests.

The glass temperature (Tg) of the adhesive should be not less than 30 °C below the end Tg of the adhesive.

A poorly cured adhesively bonded joint failed by bursting which effects the safety of the personnel. For the monitoring of the cure is recommended:
- thermocouples connected to the heating blanket or direct to the adhesive to follow time and temperature
- the WAVIN sensor on the inside of the joint, especially for thick wall joints
- additives for the adhesive which do change the colour of the adhesive at higher temperature enableing visual inspection
- finally in a laboratory the Tg can be determined with the differential scanning caloremetry (DSC) for the determination of the Tg.

The ultrasonic through-transmission method developed in the earlier project was found to be unpractical and unreliable in the field test. However, good results were obtained with the ultrasonic reflection method and X-ray projection method. From the results it is concluded that both methods can detect lack of areas under certain conditions. The minimum detectable defects are smaller in size than allowed on the basis of the criteria for good workmanship.

Applications

Adhesively bonded joints must be made by qualified personnel following the "practical guidelines".

The good workmanship criteria for detectable defects shall be used in the certification of personnel in order to increase the quality of the GRP piping system.

Pressurizing the pipe system before commissioning reveals most of the defects and is recommended.

The NDT methods can be used for proving the good workmanship or in critical GRP applications (fitness for purpose) inspections of all the joints for even more security. Several techniques for monitoring the cure of the adhesive can be applied in order to prevent the dangerous bursting of the joint.

Their should be an international certification system for GRP pipes.

The results obtained contribute to the acceptance of GRP pipes.

Further information

This is a BvM/NIL project (Association for Materials Knowledge and Dutch Institute of Welding Technology). The project was realized with support and contribution of:
AIMS NDT, AKZO-Nobel, Ameron, BvM, Corresist, DSM, Dutch utilities, Future Pipe Industry, General Electric Plastics, Hoogovens Technical Service, Stoomwezen, KIWA, Shell, TNO-TPD, KIM-MML, RTD, StarFiber Glass Systems, Visser & Smit Hanab, KEMA

Project leader: dr. C.A.M. van den Ende
                    KEMA Nederland B.V.
                    P.O. Box 9035
                    6800 ET ARNHEM
                    Tel.: +31 26 356 24 02
                    Fax: +31 26 445 46 59

Comparison of warp knitted and stitched non-crimp fabrics

Henk Pattyn [1], Ignaas Verpoest [1], Jan Ivens [1], Esteban Villalon [2]

[1] Department of Metallurgy and Materials Engineering, KULeuven,
de Croylaan 2, B-3001 Leuven, Belgium
[2] Hexcel Fabrics,
av. Franklin Roosevelt 33, FR-69153 Decines Cedex Lyon, France

KEYWORDS: multi-axial, warp knitting, stitching, non-crimp, Liba, Paramax, tape

Introduction

Warp knitting with multi-axial weft insertion is a well-known technique to produce tailored multi-layered preforms for structural composite parts. This material technology is also named Multiaxial (by *Karl Mayer*) or Paramax (by *Liba*). Further on, it will be referred to as 'Liba'. This Liba material is compared with a new multi-layered, multi-axial, stitched preform produced by Hexcel fabrics. Further on, it will be referred to as 'stitched multi-axial'. For both materials, quasi-isotropic lay-ups (8 plies) were considered, both in glass and carbon. The preforms were processed with hand lay-up and autoclaving, using an epoxy resin. The mechanical in plane performance and the resistance to damage development were evaluated.

Influence of preform manufacturing on fibre architecture in the composite

The Liba material is constructed by laying down weft yarns, oriented layer by layer. At both sides, a continuous chain of hooks keeps the yarns straight and well in place. These chains transport the yarn layer assembly to the knitting unit, where the layers are bonded together into the final stable preform. This process realises flat filament winding in a continuous way.

For the stitched multi-axial, heavy tows (12k up to 80k) are spread and are laid down as a tape, also oriented layer by layer. A belt transports the lay-up to the stitching unit, which turns it into the final preform.

Compared to Liba, the stitched multiaxial offers complete flexibility in ply orientation and stacking sequence, overcoming the limitations posed by the side chains with hooks. This technique allows the creation of a multiaxial lay-up with very fine plies, starting from heavy tows. Laying up tape does not introduce big gaps in the preform (see below). This promotes a more homogenous fibre distribution and better surface quality.
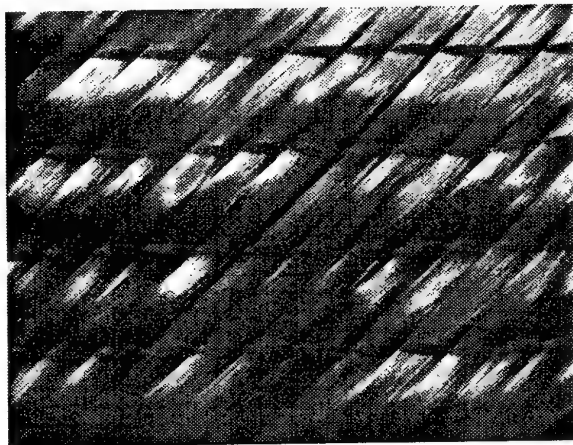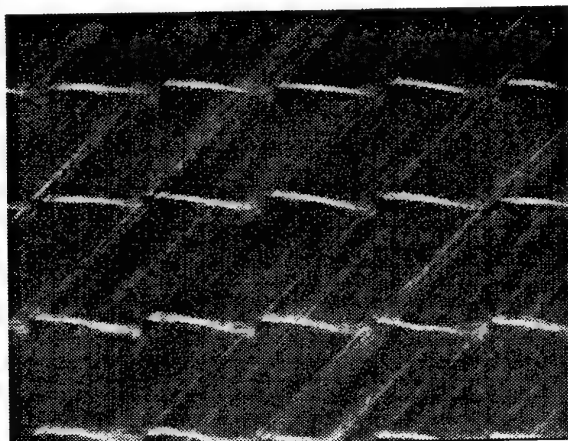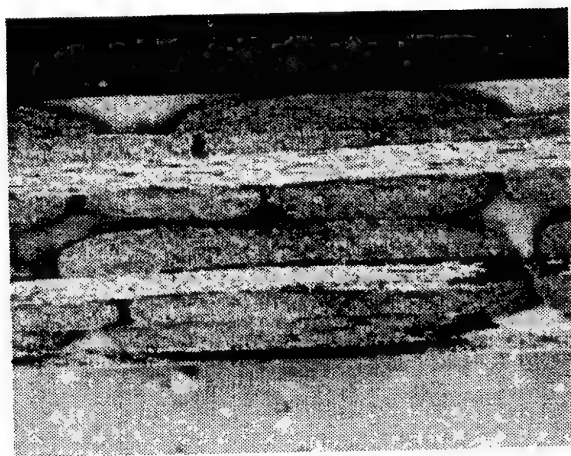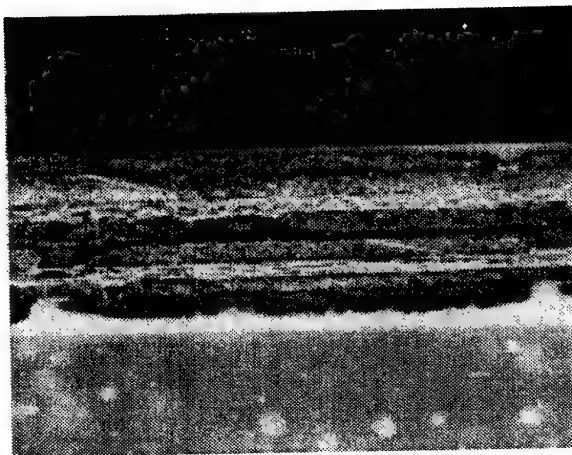

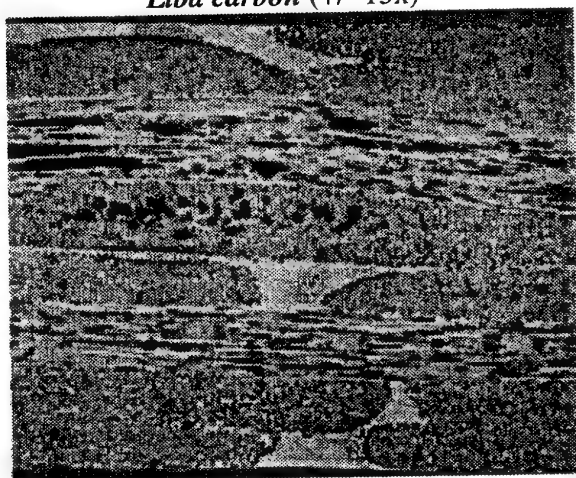*Liba glass*   *Stitched multi-axial glass*

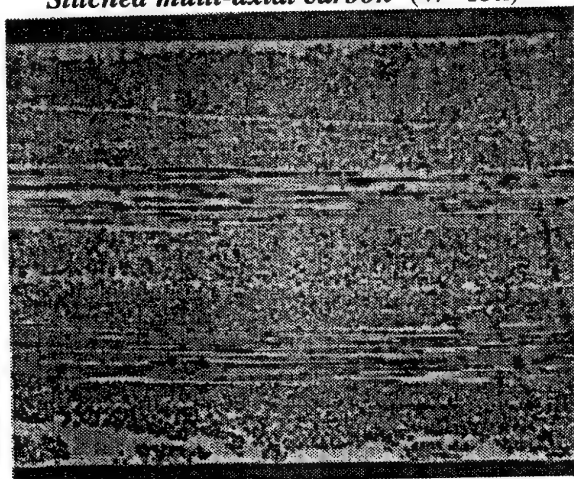The difference in fibre distribution in the final composite is shown below.

Liba carbon (+/- 15x)

Stitched multi-axial carbon (+/- 15x)

Liba glass (+/- 35x)

Stitched multi-axial glass (+/- 35x)

During autoclave processing, the squeeze out of resin is 2 to 3 times higher for the Liba material. The gaps between yarns of the Liba material act as "channels" for the resin. The in-plane permeability is lower for the stitched multiaxial than for Liba, requiring more careful processing.

Mechanical in-plane performance

First, the mechanical in-plane performance was characterised with tensile tests. In the case of carbon fibre, the normalised E-modulus was the same for both Liba and stitched multi-axial. However, in the case of glass fibre, the stitched multi-axial had a slightly higher normalised E-modulus compared to the Liba. The normalised strength was higher for the stitched multi-axial than for the Liba: + 50% for glass fibre, + 15% for carbon.
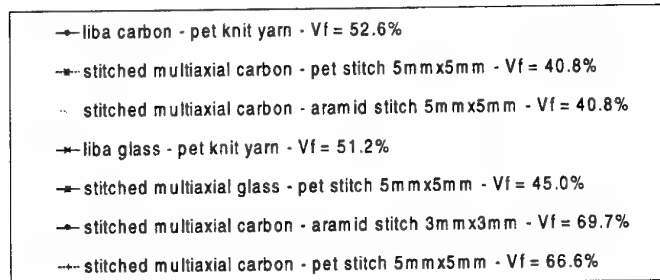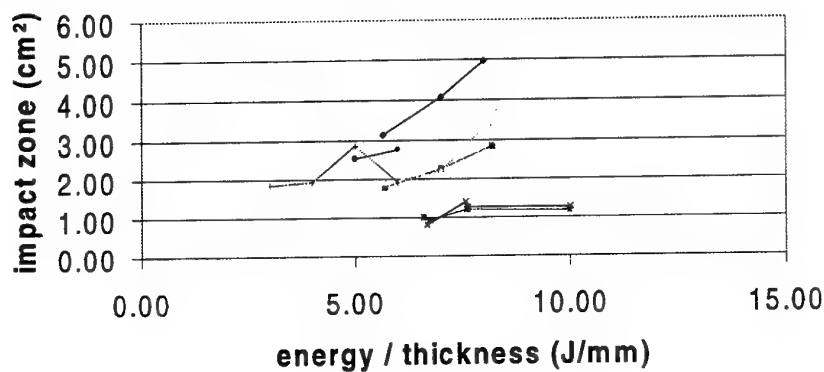
Resistance to damage development

The mechanical out-of-plane performance was first investigated with the Charpy test. The Charpy impact strength turned out to be higher for the stitched multi-axial than for the Liba.

Drop weight impact testing was used to characterise the resistance of the materials to damage development. The damaged zone was used as an evaluation parameter. For the glass-epoxy specimens, the damaged zone could be observed visually, as these were semitransparent. For the carbon-epoxy specimens, the damaged zone was determined using ultrasonic C-scanning (see example below).
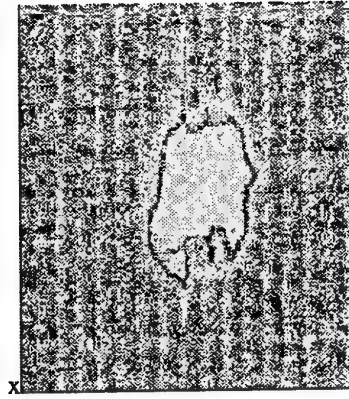
C-scan of impacted Liba carbon specimen *(8 J/mm thickness)*

The results are summarised in the figure below.

→ liba carbon - pet knit yarn - Vf = 52.6%

→ stitched multiaxial carbon - pet stitch 5mmx5mm - Vf = 40.8%

·· stitched multiaxial carbon - aramid stitch 5mmx5mm - Vf = 40.8%

→ liba glass - pet knit yarn - Vf = 51.2%

→ stitched multiaxial glass - pet stitch 5mmx5mm - Vf = 45.0%

→ stitched multiaxial carbon - aramid stitch 3mmx3mm - Vf = 69.7%

→ stitched multiaxial carbon - pet stitch 5mmx5mm - Vf = 66.6%

The glass variations can absorb much more energy than the carbon variations. Taking into account the fibre volume fraction, the stitched multi-axial glass performs slightly better than the Liba glass. The stitched multi-axial carbon performs significantly better compared to the Liba carbon. The difference between the pet stitching and aramid stitching is small. Comparing the stitched multi-axial with 3mmx3mm aramid stitching with 5mmx5mm does not reveal a major difference.

After impact, the Liba specimens show large cracks among the fibre bundles whereas for the stitched multi-axial specimens, cracks among the fibre bundles are smaller. The damaged zone is more restrained for the stitched multi-axial. In the impact zone, the stitched multi-axial specimens show more fragmentation of the fibre bundle. Finer fibre distribution promotes fibre bundle cracking instead of inter fibre bundle cracking, so that the stitched multi-axial can absorb, locally, more energy and is more damage tolerant.

PREDICTING THE DURABILITY OF PMR-15 COMPOSITES AGED AT ELEVATED TEMPERATURES.

Kenneth J. Bowles

Polymers Branch, Materials Division
National Aeronautics and Space Administration
Glenn Research Center
Cleveland, Ohio 44135 USA

Earlier work pointed out the apparent influence of a surface layer formation and growth on the retention of compression properties of polymer matrix composites (PMC's) during extended aging times[1]. This layer was found to change in its composition and features as the aging temperature changed. Microcracks and small voids initiated and advanced inward at all temperatures.

The material that was studied was PMR-15 reinforced with T650-35, 24 by 23, 8 harness, satin-weave graphite fiber fabric[2]. The materials were processed at the General electric Aircraft Engine Inc. in Evendale, Ohio.

The composite materials used were aged in air-circulating ovens at temperatures of 204, 260, 288, 316 and 343°C and an air flow maintained at 100 cm^3/min. The laminates were removed periodically, allowed to cool in a desiccator, weighed, and either returned to the oven or permanently removed for testing. The aging time was considered completed when the weight loss exceeded 10%.

All specimens were conditioned at 125°C for 16 h before compression tests were conducted. All compression tests were performed as specified in Test Method for Compressive Properties of Rigid Plastics (ASTM D 695M). No end tabs were used. Strain was measured with an extensometer, and moduli were measured using strains and loads at 500 and 1500 microstrain[2]. The surface layer thickness measurements were made from photomicrographs that were taken.

Figure 1 shows a schematic of the surface damage growth during the duration of aging. The depth of the cut surface damage increased with increasing specimen thickness. Because of this, weight loss data cannot be compared for specimens of different thicknesses.

Figure 2 shows the dependence of the thickness of the resin-rich surface damage layer with the aging time at all temperatures. The relationships appear to be linear at all five temperatures, with slower growth rates at the lower temperatures. The data from the two lower temperature tests indicate what may be an initial fast rate of growth and then a slower steady rate after 1000 h of aging. This may be normal scatter however.

Figures 3-5 present compression strength, plotted as a function of layer thickness of the composite at various temperatures. Each figure contains data for one thickness of specimen. The thicknesses are 1.27, 2.77 or 6.73 mm (4, 8, or 20 plies respectively). The scatter in the data in Figure 3 appears to be greater than that of the 8 and 20 ply specimens (Figures 4 and 5 respectively)). The half thickness of the specimens (denoted by the vertical dashed line) is nominally 0.635mm. When the surface layer thickness reaches this value, the entire cross section of the specimen is damaged and consists of surface layer material. The normalized compression

strength seems to reach a minimum at 20 to 25 percent. The surface layer thickness values to the right of the half-thickness line are taken from Figure 2, and are the thicknesses the layer would reach in a thicker specimen during the time the 4 ply specimen was aged. The half-thickness of the 8 ply specimen is 1.38 mm. Figure 4 indicates that when the surface layer thickness approaches this value and the entire cross section is composed of damaged material, the residual compression strength approaches 20%. The data from the 20 ply composite, shown in Figure 5, extrapolate to a surface layer thickness of 2.7 mm. at 20% residual strength. The half-thickness value is 3.4. The minimum value appears to be offset to a point less than the half-thickness. Indications are that the offset increases with specimen thickness (or aging time).

The modulus data in Figure 6 show an extreme amount of scatter and have been separated into two separate curves. This is because the composite modulus is affected by the modulus of the reinforcement and only slightly by the matrix. This effect becomes less noticeable as the thickness of the specimen increases. The thicker modulus data at all temperatures collapse onto one linear curve in Figures 7 and 8.

Specimen thickness is a significant factor in compression property deterioration during such periods of exposure. It is apparent from viewing Figures 3-5 that the influence of the surface layer diminishes and the core strength becomes more important as the composite thickness increases. Initially, although the surface layer thickness is a good indicator of the magnitude of property degradation, the core material is the main contributor of strength for composites with thicknesses of 8 ply and above. As the layer thickens, its influence increases. Estimates of structural lifetimes for PMR-15 composites reinforced with T650-35 fabric can be made using Figure 2 in conjunction with a plot like those shown in Figures 3-5. Accelerated testing may be possible as shown in Figure 9, which is an adjustment of Figure 5. Once a straight line can be assumed with a minimum amount of data points, it can be extrapolated to the desired normalized strength. This can then be converted to operating time.

REFERENCES
1. Bowles, Kenneth J., Thermal and Mechanical Durability of Graphite Fiber Reinforced PMR-15 Composites, *Progress in Durability Analysis of Composite Systems,* K.L.Reifsnider D. A. Dillard, and A. F. Cardon, eds. Proceedings of the third international Conference on Progress in Durability Analysis of Composite systems, Blacksburg, Va., USA, 14-17 September, 1997, PP71-75.
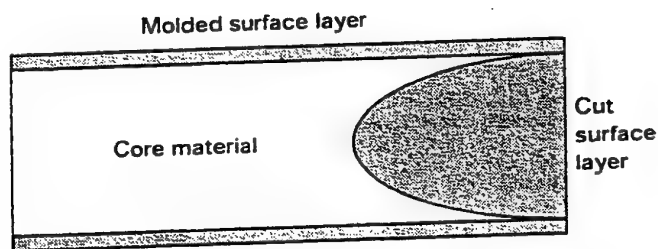2. Bowles, K. J., Roberts, G. D. and Kamvouris, J., ASTM STP 1302, 1997.

Figure 1.. Microcrack and oxidation layer growth during isothermal aging
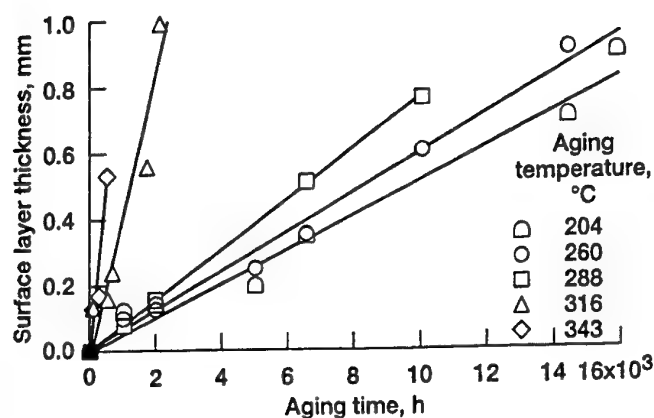
Figure 2. Surface layer thickness as a function of aging time at various temperatures.
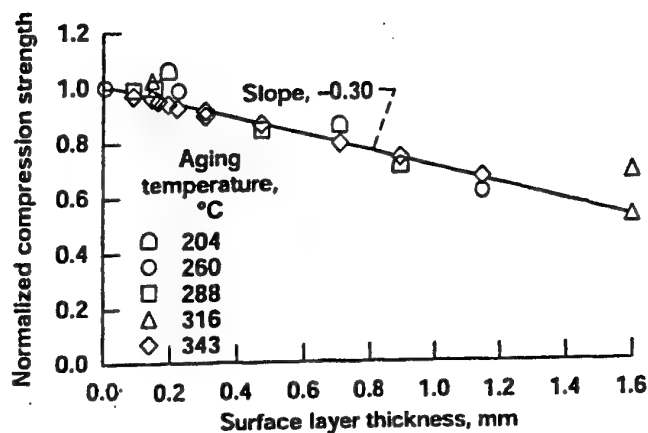

Figure 5. Composite compression strength as a function of surface layer thickness at various temperatures. Number of plies, 20.
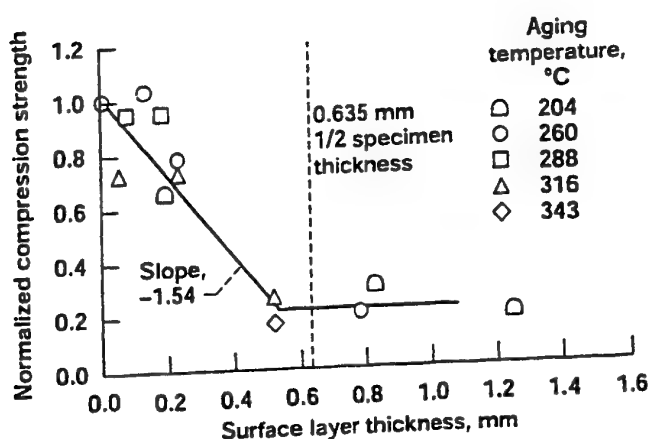

Figure 3. Composite compression strength as a function of surface layer thickness at various temperatures. Number of plies, 4.
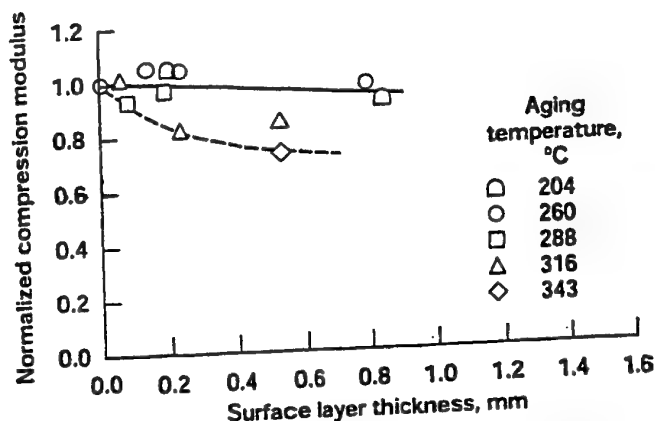

Figure 6. Compression modulus as a function of surface layer thickness at various temperatures. Number of plies, 4.
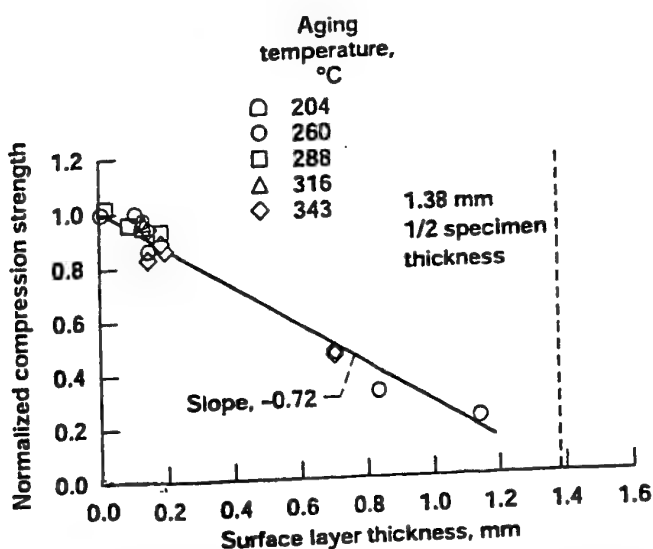

Figure 4. Composite compression strength as a function of surface layer thickness at various temperatures. Number of plies, 8.
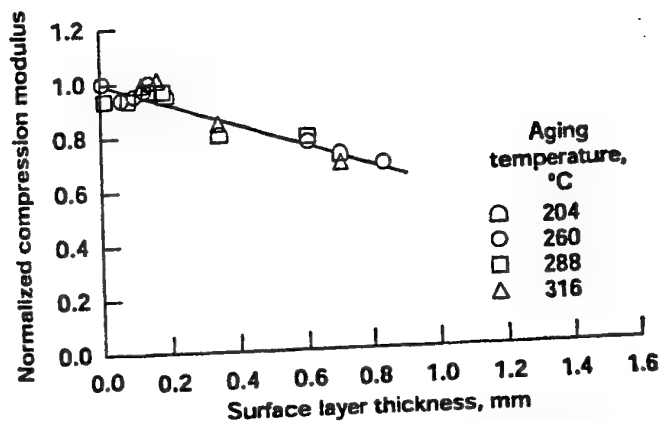

Figure 7. Compression modulus of composites as a function of surface layer thickness at various temperatures. Number of plies, 8.
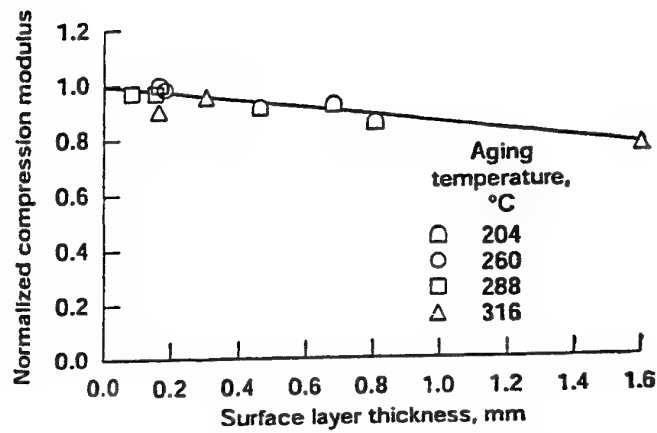
Figure 8. Composite compression modulus as a function of surface layer thickness at various temperatures. Number of plies, 20.
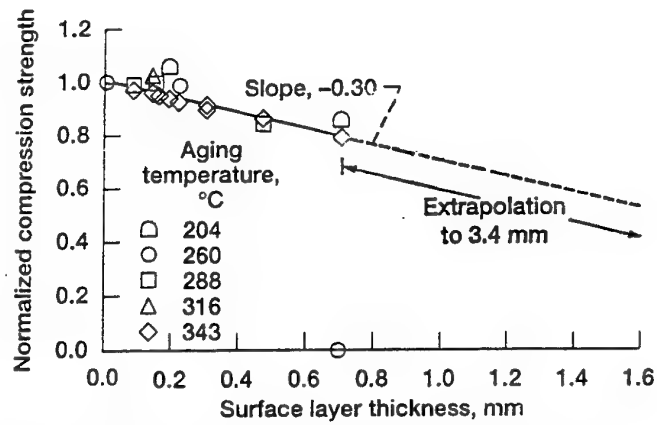

Figure 9. Extrapolation of short time data set to one-half specimen thickness.

Durability of Adhesive Joints Subjected to Elevated Temperature Aging

David R. Veazie[1], Jianmin Qu[2], and Josiah Lindsay[2]

[1] Department of Engineering, Clark Atlanta University, Atlanta, GA 30314
[2] School of Mechanical Engineering, Georgia Institute of Technology, Atlanta, GA 30332

The aerospace industry has become increasingly interested in the use of structural adhesive joints in the design of new aircraft. The impetus for this interest is the many advantages adhesively bonded joints posses over traditional fastening techniques such as rivets and bolts. Adhesive joints are usually lower in weight, allow the bonding of dissimilar materials, and have lower fabrication costs. Several structural adhesive joints are in service on military and commercial aircraft [1,2], however, these bonded joints have been limited to secondary structures partly because the environmental durability of these joints have not been extensively characterized. Since structural adhesive joint systems are composed of adherends, adhesives, and interphase regions, detailed analyses of these joints must be performed not only in their fabricated condition but also after they have been exposed to elevated temperature and other environmental conditions.

Commercial supersonic aircraft capable of traveling at speeds in excess of Mach 2, could be subjected to temperatures near 177°C in wing and fuselage structures. It is believed that the key to develop advanced adhesive joints to meet future challenges of elevated temperature, environmental exposure, and durability is to understand the mechanics of the adhesive joints based on the adhesive's microstructure and the physics of interfacial adhesion. To obtain this understanding is the rational for a comprehensive study aimed at 1) establishing a correlation between the microstructural changes and the long term bond strength in adhesive joints by the use of interfacial fracture mechanics to characterize interfacial toughness as a function of the mode mixity at the debonding crack-tip and 2) developing finite element computations to obtain a calibration between the applied load and the energy release rate based on the load and specimen geometry.

This research investigates the physics of degradation mechanisms and the long term effects of time and temperature on polymer bonded joints through an experimental study. Fracture toughness parameters (G_c) are obtained for possible use in a predictive scheme to estimate the remaining life of a bonded joint. To this end, room and elevated temperature (-54°C and 177°C) tests are conducted. The adhesive system used for the study is comprised of Ti-6Al-4V titanium adherends bonded with an adhesive (FM®x5) based on a polyimide developed at the NASA-Langley Research Center (LaRC™-PETI-5). Room and elevated temperature Mode I, Mode II and Mixed-Mode I and II fracture toughness results are obtained from double cantilever beam (DCB), end notch flexure (ENF), and cracked lap shear (CLS) tests, respectively. Testing was performed on specimens with no environmental exposure (as-received), as well as isothermally exposed for 5,000 hours at 177°C, and isothermally exposed to a hot/wet environment (80°C, 90%+ relative humidity).

Specimens cut from a 95.3 cm. by 69.9 cm. bonded panel were provided by Boeing. The unaged glass transition temperature, T_g, of the adhesive as measured by Dynamic Mechanical Analyzer (DMA) G'' peak was 250°C. The titanium adherend thickness was 0.25 cm., whereas the adhesive measured 0.04 cm. thick. To enhance the durability of the joints, a Sol Gel chemical pretreatment process was performed on the surface of the titanium adherends. The inclusion of non-adhesive Kapton™ film provided the crack initiation sites, and slots were incorporated in the panel for venting of volatiles during cure.

DCB and ENF tests were performed to obtain the Mode I and Mode II fracture toughness parameters, respectively. The DCB and ENF specimen configurations are identical, and consist of two adherends joined by the adhesive with a mid-plane embedded insert (Kapton™) at one end. The insert prevented bonding of a nominal 5.08 cm. region. DCB and ENF specimens used for this research were nominally 1.90 cm. wide and 26.67 cm. long, as shown in Figures 1 and 2. The CLS specimen consists of a 30.48 cm. long beam (lap) bonded to a 26.67 cm. shorter beam (strap), as shown in Figure 3. All of the fracture tests were performed at atmospheric pressure in laboratory air (23°C, 50% RH) on a 100 kN servo-hydraulic test frame equipped with digital controller and computer data acquisition. To reduce experimental error, several replicate tests were performed, permitting the calculation of multiple G_c values for each specimen.

MODE I (G_{Ic}) CLOSED FORM SOLUTION

The DCB specimen was first introduced for fracture toughness testing by Ripling et. al. [3]. For DCB specimens with two adherends of the same material and thickness, the strain energy release rate, G_{Ic}, may be calculated by using Equation (1)

$$G_I = \frac{P^2}{2b}\frac{dC}{da}$$ (1)

where:
P = load
b = specimen width
C = specimen compliance (δ/P)

a = crack length
δ = crosshead opening displacement

By using beam theory and assuming that the DCB specimen consists of two cantilever beams with a built-in-support on the end opposite the load application point, Equation (1) reduces to

$$G_I = \frac{3P\delta}{2ba}.$$ (2)

Equation (2) can be modified to account for the relationship between specimen compliance and observed crack length using

$$G_I = \frac{3P\delta}{2b(a+|\Delta|)}.$$ (3)

The value Δ is the intercept of the a- axis obtained from a linear relationship between $C^{1/3}$ and a. The Δ term serves as a correction term to account for the false assumption that the cantilever beams were built end since the uncracked end of the DCB specimen is free. For the monotonic test, the critical load, P, corresponded to the load at which the load versus displacement data deviated from linearity.
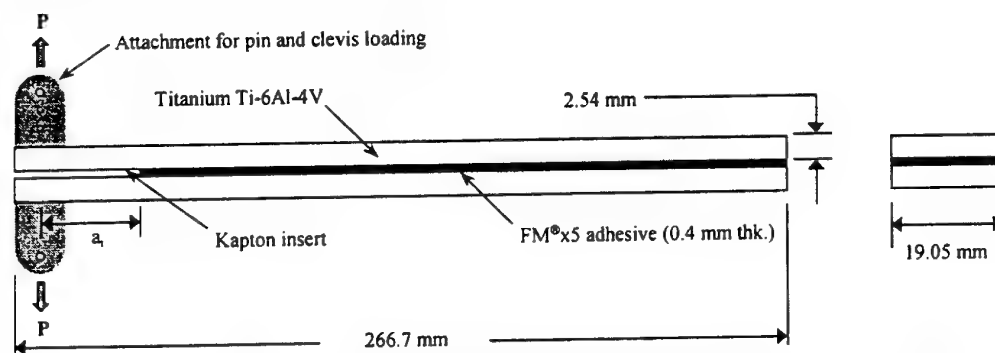

Figure 1. Schematic for the Ti-6Al-4V/FM®x5 double cantilever beam specimen.
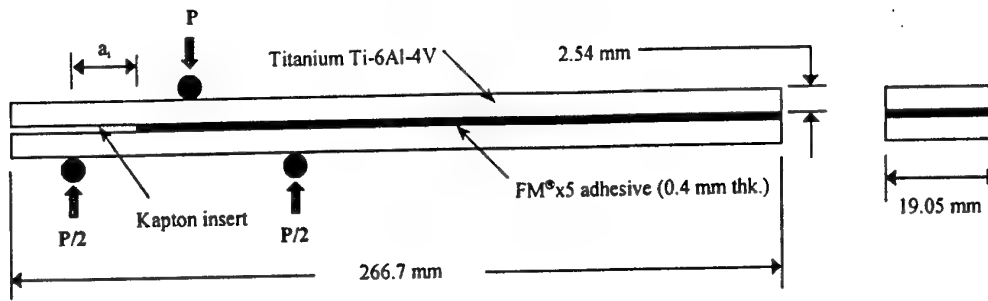
Figure 2. Schematic for the Ti-6Al-4V/FM®x5 end notch flexure specimen.

MODE II (G_{IIc}) CLOSED FORM SOLUTION

Determination of the applied Mode II strain energy release rate, G_{IIc}, from ENF specimens was carried out using the beam theory method. The method is discussed by Carlsson, et al. [4], and the formula for the beam theory is given as

$$G_{IIc} = \frac{9P^2 a^2}{16Eb^2 t^3} \qquad (4)$$

where:
P = load
a = crack length (2.54 cm)
E = adherend elastic modulus

b = specimen width
t = thickness of one adherend

Similar to the DCB tests, crack growth was observed to begin at or near the onset of nonlinearity in the load versus displacement curve. A note should be made that this analysis does not take into account friction between the adherends. In previous analyses, friction was neglected due to the smooth surface of interlaminar cracks in composites. However, this assumption may not be valid here due to the increase in G_{IIc} values as multiple tests were taken on the same specimen.

MIXED MODE I & II (G_{Tc}) CLOSED FORM SOLUTION

The CLS specimen geometry was devised by Brussat, et al. [5], and its closed form solution is based upon beam theory, given as

$$G_{Tc} = \frac{P^2}{2b^2}\left[\frac{1}{E_s t_s} - \frac{1}{E_s t_s + E_l t_l}\right] \qquad (5)$$

where:
P = load
b = specimen width
E_s = strap elastic modulus

E_l = lap elastic modulus
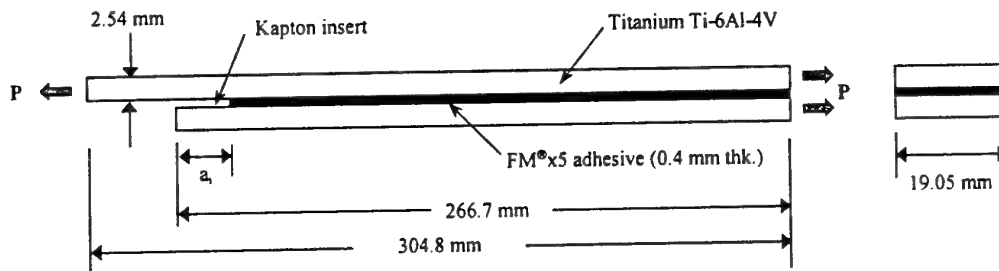t_s = strap adherend thickness
t_l = lap adherend thickness

Figure 3. Schematic for the Ti-6Al-4V/FM®x5 crack lap shear specimen.

Note that this Equation (5) does not provide for the determination of the individual Mode I and Mode II components present in the cracked lap shear specimen. Currently, research still continues on ways to separate these two distinct strain energy release rate modes using a closed form solution.

RESULTS AND DISCUSSION

The effects of environmental exposure on the Mode I, Mode II, and Mixed Mode I & II critical strain energy release rates from DCB, ENF, and CLS tests at room temperature and elevated temperatures (177°C and -54°C) are compared in Figures 4-6, respectively. The error bars represent the ±95% confidence interval. In most Mode I cases, crack growth in the Ti-6Al-4V/FM®x5 specimens was cohesive (i.e. contained within the adhesive bondline). DCB tests showed a moderate reduction in the Mode I fracture toughness due to 5,000 hours of aging and elevated temperature testing. Mode II cases primarily showed an interfacial failure (i.e. adhesive layer debonds from the adherend). ENF results showed more of a reduction in the Mode II fracture toughness due to 5,000 hours of environmental exposure and elevated temperature testing. In most Mixed Mode I & II cases, an alternating failure (i.e. both cohesive and interfacial failure) was observed. Critical strain energy release rate results from CLS tests showed a significant reduction in fracture toughness, especially due to the 'hot/wet' exposure and elevated temperature testing. There was no evidence that elevated temperature testing or exposure to either 'hot/dry' or 'hot/wet' environments caused a change in the crack growth paths.

In all loading cases except Mode I, the threshold strain energy release rates were reduced as a result of 5,000 hours of aging and elevated temperature testing. From the critical strain energy release rate results presented here, failures from Mixed Mode I & II tests appear to be more susceptible to degradation by environmental exposures and elevated temperature testing than failures by Mode I or Mode II tests alone. Although the results presented here are specific to the materials, loading modes, and the environments examined, the sensitivity of the fracture toughness to environmental exposure and elevated temperature testing imply that a predictive scheme to estimate the remaining life of a bonded joint must account for elevated temperatures and moisture. This implication would also hold true when considering the development of accelerated test methods based upon the changes in the adhesive's microstructure and the physics of interfacial adhesion due to temperature and moisture.
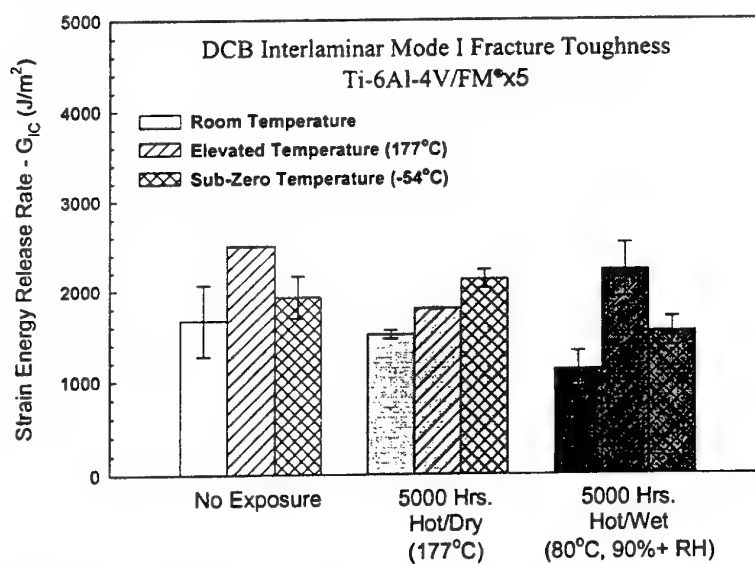

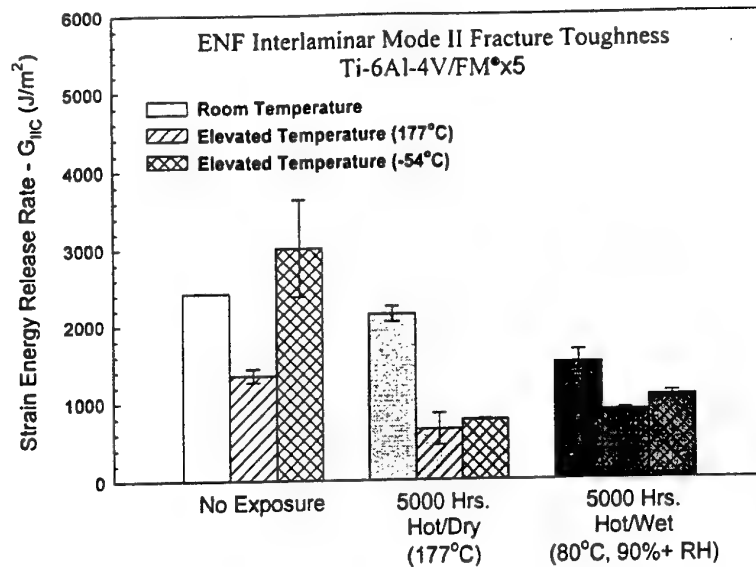Figure 4. Effect of environmental exposure on Mode I fracture toughness.

Figure 5. Effect of environmental exposure on Mode II fracture toughness.

REFERENCES

1. Baker, A. A., 1994. "Bonded Composite Repair of Metallic Aircraft Structures." in *Composite Repair of Military Aircraft Structures:* Proceedings of the 79th Meeting of the AGARD Structures and Materials Panel, Seville, Spain.
2. Belason, E. B., 1994. "Status of Bonded Boron/Epoxy Doublers for Military and Commercial Aircraft Structures." in *Composite Repair of Military Aircraft Structures:* Proceedings of the 79th Meeting of the AGARD Structures and Materials Panel, Seville, Spain.
3. Ripling, E. J., Mostovoy, S., and Patrick, R. L. 1964. "Measuring Fracture Toughness of Adhesive Joints," *Materials Research and Standards*, American Society for Testing and Materials, Philadelphia, PA.
4. Carlsson, L. A., Gillespie, J. W., and Pipes, R.B. 1986. "On the Analysis and Design of the End Notched Flexure (ENF) specimen for Mode II Testing, "*Journal of Composite Materials*, Vol. 20.
5. Brussat, T. R., Chiu, S. T., and Mostovoy, S. July 1977. "Fracture Mechanics for Structural Adhesive Bonds - Final Report," Lockheed Co., Burbank, CA for the USAF Materials Laboratory, AFML-TR-77-163.
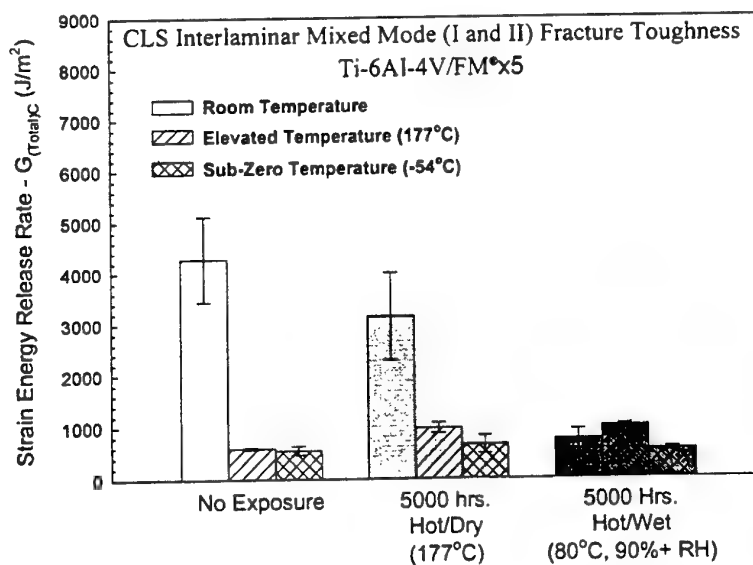
Figure 6. Effect of environmental exposure on Mixed Mode I & II fracture toughness.

On The Use of Acoustic Emission and Scanning Electron Microscopy to Investigate Fatigue Damage in Plain -Woven Fabric Composites

Surya D. Pandita, Gert Huysmans, Martine Wevers, Ignaas Verpoest

Department of Metallurgy and Materials Engineering, Katholieke Universiteit Leuven, De Croylaan 2, B-3001 Leuven, Belgium

1. Introduction

Woven fabric composites are a class of textile composites that are widely used for many structural applications. The use of textile fabrics has generally offered a lower cost to composite manufacturing and higher damage tolerance for impact loading. Woven fabrics are produced by interlacing two or more yarns on a loom. The mechanical properties of woven fabric composites, such as strength and stiffness, are strongly determined by weave parameters (weave geometry, yarn size, yarn spacing, and yarn crimp, fiber type), and laminate parameters (fiber orientations and overall fiber volume fraction), and the inherent material properties of fiber and matrix.[1,2]

During service, composite structures can be subjected to fatigue loads. The fatigue load creates fatigue damage. The major damage types in fiber reinforced composite materials are fiber fracture, matrix cracks, matrix-fiber debonding, and delamination. Those damage types were also detected in woven fabric composites that were subjected to fatigue loads. In general, the accumulation of fatigue damage is accompanied by a reduction in stiffness and strength, and an increase in the size of the hysteresis loop. Residual stiffness and hysteresis change are not easily measured during the fatigue test, unless the test is stopped or the fatigue tests are run on a sophisticated fatigue machine where data processing is possible during the measurement. Acoustic emission (AE) is the only non-destructive test technique capable of detecting all of the above mentioned damage types and of providing information of damage accumulation during fatigue loading.

However, the major disadvantage of AE is that great skill is needed in order to correlate AE information with damage mechanisms in a material. The interpretation of AE signals coming from different damage types is not straightforward. In order to facilitate AE interpretation, researchers often compare AE data with other damage characterisation techniques (ultrasonic C-scan, radiography and scanning electron microscopy). Microscopic techniques such as scanning electron microscopy (SEM) have often been used to complement acoustic emission. The main disadvantage of SEM is that it is a destructive technique. It means that an investigated specimen can only be subjected to a certain damage level or a specific number of fatigue cycles. The specimen then needs to be cut and analysed either at the edge or over a cross-section of the specimen.

This paper focuses on the use of acoustic emission and scanning electron microscopy to investigate tensile-tensile fatigue damage in plain-woven fabric composites. Woven Fabric composites were subjected to fatigue load in the on-axis direction.

2. Results and Discussion

A symmetric plain woven fabric, having similar yarn properties in both warp and weft direction, is used. Because of this symmetry, fatigue tests were performed in one of these two directions. Fatigue tests on woven fabric composites were performed on the weft direction.

E-glass woven fabrics (R/420) were supplied by the Company SYNCOGLASS, Belgium. The woven fabrics were impregnated by epoxy resin films F533 from HEXCEL and cured in an autoclave at a temperature of 125 degree Celsius and a pressure of 3 bar.

Plain weave fabric composites were subjected to tensile fatigue loading at a stress ratio R ($\sigma_{min}/\sigma_{max}$) of 0.1 and a frequency of 3 Hz. In this paper, we only focus on damage accumulation of woven fabric composites subjected to a fatigue load S_{max} ($\sigma_{max}/\sigma_{ult}$) of 0.5 and 0.7. Two AE sensors were attached on the fatigue specimen. The distance between the two AE sensors is 50 mm or 30 % of the gauge length of the specimen. The tested specimens have a thickness of 25 mm and a length of 230 mm. End tabs with a length of 40 mm were glued at the corner of the specimen

2.1 Static Tensile results.

Before investigating the fatigue behaviour of a particular material, its static behaviour must be discussed first. Figure 1 shows the static tensile test result of the investigated woven fabric composites. The tensile test was performed at a strain rate of 2 mm/s, which is much slower compared to the cyclic displacement rate in a fatigue test whose frequency is 3 Hz. At 50 % of the   ultimate tensile stress, damage has been created in the specimen because the stiffness of the specimen has already decreased to 75 % of the initial stiffness. Therefore, a fatigue load. S_{max} of 0.5 has been selected for the fatigue tests.
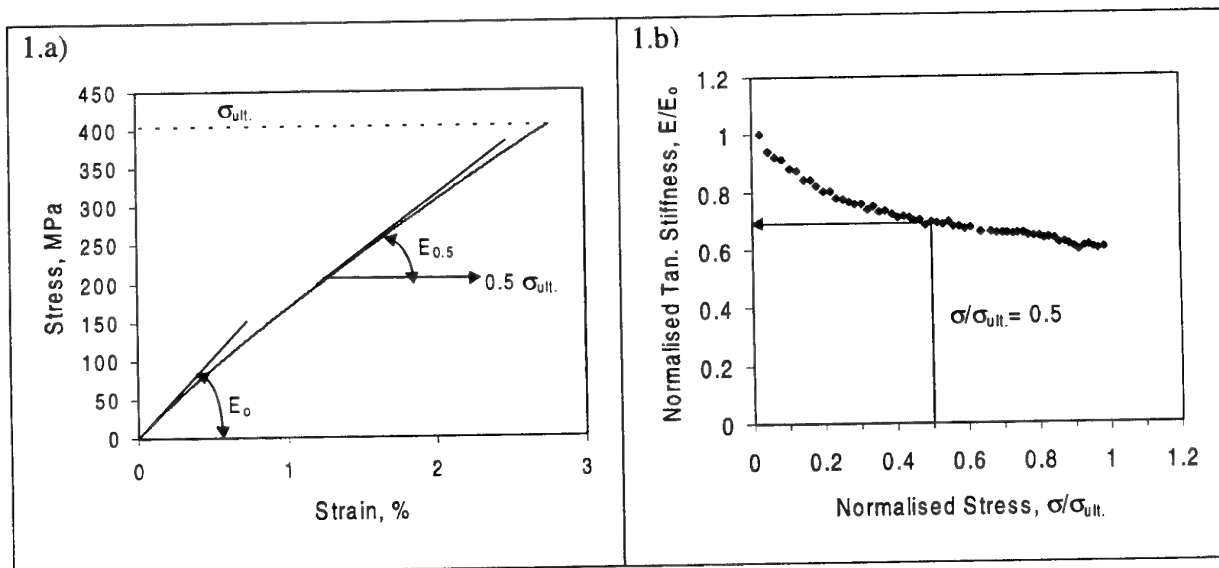

Figure 1. Static tensile result of woven fabric composite R/420

2.2. Fatigue Results.

Figure 2 shows the S-N curve of woven fabric composites subjected to tensile-tensile fatigue loading. The fatigue life at a fatigue load S_{max} of 0.5 is 65.000 cycles and at S_{max} of 0.7 is 2.700 cycles.

The fatigue behaviour of woven fabric composites generally consists of three stages, in which transverse bundle cracks, meta-delaminations and fiber fracture develop consecutively. A meta-delamination is created when a transverse bundle crack is being deflected by a longitudinal fiber bundle within the same fabric layer. For the investigation of the damage mechanisms of woven fabric composites, two fatigue loads were selected with

2

maximum fatigue loads S_{max} of 0.5 and 0.7. These fatigue loads were selected based on the related fatigue lifes.
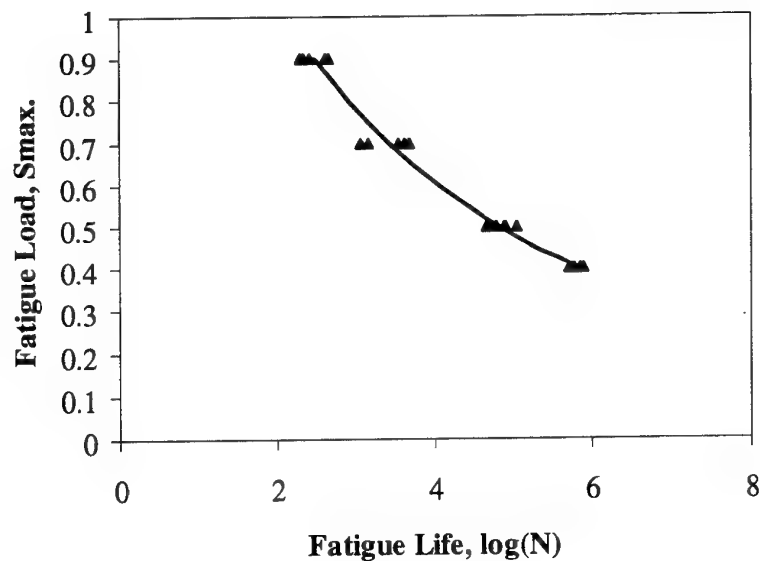

Figure 2. S-N curve of woven fabric composites in weft direction.

Based on the acoustic emission and SEM investigation, the fatigue damage development at the fatigue load S_{max} of 0.5 consists of 4 stages. The first stage is defined by the absence of the AE activities. Based on the static test, which a stiffness decrease about 25 % from the initial stiffness was observed, fatigue damage was expected to be detected by acoustic emission at the beginning of the fatigue tests. However, the acoustic emission device only detected AE activity after 12.000 cycles. The stiffness in the fatigue test was only dropped to 95 % of the initial stiffness when the first AE event was detected. Compared to the static results, the stiffness degradation during fatigue tests is less pronounced. It indicates that the mechanical response of woven fabric composites is strongly influenced by the strain rate. Figure 3 shows the hysteresis loop and the residual stiffness at a fatigue load S_{max} of 0.5.

Although the stiffness decreased after 12.000 cycles, no AE events were detected. There are two justifications for this observation. First, the AE events of fatigue damage introduced outside the investigated area, will be filtered out. The second reason is that the AE intensity of the first fatigue damage is too weak. Small fatigue damage phenomena such as fiber-matrix debonding near the edge of the specimen may result in low AE intensity.

In the second stage, AE events related to fatigue damage were detected increasingly when the number of fatigue cycles increased. A complementary fatigue test on another sample was performed and stopped at 15.000 cycles where the second stage was expected to happen. The specimen was then cut and analysed microscopically at its cross-section. From the SEM inspection, the fatigue damage at 15.000 cycles consists of transverse bundle cracks in the fatigued specimen. The AE amplitude of the AE events at the second stage is mostly between 45 and 50 dB. Another test was stopped and analysed by SEM at 45.000 cycles, which is close to the end of the second stage. The fatigue damage in stage 2 did not only consist of transverse cracks, but also of meta-delamination. Up to 45000 cycles, the amplitude of the AE events did not show a significantly different value. Most of the

amplitudes are still between 45 and 50 dB. As the meta-delamination process consists of fiber-matrix debonds and matrix cracks that are also present with a transverse crack but in different direction, the AE waveform of the meta-delamination process can be similar to the AE waveform of the transverse crack. Few AE events have the amplitude higher than 60 dB. These events might result from the few premature fiber failures.
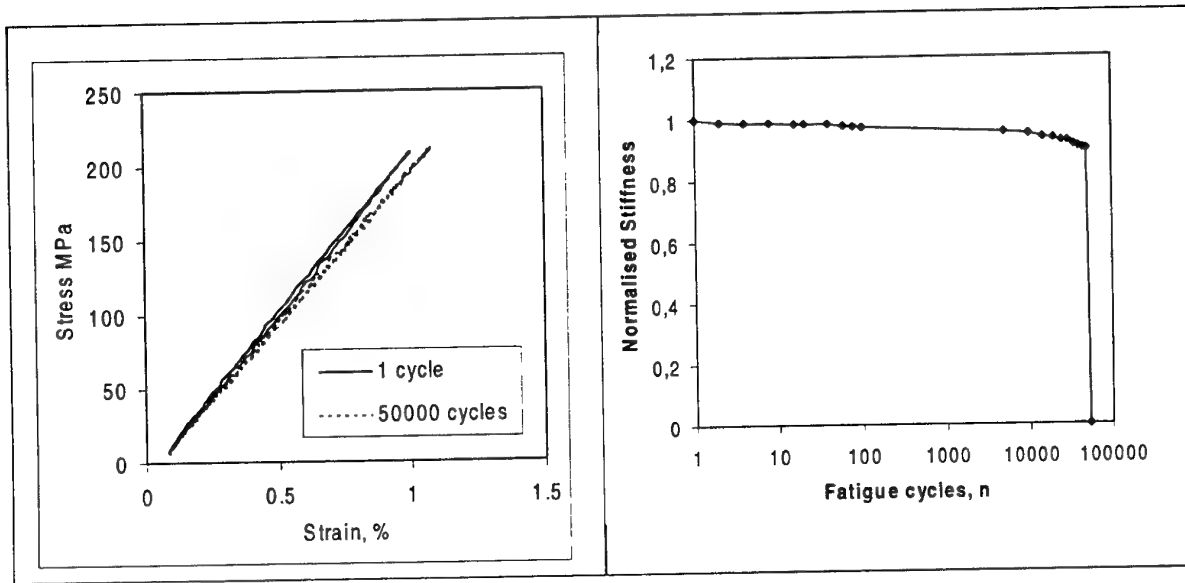

Figure 3. Fatigue profile at the fatigue load S_{max} of 0.5

However, the growth of the AE event rate stabilises after all transverse bundles are damaged by transverse cracks and meta-delaminations. This condition is defined as the third stage. Some events are still detected, resulting from either the propagation of transverse cracks into the matrix area or friction phenomena occurring at the meta-delaminations. However, the accumulative events in this stage are much lower than the accumulative events in the second stage.
The last stage is the final failure that takes place locally and is indicated by a heavily increasing amount of AE events. The final failure is dominated by fiber fractures. The AE amplitudes associated with fiber fracture are higher than 60 dB.

At the maximum fatigue load ratio S_{max} of 0.7 σ_{uts}, the fatigue damage development stages are not well separated. At this fatigue load, the fatigue damage only consists of the initial damage stage (transverse cracks and meta-delaminations) and fiber failure respectively. A correlation between the mechanical properties, such as residual stiffness, and damage content (figured by the AE events), was also investigated.

3. CONCLUSIONS

The combination of acoustic emission and SEM was used to analyse tensile fatigue damage development in woven fabric composites. For a global analysis, this combination of techniques is better than using for instance only X-radiography[3] for visualisation of damage. The geometry of transverse cracks is not linear in the fatigued woven fabric composites and they are difficult to be filled by liquid penetrants. Interpretation of AE results is however not straightforward, which can be a drawback of this technique.

At the fatigue load S_{max} of 0.5, the fatigue damage development was observed in 4 stages. In the first stage, AE events were not detected up to 12.000 cycles when the second stage starts. Transverse cracks and meta-delamination were observed in the second stage. The third is a transition stage in between the initial damage and the final failure. The final failure was terminated by fiber fractures. However, at the fatigue load S_{max} of 0.7, the fatigue damage development is more continuous or can therefore not be classified into any stages
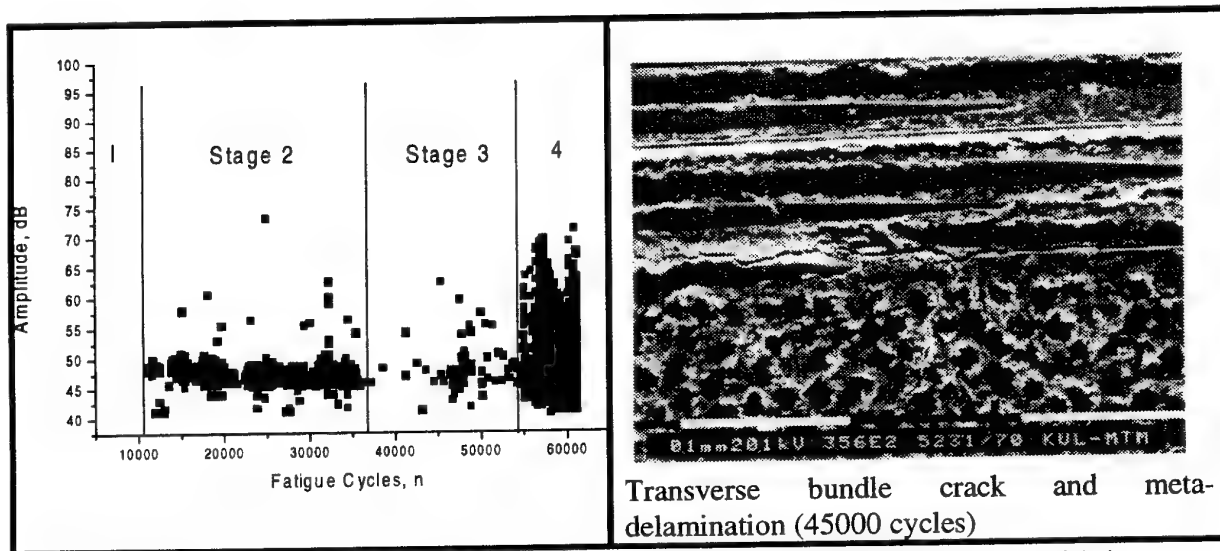

Transverse bundle crack and meta-delamination (45000 cycles)

Figure 4. Accumulative AE amplitude and fatigue damage (SEM) of a woven fabric composite, subjected to a maximum fatigue loads S_{max} of 0.5 σ_{uts}

ACKNOWLEDGEMENTS

REFERENCES

1.   Naik, R.A., "Failure Analysis of Woven and Braided Fabric Reinforced Composites", *Journal of Composite Materials*, Vol. 29, No. 17, 1995, pp. 2334-2363.

2.   Vandeurzen, P., "Structrure-Performance Modelling of Two Dimensional woven Fabric composites", *Doctoral Thesis*, Katholieke Universiteit Leuven, Belgium 1998.

3.   Fujii, T., Amijima, S., Okubo K,. "Microscopic Fatigue Processes in Plain Weave Glass Fiber Composites", *Composites Science and Technology*, vol. 49, 1993, pp. 327-333.

STUDY OF THE EFFECT OF FIBER ORIENTATION ON THE NONLINEAR VISCOELASTIC BEHAVIOUR OF CONTINUOUS FIBER POLYMER COMPOSITES

S.P. Zaoutsos, G.C. Papanicolaou

Composite Materials Group
Department of Mechanical and Aeronautical Engineering
University of Patras, 265 00 Patras, Greece

Polymers and Polymeric Matrix Composites (PMC's), meet plenty of engineering needs as structural parts in a variety of applications of crucial importance. Their excellent mechanical properties together with advantages as lightweight and resistance to corrosion necessitate the use of this class of materials. However, an important feature of these materials is the time dependency of their mechanical response. This behaviour becomes highly nonlinear with the application of specific loading conditions.

The current work is an attempt for studying and modeling the effect of fiber orientation on the nonlinear time dependent response of a carbon/epoxy composite. Schapery's[1] modified nonlinear viscoelastic/viscoplastic model[2] is used for the description of the nonlinearity[3] occurring in the viscoelastic response of a unidirectional carbon/epoxy composite.

Assuming uniaxial and isothermal conditions, the nonlinear viscoelastic response can be accurately described, as:

$$\varepsilon(t) = g_0 D_0 \sigma_0 + g_1 \int \Delta D(\psi - \psi') \frac{d(g_2 \sigma_0)}{d\tau} d\tau + \varepsilon_{vp}(t)$$

where D_o and $\Delta D(\psi)$ are the instantaneous and transient components of creep compliance, while ψ and ψ' is the so-called *"reduced times"* defined by :

$$\psi = \int_{0^-}^{t} \frac{dt'}{\alpha_\sigma} \qquad \text{and} \qquad \psi' = \psi(\tau) = \int_{0^-}^{\tau} \frac{dt'}{\alpha_\sigma}$$

and g_0, g_1, g_2, α_σ are stress and temperature dependent nonlinear parameters.
The additional term $\varepsilon_{vp}(t)$, accounts for the viscoplastic strain which is developed during the creep test.

Using an appropriate data reduction method, developed by the authors[4], the estimation of the nonlinear parameters can be easily performed from data resulting from creep/recovery tests at different applied stress levels[5]. Each of the factors is modeled using the following generic function:

$$G_i = \begin{cases} 1 & \text{for } \sigma \rangle \sigma_c \\[2em] \dfrac{1 - K_i}{1 + \dfrac{\sigma - \sigma_c}{\sigma_u - \sigma} e^{\left(\frac{\sigma - \sigma_c}{\sigma_u - \sigma}\right)}} + K_i & \text{for } \sigma \langle \sigma_c \end{cases}$$

where G_i stands for g_0, g_1, g_2 and a_σ, σ_u is the ultimate tensile stress, σ_c is the critical stress from linear to nonlinear transition and K_i is the maximum G_i value when the applied stress tends to the σ_u value. It has to be noted that the K_i parameters included in (4), have different values, depending on the G_i parameter of interest.

The model has been already tested for the case of 90° degrees fiber angle and an extension is performed for the case of fiber angles other than 90° degrees. In that case the model is transformed to the following form :

$$G_{i\theta} = \begin{cases} 1 & \text{for } \sigma \rangle \sigma_{c\theta} \\[2em] \dfrac{1 - K_{i\theta}}{1 + \dfrac{\sigma - \sigma_{c\theta}}{\sigma_{u\theta} - \sigma} e^{\left(\frac{\sigma - \sigma_{c\theta}}{\sigma_{u\theta} - \sigma}\right)}} + K_{i\theta} & \text{for } \sigma \langle \sigma_{c\theta} \end{cases}$$

The experimental program performed for the verification of the model consisted of creep and recovery tests under different stress levels in specimens at different fiber angle orientation. The composite system used in the test was a carbon/epoxy, provided by FIBREDUX-920-TS-5-42 prepregs from CIBA-GEIGY. The manufacturing of the specimens was conducted in the Department of Structures and Applied Mechanics of the Free University of Brussels (VUB) while the experiments performed in the National Technical University of Athens in the Laboratory of Strength of Materials.

Static tests were conducted for the estimation of the ultimate tensile stress $\sigma_{u\theta}$ in five specimens at each fiber angle. Experimental values of the ultimate tensile stress $\sigma_{u\theta}$ as a function of the fiber angle are shown in Figure-1. The loading mode applied for the viscoelastic characterization of the current composite system, was a simple tensile loading mode, consisted of an initial applied tensile loading, followed by an 8 hours constant stress level, σ_0, and an 8 hours recovery.

In this way, five different stress levels σ_0 corresponding to 30%, 40%, 50%, 60% and 70% of the ultimate tensile stress σ_u were applied for a series of specimens at 75° and 60° fiber angles. A typical creep - recovery response of the carbon epoxy tested at the applied stress levels is shown in Figure-2. The results are also compared with experiments in specimens at 90° fiber angle.

The estimation of the nonlinear parameters shows a dependency from the fiber angle. Predictions of the nonlinear parameter g_1 as a function of stress is shown in Figure-3. The proposed model predicts well this influence and can be accurately used in the case of off axis loading. All the parameters included in the model have a clear physical meaning and they are fiber angle dependent.
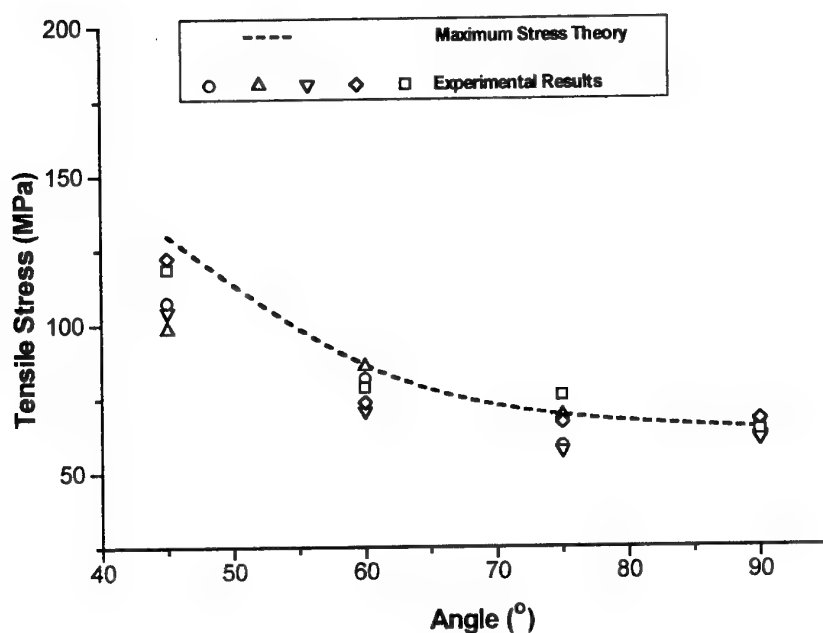

Figure 1.Values of the ultimate tensile strength as a function of the fiber angle.
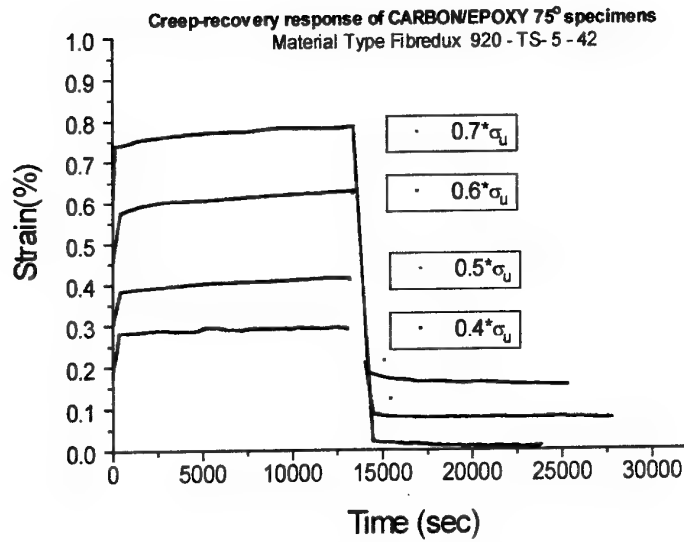
Figure 2. Typical creep and creep-recovery response of the 75° carbon/epoxy system at different stress levels applied.
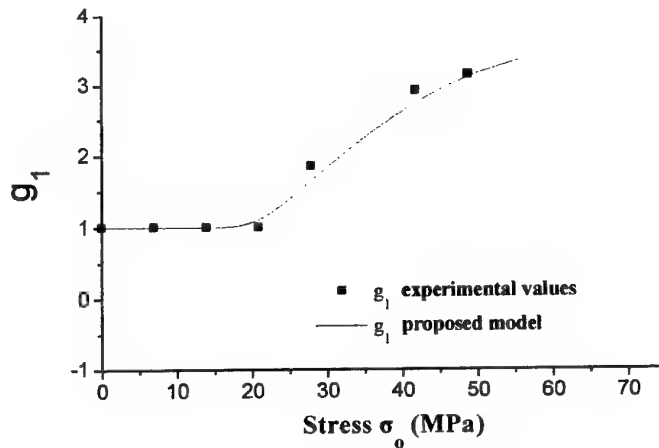
Figure 3. Comparison between predicted and experimental values of the nonlinear factor g_1 as a function of the applied stress at different fiber angles.

[1] Schapery R. A., "On the Characterization of Nonlinear Viscoelastic Materials", Polymer Engineering and Science, 9, (4), pp.295-310, 1969.

[2] Zaoutsos S.P. & Papanicolaou G.C., Cardon A.H., "On the Nonlinear Viscoelastic Behavior of Polymer Matrix Composites", Composites Science and Technology, 58, (6), pp. 883-886, 1998.

[3] Fidley, W. N., Lai J.K., & Onaran K., "Creep and Relaxation of Nonlinear Viscoelastic Materials", Dover Publications, New York, 1976.

[4] Papanicolaou G.C., Zaoutsos S.P., & Cardon A.H, "Further Development of a Data Reduction Method for the Nonlinear Viscoelastic Characterization of FRP's", Composites Part A : Applied Science and Manufacturing, 30, (7), 839-848, 1999.

[5].Papanicolaou G.C,.Zaoutsos S.P & Cardon A.H, "Prediction of the Non-Linear Viscoelastic Behaviour of Polymer Matrix Composites" Composites Science and Technology, Volume 59, Issue 9, pp.1311-1319, 1999.

DAMAGE MODELLING OF COMPOSITE STRUCTURES VISCOELASTIC EFFECTS

M.CHAFRA, Y. CHEVALIER
Institut Supérieur des matériaux et de la construction Mécanique (ISMCM) - LISMMA-Rhéology and Structure Group- 3 Rue Fernand Hainaut- F- 93407 SAINT-OUEN CEDEX

Fibres orientation create directional effects in composite materials. This anisotropic behaviour generates difficulties towards mechanical behaviour modelling : some orientation are more sensitive to strain fracture and failure. This sensitivity depends on the kind of solicitation [CHE 98]. This approach is a tridimensional modelling used to study advanced fabric composite materials including damage and viscoelasticity. The model takes into account the features of loading (type and direction), and the mechanical behaviour of the composite (linear or non linear). An increment procedure on stress and strain permits step by step computations for any type of loading which is also expressed as increments. Concerning the coupling between damage and viscoelasticity a new description of degradation in composite is proposed. The type of loading and the structural anisotropy of the material are also taken into account and we bring in a damage oriented parameter which depends on the strain velocity with the framework of linear behaviour . We suggest a model able to identify mechanical properties in various direction by using isostrain quadratic surfaces [CHA 95]. For non-linear behaviour the loading process is spliced up into increments and each loading increment is analysed as a linear case with tangent viscoelastic properties. An identification procedure has been performed on Carbon/PMR15 fabric composites [AUS 97]. The coupling between viscoelastic behaviour and damage is dominating in off axes loads: The effect of strain velocity is important.
In conclusion the dynamic approach of damage must be taken into account in organic composite material.

REFERENCES

[CHE 98] Y. CHEVALIER. M.LOUZAR, M.CHAFRA. G.A MAUGIN
Damage modelling of composite structures : Static and dynamic approach
Progress in durability analysis of composite systems in K.Reifsnider. D.Dillard and A.Cardon. (ed). A.A.Balkema/Rotterdam/Brookfield/ 1998.

[CHA 95] M.CHAFRA. A.BALTOV, T.VINH - Tridimensional modelling of composite materials damage and failure - Actes EUROMECH 334. Lyon. pp154-163-1995.

[AUS 97] E.AUSSEDAT-YAHIA Comportement et endommagement du composite tissé Carbone/PMR15 soumis à des chargements mécaniques et thermiques. Thèse de Doctorat. Ecole Nationale Superieure des Mines de Paris 1997.

ULTIMATE BEARING CAPACITY OF CEMENT COMPOSITE SECTIONS UNDER LONG TERM PHYSICO-CHEMICAL EXPOSURE

TOMASZ BŁASZCZYŃSKI
Poznań University of Technology

Summary

Bearing capacity of transverse concrete composite sections subjected to bending and eccentric compression with relation to oil influence is evaluated. Two oil conditions are considered: nonoiled (dry) and oiled after 12 months of influencing. Ultimate bearing capacity of reinforced sections influenced by crude oil products is defined numerically by the limit state interaction diagrams. The analysis is carried out for rectangular section with tension and compression reinforcement. In the case of oiled condition bearing capacity of a section decreases up to 50%, when compared with the nonoiled state.

1. INTRODUCTION

The RC sections bearing capacity is presented in many papers. In most cases it concerns an analysis of bearing capacity without taking into account the service conditions of the element. Properties of concrete, such as strength and deformability depend on various environmental influence, e.g. temperature, humidity or aggressive agents. The bearing capacity of RC sections therefore depends not only on the strength and deformation parameters of concrete, but is also influenced by environmental factors.

The article presents an evaluation of crude oil products like mineral oils influence on bearing capacity of RC sections subjected to bending or compression with bending. This main issue is solved using limit state interaction diagrams for the sections. Interaction diagrams have been established for oiled and nonoiled state of concrete.

2. CRUDE OIL PRODUCTS INFLUENCE ON CONCRETE STRENGTH AND DEFORMABILITY

Long term laboratory experiments have been conducted to assess the changes of physico-mechanical characteristics of oil contaminated concrete. The compressive strength was determined from 100 mm cubes for concrete type B-25 (29,8 MPa) as most commonly used for industrial RC structures in Poland, the average 28 day compressive strength of concrete is shown in brackets. The water-cement ratio was 0,59 and aggregate-cement ratio was 6,70.

Concrete was impregnated with the most commonly used industrial oils of different kinematic viscosities namely turbine oil TU-20 (81 mm^2/s), machine oil M-40 (211 mm^2/s) and hydraulic oil H-70 (383 mm^2/s). These oils have low neutralisation numbers with values between 0,05 and 0,75 mgKOH/g. The oils was first applied to concrete 2 months after casting, subsequently the specimens were examined every 4 or 12 months during total period 72 months. The control specimens (samples) were additionally examined after 28 days and 2 months.

The results clearly show, that as a result of the influence of the oils used , the significant decrease of f_c with oil contamination. Comparison of the influence which the oils had on the compressive strength shows that oils TU-20 and H-70 decrease f_c the most.

Contamination of concrete by hydrocarbons gives an almost new material, which behaves differently. The results of the stress (σ) - strain (ε) relation in dry state and after 12-months of oiling by mineral oil TU-20 for concrete B-25 in function of the longitudinal strains are different. The non-linear behaviour of strength and strain variations depends on the contents of hydrocarbon and its type. It can be noticed that the strain ε_R, corresponding to the maximum stress, is lower for oil saturated concrete then for dry concrete. On the other hand, the maximum limit strain ε_m is correspondingly higher.

3. THE METHOD OF SOLUTION

The influence of mineral oils on the bearing capacity of RC sections was assessed by the limit state interaction diagrams.

The following assumptions were adopted in calculations of the bearing capacity:
– plane sections remain plane,
– strains of tension and compression reinforcement are the same as strains of the surrounding concrete,
– for section under axial compression the concrete compressive strain is limited to ε_R,
– for sections compressed in part, the limit concrete strain is assumed to be ε_m,
– the tensile strength of concrete is neglected,
– the σ-ε relation for concrete follows the Saenz function,
– the σ-ε relation for steel is based on the following formulae
  $\sigma(\varepsilon) = E_a \cdot \varepsilon_a$ for $\varepsilon_a < \varepsilon_o$ and $\sigma(\varepsilon) = f_{ak}$ for $\varepsilon_o \leq \varepsilon_a \leq \varepsilon_k$,

Limit state interaction diagrams for concrete sections have been defined using the equilibrium conditions at limit bearing capacity state.

The (M, N) co-ordinates of the interaction diagram have been defined from equilibrium conditions, taking advantage of Gauss quadratic formula in numerical integration. According to graph showing the strains, appropriate ranges of co-ordinates were adopted for the limit state diagram curves.

The (M, N) co-ordinates were approximated using n-th order polynomial. The order of the polynomial was chosen in such a way, that the discrepancy in the approximation did not exceed 0,1%.

The numerical analysis of the bearing capacity of a section using the limit state interaction diagrams was carried out for nonoiled and contaminated state. In order to compare the influence of oiling on the bearing capacity of RC section, presented in the form of limit state interaction diagram, the discrepancy R_w was introduced between the bearing capacity areas defined for concrete in dry and oiled state.

It follows that,

$$R_w = \frac{r_2 - r_1}{r_1} 100$$
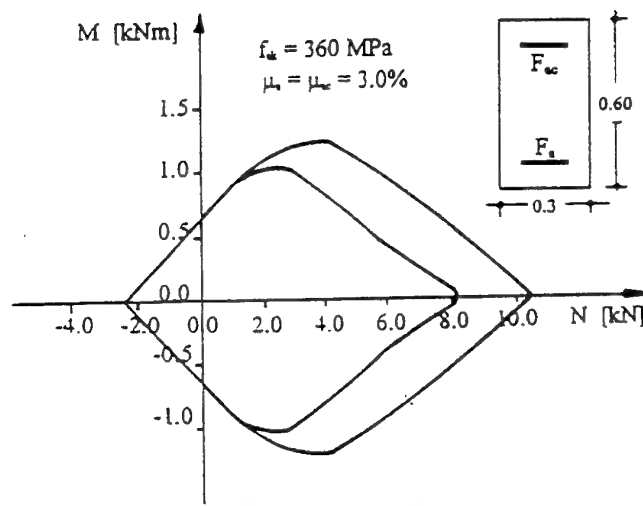
Fig. 1. Limit state interaction diagrams for RC section with symmetrical reinforcement and to extreme cases of oiling in concrete B-25.
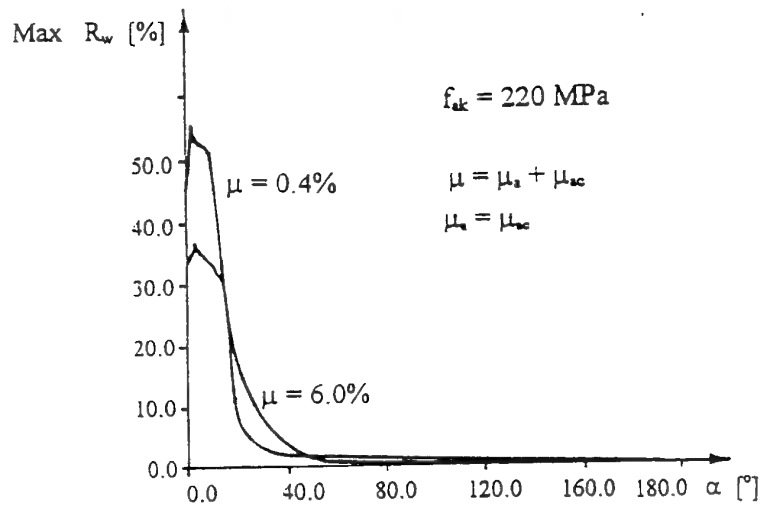

Fig. 2. Discrepancy between the limit state interaction diagrams for section with symmetrical reinforcement of $f_{ak} = 220$ MPa at two extreme percentages of steel area.
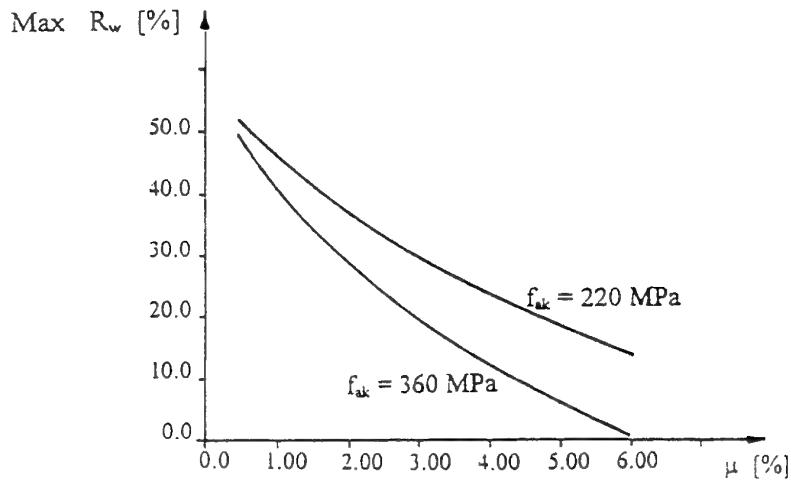

Fig. 3. The maximum discrepancy values in concrete B-25 section with symmetrical reinforcement, subjected to bending as a function of the total reinforcement percentage.

4. NUMERICAL ANALYSIS

The numerical analysis of RC section bearing capacity was carried out for oiled and nonoiled states.

The coefficients of the Saenz function were find by the numerical calculation using APROKS software. In order to find the values of the limit strains ε_m, the ratio $\varepsilon_R/\varepsilon_m$ was taken to be 0,75 for nonoiled concrete and 0,5 for oiled concrete according to.

Therefore:

– for oiled B-25 concrete (after 12 months of oiling)

$$\varepsilon_m = \frac{\varepsilon_R}{0,9} = \frac{0,00161}{0,5} = 0,00322$$

– for nonoiled B-25 concrete (in the same age)

$$\varepsilon_m = \frac{\varepsilon_R}{0,9} = \frac{0,00277}{0,75} = 0,003692$$

Rectangular concrete section with tension and compression reinforcement was examined by numerical analysis. The analysis was carried out for two extreme values of total reinforcement percentage ($\mu_{max} = 6\%$, $\mu_{min} = 0,4\%$) and for two classes of reinforcing steel ($f_{ak} = 220$ and 360 MPa).

An example diagram of the limit state interaction curves for both states is shown in fig. 1. This figure refers to the section with steel of $f_{ak} = 360$ MPa and a maximum percentage of reinforcement.

The distribution of discrepancy R_w (in function of angle α) between the areas of bearing capacity of oiled and nonoiled states, for steel with $f_{ak} = 220$ MPa and two extreme percentages of reinforcement is presented in fig. 2. Angle $\alpha = 0°$ refers to axial compression, $\alpha = 90°$ refers to bending and $\alpha = 180°$ refers to an axial tension of the section.

In fig. 3. the discrepancy R_w is shown as a function of the total percentage of reinforcement in the section subjected to bending ($\alpha = 90°$) with symmetrical tension and compression reinforcement.

5. CONCLUSIONS

As the presented numerical analysis proves, the limit state interaction diagrams are determined by oiling in concrete. The loss of bearing capacity of RC section using concrete in mineral oil environment extends up to 50%, for high contribution of shear force and the lower percentage of reinforcement. The discrepancy rises also with the lowering of steel strength.

Important lowering of bearing capacity of RC oiled sections points to the necessity of taking this fact into account in the design and asses process.

DAMAGE IDENTIFICATION OF COMPOSITE MATERIAL DURING STRESS RUPTURE USING ACOUSTIC EMISSION TECHNIQUE

Prof. A. Rotem

Faculty of mechanical engineering

Technion IIT, Haifa, ISRAEL

ABSTRUCT

Composite material laminates, fabricated 19 years ago were used in this research, to find aging influences. The material was T300/5208 carbon fibers in an epoxy matrix. Rectangular specimens in the dimensions of 220X12.7 mm and nominal thickness of 1.1 mm were cut from various types of laminates. A lever type creep apparatus with a dead load, was build for performing the rupture tests. A single channel Acoustic Emission system, was used to detect the emitted elastic waves. A transducer was attached to the free surface of the specimen and the signal was amplified by a factor of 10^5. The AE signals were fed in parallel to a totalizer and a Pulse Height Distribution Analyzer. The load was applied by weights and the creep was measured by LVDT. All these information was then logged to a dedicated computer. Specimens were cut from uniaxial and $\pm45°$ angle ply laminates. Perpendicular slits were added to the uniaxial specimen (0°) in order to use it as a shear specimen. The uniaxial specimens represent pure axial shear behavior and the $\pm45°$ specimen represent shear mechanism with the addition of interlaminar shear.

The AE and creep history of the two types of specimens are shown in the following figures, as well as the PHA. The TAE almost pace the creep history, with accelerated activity towards the rupture, thus can serve as a durability sensor. The PHA is different for each specimen type, with linear behavior but different slope for the 0° and the $\pm45°$. The PHA is typical for each kind of specimen and shows the same characteristic, regardless where in the load history the AE was taken. Therefore, the relation between

high and low energy elastic waves which emits from the degradation process of the material, is typical for the kind of the stress field in the specific laminae.

It was found that aging does not play a significant roll in the strength and the AE behavior. In fact, by comparison with data that was taken 16 years ago from testing of the same material, no difference was noticed as shown in the figure (17) below [1]. Also It was found that AE activity increases toward the end of the creep life, and can serve as a detector to material failure. It was also found that the AE signature by the PHA is different for the different stress component and can determine the mode of failure in a more complex laminate configuration.

Reference

1. A. Rotem, "Fracture modes identification of composite materials by A.E. analysis", Composite Technology Review, Vol. 6, No. 4, Dec. 1984, pp. 145-158.
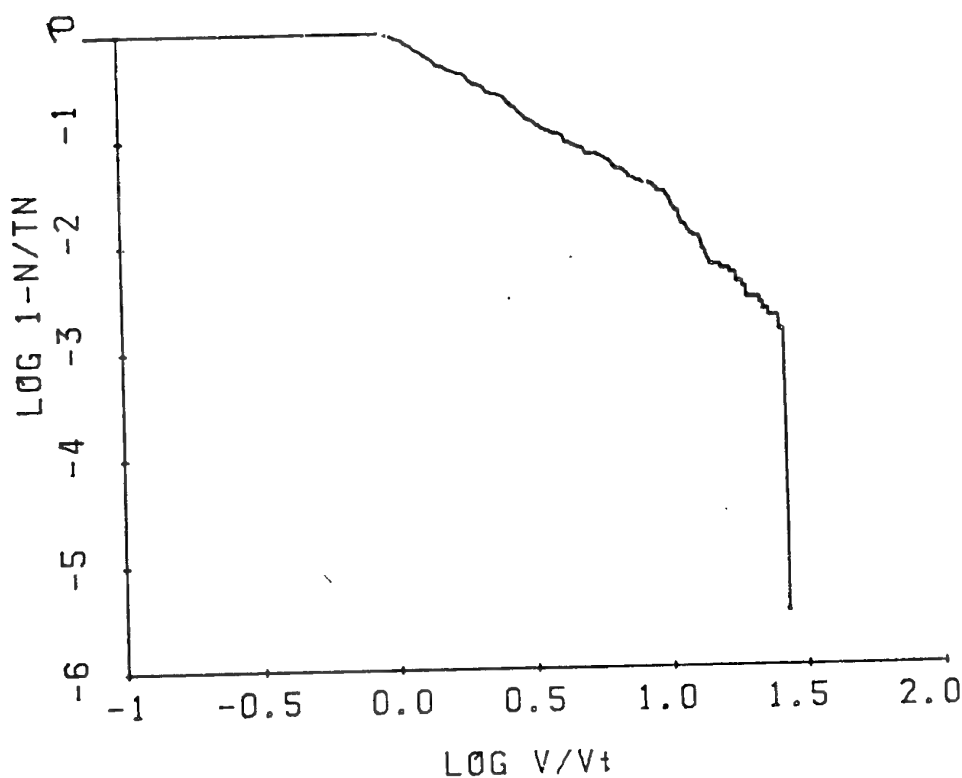
FIG.17 GRE+-45 W DEF 30% FL
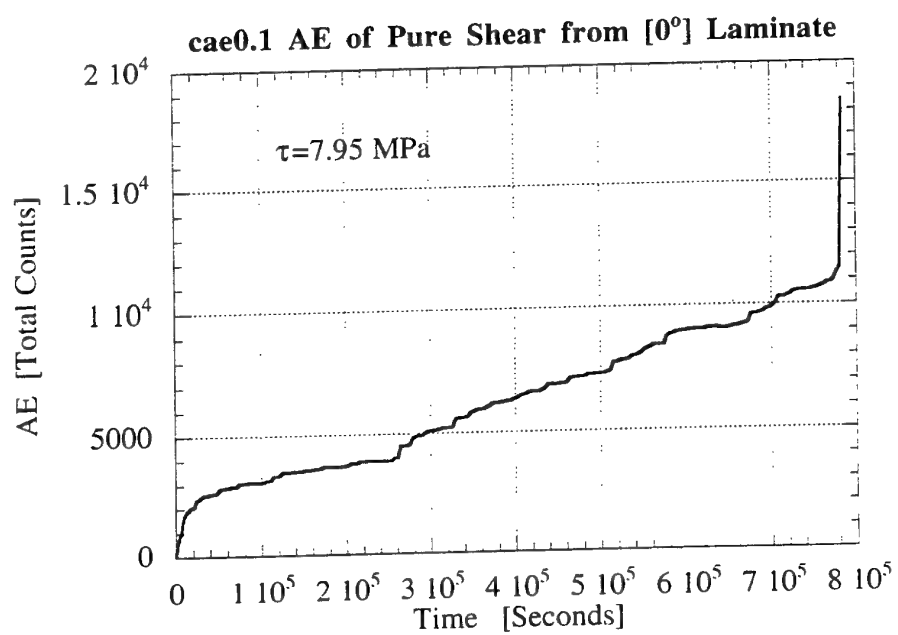
caes0.1b Pulse Height Slope of Shear on 0°

B=-0.92851

Log (1-n/N)

Log (h/H)

cae0.1 AE of Pure Shear from [0°] Laminate

τ=7.95 MPa

AE [Total Counts]

Time [Seconds]

cae45 Creep and AE of ±45° Laminate

caes45c0 PHA Slope of ±45° laminate
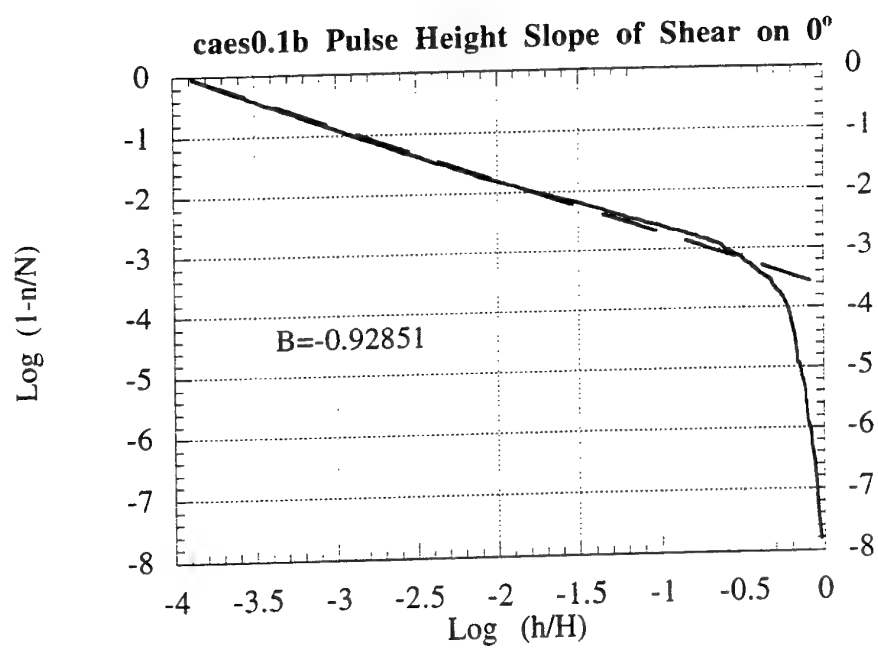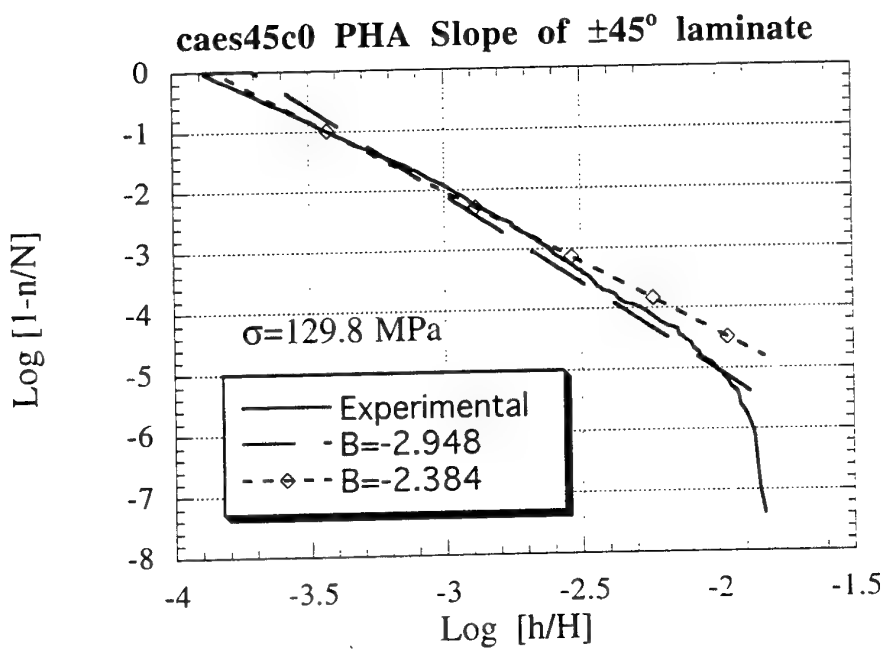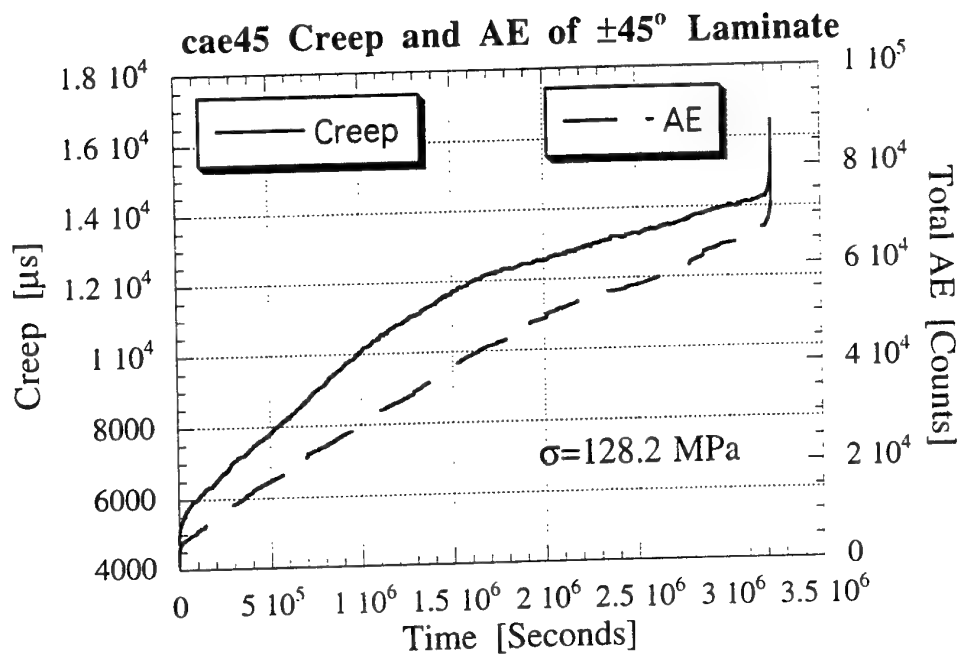
The Influence of Moisture on the Physical Aging Response of Epoxy: Experimental Results and Modeling Considerations

W.H. Han
Polymers Division, NIST, Gaithersburg, MD, USA

G.B. McKenna
Polymers Division, NIST, Gaithersburg, MD, USA

ABSTRACT: We have investigated the hygrothermal effects in thin epoxy films (c.a. 50 μm thick) using mass uptake, swelling, and uniaxial creep compliance measurements inside a dew formation-free transparent chamber capable of arbitrary relative humidity and temperature controls. We show that the physical aging behavior in humidity down-jumps is equivalent to temperature down-jumps such that the time-aging time superposition principle holds for both cases. Furthermore, we demonstrate that moisture-jump experiments exhibit memory and asymmetry of approach similar to those found in temperature-jump experiments. A modified form of the TNM-KAHR model of structural recovery is proposed to account for the observations.

1. INTRODUCTION

In previous work [1] we presented evidence that a relative humidity jump experiment results in mechanical responses that are similar to those obtained in temperature jumps. Hence, we were able to make the argument that the models of structural recovery or physical aging that govern a glass forming material's viscoelastic responses should be able to extend to moisture effects as well. In the following paragraphs we briefly review that work and present new experimental results that further substantiate those observations. We also summarize the TNM-KAHR [2-5] models and present an extension of the models that we propose to account for the humidity induced structural recovery or physical aging response. We present preliminary results needed to obtain the TNM-KAHR material parameters for moisture induced structural recovery.

2. HUMIDITY-TEMPERATURE "EQUIVALENCE"

Conceptually it is possible to think that changes in the moisture content of a glassy polymer have much in common with changes in temperature because of the well known effect of moisture as a plasticizer [6]. Because water depresses the glass transition temperature, one could imagine that an isothermal change in moisture content could be treated as a change in temperature, i.e., a change in the distance from the glass transition temperature T_g.

Previously [1], we showed that a moisture jump experiment in an epoxy material produced results similar to a temperature jump experiment to the same final conditions. Figure 1 shows the comparison of the aging time shift factors a_{t_e} vs aging time t_e after a humidity or temperature jump to the same final temperature and humidity conditions. Clearly, the responses are similar. The interpretation of such behavior is given schematically in Figure 2 where we depict a 3-dimensional Volume-Temperature-Humidity surface. If the mobility of the material depends on the volume, then, performing a RH-jump from above the RH-induced glass transition H_g to below it is equivalent to performing a temperature-jump from above to below T_g.

3. EXTENDED TNM-KAHR MODEL

The temperature history dependence of the relaxation response in glassy materials is often analyzed in terms of the so-called TNM-KAHR [2-5] model of structural recovery. The time evolution of the departure δ from

$$\delta(z) = -\Delta\alpha \int_0^z R(z-z')\frac{dT}{d'z}d'z$$

$$\text{where}$$

$$z = \int_0^t \frac{d\xi}{a_T\, a_\delta}$$

the equilibrium volume is written in the form of a convolution integral:

and a_T and a_δ are shift factors for temperature T and departure from equilibrium δ. The departure from equilibrium is defined as $\delta=(v-v_\infty)/v_\infty$ where v and v_∞ (or v_{liq}) are the volume at time t and in equilibrium, respectively, for a given temperature T. $\Delta\alpha$ is the change in the coefficient of thermal expansion upon traversing the glass transition temperature. $R(t)$ is a viscoelastic response function for the structural recovery and z is the reduced time. Similar equations can be written for the enthalpy as well, but we limit ourselves here to the volume formulation. We add that the concept of physical aging [7] results in the viscoelastic response (creep or relaxation) times shifting with the same a_T and a_δ shift factors as the structure. The shift factors have been represented by

$$\frac{\tau_i(T,\delta)}{\tau_{i,r}} = a_T \, a_\delta = e^{-\theta(T-T_r)} \; e^{\frac{(1-x)\theta\,\delta}{\Delta\alpha}}$$

[2]:
where the first exponential term is a_T and the second is a_δ. $\tau_i(T,\delta)$ is the relaxation time at the relevant values of temperature and structure and the $\tau_{i,r}$ refers to the relaxation time at the reference state, generally taken for $T_r=T_g$ and $\delta=0$. The parameter x is a partition parameter $(0\leq x\leq 1)$ that determines the relative importance of temperature and structure on the relaxation times. The parameter θ is a material constant that characterizes the temperature dependence of the relaxation times in equilibrium. KAHR used $\theta\approx E_a/RT_g^2$ where E_a is an activation energy and R is the gas constant.

In the case of the temperature-jump experiment, the parameters to be determined are x, θ (or E_a), $R(t)$ and $\Delta\alpha$. This can be a non-trivial task, though procedures for parameter estimation have been developed [8,9]. To extend this sort of formalism to the case of the humidity-jump experiment, we assume that the effects of volume and moisture are additive and, then,

$$\delta(z) = \int_0^z d'z \, [\Delta\alpha_T \, R_T(z-z') \frac{dT}{d'z} +$$
$$+ \Delta\alpha_h R_h(z-z') \frac{dh}{d'z}]$$
$$where \quad z = \int_0^t \frac{d\xi}{a_T \, a_\delta \, a_h}$$

equation 1 can be modified as follows:
and the aging problem now requires not only the temperature factors to be obtained but also appropriate parameters for the humidity terms. The reduced time now includes a shift factor a_h due to the changing moisture in the material.

To first approximation, one would anticipate that $R_T(t)=R_h(t)$ and the mechanical test data leading to Figure 1 support this contention [1]. The shift factors a_T and a_h can be obtained by performing isothermal and constant humidity experiments, as appropriate. The determination of a_δ requires implementation of procedures similar to those used in temperature experiments [8,9]. The value of the change of volume with humidity $\Delta\alpha_h$ at H_g is more problematic, as will be seen in the results section. However, the formalism offers the possibility of describing the change of the relaxation response of a material when both temperature and humidity are changed. In the following we present data typical of that required to determine the function $\Delta\alpha_h$. We also present further results from RH-jump experiments that justify the continued examination of equation 3 to describe moisture induced aging effects.

4. EXPERIMENTAL [10]

4.1 Materials

Diglycidyl ether of bisphenol A(DGEBA, DER 332, Dow Chemical, USA) epoxide monomer was mixed with a curing agent, amine terminated poly(propylene oxide) (Jeffamine, T403, designation of Texaco Chemical Company) in a stoichiometric ratio. The mixture was degassed for 20 min at 23 °C, then cast into smooth TEFLON molds with dimensions 6 mm X 0.06 mm X 210 mm. To prevent bubble formation, thin samples were cured at high pressure (2MPa) and at temperature of 100 °C for 16 hours. The samples were then slowly cooled overnight. The glass transition temperature of this material measured by standard DSC is 72.3 °C [11].

4.2 Moisture Uptake Measurements

The in-situ moisture uptake measurements were done in a double layer transparent hygrothermal chamber built in this laboratory [1]. The temperature of the mixture of air and moisture inside the hygrothermal chamber is controlled within ± 0.1 °C. The humidity was controlled to within ± 0.5 % relative humidity (RH). In-situ measurements of weight changes of the epoxy films were carried out using cathetometers and quartz springs which allow us to detect ± 1 µg changes. Volume change was monitored by using a thin epoxy strip which was hung freely. To this was attached a tiny magnetic core for a hermetically sealed LVDT, the voltages from which were read via a PC. The expanded uncertainty in the measurements of the relative volume change is estimated to be 1.25x10⁻⁵ based on sample geometry and the response characteristics of the LVDT [1].

4.3 Creep Measurements

Subsequent to a humidity or temperature change, aging experiments were performed following Struik's protocol [7]. The thin films were loaded in a miniature tensile machine maintained at the same temperature for creep compliance tests at different aging times. The apparatus uses linear differential transformers (LVDTs) (Schaevitz Inc.) connected to a microprocessor based signal conditioner (MP/2000, Schaevitz Inc.) and sets of weights which can be loaded and unloaded by a geared lift powered by a high humidity temperature resistant D.C. motor (Motor Technology Inc). An AD/DA converter card installed in an IBM PC receives the creep compliance voltages from the LVDT conditioners, and send out signals to a motor controller for the motor operation. Repeat experiments provide an estimated expanded uncertainty in the measurements of approximately 5 % of the measured load. The uncertainty of a single set of aging experiments is considerably less than this.

5. RESULTS

5.1 Coefficients of Thermal and Moisture Expansion

At a constant cooling rate of 0.1 °C/min. the length changes of the thin epoxy strips were measured in constant humidity conditions. Similarly, isothermal measurements were performed by reducing the RH at a rate of 0.02/min. From the sample strip length data, assuming isotropic dimensional change, we directly calculate the corresponding volume change. In independent experiments of mass uptake, the diffusivity of the epoxy sample was experimentally measured to be approximately $1.6 \times 10^{-8} cm^2/s$ using the Fickian diffusion equation [12] for the lowest temperature (T=45 °C). For this value of diffusivity and the sample thickness (60 µm), the diffusion half time is less than 2 min. which is significantly shorter than the experimental time scale. Figures 3a and 3b depict the volume-temperature response of the epoxy at different relative humidities and the volume-RH response at different temperatures, respectively. Clearly the T_g decreases with decreasing RH, however, the behavior of the volume as a function of RH does not lead to a clear definition of a humidity induced glass transition H_g. Hence, while it is possible to determine $\Delta \alpha_T$ for input into equation 3, the value of $\Delta \alpha_H$ is less clearly ascertained from the data. Figure 4 indicates this to be the case. In 4a we plot the value of the coefficient of thermal expansion from the constant Clearly, the behavior seen in humidity-jump and temperature-jump experiments is similar in nature. The plasticizing effect of the moisture in the sample leads to a depression of the glass transition. Then, in an isothermal experiment, a change in moisture content (induced by a change in RH) is the equivalent

humidity experiments both above and below T_g. It can be seen that the difference $\Delta \alpha_T$ between the glassy and liquid values is constant within the experimental error. Fitting polynomials to the low humidity and high humidity data of Figure 3b provides a means to estimate $\Delta \alpha_H$. The result of such a treatment for the estimated behavior of $\Delta \alpha_H$ is shown in Figure 4b where it is clear that the isothermal values of $\Delta \alpha_H$ are functions of both temperature and humidity.

5.2 Asymmetry of Approach Experiments

One other point to be made here arises from volumetric measurements subsequent to RH-jumps. Previously we had shown that the retardation times in RH-jumps followed a similar behavior to temperature-jumps (see Introduction). One of the classic T-jump experiments that show the non-linearity of structural recovery is the so-called asymmetry of approach. Here we illustrate the first asymmetry of approach results from experiments in RH-jump conditions.

In the T-jump experiments of Kovacs [12], the sample was tested in up- and down-jumps to a final temperature T_0. The magnitude of the up and down-jumps was the same and non-linear response was deduced from the observation that the up-and down-jump δ vs log (time) curves were not symmetric about the $\delta=0$ line. For the RH-jump experiments, we take a similar approach, expecting the responses from nearly similar values of ΔRH in magnitude would be mirror images in the up- and down-jump conditions if the response were linear. Figure 6 shows first results from such an experiment in which a sample was equilibrated at RH=0.75, T=65.5 °C and jumped to RH=0.50, T=65.5 °C and the volume recovery followed. Also plotted in the figure is the result for a sample equilibrated at RH=0.28, T=65.5 °C and jumped to RH=0.50, T=65.5 °C. The figure shows clearly that the response in the up-jump experiment is much slower than in the down-jump. This behavior is very similar to what was observed by Kovacs [12] for T-jumps and rationalized by equations 1 and 2. The similar result shown in Figure 6 provides further rationalization for an equation of the sort of equation 3 in which the humidity history has a similar impact on glassy behavior as does the thermal history. Further work will establish the level of reproducibility and uncertainty in such measurements.

6. DISCUSSION

of a change in temperature because the 'distance' from the T_g has been changed. Equation 3 partially quantifies this observation.

At the same time, the formalisms that have been explored for determining the material parameters for

temperature-jump experiments. have not been developed for humidity-jump experiments. Models for changing moisture content and its effect on T_g [6,14,15] do exist. To our knowledge. however, equation 3 has not been previously proposed. That being said. the determination of the moisture or RH parameters in equation 3 that are equivalent to the temperature parameters for equation 1 (given in equation 2) are not so straight-forward. In this work, values of $\Delta\alpha_H$ have been determined. Further work is required to determine how well the other parameters can be obtained from the RH-jump experiments themselves.

7. CONCLUSIONS

An equivalence between humidity-jump and temperature-jump experiments has been demonstrated. Mechanical experiments show that physical aging occurs after RH-jump experiments in a fashion similar to classical T-jump experiments. An equation building on the TNM-KAHR formalism has been proposed to take into account the moisture (RH) history of the sample. Experiments were performed in isothermal conditions to obtain the values of the coefficient of moisture (RH) expansion and its change $\Delta\alpha_H$ at H_g. The current results suggest that $\Delta\alpha_H$ is not a constant and further work is required to implement the model. Finally. the first experiments that exhibit an asymmetry of approach in RH-jump conditions were presented. further justifying continued exploration of the value of extending the TNM-KAHR formalism to plasticizing environments.

8. ACKNOWLEDGEMENTS

9. REFERENCES

1. A) Han. W.H. and McKenna. G.B. (1997) SPE ANTEC. II. 1539. B). Han. W.H. and McKenna. G.B. (1997). Proc. NATAS. **25**. 382.

2. Kovacs. A.J.. Aklonis. J.J..Hutchinson. J.M.. and Ramos. A.R. (1979) Journal of Polymer Science. Polymer Physics Edition. **17**, 1097.

3. Tool. A. Q. (1946) Journal of Research of the National Bureau of Standards (USA) . **37**. 73.

4. Narayanaswamy. O.S.(1971) Journal of the American Ceramic Society. **54**. 491.

5. Moynihan. C.T.. Macedo. P.B. Montrose. C.J.. Gupta. P.K. DeBolt. M.A.. Dill. J.F.. Dom. B.E.. Drake. P.W.. Esteal. A.J.. Elterman. P.B.. Moeller. R.P.. Sasabe. H.. Wilder. J.A. (1976) Annals of the New York Academy of Sciences. **279**. 15.

6. Knauss. W.G. and Kenner. V.H. (1980) J. Appl. Phys.. 51. 5131.

7. Struik LCE (1978) Physical Aging in Amorphous Polymers and Other Materials. Elsevier. Amsterdam.

8. Hodge. I.M. (1994) Journal of Non-Crystalline Solids. **169**. 211.

9. Scherer. G.W. (1986) Relaxation in Glass and Composites. Wiley. New York.

10. Certain commercial materials and equipment are identified in this paper to specify adequately the experimental procedure. In no case does such identification imply recommendation or endorsement by the National Institute of Standards and Technology. nor does it imply necessarily that the product is the best available for the purpose.

11. Lee.A. and McKenna.G.B.(1988) Polymer. **29**. 1812.

12.Vieth. W.R. (1991) Diffusion In and Through Polymers: Principles and Applications. Hanser. New York.

13. Kovacs. A.J. (1963) Fortschritte der Hochpolymeren-Forschung. **3**. 394.

14. McKenna GB (1989) in Comprehensive Polymer Science: Volume 2 Polymer Properties. ed. by C. Booth and C. Price. Pergamon. Press. Oxford. 311-362.

15. Gibbs. J.H. and DiMarzio. E.A. (1958) Journal of Chemical Physics. **28**. 373.
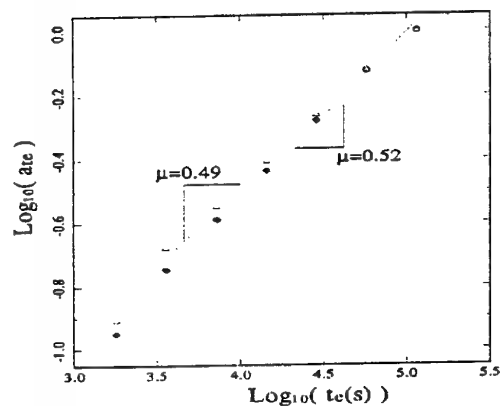
Figure 1. Aging time shift factors vs aging time for an epoxy glass subjected to RH-jump or T-jump conditions. Filled circles are for a RH-jump from RH=0.75 to RH=0.50 at T=68 °C. Open triangles are for T-jump from 85 °C to 68 °C at RH=0.50.
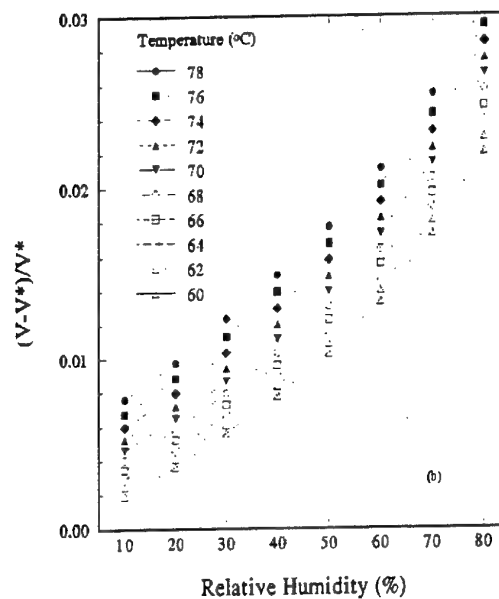
Figure 3. Epoxy-Moisture Effects: **(a)** Relative volume vs Temperature at constant RH. **(b)** Relative volume vs RH at constant temperature. V* is the volume at 55 °C and RH=0.20. (See text for discussion).
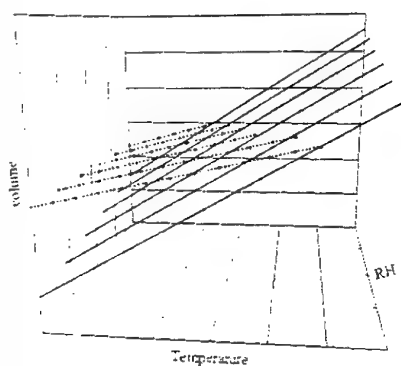
Figure 2. Schematic of Volume-Temperature-RH surfaces for equilibrium and glassy states of a moisture sensitive polymer glass. (See text for discussion).
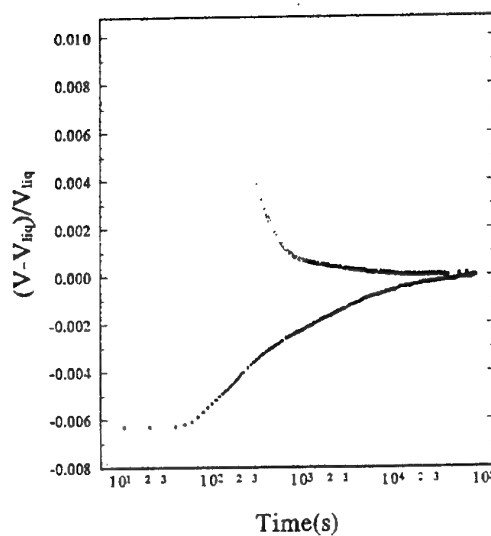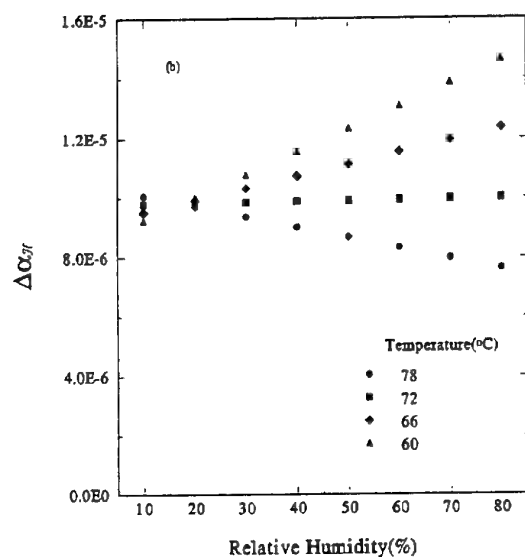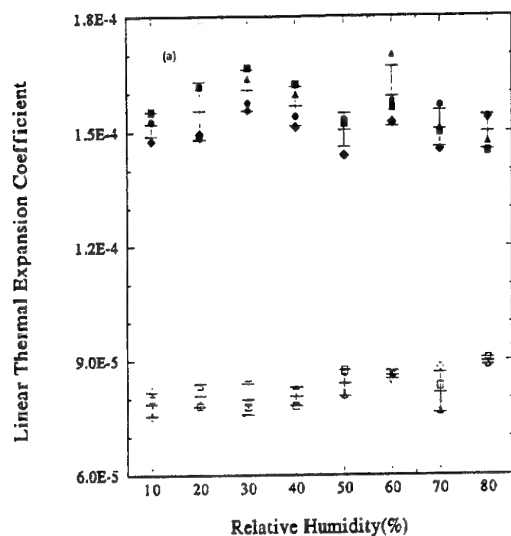
Figure 5. Asymmetry of approach: volume departure from equilibrium vs log time following relative humidity jumps from RH=0.75 to RH=0.50 (upper curve) and from RH=0.28 to RH=0.50 (lower curve) for an epoxy glass at T=65.5 $^{\circ}$C. (See text for discussion).

Figure 4. Expansion coefficients in epoxy: **(a)** Thermal expansion in the glassy (open symbols) and rubbery (filled symbols) states vs RH. Points represent individual experiments. Error bars represent single standard deviation from the repeat experiments. **(b)** Estimates of the parameter $\Delta\alpha_H$ in equation 3 from data of Figure 3b at different temperatures. (See text for discussion.)

Hybrid composites with nonlinear behaviour for forcing of concrete

V. Tamuzs
Institute of Polymer Mechanics, University of Latvia, Riga, Latvia
R. Tepfers
Chalmers University of Technology, Göteborg, Sweden

Up-to-date situation in production, consumption and applications of advanced composites.

Commercial production of advanced fibers for composites started substantially in the early 1970s. At that time various reinforcement fibres were developed, namely boron, carbon from viscose and PAN, aramid, alumina, silica, etc. One of the typical sort of fibers are carbon fiber. Since specific elastic modulus and specific tensile strength of carbon fibres from PAN and mesophase pitch are very high, these fibres have gained an advantageous position as reinforcements of advanced composite materials. For the structural parts of aircraft, spacecraft, F1 cars, yachts, bicycles, tennis rackets, golf clubs, fishing rods, etc. PAN based carbon fibres have gained a majority share. According [1] current world production capacity of carbon fibers in 1993 was about 10,000 tons per year (50% Japan, 30% USA and 15% Europe). Consumption was 6500 tons per year (35% USA, 23% Japan, 20% Europe and 23% the other countries). In 1986 to 87 aeronautic use counted for 42-50% versus sporting goods 40-37%. The world-wide recession and a cutback of military spending in the USA and Europe hit the aircraft industry, resulting in aeronautic use going down to 20% and the share of sporting goods increasing up to 55% in 1993 [1]. In early nineties the application of fiber composites in infrastructure started to uncrease. The main consumption of advanced composites in civil engineering is the repairing and retrofit of old and damaged concrete structures by external reinforcement. It can be estimated [2] that in Japan in late nineties the amount of carbon composites used in concrete industry equaled 300 tons per year. The dynamics of composite amount used in civil engineering in Swiss is given in [3] Fig. 1. Besides of external reinforcement also some attempts have been done to replace the traditional concrete steel bar reinforcement by composite bar reinforcements.

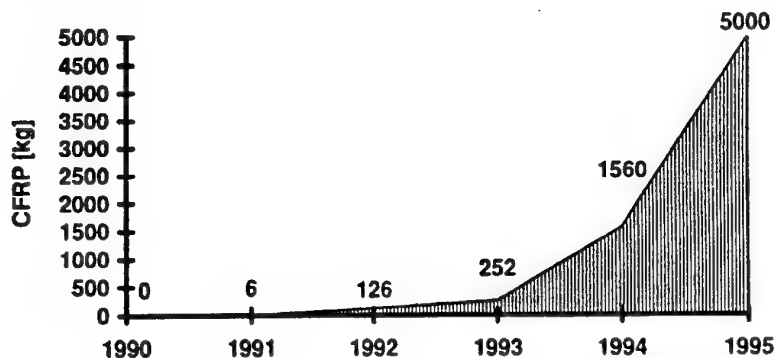Fig. 1. Use of CFRP-Laminates for strengthening purposes in Switzerland Source: Stesalit AG, Zullwil, Switzerland [3].

Composite bars as reinforcement for concrete.

At present some comercial available products can be mentioned: CFCC (Tokyo Rope Carbon Fiber Composite Cable), Arapree - aramid reinforced composite bars, Technora-aramid reinforced bars, unidirectional glass fiber composite rods etc.

The main advantage of composite reinforcement is its resistance to corrosion and consequent durability in contrary to steel. The light weight and transparence to electromagnetic waves also can be desirable in specific cases.

The main disadvantages are the follow:
1. high material price (carbon and aramide)
2. creep (aramide fibers)
3. sensibility to alkaline attack (glass fibers)
4. low ultimate strain (especialy carbon fibers)
5. low modulus (aramide and glass fibers)
6. linear behaviour till the failure without extended plasticity.

Some of these undesirable features can be reduced by using the hybrid composite rods: carbon + glass or carbon + aramide fibers: a) increase of modulus comparably with aramide or glass composite, b) reduction of price comparably with carbon composite rods, c) appearance of nonlinear "ductile" behaviour at high stress level.

Ductility of concrete structures is necessary due to safety requirements to avoid brittle fracture. In traditional steel reinforced concrete structures the ductility is guaranteed by ductile behaviour of cold worked reinforcing steel.
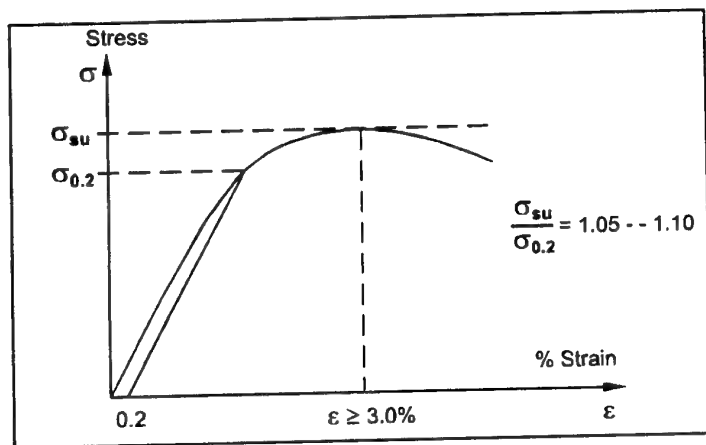
Classical stress strain diagram for steel is shown on Fig. 2. A fictitious yield stress is stipulated as the stress $\sigma_{0.2}$ at which the permanent elongation after removing the load is 0.2%. Further the steel must have a strain at maximum load of at least 3.0%. Moreover there should be a load increase between the $\sigma_{0.2}$ and the stress at maximum load σ_{su}. The relation between

Fig. 2. Stress-strain diagram for cold worked steel.

$\sigma_{su}/\sigma_{0.2}$ should be at least somewhere in between 1.05 and 1.10 according to code requirements in different countries. It is desirable to about reproduce for FRP this stress-strain relationship.

Estimation of modulus and nonlinearity of hybrid composites.

Let us analyze the behaviour of hybrid composite, where two sorts of fibers with different modulus, ultimate elongation and strength properties are mixed.

The initial modulus E_c of hybrid composite with great accuracy can be expressed by simple rule of mixture

$$E_c = E_{Hf}\mu_H + E_{Lf}\mu_L + E_m(1 - \mu_H - \mu_L) \tag{1}$$

where indices H and L denote the high and low modulus fibers, m - matrix and μ_f is the volume fraction of fibers.

Let ultimate deformation $\varepsilon_H < \varepsilon_L$. At $\varepsilon = \varepsilon_H$ the H fibers start to break transferring the load

$$N = \mu_H E_H \varepsilon_H + \mu_L E_L \varepsilon_L$$

to L fibers. It is necessary that stress in L fibers after breaking process of H fibers and nonlinear deformation don't exceeds the ultimate strength of L fibers allowing to load slightly increase (up to 20%) analogicaly as it is in fig. 1 for steel.

Therefore

$$\mu_H E_H \varepsilon_H + \mu_L E_L \varepsilon_L = 0.8 E_L \varepsilon_L \qquad (2)$$

So the desirable volume fraction ratio $\dfrac{\mu_H}{\mu_L}$ depends on the ratio of fiber moduli and fiber

strength:

$$\frac{\mu_H}{\mu_L} = \frac{E_L}{E_H}\left(\frac{0.8\varepsilon_L}{\varepsilon_H} - 1\right) = 0.8\frac{\sigma_L}{\sigma_H} - \frac{E_L}{E_H} \qquad (3)$$

Of course it is very rough estimation and more detailed analysis is based on the statistical model of fiber fragmentation in hybrid composites [4].

The main assumption used in [4] was that hybrid composite has been formed by well mixtured fibers of low and high elongation (high modulus (HM) and low modulus (LM) respectively) Fig. 3. For fracture process prediction it was necessary to know besides of elastic constants the fiber strength statistical distribution for both fibers and their ineffective lengths l_H and l_L. It was assumed, that strength distribution follows the Weibulls rule for both types of fibers. Stress concentration coefficients in fibers around the defects have been calculated in [5] and for particular case referred in [4].
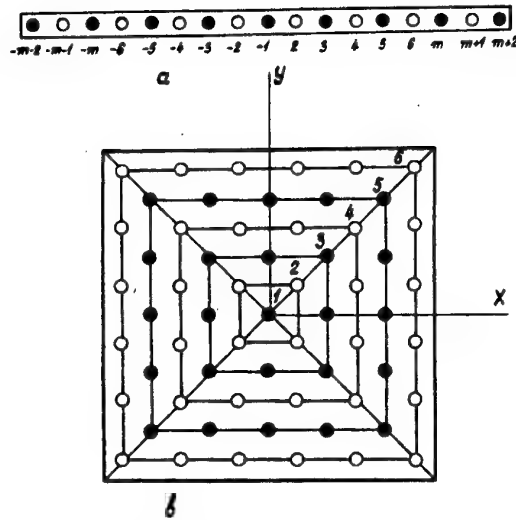
The breaking sequence of HM and LM fibers mixed regularly as shown on Fig. 3. can be very different and depends on strength and stiffness properties of fibers. In [4] the algorithm of the most probable failure sequence seeking was formulated and particular numerical results were obtained. For our aims it is important to note, that the damage level of H fibers obtained in hybrid composite was 20 times more high than the damage level calculated in regular H fibers composite (8.3% and 0.47% respectively). The result obtained quite evident because of different ultimate elongation of fibers in hybrid composite. The ultimate damage level can be even 2-3 times more high depending on the ratio of properties of both fibers. It means that

Fig. 3. Schematic of unidirectional hybrid composite (a) single layer and (b) multilater [4].

in the ideally organized (mixtured) hybrid composite the high modulus fibers will split into fragments with mean length equal approximately 5-10 "ineffective lengths" i.e. 100-500 diameters of fibers. The reducing of modulus because of arosed damage can be calculated by two approaches [6, 7].

The first aproach consists in taking the virgin composite modulus as an initial one and to calculate the reducing of modulus as a result of arising of small cracks in transverse isotropic body [6]. Another possibility consists in taking the matrix modulus as initial and to

calculate what will be the value of modulus of material by reinforcing the matrix with the system of straight parallel fiber fragments [7].

However in practise such sofisticate approach is rather useless. The Weibul's statistics for fibers are not known and what is even more important the mixture of fibers in real composite rod is far away from that on Fig. 3. The rod consists on rather irregularly mixtured bundles of both sorts of fibers. Strongly speaking the new theoretical model of fracture, damage and nonlinear stress strain behaviour in such composite should be elaborated. For practical needs the elementary formula (3) can be used.

Experimental results.

Two kinds of hybrid unidirectional composites were produced: carbon-armide-polyester (CAP) and carbon -glass-polyester (CGP) [8]. The raw materials used for specimens were "Toray" carbon fiber, T400HB-6K-40D produced in Japan; aramid fiber ZSVM-300, produced in Russia; E-glass fiber produced in Valmiera, Latvia; and polyester resin NORPOL440M850, made in Norway. The characteristics of materials are given in table 1.

Table 1

Type of fiber	E, GPa	$\sigma *$, Gpa	$\varepsilon *$, %
E-glass	72-75	1.25-3.8	2.64
Aramid ZSVM - 300	11-135	3.8-4.2	3.29
Carbon fiber T400HB	250	4.49	1.21

Carbon-aramid rods were made of T400HB carbon fiber and Russia-made ZSVM - 300 aramid fiber. The required proportion of the fiber kinds was found using (3). Due to some practical reasons actual fibers contents in specimens was a little different: 76% aramid and 24% carbon. Total volume fraction of fibers in the rod was $\mu_{tot} = 0.36$. Cross section of rod was 195 mm^2 (diameter 16 mm).
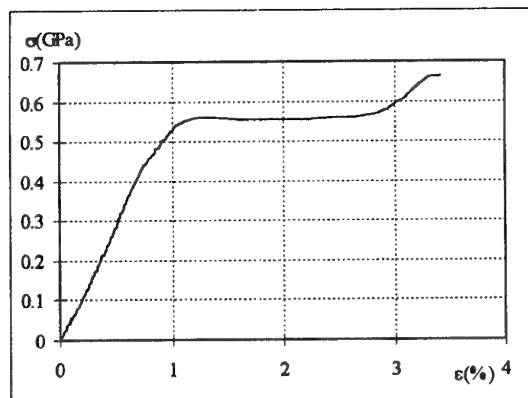
Figure 4. Carbon-aramid hybrid composite $\sigma - \varepsilon$ diagram.

Figure 4 shows $\sigma - \varepsilon$ curve obtained on carbon-aramid specimen in tension and it is seen, that desirable nonlinearity is achieved.

According to calculations, the initial modulus of the material is $E = 51.7\ GPa$. Experiments give $E = 52\ GPa$. The calculated value of the modulus in the final stage of loading is 22.4 GPa (the modulus of the aramid fiber used decreases as strain grows so that just before rupture it is about 75% of the initial value; this effect is taken into account here). Experimental value is $\approx 20\ GPa$. Therefore, the experiment

confirms that the wanted hybrid effect was attained. The ultimate load capacity was 17 tons. It is worth to note that this nonlinear effect was achieved only on specimens with relatively large diameter, (16 mm) and absent on thin unidirectional hybrid specimens. In such specimens the failure onset was observed just after first break of carbon fiber bundle. Increasing the specimens cross-section decreases ratio of the fiber bundle cross-section to the total specimen cross-section and improves homogeneity of fibers mixing.

Glass fiber is much cheaper than aramid fiber, which makes prospective its using for concrete reinforcing very attractive and motivates research in hybrid rods with E-glass fibers instead of aramid. Calculations using (3) show that such a material must contain 81% glass fiber and 19% carbon fiber. Hybrid composite specimens containing 80% E-glass fiber and 20% T400HB carbon fiber were made and tested. Total volume fraction of the fibers was $\mu_{tot} = 0.47$. The tension tests were carried out at a constant loading rate of 20.8 N/s. Figure 5 shows the results of these experiments.
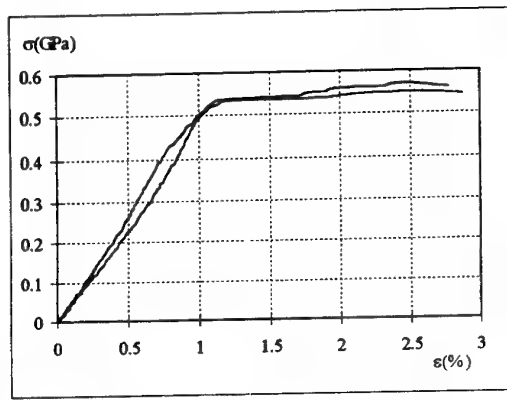

Figure 5. Carbon-glass hybrid composite $\sigma - \varepsilon$ diagram.

It is seen that also this hybrid composite has a plateau. 3% strain was almost reached in these first experiments and the stress growth before the rupture was about 3% to 5%.

The creep tests of hybrid composites are still in progress, but during 3 months no creep was observed under load equal 0.7 of static strength.

Finaly the bending test of concrete slab containing two CGP rods was performed. The details of test are reported in [9]. Shortly it can be stated, that indirect estimation of ultimate strain in CGP rods reached 2.5%.

After test the rods were extracted and matrix burned out. It revealed the partial fragmentation of carbon fibers during loading, but the length of fragments considerably exceeded that predicted by statistical theory. Also the distinctive yielding of concrete beam was not observed, therefore the rotational capacity in the classical sense was not revealed.

Conclusions.

1. It is possible by appropriate choose of hybrid composite fibers to obtain nonlinear "quasiplastic" behaviour of hybrid composite rods till the ultimate strain 3%.
2. The fiber mix proportion, mixing uniformity, size of fiber bundles, resin impregnation procedure and size effect of rod are very important to achieve a desirable performance of hybrid rods.
3. Hybrid composites having carbon fibers up 20% of total fiber amount don't reveal tensile creep deformation at stress level 0.7 of static strength.
4. The ductile behaviour of hybrid rods in concrete structures should be investigated more completely.

References.

1. Junichi Matsui "PAN based carbon fibres". In Proceedings ECCM-6 (Euro-Japanese colloquium on ceramic fibres) 1993, pp. 38 - 54.
2. Tamon Ueda - private communication.
3. U.Meier "Composites for structural repair and retrofitting" in Fiber Composites in Infrastructure, ICCI 96 Tucson, pp. 1203-1216.
4. J.Gutans, V.Tamuzs "Strength probability of unidirectional hybrid composites". Theoretical and Applied Fracture Mechanics, 7 (1987), pp. 193-200.
5. J.Gutans "Analysis of stress concentration in hybrid composites". Mechanics of Composite Materials, Vol. 21(2), (1985).
6. I.Grushecky, M.Mikelson, V.Tamuzh "Change of stiffness of the unidirectional fiber reinforced composite due to fiber breaking", Mechanics of Composite Materials, Vol. 18(2), (1982).
7. R.Maksimov and V.Kochetkov "Description of the deformation of a hybrid composite with allowance for the effect of fibre fracture", Mechanics of Composite Materials, Vol. 18(2), pp. 157-162 (1982).
8. R.Apinis, J.Modniks, V.Tamuzs, R.Tepfers "Ductility of Hybrid Fiber Composite Reinforcement FRP for Concrete". Proceedings of ECCM-8 Naples, Vol. 2, pp. 89-96.
9. R.Apinis, V.Dejke, J.Modniks, V.Tamuzs, R.Tepfers "Rotation Capacity of Concrete Beams with Ductile Hybrid CFRP + GFRP and Elastic CFRP Tensile Reinforcement. To be appeared in Proceedings IRACC-99 Baltimore USA, November 1999.

Freeze-Thaw Durability of Polymer Matrix Composites in Infrastructure

N. Verghese[1], J. Haramis[2], and J. J. Lesko[1]
Virginia Polytechnic Institute and State University, Blacksburg,
Virginia 24061-0219, USA.

Abstract

The present paper discusses the features of freeze-thaw damage in polymer matrix composites. We highlight results obtained using a differential scanning calorimeter (DSC) on both the unreinforced polymer as well as a glass fiber reinforced, vinyl ester matrix composite. The DSC data obtained shows that the neat resin, although saturated, did not contain any freezable traces of water, whereas the composite system does show the presence of freezable water. Thermal cycling experiments were also performed on the composite using the DSC. A reasonable thermal cycle was chosen based in part, according to ASTM C666 (temperature range; 18°C to +4°C) and a rate by choice of 5°C/minute. Data shows significant trends in terms of changes in the profile of the melt endotherm that occurred after the initial couple of cycles which then remained constant over the remainder of the test. Scanning electron and optical micrographs taken on composite cross-sections indicate clearly the presence of both interfacial cracking upon saturation along with some cracks in the resin rich areas of the pultruded component. This lead the authors to believe that water tends to reside in these locations and that the size of these cracks are large enough (namely greater than 40 Å from the Thompson equation) permitting water to freeze. This cannot occur in the case of the neat resin because water resides primarily in the free volume (6-20 Å).

Introduction

Fiber reinforced polymer (FRP) composite materials are under serious consideration for use and investigation for civil infrastructure within the U.S. The high strength and stiffness to weight ratios along with their flexibility in designing specific structural characteristics make them attractive for various structural applications. In addition, the serviceability and functional service life of a composite superstructure such as a bridge may be greater than those built using conventional materials. An uncertainty that plagues the community in its attempt to routinely implement FRP in highway structures is the proof of their environmental durability. A comprehensive database of information does not exist as of today nor does a fundamental understanding of the physics of the problem at hand.

One such environmental condition that remains an unknown is that of freeze-thaw resistance. Limited research has been conducted in this area; primarily with regards to aerospace applications[1]. When considering civil infrastructure applications, Gomez and Casto[2] have reported mechanical data on freeze-thaw tests conducted on insopthalic polyester and vinylester pultruded glass reinforced composites. These specimens were aged in accordance with ASTM C666 (namely, 40°F to 0°F followed by a hold at 0°F and a ramp up to 40°F followed by a hold) while submerged in 2% sodium chloride and water. Specimens were removed after every 50 cycles and tested in flexure mode. The results clearly indicated reduction in flexure strength and modulus after 300 cycles.

Lord and Dutta[3] were according to the authors one of the first to highlight the importance of cracks in the matrix and fiber-matrix interface as being the cause of the damage in composite materials. When these cracks form beyond a certain critical size and density, they coalesce to form macroscopic matrix cracks. This then increases the diffusion of water into the system so that now condensed matter could settle within these cracks and

---

[1] Department of Engineering Science & Mechanics
[2] Via Department of Civil and Environmental Engineering

result in crack propagation as well the formation of micro as well macro level ply delamination during the expansion of water undergoing a liquid-solid phase transition. In Kevlar fabric laminates used by Allred[4] and subjected to 2 hour temperature cycles from – 20°F to 125°F, ultimate tensile strength of the laminate was found to decrease by 23% after 360 cycles and by 63% after 1170 cycles.

The work done thus far has not elucidated the controlling mechanism(s) or kinetics to explain the process of freeze-thaw damage. Thus, the primary goal of the present work is to therefore examine the occurrence, extent and mechanisms controlling freeze-thaw degradation in composite materials. The problem has been broken down to examine the response of each of the constituents (fiber, matrix and interphase/face) to the presence of moisture under cyclic thermal conditions. Differential scanning calorimetry (DSC) will serve as an initial technique to study the freeze-thaw process in an effort to identify the nature and presence of freezable water within each constituent. Subsequent work will examine the nature of freeze thaw damage within the composites and their effects on residual properties.

Material System and Experimental Procedure

A commercial vinylester was used as the neat, unreinforced resin. This resin is produced by the Dow Chemical Company and marketed under the brand name Derakane 441-400. Styrene is added as the co-monomer and helps reduce the room temperature viscosity of the resin. Benzoyl peroxide is added to the system and the resin undergoes a rapid, free radically initiated addition polymerization to form the crosslinked network.

The glass transition temperature, T_g for the pure resin is around 135°C (from DSC) and that of the composite is around 126°C. The lower T_g for the composite can be due to the fact that the pultrudable resin contains fillers and other additives such as mold and air release agents that could plasticize the resin. The composite is a $(0°/90°)_{3s}$, glass fiber, vinyl ester system, pultruded at Hexcel Corporation using the continuous resin injection technique.

A Perkin Elmer, Pyris 1 differential scanning calorimeter was used to perform the freeze-thaw experiments. Liquid nitrogen was used to achieve the cryogenic temperatures needed for the experiment. The base line of the instrument was constructed on a daily basis to ensure experimental accuracy. Regular aluminum pans were used for the single cycle experiments whereas special Perkin Elmer, pressure pans had to be used in the cyclic experiments. These are pans with special threaded lids to prevent leakage due to pressure build up inside the pans leading to subsequent opening of the seal. In the case of the cyclic experiments a few drops of water was dispensed into the pan in addition to the saturated specimen in order to investigate the role of this free-water. Circular disks of the material were punched out in the case of the resin and machined in the case of the composite so as to prevent having to cut or punch material out for DSC after moisture saturation. A temperature cycle of -150°C to +50°C was used for the single cycle experiment and –18°C to +4°C for the cyclic experiment. In both cases a rate of 5°C/min was used and the melt endotherm was monitored owing to its greater reliability as explained by McKenna.[5] This thaw rate is clearly much greater than that observed in our terrestrial environment (5°C/hr.). In each case two samples were examined and a dwell time of about 3 minutes was given to the sample at the extreme temperatures in order to maintain thermal stability in the system.

Results and Discussion

Heat flow measurements as obtained by DSC, under the above stated thaw conditions for a neat, un-reinforced resin sample, subjected to a single cycle, showed no endotherm. Again, this resin has been saturated in a water bath at 65°C and has an equilibrium moisture content of 0.9% by weight (Table 1). The lack of a melt endotherm indicates the absence of freezable water in the pure resin. This is not surprising considering the fact that the water

essentially resides in the free volume of the resin and this free volume size is of the order of about 6-20 Å. According to the Thompson's equation this void size is too small thermodynamically for water to freeze. In addition, Verghese et.al[6] have reported that specific interactions in the form of hydrogen bonding exist in the presence of water for this vinyl ester resin. These specific interactions bind the water to the resin backbone inhibiting crystallization.

The melt endotherm region in a similar heat flow experiment that was carried out on a saturated (at 65°C) E-glass/Derakane 441-400 composite sample is shown in Figure 2. The existence of a weak melt endotherm is clear, indicating the presence of freezable water. From this melt endotherm region the enthalpy under the peak can be estimated. Using the enthalpy of fusion of water (333 J/grm), the amount of freezable can be ascertained (Table 1). A supression in the freezing point is seen to exist and this is conceivable, as the degree of supercooling is a function of the crystal size (diameter in the case of a spherical crystal).

Table 1: Saturation and DSC data obtained on both the neat resin as well as composite

| Sample	Number	Maximum Moisture Content (wt.%)	Amount of Water, W1 (mg)	Area under Endotherm (mJ)	T_m (°C)	Freezable Water, W2 (mg)
Derakane 441-400	1	0.9	0.2	None	—	None
	2	0.87	0.2	None	—	None
Composite	1	0.53	0.1	1.05	-6.34	0.038
	2	0.55	0.1	1.51	-6.48	0.045
	3	0.56	0.1	1.28	-6.83	0.039
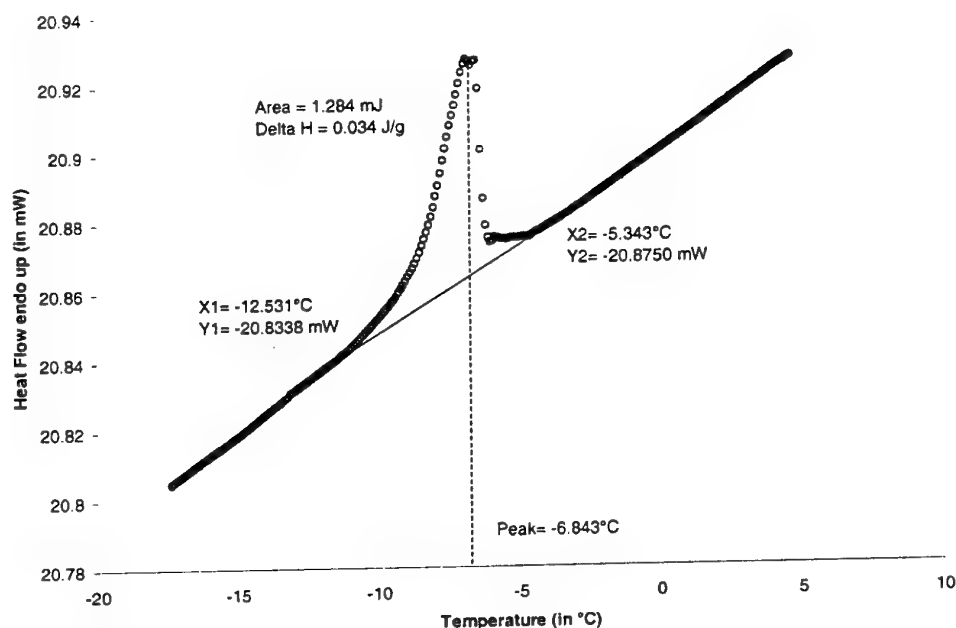
Figure 2: Melt endotherm region for the composite specimen. Indicated here are both the position of the melt endotherm at –6.8°C and the area under the peak

The melt endotherm portion of several freeze-thaw cycles is shown in Figure 3. Again, the composite specimen was saturated in a 65°C water bath before testing. In this experiment, a few drops of water was dispensed into the pan in addition to the saturated specimen in order to investigate the role of free versus bound water. It is clear that certain features of the curve change as freeze thaw cycles proceed. Initially, a shoulder appears at the lower temperatures and is attributed to the water contained inside the saturated specimen. The position of the peak seems to be shifted to around -4°C as opposed to –6°C and this is because these samples were saturated in distilled water as opposed to tap water. The second more prominent peak is associated due to its shear magnitude to the melting of the free water. After 5 cycles this low-end shoulder disappears. We speculate that this is due to the accumulation of damage in the composite that then opens up the size of these spaces and allows the water to freeze in an increased free-water like manner. This however needs to be inspected with further testing.
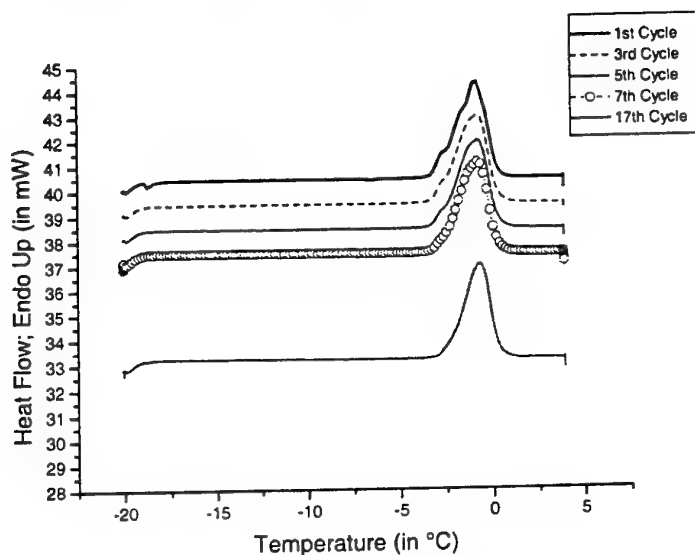
Figure 3: Cyclic DSC data on the composite specimen. The pan contained both the saturated specimen as well as a few drops of free-water.
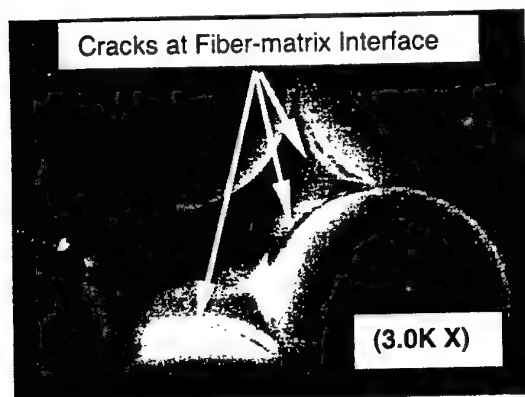

Figure 4: Scanning electron micrographs of fresh water aged material at two different magnifications.

This increase in damage can be associated with fiber matrix interface failure as well as preexiting flaws within the composite. Scanning electron micrograph of a saturated glass/vinyl ester composite (EXTREN™)[7] clearly show interfacial cracks. The sizes of these cracks along with that shown in Figure 5, which is an optical micrograph, are large enough to harbor freezable water. The crack in Figure 5 is formed in the resin rich regions of the "as received" material detailed in the experimental section. This processing flaw is due to the large cure shrinkage associated with the vinyl ester resin (~6% by volume) and the mismatch in coefficient of thermal expansion between glass fibers and vinyl ester[8]. The authors therefore have sufficient reason to believe that water can reside in these areas in the composite and that these regions are large enough to facilitate the freezing of water during aging.
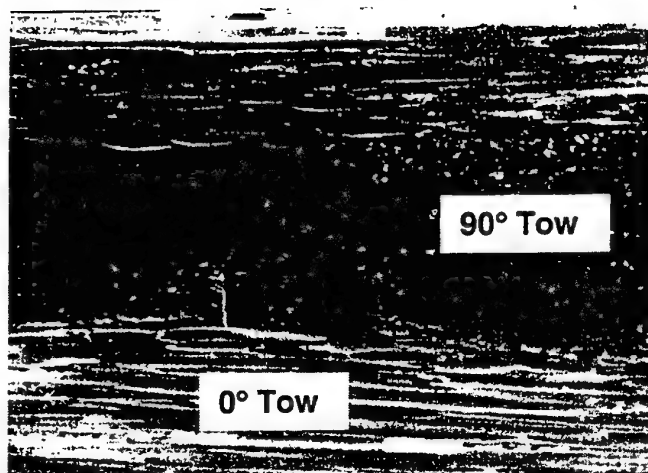
Figure 5: Optical micrograph of the "as received" pultruded cross ply laminate (E-glass/Derakane 441-400) viewed from the transverse direction; a microcrack (8mm long by 1mm wide) is observed in the resin rich region.

Conclusions and Future Work

It is virtually impossible to freeze water in a highly crosslinked amorphous polymer like vinyl ester. This is in part due to the geometric space constraints and due to hydrogen bonding that further impedes the process. In the composite system however, the crack dimensions are large enough to facilitate the freezability of water. The authors believe that it is this mechanism then of freezing and the associated volume increase during the transition that leads to the propagation of cracks and the accumulation of damage. Presently, work is underway to understand the effects of fatigue, moisture and freeze-thaw on the remaining tensile strength of $[0°/90°]_{3s}$, glass/vinyl ester composites. This work will help further our understanding of the effects of different environmental conditions in particular, free-thaw.

Acknowledgements

References

1) Mitra, Dutta and Hansen, "Thermal Cycling Studies of a Cross-plied P100 Graphite Fiber Reinforced 6061 Aluminum Composite Laminate", *Journal of Materials Science*, **26**, November 1991

2) Gomez, J. P. and Casto, B., "Freeze-Thaw Durability of Composite Materials", *Virginia Transportation Research Council*, 1996

3) Lord, H. W., and Dutta, P. K, "On the Design of Polymeric Composite Structures for Cold Regions Applications", *Journal of Reinforced Plastics and Composites*, **7**, 1988

4) Allred, R. E., "The Effects of Temperature and Moisture Content on the Flexural Response of Kevlar/Epoxy Laminates: Part II [45/0/90] Filament Orientation", *Environmental Effects on Composite Materials*, **Volume 2**, George Springer, editor, Lancaster, PA: Technomic Publishing Company, Inc., 1984

5) McKenna, G, and Catheryn, L. J., "On the Anomalous Freezing and Melting of Solvent Crystals in Swollen Gels of Natural Rubber", *Rubber Chemistry and Technology*, **64**, 1990

6) Verghese, K. N. E, Hayes, M. D., Garcia, K., Carrier, C., Wood, J., and Lesko, J. J., "Effects of Matrix Chemistry on the Short Term Hygrothermal Aging of Vinyl Ester Matrix and Composites", *Journal of Composite Materials*, In Press

7) McBagonluri, F, Garcia, K, Hayes. M. D, Verghese, K. N. E, and Lesko, J. J, "Characterization of Fatigue and Combined Environment on Durability Performance of Glass/Vinyl Ester Composite for Infrastructure Applications", *Submitted to the International Journal of Fatigue*

8) Phifer, S., " Quasi-Static and fatigue Evaluation of Pultruded Vinyl Ester/E-Glass Composites", *Masters Thesis, Virginia Polytechnic Institute and State University*, January 1999

Durability of Fiber Reinforced Composites in Civil Infrastructure - Issues, Results and Implications

V.M. Karbhari and S. Zhang
Department of Structural Engineering, MC-0085
University of California, San Diego
La Jolla, CA 92093-0085, USA

Fiber reinforced polymer (FRP) matrix composites are increasingly being considered for use in civil infrastructure in applications ranging from the seismic retrofit of columns and strengthening of slabs and beams, to use in all-composite replacement bridge decks and in new structural systems. Although the performance advantages of FRP composites make them very attractive for use in these applications, the eventual acceptance of these materials is predicated on the resolution of a few critical aspects, foremost among which are the aspects of durability and cost. It should be noted at the outset that cost is paramount in the area of civil infrastructure, especially as new materials and technologies are compared with conventional materials on an acquisition cost rather than a life-cycle cost basis. Further, civil infrastructure components such as bridges are designed for life-times ranging from 75-150 years. The use of composites in aerospace applications has been predicated on extensive materials testing for the purposes of qualification, followed by strict adherence to prescribed specifications for autoclave based fabrication in highly controlled factory environments. These materials and processes are unlikely to find significant application in civil infrastructure due to cost and processing specific aspects. Civil applications, at present, are more likely to (a) use processes such as wet lay-up, pultrusion and resin infusion than autoclave molding, (b) fiber and resin as separate constituents rather than in the form of preimpregnated material, and (c) resin systems such as polyesters, vinylesters, phenolics and lower temperature cure epoxies rather than the higher temperature curable epoxies and thermoplastics. Further, there is likely to be extensive use of processes under ambient conditions in the field, rather than fabrication in factory controlled environments. Thus, the civil engineering environment not only brings with it new challenges for the control of quality and uniformity of composites, but also makes it difficult (if not impossible) to use the well established databases generated by DoD sponsored research (such as those for AS4/3501-6 or T300/5208 based systems). Environmental conditions likely to be faced by these composites range from extremes in temperature (heat as in Saudi Arabia, cold as in Alasksa), significant variation in humidity levels, potential for routine submersion or immersion (such as for structures in flood plains), exposure to chemicals, including road salt, and widely varying load conditions. It is important that these issues be kept in mind while selecting materials and processes for the fabrication of FRP composites for civil infrastructure. This paper attempts to raise the awareness of the effect of a number of these materials-process-environment systems on the durability of the structure, while emphasizing the implication of such factors on overall design and use.

It is important to note that the use of composites in infrastructure renewal can be classified into the different classes of rehabilitation and new structural systems. Within the scope of rehabilitation of concrete structures, it is essential that we differentiate between repair, strengthening and retrofit, terms which are often erroneously used interchangeably, but in fact refer to three different structural conditions (Figure 1). In "repairing" a structure, the composite material is used to fix a structural or functional deficiency such as a crack or a severely degraded structural component. In contrast, the strengthening of structures is specific to those cases wherein the addition or application of the composite would enhance

the existing designed performance level, as would be the case in attempting to increase the load rating (or capacity) of a bridge deck through the application of composites to the deck soffit. The term retrofit is specifically used as related to the seismic upgrade of facilities, such as in the case of the use of composite jackets for the confinement of columns. The differentiation is important not just on the basis of structural functionality, but also because the specifics related to the use of the material in conjunction with existing conventional materials, and its expected life have a significant effect on the selection (or rejection) of fiber-resin combinations from a variety of alternatives.

The use of composites in seismic retrofit and strengthening of reinforced concrete columns has received a large amount of attention in recent years due to the critical need for materials/technologies that would allow for rapid installation of jackets for confinement. The corrosion resistance, light weight and anisotropy of FRP composites provides an ideal match for this application wherein use of conventional isotropic materials generically results not only in the desired enhancement of hoop confinement, but also an undesired increase in structural stiffness. In the case of seismic retrofit, FRP composite jackets are generically unstressed and hence both glass and carbon fiber can be used as primary reinforcement. However, load levels need to be carefully considered in cases of strengthening since it is expected that the composite jacket would bear a significant amount of the axial load capacity in addition to providing confinement. The NOL ring burst test has been identified as an efficient test that combines both materials and structural aspects for the determination of design properties and durability of the FRP jacket. Figure 1 shows the dimensions of a standardized ring, whereas Figures 2-4 show a range of failure modes. It should be apparent that each is characteristic of a materials-process combination and although functionally sufficient under short-term conditions, overall performance could be significantly affected by environmental conditions (moisture, freeze, freeze-thaw both with and without road salt, elevated temperature, humidity etc.) over the long-term.
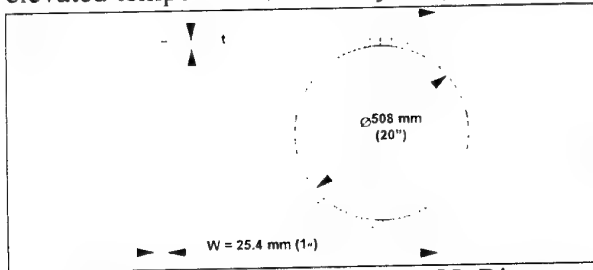
Figure 1: Schematic of the NOL Ring Showing Pertinent Dimensions

Figure 2: Tensile Failure Showing Well-Consolidated and Cured Specimen

Figure 3: Failure Initiated At Adhesive Level in a System Using Prefabricated Adhesively Bonded Sections

Figure 4: Failure Through Layer Separation Due to Poor Wet-Out/Interply Bonding

The time-temperature history for freeze-thaw exposure of E-glass and carbon fiber reinforced composite wrapped concrete specimens is shown in Figure 5, whereas the effects

of this exposure on performance metrics is shown in normalized form in Figure 6. It was noted that freeze-thaw exposures resulted in significant changes in damage mechanisms and failure modes due to effects on the resin and at the level of the fiber-matrix interphase. It was also noted that although overall energy did not change significantly, there was a discernable increase in energy levels measured at the initiation of bilinear response in compression for the system, indicating change in failure initiation mechanisms (Table 1)
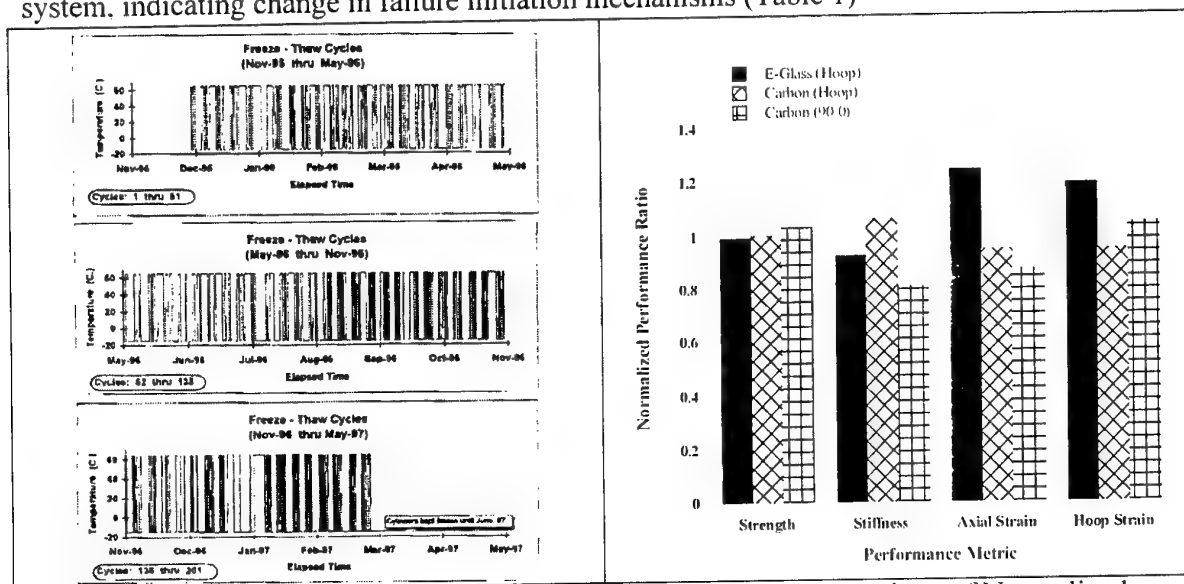

Figure 5: Record of 201 Freeze-Thaw Cycles Used For Exposure of FRP Composite Wrapped Concrete Specimens

Figure 6: Comparison of Normalized Performance Metrics on the Basis of Wrapped Cylinders Only ($P_{\text{freeze-thaw}}/P_{22.5°C}$)

Table 1: Comparison of FRP Composite Jacketed Specimens on the Basis of Energy Response. (Values obtained as a result of freeze-thaw cycling are normalized by those obtained after 22.5°C exposure)

System	Normalized Energy Till Kink Point	Normalized Energy At Failure
Glass (0°)	1.36	1.01
Carbon (0°)	1.52	0.99
Carbon (90/0)	1.43	1.15

In addition to the case of FRP composite reinforcement being used as a replacement for conventional steel rebar, in a number of rehabilitation applications there is the potential for the FRP composite to be in contact with fresh concrete or with solutions/moisture that have diffused to the FRP surface through the concrete (as in the case of exposed slabs). Since E-glass fiber is known to be highly susceptible in the bare state to alkalinity induced degradation, there is a level of concern related to the use of these materials for strengthening and repair of primary structural elements. In order to simulate effects due to migration of water through concrete to the composite, alkaline solutions were prepared by placing disks of concrete of 150 mm diameter and 25 mm height in water and allowing alkaline salts to collect in the water directly from the concrete itself. For purposes of comparison concrete disks from two different sets of ordinary Portland Cement Concrete were used, the first resulting from cylinders allowed to cure for 28 days (New Concrete) and the second resulting from cylinders that were allowed to age 10 years before use (Old Concrete). To further compare effects a cementitious extract was prepared at the same time as pouring of the "New" Concrete by collecting the solution that formed after settling of the aggregate and diluting the

solution by the same level of water added to the concrete disks used previously. Standard potassium buffer solution providing a pH of 10 was also used. Further water by itself was also used as a comparative test solution. pH levels of these solutions (with the exception of the buffer) were measured over an extended period of time and results are shown in Figure 7. As can be seen the pH levels of the "New" Concrete solution, "Old" Concrete solution, and Cementitious extract are different at the beginning with the extract solution having the highest pH and the "Old" concrete solution having the lowest. The two solutions that derive alkali salts and pH from actual concrete both drop to a pH level of 8.5 fairly rapidly (60-80 days) whereas the cementitious extract solution falls to a level of about 8.5 in about 250 days. It is interesting to note that if the concrete containing water was placed in isolation (in this case in a sealed dessicator) the pH level does not fall but stays relatively constant at a level of 12-12.5. This is in line with the effect of carbon dioxide on carbonates in forming calcium bicarbonate which results in a lower pH level. The effect, however does raise questions related to effects arising from situations wherein the concrete in question is isolated from free atmospheric interaction, which would seemingly result in maintenance of higher pH levels as well as of salt concentrations that conceivably would be more degrading to glass fiber reinforced concretes, than others.
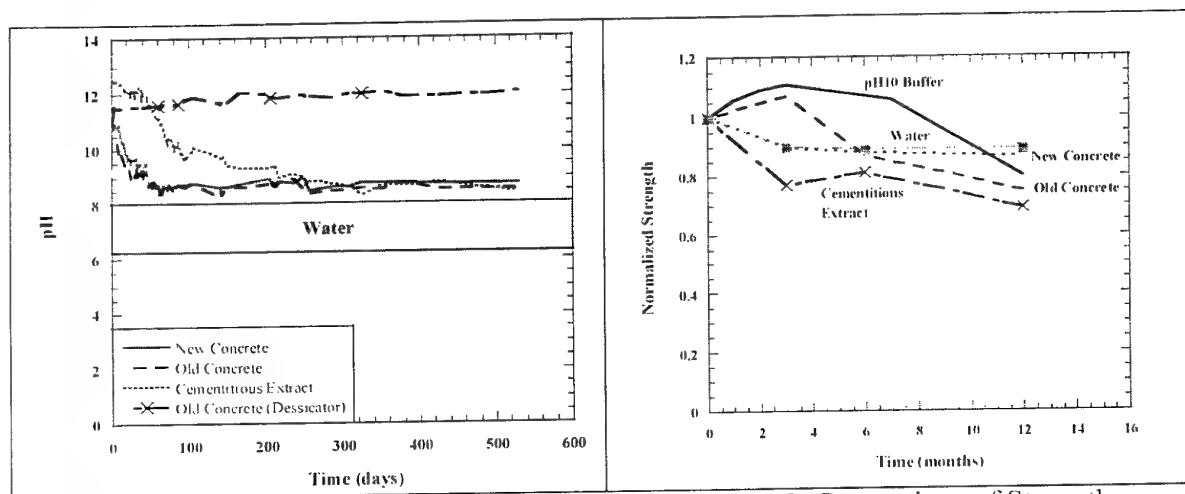

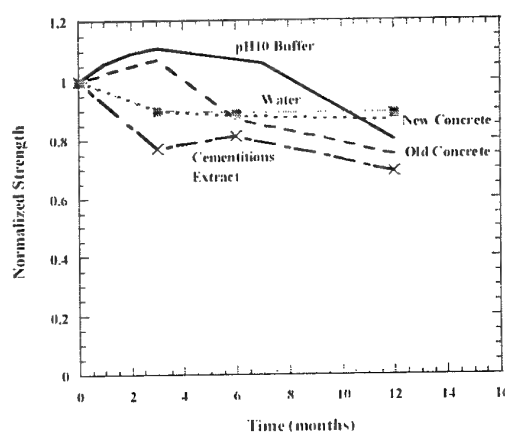Figure 7: Effect of Time and Exposure Conditions on pH Levels

Figure 8: Comparison of Strength Degradation

The effect of 12 months exposure of these solutions on a E-glass/Vinylester composite cured under ambient conditions is shown in Figure 8. As can be seen in Figures 9 and 10, the different solutions result in differing failure initiators at the fiber, and fiber-matrix level. Micrographic and EDAX analysis shows that the damage at the interphase level is initiated by moisture in a highly alkaline medium, whereas that at the fiber level is due to initial formation of a calcium hydroxide crystal with notches and abrades the fiber itself. Both these effects could conceivably be aggravated further through the introduction of stress, and could be potentially negated through the use of appropriate fiber sizings/finishes and use of resin systems such as polyurethane modified vinylesters which have been shown to be more resistant to moisture and alkali related degradation.

In the past glass fiber reinforced FRP composites have been successfully been used for marine applications through the use of a factor of safety of 4-6, and these materials have been used for underground storage tanks with a factor of safety of 10-12. It should be noted, however, that the environment and load conditions are different as related to bridges and

buildings and due care has to be taken in determining the effects of these conditions both on short-term and long-term performance.
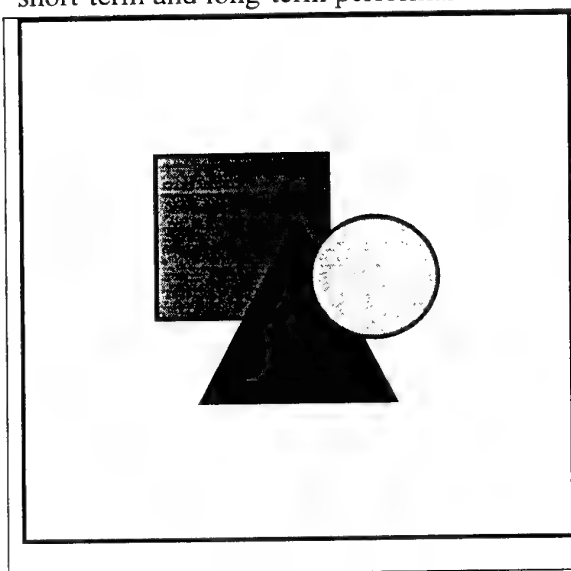

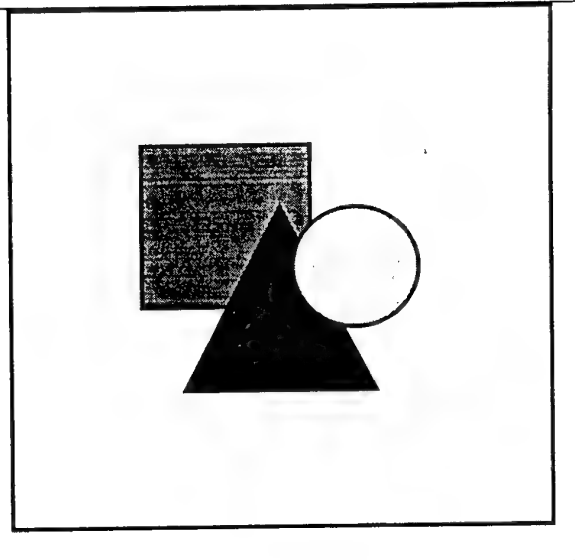Figure 9: Fiber Pitting and Interphase Level Degradation Due to "Old Concrete" Leachate

Figure 10: Fiber and Resin Degradation Due to Exposure to Cementitious Extract.

The influence of ambient temperature cure as applied to processes such as wet layup conducted in the field on substrates such as concrete which may not be completely dry should also be considered, especially in light of the fact that there is likely to be significant use of resin systems such as polyesters and vinylesters, both of which do not reach full cure for extended periods of time and are thus susceptible to creep relaxation and moisture induced degradation. Although carbon fibers are generically considered to be inert to most environmental influences there is potential for degradation at the level of the resin and fiber-matrix interphase as well, both of which can result in severe deterioration of composite performance. Now more than ever before there is a critical need for the development of an integrated materials-structures model for prediction of durability (Figure 11) especially since structures differ in terms of criticality of strength, stiffness or failure strain levels vis-à-vis design, not all of which degrade at the same rates or to the same relative levels.
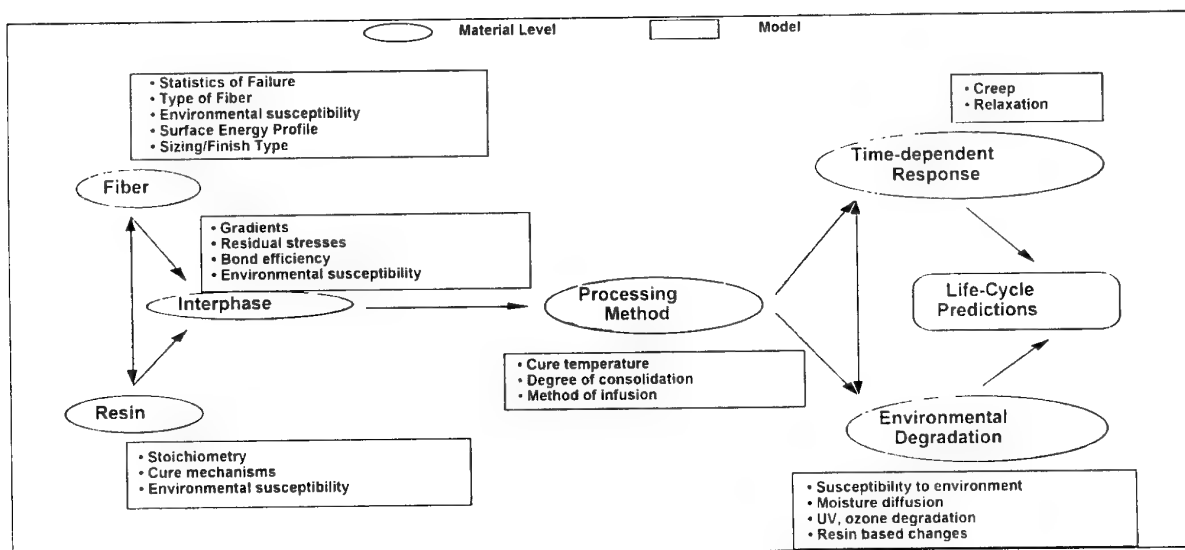

Figure 11: Schematic of a Model for Life-Cycle Response Predictions

Durability of reinforced concrete beams
repaired by composites under creep and fatigue loading

E. Ferrier, G. Lagarde, P. Hamelin.
Materials, Mechanical engineering Laboratory
Université LYON 1-IUT A Génie civil
43 bd du 11 novembre 1918
69622 Villeurbanne cedex France

Abstract

The external bonding of fiber reinforced plastic to concrete structures is an effective method so as to increase the structural capacity of such structures. But, for the design of the reinforcement, one has to take into account the long-term behavior of each material. If the influence of natural exposure on the durability of reinforced structure begins to be well identified, only few works study the long-term behavior under creep and fatigue loads [1].
The use of composite glued on the concrete support requires the identification of the adhesive layer. This adhesive layer is usually an epoxy polymer. This paper deals with the fatigue and creep behavior of this part of the reinforced structure. Then, the influence of the delayed behavior of the polymer is taken into account in predicting the behavior of a composite reinforced concrete beams.

Introduction

The design of the composite reinforcement is determined by a software developed by P. Hamelin, H. Varashtepour and H. Nasseri [2] using a non-linear calculation method. The design method of those reinforcements is based on classical methods used for RC structures, taking into account the slip phenomena in the adhesive layer, considering the mechanical behavior of each material and specific failure mode of RC beam with FRP. Fatigue, creep, or aging solicitation acts on the evolution of the interface behavior with the increasing of the slip phenomena. The calculation method takes into account this evolution for each step of loading. It allows designing the suitable anchorage length of the composite. To design composite reinforcement for a RC beam under fatigue, creep load or composite aging, one has to assess the mechanical behavior of each material and above all, of the adhesive layer.

Delayed calculation method

This calculation method uses standard principle in predicting delayed properties of a steel reinforced concrete beams. This method discribed by Triantafillou and Plevris [3] uses the delayed properties of each material of the beam. It means that the behavior of steel, concrete, adhesive and composite has to be taken into account. The delayed properties of steel and concrete under creep and fatigue loading have been assessed by several authors [4],[5],[6]. But only few researches have been done on the composite and the adhesive layer delayed properties. This identification has been done by using a tensile test for the composite and a tensile shear test for the adhesive. When all the mechanical properties under creep and fatigue are assessed the evolution of curvature is calculated with all the identified mechanical law. This calculation is done for a moment or at the end of N cycles. With the software expanded by the Mechanical Materials engineering Laboratory the calculation is done using two hypothesis. First, the adhesion beetween concrete and composite is perfect, then the sliding between the two materials is taken into account (fig. 1).
The curvature is calculated with the equilibrium of the section (equation (1)).
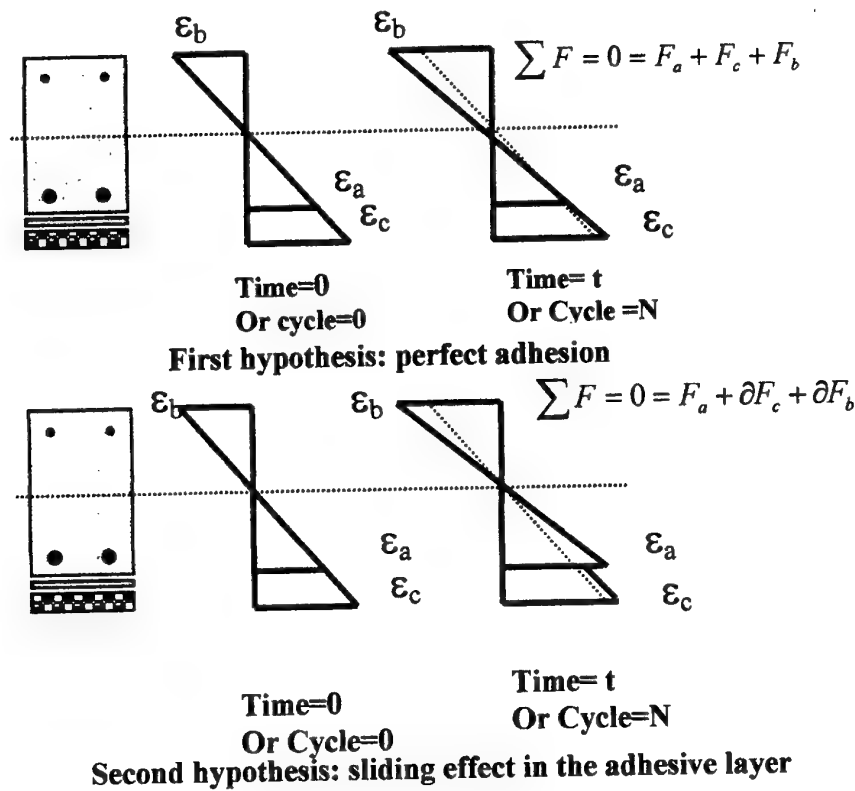
$$\sum F = 0 = F_a + F_c + F_b$$

Time=0
Or cycle=0

Time= t
Or Cycle =N

First hypothesis: perfect adhesion

$$\sum F = 0 = F_a + \partial F_c + \partial F_b$$

Time=0
Or Cycle=0

Time= t
Or Cycle=N

Second hypothesis: sliding effect in the adhesive layer

Fig. 1: Delayed behavior calculation method

This equilibrium is assessed taking into account all the material properties of the structure (concrete in compression (b), concrete in tension (t), steel (a), composite (p)).

$$\Sigma F_x = 0 \qquad N_b + N_a + N_t + N_p = 0$$
$$\Sigma M = 0 \qquad M = M_b + M_a + M_t + M_c + M_p \qquad (1)$$

For the second hypothesis, the shear stress in the adhesive layer has to be estimated. Several authors propose analytic solution to assess this shear stress in case of beam. We have compared those methods with finite element and experimental solutions. All the solutions show a localization of high stress at the end of the composite plate. We have chosen the solution given by the analytical calculation method assessed by Täljsten [7].

Identification of creep and fatigue adhesive layer properties

The adhesive layer study has been done with a tensile-shear test. Composite reinforcements are made of two carbon fabric strips of 425.60 mm^2. The strips assemble two concrete blocks. We have carried out a set of tests with fatigue cycles on the interface and a set of creep tests with the same device. The first test has been conducted to failure with several levels of shear stress with two composites (B and C table 1). The second is conducted on polymers (A, B, C: table 1) to estimate the influence of time-temperature-loading on the viscoelastic behavior.

Tableau 1 : Composites mechanical properties			
	Composite A	**Composite B**	**Composite C**
E (MPa)	65000	50000	56000
R (MPa)	600	550	430
Allongement à rupture (%)	0.8	1.05	0.07
Tg (°C)	46.7°C	51.8°C	83.7°C

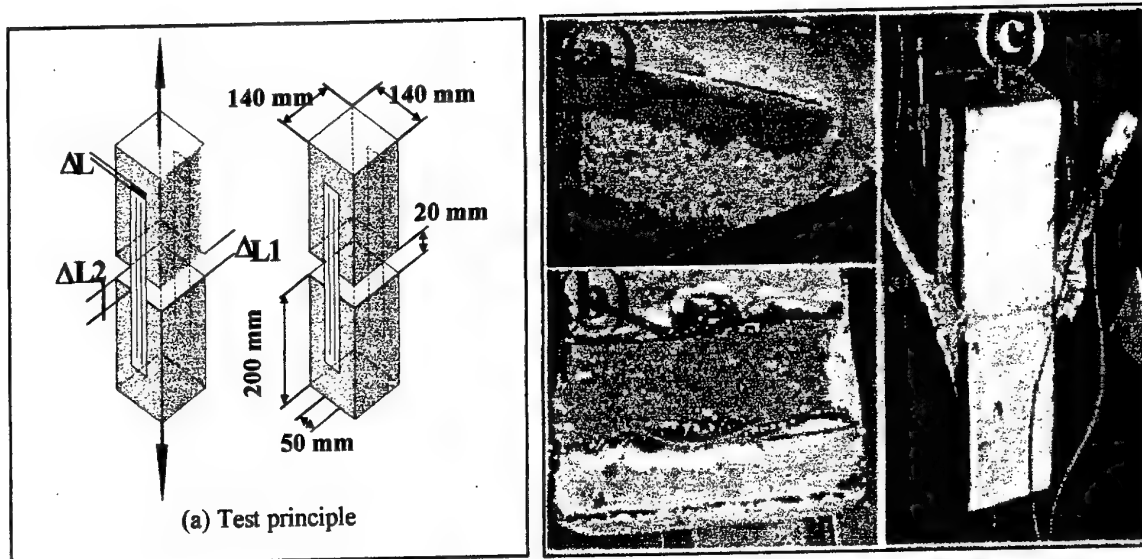The test principle using for creep, fatigue and polymer aging is given by figure 2.

Fig. 2: Test principle, failure mode

Aging

The aging of the reinforcement has been tested on the composite, the polymer and the adhesive layer with the double lap joint device test. The aging is done by moisture exposition. The main conclusions of this test are a first increase of polymer properties due to post curing and then a decrease of materials properties is noticed. With the double lap joint, the failure mode on the non-exposed mode is cohesive, after 1000 hours of moisture aging, this failure mode is non-cohesive, a decrease of joint properties is also noticed.

Creep

The creep test allows setting up the creep of the composite reinforcement under combined effects of stress and environment. Three composites have been tested (A, B, C), the main difference between all the composites is the glass transition temperature. The parameters of the rheological model (2) are identified conducting several tests with several temperatures.

$$\gamma(t,T) = \tau_0 \cdot D(t,T)$$

$$D(t) = \frac{2}{G_0(T)} + \frac{G_0(T) - G_\infty(T)}{G_0(T) \cdot G_\infty(T)} \cdot e^{\frac{-t(G_0(T)(G_\infty(T) - G_0(T)))}{\eta_1 \cdot G_\infty(T)}} + \frac{G_0(T) - G_\infty(T)}{G_0(T) \cdot G_\infty(T)} \cdot e^{\frac{-t(G_0(T)(G_\infty(T) - G_0(T)))}{\eta_2 \cdot G_\infty(T)}}$$

with: $G_0(T)$, $G_\infty(T)$, $\eta 1$, $\eta 2$ (rheological parameters)

The result of the test assessed in dry or moisture environment shows an important creep for the composite A when the temperature increases. The main conclusion of this part is that the Tg effect should be limited to 55°C or upper to limit the creep in the adhesive layer [8].

Fatigue

The tensile-shear test sets up the fatigue life for several levels of shear stress in the interface and then allows to assess the maximum fatigue stress curve (S)– number of cycles (N).

$$\Delta\tau = m.\log(N) + b \qquad (3)$$

With m=-0.07 and b=0.98

The coefficients m, b depend on composite characteristics and concrete surface treatment. This average shear stress allows calculating the anchorage length of the reinforcement.
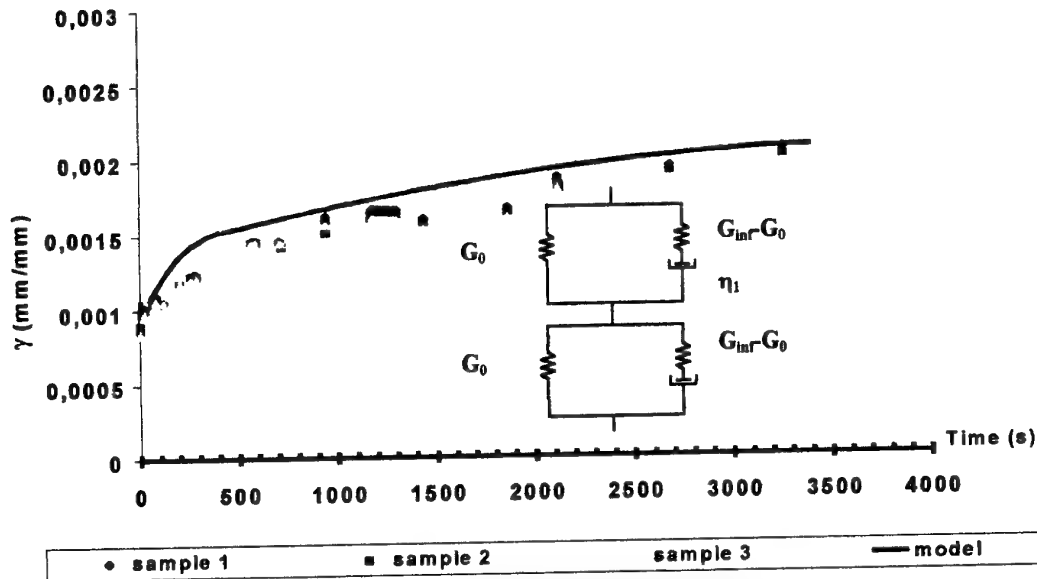
Fig. 3: Creep result on the adhesive layer (polymer B, 35 °C)

This average shear stress allows calculating the anchorage length to take into account a flexural design. The failure occurs with a partly cohesive delamination in the concrete and with a diagonal failure in the concrete at the beginning of the adhesive joint. A calculation using Ansys finite element calculation code shows that in this part of the concrete, a high concentration of strength occurs. Tensile tests are carried out on composite plate, the failure occurs with an average tensile stress of 600 MPa. The constant stress fatigue response and life prediction for carbon-fiber composites is assessed with test under a stress level of 500 MPa.
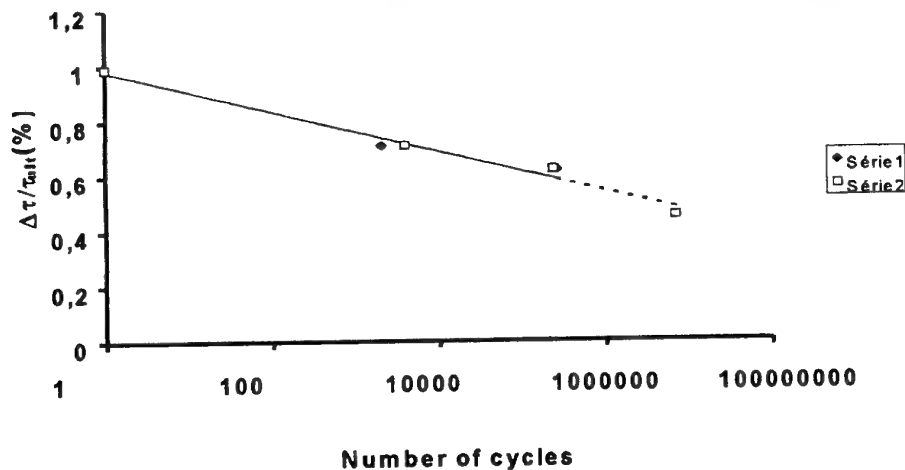
Fig. 4: Test fatigue result on the adhesive layer

Influence of creep on the reinforced concrete beams

The evolution of the deflection is calculated for a load corresponding to 60% of the failure load. The conclusion of this calculation is that the adhesive layer does not affect the behavior of the beam when the temperature is low.

In this case, the difference between the perfect adhesion hypothesis and the sliding effect is low (fig.5). But for the composite A, when the temperature increases this sliding effect in the polymer becomes very important in the global behavior of the structure.

With a polymer with a low Tg (<50°C), the increase of temperature during permanent loading creates an increase of the creep in the adhesive. With this kind of polymer, the loading should be limited to avoid prematurated failure.
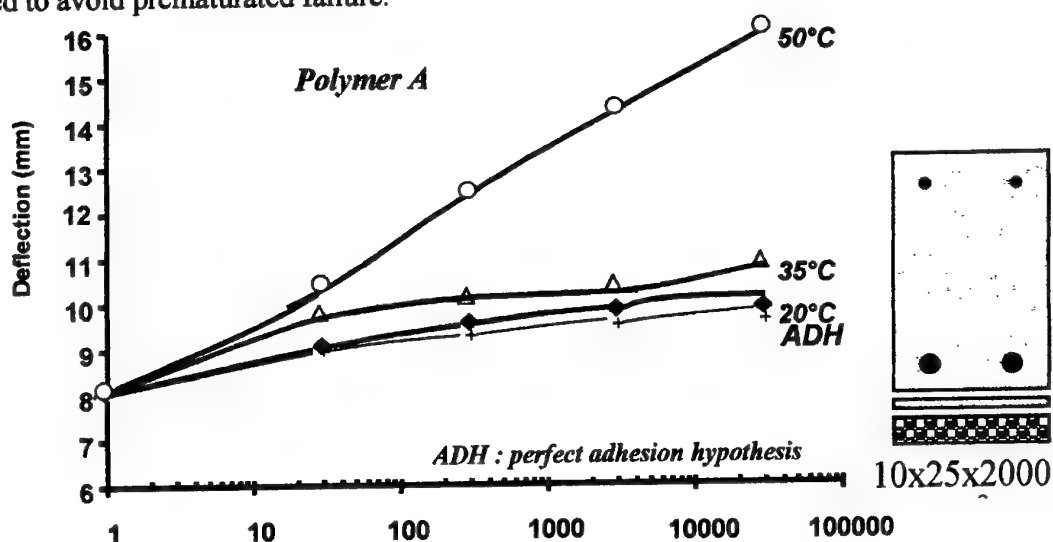
Fig. 5 : Evolution of deflection under creep loading (composite A 60% of failure load)

Influence of fatigue on the reinforced concrete beams

In case of loading, the calculated result has been compared with experimental result. (fig. 6).
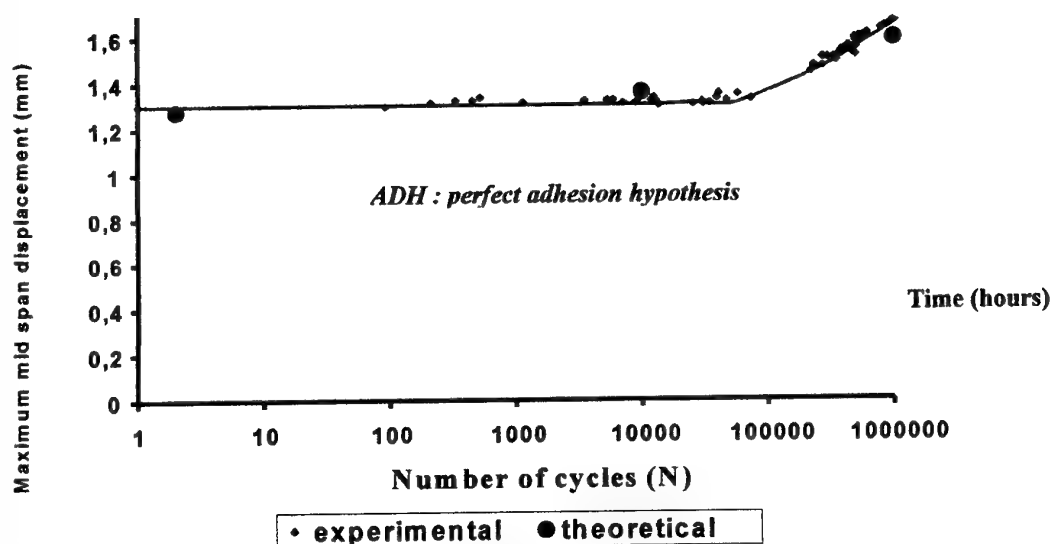
Fig. 6: Evolution of mid span displacement as a function of number of cycles

This result shows that the delayed behavior is estimated with a good accuracy. The main conclusion is that, with a fatigue loading under a temperature of 20°C, the behavior of the structure is not really affected by the fatigue. In this case, the composite (carbon epoxy) and the adhesive layer show a good behavior. The main evolution of the deflection is caused by concrete cracking. Others tests are under-going for higher loads on beams.

CONCLUSION

The safety factor to apply for a long-term behavior of a reinforced concrete beam can be assessed with those laws and with the software. Suitable range of loads for concrete, steel, composite and interface are assessed to predict the life under fatigue and creep load of the reinforced concrete beams. Flexural tests on RC beams with FRP show that, with suitable length of anchorage determined with the first test and with suitable range loads, the long life of reinforced concrete structure can be predicted with reasonable accuracy. The identification of concrete-composite shear behavior law with various environmental conditions allows taking into account the combined effect of time – temperature – loading of a reinforced concrete structure. The same identification can be done for time temperature and moisture. This effect can be more or less predominant according to the structure exposure (building or civil engineering structure). The authors believe that the use of high modulus carbon fiber should improve mechanical behavior of beam, by decreasing composite strength and beam curvature evolution. The result of the test and the design determine the fact that the adhesive joint and the composite plate are strong enough for a fatigue loading of 10^6 cycles (1 Hz). The material that limit the loading in case of fatigue tests is concrete and steel strength. Using the evolution under cyclic loading of mechanical law behavior of each material and the software, the evolution of mid span displacement of a RC beam with FRP is calculated with a good accuracy

The research assessed in this paper shows that polymer with higher Tg than 55°C should be chosen for composite reinforcement in civil engineering structures. All the conclusions assessed by those researches do not take into account the aging of the polymer or the concrete. Studies on polymer aging are undergoing in the laboratory L2M to see the influence of those parameters on the global behavior.

Bibliography

[1] M. Shahawy, T.E. Beitelman, *Fatigue performance of RC beams strengthened with CFRP laminates*, CDCC, Sherbrooke (Québec) 1998.

[2] H. Varastehpour, P. Hamelin, *Analysis and study of failure mechanism of RC beam strengthened with FRP plates, Second international conference on composite material for bridge and structure*, Montreal (Canada), 11-15 August 1996.

[3] N. Plevris, T.C Triantafillou, *Time dependent behavior of RC members strengthened with FRP laminates, Journal of structural engineering*, vol 120 n°3, p 1016-1042, March 1994.

[4] A.K Jakobsen, *Fatigue of concrete beams and columns*, bulletin n°70-1, NTH Institut for beton konstruksjoner, Trandheim, sept 1990.

[5] B.Balagru and S.P Shah, *A method of predicting crackwidth and deflections for fatigue loading*, Fatigue of concrete structures ACI publications SP-75.

[6] M. Kashani, *Etude de l'évolution des déformations du béton soumis à des actions cycliques, applications aux éléments fléchis en béton armé*, thèse de docteur-ingénieur, INSA de LYON 1994.

[7] B. Täljsten, *Strengthening of beams by plates bonding*, Journal of materials in civil engineering, vol 9, n°4, p 206-212, November 1997.

[8] E. Ferrier, G. Lagarde, D. Prin, P. Hamelin, *Durability of reinforced concrete beams repaired by composites*, CDCC 98 Sherbrooke University Canada 1998 p 351-360.

A MODEL ON TEHRMAL DEGRADATION OF FATIGUE STRENGTH AND ITS APPLICATION IN FATIGUE LIFE PREDICTION OF POLYMER COMPOSITES WITH HYSTERETIC HEATING

X.R.Xiao and I.Al-Hmouz

Concordia Center For Composites
Concordia University, Montreal, Canada

INTRODUCTION

Due to the viscoelastic nature of polymer matrices, polymer composites exhibit hysteretic heating under cyclic loading. In some cases the temperature rise resulted from hysteretic heating can be substantial such that it leads to thermal degradation and hence a significant reduction of fatigue life.

In viscoelastic media, the time-temperature, time-stress superposition approaches are the framework used in the modeling of the time-dependent mechanical responses such as creep and relaxation. This type of approach has also been extended to model the fatigue behavior of polymer composites. The published works, however, are for the isothermal conditions, whereas the temperature effect associated with hysteretic heating is a non-isothermal one.

This paper presented a simple prediction scheme which correlates the fatigue life to the thermal degradation of fatigue strength. Shifting factors similar to the time-temperature shifting in viscoelastic media were employed to account for the temperature effect on the fatigue strength and an iso-strength plot was introduced for fatigue life prediction under non-isothermal conditions. The scheme presented in this paper can predict the load frequency effect associated with hysteretic heating from limited basic material information.

The load frequency effect on the fatigue life of thermoplastic composite AS4/PEEK ±45 laminate was investigated at 1 Hz, 5 Hz and 10 Hz. At each frequency, fatigue tests were conducted at three stress levels: 60%, 70% and 80% of the ultimate tensile strength. The fatigue life prediction for 5 Hz and 10 Hz based on SN data at 1 Hz was demonstrated. The predictions were in a reasonably good agreement with the experimental data.

FATIGUE STRENGTH UNDER NON-ISOTHERMAL CONDITIONS

Rotem and Nelson [1] introduced temperature shifting factors to predict long-term fatigue strength from short-term testing at elevated temperatures. For isothermal conditions, assuming that the S-N curve of a composite laminate at a reference temperature T_0 has the following form

$$\sigma(T_0) = f(N) \qquad (1)$$

then the S-N curve at a arbitrary temperature T will be

$$\sigma(T) = f[N, a_T(T), b_T(T)] \qquad (2)$$

where a_T and b_T are the shifting factors. b_T corresponds to a vertical shift due to the changes in the static strength with temperature; a_T to the rotation of S-N curve with temperature. The form of f function and the values of a_T and b_T are to be determined from experimental results. A series of isothermal S-N curves described by Eq.2 are shown schematically in Fig.1.

The fatigue strength in a non-isothermal condition can be presented by plotting iso-strength fatigue curves in a temperature-number of cycles plot, as shown schematically in Figure 2. The iso-strength curves is constructed based on Figure 1. A horizontal iso-stress line is drawn to intercept isothermal S-N curves at different fatigue lives. The data taken at these intercepts constitute one iso-strength curve in Figure 2. A number of iso-strength curves may be constructed by this way. Another important element in Figure 2 is the horizontal line, which corresponds to the temperature when the static strength decreases to the iso-strength value.

By overlaying the predicted transient temperature curve of a sample cycled at a stress level equal to the iso-strength value on Figure 2, one can predict the fatigue life under non-isothermal condition. Fatigue failure occurs when the transient temperature curve intercepts the iso-strength curve. If the temperature rises rapidly, the transient temperature curve may intercept the horizontal line before meeting the iso-strength curve, i.e., the static strength of the material thermally degrades to the applied cyclic stress level and hence the material fails as in a static test before fatigue failure. For both cases, the number of cycles corresponding to the crossing point gives the fatigue life prediction.

FATIGUE LIFE PREDICTION

The data on fatigue strength - number of cycle to failure (S-N) obtained are presented in Table 1. The values of the equilibrium or the maximum temperature recorded during fatigue tests are also listed. As seen, increasing frequency reduces the fatigue life and this life reduction effect appears to be larger at lower stress levels.

The SN curve at 1 Hz is used as the reference curve. In this work, the SN curve is modeled by a four-parameter power law relation:

$$p = p_0 + \frac{1-p_0}{(1+\tau N)^n} \qquad (3)$$

In Eq.3, the cyclic stress appears in a normalized form, $p=\sigma/\sigma_u$ and $p_0=\sigma_0/\sigma_u$, in which σ_u and σ_0 are the static strength and the fatigue limit, respectively; τ is a dimensionless parameter related to a characteristic time or number of cycle; and n is an exponent. τ and n are to be determined by curve fitting. The parameters in Eq.3 for the SN curve at 1 Hz were determined by curve fitting. It turned out to be $\tau=0.0004$ and $n=0.5$. The p_0 was estimated to be 0.55 based on the SN data at 1 Hz. In Fig.3, the SN curve at 1 Hz described by Eq.3 (the solid line) is compared with experimental data (symbols). As seen Eq.3 fits the data reasonably well over an entire stress range from the static strength to the fatigue limit.

The SN curves at elevated temperatures are estimated by shifting the reference SN curve,

$$p = b_T \left(p_0 + \frac{1-p_0}{(1+a_T\tau N)^n} \right) \qquad (4)$$

where a_T and b_T are the shifting factors defined earlier. In this work, the rotation shifting factor a_T was assumed to be 1. This assumption was based on literature data [1,2] which have shown that the slope of SN curves of angle-ply laminates remains almost the same over a wide temperature range. The vertical shift factor b_T was equal to the ratio of the static strength at temperature T to that at the reference temperature. For AS4/PEEK ±45 laminate, the following data are available in literature [3]:

Relative Tensile Strength of ±45 AS4/PEEK Laminate

Temperature (°C)	23	120	180
Relative Strength	1	0.75	0.65

The b_T values were determined by interpolation of the above data:

Temperature (°C)	40	75	110	135	175
b_T	1	0.9	0.82	0.75	0.67

A series isothermal SN curves generated using Eq.4 are plotted in Fig. 3, together with the reference SN curve.

Following the procedure presented above, iso-strength curves corresponding to 60%, 70% and 80% load levels are constructed in Fig.4. The predicted transient temperature curves for the three load levels are also plotted. The crossing points of these two groups curves at the same load level give the fatigue life, as shown by the crossing marks.

Figs.5 and 6 compares the fatigue life prediction for 5 Hz and 10 Hz with experimental results, respectively. The solid symbols in these two figures are the temperatures measured at the moment of fatigue failure. As seen, most of the data fall close to the predicted failure points. This supports a basic assumption in our prediction that the thermal effect is the dominant factor for the frequency dependence of the fatigue life for materials with large hysteretic heating.

As noted, the maximum temperature values in Table 1 appear to be controversy. The maximum temperatures measured on samples tested at 10 Hz somehow were lower than those measured at 5 Hz at the same load level. Also, the measured maximum temperatures were lower on samples tested at higher levels as compared to those at lower load level at the same frequency for 5 Hz and 10 Hz cases. Figs. 5 and 6 clearly indicate that the maximum temperature that might be reached in a fatigue test depends upon the number of cycles a sample can endure before failure and its value is predictable using the present scheme. The predicted maximum temperature rises are compared with the experimental average values in Table 2. As seen, the predictions are in a good agreement with the experiment. For 5 Hz cases, the predictions are within the scatter in experimental data. Lower value measured in 10 Hz tests might be due to the delay in heat transfer. Continue temperature rise after the load had been removed was noted in 10 Hz tests.

The temperature prediction capability in the present scheme has solved a key problem for models relying on curve fitting. To account for the hysteretic heating effect, the temperature rise has to be included as a variable in this type of models, either directly or indirectly. On one hand, using experimentally measured maximum temperature value will limit the predictive capability of a model. On the other hand, from analysis one can only predict the maximum equilibrium temperature but not the temperature at failure, i.e. the predicted maximum temperature rise is always higher for a sample tested at a higher frequency and load level. Actually, this problem cannot be solved by using a single equation.

The predicted fatigue lives are compared with the test results in Table 2. As seen, the predictions are in a good agreement with the experimental results for 10 Hz at 70% and 80% levels, and for 5 Hz at at 80% load levels, i.e. within the scatter of experimental data. The prediction overstimates the fatigue life at 60% load level for about 40% for 5 Hz and 80% for 10 Hz cases while underestimate the fatigue life at 5 Hz, 70% level for about 50%. Nevertheless, these predictions are still in a reasonably good agreement with experiment data considering the standard deviations of the data were about ±30% in our results.

REFERENCES

1. A.Rotem, H.G.Nelson, "Fatigue behaviour of graphite-epoxy laminates at elevated temperatures", Fatigue of Fibrous Composite Materials, ASTM STP 723, 1981, 152-173.
2. Y.Miyano, M.K.McMurray, "Loading rate and temperature dependence on flexural fatigue behaviour of a satin woven CFRP laminate", J. Composite Materials, Vol.28, No.13, 1994, 1250-1260.
3. F.N.Cogswell, Thermoplastic Aromatic Polymer Composites, Butterworth-Heinemann Ltd, 1992.

TABLE 1. FATIGUE TEST RESULTS FOR AS4/PEEK ±45 LAMINATE

Load Level (% of σ_u)	Frequency (Hz)	Number of Cycles To Failure	Maximum Temperature (°C)
60%	1	1,400,000*	34
		1,200,000*	32
65%	1	50,7000	-
70%	1	20,650	43
		16,000	40
		21,000	45
		18,800	46
80%	1	2,900; 3,000	45; 45
		3,850; 3,570	- ; 52
93%	1	1,500	-
60%	5	100,000	84
		186,000	84
70%	5	2,200 1,500	127; -
		1,100; 2,600	135; 152
		2,620	127
75%	5	350	100
80%	5	200; 220	110; 97
		200	108
60%	10	550; 575	152; 140
		1,040; 580	-
70%	10	450; 260	136; 95;
		280; 470	-; 119
80%	10	200; 180; 315	110; 102; 135
		120; 100	-; 90

* sample did not fail

TABLE 2 COMPARISON OF PREDICTED FATIGUE LIVES AND TEMPERATURE AT FAILURE WITH EXPERIMENTAL RESULTS

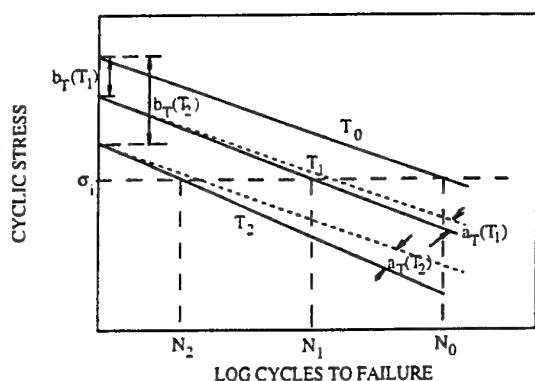| Load Level (% of σ_u)	Frequency (Hz)	Number Of Cycles To Failure		Temperature At Failure (°C)	
		Experiment (Mean±S.D.)	Prediction	Experiment (Mean±S.D.)	Prediction
60%	5	143,000±4300	200,000	84	79
70%	5	2,004±679	950	135±12	130
80%	5	207±11	235	105±7	101
60%	10	686±236	1230	146±8	200
70%	10	365±110	470	117±21	140
80%	10	183±85	190	109±19	101

*S.D.=standard deviation

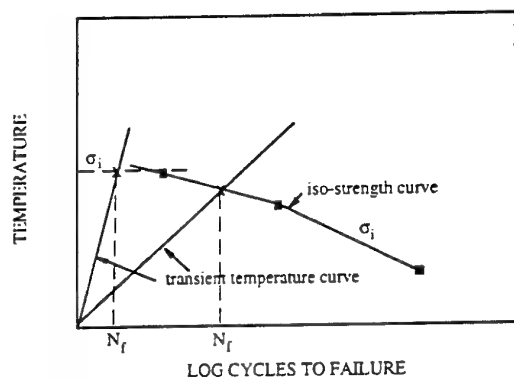Fig.1 Schematic isothemal SN curves and shifting factors.

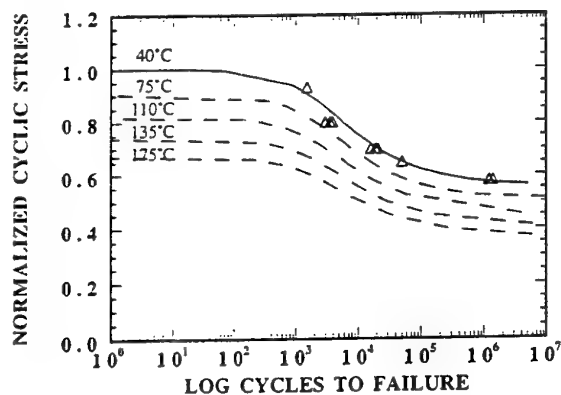Fig.2 A schematic iso-strength curve and the prediction of fatigue life for non-isothermal conditions.

Figure 3. SN curve fitting using Eq.3 (solid line) for 1 Hz data (symbols) and the iso-thermal SN curves obtained by shifting the reference SN curve using Eq.4 (dashed line).
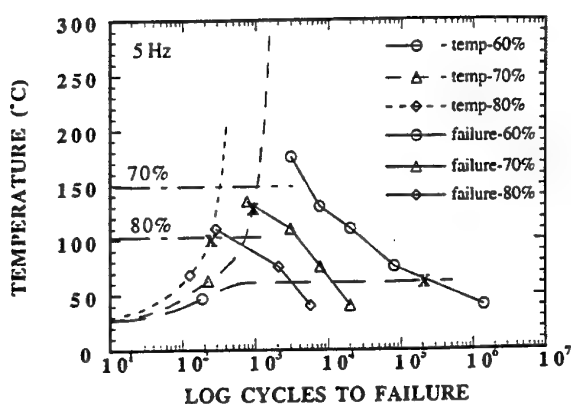

Figure 4. The iso-strength curves for 60%, 70% and 80% load levels and the fatigue life prediction for 5 Hz.
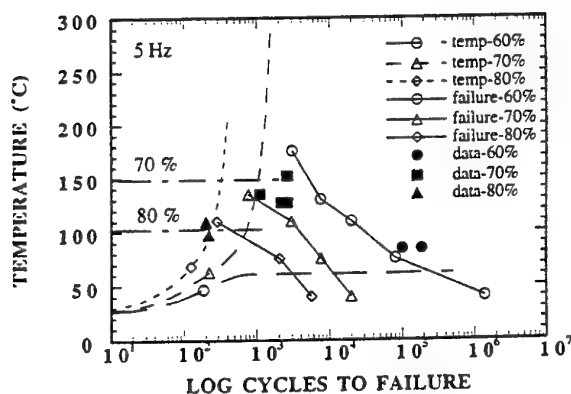

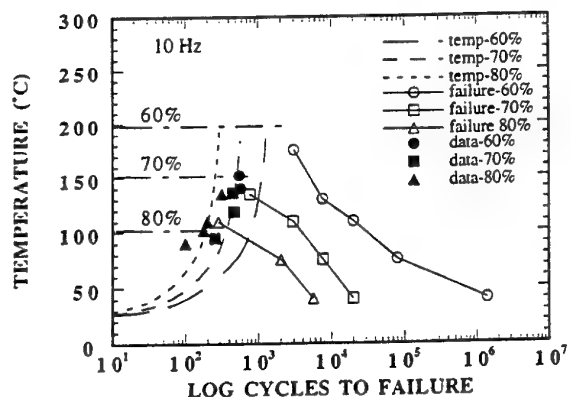Figure 5. Fatigue life prediction for 5 Hz. The symbols are experimental data.

Figure 6. Fatigue life prediction for 10 Hz. The symbols are experimental data.

Long Term Prediction of Fatigue Life for FRP Joint Systems

Masayuki Nakada, Yasushi Miyano, and Stephen W. Tsai [*].

Materials System Research Laboratory, Kanazawa Institute of Technology
Yatsukaho, Matto, Ishikawa 924-0838, Japan
* Department of Aeronautics & Astronautics, Stanford University
Stanford, California 94305-4035, U.S.A.

INTRODUCTION

The mechanical behavior of polymer resins exhibits time and temperature dependence, called viscoelastic behavior, not only above the glass transition temperature T_g but also below T_g. Thus, it can be presumed that the mechanical behavior of polymer composites and structures also significantly depends on time and temperature even below T_g which is within the normal operating temperature range.

The time-temperature dependence of the tensile failure load under constant elongation-rate (CER) and fatigue loadings for GFRP/metal conical shaped joint and GFRP/metal adhesive joint using brittle epoxy adhesives has been studied in our previous papers. It was observed that the fracture modes are almost identical under two types of loading over a wide range of time and temperature, and the same time-temperature superposition principle holds for CER and fatigue failure loads. Therefore, the master curve of fatigue failure load can be obtained from results of the CER tests under various CERs and temperatures and the fatigue tests at a single frequency under various temperatures. The fatigue failure loads of these GFRP/metal joints under a wide range of time and temperature can be characterized using the master curve of fatigue failure load.

In this paper, the tensile fatigue tests as well as tensile CER tests for GFRP/metal adhesive joint using ductile PMMA adhesives are carried out under various loading rates and temperatures. The time and temperature dependence of tensile fatigue behavior for this FRP joint is characterized by using the master curve of fatigue failure load and is compared with those for other joint systems mentioned above.

EXPERIMENTAL PROCEDURE

The GFRP/metal adhesive joint (FRP joint) was made from a GFRP pipe, ductile cast iron rod, and adhesive resin as shown in Fig.1. The adhesive resin is PMMA resin, PLEXUS® AO425 (ITW Adhesives). Ductile cast iron rod is made from ductile iron castings Grade 80-55-06 (ASTM A 536-84). The adhesive resin thickness and length of FRP joint are respectively 4mm and 28mm.

The tensile tests under CER and fatigue loadings were carried out for various loading rates and temperatures. The tensile CER tests were conducted at 5 testing temperatures between T=25 and 90°C by using an Instron type testing machine. The tensile load was applied at both end screws of the FRP joint. The loading-rates (crosshead speeds) were 0.01, 1, and 100mm/min. The tensile fatigue tests were conducted at 5 testing temperatures between T=25 and 70°C at a frequency f=5Hz, and 10, 50°C at f=0.05Hz, by using an electro-hydraulic servo testing machine. Load ratio R (minimum load/maximum load) was 0.05.
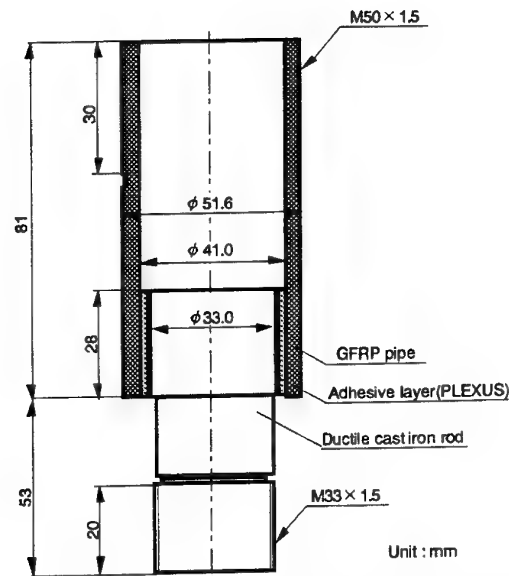
Fig.1 Configuration of GFRP/metal adhesive joint

RESULTS AND DISCUSSION

The CER and fatigue failure of FRP joint occurred in the adhesive resin nearby the interface between cast iron rod and adhesive resin. All failed specimens are similar regardless of loading pattern. We consider, therefore, that the failure mechanisms are the same for CER and fatigue loadings.

Master Curve of CER Failure Load

The left side of Fig.2 shows the tensile CER failure load P_s versus time to failure t_s at various temperatures for FRP joint, where the t_s is defined as the time period from initial loading to P_s in CER test. The master curve of P_s versus reduced failure time t_s' at a reference temperature $T_0 = 40°C$ as shown in the right side of Fig.1 were constructed by shifting P_s at various temperatures along the log scale of t_s until they overlapped each other. Since P_s at various temperatures can be superimposed smoothly, the time-temperature superposition principle is applicable for P_s.
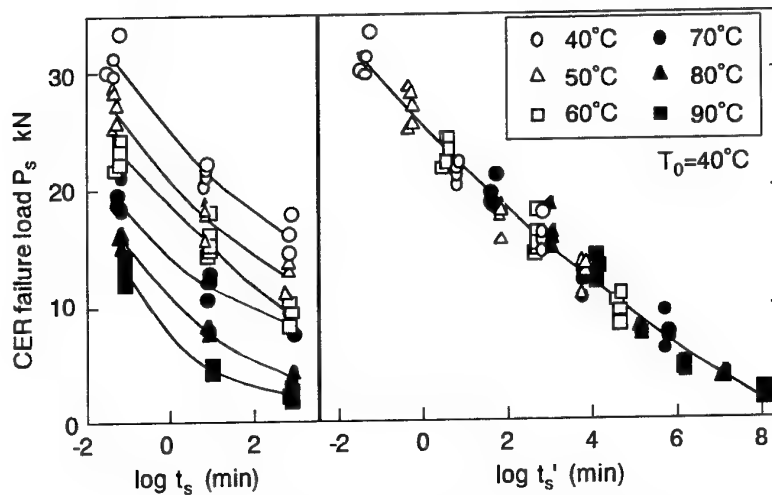

Fig.2 Master curve of CER failure load P_s

Figure 3 shows the time-temperature shift factor $a_{T_0}(T)$ for the master curve of P_s of FRP joint. The $a_{T_0}(T)$ is quantitatively in good agreement with Arrhenius' equation using two different activation energies. The dotted line in this figure shows $a_{T_0}(T)$ obtained experimentally for the creep compliance D_c of the adhesive resin. The $a_{T_0}(T)$ for P_s of FRP joint is slightly different from that for D_c of adhesive resin.
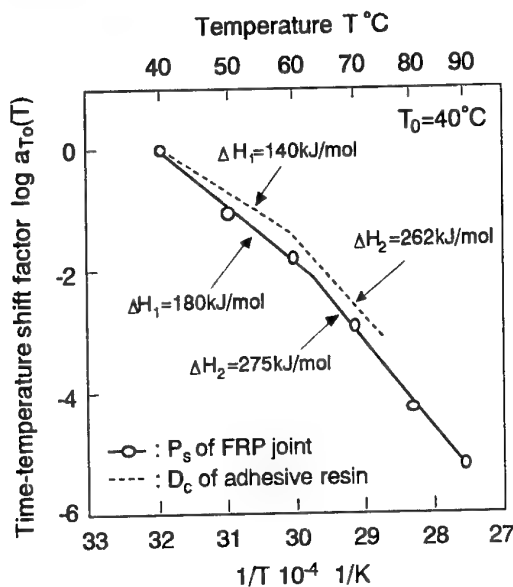
Fig.3   Time-temperature shift factor

Master Curve of Fatigue Failure Load

The tensile fatigue failure load P_f versus the number of cycles to failure N_f (P_f-N_f curve) for FRP joint at frequency f=5Hz are shown in Fig.4.   In this figure, P_f at N_f=1/2 corresponds to the CER failure load P_s at t_s=1/(2f).
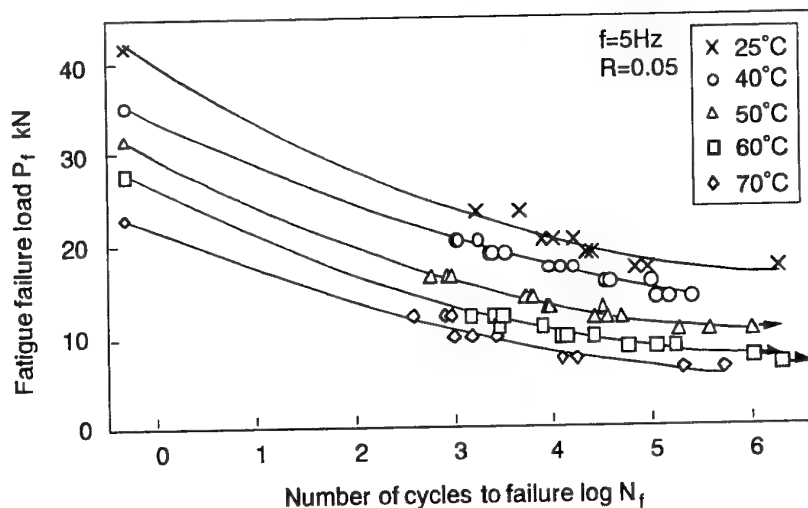
Fig.4 P_f-N_f curves at f=5Hz

The upper portion of Fig.5 shows P_f versus reduced time to failure t_f', where the t_f' is obtained from Eq.(1) based on the time-temperature superposition principle which holds for the CER failure load of this FRP joint.

Each point on these master curves of constant reduced frequency f' represents a number of cycles to failure.   Connecting the points of the same N_f with these curves, the master curves of P_f for constant N_f are constructed as shown in the lower side of Fig.5.

$$t_f' = \frac{t_f}{a_{T_0}(T)} = \frac{N_f}{f'}, \quad f' = f \cdot a_{T_0}(T) \qquad (1)$$

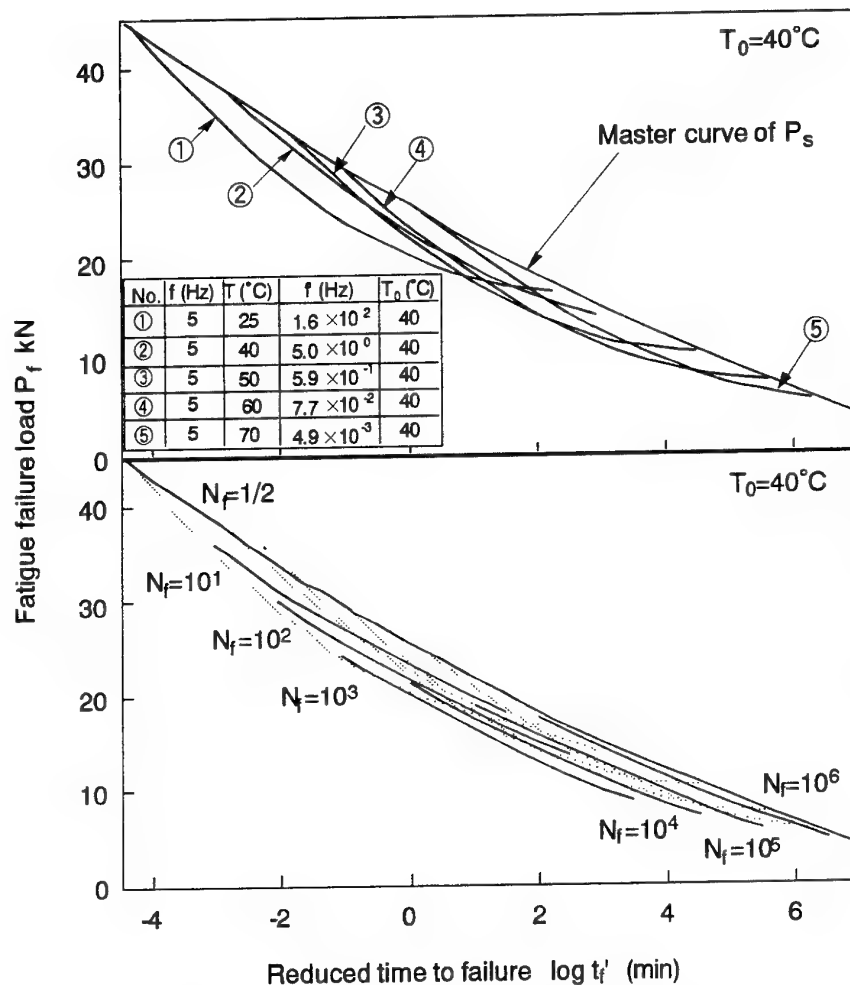| No.	f (Hz)	T (°C)	f' (Hz)	T_0 (°C)
①	5	25	1.6×10^2	40
②	5	40	5.0×10^0	40
③	5	50	5.9×10^{-1}	40
④	5	60	7.7×10^{-2}	40
⑤	5	70	4.9×10^{-3}	40

Fig.5   Master curves of fatigue failure load P_f

Comparison of the Master Curves of Fatigue Failure Load

Figure 6 shows the master curves of tensile fatigue failure load for GFRP/metal conical shaped joint and GFRP/metal adhesive joints using brittle epoxy adhesives and ductile PMMA adhesives.   The tensile fatigue failure load for the GFRP/metal conical shaped joint depends slightly on time to failure and temperature, however the fatigue failure load decreases remarkably with increasing number of cycles to failure N_f.   The tensile fatigue failure load for the GFRP/metal adhesive joint using brittle epoxy adhesives depends on both time to failure (temperature) and N_f.   The fatigue failure load for GFRP/metal adhesive joint using ductile PMMA adhesives depends remarkably on time to failure and temperature, however the fatigue failure load decreases scarcely with increasing N_f.
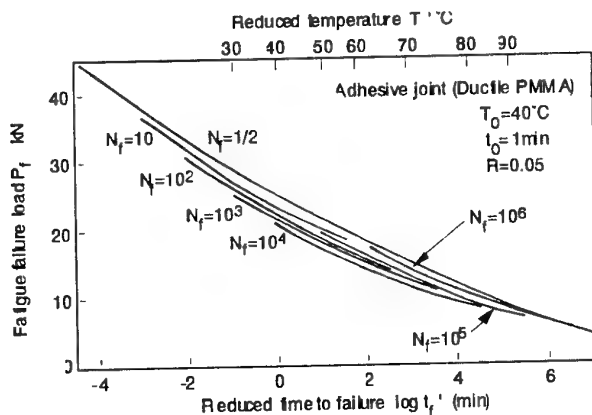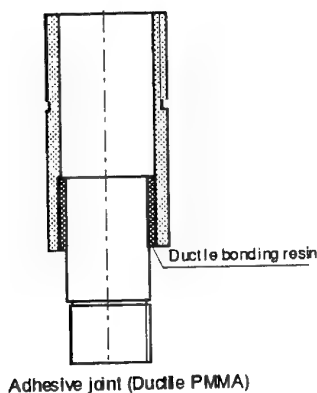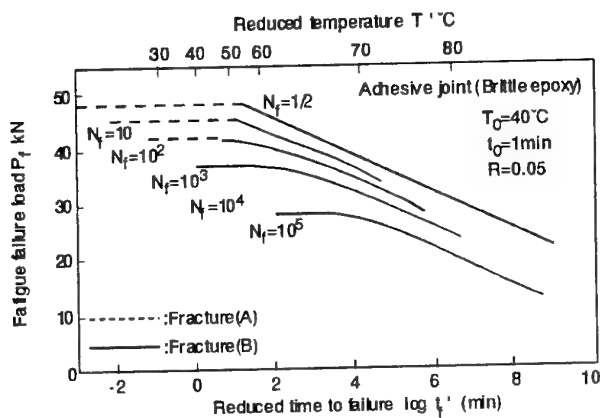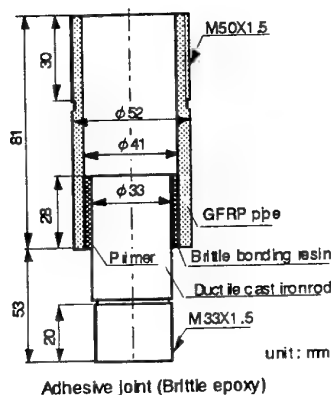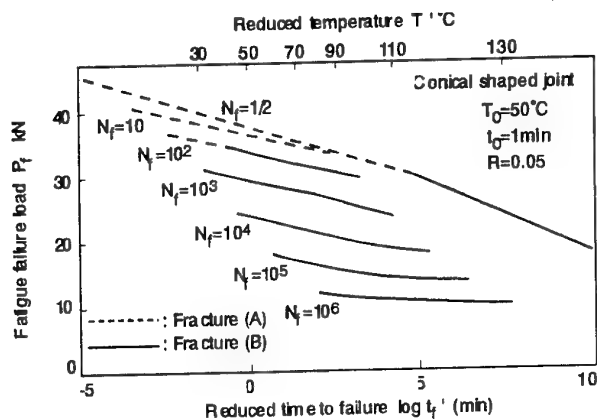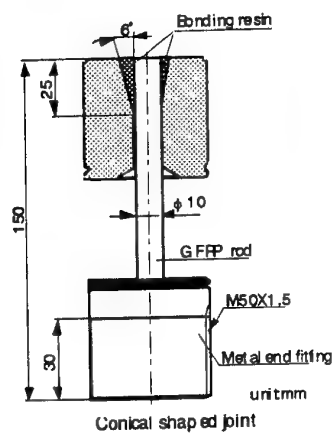
Fig.6   Comparison of the master curves of fatigue failure load

CONCLUSION

The time and temperature dependence of tensile fatigue behavior for GFRP/metal adhesive joint using ductile PMMA adhesives is determined experimentally and is compared with those for other joint systems, GFRP/metal conical shaped joint and GFRP/metal adhesive joint using brittle epoxy adhesives.   The time-temperature superposition principle holds for tensile fatigue failure loads for all of these joints, therefore, the master curves of fatigue failure load for these joints can be obtained.   The master curves of fatigue failure load show very characteristic behavior due to the structure and the combination of materials of joints.

Failure of Laminated Composites at Thickness Discontinuities Under Complex Loading and Elevated Temperatures

S. Lee[1] and W. G. Knauss[2]
Graduate Aeronautical Laboratories
California Institute of Technology
Pasadena, CA 91125 USA

A recurring problem in designing structures with fiber reinforced composite materials is the potential failure at thickness variations in the lay-up associated with the induced stress concentrations. Such questions arise in connection with stress variations in the vicinity of geometric discontinuities in the ply drop-off problem as well as with attachments of stringers and other frame structures to the skin of aircraft, for example. Within the framework of solid mechanics any failure emanating from "sharp" corners elicits immediately the vision of stress singularities and analyses associated with the discipline of fracture mechanics. The stress field surrounding a step discontinuity in a composite was of the form $\sigma_{ij} = \Psi_{ij} r^k$. This solution was valid, however, only for distances of less than $10^{-1} \mu m$ from the corner. Considering that the diameter of an individual fiber is about 5-7 μm, the power law is valid in such an extremely small region that continuum concepts for "smeared-out" ply properties are not applicable. Consequently, one must call the treatment of failure from a corner in a composite lay-up by means of singularity analyses into question. From a design point of view it is desirable to evaluate structures in terms of "strength of materials" loads such as moments, (average) shear and tension stresses. At issue is thus whether a failure criterion can be established that lends itself to structural applications. Even if the basis of such a criterion rests ultimately in the mechanics at the micron or submicron scale, it may be possible to identify a structural or "macroscopic" criterion or criteria, such that subsequently a minimum of test data suffices to establish a design guide. The tenor of this study is primarily experimental in nature, with, however a strong component of numerical analysis to examine an analytical basis for the observed failure behavior.

Four types of specimens with different stacking order are made of AS4/3502 carbon fiber reinforced epoxy. All of the specimens were fabricated as a single, stepped plate, which was then cut into strips after the curing/cooling cycle was completed. Each of the cut specimens was C-scanned to ensure that no delaminations nor inclusions were present. For ready visualization of the interface arrangement these are also depicted in Figure 1 without recording all of the laminae far from the interface. Two devices were designed to apply combined loads to the specimens. One of these devices employed the tension/torsion modes of an MTS testing machine to provide tension and bending by converting the twisting motion through linkages into lateral loads so as to impose bending and tension loads in arbitrary sequence (non-proportional loading). A second device provided tension and bending in proportional loading through mounting the specimen eccentrically and subjecting the grips to tension only. By adjusting the off-set, a range of bending/tension combinations is achieved, including zero bending. The operation of this appliance was much simpler than the previous one, and was used primarily. At room temperatures observations of failure initiation were made with the aid of a microscope while the specimen was under load. Attachment of an optical camera to the microscope and a polished surface finish on the specimen edge allowed thus the recording of the various features in the damage development during the (room temperature) tests.

---

[1] Graduate Student
[2] Professor of Aeronautics and Applied Mechanics

A summary of the failure patterns associated with the four stacking sequences is sketched in Figure 1. Depending on the stacking sequence next to the "interface" of the step either transverse ply cracking or delamination occurs. Specimen containing fiber orientations on either side of the "interface" and having an orientation component deviating (significantly) from the zero direction (specimen Types I, II, and III) fail by ply-fracture normal to the fiber orientation in the top ply of the plate. On the other hand, when the interface between the steps is contained between two layers of zero-oriented fibers (specimen Type IV) a delamination-type failure results. The interaction between moment and tension at failure initiation for the two lay-ups I and IV are presented in Figure 2. We note that in spite of the large deformations, the interaction between moment and tension at failure is roughly linear (Types I, II, and III) and parabolic (Type IV). The specimens exhibiting the delamination mode of failure (Type IV specimens) provided the highest strength as measured by load carrying ability. They are nearly twice "as strong" as the other types of specimens which failed by ply fracture. However, the "stronger" configuration allowed for a markedly smaller (10%) difference between loads at failure initiation and final (total) failure than the ply-failure modes; the latter provided an additional load carrying capability of about 20 to 30% beyond that at failure initiation.

We take recourse to finite element analysis for examining the conditions prevailing at failure initiation. The analysis was fully three-dimensional, each lamina being represented by a homogeneous, anisotropic medium; use of the ABAQUS code typically involved over 13,000 degrees of freedom for the base problem on a Cray 90. Both stress (strain) criteria in terms of the Tsai-Hill criterion as well as a discretized energy release rate approach have been used to analyze the data. To inquire whether a common criterion exists for the failure initiation process in all specimens, we pursue both criteria for all test situations; however, it will be found that no single set of material failure parameters for either type of failure characterization describes the data unequivocally, though broad rules for analysis can be outlined. We note that either criterion provides for an essentially linear interaction between tension and bending for Types I, II and III, but a roughly parabolic characteristic for those of Type IV. Although the functional representation of the failure data by the energy criterion appears to be good, one must question this uniformity in terms of the single-valuedness of the energy release rate parameter. Type I and II specimens should involve essentially the same parameter by virtue of the fact that the lay-up is very similar. Apart from this similarity, there are then three groups of specimens which involve significantly different energy parameters: Specimens I and II yield 140.5 J/m^2, Type IV requires 212.0 J/m^2, and Type III specimens are consistent with a value of 14.0 J/m^2. Clearly, this "problem" invites further attention. On the other hand, the Tsai-Hill criterion produces a correlation with the test data through a single set of material parameters, which, however, does not replicate the shape of the interaction curve very well for the type IV specimens.

The same procedures were followed to investigate failures under elevated temperatures for several of the stacking sequences. Two temperatures, 100°C and 150°C, were chosen, considering that the glass transition temperature of the matrix is 198°C. In the range studied, the effect of temperature on the failure manifests itself primarily in a lowering of the load levels, leaving the modes of failure unaltered. While at temperatures within a few degrees of the glass transition this behavior may change, particularly as the result of more time dependent material response, in the presently used environment higher temperatures primarily reduce the material strength. The finite element analysis accompanying the high temperature experiment accounted for both the mechanical loading as well as for temperature induced stresses, assuming the specimens to be stress-free at 25°C. Changes in the mechanical properties with temperature were also taken into account. This critical energy value of Type IV specimens dropped by about 0.7 J/m² per degree °C.

2

Figure 1. Failure modes

(a) Type I

(b) Type IV
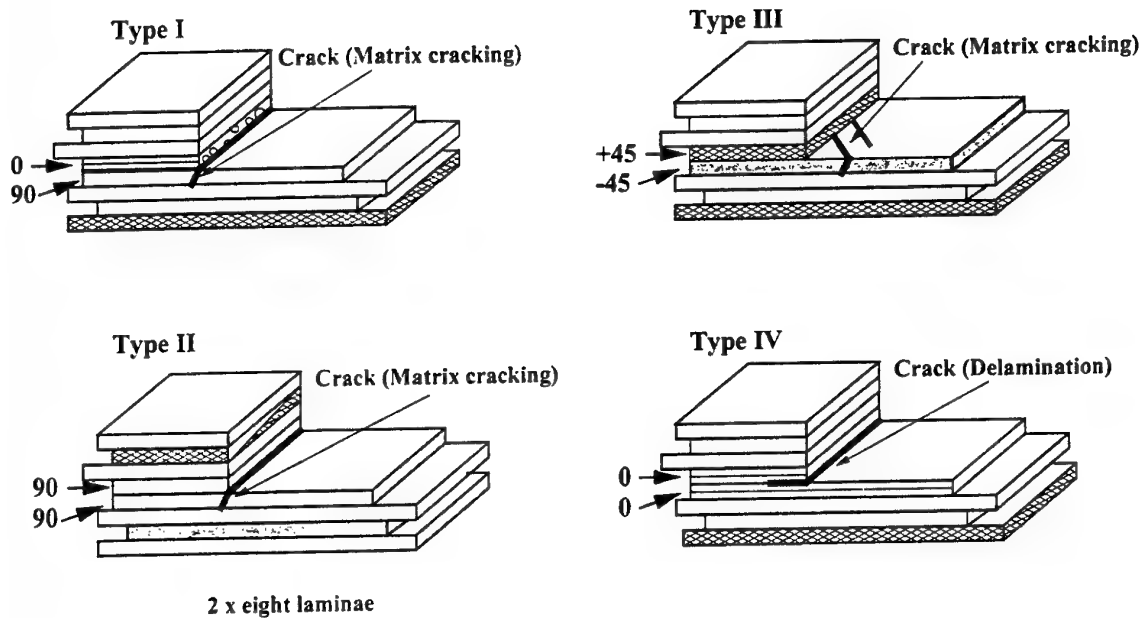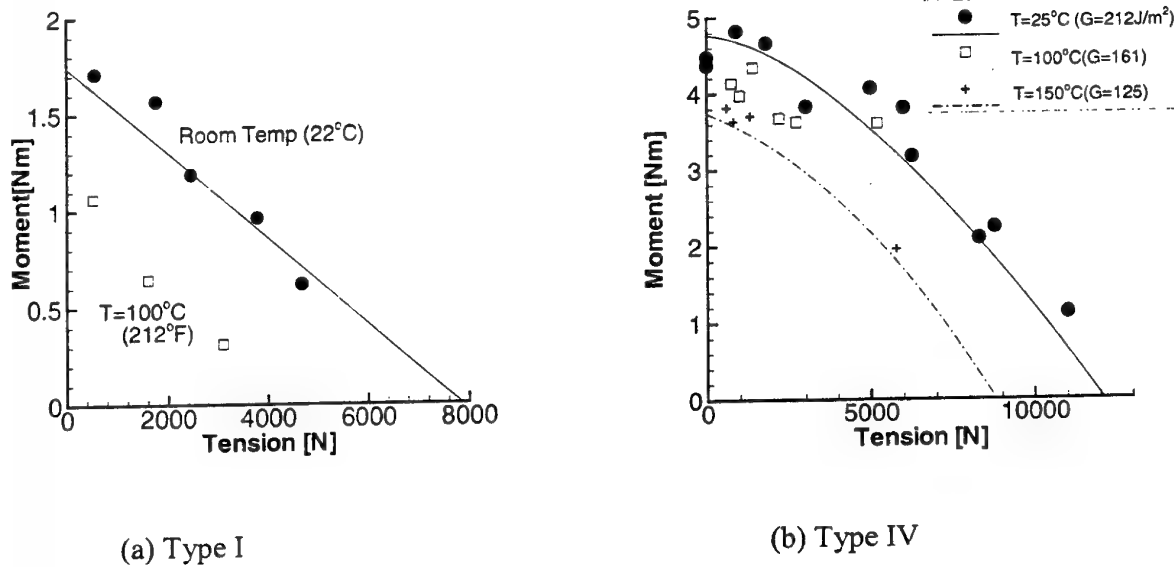
Figure 2. Moment-tension interaction at failure initiation for Type I and IV specimens

Durability Assessment of Polymeric Composites for High Speed Civil Transport

Thomas S. Gates
NASA Langley Research Center
Hampton, Virginia, 23681 USA

ABSTRACT

The NASA High Speed Research (HSR) Program was conceived as a means for NASA and the United States aerospace industry to develop the technology necessary for the eventual design and construction of a new generation High Speed Civil Transport (HSCT). The HSCT was envisioned as a 300 passenger, supersonic aircraft capable of servicing the Pacific Rim market. One of the critical technologies required by such a revolutionary aircraft was in the area of Composite Materials Durability.

The overall objective of the Materials Durability task for HSR was to demonstrate the ability of candidate materials to withstand the harsh environment associated with a HSCT flight vehicle. It was recognized that materials used on a HSCT aircraft must withstand exposure to mechanical loads, elevated temperatures, and other environmental factors for up to 60,000 flight hours without significant degradation of mechanical properties. The HSCT vehicle was envisioned with a design life of 72,000 flight hours and will require materials capable of withstanding a maximum temperature of 350°F during Mach 2.4 flight.

In the HSR Materials Durability program, tests were conducted to develop a material durability database for selected composite materials. A material selected for testing either showed promise for eventual application on a HSCT or were representative of classes of materials such that they could provide validation data for analytical models of durability performance. The database included data on the properties of these materials after short-term and long-term exposure to the HSCT mechanical, thermal, and chemical environments. Testing programs were designed to determine the degradation in material properties due to each of the elements of the HSCT environment and the extent of synergistic effects due to simultaneous exposure to multiple elements. Composite material properties of interest included static strength, elastic modulus, fatigue life, solvent resistance, creep resistance, and residual strength. Standard test specimen configurations and procedures, conforming to the High Speed Research Composites Durability Test Guide and Recommended Test Procedures documents, were used whenever possible. Thermal-mechanical fatigue test profiles were also developed for use in mission simulation tests. Potential NDE methods for detecting manufacturing flaws and degradation due to test environments were evaluated in the course of making and testing specimens.

It was expected that materials chosen for this vehicle would experience at least one lifetime of loads, temperatures, and environments typical of the HSCT before production go-ahead was given. Considering that a 60,000-hour exposure test will require at least 7 years of testing time, it is not likely that all of the necessary information could be obtained in real-time testing. The prohibitive times and costs of testing for 60,000 hours necessitated the development of accelerated test methods and durability performance prediction methods.

Verified accelerated test methods were needed to accurately and economically assess the long-term durability performance of new materials and to provide guidance for structural testing. Life, strength, and stiffness predictive models were required for design because adequate databases for all stress/temperature/time scenarios cannot be established.

Accelerated aging methods were also required to allow the introduction of new materials later in the program. Comparing mechanical properties, damage modes, and physical parameters, such as weight loss, with those from specimens tested under real time conditions allowed for validation of the empirical and semi-empirical accelerated methods. The development of accelerated aging profiles required extensive testing to define critical parameters and their interactions that drive physical aging and chemical degradation. This testing provided the insight into how these materials behave and allowed for the development of analysis methods to predict material performance when subject to different combinations of load, temperature, and environment. Options have been explored for changing the test parameters from the expected HSCT operational values in order to reduce the test time required to achieve a desired end-state damage, but without changing the damage mechanisms identified for the operational environment.

Degradation mechanisms associated with elements of the operating environment were identified and quantified in the initial exploratory test programs. Predictive modeling strategies were selected to account for the effects of the degradation mechanisms on fatigue life, stiffness, and residual strength. The predictive models are being evaluated and refined as necessary as the program progresses by comparing predictions to results from accelerated and long-term tests.

Therefore, the specific objectives of the Materials Durability program were to:

1) generate a limited short-term and long-term (up to 60,000 hours) durability database for selected materials

2) develop and verify accelerated test methods that will experimentally simulate long-term durability performance

3) develop and verify analytical methods that will predict long-term durability performance

4) develop a set durability validation protocols.

This paper will provide an overview of the progress in technology development in these four objectives by relating program issues unique to composite materials durability for HSCT, discussing recent developments in analytical and experimental methods, and providing work-in-progress results of selected program elements.

Investigation into honeycomb durability through an in-flight service evaluation

J. C. Seferis

Polymeric Composites Laboratory, Department of Chemical Engineering, University of Washington, USA.

ABSTRACT: Thirteen commercial wing panels were fabricated and flown on a commercial aircraft to investigate the mechanisms of water migration through various honeycomb cores. A 12.2 J impact damage was not observed to cause damage propagation in aluminum and Korex® honeycomb materials. This was attributed to the ability of the cores to localize the impact damage. In Nomex® and fiberglass cores a different damage propagation mechanism was observed. In these cores, the damage was not confined to the localized area around the impact. Instead, facesheet and core damage was seen as far as 2.6 cm from the point of impact. This increased core damage allowed the core to retain water. The retained water helped propagate the impact damage through a freeze thaw mechanism. Speed tape repairs were only found to be statistically significant when water migrated through the core. Ultimately this work provides the tools for understanding and developing damage and water tolerant honeycomb structures.

1 INTRODUCTION

When honeycomb composite structures are fabricated for the aerospace industry, they are designed to be closed to their operating environment for the life of the composite structure (Coggeshall, 1983). Although, once in-service, this design often breaks down. Airline operators sometimes find that composite honeycomb structures absorb and retain large amounts of water while in-service. Water absorption in honeycomb composite structures represents a large problem for aircraft operators. It can cause mechanical deterioration of honeycomb core, delamination of the facesheet from the honeycomb core and increased operating and maintenance costs for the composite structures (Abrate, 1997).

Several researchers have investigated water ingression and migration through honeycomb core, but no investigators have attempted to statistically understand the mechanisms of water ingression and migration through honeycomb core as a function of in-service cycling (Cise & Lakes, 1997; Wong & Abott, 1990; Jackson & O'Brian, 1988). This paper represents part two of a two-part investigation to study the scope and mechanisms of water ingression and migration through honeycomb core. In the first part of this study, the extent of honeycomb water ingression problems were explored. An investigation was conducted to determine whether water ingres-

sion is a localized problem which occasionally occurs, or whether water ingression in honeycomb sandwich structure represents a systemic composite problem. (Shafizadeh et al, submitted) To quantify the extent of water ingression and migration problems, non-destructive infrared thermographic inspections were performed on 35% of United Airlines Boeing 767's. The second part of this study focuses on a Design Of Experiment (DOE) to understand how water migrates through the core once it is ingressed. For the DOE, an in-flight service evaluation was conducted on thirteen outboard fixed trailing edge panels. From these panels, the effects of core type, impact damage, and tarmac repair procedures were examined. Together, these studies represent the most comprehensive attempt to understand the in-service durability of honeycomb structures. Ultimately the research performed in these two studies will aid in the understanding and design of future honeycomb composite sandwich structures.

2 EXPERIMENTAL *PROCEDURE*

2.1 *Panel Fabrication*

A total of sixteen modified Boeing 767-200 upper wing fixed trailing edge panels were fabricated and flown to study the mechanisms of water ingression and migration through honeycomb core. Upper wing

fixed trailing edge panels were chosen for study due to their ease of fabrication and location on the wing. As shown in Figure 1, these panels are located on the outboard section of the wing behind the rear spar.

The wing fixed trailing edge panels are lightly loaded wing panels and are manufactured with fiberglass facesheets and honeycomb core. The facesheets of the panels were fabricated from Hexcel F-155 prepreg qualified to Boeing Material Specification (BMS) 8-79 (Anon, 1989). The F-155 prepreg used was a 121°C cure, self-adhesive, epoxy based, prepreg system which was impregnated in a 7781 style fiberglass fabric. The panels were constructed using a vacuum bagging process where five plies of prepreg were used on the tool, or aerodynamic, side of the panel.
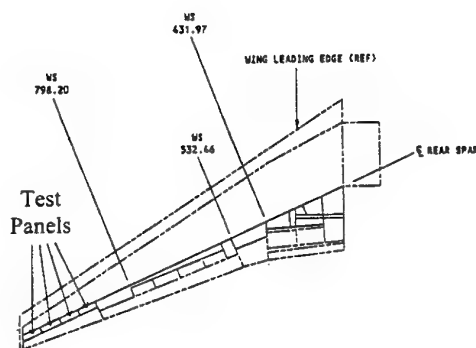

Figure 1. Diagram showing the wing location of the upper wing fixed trailing edge test panels (Anon, 1994).

The honeycomb core bays used in production trailing edge panels are fabricated from 3.2 mm cell size Nomex® honeycomb core with a nominal density of 50 kg/m^3. In this study, the usual Nomex honeycomb material was substituted with one of four different types of honeycomb core which included aluminum, Korex®, Nomex and fiberglass based cores. The Nomex, fiberglass, Korex and aluminum cores used were all provided by Hexcel and had the following respective Hexcel designations: HRH-10-1/8 3.0, HFT-1/8-3.0, Korex-1/8-3.0, and CRIII-1/8-5052-0.001-4.5. The cell size on all honeycomb cores was 3.2 mm and all cores had a nominal density of 50 kg/m^3, except the aluminum core. The aluminum core had a nominal density of 75 kg/m^3 and was anodized with phosphoric acid to prevent corrosion

In production upper wing fixed trailing edge panels, the size of the honeycomb core bays ranges from 99 to 39 cm in length and 27 to 33 cm in width. In modifying the honeycomb core bay materials, the overall size of the core bays was fixed by Boeing specification drawings. Therefore all modified core bays had to conform to the dimensions of

the production core bays. In complying with this design constraint, the overall size of the core bays was divided into one, two or three smaller core bays, or sub-bays. The core sub-bays were manufactured from the different core materials listed above and spliced together with a foaming adhesive from Sovereign Specialty Chemicals (PL 685). After the bays were spliced together a 20° chamfer was machined out of the core to match the part specification drawings. The spliced core bays had the same dimension as the original production core bays. Each sub-bays was approximately 650 cm^2 in size. After fabrication, the wing panels were installed on two different United Airlines 767-200s and flown on domestic US routes for fourteen months.

2.2 Design of Experiment

In order to statistically understand and isolate the mechanisms of water migration through honeycomb core, a Design of Experiments (DOE) was constructed. The DOE was fabricated to study the interactions between different honeycomb core materials and the honeycomb operating environments as a function of core composition, damage size and limited repair procedures. The DOE is outlined in Table 1. The face sheets over each core bay were intentionally compromised to allow water into the honeycomb core and create a known leak path for water ingression. Three holes, 1.6 mm in diameter, were drilled in the center of the aerodynamic facesheet of each core bay. The holes were drilled in the centers of three adjacent core cells forming a triangle with the centers of the holes located 3.2 mm apart.

Table 1. DOE for evaluating the effects of core material, impact damage and speed-tape repair as a function of water migration and damage growth.

Core Bay	Core	Speed Tape	Impact	Plane
1	Korex	No	Yes	A
2	Nomex	No	No	A
3	Fiberglass	Yes	No	A
4	Aluminum	Yes	Yes	A
5	Aluminum	No	No	A
6	Korex	Yes	No	A
7	Nomex	Yes	Yes	A
8	Fiberglass	No	Yes	A
9	Korex	No	No	B
10	Korex	Yes	Yes	B
11	Nomex	Yes	No	B
12	Nomex	No	Yes	B
13	Fiberglass	No	No	B
14	Aluminum	No	Yes	B
15	Aluminum	Yes	No	B
16	Fiberglass	Yes	Yes	B

Some honeycomb bays were also impacted to study the growth of impact damage as a function of

water migration through the core. According to the Structural Repair Manual (SRM) for the Boeing 767-200, the maximum allowable damage size before a repair is necessary for a single damage site in a honeycomb core area is 5.1 cm (Anon, 1994). The panels were damaged such that all damage locations were approximately the same size. The panels were damaged with an impact drop tower. The impact energies and damage sizes for each core bay are presented in Table 2.

Table 2. Impact energies and their resultant honeycomb bay damage sizes.

Core Type	Core Bay	Impact Energy	Damage Size (Diameter)
		J	cm
Nomex	7, 12	8.1 J	2.14
Korex	1, 10	12.2 J	2.09
Aluminum	4, 14	12.2 J	2.00
Fiberglass	8, 16	4.1 J	3.53

The effectiveness of speed tape repairs to prevent water ingression through a known ingression path was also explored in the DOE.. In a speed tape repair, the damaged area is cleaned with an appropriate solvent and an aluminum foil tape is applied over the damaged area. For the modified fixed wing trailing edge panels, a square 103 cm² piece of speed tape was place over the holes or damage location before the panels were installed on the aircraft. Two core bays of each construction were manufactured to insure result reproducibility.

2.3 Panel Inspection

Before and after the in-flight service evaluation, through-transmittance ultrasound (TTU) inspections were performed on the panels to measure the size of the damaged area in each honeycomb core bay. During the TTU inspections, the panels were scanned with waterjet coupled transducers 1.91 cm in diameter. The panels were scanned at a rate of 25.4 cm/sec at a frequency of 1 MHz while being indexed in increments of 4.06 cm.

While cycling for fourteen months on the two 767 aircraft, the panels saw an average service time of 4,400 flight hours with 2 takeoffs and landing per day with an average flight time of 5 hours per takeoff. After the in-service cycling, the panels were removed from the aircraft and a 420 cm² square was cut from the center of each core bay. The individual core bays were weighed and dried in a vacuum oven at 75°C under a constant pressure of 4.8 kPa for 121 hours. After drying the core bays were weighed and the difference between the initial and final weights was reported.

3 RESULTS AND DISCUSSION

There are two basic statistical models for analyzing and interpreting Design of Experiments: factorial models and hierarchical models (Hicks, 1982). Factorial models assume that all of the measured response variables can be analyzed independently of their source of variance. Hierarchical models assume that the response variables are interrelated with their respective sources of variance. In understanding the response of different honeycomb cores to water absorption and impact damage, a hierarchical model must be applied. The mechanisms of water migration and damage growth in honeycomb composite structures are unique to each type and density of core. Subsequently, the sources of variance must be analyzed as a function of core type. In Table 3, the statistically significant variables that affect the water absorption characteristics of the different honeycomb cores are presented.

Table 3. Statistical analysis of variance for water absorption of different honeycomb cores using a hierarchical DOE model.

Source of Variance	Core Type			
	Aluminum	Korex	Nomex	Fiberglass
Location				
Impact			XX	XX
Speed Tape			X	XX
Impact & Speed Tape			X	XX

XX – Significant at 1% confidence level
X – Significant at 5% confidence level

As shown in Table 3, the locations of the individual core bays on the aircraft were not found to play a statistically significant role in water absorption. This is an important non-factor because it indicates that all core bays experienced comparable flight conditions during the fourteen-month service evaluation, independent of the individual aircraft's flight schedule or the location of the bays on the aircraft.

The absorption of water by the aluminum and Korex core bays was also found to be unaffected by a 12.2 J impact. The lack of an affect may be attributable to a few possible causes. It is first possible that the panels were not in service long enough to allow sufficient time for damage propagation. Korex and aluminum are relatively strong web materials when compared to Nomex and fiberglass. These materials may have required a longer service time to reveal the degradative effects of continuous environmental cycling.

It is also possible that while in service, water did not accumulate or remain in the core bays long enough the significantly damage the core. In Figures 2 and 3, photomicrographs of the impact damage to the aluminum and Korex core bays are shown. For

these composite structures, the damage to the honeycomb cores and facesheets extended only one or two cells beyond the point of impact. Outside the small damage area, the core and facesheet were unaffected by the impact, as confirmed through optical microscopy. The localization of the impact damage prevented the creation of a volumous reservoir for the accumulation of water inside the core. By minimizing the amount of water in the cells the detrimental mechanical effects from the water continually freezing and thawing were diminished.

Figure 2. Photomicrograph of an aluminum core bay impacted with 12.2 J at 25X magnification.

Figure 3. Photomicrograph of a Korex core bay impacted with 12.2J at 25X magnification.

The localization of the impact damage may have also aided in removing the water from the core during flight. During flight, high-speed air flowing over the damaged honeycomb core bays creates a negative pressure gradient inside the honeycomb core (Giancoli, 1988). This pressure gradient will lower the vapor pressure of the water or ice and increase the rate of evaporation or sublimation. Because all of the water in the panel was confined to a small area near the point of ingresssion, most of the water could be removed through this mechanism.

For the Nomex and fiberglass cores, impact damage was found to have a statistically significant effect on water ingression and migration through the sandwich structure. This is attributed to the mechanism of damage propagation through the core. When the Nomex honeycomb composite structure was impacted, both the core and facesheet sustained a great deal of damage, as shown in Figure 4. In this figure, only the area immediately surrounding the impact location is shown, however, small microcracks

could be observed in the honeycomb core as far away as 1.5 cm from the impact location. The relatively weak nature of the sandwich structure delocalized the impact and resulted in extensive damage around the impact. This allowed water to migrate away from the ingression point and further into the core. At altitude, the pressure gradient for water removal is largest around the point of ingression. As the distance from the impact location increased, the pressure drop from cell to cell decreased and the effective driving force for water removal decreased. The net result was a greater amount of water retained by the honeycomb core. Retained water can cause freeze-thaw damage in the core, which further damages and fractures the core, and ultimately increase the water retention volume of the core.

Figure 4. Photomicrograph of a Nomex core bay impacted with 8.1 J at 25X magnification.

Figure 5. Photomicrograph of a fiberglass core bay impacted with 4.1 J at 25X magnification.

For the honeycomb composites manufactured with fiberglass core, a similar story can be told. After being impacted, the facesheets of composite structures microcracked and small sections delaminated, as shown in Figure 5, but unlike Nomex, the facesheet damage was limited to the immediate area around the impact. Although, the facesheet did not show extensive damage, the core and the skin-to-core fillets were observed to have widespread failures. From the TTU inspections, the initial diameter of the core damage was observed to be 3.53 cm, but through microscopy, buckling and small mi-

crocracks were observed to extend as far as 2.0 cm from the center of the impact. From the photomicrographs and TTU inspections, it can be concluded that the fiberglass core absorbed the brunt of the impact damage. The fiberglass core sustained a greater amount of damage than the Nomex, Korex or aluminum cores in spite of the fact that smaller impact energies were used on the fiberglass cores. The larger amount of core damage allowed a greater amount of water to be trapped within the core. The extensive damage away from the small impact center also reduced the ability of the core to dry during flight, as described earlier.

Speed tape and speed tape over an impact were not found to be significant factors for the absorption of water in the aluminum and Korex cores. The accumulation of water in the core can be viewed as function of the volume of core damaged or compromised during the service life of the composite parts. If the impact damage did not grow over time and was not found to be a significant factor then a repair over the damaged area should also have no effect. Speed tape alone should also have no effect if water did not accumulate in the core over time.

Speed tape and speed tape over an impact were found to play a role in the absorption of water by the fiberglass and Nomex cores. The fact that speed tape alone played a role implies that water was able to enter and different honeycomb cores during the fourteen-month service evaluation, even though it did not affect the Korex or aluminum cores. From the analysis of variance, the speed tape and speed tape with repair were found to have negative correlation coefficients. The negative correlation coefficients imply that the speed tape decreases the tendency of the parts to absorb water. However it only played a role when water migration through the core played a role.

4 CONCLUSIONS

In this work, the mechanisms of water ingression and migration through honeycomb core were explored using an in-service Design of Experiment. The effects of impact damage and speed tape repair on water absorption and damage propagation through the core were investigated for four different honeycomb cores. When fiberglass and Nomex based sandwich panels were impacted, extensive damage was seen throughout the facesheet and core. This damage allowed water to accumulate in the core and migrate through a freeze-thaw mechanism. For Korex and aluminum cores, the impact damage was localized around the point of impact. The localization of this impact allowed the core to dry during flight. From the air flowing over the impact

location, a negative pressure gradient was created inside the core. This pressure gradient provided a driving force for the removal of water around the point of impact. This effect was not seen in the Nomex or fiberglass cores due to the extent of damage. In addition, speed tape repairs were found to be an effective repair only when water was found to migrate through the core. From these investigations it can be shown that damage and water alone are not sufficient for the propagation of water through honeycomb core. Other factors, such as core type and damage size, need to be considered in evaluating the durability of honeycomb composite sandwich structures.

6 REFERENCES

Abrate, S. 1997. Localized impact on sandwich structures with laminated facings. *Applied Mechanics Reviews* 50(2): 69-82.

Anonymous 1989. *Boeing material specification 8-79 for 250°F epoxy prepreg systems.* Seattle: Boeing Commercial Airplane Group.

Anonymous 1994. Boeing 757-200 structural repair manual. Seattle: Boeing Commercial Airplane Group.

Cise, D. & R. S. Lakes 1997. Moisture ingression in honeycomb core sandwich panels: directional aspects. Journal of Material Engineering and Performance, 6(6): 732-736.

Coggeshall, R. L. 1983. Service experience with composites on Boeing commercial aircraft. 15th National SAMPE Technical Conference 15: 310-320.

Giancoli, D. G. 1988. Physics for scientists and engineers, Englewood Cliffs: Prentice Hall.

Hicks, C. R. 1982. *Fundamental concepts in design of experiments.* Orlando: Saunders College.

Jackson, W. C. & T. K. O'Brien 1988. Water intrusion in thin-skinned composite honeycomb sandwich structures. *Journal of the American Helicopter Society* 35(4): 31-37.

Shafizadeh, J. E., J. C. Seferis, E. F. Chesmar, & R. Geyer (Submitted). Evaluation of the in-service performance of honeycomb composite structures. *Journal of Materials* Evaluation *and Performance.*

Wong, R. & R. Abbott 1990. Durability and damage tolerance of bonded sandwich panels. *35th International SAMPE Conference* 35: 366-380.

Investigation of the hygrothermal ageing of composites by means of Raman spectroscopy

A. Cervenka, R. J. Young and D. J. Bannister

Manchester Materials Science Centre, UMIST/University of Manchester

Phenomena relevant to the issues of the composite durability are investigated monitoring the strain that develops along an embedded fibre due to non-mechanical loading and as a result of hygrothermal effects in the constituents. The reported study is focused on three aspects: 1) determination of the diffusion coefficient of the matrix, 2) monitoring degradation of the interface to complete debonding and 3) comparison of the hygrothermal behaviour with respect to the state of water: vapour or liquid. Two variables are involved in these investigations: a) the exposure time and b) the surface treatment of a Twaron fibre.

Experimentally, Raman spectra are obtained for specimens conforming to two configurations: i) A 'double-fibre pull-out' (DFPO) arrangement in which a single fibre spans the entire length and the fibre ends protrude through the matrix bloc and ii) a 'diffusion slab' (DS) type where a fibre monofilament is fully embedded at varying depths in the resin. The fibres under investigation are three variants of Twaron®1055 aramid fibre supplied by AKZO Nobel Central Research (Arnhem, The Netherlands), namely: The fibre coded HM (as spun and without any surface modification), HMA (with an activated finish) and HMF (containing a surface finish). The matrix is a two-part epoxy LY5052 resin cured at the ambient temperature with HY5052 hardener, both obtained from Ciba-Geigy. Microcomposites are immersed either in distilled water or exposed to saturated vapour at ambient temperature for periods of time exceeding 18 months. The Raman spectra are obtained using 632.8 nm red line of a 15 mW He-Ne laser with the beam focused to give a spot size of 5µm and polarised in the fibre directions. Olympus BH-2 optical microscope connected to a Spex 1000M monochromator and a 'Wright instruments' charge-couple camera are elements of the setup used to record the actual Raman spectra using the shift in the 1610 cm^{-1} aramid band to quantify the axial fibre strain. In addition, weight increments in both specimen types are monitored gravimetricly.

From the theoretical point of view, two approaches are used to analyse the Raman spectra: a) the shear-lag theory[1] and b) the Fick's second law acknowledging the finite dimensions of our specimens[2]. The shear-lag theory relates strain profiles $\varepsilon(x,t)$ along a fibre at $L/2 \geq x \geq -L/2$ to the mid-fibre strain $\varepsilon(x=0,t)$, exposure time t, the Raman parameter n and the fibre geometry: its length L and the radius r. The Fickean diffusion model is used to formulate relationships between the specimen geometry $|a/2| \geq x$, $|b/2| \geq y$, $|h/2| \geq z$ and both the total water content M(t) and the local concentration c(x,y,z,t) to be expected after an exposure time t. Having established the saturation values $\varepsilon(x=0,t=\infty)$ and $M(t=\infty)$, the dimensionless quantities $M(t)/M(t=\infty)$ and $\varepsilon(x=0,t)/\varepsilon(x=0,t=\infty)$ are to be related to the matrix properties: its diffusion coefficient D_M and the swelling characteristic β_M. Following the procedure of Galiotis[3], the Raman parameter n derived by fitting the $\varepsilon(x,t)$ profiles of the DS specimens is used as a yardstick reflecting gradual deterioration in the stress transfer efficiency between a fibre and the matrix, i.e. ageing of the interface.

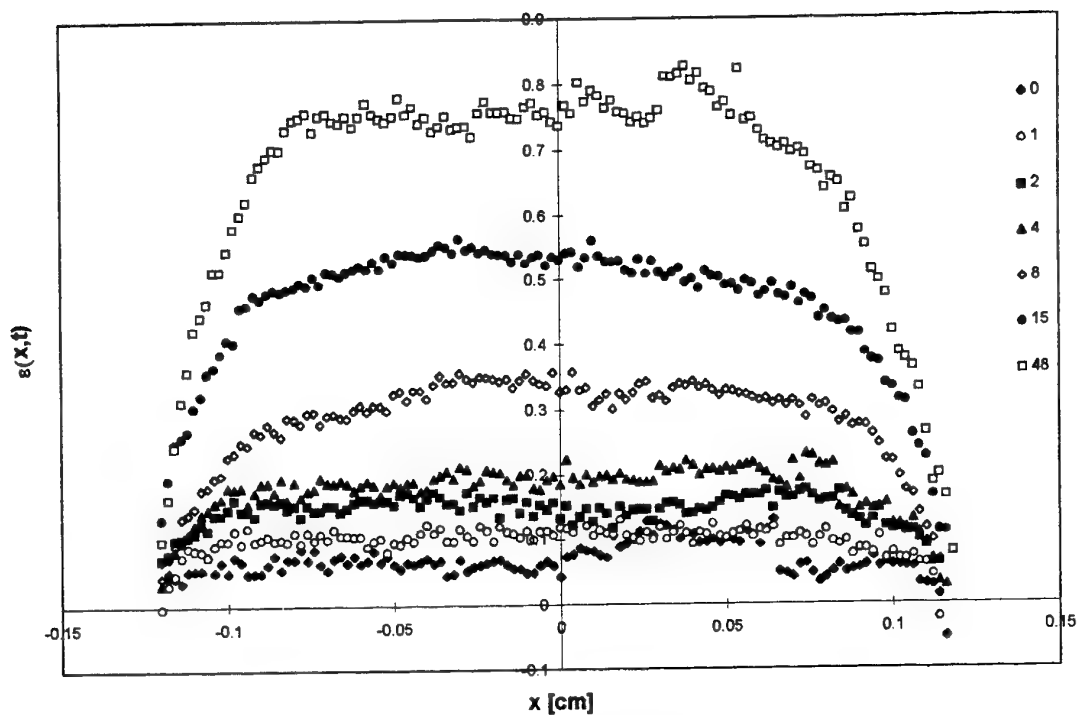Exposures of DS and DFPO specimens lead to different $\varepsilon(x,t)$ profiles - Figs. 1 and 2.

Figure 1: Example of the Raman data for the DS specimen; Fibre is HMA, The legend gives exposure times [week]
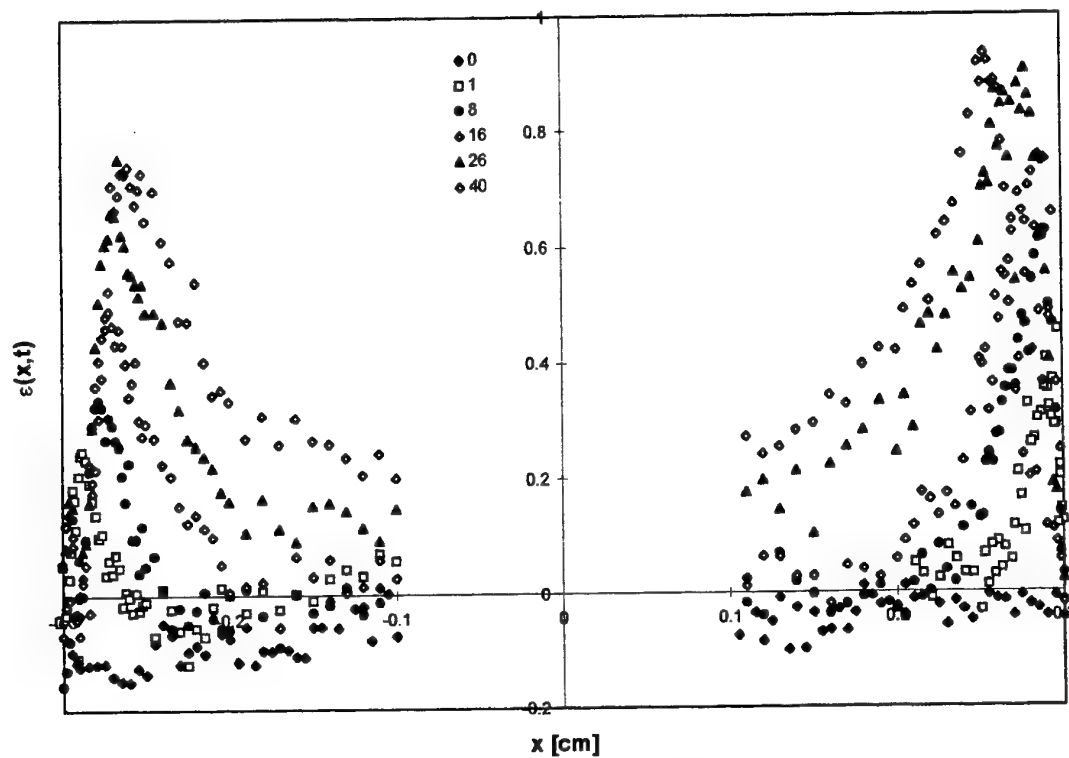

Figure 2: Example of the Raman data for the DFPO specimen; Fibre is HM, The legend gives exposure times [day]

Profiles for the DS specimens conform to the classical shear-lag theory with zero strains at both ends of a fibre and a maximum strain defined by a broad plateau in the $x \rightarrow 0$ region. As the time progresses, the $\varepsilon(x=0,t)$ values rise and gradually converge to the saturation value in the manner as predicted by the theory for the $M(t)$ quantity. The mid-fibre strains are used for deriving the value of the diffusion coefficient as illustrated in Fig. 3. The values $\varepsilon(x=0,t)$ values are normalised on the saturated value $\varepsilon(x=0,t=\infty) = 1.8\%$, corrected for the specimen geometry and plotted as a function of the square root of time. Thus the same procedure as that developed for handling the gravimetry data[2] is used. The linear correlation in Fig. 3 is independent of the fibre type and gives $D_M=1.44 \times 10^{-14}$ m^2/sec. Non-linear parts of the strain profiles $\varepsilon(x,t)$ in the regions $x \rightarrow |L/2|$ for this specimen type are used to derive the dependence of the Raman parameter n on the exposure time. The n values derived for each exposure time and the type of the fibre surface treatment are iterated from the ascending and ascending parts by a simple data-fitting procedure facilitated by the Excel software. The outcome is illustrated in Fig. 4 which clearly illustrates the parameter n to be a decreasing function of the time. There is an appreciable scatter leading to low correlation coefficients $0.64 > R^2 > 0.36$ for the semi-logarithmic dependence of the type $n = C_1 - C_2 \ast \log t$. The constant $C_1 = 0.123$ approximates well the value derived[4] from the constituent properties, the slope satisfies $0.06 > C_2 > 0.05$. The fibre treatment does not appear to influence the C_1 nor C_2 values.

The strain profiles for the DFPO specimens are more complex: in addition to the feature described for the DS type, well pronounced maxima are observed in the regions $x \rightarrow |L/2|$ for shorter exposure times. These maxima attain higher values and move towards the fibre centre as the exposure time increases. This trend amplified by $\varepsilon(x=0,t)$ being also an increasing function of the time causes the 'humps' to become less prominent and eventually to resemble the behaviour of the DS specimens. A very similar behaviour has been observed also for the alumina fibre and thus the observed 'humps' are not related to features of the water transport through polyarylamide fibres. Qualitatively, we feel that the 'humps' might be attributable to the local water concentration $c(x,y,z,t)$ in the constituents amplified by possible mismatch in the swelling characteristics. More sophisticated analytical models and Finite Elements codes are being developed with the aim to simulate the observed behaviour theoretically. The DFPO specimens exposed to the water vapour behave identically to those immersed in the liquid. This conclusion is based on both the analysis of the $\varepsilon(x,t)$ profiles and the gravimetry data. Thus any possibility for the 'wicking' action (fast transport of the liquid along the fibre surface) can be eliminated.

Finally, the Raman spectroscopy allows unambiguously the total debonding to be pinpointed. The case is illustrated in Fig. 5 in which the $\varepsilon(x,t)$ profile changes drastically after 2514 hours of exposure due to debonding of both fibre ends. Whilst the mid-fibre section still conforms to the shear-lag theory, the $\varepsilon(x,t)$ profiles near the fibre ends are linear and their shallow slope reflects the microcomposite integrity being maintained due to weak clamping forces only.
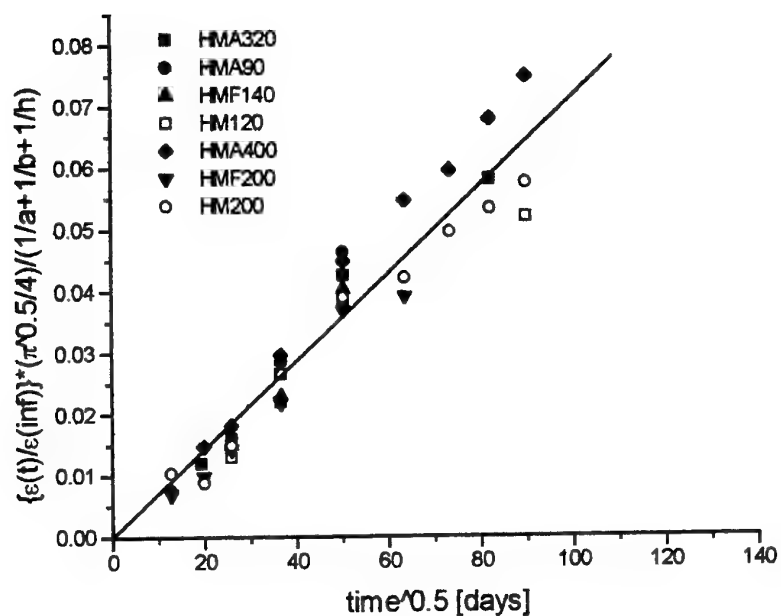
Figure 3: Determination of the diffusion coefficient D_M from the Raman data for the DS specimens
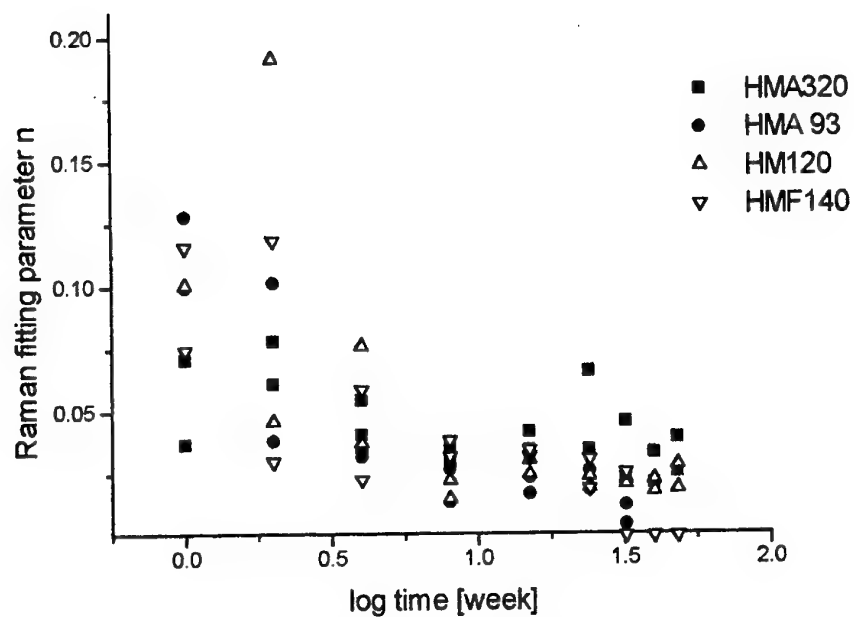

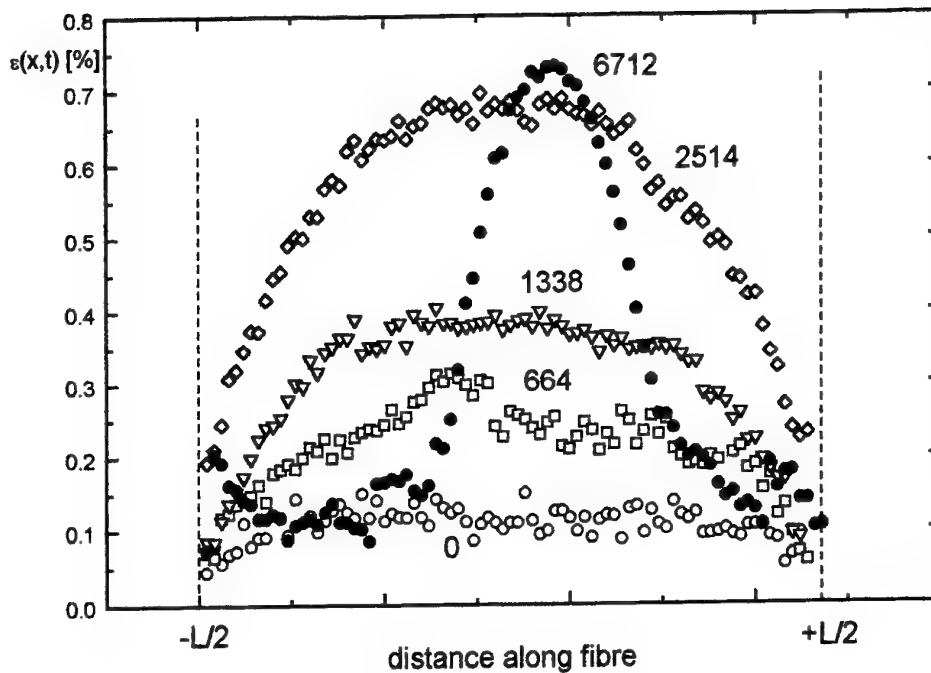Figure 4: Time dependence of the Raman parameter n from the DS measurements

Figure 5: Exposure of the HMF140 specimen associated with debonding; the legend identifies the exposure times in hours

References:

1)   A. J. Cervenka, D. J. Bannister and R. J. Young: Moisture absorption and interfacial failure in aramid/epoxy composites, *Composites Part A* **29A** *(1998) 1137-44.*

2)   M. T. Aronhime, S. Neumann and G. Marom: The anisotropic diffusion of water in Kevlar-epoxy composites, *J. Mater. Sci* **22** *(1987) 2435-46.*

3)   C. Galiotis and A. Paipetis: Definition and measurement of the shear-lag parameter as an index of the stress transfer efficiency in polymer composites: *J. Mater. Sci* **33** *(1998) 1137-43.*

4)   S. Chua and M. R. Piggott: in *'Load-bearing Fibre Composites'*, M. R. Piggott, Ed, Pergamon Press, Toronto, 1982, p.82.

FAILURE MECHANICS OF THIN COATINGS UNDER MULTIAXIAL LOADING

Y. Leterrier, D. Pellaton, J. Andersons*, J.-A. E. Månson#
Laboratoire de Technologie des Composites et Polymères
Ecole Polytechnique Fédérale de Lausanne, CH-1015 Lausanne, Switzerland
(*) Institute of Polymer Mechanics, 23 Aizkraukles st., Riga, Latvia, LV-1006
(#) Corresponding author

Introduction

Thin coatings adhering onto polymer substrates find increasing interest in applications as diverse as multilayered optical lenses, microelectronic devices, and gas barriers for pharmaceutical and food packaging [1]. The thickness of the coating and its adhesion to the substrate are among the key characteristics to be tailored for both performance and cost optimization. Reduced thickness without impaired reliability enables cost savings. However, coatings with thickness down in the nanometer range are often associated with growth heterogeneities and high residual stresses generated during the deposition process. The influence of these factors on the mechanical properties of the coating and adhesion to the substrate, and therefore on the functional reliability of the coated parts is a major concern. The failure mechanisms of elastic thin coatings under multiaxial loading are investigated in this work to simulate the complex stress loadings present during manufacture and service.

Particular attention is paid to modeling crack onset strain in thin, brittle coatings, which is also relevant to off-axis ply cracking in composite laminates. A novel hypothesis of a perfectly plastic interface is introduced, and the effect of uniaxial and equibiaxial tension is considered. The analysis of the stress transfer and durability of such multiphase materials is further expected to refine the understanding of the interfacial behavior in polymer composites. A promising output of this approach is the generation of tailored interfaces for improved durability, which is still a challenge for this class of materials if one aims at increasing their use in advanced applications.

Theoretical derivation of crack onset strain

Cracking of brittle coatings shows close analogies with off-axis ply cracking in brittle-matrix composite laminates subjected to tensile load. In both cases a crack, once initiated, usually propagates instantaneously, spanning the whole width of the specimen, stopping at the interface with adjacent plies in the laminate case. An important difference concerning the direction of intralaminar crack propagation is in that it is governed by reinforcing fiber direction in laminates, while in isotropic coatings crack trajectory is determined by the stress state in the coating, i.e. by applied loading. Crack onset strain is a key feature in durability analysis, and its modeling has motivated various approaches which are briefly reviewed. Under uniaxial tension, the weakest link model with two-parameter Weibull strength distribution has been extensively used, where the fracture of a brittle material results from flaws located both on the surface and within the bulk. The Weibull strength model was reported to underpredict the measured increase of crack onset strain with decreasing coating thickness [3]. This result was also observed for fibers, for which, although both length and diameter effects on strength agree with Weibull model, the shape parameter associated with diameter is substantially lower than that related to fiber length [2].

Alternatively, linear elastic fracture mechanics (LEFM) models have been successfully employed for crack onset and crack density prediction in laminated composites, and also extended to coating cracking analysis under uniaxial loading [4]. The corresponding energy balance equation for crack propagation implies that the strain energy released due to crack growth equals the fracture toughness of either the transverse ply or the coating. The simplest analytical approach for stress redistribution calculation is the shear lag model. Applying the energy release rate relation derived in the work of Laws and Dvorak [5] to the coating-substrate system in consideration and neglecting residual stresses leads to the following expression for crack onset strain:

$$\varepsilon_{onset} = \sqrt{\frac{2 G_c \xi h_s E_s}{h_c (h_s + h_c) E_c E}} \qquad (1)$$

where G_c is the coating fracture toughness, E_s, E_c and E are the substrate, coating and film moduli, respectively, and h_s and h_c are the corresponding thicknesses. The factor ξ is a non-dimensional shear lag parameter, determined by fitting the above equation to experimental data. Another approach was proposed recently by Yanaka et al. to calculated the crack onset stress, with the assumption that the additional displacement in the substrate due to cracking varies linearly in the thickness direction [6]. The corresponding crack onset strain is found inversely proportional to $h_c^{1/4}$:

$$\varepsilon_{onset} = \sqrt{\frac{2G_c}{3E_c\sqrt{(1+v_c)h_c h_s}}}$$ (2)

A further expression for strain energy release rate was derived by Nairn and Kim by minimizing the complementary energy of the film, assuming that the axial stress in coating and substrate does not depend on the thickness coordinate [4]. Due to complexity, the resulting expression for first crack strain is not given here. Both shear-lag and variation mechanics solutions can be applied to extrapolate crack onset strain vs. coating thickness, providing that the parameter ξ or the coating toughness G_c are fitted by testing one film with a given coating thickness.

Case of a plastic interface

The above approaches assume linear elastic behavior of the material system. For a ductile substrate, crack propagation can also involve small-scale yielding at the coating-substrate interface [7] caused by shear stress, and part of the released strain energy is dissipated. Accounting for that, the energy balance takes the form:

$$G_c h_c + W_d = \Delta A - \Delta W$$ (3)

where W_d, ΔA and ΔW are accordingly the energy dissipated by deforming the plastic interface, the work done by the applied load, and the strain energy released due to crack extension through the coating (all per unit width of the film). Crack onset strain for a thin film under plane-stress conditions is derived below, assuming that the coating and substrate are elastic in the strain range of interest, and that the coating-substrate interface is perfectly plastic with a shear strength τ. The energy terms in Equation (3) are derived from the expressions for stresses σ_x and σ_y, and displacements u_x in the presence of the crack:

$$W_d = 2\int_0^\delta \tau(u_{xc} - u_{xs})dx$$

$$\Delta A = 2\sigma(h_s + h_c)\Delta u_x$$ (4)

$$\Delta W = \sum_{i=c,s}\frac{h_i}{E_i}\int_0^\delta (\sigma_{xi}^2 + \sigma_{yi}^2 - 2v_i\sigma_{xi}\sigma_{yi})dx - \sum_{i=c,s}\frac{h_i}{E_i}\int_0^\delta \left[(\sigma_{xi}^0)^2 + (\sigma_{yi}^0)^2 - 2v_i\sigma_{xi}^0\sigma_{yi}^0\right]dx$$

Coating crack onset strain is obtained by routine but tedious calculations, yielding:

$$\varepsilon_{onset} + \varepsilon_{rc}\frac{1-v_c}{1-vv_c} = \frac{1-v_c^2}{1-vv_c}\sqrt[3]{\frac{3G_c\tau}{E_c^2 h_c\left(1-v_c^2 + \frac{E_c h_c}{E_s h_s}(1-v_s^2)\right)}}$$ (5)

This model includes residual compressive stresses, ε_{rc}, measured from the radius of curvature of the coated films, and found to decrease from approx. -0.5 % for 50 nm coatings to -0.3 % for 100 nm coatings, in excellent agreement with values published in a recent work [6].

In the equibiaxial loading case, the stress is applied to the film in both x and y directions, and $\sigma_x=\sigma_y=\sigma$. The presence of the applied load component parallel to the straight crack is reflected in the model via the appropriate far-field stress and strain values. The perturbation of strains and displacements in y-axis direction by the presence of the crack is neglected. Therefore neither plastic slip occurs along the crack, nor additional work is done by load component σ_y, and Equation (4) remains valid for biaxial load. Finally, crack onset strain under equibiaxial tension is given by:

$$\varepsilon_{onset} + \varepsilon_{rc} = (1-v_c)\sqrt[3]{\frac{3 G_c \tau}{E_c^2 h_c \left(1-v_c^2 + \frac{E_c h_c}{E_s h_s}(1-v_s^2)\right)}} \tag{6}$$

Experimental techniques

The materials investigated are 12 µm thick biaxially stretched PET films coated by physical vapor deposition (PVD) with SiO_x layers, of thickness ranging from 30 nm to 156 nm [3]. The elastic properties of the materials are $E_s = 3920$ MPa; $v_s = 0.44$; $E_c = 79500$ MPa; $v_c = 0.2$; $v = 0.4$; and E was derived using the rule of mixtures. The interfacial strength τ was assumed to be equal to the VonMises yield shear stress of the polymer substrate, which is equal to 49 MPa.

The techniques developed to analyze the fragmentation process of the thin coating under uniaxial and biaxial loads were detailed in separate publications [8,9]. A summary of the main features of each test is given in the following. Fragmentation tests under uniaxial tension were performed at a constant strain rate of $2.1 \ 10^{-4} \ s^{-1}$ by means of a Polymers Labs Minimat tensile tester mounted on a Olympus SH-2 optical microscope stage, and the crack development during straining was recorded via a CCD camera connected to the microscope. Fragmentation tests under equibiaxial plane stress conditions were performed using a bulging cell installed on the optical microscope stage. Circular specimens were pressurized stepwise by means of a precision pressure controller. Theoretical modeling of film deformation process was carried out to derive stresses and strains in the membrane as a function of applied pressure and displacement of the top of the inflated calotte. A closed-form solution was derived by Hencky for a circular membrane loaded by an uniform pressure [10]. In order to assess the accuracy of the analytical solution, FEM calculations were performed by NISA2 software [11]. 3-D general shell elements accounting for membrane, bending and transverse shear stresses were applied to model one quarter of the circular membrane with appropriate symmetry and boundary conditions. 510 nodes were used. As shown in Figure 1, a good agreement is obtained between the FEM and the analytic results. Upon plastic yield of the polymer substrate, the above elastic derivation is not applicable, and a simplified geometrical calculation was used, assuming an homogeneous equibiaxial strain in the membrane.

Results and discussion

Experimental values and theoretical crack onset strain of the SiO_x coatings under uniaxial loading are compared in Figure 2. Since a direct measurement of the coating fracture toughness G_c is not possible, curve fit to experimental data was done with adjustable ξ (Equation 1) or adjustable G_c (Equations 2 and 5, and variational mechanics approach) values.

All models fit the experimental findings with reasonable accuracy, however with considerably different values. The first shear lag model (Equation 1) is hampered by the presence of the empirical parameter ξ. The apparent coating toughness G_c is found to be equal to 30 J/m^2 in the case of the variational model, and to 16 J/m^2 in the case of the shear lag model including the linear variation of the additional displacement in the substrate due to cracking (Equation 2). The former value is very high, and the latter still high, compared to the fracture toughness of bulk glass that, depending on the composition, is of the order of 10 J/m^2 [12]. This discrepancy is likely to arise from neglecting plastic effects in the substrate, at the interface vicinity. By contrast, the assumption of a perfectly plastic interface whose strength equal the yield strength of the substrate (Equation 5) leads to a low fracture toughness equal to 2.9 J/m^2.

Modeling of the crack onset strain under equibiaxial load (Equation 6) is reported in Figure 3, using the fracture toughness determined in the uniaxial case. In the biaxial geometry, the model is only accurate for the thicker coating, whereas it underestimates crack onset strains of thinner coatings. The deviation of the prediction from experimental data with coating thickness reduction is likely to be caused by plastic yield of the substrate, which is assumed to be elastic in the model.

Estimation of substrate stress in the center of the inflated film, shown in Figure 1 for the 103 nm coated film, revealed that only in the 156 nm coating case the equibiaxial stress in the PET substrate at crack onset was well below the nominal PET tensile yield stress of 85 MPa. For the 103 nm coating case, the calculated stress in PET at coating crack onset was close to plastic limit, while for thinner coatings – exceeded it. The presence of substrate plasticity in the pressure range of interest for $h_c \leq 103$ nm was also indirectly corroborated by the measured calotte top displacement exceeding considerably the elastic analysis prediction.

The comparison of these various approaches to fracture mechanics of thin coatings highlights the importance of accounting for the behavior of the polymer/coating interface for reliable durability predictions.

Conclusions

The failure mechanisms of SiO_x coatings of thicknesses ranging from 30 nm to 156 nm on PET substrates developed for packaging applications were modeled under uniaxial and equibiaxial tension, to simulate relevant stress conditions achieved during the manufacture and service of the bilayer material system. The crack onset strain was found to increase with decreasing coating thickness, and this evolution was analyzed using several fracture mechanics-based models, also relevant for transverse cracking in composite laminates.

In the uniaxial loading case, all models show a good agreement with experimental data. Elastic shear-lag and variational mechanics approaches lead to oxide fracture toughness values beyond practical limits for silicon oxide. On the contrary, the shear-lag model with a perfectly plastic interface developed in this study leads to a low fracture toughness, equal to approx. 3 J/m^2. In the biaxial loading case, substrate plasticity leads to an underestimation of the crack onset strain at small coating thickness.

Acknowledgments

References

[1]   Society of Vacuum Coaters, *Proc. 41st Ann. Tech. Conf., Boston, Apr. 18-23*, (1998).
[2]   Wagner, H.D., in *"Composite Material Series. Vol. 6. Application of Fracture Mechanics to Composite Materials"*, Elsevier Science Publishers, New-York, 39 (1989).
[3]   Leterrier, Y., Andersons, J., Pitton, Y., Månson, J.-A.E., J. Polym. Sci. B: Polym. Phys., **35**, 1463 (1997).
[4]   Nairn, J.A., Kim, S.-R., Eng. Fract. Mech., **42**, 195 (1992).
[5]   Laws, N., Dvorak, G.J., J. Compos. Mater., **22**, 900 (1988).
[6]   Yanaka, M., Miyamoto, T., Tsukahara, T., Takeda, N., Proc. ICCI7, Shonan Inst. Technol., Japan, May 9-13, also submitted to Compos. Interfaces, (1998).
[7]   Hu, M.S., Evans, A.G., Acta Metall., **37**, 917 (1989).
[8]   Leterrier, Y., Pellaton, D., Mendels, D.A., Glauser, R., Andersons, J., Månson, J.-A.E., to be submitted.
[9]   Leterrier, Y., Boogh, L., Andersons, J., Månson, J.-A.E., J. Polym. Sci. B: Polym. Phys., **35**, 1449 (1997).
[10]   Hencky, H., Z. Math. Physik, **63**, 311 (1915).
[11]   Users Manual for NISAII. Version 94.0 (1994).
[12]   Wiederhorn, S.M., J. Amer. Ceram. Soc., **52**, 99 (1969).
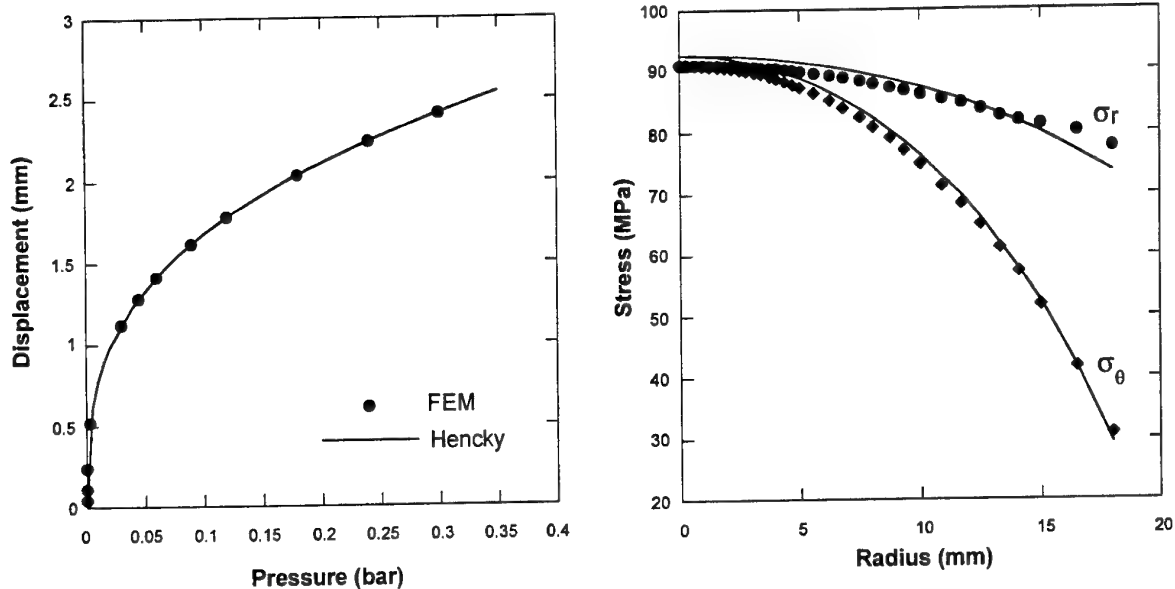
Figure 1. Comparison of FEM results (dots) and Hencky's analytical model prediction (lines) for the bulge test of PET film with a 103 nm SiOx coating. Left: dependence of calotte top displacement on applied pressure; right: radial and circumferential stress distribution at a pressure equal to 0.3 bar.
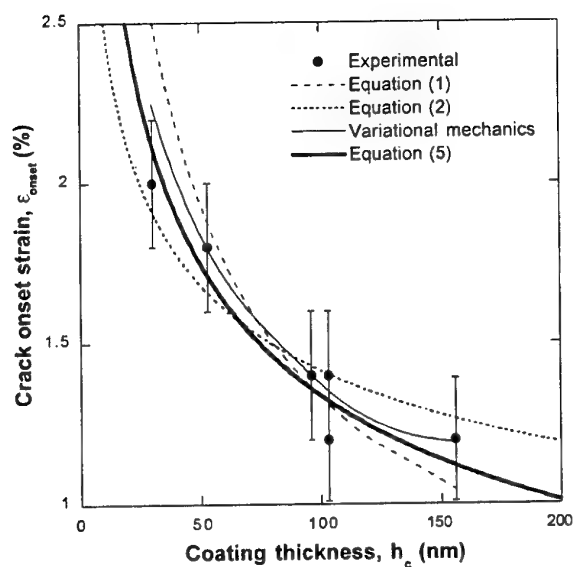

Figure 2. Dependence of the SiO_x coating crack onset strain under uniaxial load on coating thickness, and comparison of experimental data with models.

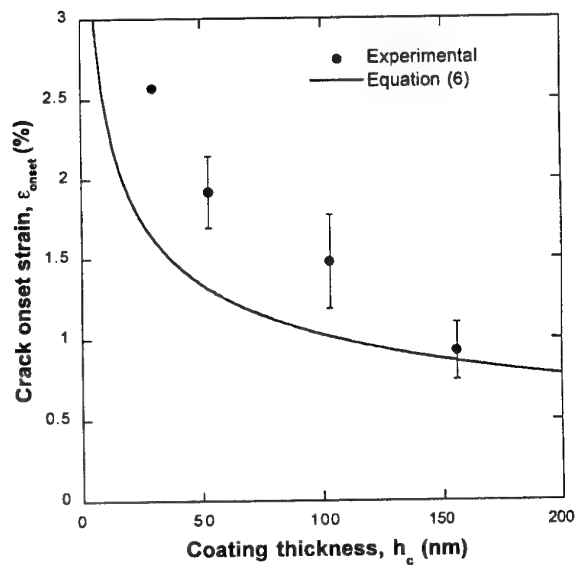*Figure 3. Dependence of the SiO_x coating crack onset strain under biaxial load on coating thickness. The dots are experimental data, and the line represents Equation (6).*

Effect of Temperature and Strain Rate
on Polymeric Composites

K. Reifsnider, C. Mahieux, B. Walther and F. Sun
Virginia Polytechnic Institute and State University

ABSTRACT

The effect of temperature and strain rate during deformation on the properties and performance of materials has been a long-standing subject of engineering interest, driven by the observation that significant differences in strength, stiffness and life can be induced by these effects. In polymer-based materials, the discussion of such effects usually centers on viscoelastic response and changes in stiffness. The present paper examines subjects that are related to strength, life, and to accelerated testing. Micromechanical effects are identified and discussed, and new concepts are introduced to assist in the interpretation and representation of physical behavior, over ranges of strain rate from impact to quasi-static testing, and temperature from glassy to flow behavior.

STRAIN RATE EFFECTS

The behavior of materials, especially polymeric matrices in composites under dynamic loads, is a very important issue in practical engineering, essential for any work involving polymeric composite materials and structures in aerospace and ocean applications (1). Most of the prior research dealing with the dynamic properties of composites has concentrated on the strain rate dependent behavior of composite laminates and structures, and on macro-mechanics analysis (2-4).

In order to fully understand the strain rate dependent mechanisms and to develop better impact-tolerant composites through a micro-mechanics approach, it is necessary to know the strain rate dependent properties of the constituents, i.e., the fibers and matrices. It is only in fairly recent years that tensile impact techniques for fiber bundles and matrix have been established (5-7). There are some tensile impact data showing that the strength of epoxy, widely used as a matrix in polymeric composites, increases with strain rate (8,9). However, few quantitative analyses for the strength variations and rate dependent mechanisms for this material have been found so far, and few explanations of strain rate effects on polymeric matrices have been offered.

On the other hand, it is common knowledge that the mechanical properties of polymeric matrices change with strain rate as well as with ambient temperature. For very long-term deformations, such as creep and relaxation, time-temperature equivalence, e.g., WLF superposition principles may apply (10). Mechanical properties of polymers at times over several decades of significance can be predicted from data at a higher temperatures over short times. But this equivalence is not generally valid at temperatures below Tg, and few data support the application of WLF principles to the relationship between temperature and strain rate for polymeric matrices. It is only reported qualitatively that there exists an "equivalence" between strain rate in impact process and temperature, for polymeric resins (11,12), and for elastomers within the range of rubbery behavior (13); there are no quantitative descriptions regarding this equivalence.

MODELS FOR STRAIN RATE AND TEMPERATURE EFFECTS

In this paper, "material properties" refers mainly to mechanical properties, especially, strength, stiffness, strain to failure and time to failure of epoxy, in the temperature range below Tg.

It is reported that Young's modulus, strain to failure and strength for epoxy (18, 27) are proportional to the log (strain rate), as follows:

$$E = B_1 \cdot \log \dot{\varepsilon} + C_1$$

$$\varepsilon_b = B_2 \cdot \log \dot{\varepsilon} + C_2 \tag{1}$$

$$\sigma_b = B_3 \cdot \log \dot{\varepsilon} + C_3$$

Data from references 17-28 were used to construct examples of such variations in Figs. 1 and 2, below.

Youngs modulus (GPa)
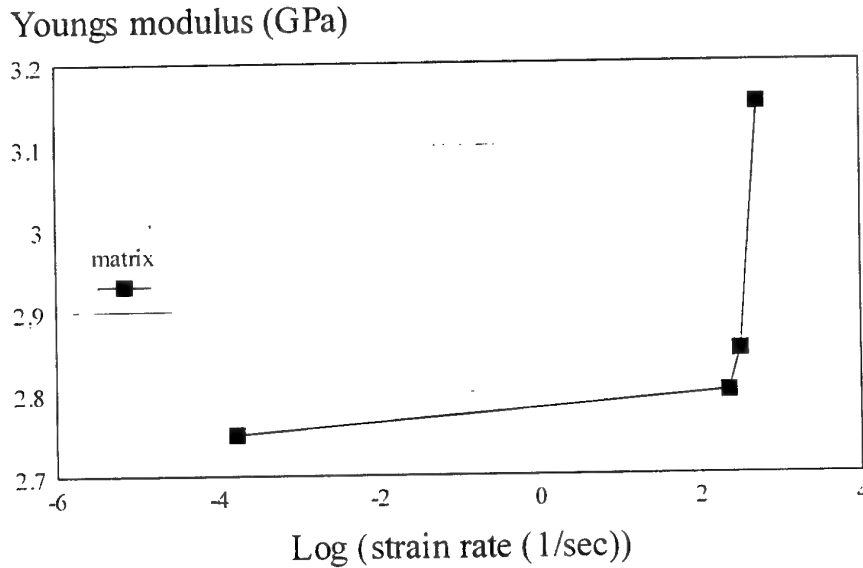
Figure 1 Variation of the stiffness of epoxy with strain rate

These data indicate several important and typical features. The fiber, matrix and composite show little strain rate dependence for low strain rates. At high strain rates there is a strong dependence, which seems to be linear or nearly linear. It is also seen that the strain rate dependence of the composite stiffness follows the form of the epoxy behavior. It should be noted that the significance of high strain rates is not limited to engineering situations involving impact or other high deformation rates at the macroscopic level. Local fracture events (driven by fiber fracture or the fracture of fiber tows) are high-rate deformation events. In general,

Youngs modulus (GPa)
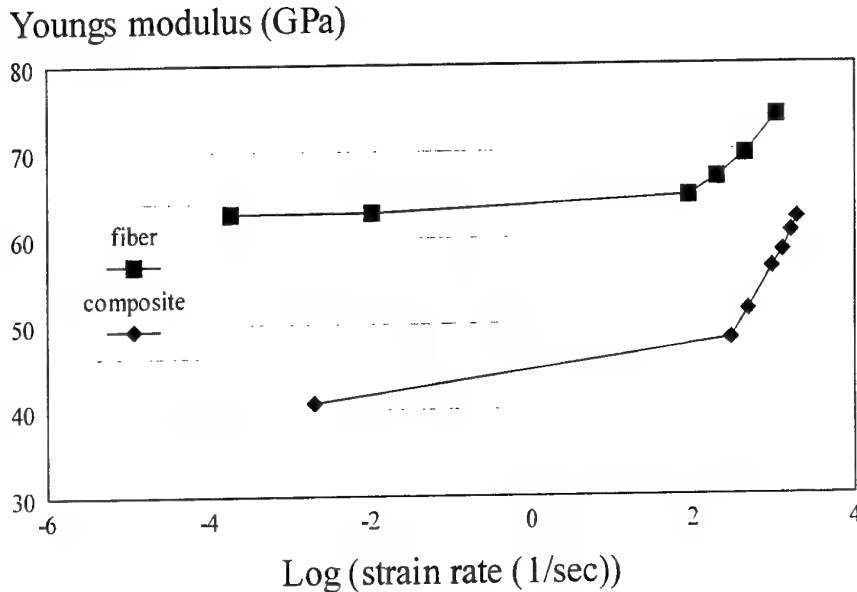
Figure 2 Variation of stiffness of glass fiber and glass-reinforced
epoxy composite, as a function of strain rate.

progressive damage processes in high-stiffness, low strain to failure composites are high strain
rate events.

TEMPERATURE EFFECTS

The effect of temperature on the mechanical response of polymers and polymer based
composites is often discussed in terms of viscoelastic response. However, engineering
applications are generally designed to minimize time-dependent deformation (creep and creep
rupture). This is most often done by constraining the viscoelastic deformations with reinforcing
fibers in load-bearing directions. However, our recent data show that although fiber-dominated
composites may not creep as a result of elevated temperature, the instantaneous properties (fast-
fracture stiffness and strength) can be greatly affected by temperature. Indeed, fiber-direction
stiffness of unidirectional carbon/PPS composites can vary by of the order of 15 percent, and
strength in the fiber direction by more than 30 percent as temperature is varied from values that
correspond to glassy response of the polymer to values well above Tg (31).

The present paper will propose a robust model for the instantaneous stiffness variations of
polymers across all temperature transitions, and apply that model to micromechanical models of
composite stiffness and strength to attempt to estimate and explain such unusual variations. A
schematic diagram of the problem addressed is sketched in Fig. 3. The model presented is based
on statistical arguments and representations of the mobility of macromolecules as energy is
supplied by increasing applied temperatures. A universal relationship is derived.
Micromechanical models of composites match experimental observations well.

3
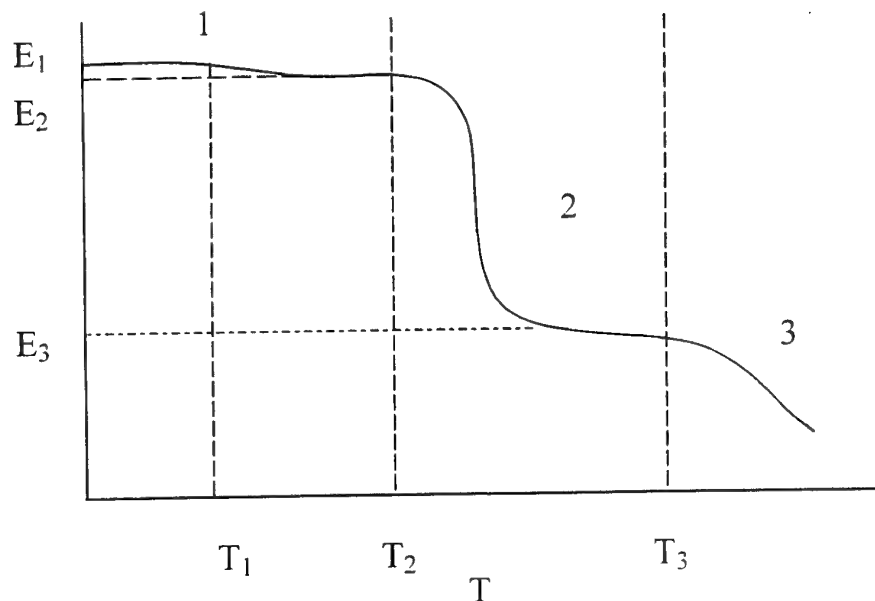
Figure 3 Schematic diagram of the variations of instantaneous stiffness of polymers across transitions in properties.

REFERENCES

1. Robert L. Sierakowski and Shive K. Chaturvedi, Dynanic Loading and Characterization of Fiber-Reinforced Composites, Published by John Wiley & Sons. Inc..1997.
2. C.A.Ross and R.L.Sierakowski, " Studies on the Impact resistance of Composites", Composites, July 1973. pp.157-161..
3. S.R.Finn and G.S.Springer, " Composite Plates Impact Damage", Technomic publishing Co.. Inc.. 1991.
4. D.Hull. " A Unified Approach to progressive Crushing of Fiber- reinforced Composite Tubes". Composites Science and Technology, 40. pp.377-421. 1991.
5. J.Harding and L.M. Welsh. " Impact testing of Fiber – Reinforced Composite materials", Proc. ICCM 4. pp.845-852. Tokyo. Japan, 1982.
6. K.Kawata. S.Hashimoto and N.Takeda, " Mechanical Behaviors in High Velocity Tension of Composites", Proc. ICCM 4, pp.829-836, Japan, 1982.
7. Y.Xia. B.Yang L.Dong and D.Jia. " Experimental Study of Constitutive Relation for Unidirectional Glass Fiber Reinforced Resin under Tensile Impact". Proc. of ISCMS. Beijing. China. pp.997-1002.1986.
8. J.Harding and L.M. Welsh. A Testing Technique for Fiber – Reinforced Composites at Impact rates of Strain". J. of Materials Science, 18. pp.1810-1826. 1983.
9. L.Dong. Y.Xia and B.Yang. " Tensile Impact Testing of fiber Bundles". ICSTAD proceedings. India. pp.184-189. July 29 – Aug.3.1990.
10. M.L.Williams. R.F.Landel and J.D.Ferry, The temperature Dependence of Relaxation Mechanisms in Amorphous Polymers and Other Glass-Forming Liquids". J. American Chemical Society. 77. pp.3701-3707.1955.
11. L.E.Nielsen and R.F.Landel. Mechanical Properties of Polymers and Composites, 2nd ed.. Published by Marcel Dekker. Inc.. pp.256. 1994.
12. C.Hall. Polymer Materials. Published by John Wiley & Sons. pp.73.1981.

13. T.I.Smith and P.J.Sterdy, " Time and Temperature Dependence of the Ultimate Properties of an SBR Rubber at Constant Elongations", J.of Applied Physics, 31, No.11, pp.1892-1898, 1960.
14. L.Dong, Y.Xia and B.Yang, Tensile Impact Testing of Fiber Bundles, ACTA MATERIAE COMPOSITAE SINICA, pp.9-14, Dec. 1990 (in Chinese).
15. D.R.Hartman, M.E.Greenwood and D.M.Miller, Technical Paper-High Strength Glass Fibers, Published by Owens-Corning Fiberglass Corparation, (Figure 2), Mar. 1994.
16. Y.Xia, L.Dong, S.Rao and B.Yang, "Energy Transition of Fiber-Bundle and Their Unidirectional Composites under Tensile Impact", Proc. ICCM 8, Hawaii, pp.29-O-1-8, 1991.
17. T.S.Gates, " Matrix-Dominated Stress/Strain behavior in Polymeric Composites : Effects of Hold Time, Nonlinearity, and Rate Dependency", ASTM STP 1206, E.T.Camponeschi, Jr., Ed., Philadelphia, pp.177-189, 1993.
18. Y.Xia, B.Yang and M.Li, "Tensile Impact Response of Resin Matrices and their composites", ACTA MATERIAE COMPOSITAE SINICA, Vol. 4, No.2, pp.59-65, 1987 (In Chinese).
19. M.F.Ashby and D.R.H.Jones, Engineering Materials 2, Pergamon Press, pp.226-231,1986.
20. Y.Xia, J.Yuan and B.Yang, " A Statistical Model and Experimental Study of the Strain – Rate Dependence of the Strength of Fibers", Composites Science and Technology, 82, pp.499-504, 1994
21. Y.Xia, and W.Xing, " Constitutive Equation for Unidirectional Composites under Tensile Impact", Composites Science and Technology, 56, pp.155-160, 1996.
22. G. Carrington, Basic Thermodynamics, 2nd ed., Oxford Science Publications, pp.275-280, 1994.
23. S. L. Rosen, "Fundamental Principles of Polymeric Materials", John Wiley and Sons, Inc., P242, 1982.
24. H.E.Evans, "Mechanisms of Creep Fracture", Elsevier Applied Publishers, p.20,1984.
25. G.M.Bartenev and Yu.S.Zuyev, translated by F.F. and P. Jaray, Strength and Failure of Visco-elastic Materials, Pergamon Press, p.102, 1968.
26. Y.Xia, X.Wang and B.Yang, " Brittle-ductile-brittle transition of glass fiber-reinforced epoxy under tensile impact", J.Materials Sci.Lett., Vol.12, pp.1481-1484, 1993.
27. G.Hartwig, "Mechanical and Electrical low temperature properties of high polymers", Nonmetallic Materials and Composites at Low Temperatures, edited by A.F.Clark, R.P.Reed and G.Hartwig, Plenum Press, 1978, pp.33-50.
28. P.K.Dutta, K.L.Faran and D.Hui, "Influence of Low Temperature on Energy Absorption in Laminated Composites", Proc. ICCM 9, 1993, pp.311-320.
29. K.Padmanabhan, "Time-Temperature Failure Analysis of Epoxies and Unidirectional Glass/Epoxy Composites in Compression", Composites, Part A, Vol.27A (1996), pp.585-596.
30. Y. Miyano and M.Kanemitsu, "Time and Temperature Dependence of Flexural Strength in Transversal Direction of Fibers in CFRP", Fiber Science and Technology, Vol.18, pp.65-79, 1983.
31. Walther, B.M., "An Investigation of the Tensile Strength and Stiffness of Unidirectional Polymer-Matrix, Carbon-Fiber Composites under the Influence of Elevated Temperatures." Thesis, College of Engineering, Virginia Polytechnic Institute and State University, Blacksburg, VA, 1999

EVOLUTION OF MATRIX CRACKING IN CROSS-PLY CFRP LAMINATES : DIFFERENCES BETWEEN MECHANICAL AND THERMAL LOADINGS

C. HENAFF-GARDIN, I. GOUPILLAUD, M.C. LAFARIE-FRENOT,
Laboratoire de Mécanique et de Physique des Matériaux, ENSMA
1 avenue Clément Ader
86960 Futuroscope-Chasseneuil, France
henaffc@lmpm.ensma.fr

1. Introduction

In aeronautical applications, structural parts can be submitted to large cyclic temperature variations. Large thermal stresses may develop in composite CFRP laminates due to the mismatch in the coefficients of thermal expansion of the fibers and the matrix, at a microscopic level, and consequently of adjacent plies stacked with different orientations in the laminate. So, in a cross-ply laminate for example, cyclic temperature variations induce cyclic biaxial in-plane strains in every layer. In that case, cyclic thermal exposure is likely to enhance damage similar to that observed under mechanical fatigue (1).

Damage mechanisms induced in CFRP laminates by mechanical fatigue have been extensively studied during the last twenty years. Comparatively, only few experimental works have concerned thermal fatigue of composite laminates. The aim of the present paper is to compare the matrix cracking evolution in cross-ply composite laminates subjected to 'equivalent' mechanical or thermal cyclic loadings. This first experimental program has for objective to put in light the limitations of a purely mechanical approach for the prediction of matrix cracking due to cyclic thermal exposure.

2. Material and experimental procedures

The material chosen for the present work (carbon/epoxy T300/914), was intended solely as a model material and not as a candidate for an elevated temperature usage. It was chosen essentially because it was previously well characterised in mechanical fatigue (2).

Two cross-ply laminates $[0_3/90_3]_s$ and $[90_3/0_3]_s$ have been tested in uniaxial tension fatigue, at a frequency of 10 Hz and with a load ratio equal to 0.1. The same laminates have been submitted to thermal cycles, between +150°C and -50°C, with ±4°C/mn cooling and heating rates, corresponding to a $1.7\ 10^{-4}$ frequency. For mechanical fatigue tests, the maximal applied stress value was determined in order to have, in the 90° plies, about the same cyclic amplitude of σ_{22} (transverse ply stress) than that induced by the thermal variation in the specimens exposed to temperature. In our case, this value was found equal to 50% of the static failure stress value. Nevertheless, the minimum value of this stress is really higher under fatigue loading. This implies that the maximum transverse stress is approximately twice higher under mechanical fatigue.

The damage development, particularly the evolution of 0° and 90° cracks, was investigated throughout tests by means of penetrant enhanced X-radiography.

after 50 cycles (figure 1e.). In $(0_3/90_3)_s$ laminate, such longitudinal cracks initiate after approximately $5\ 10^4$ cycles.

The transverse and longitudinal cracks multiply and propagate when the cycle number increases, resulting in a regular array of cracks of both directions 0° and 90° that corresponds with a quasi saturation of fatigue damage (figures 1d. and 1f.). For $(0_3/90_3)_s$ laminate, such a regular array of cracks is obtained far much later in the fatigue life of the coupons. When cracks are fully developed in both 0° and 90° layers, delaminations initiate and propagate along the cracks of the external layers.

3.2. Edge crack density

The figure 2 gives a representation of the edge crack density values versus the cycle number, under mechanical fatigue and thermal cycling. In figure 2a. the edge crack density values obtained in the external layers of the specimens tested under thermal cycling are compared to those measured in the external 90° layers of the $[90_3/0_3]_s$ laminates subjected to mechanical fatigue. In the same way, in figure 2b., the cracking evolution of the internal layer of the specimen exposed to temperature variations is compared to that of the 90° inner ply of the $[0_3/90_3]_s$ laminate submitted to fatigue.
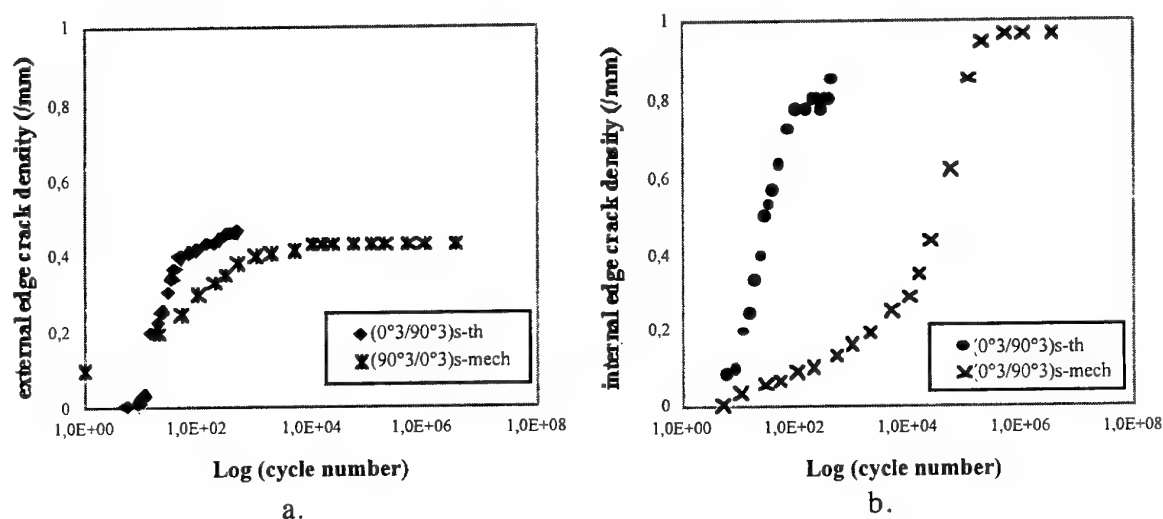

Figure 2 : Evolution of edge crack density with loading cycle number : comparison between mechanical and thermal loadings.

On these figures 2a. and 2b., it can be seen that the cracking development is far much faster in the specimens exposed to cyclic temperature variations than in those tested under mechanical fatigue ; the cycle number necessary to reach a quasi saturation of the edge crack density is equal to 500 under temperature where as, under fatigue, $5\ 10^4$ and $1\ 10^6$ cycles are respectively necessary for saturation in the external and internal 90° layers of studied laminates.

The obtained ultimate values of the edge crack density are analogous under thermal and mechanical cyclic loadings, in both internal and external layers. Moreover, it must be noted that the ultimate edge crack densities are approximately twice higher in the internal layers.

4. Analysis

All these experimental results have been analyzed using a fracture mechanics approach developed earlier and validated for fatigue matrix cracking of various cross-ply laminates (4).

In the analysis, the studied cross-ply laminates are assumed to present a symmetric and periodic stacking sequence such as $(0_m, 90_n)_s$. The laminate is subjected to biaxial loading

3. Results
3.1. X-ray observations

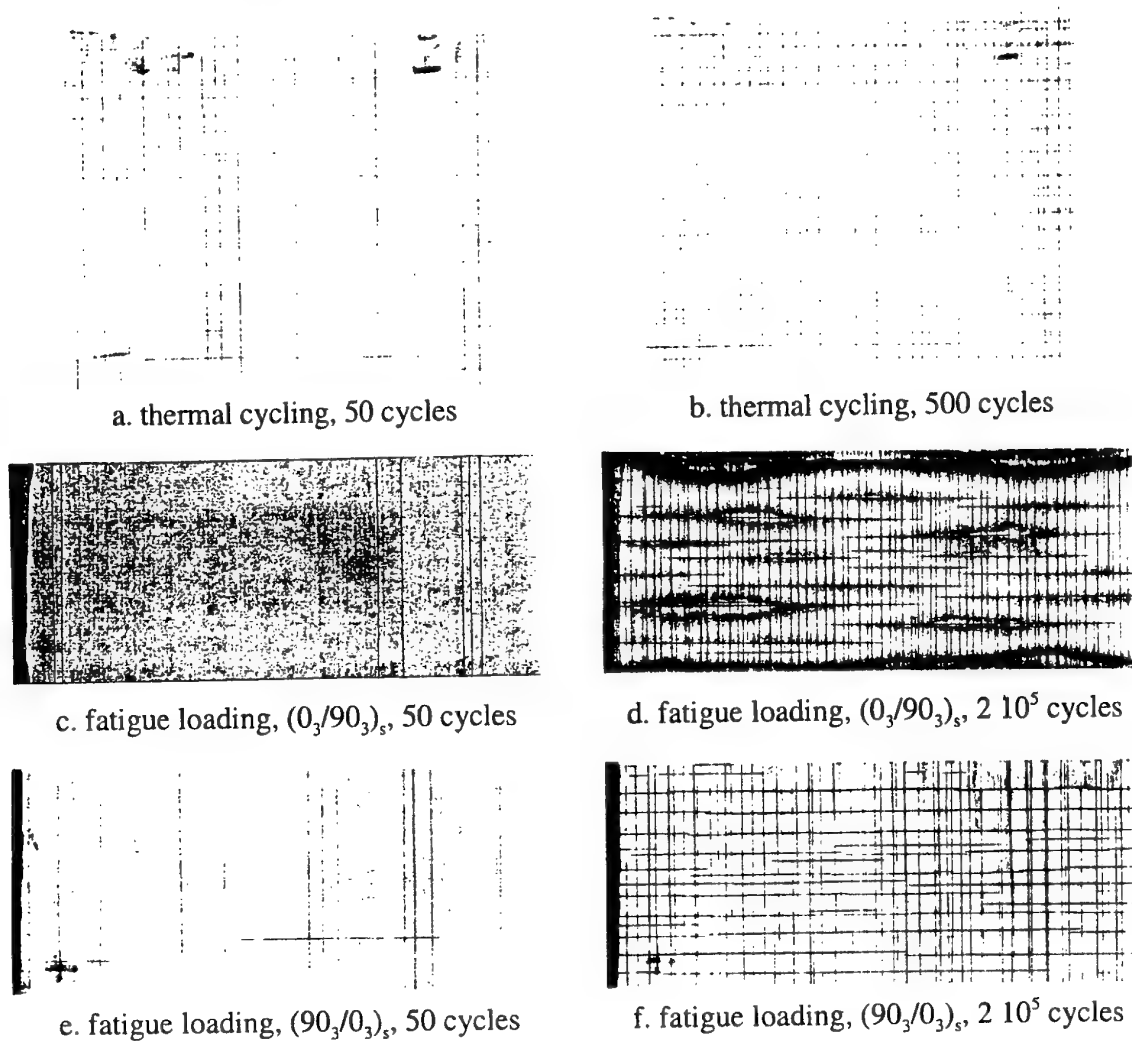X-radiographs illustrating damage development throughout mechanical fatigue and thermal cycling are given in figure 1.

a. thermal cycling, 50 cycles

b. thermal cycling, 500 cycles

c. fatigue loading, $(0_3/90_3)_s$, 50 cycles

d. fatigue loading, $(0_3/90_3)_s$, $2\ 10^5$ cycles

e. fatigue loading, $(90_3/0_3)_s$, 50 cycles

f. fatigue loading, $(90_3/0_3)_s$, $2\ 10^5$ cycles

Figure 1 : X-radiographs under mechanical and thermal cyclings

As far as thermal cycling is concerned, the two studied laminates $(0_3/90_3)_s$ and $(90_3/0_3)_s$ are equivalent, as temperature leads to biaxial loading. So, the layers will be refereed as external and internal layers.

During thermal cycling, the first cracks initiate in the very first cycles, in majority in the external layers, from the specimen free edges, and they are essentially crossing the entire layer. These cracks increase in number. New cracks then initiate in the internal layer. Most of those initiate at the free edges, and half of them are crossing the specimen width. The other half of the cracks propagate as thermal cycle number increases, but they never reach the opposite side because they are facing each other. At the end of tests, after 500 thermal cycles, the crack distribution in the internal layer is still heterogeneous, with a lower crack density in the earth of the coupon than at the free edges (figure 1b.).

Under fatigue, transverse cracking always appears first, and is already developed after 50 cycles (figures 1c. and 1e.), with cracks spanning the entire specimen width. Although the loading axis is parallel to 0° fibers, some longitudinal cracks are present in $(90_3/0_3)_s$ laminate

in both x and y directions, and to temperature variations ΔT. Two damage parameters have been chosen : the crack density d_{90} in inner 90° layer, and d_0 in each outer 0° layer. The displacements are assumed to be parabolic in the cracked layer, and constant in the uncracked one . A general governing equation set is derived for $(0_m, 90_n)_s$ laminates that involves only in-plane displacements in both layers, based on equilibrium, continuity and boundary conditions. Stress distributions, elastic constants and strain energy release rate under mode I opening (as the derivative of the stored elastic energy with respect to the cracked surface area per unit volume of the specimen) have been obtained as functions of the crack densities d_0 and d_{90} in 0° and 90° layers of the laminate.

This analysis has been applied for many mechanical fatigue tests, and a propagation law under fatigue has been introduced, This law has been validated for damage evolution in the internal layer of $(0_m/90_n)_s$ laminates. Moreover, the analysis has been improved in order to predict damage development in the external layers of $(90_m/0_n)_s$ laminates. The analysis then allows to predict :
- the cycle number necessary for the initiation of cracks,
- the kinetics of crack development,
- the cycle number necessary to reach crack saturation,
- the corresponding crack density.

In this study, this analysis has been applied, without modification, to the case of thermal cycling :

- concerning the cycle number necessary for crack initiation, the predictions are in good agreement with the experiments ,

- the table 1 allows to compare the predicted values of the saturation crack densities to the experimental ones. In the particular case of the internal layer under thermal cycling, where, at the end of tests, the damage is still heterogeneous in the specimen, the given experimental density corresponds to the edge one (indicated by *). It can be observed in this table that there is a very good agreement between the predicted and the observed crack densities, in all the cases,

	d_{sat} (mm^{-1})	$(0_3/90_3)_s$		$(90_3/0_3)_s$	
		internal layer	external layer	internal layer	external layer
mechanical	prediction	0.86	//	//	0.44
fatigue	tests	0.94	//	//	0.43
thermal	prediction	0.86	0.44	0.86	0.44
cycling	tests	0.84*	0.46	0.84*	0.46

Table 1 : Values of saturation crack densities : comparison of predictions and experiments for the two stacking sequences and the two types of loadings (* : edge density values)

- under mechanical fatigue loading, the analysis can predict the kinetics of damage development with cycle number. Unfortunately, under thermal cycling, the current modeling is unable to estimate the cycle number necessary to reach the saturation of crack density, as kinetics are far much faster with cyclic temperature. As an example, in the case of the internal layer of $(0_3/90_3)_s$ laminate, the analysis predicts a damage saturation after $2.1 \ 10^6$ cycles ; experimentally, the saturation is obtained after $1 \ 10^6$ cycles under mechanical fatigue, but only after 400 cycles under thermal cycling !

5. Conclusion

This study is concerned with the damage development under both mechanical fatigue and thermal cyclic loadings of $(0_3/90_3)_s$ and $(90_3/0_3)_s$ T300/914 laminates.

Under mechanical fatigue loading, matrix cracks initiate first in the 90° layers, followed by longitudinal cracks. Under thermal biaxial cyclic loading, cracks initiate almost at the same time in both internal and external layers. The crack densities at the end of tests are similar under thermal cycling and fatigue, but the kinetics of crack development are far much faster under thermal cycling.

A fracture mechanics analysis, previously developed in the case of mechanical fatigue loading in $(0_m/90_n)_s$ stacking sequences, has been applied without modification to the case of thermal cycling : it presently allows to predict initiation and crack density values at saturation. Nevertheless, this model still need to be modified to be able to predict the kinetics of damage development under thermal variations.

References

1. Fang, G., Schapery R.A., and Weitsman, Y., (1989), "Thermally-induced fracture in composites", Eng. Fr. Mech., 33 (4), 619-632

2. Henaff-Gardin C., Lafarie-Frenot M.C., Goupillaud I., (1997), "Prediction of cracking evolution under uniaxial fatigue loading in cross-ply composite laminates" Proc. of Int. Conf. on Fatigue of Composites, Paris, 3-5 Juin 1997, pp. 189-196.

3. Henaff-Gardin C., Lafarie-Frenot M.C., Gamby D., (1996) "Doubly periodic matrix cracking in composite laminates. Part 1 : General in-plane loading ; Part 2 : Thermal biaxial loading" *Composites Structures,* Vol 36, No. 1-2, pp. 113-140.

4. Henaff-Gardin, C., I. Goupillaud, M. C. Lafarie-frenot and S. Buhr 1999. Modelling of transverse cracking under uniaxial fatigue loading in cross-ply composite laminates : experimental validation. *12th International Conference on Composite Materials,* Paris, France, 5-9 July 1999.

DURABILITY OF TITANIUM-GRAPHITE HYBRID LAMINATES

Dennis A. Burianek and S. Mark Spearing
Technology Laboratory for Advanced Composites
Aeronautics and Astronautics Department
Massachusetts Institute of Technology
Cambridge, MA 02139, USA

Titanium-graphite (TiGr) fiber metal hybrid laminates (FMHL) offer the potential to achieve a high degree of structural durability for elevated temperature airframe and engine applications. These materials consist of polymer matrix composite (PMC) plies interspersed with titanium foil layers. The use of titanium as the outer plies protects the PMC core from environmental effects such as oxidation and moisture ingress as well as potentially providing improved impact resistance and bearing properties. In order to assess the suitability of these materials for their target applications it is essential to obtain valid durability test data under service environments. Furthermore, given the cost of long duration testing, it is desirable to construct models for the material response that are capable of guiding accelerated testing and of underpinning durability assessments out to service lifetimes in excess of 10,000 hours.

Experimental and analytical results are presented for elevated temperature (177°C), tension-compression fatigue tests performed on titanium-graphite (TiGr) hybrid laminates containing open holes. The material consisted of titanium 15-3-3-3 foils and IM7-PIXA polymer matrix composite plies in a $(Ti/0/90/0_2)_s$ laminate. The overall laminate thickness is 1.6 mm, specimens were 37 mm wide and the notches were 6.4 mm in diameter. The evolution of notch tip damage was observed by cross-sectioning specimens after predetermined numbers of cycles. Figure 1 shows a schematic of damage in a specimen exposed to 30,000 cycles at 177° C, R= 0.1, and σ_{max}=30% of the open hole tension strength strength. The titanium facesheet cracks extend approximately one third of the way across the facesheet ligaments and are accompanied by splitting, facesheet delamination and transverse ply cracking. Further cycling causes the facesheet cracks to reach the edge of the specimen and subsequent damage consists of extensive delamination of the facesheets.
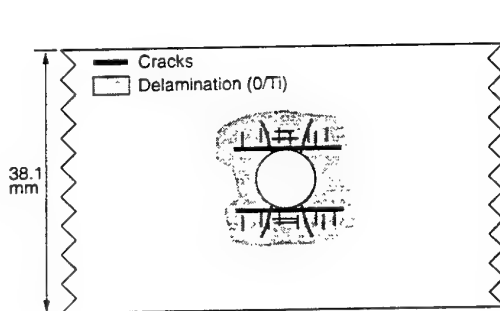

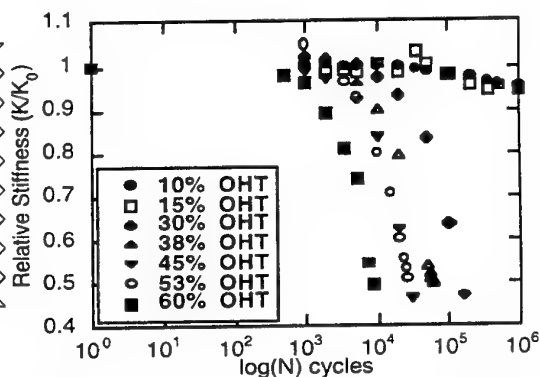Figure 1: Schematic of damage after 30,000 cycles.

Figure 2. Stiffness vs. cycles at seven stress levels

Damage progression was monitored non-destructively during testing by periodically measuring the local stiffness using an extensometer mounted across the open hole. Data from these measurements are shown in figure 2. The growth of damage during fatigue resulted in a significant reduction of the local stiffness of the material adjacent to the hole. The relative stiffness degradation was observed to increase monotonically with applied load level and number of cycles. Furthermore, the rate of stiffness degradation, and thus the damage growth was a strong function of the test temperature, as shown in figure 3. Tests were continued until either catastrophic fracture or a 50% reduction in local stiffness occurred. The data from these measurements are shown in figure 4, which indicate a relatively steep decrease in fatigue life with increasing stress level.
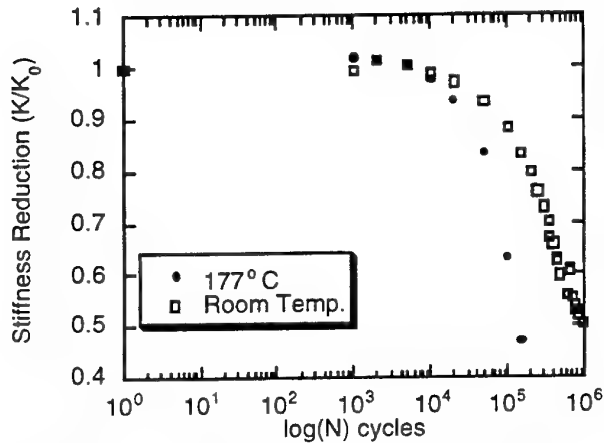

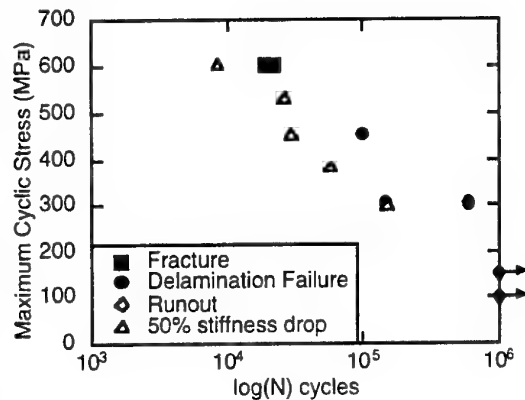Figure 3. Comparison of stiffness reduction at room temperature and 177°C.

Figure 4. S-N representation of data for specimen failure as a function of stress level and number of cycles.

Fracture mechanics-based models have been developed for the growth of the sub-critical damage modes of delamination and facesheet cracking. In combination with laminated plate theory models for residual stiffness, these reveal that facesheet delamination is the damage mode which dominates the stiffness reduction presented in Fig. 2. Tests were conducted to isolate facesheet delamination by cyclically loading unnotched specimens with seams in the facesheet orientated across the specimen width. These tests revealed that the delamination growth rate conformed to a power law relationship between growth rate and applied strain energy release rate as shown in Figure 5. The power law exponent on strain energy release rate is approximately 1.9. The data in Fig. 5 clearly shows that the fatigue delamination growth rate is accelerated by increasing temperature, by approximately an order of magnitude between room temperature (20°C) and 177°C. This provides a clear explanation for the accelerated stiffness loss observed in open hole tension specimens at elevated temperatures presented in figure 3.

Use of the stiffness reduction model allows the determination of the effective delamination growth rate – strain energy release rate dependence for the notched specimen data presented in figure 2. This reduced data is presented in Figure 6. Again a power law links the delamination growth rate and the applied strain energy release rate, with an exponent of approximately 2.0, confirming the importance of delamination in the notched response.
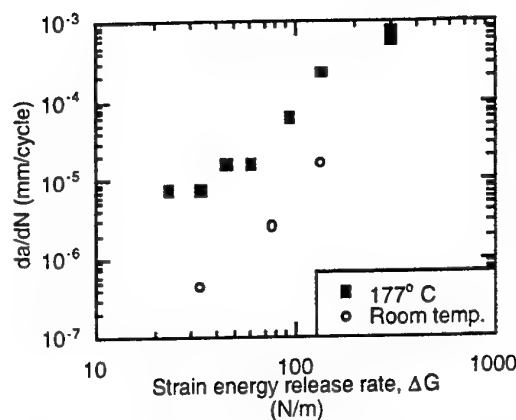
Figure 5. Facesheet delamination growth rate vs. cyclic strain energy release rate amplitude for two temperatures.
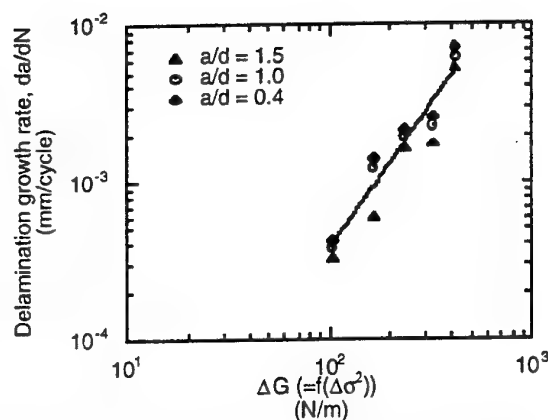
Figure 6. Effective damage growth rate vs. effective strain energy release rate for open hole specimens.

Fractographic microscopy of the delaminations revealed that the delamination generally ran in the polymer matrix rather than at the titanium/PMC interface, indicating that a strong bond was achieved and that the durability of the hybrid laminate is to a large extent determined by the elevated temperature fatigue delamination response of the PMC.

This study of a specific material system illustrates important concepts that potentially can be more generally applied to modeling the contribution of fatigue process to the durability of composites. Key features are; the identification of the key damage modes in representative structural configurations; the subsequent isolation of these damage modes and the effect of the environment on determining their rate of propagation and the construction of models for individual damage modes that can be linked to describe the structural response. Furthermore the use of fracture mechanics models to characterize damage growth, particularly under cyclic loading conditions, offers the potential to develop a damage tolerant design philosophy for composites analogous to that currently used for metallic aerospace components.

Initiation versus Growth Criteria for Transverse Matrix Cracks

Peter Gudmundson
Department of Solid Mechanics
Royal Institute of Technology (KTH)
SE-100 44 Stockholm, Sweden

The conditions for initiation and growth of transverse matrix cracks in glass or carbon fibre reinforced composite laminates have been investigated by several researchers over the last twenty years, see for example [1-7]. Almost exclusively, tensile test specimens have been applied. Experimental data have been presented in the form of transverse crack density versus applied loading for various laminate layups, ply thicknesses and material combinations. These investigations have provided information about conditions for initiation of cracks, but it is not obvious how to extract information about crack growth criteria, since the cracks are results of initiation and subsequent growth. For small ply thicknesses one can argue that initial flaws exist which span the ply thickness and hence the initiation is a result of crack growth from these flaws. Crack initiation data for small ply thicknesses have successfully been interpreted in this way. In order to perform direct measurements of crack growth conditions, a well defined initial crack must exist and conditions for growth of this crack should be considered. The effects of notches on the transverse layer have been investigated by Boniface et al. [8]. They found that the notches had a significant influence on the conditions for crack initiation in thick transverse plies, whereas the effect was smaller for thin plies. These observations indicate in a nice way for the difference between initiation and growth criteria.
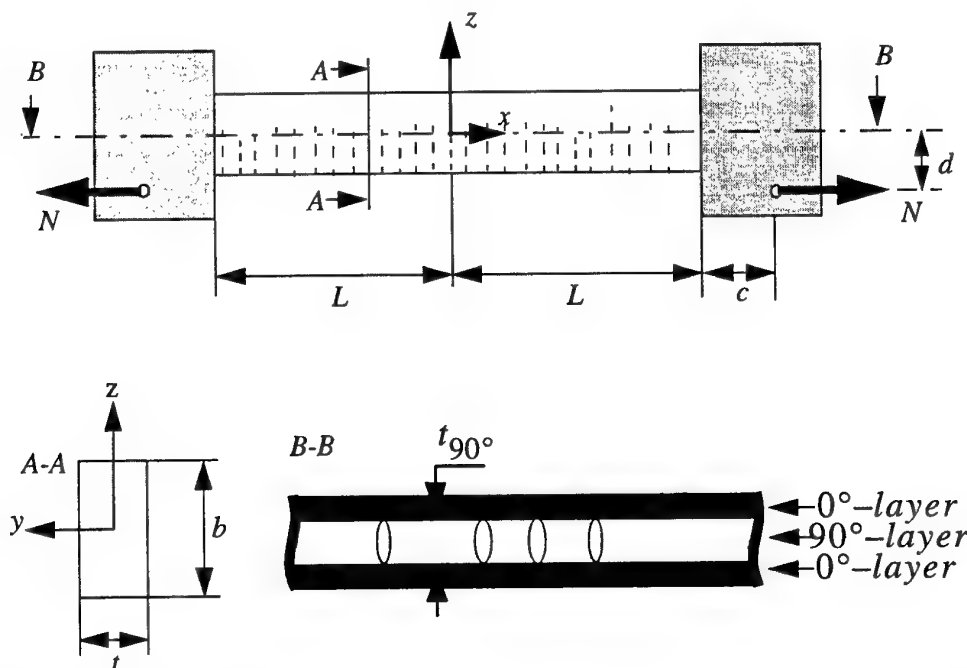

Figure 1. Experimental setup. The dashed lines in the upper figure symbolize transverse matrix cracks.

The present investigation is aimed at well controlled crack growth measurements for determination of a relevant crack growth criterion. An experimental technique is developed that makes it possible to introduce transverse matrix cracks which start from one edge of a specimen and arrest before reaching the other edge. This is achieved through a combination of extension and

bending loading of tensile specimens, see Figure 1. As the external loading increases, already existing matrix cracks continue to grow in a step-wise fashion and new cracks initiate. Matrix crack positions and lengths are registered through optical images which are captured at regular external load intervals.

The local stress and strain state as well as energy release rates of individual matrix cracks are determined from a combined global and local analysis. The average stress and stress state as a function of the loading N in the beam described in Figure 1 is modelled by beam theory including the stiffening effect of the axial force. For each load level, the average matrix crack length is determined from the optical images. The decrease in beam stiffness in the cracked part of the specimen is estimated from the model described in [9]. To check the accuracy of the beam model for prediction of the global strain state, strain gages were mounted on the edges $z = 0.5b$ and $z = -0.5b$ in the middle of the beam ($x = 0$). In Figure 2 the measured strains are compared to the beam model predictions. It can be observed that a quite good agreement is obtained.
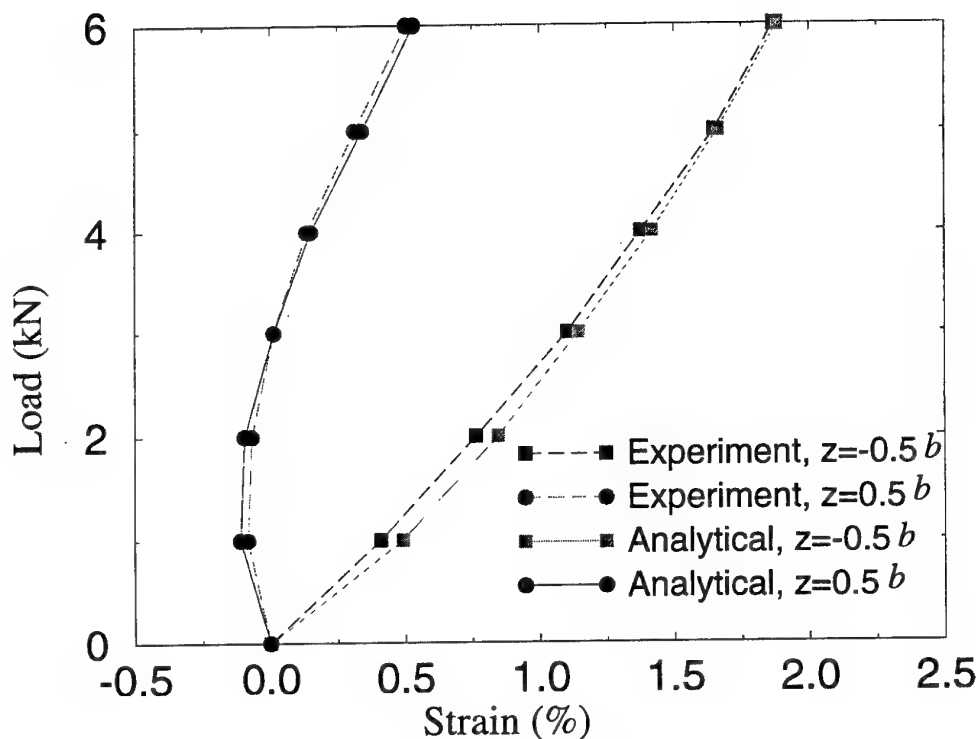

Figure 2. Comparison between measured and calculated strains for the $[0_2, 90]_s$ specimen. The position of the measured and calculated strains correspond to the top ($z = 0.5b$) and the bottom edge ($z = -0.5b$) in the middle of the beam according to Figure 1.

Based on extensive finite element calculations, a model for determination of local energy release rates for individual matrix cracks was developed. It was found that the stress intensity factor of a matrix crack is controlled by the lengths of the crack under consideration and the two neighbouring matrix cracks. If the crack is longer that its two neighbours, the interaction effect from the neighbours can be neglected. In the case that one or two of the neighbouring cracks are longer, correction factors depending on the distance between the cracks are derived based on extensive finite element calculations. For some load levels, the above mentioned simplified method for determination of individual stress intensity factors were compared to full three-dimensional finite element calculations of the whole specimen. In Figure 3 comparisons between the approximative analytical formula based on correction factors for determination of

stress intensity factors and results from full three-dimensional finite element calculations are presented. It is observed that an acceptable accuracy is obtained by use of the approximative method. All specimens, load levels and corresponding crack states determined from the optical images are then analysed by use of the beam model for determination of the global strain state and by the derived formula for calculation of stress intensity factors (energy release rates).
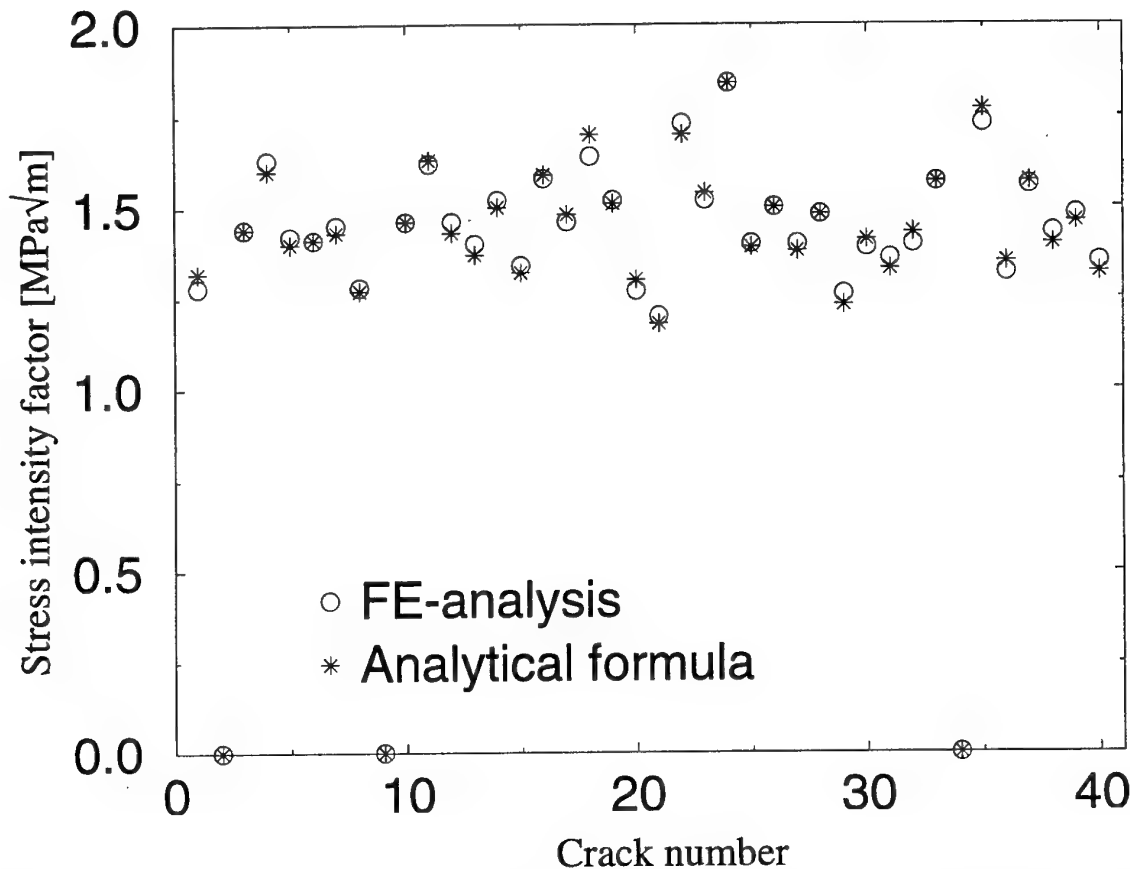

Figure 3. Comparison between approximative estimates of stress intensity factors and three-dimensional finite element calculations for the [0₂, 90]ₛ laminate.

An analysis of the conditions for reinitiated growth of already existent matrix cracks makes it possible to evaluate crack propagation criteria. Also conditions for initiation of new cracks can be analysed from the experiments. In this way, initiation and growth can be separated in an unambiguous way. Since several transverse matrix cracks appear in each specimen and crack growth can be observed at different load levels, a single macroscopic specimen generates lots of data. Experiments on $[0_2, 90]_s$ and $[0_2, 90_2]_s$ glass/epoxy cross-ply laminates are presented. About 40 transverse matrix cracks at 15 load levels were analysed for each specimen. This resulted in more than 400 crack growth observations and about 40 crack initiations for each specimen.

The results indicate that the energy release rate is a controlling parameter for crack growth whereas the strain state controls the crack initiation. A small transverse ply thickness dependence was however observed. The critical energy release rates for the $[0_2, 90]_s$ and $[0_2, 90_2]_s$ were found to be 151±45 N/m and 124±28 N/m respectively. The initiation strains were determined as 0.74±0.12% and 0.62±0.05%. The present investigation clearly demonstrate that separate criteria for initiation and growth of transverse matrix cracks must be applied in evaluations of test data as well as in applications.

[1] Garrett, K.W. and Bailey, J.E., Multiple Transverse Fracture in 90° Cross-Ply Laminates of a Glass Fibre-Reinforced Polyester. *J. Mater. Science,* 1977, **12**, 157-168.

[2] Garrett, K.W. and Bailey, J.E., The Effect of Resin Failure Strain on the Tensile Properties of Glass Fibre-Reinforced Polyester Cross-Ply Laminates. *J. Mater. Science*, 1977, **12**, 2189-2194.

[3] Parvizi, A., Garrett, K.W. and Bailey, J.E., Constrained Cracking in Glass Fibre-Reinforced Epoxy Cross-Ply Laminates. *J. Mater. Science,* 1978, **13**, 195-201.

[4] Bailey, J.E., Curtis, P.T. and Parvizi, A. On the Transverse Cracking and Longitudinal Splitting Behaviour of Glass and Carbon Fibre Reinforced Epoxy Cross Ply Laminates and the Effect of Poisson and Thermally Generated Strain. *Proc. R. Soc. Lond.,* 1979, **A366**, 599-623.

[5] Flaggs, D.L. and Kural, M.H., Experimental Determination of the In Situ Transverse Lamina Strength in Graphite/Epoxy Laminates. *J. Comp. Mat.,* 1982, **16**, 103-116.

[6] Harrison, R.P. and Bader, M.G., Damage Development in CFRP Laminates Under Monotonic and Cyclic Stressing. *Fibre Science and Technology*, 1983, **18**, 163-180.

[7] Boniface, L. and Ogin, S.L., Application of the Paris Equation to the Fatigue Growth of Transverse Ply Cracks. *J. Comp. Mat.*, 1989, **23**, 735-754.

[8] Boniface, L., Smith, P.A., Bader, M.G. and Rezaifard, A.H., Transverse Ply Cracking in Cross-Ply CFRP Laminates - Initiation or Propagation Controlled?. *J. Comp. Mat.*, 1997, **31**, 1080-1112.

[9] Adolfsson E. and Gudmundson P., Thermoelastic properties in combined bending and extension of thin composite laminates with matrix cracks. *Int. J. Solids Structures*, 1997, **34**, 2035-2060.

APPLICATION OF HIGH FREQUENCY DIELECTRIC SPECTROSCOPY FOR THE ASSESSMENT OF DURABILITY OF ADHESIVELY BONDED COMPOSITE STRUCTURES

P. Boinard and R.A. Pethrick[*]
Department of Pure and Applied Chemistry,
University of Strathclyde,
295 Cathedral Street, Glasgow, G1 1XL, Scotland, UK.

W.M. Banks
Department of Mechanical Engineering,
University of Strathclyde,
75 Montrose Street, Glasgow, G1 1XJ, Scotland, UK.

1. INTRODUCTION

Adhesively bonded composite structures are being used in a wide range of applications, including situations where they become exposed to high levels of moisture. Ingress of moisture into a polymeric adhesive will lead to changes in its mechanical properties related to plasticisation and hydrolysis effects (Comyn 1991 and Shaw 1993). In bonded composite structures, water ingress can influence not only the mechanical properties of the adhesive but also those of the composite matrix, fibre-matrix interface and adhesive-adherent interface.

Over the last ten years, the application of high-frequency dielectric techniques to the characterisation of adhesively bonded metallic structures has been extensively investigated by the co-authors (Pethrick *et al* 1995,1996,1997a to c). In such a structure, the metallic adherents can be used as wave-guides allowing characterisation of the adhesive layer which acts as a dielectric. Changes in the dielectric characteristics of such a structure can be used to monitor its ageing and degradation.

Carbon fibre reinforced plastics (CFRP), while less conductive than aluminium, are sufficiently conductive to sustain the propagation of high-frequency dielectric signals. This paper discusses the application of high-frequency time domain response (TDR) analysis to CFRP adhesively bonded structures and indicates that the success obtained in its application to aluminium structures regarding assessment of water ingress is also applicable to CFRP bonded structures. This paper not only suggests a new way to assess the integrity of a structure but also produces new insights into the application of TDR measurement to non-isotropic materials.

2. EXPERIMENTAL METHODS

2.1 Materials

Carbon fibre reinforced plastic (CFRP) adherents were manufactured from Hexcel Composites Ltd unidirectional carbon fibre pre-impregnated film, trade named 914C-TS(6K)-5-34%. The adhesive system used, a nylon woven fibre supported epoxy resin, was a 3M structural epoxy system trade named Scotch-Weld Brand AF-163-2U. Samples were manufactured using a vacuum bag procedure in an autoclave.

2.2 Dielectric Measurements

Dielectric measurements were carried out in reflection mode over the frequency range 300kHz to 3GHz using a Hewlett Packard 8753A Network analyser. The system was calibrated using three independent standards whose reflection coefficients are known over the frequency range of interest. Details of the measurement technique and theory have been presented elsewhere (Pethrick *et al*, 1995 & 1997b).

---

[*] To whom correspondence should be addressed.

I

3. RESULTS AND DISCUSSION

3.1 Effect of Orientation of the Carbon Fibre Layers on the TDR

During high frequency dielectric spectroscopy, an electric field appears between the CFRP plates producing a magnetic field, which propagates a transverse electro-magnetic (TEM) wave at the adherent/adhesive interface. When good contacts exist between the fibres of CFRP laminates, the composite adherent structure is able to transmit the electric field at the adherent/adhesive interfaces, therefore polarising the adhesive. Different joint designs were examined (Fig.1), but after consideration of the mechanical experiments following this study, the design presented in Figure 1, bottom was chosen. Typical TDR results for unidirectional carbon fibre plate joints are presented in Figure 2 where several reflection peaks are observed (solid line). However, when all the fibres are perpendicular to the dielectric wave propagation direction, the dissipation of the impulse energy in the first millimetres of the joint prevents the development of secondary reflection peaks. There is a sufficient contact between the laminate fibres and enough energy supplied to percolate through the thickness of the plate, as shown by the presence of a first upward peak. However, the high resistivity of the laminate matrix prevents propagation of the pulse along the joint.

To improve the conductivity of the adherent in the direction of the electro-magnetic wave propagation, unidirectional fibres were aligned in the direction of propagation. Five different lay-ups following the sequences $[0_{14}]$, $[0_2/90/0_2/90/0]_S$, $[0/90_3/0/90_2]_S$, $[90_2/0/90_2/0/90]_S$ and $[90/0_3/90/0_2]_S$ were manufactured. The main differences between these lay-ups are the direction of the last laminae at the adherent-adhesive interface and the percentage of fibres in each direction. A 90° fibre direction means that the fibres are perpendicular to the dielectric wave direction of propagation (Figure 1, bottom). Figure 3a presents the TDR spectrum of the $[0_{14}]$, $[0_2/90/0_2/90/0]_S$ and $[0/90_3/0/90_2]_S$ joint: 100%, 74% and 26% of the carbon fibre at 0°, respectively, with the direction of the fibre of the laminae at the interface being at 0°. Figure 3b presents the TDR spectrum of the $[90_2/0/90_2/0/90]_S$ and $[90/0_3/90/0_2]_S$ joint: 74% and 26% of the carbon fibre at 0°, respectively, with the direction of the fibre of the laminae at the interface being 90°. The sequence of the layers does not have an influence on the response and, as seen in Figure 3b, and the presence of some layers at 90° does not significantly disturb the TDR as shown by the comparison between the $[0_{14}]$ response and the other laminate responses.

Following these results, the $[90_2/0/90_2/0/90]_S$ configuration was selected for the adherent plates of the new design. This implies 14 layers of carbon fibres, 10 at 90° and 4 at 0°, representing 74% of fibres at 90° and 26% at 0°. Figure 4 presents a comparison between the TDR of the $[0_{14}]$ design and the new design. The lower amplitude in the impulse (downward) peak indicates a better balance between the impedance of the measuring system and the joint structure. The higher amplitude of the first response (upward) peak corresponds to an improved polarisation of the CFRP-adhesive interfaces. The displacement of the peaks towards longer response time is consistent with the high resistivity of the new design, which decreases the velocity of the TEM wave.

3.2 Moisture Absorption in the Joint Structure

Gravimetric measurements during ageing were performed by removing the samples from a water bath held at a constant temperature of 60°C and rapidly blotted and weighted using an electronic balance with an accuracy of ±0.1mg. Figure 5 presents the results for the joint structure, the CFRP adherents alone and the adhesive. The amount of water present in the adhesive has been estimated by subtracting the amount of water present in the joint to the amount of water present in the CFRP plates. The latter has been calculated from gravimetric results of CFRP plates exposed to identical ageing conditions. From these results, it is possible to differentiate the amount of water in the adherent from the amount of water absorbed by the adhesive.

3.3 Effect of Water on the TDR of Adhesively Bonded Composite Structures

TDR measurements were performed during ageing and the results are presented in Figure 6. The time difference between two neighbouring peaks is related to the effective permittivity $\bar{\varepsilon}$ of the material between the wave-guides (Pethrick et al., 1997a) by:

$$\bar{\varepsilon} = \left(\frac{c}{2 \cdot l / \Delta t}\right)^2 \qquad (1)$$

where c is the velocity of light in vacuum, l is the physical length of the joint and Δt is the time difference between the impulse peak and the first response peak. Figure 6a shows the displacement of the response peaks towards longer response time values. This is caused by the evolution of the dielectric permittivity of the adhesive due to the absorption of water which decreases the electrical wave velocity, consequently increasing the response time. Figure 6b presents the evolution of the average dielectric permittivity as a function of exposure time.

3.4 Correlation Between Water Uptake and TDR of Adhesively Bonded Composite Structures

In order to compare the time domain results with the gravimetric results, normalisation of the data was performed using Equation 2:

$$Data_{Norm} = \frac{Data_t - Data_0}{Data_\infty - Data_0} \qquad (2)$$

where $Data_t$ is the value at time t, $Data_0$ is the initial value, $Data_\infty$ is the final value at equilibrium and $Data_{Norm}$ is the normalised value. A correlation coefficient of 0.96 over 10 points between the TDR results with the gravimetric results shown in Figure 7 confirms that water penetration in adhesively bonded structure could be assessed by high frequency TDR measurement.

4. CONCLUSION

This study has shown the importance of the carbon fibre orientation on the high-frequency time domain analysis, has established that non-isotropic adherents, when properly designed, provide good wave-guide permitting TDR measurements and has validated the use of TDR to identify the change in the dielectric permittivity of the bond line. Correlation between the gravimetric and TDR data established its capacity to assess water uptake in the adhesive of a joint structure.

This study on adhesively bonded composite structure has shown the potential of high frequency dielectric TDR as a non-destructive evaluation method to assess the integrity of the bond line present in aircraft primary and secondary bonded structures.

ACKNOWLEDGEMENTS

REFERENCES

Comyn J., 1981, *Developments in Adhesives – Part 2*, Applied Science Publishers, London, pp. 279-314.

Pethrick R.A., Banks W.M., Hayward D., Joshi S.B., Li Z-C. and Jeffrey K., 1995, *Insight*, Vol. 37, No. 12, pp. 964-968.

Pethrick R.A., Banks W.M., Dumoulin F., Hayward D. and Li Z-C., 1996, *Journal of Physics Part D, Applied Physics*, Vol. 29, pp. 233-239.

Pethrick R.A., Li Z-C., Hayward D. and Gilmore R. , 1997a, *Journal of Materials Science*, Vol. 32, pp. 879-886.

Pethrick R.A., Li Z-C., Joshi S., Hayward D. and Gilmore R. , 1997b, *Non-Destructive Testing & Evaluation International*, Vol. 30, No. 3, pp. 151-161.

Pethrick R.A., Joshi S., Hayward D., Gilmore R. and Yates L.W. , 1997c, *Journal of Adhesion*, Vol. 62, pp. 281-315.

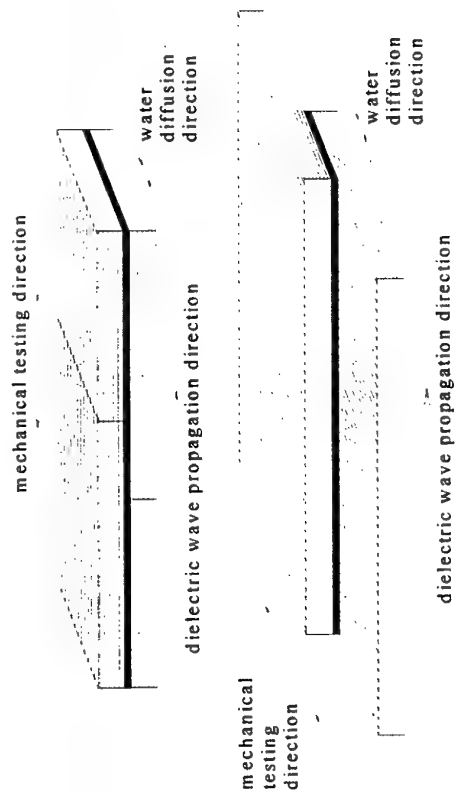Shaw S.J., 1993, *Chemistry and Technology of Epoxy Resins*, Blackie Academic & Professional, Glasgow, pp. 206-255.

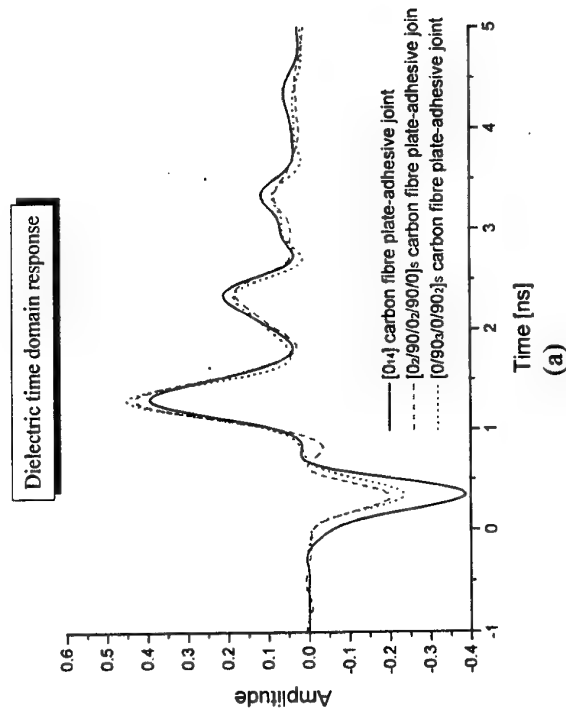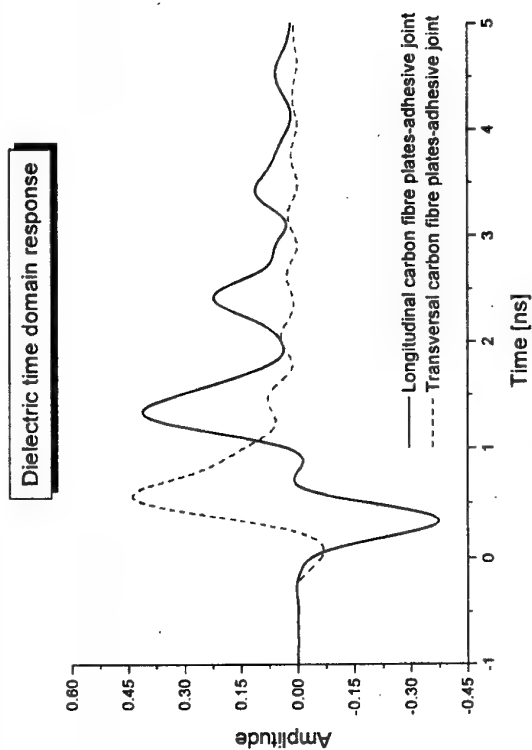Figure 1: *Previous joint design (top) and new joint design (bottom).*

Figure 2: *TDR of longitudinal and transversal CFRP joints.*
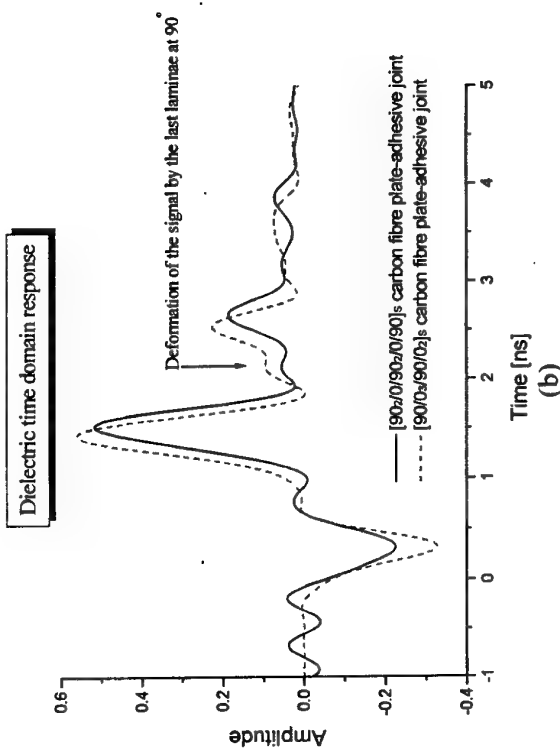

Figure 3: *TDR of different carbon fibre lay-up: (a) laminae at the interface at 0° and (b) laminae at the interface at 90°.*
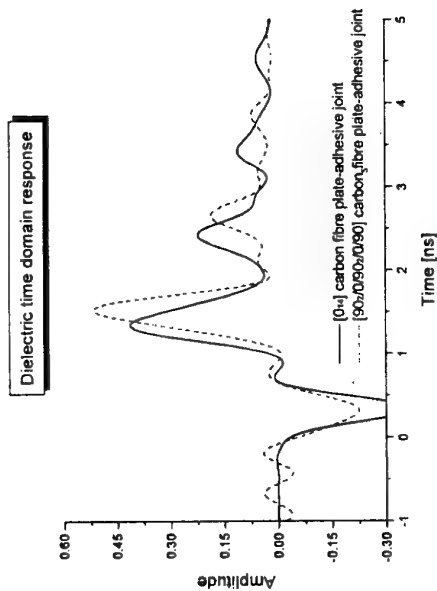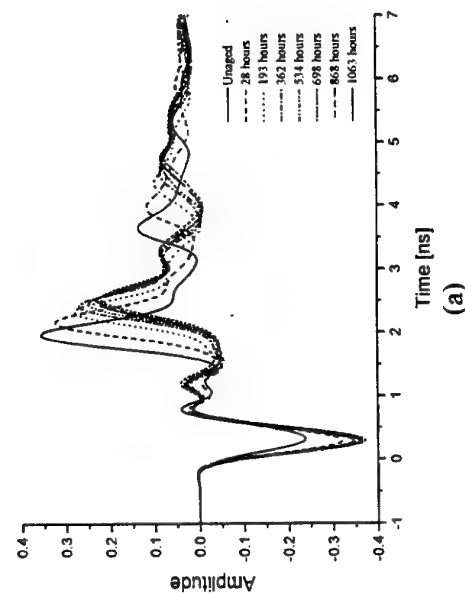
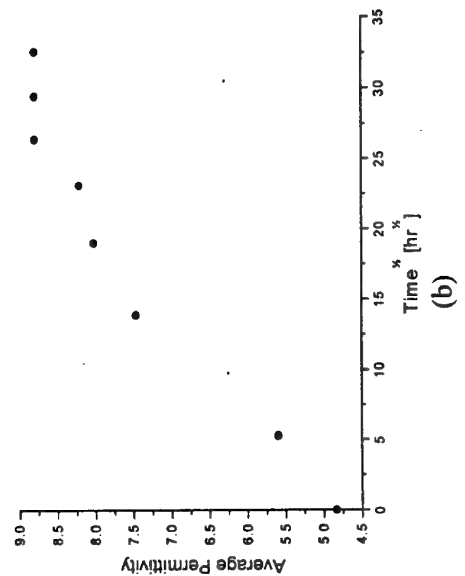**Figure 4:** TDR of [0₁₆] and [90₂/0/90₂/0/90]s CFRP joints.

[0₁₆] carbon fibre plate-adhesive joint
[90₂/0/90₂/0/90] carbon fibre plate-adhesive joint

Dielectric time domain response

Amplitude — Time [ns]

Figure 5: Water uptake of (■) joint structure, (●) CFRP adherents and (▲) adhesive.

% Water Uptake — Time ½ [hr ½]

Figure 6: Evolution during ageing of (a) the TDR and (b) the average permittivity.

Unaged
28 hours
193 hours
362 hours
514 hours
698 hours
868 hours
1063 hours

Amplitude — Time [ns]
(a)

Average Permittivity — Time ½ [hr ½]
(b)
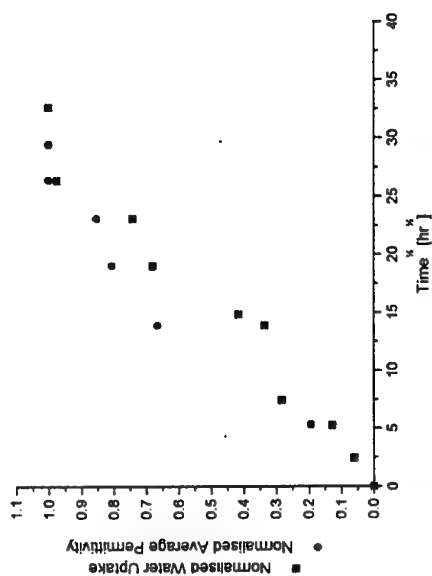
Figure 7: Correlation between normalised adhesive water uptake and average dielectric permittivity.

■ Normalised Water Uptake
● Normalised Average Permittivity

Normalised Average Permittivity — Time ½ [hr ½]

X-RAY MICROTOMOGRAPHY: A NEW TECHNIQUE FOR ANALYSIS OF COMPOSITE MATERIALS

R. Pyrz

Institute of Mechanical Engineering, Aalborg University,
Pontoppidanstræde 101, 9220 Aalborg East, Denmark

INTRODUCTION

The physical properties of a material are strongly influenced by the microstructure which is designed during processing. Amount of constituent elements forming the material is in many cases known beforehand as for example the volume fraction of reinforcing phase in composite materials. However, the final architecture of a microstructure is controlled only to a limited extent, and on the microscale the geometrical arrangement of second-phase inclusions is a result of complex and interacting processing micromechanisms rather than a design variable. This seems to create an obstacle in modelling the relation between microstructure and overall material properties.

In order to overcome this difficulty it is customarily assumed that the geometrical features of a microstructure are randomly distributed without any precise explanation of what randomness means and how it can be quantified. On the other extreme lies the assumption that the dispersion of fillers is regular. It significantly simplifies calculations, especially with the finite element method, and provides satisfactory results as far as highly nonlinear phenomena are not concerned. For strongly localized effects such as initiation of microcracks and plastic zones which subsequently propagate at different scale lengths, the regularity assumption may lead to seriously erroneous results. Therefore, it is important to describe dispersion characteristics of the microstructure in an unambiguous way by quantitative factors which eventually could be related to physical properties of the material.

When we examine the microstructure of a material we are looking at a very small sample of the structure. From this limited view we have tried to understand how the properties of the material relate to microstructure. The approach must necessarily be statistical in particular with respect to the measurements of the microstructure. A selection of representative volume elements where we seek to find microstructure-property relations must be based upon sound sampling techniques. Furthermore, the investigation of three-dimensional microstructures is possible in most cases only on the internal surfaces generated by taking planar sections for microscopy. This necessary step from spatial microstructures to their planar sections involves a great loss of information.

X-RAY MICROTOMOGRAPHY

Developments of X-ray microscopy and computer tomography provide a new tool for the assessment of materials morphology. A common problem in morphological analysis is that three-dimensional information of microstructure is required, but its images are two-dimensional. In X-ray microtomography, the object is rotated so as to obtain radiographic projections from different viewing angles. An enlarged radiograph of the object is recorded

by an X-ray sensitive camera after the object has been traversed by the conical X-ray beam. All these projections are used in a reconstruction algorithm which calculates a set of serial non-destructive sections where the interpretation of the image, i.e. cross section, can be done in terms of attenuation of the X-rays in the object. Then, a three-dimensional image of the specimen can be reconstructed from serial sections and can be processed to show and measure three-dimensional features.

X-ray microscopy is a relatively new technique that has not been applied to any significant extent in materials science. Most X-ray microscope development has so far been made using large synchrotron sources. This has limited X-ray microscopy to a research tool available only at the major synchrotron facilities. The use of X-ray tubes with a very small focus together with a very sensitive recording devices enable the design of a bench-top X-ray microscope with a spatial resolution less than 8 micrometers.

ANALYSIS

In the present context we are concerned with a well-defined shape of the inclusions such as spherical particles and continuous fibres. The following question arises if we attempt to characterize the distribution of centre points of fibres in unidirectional composites recorded on the transverse sections or the centre points of spherical particles' traces in particulate composites: "What is the shape of a set of points and how it can be quantified.

The distribution is neither regular nor random in a strict sense of the word. On the other hand it is generally recognized that dispersion pattern of fillers strongly influences the mechanical properties of composites and, in particular, causes extreme fluctuations of local stresses that may exceed a microfailure threshold. Hence, relevant data concerning classification of the inclusion distribution, i.e. as to whether it is random, non-random, clustered or any other is necessary. The characterization of complex aspects of disorder is performed using the idea of fractal dimension: a dimension that corresponds in a unique fashion to the geometrical entity under study and often is not an integer.
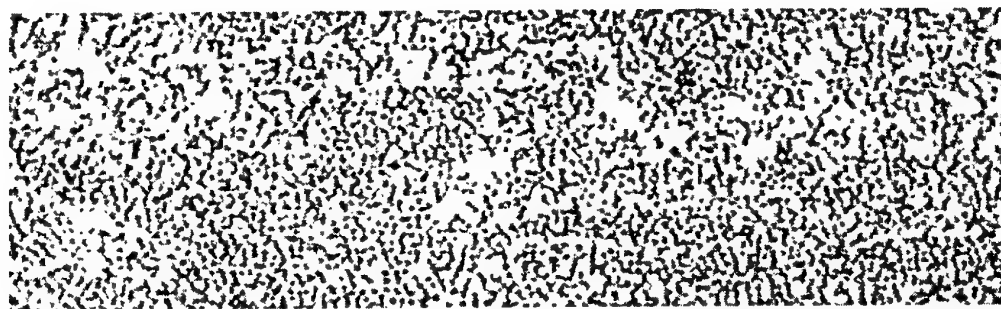

Figure 1

Figure 1 presents one reconstructed cross section through a unidirectional glass fibre epoxy composite. This nondestructive image allows to determine the centre position of all fibres to characterise a dispersion pattern by quantitative terms, simultaneously giving a visual impression about homogeneity of fibres dispersion. The precision and accuracy of the image is slightly disturbed by a statistical noise which cannot be eliminated from microtomographis scans. However, the post-recostruction filtering and image enhancement can to a large extent eliminate its influence. This is illustrated in Fig.2 where only a small part of the original image is shown. In the post-reconstrucrion filtering procedure a major part has been played by
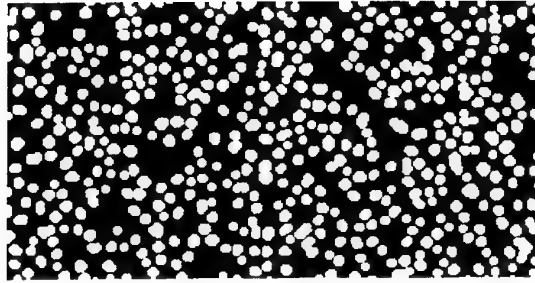
Figure 2

a proper selection of morphological filters and thresholding. Taking the nondestructive slices at relatively small intervals of approximately 40 μm indicate that the fibres are not parallel as illustrated in Fig. 3. That is to say that the dispersion characteristics of fibre centres vary with
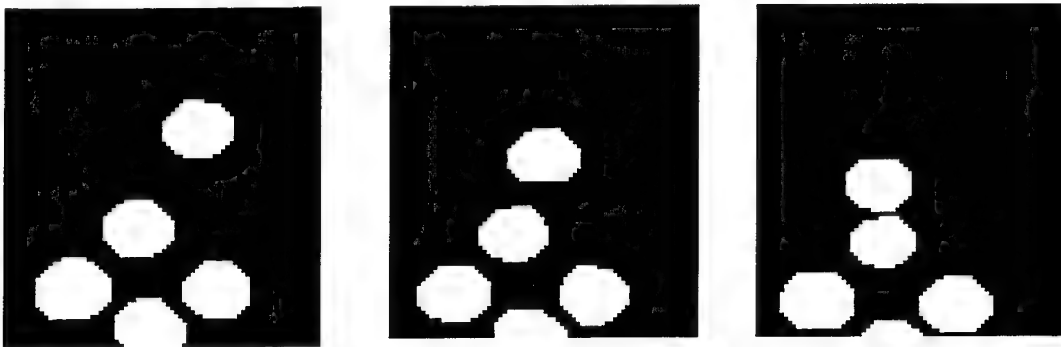

Figure 3

the position of the cross section. These kind of images may be used to disclose fibre waviness, a geometrical factor of the reinforcing fibres which controls compressive properties of the composite.

For the particulate composite a correlation map has been established between particles diameters and corresponding diameters of traces measured on reconstructed nondestructive cross sections.

CONCLUSION

The most important aspect of X-ray microtomography is that the method is nondestructive. Thus it is possible to characterise samples in situ and observe how the microstructure evolves under the influence of mechanical and/or other types of loadings.

IN-SITU INVESTIGATION of TIME-DEPENDENT BEHAVIOR of POLYMERIC COMPOSITE SUBJECT to SHEAR LOADS

Ai-Chang Zhan, Yong-Qi Sun and Jiong Tian

Laboratory for Nonlinear Mechanics of Continuous Media, Institute of Mechanics,
Chinese Academy of Sciences, Beijing, 100080, China
Northwest Institute of Textile Sci. & Tech., Xian, 710048, P. R. China

INTRODUCTION

It is well known that the viscoelastic nature of polymeric materials cause them to exhibit considerable rate-sensitivity. For the polymer matrix composites, their behaviors of deformation, damage and fracture during being loaded depend upon not only the load level, but also the duration of loading . Therefore, a good understanding of the long term behavior of these composites become more and more important. The objective of current investigation is to gain insight into the micromechanisms of the time-dependency of damage in composites through in-situ observation of the dynamic processes of initiation and evolution of damage by loading specimen inside of a scanning electron microscope (SEM) equipped with a mechanical stage and measuring system.

EXPERIMENTAL PART

The material chosen for this investigation was the fiber reinforced epoxy AS4/3502 manufactured by Hercules Corporation. The epoxy 3502 is a highly cross-linked resin.

Miniature end notched flexure (ENF) specimens approximately 30mm long, 5mm wide and 1mm thick were cut from a unidirectional laminate. The specimen surface to be observed was ground with sand paper and polished with alumina powder to 0.3 micron finish on an automatic polisher, cleaned, dried, and finally sputter coated with approximately 100 angstrom of gold.

The shear loading was performed inside the SEM by using a three − point bend fixture. The specimen was loaded until a certain load level was reached. At this point, the load was kept approximately the same, and the duration of loading was extended.

The time-dependency of microcracking behavior of a material in the damage zone was directly and continuously observed, recorded, then measured and analyzed. The shear strain corresponding to various spans of duration was calculated.

RESULTS AND DISCUSSIONS

Results show by several sets of valuable SEM micrographs which recorded what were really happening in detail during test. It was found that the microcracking behavior of material in the crack tip damage zone was closely related with the duration of loading under certain load level. A domain or microscopic region (about 24×14 square micron) between fibers in the crack tip damage zone was focused on, the time-dependent behavior of the material in the region was continuously observed, which includes the initiating, growing and coalescing of microcrack.

Shear strains $\gamma = \tan\theta$ corresponding to each span of duration were measured and listed in Table 1.

Table 1

duration of loading (min)	shear strain
15	0
35	0.14
60	0.27
70	0.51
100	0.65
115	0.90

It was found that shear strain depends on stress, loading time, local boundary conditions, etc.

$$\gamma = \gamma(\tau, t, b)$$

In the case discussed here, the shear strain depends mainly on the duration of loading. It was also noted that the manner of strain increasing with time was jumping which resulted from the damage localization. It seems that there exists a principle of equality between load and duration, for developing a given strain value, increasing the duration of loading equal to increasing load level. When the attention was paid to an entire crack tip damage zone (270×14 square micron), about the same result was observed. In the early phase of duration, the microcracks were observed to initiate and grow but no microcrack coalescence occurred. So the microc-

racking behavior of the system in this stage may be described by using the following equation:

$$\frac{\partial n}{\partial t} + \sum_{i=1}^{i} \frac{\partial(nP_i)}{\partial p_i} = n_N$$

Where n is the number density of microcrack, t is the duration of loading, P_i and p_i are variables related to the size of microcrack, and n_N is the nucleation rate of the n.

When the system is in a state of dynamic equilibrium, within certain period of duration, the number of microcrack newly initiated approximately equals to the number of microcrack disappeared due to the coalescing. The evolution of microcracking probably follows the following equation:

$$\frac{\partial n}{\partial t} + \sum_{i=1}^{i} \frac{\partial(nP_i)}{\partial p_i} = n_N - n_A \doteq 0$$

Where n_A is the disappearing rate of microcrack number density.

Influence of quasi lifetime treatments on the static and fatigue durability of continuous glass fibre reinforced polypropylene

J.F. Neft*, P. Schwarzer* & K. Schulte[#]

*Volkswagen AG, Central Labs, Wolfsburg; [#]Technische Universität Hamburg-Harburg, Hamburg

Ongoing efforts in the automobile industry to increase the fuel efficiency of cars by an overall weight reduction have led to an increased interest in lightweight materials and design. In addition to aluminium and magnesium, fibre reinforced polymers (FRP) show a high potential to reach the lightweight targets. During the past 3 decades, continuous fibre reinforced polymers have been employed successfully as substitutes for steels and aluminum alloys in aerospace industry. However, these carbon fibre reinforced thermosets (CFRP) are not suitable for automobile applications due to their high costs and processing difficulties yet. On the other hand, the fairly new group of FRP, the continuous glass fibre reinforced thermoplastics (GFRT), is considered as potential material in the automobile industry. Advantages of GFRT include low cost and manufacturing processes comparable to GMT.

Many international projects have already dealt with the aspects of production and implementation of GFRT [STU 98, MAE 96, ENG 93, FUN 97, DAV 94]. Results of mechanical tests showed the potential of GFRT for industrial application [MAE 95, OEV 98, THO 94]. Paramount to the introduction of GFRT into automotive applications is a wide database of their durability behaviour. A comprehensive understanding of the mechanical behaviour and the damage mechanisms under service conditions is necessary for a successful application.

This study investigated the mechanical properties, including static, fatigue and thermomechanical behaviour, of a continuous GFRT, with the trademark name Plytron© from Borealis (Norway). The material consisted of prepregs with E-glass fibre as reinforcement and isotactic polypropylene as matrix material with a fibre volume fraction of about 35%. Both unidirectional and cross-ply stacking sequences were used. The material was investigated in three different conditions: I) as delivered, II) aged (90°C, 100 days) and III) aged under a special 125 day climate cycle consisting of high and low temperature and humidity levels. The material was characterised by means of a thermo analyzer (DMA) and tested under tension, compression and bending stresses. Fatigue testing was performed at two different stress ratios, R=0.1 and R=-1, at a frequency of 10 and 5Hz respectively and room temperature. A special test fixture was designed for performing both static and fatigue compression stresses under the same conditions. Damage mechanisms and influence of material treatment were studied by optical microscopy, SEM and replica technique.

Figure 1 and 2 display the results. Figure 1 shows that the treatments influenced the material strength, however this depended on the loading conditions. The as delivered material showed the highest strength in transverse tension and compression while the aged specimens showed the highest strength in tension and bending. The SEM micrographs showed that the different stress treatments led to different micromechanical failure. Failure mechanisms could be correlated with the material conditions. The cross-ply laminates had comparable results.
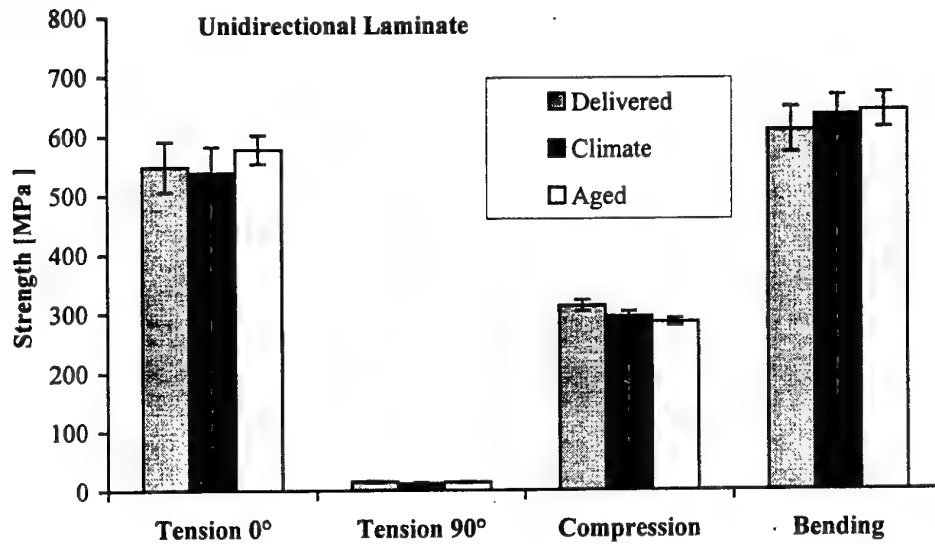
Figure 1: Strength of the unidirectional laminates under tension, transverse tension, compression and bending for all three treatments: I) as delivered, II) conditioned with a special climate cycle and III) aged.

Figure 2 shows the S/N-curves for tension-compression loading (R=-1). The as delivered material showed the best fatigue resistance and the aged material showed the worst up to 10^4 cycles. However S/N-curves are not an accurate representation of the fatigue behaviour of FRP. A better understanding of fatigue failure mechanisms can be achieved by fractography and the observation of stiffness reduction during fatigue. It is shown that the different fracture behaviour is mainly influenced by the matrix and the fibre-matrix interface.
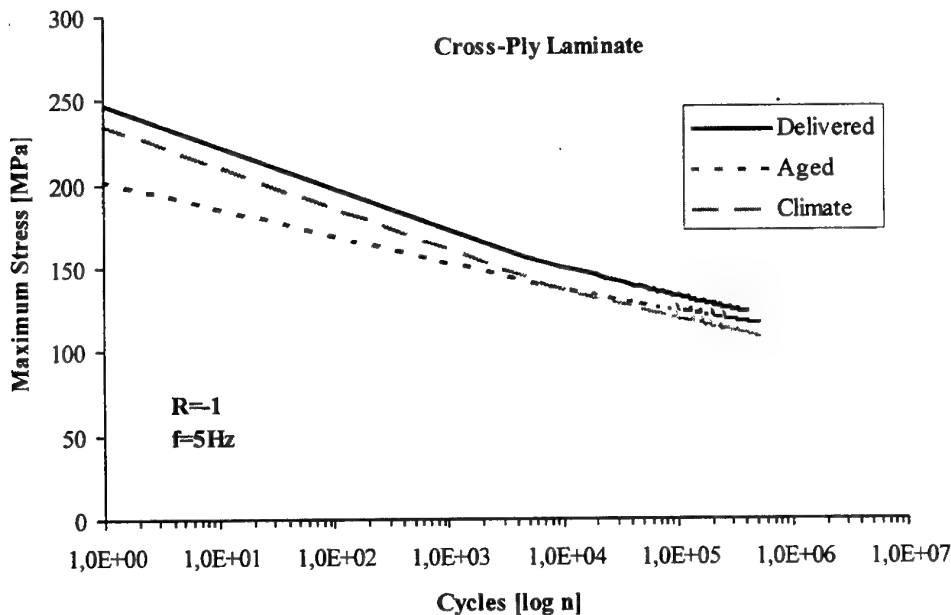

Figure 2: S/N-curves for all three treatments: I) as delivered, II) conditioned with a special climate cycle and III) aged. R=-1 and f=5Hz.

Literature

DAV 94   P. Davies, W.J. Cantwell; Fracture of glass/polypropylene laminates: influence of cooling rate after moulding; Composites 25 (1994) 869-877

ENG 93   K. Eng; Lost yarn preforming and splitt film based weft insert warp co-knitting, new routes for composite materials preforming; Verbundwerkstoffe und Werkstoffverbunde, DGM Informationsgesellschaft Verlag, 1993, 131-137

FUN 97   R. Funck, M. Neitzel, O. Christen; Innovative applicatiuons with thermoplastic filament winding techniques; Proceedings of ICCM-11, 1997, I-419 – I-425

MAE 95   Einfluß der Struktur textiler Vorprodukte auf die Eigenschaften langfaserverstärkter Thermoplaste; Technische Textilien, 38 (1995) 205-208

MAE 96   E. Maeder, K. Skop-Cardarella; Textile Hybridkordelstrukturen für langfaserverstärkte Thermoplaste; Technische Textilien; 39 (1996) 124-126

OEV 98   M. Oever, T. Peijs; Continous-glass-fibre-reinforced polypropylene composites II. Influence of meleic-anhydride modified polypropylene on fatigue behaviour; Composites, 29 A (1998) 227-239

STU 98   H. Stumpf; Study on the manufacture of thermoplastic composites from new textile preforms; Dissertation at TU-Hamburg Harburg; 1998

THO 94   J.L. Thomason, G.E. Schoolenberg; An investigation of glass fibre/polypropylene interface strength and its effect on composite properties; Composites, 25 (1994) 197-203

Fatigue Behavior of Adhesive Composite Joints

Ian Saunders and Yuris A. Dzenis
Department of Engineering Mechanics
University of Nebraska-Lincoln
Lincoln, NE 68588-0526

Adhesive bonding has a high potential for aerospace, automotive, and other structural applications. Adhesively bonded composite patches can be used to repair aerospace parts with minimum deterioration of aerodynamic contours. Although adhesive joints have been extensively studied during the past decades, the mechanisms of fatigue failure and life of the joints are not yet sufficiently understood. The objective of this paper was to study mechanical behavior and mechanisms of damage and failure in single-lap composite joints under fatigue.

Single-lap joint specimens were manufactured by the secondary curing from a high temperature Boeing certified graphite-epoxycomposite and an adhesive film used in the Air Force.
Unidirectional and cross-ply adherends were utilized. Filets of epoxy resin formed at the ends of the overlap were removed before testing. Instrumented fatigue testing of joints was performed on a digitally controlled servohydraulic testing machine. Sinusoidal tension-tension load function with the load ratio 0.1 was applied.
The load amplitude varied from 0.4 to 0.8 of the quasistatic failure load. The resulting number of cycles to failure varied between 74 and 63,166. Damage and fracture evolution was simultaneously studied on-line by acoustic emission and optical video microscopy.

Substantial acoustic emission was acquired from the specimens throughout fatigue tests. Acoustic emission signal location analysis was performed after removal of the frictional noise created by fretting microcrack faces. Higher concentration of the AE events was observed near the ends of the overlap zone indicating damage development in these areas. However, final failure of joints with both unidirectional and cross-ply adherends occurred through the bond line. The bond crack initiated within 25-50% of fatigue life.
Gradual crack growth in the bond line was then observed to failure. No indicators of the bond crack initiation were observed on the deformation diagrams. However, a jump on the cumulative AE history curves marked the bond crack initiation that was independently observed by video microscopy. The S-N curves for joints with unidirectional and cross-ply adherends overlapped in the life range from 1,000 to 70,000 cycles to failure. It appeared, however, that the S-N curves for the two adherends had different slopes. The fracture surfaces of the failed specimens were fractographically examined and the final fracture areas under fatigue were identified and measured. Plotted against the fatigue load amplitude, these fracture areas exhibited a linear variation.
This effect can be used in the development of a final failure criterion under fatigue. A nonlinear FEM model of a single-lap adhesive composite joint with a bond crack was developed. The model will be used for evaluation of stresses in cracked joints and formulation of relevant fatigue crack growth criteria.

Experimental Characterization of Damage Progress in High Temperature CFRP Laminates

Shinji Ogihara*, Nobuo Takeda**, Satoshi Kobayashi***, Mikio Oba*** and Akira Kobayashi*

*Department of Mechanical Engineering, Science University of Tokyo, 2641 Yamasaki, Noda, Chiba 278-8510, Japan
**Department of Aeronautics and Astronautics, The University of Tokyo, 7-3-1 Hongo, Bunkyo-ku, Tokyo 113-8656, Japan
***Graduate Student, The University of Tokyo

Introduction

Carbon fiber reinforced plastics (CFRP) are remarkable for their high specific modulus and strength. CFRP is a candidate for the primary structure of supersonic transport plane (SST). Surface temperature of SST can reach -55°C at taking off and landing, while it reaches 150°C-180°C on a supersonic cruise of Mach 2.2-2.4. In this point of view, matrix resins are expected to have good heat resistance. Bismaleimide (BMI) is one of the high temperature resins. BMI has higher heat-proof quality than the conventional epoxy resins. However, damage tolerance of CFRP with BMI matrix is not clarified. In the present study, microscopic damage progress in carbon/BMI composite laminates under static tension is investigated experimentally. Transverse matrix cracking which will be an important factor in designing laminated composites is focused.

Many investigations have been conducted on transverse cracking in laminated composites which consist of experimental observation and analytical modeling. Masters and Reifsnider [1] observed transverse crack behavior by using the replica technique. It was shown that transverse cracks saturated before the final fracture. Takeda and Ogihara [2] conducted in-situ observation of damage process in CFRP cross-ply laminates. The interaction between the transverse cracks and delamination was explained by using a modified shear-lag analysis which consider the delamination effect. Naim [3] derived variational stress analysis considering the thermal residual stresses for cross-ply laminates. McCartney [4] analyzed stress transfer between 0° and 90° plies in cracked cross-ply laminates. The solutions are determined to satisfy the stress-strain-temperature relations either exactly or in an average sense. These analyses can be applied only to cross-ply laminates.

Gudmundson and Zang [5] derived the thermoelastic properties of composite laminates containing matrix cracks. In the analysis, the concept of damage mechanics analysis was used. The applicability of the analysis is not limited to cross-ply laminates. Ogihara et. al. [6] derived the energy release rate associate with cracking using this analysis and modeled the transverse crack behavior.

In the present study, microscopic damage progress in carbon/BMI laminates is investigated experimentally. Based on the experimental results and damage mechanics analysis, transverse crack behavior is modeled to evaluate the transverse cracking resistance. Furthermore, results of carbon/BMI composites are compared with the results of carbon/epoxy laminates with toughened-interlaminar layers. The methodology described in the present paper will be a procedure for the selection of SST structural materials and damage tolerance design.

Experimental Procedure

Material systems used are G40-800/5260 and T800H/3900-2. G40-800/5260 is a bismaleimide-based CFRP and is a candidate for SST structural material. It is reported that G40-800/5260 material has high compressive strength and CAI strength at high temperature. T800H/3900-2 is carbon/epoxy composite with toughened-interlaminar layers. It is also reported that T800H/3900-2 material has higher hot-wet compressive strength and CAI strength [7, 8] than conventional carbon/epoxy composites. Delamination suppression around an open hole under tensile loading was also shown [9].

The size of the specimen are 150 mm long, 20 mm wide for G40-800/5260, while 25 mm for T800H/3900-2. 35 mm long GFRP tabs are glued on the end of the specimens. $[0/90]_s$ and $[\pm45/90]_s$ laminates are prepared for both material systems to clarify the difference in the

microscopic damage behavior. For G40-800/5260, $[0/90_2]_s$ and $[\pm 45/90_2]_s$ laminates are also prepared to investigate the effect of laminate configurations on the microscopic damages. Edges of specimens are polished for microscopic observation. Laminate strain is obtained by the strain gauge glued on the center of the specimen. Tensile tests are conducted at room temperature. The cross-head speed is 0.5 mm/min. Tensile testing machine is periodically stopped and the edge of the specimens is observed by using an optical microscope. The observed area is 50mm long at the center of the specimen. The number of the transverse cracks per unit length is defined transverse crack density. Internal damage progress is observed by soft X-ray radiography [10]. Iodozinc (ZnI), a dye penetrant opaque to X-rays, is applied along the specimen edge. Specimens are exposed to X-rays for 150 s at 20 kV and 2 mA. A X-ray point-source unit positioned 570mm away from the specimen is used.

Analysis
    In modeling transverse crack behavior in composite laminates, there are two important stages. The first is selection of stress transfer mechanics in laminated composites with transverse cracks. In previous studies, shear-lag analysis [1, 2], variational analysis [3] and approximate elastic analysis [4] have been developed. But application of these analyses is limited only to cross-ply laminates containing transverse cracks in the 90° plies. In the present study, damage mechanics analysis is used which can be applied to laminates with arbitrary laminate configurations. The second stage is selection of transverse cracking criterion. In the early period, the stress criterion was often used. However, to explain the constraint effect (transverse crack onset stress (strain) becomes larger in the case of thin 90° ply), the energy criterion was developed. Recently, in many papers, experimental results are compared with analytical predictions based on only the energy criterion, because thin 90° ply is usually used. The authors have shown that both the energy and the stress criteria must be considered when predicting transverse cracking in laminates with various 90° ply thicknesses. In the present study, both the energy release rate associated with transverse cracking and the average stress of 90° ply calculated by using the damage mechanics analysis is considered. The damage mechanics analysis is outlined in the following.
    Gudmundson and Zang [5] derived in-plane compliance matrix, $\mathbf{S}_{II}(\rho^k)$, of a composite laminate containing transverse cracks as

$$\mathbf{S}_{II}\left(\rho^k\right) = \left\{ \mathbf{S}_{II}(0)^{-1} - \sum_{k=1}^{N} v^k \rho^k \left(\mathbf{A}^k\right)^T \sum_{i=1}^{N} \boldsymbol{\beta}^{ki} \mathbf{A}^i \right\}^{-1} \tag{1}$$

where, v^k is volume fraction of ply k (90° ply), ρ^k is normalized transverse crack density of ply k (=transverse crack density × the thickness of ply k), $\mathbf{A}^k$ is the matrix defined by compliance matrix and normal vector of crack surface of ply k, $\boldsymbol{\beta}^{ki}$ is the matrix associated with average crack opening displacement of ply k. Young's modulus of the laminate, $E(\rho^k)$, is derived from $\mathbf{S}_{II}(\rho^k)$.
    Energy release rate associated with transverse cracking considering thermal residual stress can be derived using $E(\rho^k)$ [6]. Now, a new transverse crack is assumed to occur at the midway between the two existing transverse cracks. When normalized transverse crack density becomes ρ^k from $\rho^k/2$, the relation between the laminate stress, σ, and the energy release rate, $G(\rho^k)$ is derived as

$$G\left(\rho^k\right) = \frac{\sum_{i=1}^{N} a^i}{\rho^k} (\sigma - \sigma_T)^2 \left(\frac{1}{E\left(\rho^k\right)} - \frac{1}{E\left(\rho^k/2\right)} \right) \tag{2}$$

where d is the thickness of ply i, σ_T is a parameter to consider the effect of thermal residual stress.
    In the energy criterion, transverse cracks are assumed to occur when the energy release rate reaches a critical value G_c. Therefore, the relation between laminate stress, σ, and normalized transverse crack density, ρ^k can be expressed as

$$\sigma\left(\rho^k\right) = \sqrt{\frac{G_c \rho^k}{\displaystyle\sum_{i=1}^{N} a^i}\left(\frac{1}{E\left(\rho^k\right)} - \frac{1}{E\left(\rho^k/2\right)}\right)^{-1}} + \sigma_T \qquad (3)$$

Gudmundson and Zang [5] also derived the relation between the average stress in each plies and the normalized transverse crack density. In our previous paper [6], we derived the relation between laminate stress, σ, and the average stress of 90° ply (ply k) in the tensile direction, $\sigma^{k(a)}$, for the case that only the ply k is the cracking ply as

$$\sigma\left(\rho^k\right) = \frac{\left[\dfrac{\sigma^{k(a)}}{1 - \rho^k \boldsymbol{\beta}^{kk}{}_{(1,1)}\left(\mathbf{S}_{\mathrm{II}}\right)^{-1}{}_{(1,1)}} + \left[\left\{\alpha_{90} - \alpha_1\left(\rho^k\right)\right\}\left(\mathbf{S}_{\mathrm{II}}\right)^{-1}{}_{(1,1)} + \left\{\alpha_0 - \alpha_2\left(\rho^k\right)\right\}\left(\mathbf{S}_{\mathrm{II}}\right)^{-1}{}_{(1,2)}\right]\Delta T\right]}{\left(\mathbf{S}_{\mathrm{II}}{}^{k}\right)^{-1}{}_{(1,1)}\mathbf{S}_{\mathrm{II}(1,1)} + \left(\mathbf{S}_{\mathrm{II}}{}^{k}\right)^{-1}{}_{(1,2)}\mathbf{S}_{\mathrm{II}(1,2)}}$$

$$(4)$$

where $\mathbf{S}_{\mathrm{II}}{}^{k}$ is compliance matrix of ply k, α_0 is longitudinal thermal expansion coefficient of unidirectional composite, α_{90} is transverse thermal expansion coefficient of unidirectional composite and $\alpha_2\left(\rho^k\right)$ is transverse thermal expansion coefficient of the laminate. In the average stress criterion, transverse crack is considered to onset when average stress, $\sigma^{k(a)}$ reaches a critical average stress, σ_c. In the present analysis, both the energy and the average stress criteria are considered. This method leads the precise prediction of transverse crack behavior in various laminate configurations.

Results and Discussion

In $[0/90_n]_s$ $(n=1, 2)$ laminates, the first microscopic damage observed is transverse cracks in 90° ply in both G40-800/5260 and T800H/3900-2. Transverse cracks onset and grow in both the thickness and width directions instantaneously. No delamination is observed in all the cross-ply laminates.

In $[\pm45/90_n]_s$ laminates, first microscopic damage observed is transverse cracks in 90° ply in both material systems. In G40-800/5260 laminates, matrix cracks in -45° ply are observed at the tips of transverse cracks in 90° ply. On the other hand, in T800H/3900-2 laminates, matrix cracking in -45° ply at the tips of transverse cracks in 90° ply is suppressed by the toughened-interlaminar layers. Matrix cracks in -45° ply do not grow in the width direction extensively. Delamination at -45/90 and 90/90 interfaces are also observed in both material systems. Delamination occurs at free edge and grows in the loading and width directions.

Figures 1 and 2 show the relation between transverse crack density and laminate strain in G40-800/5260 and T800H/3900-2 laminates, respectively. Transverse crack behavior in the same laminate configurations in the two material systems is compared. First cracking strains and transverse crack densities at final fracture are larger in G40-800/5260 laminates. In G40-800/5260 $[\pm45/90]_s$ laminates, crack density in -45° ply sometimes becomes larger than that in 90° ply. This may be due to delamination at -45/90 interface reduces stress in 90° ply. In this case, $\pm45°$ ply carry more load and little matrix cracks in $+45°$ ply are also observed. In T800H/3900-2 $[\pm45/90]_s$ laminates, crack density in -45° ply is smaller than that in G40-800/5260 laminates, because matrix cracks in -45° ply at the tips of transverse cracks in 90° ply are suppressed by the toughened-interlaminar layers. Delamination was also observed in T800H/3900-2 $[\pm45/90]_s$ laminates, however, matrix crack in 45° plies are not observed until the final laminate fracture.

First cracking strain becomes larger as the thickness of 90° plies becomes thinner. Transverse crack density growth rate becomes larger as the thickness of 90° plies becomes thinner. This results in larger transverse crack density just before the final fracture in the laminates with thinner 90° plies. First cracking strain becomes larger as the stiffness of the adjacent plies becomes larger. Transverse crack density growth rate becomes larger as the stiffness of the adjacent plies becomes larger. That is, the larger stiffness of adjacent plies of 90° plies has a similar effect of thinner 90° plies.

Figures 1 and 2 show the predictions of transverse crack behavior in 90° ply based on the damage mechanics analysis. In the present study, a transverse crack is assumed to occur when both the energy and average stress criteria are satisfied. In other words, the prediction which gives lower crack density at the same strain is considered to be analytical prediction.

Analytical predictions based on the average stress criterion gives smaller transverse crack density for G40-800/5260 $[0/90_2]_s$, $[\pm 45/90_2]_s$ and T800H/3900-2 $[0/90]_s$, $[\pm 45/90]_s$ laminates. This indicates that predictions based on the average stress criterion are regarded as the analytical prediction for these laminates. Predictions are in good agreement with experimental results. But predictions of $[\pm 45/90]_s$ laminates for both material systems have some mismatch in higher strain region. This higher strain region corresponds to delamination growth which is not considered in the present analysis.

(a) $[0/90]_s$

(b) $[0/90_2]_s$

(c) $[\pm 45/90]_s$

(d) $[\pm 45/90_2]_s$

Experimental Results

○ 90° Ply

△ +45° Ply

□ -45° Ply

Analysis (90° Ply)
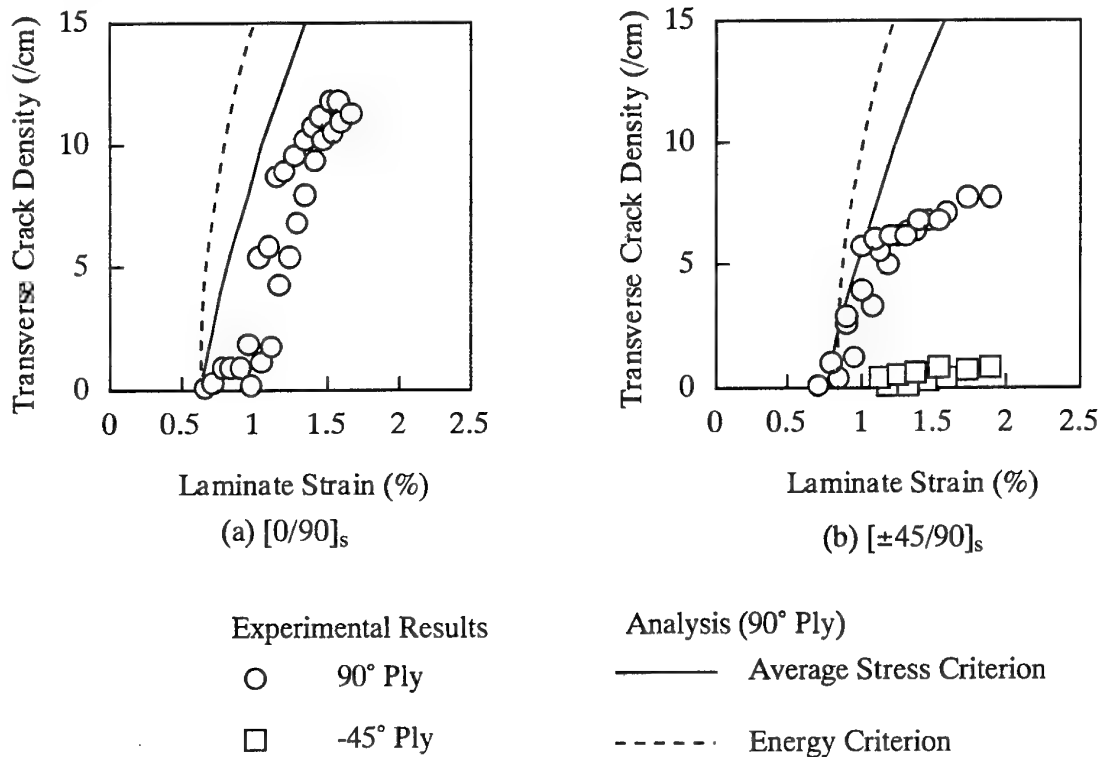
——— Average Stress Criterion

- - - - - Energy Criterion
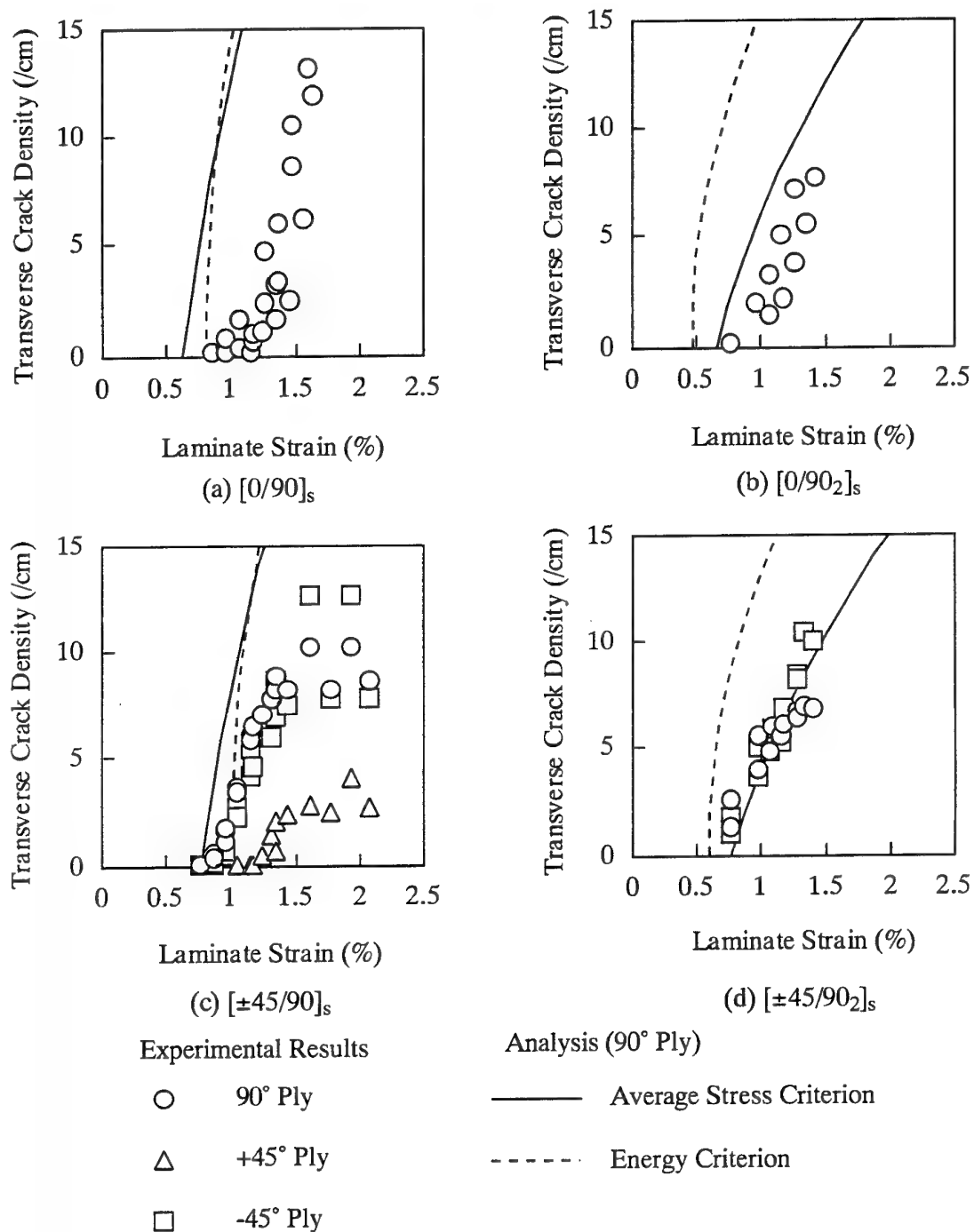
Figure 1 Transverse crack density in G40-800/5260 laminates as a function of laminate strain (experimental results and analytical prediction).

Summary

Microscopic damage progress in bismaleimide-based CFRP, G40-800/5260 laminates and interlaminar-toughened epoxy-based CFRP, T800H/3900-2 laminates are investigated experimentally. The larger stiffness of adjacent plies of 90° plies and thinner 90° plies has a similar effect on the transverse crack behavior in 90° plies. Transverse crack behavior was modeled by using damage mechanics analysis. Analytical predictions considering both energy and average stress criteria are in good agreement with the experimental result.

(a) [0/90]$_s$ (b) [±45/90]$_s$

Experimental Results   Analysis (90° Ply)

O   90° Ply   ———   Average Stress Criterion

□   -45° Ply   - - - - -   Energy Criterion

Figure 2 Transverse crack density in T800H/3900-2 laminates as a function of laminate strain (experimental results and analytical prediction).

References
[1] J. E. Masters and K. L. Reifsnider, ASTM STP 775 (1980), 40-61
[2] N. Takeda and S. Ogihara, Comp. Sci. Tech., 52, 2, (1994), 183-195
[3] J. A. Nairn, J. Comp. Mat., 23 (1989), 1106-1129
[4] L. N. McCartney, J. Mech. Phys. Solids, 40, 27 (1992), 27-68
[5] P. Gudmundson and W. Zang, Int. J. Solids Structure., 30, 23 (1993), 3211-3231
[6] S. Ogihara, N. Takeda, S. Kobayashi and A. Kobayashi, To appear in International Journal of Damage Mechanics
[7] N. Odagiri, T. Muraki and K. Tobukuro, 33rd Int. SAMPE Symp. (1988), 272-283
[8] N. Odagiri, H. Kishi and T. Nakane, ASC 6th Tech. Conf. (1991), 46-52
[9] N. Takeda, S. Kobayashi, S. Ogihara and A. Kobayashi, Adv. Comp. Mat., 7, 2 (1998), 183-199
[10] S. Ogihara, N. Takeda, S. Kobayashi and A. Kobayashi, 11th Int. Conf. Comp. Mater. (1997), V. 552-561.

INFLUENCE OF THE SHAPE OF A STRIKER
ON THE MECHANICAL RESPONSES OF COMPOSITE BEAMS

L.GUILLAUMAT

LA.M.E.F.-E.N.S.A.M.
Esplanade des Arts et Métiers 33405 Talence Cedex.

Design of structures is often made with a deterministic approach using the mean value of each variable of the system. However, this kind of design is not always efficient for industrial structures because of the variability of both mechanical behaviour and solicitation. The three most important types of loading are impact, fatigue and vibrations. The impact solicitation applied on a structure can be due, for instance, to an accidental shock such as the fall of a tool during maintenance or manufacturing. The influences of the induced damage on the reliability of the affected piece are not always well recognized and rarely used to design the structure.

This paper deals with some mechanical responses of laminated composite beams under low velocity impact loading using different shapes of the end of the impactor in order to simulate the fall of several types of tools such as hammer, screwdriver and so on

EXPERIMENTAL METHODS

The impact tests have been performed using a drop weight set-up (Figure 1).

An electric motor is used with a magnet to raise the mass. The drop height is determined by the position of a first infra-red captor which stops the motor at the desired level. A second captor located on the set-up close to the specimen activates a rebound apparatus to prevent multiple impacts on the structure.The contact load between the striker and the composite specimen as a function of time is measured by means of a piezoelectric captor which is attached to the drop weight. Two laser captors provide the striker displacement and the deflection at the centre of the composite panel versus time. The tests have been filmed by a high speed camera system Camsys+ (2,000 up to 11,000 frames/sec). All the results were recorded in a P.C. computer.

The structure is put on two steel opposite supports in bending condition. Two flexible sheets made of metal with a rubber end maintain it (Figure 2). These boundary conditions allow rotations and vertical movements.

We have chosen five shapes for the end of the impactor (Figure 3). Moreover, the total mass of the drop weight was about 1 kg and the velocity was 3.8 ms^{-1}.

MATERIAL

The composite is a glass fibres reinforced isophtalic polyester resin. Several plates of about 1 m2 were made by the hand lay-up process. All the plates are constituted of 8 layers which give a total thickness of about 3.5 mm. The stacking sequence was [0$_3$,90]s. The specimens of this study have been cut from this plates and their size was 350 mm long and 66 mm wide.

RESULTS

The contact load between the striker and the structure versus time for a hemispherical end is shown in Figure 4. Moreover, the films given by the high speed camera show that the undulations on the curve load versus time can be attributed to the eigen modes of the panel induced by the dynamic solicitation during the shock.

To separte the bending response from the vibratory response we have to filter the signal contact load versus time at about 200 Hz (Figure 4 - curve 2). The filtered signal gives only the load versus time of the bending of the structure and the difference between the curve 2 and 1 contains the eigen modes of the composite beam, the eigen modes of the drop weight and the resonance of the piezoelectric captor (Figure 5).

The mechanical results for the tests with the other ends are very similar (Table1) and suggest that the shape of the impactor has no influence on the mechanical responses of the composite beams. Although the surface of the contact between the striker and the structure is different due to the shape of the end, it seems that this surface is too small in keeping with the surface of the beam to change the mechanical responses. Consequently, the kinetic energy of the drop weight has the same effect (for a given panel) whatever ends used in this study. The mass and the velocity of the drop weight remain the main parameters.

End (Figure 3)	1	2	3	4	5
Deflexion (mm)	6.2	6.5	5.9	6.2	5.8
Time of conctact (ms)	6.6	6.7	6.7	6.7	6.8
Maximal load (N)	1204	1206	1271	1255	1290
Frequency (Hz)	346	303	296	306	306
	1310	1287	1328	1275	1352
	1795	1768	1774	1837	1861
	–	2147	2244	2193	2193
	5080	5150	–	5103	5306

Table1. *Mechanical and vibratory responses of the impact tests for different shapes of the striker.*

On the other hand, the damage induced is different according to the shape of the end of the impactor. The Figure 6 shows the damage induced by an hemispherical end and Figure 7 by a pointed end. For all the ends except for the pointed one the visible damage was only matrix cracking. We can observe long cracks parallel to the span and short craks parallel to the width. The pointed end induces matrix cracking too, delamination and the beginning of a perforation. Obviously, this last kind of damage is more severe and could modify the behaviour of impacted panels submitted to a mechanical solicitation such as fatigue for instance.

CONCLUSION

The mechanical responses of composite panels under low velocity and high mass impact solicitation are not sensitive to the shape of the end of the striker. On the other hand the damage induced is very different according to the end.

The samples used in this study will be submitted to a fatigue solicitation to analyze the influences of an accidental shock on the behaviour of the structure.
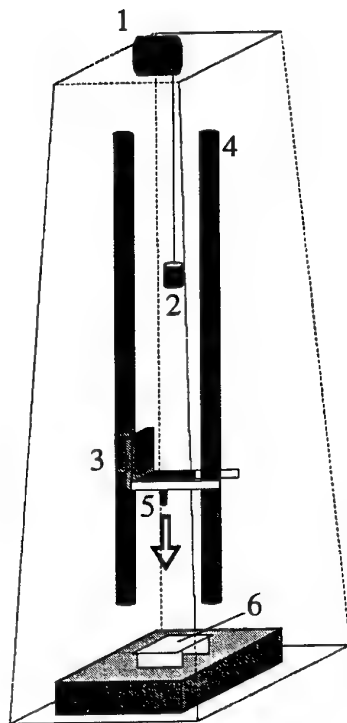
Figure 1. *Drop tower.*

1 : electric motor
2 : magnet
3 : drop weight
4 : column
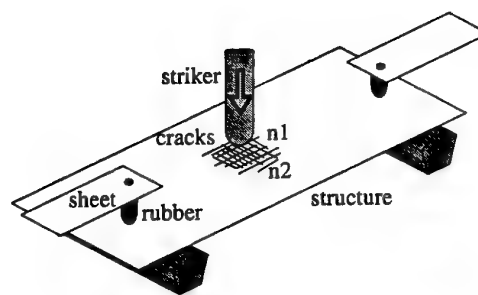5 : end of the striker
6 : structure
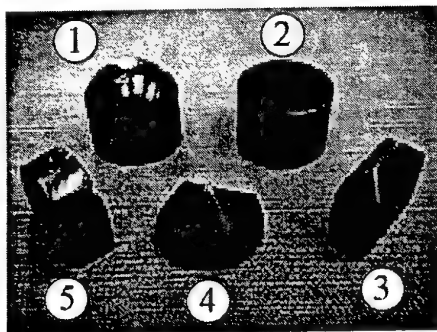

Figure 2. B*oundary conditions.*
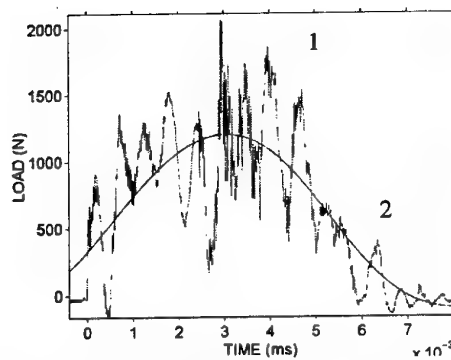

Figure 3. *Ends of the striker.*

Figure 4. *Contact load between the impactor and the composite beam.*
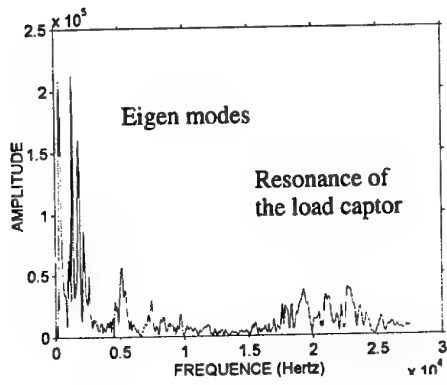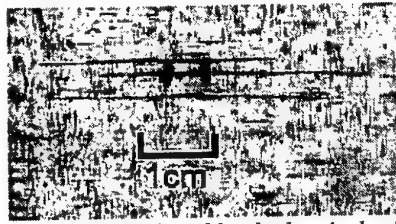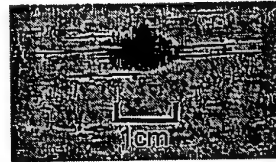
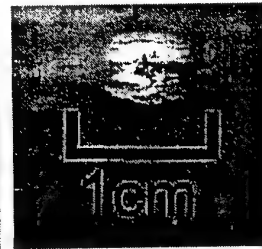Figure 5. *F.F.T. of the filtered signal.*

Figure 6. *Damage induced by the hemispherical end.*

lower face   impacted face

Figure 7. *Damage induced by the pointed end.*

Curing Conditions and Sample Preparation for the Analysis of the Transverse Creep Behaviour of Unidirectional Graphite-Epoxy Systems

Christian Van Vossole, Pascal Bouquet, A.H. Cardon
Free University Brussels

ABSTRACT: An optimisation sequence for the production and preparation of testspecimen is presented. Within the context of the mechanical long term behaviour of composite materials, unidirectional carbon fiber reinforced plates are processed in order to obtain testbeams. The manipulation in the production process and storage are critical due to the sensitive measurements. The influence of environmental and damage conditions are causes of a wide dispersion of the measurements. Utmost care has to be applied yielding to representative and repeatable testresults. The paper describes the different levels on which special attention was paid for the optimisation and control of the properties of the material through the manufacturing process of solid composite material. A closer look was given at the rupture surface of the testspecimen to distinguish eventual inhomogenities which could be the source of the rupture.

1 INTRODUCTION

Durability of materials is an important feature for structural elements. The increasing number of structural applications of fiber reinforced composites demands adequate understanding of the long term behaviour. Lifetime and specifically rupture prediction of a structure submitted to mechanical loading, are of utmost importance regarding the safety requirements. Lifetime predictions of structural elements with a complex loading history need an integrated approach, taking into account the viscoelastic/viscoplastic behaviour of the polymer matrix and the damage due to the loading history.

The aim is to apply reliable accelerated test methods capable to describe long term behaviour. Therefore accelerating parameters such as stress level, pressure or temperature are applied to speed up the test. The corresponding superposition principle allows to modelize the material behaviour at a lower stress, pressure or temperature level over a longer period of time. The fibers of the composite being almost solely elastic, the viscoelastic behaviour of the composite is mainly due to the resin. At low stress levels, we observe a linear viscoelastic behaviour on the contrary at higher stress levels a non-linear modellisation needs to be considered. For this purpose, the Schapery model can be used.

The creep behaviour of the composite is acquired from uniaxial fiber reinforced polymer matrices loaded perpendicular to the fiber direction. The stress level applied during the creep test is proportional to the ultimate stress level. A referential ultimate stress value for all testsamples had to be obtained from various production batches and samples. Since the basic data, acquired from the creep tests at higher stress levels is essential, the knowledge of the stress level as a percentage of the tensile strength has to be determined accurately. Small differences in stress level result in big differences in time to failure.

The main purpose of this work is to keep the standard deviation of the tensile strength level of different specimen within acceptable limits in order to perform repeatable and comparable creep tests. Also the variations in time should be kept to a minimum. The solution to this critical path of testing sequence and preparation will be outlined in this paper.

2 PRODUCTION OF TEST BEAMS

Tensile tests are performed on beams with all the fibers in the transverse direction of the loading. Typical dimensions of the beams are $300 \times 17 \times 1.5 mm^3$.

These beams are cut out of bigger plates, all with identical thickness, that were cured in an autoclave, under controlled temperature and pressure conditions. The plates are laminated prepregs, type
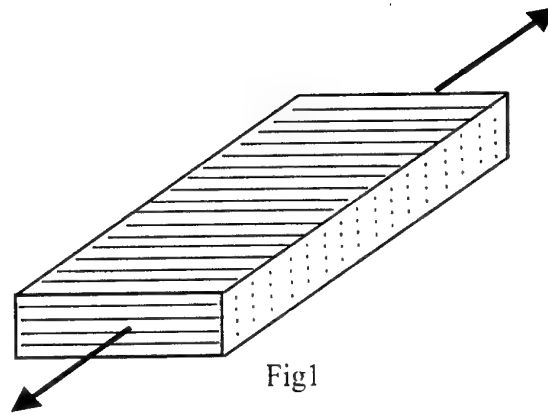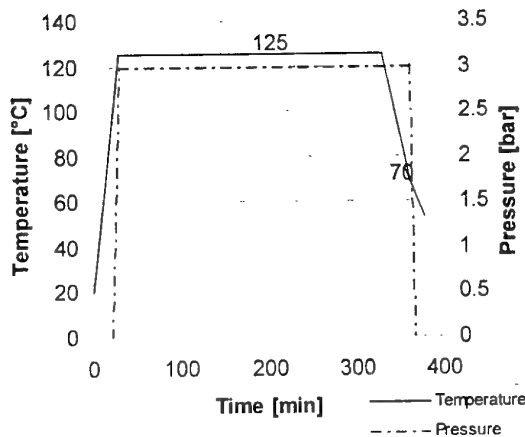 Hexcel Fiberdux 920 CX-TS-5-42

Fig1

Fig 2

This prepreg has a fiber content of 58 weight %.
Plates of 60×30 cm^2 built up of 10 layers of prepreg are vacuumized for 8 hours, and then cured.

At first, the recommended cure-cycle from the producer of this prepreg was used.

3 MECHANICAL RESULTS

Beams that were cured according to the prepreg-manufacturer's cycle, were tested for their tensile strength. Averages and standard deviations are displayed in the following table.

We noticed from the experimental results that:
- Different plates: big differences in the average tensile strength
- Within one plate: big standard deviation
- Variation in time (conservation of the specimen was at room temperature and low relative humidity)

Some factors, possible causes for these problems, had to be investigated:
- Type of epoxy groups, hardeners and additives
- Curing conditions
- Existence of fiber concentrations at fracture surface

4 CHEMICAL STRUCTURE

We were able to dissolve the prepreg resin with CHCl3 as a solvent and to separate the resin from the fibers. The solved resin was then examined in the HNMR-apparatus to identify chemical structures. Problems arose as we weren't able to identify the hardeners nor additives but only the epoxy-groups that have the following structure:
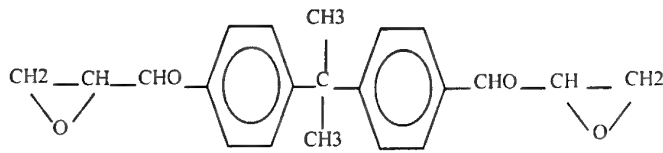
Fig3

This diglycidyl ether of bisphenol A (DGEBA) can react with amines or anhydrides.

5 FRACTURE SURFACE

When testing the specimen with the load direction transverse to the direction of the fibers, the resistance is actually provided by the resin. A strong concentration of fibers might then cause a weaker zone. The tensile strength would then be strongly dependant on the quality of the prepreg (fiber concentrations, misalignments in the prepreg).
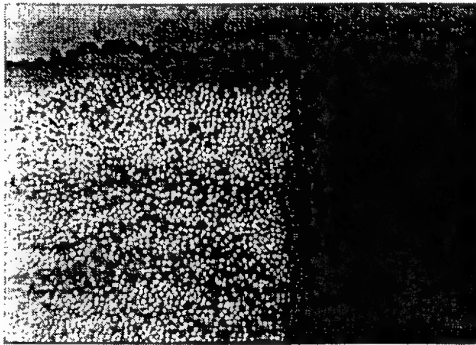

With the SEM (Scanning Electron Microscope) and an optical microscope a closer look was taken at the fracture surface.

Although the ten prepreg layers can still be easily recognized after the curing, no fiber concentrations could be observed at the fracture surface. Also no apparent cracks or irregularities were seen at the sawing edge.

Fig4 (Magnification 100x)

Polishing a set of test beams didn't raise the average tensile strength level, nor did it lower the spread between different specimen.

6 CURING CONDITIONS

The epoxy - resin in the studied composite, is an amorphous polymer. To better understand the curing process, one can use the T T T (Time-Temperature-Transformation) diagram mostly developed by Gilham et. al [Ref.1.2].

Although it has been elaborated for pure amorphous polymers, it was a good guideline to improve the curing process for the composite laminate.
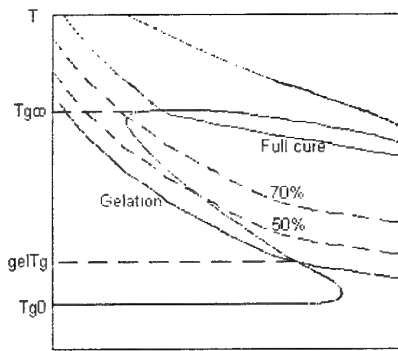

Fig5: Time-Temperature-Transformation Diagram

Since T_g is the only transition temperature for amorphous polymers, it is one of the most important material parameters. The Tg-region is a small temperature region where mechanical properties change dramatically. The material behaviour changes from a rubbery to a glassy state when going under the Tg. During the curing of the polymer, the Tg rises, and is related to the degree of conversion. From the point where network formation starts (gelation) there is a serious increase in Tg, until full conversion at $T_g\infty$.

Further on, below $T_g\infty$, vitrication can occur, due to the higher viscosity that accompanies the network formation. Then the chemical reaction gets diffusion-controlled.

$t_{reaction} = t_{chemical\ kinetics} + t_{diffusion}$

after vitrification point $t_{diffusion} >> t_{chemical\ kinetics}$

If we want to avoid too much exothermal reactions to occur in a short period of time, the reaction has to be diffusion controlled. This means that the cure-path should climb up the vitrification line, until Tg is reached.

To be able to compare mechanical properties from different specimen, full cure has to be achieved. A high $Tg\infty$ will also limit the ageing-phenomena at room temperature. A curing at a temperature above $Tg\infty$, will assure full cure. When there is risk for degradation, it can be achieved under $Tg\infty$ as well.

7 DSC- MEASUREMENTS

In the DSC-oven, the heat flow of a reference pan and a sample pan (in our case 50 micro-liter) are compared during an imposed temperature programme. With temperature modulation, Cp is measured as well.

By following up these two parameters we can observe some important features:
- the temperature at which reaction starts.
- the amount of energy released once reaction begins (how high is peak).
- Tg before and after the temperature-programme.

Results:
1/Data:uncured prepreg
temperature :
1st scan: -60°C to 220°C at 5°C/min
2nd scan: 20°C to 220°C at 5°C/min
observations:
- Tg_0= -2.55°C (region: -7.98°C to 4.19°C)
- reactions begins at 105°C (high peak)
- after 1st scan : resin is partially cured
- Tg=113.28°C

2/ Data:uncured prepreg, 2 weeks out of freezer, at room temperature (scan is not displayed)
temperature:
1st scan: -60°C to 220°C at 5°C/min
2nd scan: 20°C to 220°C at 5°C/min
observations:
- Tg_0= 0.52°C (region: -5.15°C to 6.15°C)
Even at room temperature there is some reaction going on.

3/ uncured prepreg
temperature :
1st: constant at 125°C for 100 min
2nd: scan: 50°C to 220°C at 5°C/min
3rd: scan 50°C to 220°C at 5°C/min
conclusions:
- after 40 minutes reaction is finished
2nd scan: Tg has changed after 1st scan: curing after isothermal part was not fully completed

4/uncured prepreg
temperature :
1st: constant at 105°C for 300 min
2nd: scan: 50°C to 220°C at 5°C/min

conclusions:
- after 200 minutes reaction is finished
- peak is not so high
- maximum of Tg-region of the resin: 135°C (scan is not displayed)

8 IMPROVED CURE CYCLE

The conclusions of the DSC-scans let us develop a new cure cycle. Since reaction fully starts at 105°C, a dwell is imposed at this T. From the isothermal cure at 105°C, it is observed that reaction goes on for approximately 200 minutes. Therefore, applying a margin, the dwell at 105°C in the new cycle lasts 300 minutes.

After the second scan, following isothermal cure at 105°C, the maximum of the Tg-region is 135°C. A second plateau will therefore be set at 140°C during 1 hour. Some further testing showed us that reaction was completed after this temperature programme.
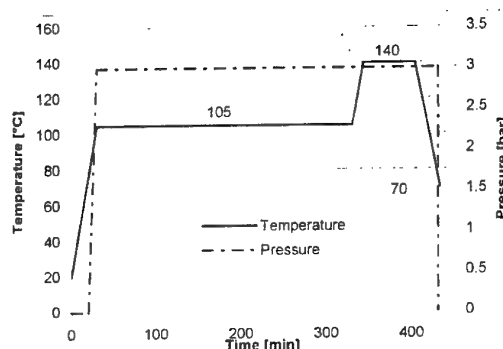

Fig 6

9 RESULTS

DSC-samples taken from beams that were cured according to this improved cure-cycle, had a Tg of 112°C. There is still a difference with the Tg of 125°C that was reached with prepreg-specimen that were cured in the DSC itself. The influence of the fiber content on the curing or the different curing conditions in the DSC versus the autoclave may be a cause for this difference.

The mechanical properties however, prove to be sufficient for the purpose of our tests.

Within one plate : beams tested for their tensile strength give following results:
Eg average: 73.62Mpa
stdev: 2.04 Mpa (= 2.78%)

When we consider the averages for several cured plates (5):
average: 74.53Mpa
stdev: 1.43 Mpa (= 1.41%)
Standard Deviation: 3MPa

Also important is that there is no observable degradation in time of mechanical properties in a time span of 5 months.

10 FURTHER RESEARCH

The results and experience obtained from the preparation of testsamples will allow to proceed in the investigation of material behaviour in the long term. Since the spread of results is largely reduced, the stress level at which current creep tests are performed is more accurately defined.

The scope of our further research is to evaluate the behaviour of fibre reinforced composites under complex biaxial loading and to evaluate the damage and its influence on the lifetime after an imposed , complex, loading history. Actual measurements clearly show the importance of a good testspecimen preparation.

11 REFERENCES

1.Gillham J.K. (1986) Formation and properties of thermosetting and high Tg polymeric materials, Polymeric Engineering and Science, vol26.
2.Aronhime M.T.,Gillham J.K. (1986)The Time-Temperature-Transformation cure diagram of thermosetting polymeric systems, Advances in Polymer Science pag.83-113

12 ACKNOWLEDGEMENTS

DURABILITY OF STRESSED E GLASS FIBRE IN ALKALINE MEDIUM

Grzegorz Świt
Kielce University of Technology, Al.1000-lecia PP. 3, 25-314 Kielce, Poland

SUMMARY: The topic of this paper is analysis of E glass fibre bunch under constant static load and in alkaline environment condition. The beginning cracking process of tested specimens was detected using acoustic emission and the influence of the alkaline medium on fibre is shown on scanning micrograph.

Keywords: Glass fibre, stress corrosion, acoustic emission,

INTRODUCTION

For the last few years in civil engineering, the composite materials have been used more and more often. They can be used both as the main element of the structure and as the element reinforcing existing constructions[1,2].

The limits in using composites as a reinforced material are caused by the fact that E glass fibres are not resistant to stress corrosion. There have been many papers publicised about stress corrosion fibre as an element of composite with polymer matrix in acid medium[3,4,5,6].

However, there is no information about behaviour of these fibres in alkaline medium. That is why I decided to establish the influence of mediums concentration and the level of load on the stress corrosion effect in alkaline medium. This is important, when, if we want to predict the durability of reinforced elements under combine influenced of stress and alkaline environment.

EXPERYMENTAL PROCEDURE

The tests were made on bunches of E glass fibres - ER-3005 produced by Glass Works in Krosno (Poland). The bunches have been taken randomly without eliminating damaged fibre. The experiment was made on rowing of boroaluminosilicate glass which contained less than 1% alkaline with text rowing 1200g/km and the nominal diameter of a single fibre was equal $\phi=10\mu m$. The number of fibres in a bunch was approximately 6000. The surface of rowing was covered by glycidoepoxysilicanian preparation . The nominal length of specimens was equal $l_{av}=275$ mm, and the cross section was equal $A_N=0.49mm^2$. The tests have been made in alkaline medium $Ca(OH)_2$ with concentration from pH12 to pH8. The static strength in the first stage of the experiments the fibre were exposed to a static load using the UTS 20 testing machine. The medium strength of a bunch of fibres was equal $P_{av} = 153.67N$.

In corrosion tests, loads in the range from 0.5 to 0.7 of mean strength were applied. To detect the beginning of fracture, the acoustic emission (AE) AET 204 and MISTRAS 2001 processors were used. To evaluate the stress corrosion, damages of the specimen surfaces after failures were analysed with a scanning electron micrograph.

INVESTIGATION OF CRACK CORROSION

Stress corrosion in alkaline medium is important when glass fibres are used as a filling material of composite to reinforce concrete and concrete elements of structures, because the concentrations mentioned above can be encountered in concrete. The concentration pH12 occurs on surface of non-corroded concrete while pH8 is observed in corroded concrete.

When analysing the AE events vs. time plots during stress corrosion cracking three intervals in damage intensity can be selected:

1. strong AE signals produced by the fracture of the fibre with unadvantageous orientation and friction between the fibres.
2. stable increase of AE signals, where AE signals may be the results of incidental fibres cracking or corrosion process
3. sudden fast increase of AE signals as the results of gross fibre breaking.
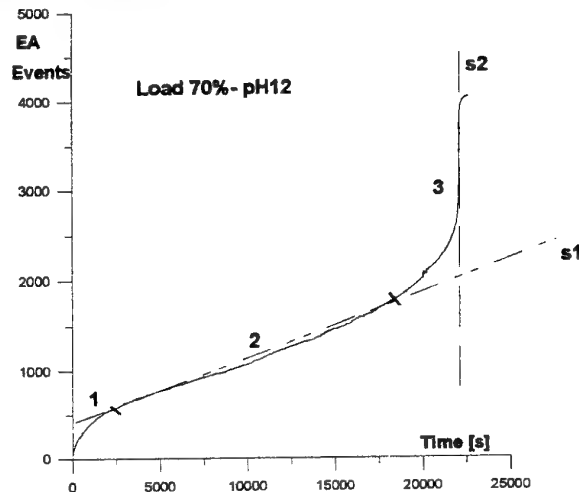
The plots mentioned above are show on figure 1.

Fig.1. Characteristic periods, which can be differentiated during a bunch fibre, stress corrosion destruction.

For further analysis assumed that the number of events equals the number of fractured fibres in a bunch, this analysing the plot given above it can be noticed that the fast process of destruction of bunch of fibre takes place when 30% of all fibres are fractured.

The service time is indicated by the point of intersection of lines s1 and s2 tangent to the EA/time diagram as it is indicated in fig. 1.

On fig. 2 plots of AE events (number) vs. time for concentration pH12 and pH8 are shown.
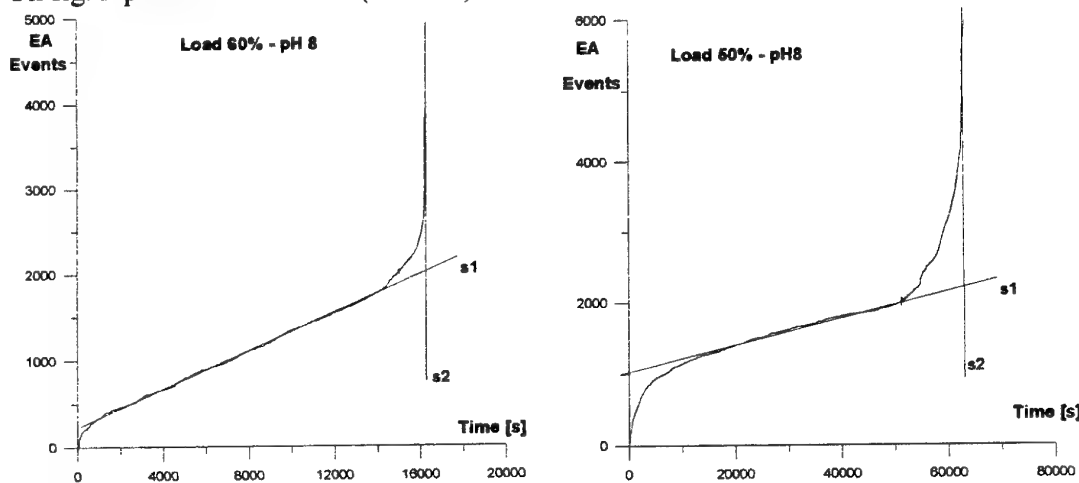

Fig.2. Comparison of plots: (AE) events (number) vs. time in dependence on concentration and load.

While comparing those plots it can be noticed that 30% of fractured fibres limited service time in corrosive environment. The number of fractured fibres at find fracture of bunches depends neither on concentration nor on the stage of load.
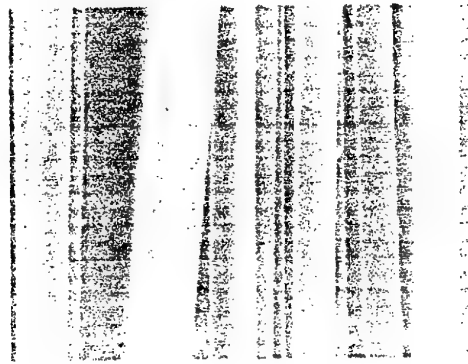
The photos of those fibres are show on fig. 4.

Figure 4. Scanning electron micrograph of E-glass fibres which had been unloaded in $Ca(OH)_2$.

In this picture there are no signals of corrosion damages on fibres surface, that leads to a conclusion that the environment surfaces aren't a sufficient condition to initiate corrosion of fibres.

CONCLUSION

While analysing of fibre corrosion in dependent on concentration and load, it can be concluded, that:
a) stress corrosion fracture of fibre bunches takes place when about 30% of all fibres are damaged,
b) the most intensive damage of stress corrosion process occurs in alkaline medium of concentration pH8
c) the damages of fibres in alkaline environment have not been noticed (pH8-pH12)

REFERENCES

1. FOCACCI F., NANNI A., FARINA F., SERRA P., CANNETI C.: „Repair and Rehabilitation of an Existing RC Structure using CFRP Sheets", ECCM-8,Woodgead Publishing Ltd., 1998, pp. 51-58
2. TASNON M., MISSIHOUN M., GERIN G.: „Lajoie, restorarion of bulding facades with composite materials", Advanced composites materials in bridges and structures, Montreal-Quebec, 1996, pp. 589-593
3. KUMOSA M., QIU Q.: „Corrosion of E-glass fibers in acidic environments", Composites Science and Technology 57, 1997, pp. 497-507
4. CHANDLER H., JONES R.: „Strength loss in „E" glass fibres treated in stronng solutions of mineral acids", Journal of Materials Science 19, 1984, pp. 3849-3854
5. DAS B., TUCKER B., WATSON J.: „Acid corrosion analysis of fibre glass", Journal of Materials Science 26, 1991, pp.6606-6612
6. GOŁASKI L., RANACHOWSKI J.: „Service life prediction of glass reinforced plastic under stress corrosion condition by acoustic emission", pp. 101-108

The fibres were immersed tested in solution with concentration: pH8 to pH12 and exposed to load equal for 50% to 70% of medium strength P_{av}.

The examples of load influence on development of stress corrosion load for 70% P_{av} and different alkaline concentration after fracture are shown on Fig. 3.
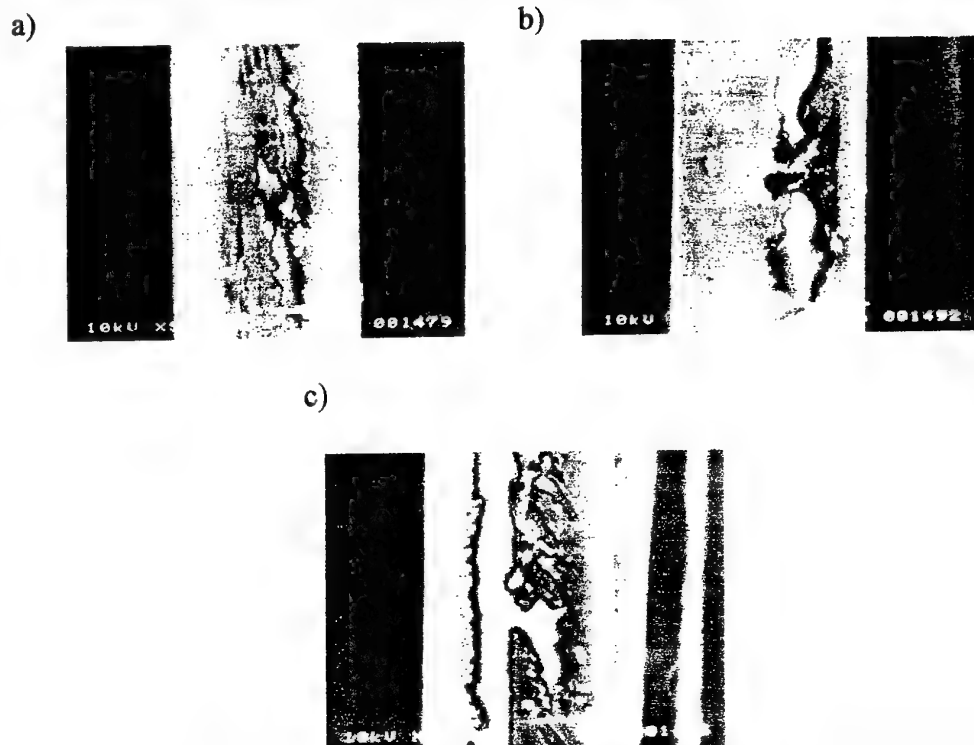
a)

b)

c)

Figure 3. The influence of strength of solution $Ca(OH)_2$ and the extent of load on development of stress corrosion E-glass fibres.

a) Scanning electron micrograph of surfaces of tested fibre in $Ca(OH)_2$ in concentration pH12 and load 70% P_{av}
b) Scanning electron micrograph of surfaces of tested fibre in $Ca(OH)_2$ in concentration pH10 and load 70% P_{av}
c) Scanning electron micrograph of surfaces of tested fibre in $Ca(OH)_2$ in concentration pH8 and load 70% P_{av}

While comparing the pictures given above, the fibre corrosion can be divided into three groups:

1. a large amount of surface elongated pits which are not connected with each other causes significant cavity of the area of fibres because of their number - fig. 3a
2. wide, deep pits with irregular edges, but not connected with each other, cavity of area because of width and depth of the pits - fig.3b
3. wide, deep pits along all corroded fibre, irregular pits and a great amount of surface pits connected with each other, a type of corrosion which is the sum of mechanisms mentioned above – fig.3c

While analysing the stress corrosion damages probably take place in accordance with the equation on the chemical process indicated below: $Ca(OH)_2 + SiO_2 \rightarrow CaSiO_3 + H_2O$.

To estimate if the fibre damage is a result of combined influence of stress and environment, unloaded fibres were immersed for 7 days in bathes with concentration from pH12 to pH8.

EFFECT OF MARINE EXPOSURE ON WEATHERABILITY OF FRP LAMINATES

H.Takayanagi, K.Kemmochi
National Institute of Materials and Chemical Research
Tsukuba, Ibaraki, 305-8565, Japan

I.Kimpara
University of Tokyo
Bunkyo-ku, Tokyo, 113-0033, Japan

ABSTRACT: We fabricated eight kinds of fiber-reinforced plastic from the matrices of unsaturated polyester resin and epoxy resin with glass fiber (i.e., a glass surface mat, glass chopped-strand mat, glass roving cloth, and glass cloth) and carbon cloth. The FRP laminates were attached to the side of a large structure floating in Tokyo Bay. The FRP laminates were removed after one and two years, and mechanical property tests were conducted to assess the degradation. The results clearly indicated that Young's modulus and the bending modulus were the smallest for the specimens exposed at the waterline. The tensile and bending strengths of the specimens exposed for one and two years exceeded the initial values, and were reduced compared to the one-year specimens, respectively. The compatibility of reinforcing carbon fiber and epoxy resin was superior to the other combinations.

1 INTRODUCTION

In the future, electrical power will be produced extensively using the force of the sea as a practical natural energy resource. We have proposed the Mighty Whale Project and have conducted sea experiments to demonstrate the multipurpose production of electrical power. New high-polymer materials will be applied to marine structures to utilize this energy resource. Durability is an important feature of these new materials[1~2]. There are relatively few existing studies into the degradation caused by marine exposure.

We fabricated eight kinds of fiber-reinforced plastic (FRP) from the matrices of unsaturated polyester resin, epoxy resin with glass fiber, and carbon fiber reinforcing materials. The resultant FRP laminates were exposed on the side of a large structure floating in Tokyo Bay. The FRP laminates were removed after one and two years and mechanical property tests were conducted to assess the degradation.

2 EXPERIMENTAL PROCEDURES

2.1 Specimen

Two lamination systems, MR lamination (a combination of glass roving cloth and glass chopped-strand mat) and plain woven cloth lamination, were used on the large marine structure shown in Table 1. Glass fiber, above the cost performance, and carbon cloth, above the specific strength and rigidity, were used for reinforcement. A resin-rich layer consisting of a surface mat was applied to both surfaces to increase the corrosion resistance. In addition, an ivory-colored, gel-coated specimen was included to increase the weather resistance. The following resins were used for matrices: that is unsaturated polyester resin, epoxy resin and gel-coat resin.

2.2 Experimental method

The experimental floating structure has been 200 m off the shore of Kanagawa Prefecture. The mean temperature was 15.4 ℃. Specimens were attached to the south wall of

Table 1 Lamination of FRP.

Type	MRS-UP	MRS-EP	MRG-UP	MRG-EP	C₁S-UP	C₁S-EP	C₂S-UP	C₂S-EP
Size(mm)	1000×500		1000×500		1000×500		1000×500	
Thickness(mm)	5.2		5.2		3.6		3.6	
Reinforcing fiber *[1]	S_1 R M R S_1	×1 ply ×1 ×4 ×1 ×1	G S_2 R M R S_2 G	×1 ply ×1 ×4 ×1 ×1	S_1 C_1 S_1	×1 ply ×13 ×1	S_1 C_2 S_1	×1 ply ×9 ×1
Matrix*[2]	UP	EP	UP	EP	UP	EP	UP	EP

*[1] S_1, S_2 : Surface mat, R: Glass roving cloth, M: Chopped-strand mat, G: Gel-coat
　　　　C_1: Glass cloth, C_2: Carbon cloth
*[2] UP: Unsaturated polyester resin, EP: Epoxy resin

the floating structure agreed with the water-line

The tensile strength, tensile modulus, and Poisson's ratio were measured. The bending strength, bending modulus, and maximum deflection were measured, based on the four-point bending test.

3 RESULTS AND DISCUSSION

3.1 *Effect of exposure position on weather resistance*

In order to clarify the effects of exposure position on the Young's modulus, we used a three-way classification. Three factors were the reinforcing fiber, matrix and exposure position. Each factor was significant at the one-percent level. The confidence limits at 95% confidence coefficient were shown in Fig. 1. The order of the reinforcing fiber on the Young's modulus was C_2S, C_1S, MRS and MRG. The order of the matrices was UP and EP. We observed that the Young's modulus of the specimens exposed at the waterline was the smallest as shown in Fig. 1. We assume that the repeated force applied by waves, the weather, and their interactions caused the severe degradation at the waterline.

The effect of the exposure position on the bending strength and modulus was significant at the one-percent level. The bending modulus of the specimens exposed at the waterline was the smallest.
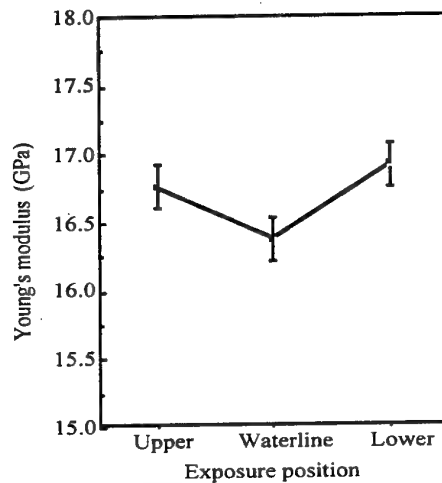

Fig. 1 Relation between Young's modulus and position.

The exposure position did not significantly affect the Sharpy impact value after two years of exposure.

3.2 *Effect of matrices on weather resistance of specimens exposed at different exposure positions*

The relation between bending strength and matrix was shown in Fig. 2. Concerning to bending strength, there was a large interaction between the reinforcing fiber and matrix. The bending strength of C_2S-EP was about two
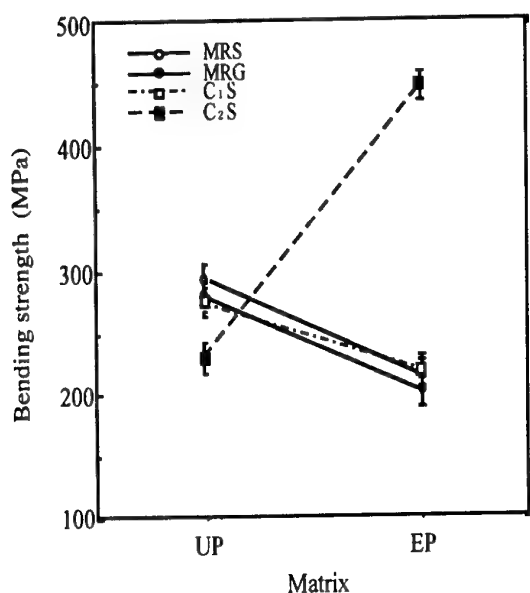
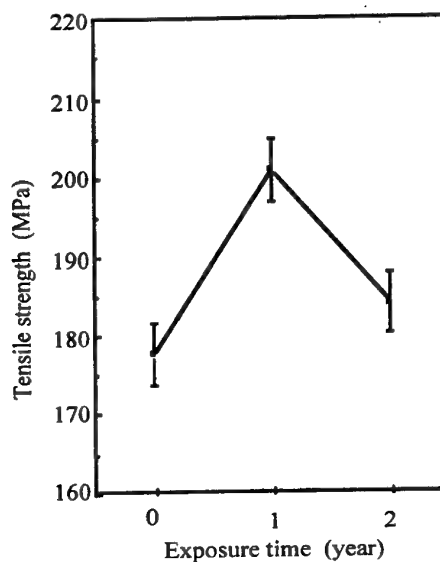Fig. 2 Relation between bending strength and matrix.

Fig.3 Effect of exposure time on tensile strength.

times the other specimens. As for the failure mode, there was a difference between C_2S-EP and the other specimens. The failure mode of C_2S-EP was fiber breakage on the tension side, the failure mode of the other specimens, however, was buckling of surface mat on the compression side.

3.3 *Effect of exposure time on weather resistance*

In order to clarify the effects of exposure time, that is, before exposure, after one year and after two years, on the Young's modulus and tensile strength, we used a three-way classification. Three factors were the reinforcing fiber, matrix, and exposure time. The values at the waterline were used as the data for exposure hereinafter. Each factor was significant at the one percent level except that the factor "matrix" concerning to tensile strength was significant at the five percent level. We observed that the tensile strength of the specimens exposed for one and two years increased by 13% and 4% the initial value, respectively, as shown in Fig. 3. The cure of the resin of the specimens exposed for one
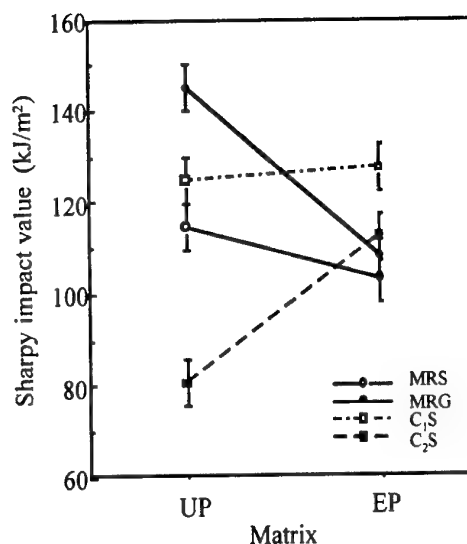

Fig.4 Relation between Sharpy impact value and matrix.

year increased over the initial value.

We observed that the bending strength of the specimens exposed for one and two years increased by 36% and 24% the initial value, respectively.

The Sharpy impact value of the specimens exposed for one and two years increased by

34% and 18% the initial value, respectively. We assume the same explanation as in the case of tensile strength.

3.4 *Effect of matrices on weather resistance of specimens exposed for two years*

The relation between Sharpy impact value and matrix was shown in Fig. 4. With respect to the Sharpy impact value, there was a large interaction between the reinforcing fiber and matrix. The Sharpy impact value of C_2S-EP surpassed extensively that of C_2S-UP.

4 CONCLUSIONS

As the effect of exposure position on modulus, the Young's modulus and the bending modulus of the specimens exposed at the waterline was the smallest. It is assumed that the repeated force produced by waves, weather, and their interactions resulted in the degradation.

As the effect of exposure time on strength, the tensile strength, the bending strength, and the Sharpy impact values of the specimens exposed for two years exceeded the initial value and decreased from those exposed for one year. It is considered that the cure of the resin during one year of exposure exceeded the degradation, and the cure finished mainly after two years.

As the compatibility of reinforcing fiber and resin, the carbon fiber in combination with epoxy resin was superior to the others on the bending strength.

5 ACKNOWLEDGMENTS

REFERENCES

1) Kemmochi, K., H.Takayanagi, C.Nagasawa, J.Takahashi & R.Hayashi 1995. Advanced Performance Materials, 2, 385-394.
2) Takayanagi, H., N.Koshizaki, K.Kemmochi & R.Hayashi 1990. Bulletin of Industrial Products Research Institute, No.117, 23-34.

Accelerated marine aging of composites and metal/composite joints

P. Davies*, A. Roy**, E. Gontcharova***, JL Gacougnolle***

* Marine Materials Laboratory, IFREMER, France
** CRITT Matériaux Poitou-Charentes, Rochefort, France
*** Laboratoire de Mécanique et de Physique des Matériaux, ENSMA Poitiers, France

ABSTRACT

Long term predictions of the integrity of marine structures require quantitative assessment of the evolution of material properties. In order to obtain such data in a reasonable time it is necessary to accelerate tests, usually by raising temperature. This paper will present data from a study in which the validity of such tests is examined. Three composite sytsems (polyester and epoxy reinforced with woven and stitched glass fabrics) and a steel/composite bonded joint have been aged at sea in the Brest estuary for up to 2 years. Specimens were removed regularly for mechanical testing in tension and flexure. At the same time specimens of identical geometry were aged in the laboratory using temperatures up to 50°C to accelerate aging. There are analogies between the aging of joints in the tidal zone and in demineralized water, for which the aging is dominated by diffusion, whereas continuous immersion in sea water results in oxidation of the steel at the steel/adhesive interface The comparison of residual mechanical and physico-chemical properties has enabled the correlation between the natural and accelerated aging procedures to be established.

Introduction

The use of composites in the marine industry is widespread [1-3]. The materials used are mostly polyester thermosets, with some vinylesters and epoxies are also employed. The fibre reinforcement is mostly glass, principally woven fabric or random mat, although more stitched fabrics are also being introduced. While some applications involve complete composite structures, generally produced by hand lay-up, in many cases composites are joined to other materials, mostly metals and particularly steel. These marine structures are usually designed for long service lives, tens of years, and the good reputation for corrosion resistance of composites in seawater is frequently a major selling point. However, the designer is required to guarantee that service life and the usual procedure is to apply a significant 'safety factor' for long term performance. This generally results in satisfactory behaviour but may significantly over-dimension the structure. When weight is critical, as in high speed vesels, this may not be acceptable.

Given the long experience with composites in this industry it might be thought that all necessary design data would be available from previous studies. Weitsman has recently summarized available data [4] and indeed, some long immersions have been noted, particularly associated with minesweeper programmes, but few results have appeared in the published literature. A brief summary of French naval tests was published [5], based on 21 years of immersion. Although few experimental details were presented this is a valuable contribution, showing a correlation between a change in mechanical behaviour observed after 15 years of natural aging at sea and 1000 hours accelerated ageing at 70°C.

The main value of long term immersion data is to validate the short accelerated tests which many laboratories are obliged to run to find answers to questions from designers both qualitatively such as 'does this new resin we want to use have as good long term aging resistance as the one we currently use?', or quantitatively 'what safety factor should we use to

take account of mechanical property degradation over a 20 year lifetime ?'. This study was performed in order to address the second type of question. The aim was to take samples with the same geometry from the same batches of fibre and resin materials, produced at the same time, and characterise their mechanical behaviour using the same test procedures after different natural and accelerated aging periods and conditions.

Materials
Three composite systems (polyester and epoxy reinforced with glass fabrics) and a steel/composite bonded joint have been studied. Table 1 shows the resin and fibre combinations. The joints were prepared by abrading and alcohol cleaning the surfaces and applying a Ciba Geigy Redux 420 two part adhesive (amine hardener) and curing for 2 hours at 70°C.

Table 1. Materials tested

Specimen	Fibre	Resin	Form
Composite 1 RM/ISO	Rovimat (Chomarat 500/300 g/m²) 5 layers	Isophthalic polyester Scott Bader 491PA	Panels 100 x 250mm Thickness 6mm
Composite 2 QX/EP	Quadriaxial stitched (Cotech 1034 g/m²)3 layers	Epoxy (Sicomin 1500/2505 amine)	Panels 100 x 250mm Thickness 4mm
Composite 3 QX/ISO	Quadriaxial stitched (Cotech 1034 g/m²) 6 layers	Isophthalic polyester Scott Bader 491 PA	Panels 100 x 250mm Thickness 6mm
Mild steel (2xmm) bonded (Redux 420) to Composite (6 mm),	Rovimat (Chomarat 500/300 g/m²) 5 layers	Isophthalic polyester Cray T7039	Lap shear specimens 25mm wide, 25mm overlap

The composites were immersed at sea at a test site in the Brest estuary for up to 2 years. Panels were fixed to immersion baskets, placed at 5 metres depth, and periodically removed by divers. Some joint specimens were also immersed, others were placed in the tidal zone. Table 2 shows the natural and accelerated test conditions. These tests are continuing and the QX/polyester series started after the other two materials so results will be presented later.

Table 2. Aging conditions

Specimen	Natural aging (months)	Laboratory aging (months)
Composite 1 RM/ISO	SW 3, 6, 9, 12, 18, 24	16°C DW, 9 50°C DW 1, 2, 3, 9
Composite 2 QX/EP	SW 3, 6, 9, 12, 18, 24	16°C DW, 9 50°C DW 1, 2, 3
Composite 3 QX/ISO	currently underway	
Mild steel bonded to Composite (Redux 420)	Tidal zone 1, 3, 6, 9, 12 Immersion SW 3, 12	25.C DW, 1, 3, 6, 9, 12 40.C DW, 1, 3, 6, 9, 12 50°C SW 1, 2, 3

DW: distilled water, SW: Sea water

After aging specimens were placed in a temperature (20°C) and relative humidity (50%) controlled laboratory for 2 weeks to stabilize them, before testing then in the same laboratory. The sea aged specimens were covered with marine growth, and this was carefully removed before stabilization. Weight gains of all specimens were recorded.

Tests performed.
All the composite panels were cut in the same way, as shown in Figure 1, using a diamond wheel.
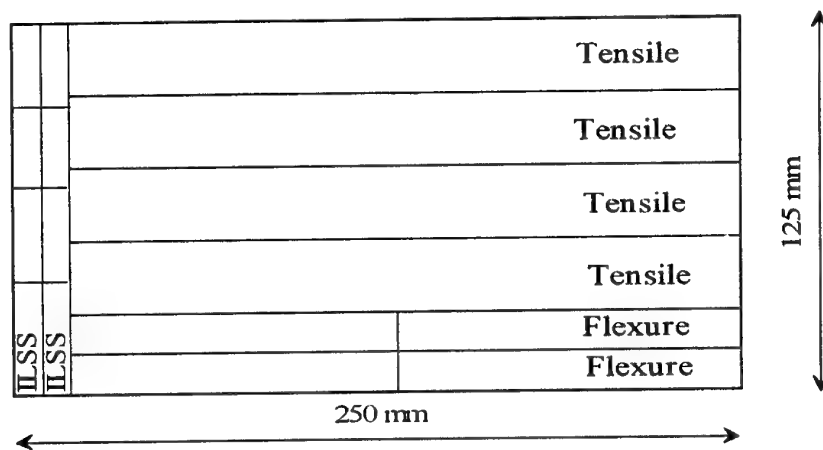

Figure 1. Specimens taken from each aged panel.

Each panel provided 4 tensile specimens, 4 flexure specimens and at least 6 interlaminar shear specimens. The test procedures were as follows:

Tensile tests
Loaded up to 1 ton force, with a clip-on extensometer, unloaded, then tested to failure. Loading rate 2 mm/minute. This provides:
- tensile modulus E_t , strain at knee on stress-strain plot (indicative of damage in 90° reinforcement), ε_d , failure stress (maximum stress), σ_t
Flexure tests
Loaded to failure at 2 mm/min, three point flexure fixture, span of 16 times thickness,. providing:
- flexure modulus E_f, flexural strength σ_f
Interlaminar shear tests
Loaded to failure at 5 mm/min, three point flexure fixture, span of 5 times thickness,. providing:
- apparent interlaminar shear strength τ.

The joint specimens were loaded to failure at 1 mm/minute. Tabs were bonded to the ends to allow symmetrical loading. An extensometer was placed on the specimen, fixed above and below the bonded overlap, to measure apparent strain (including tensile, shear and rotation contributions). Some laboratory-aged joint specimens were dried before testing. These tests provide two values:
- force at damage initiation F_d , force at failure, F_r

Results

a) Composite panels
Examples of the influence of aging on composite behaviour are shown below. The tensile stress-strain plots show a clear knee as damage occurs in the regions containing off-axis reinforcement.in the 90° weave and mat layers for the rovimat, and in the 90° layers in the quadriaxially reinforced composite. This is one of the parameters which can be correlated, but in the limited space available here only the failure stresses will be considered. Figures 2-4 show

tensile, flexure and interlaminar shear strength results, for RM/polyester and QX/Epoxy composites aged naturally and in the laboratory.
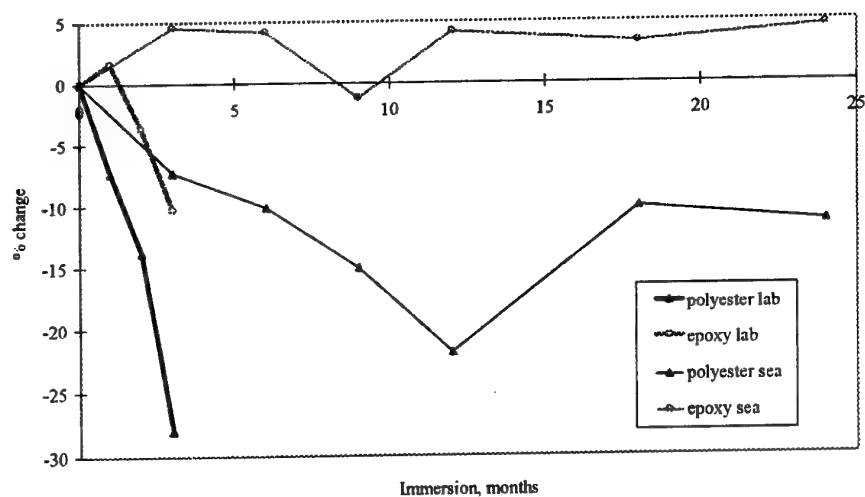
Figure 2. Tensile strength

Figure 2. Tensile strength

Figure 3. Flexural strength

Figure 3. Flexural strength

Figure 4. Interlaminar shear strength

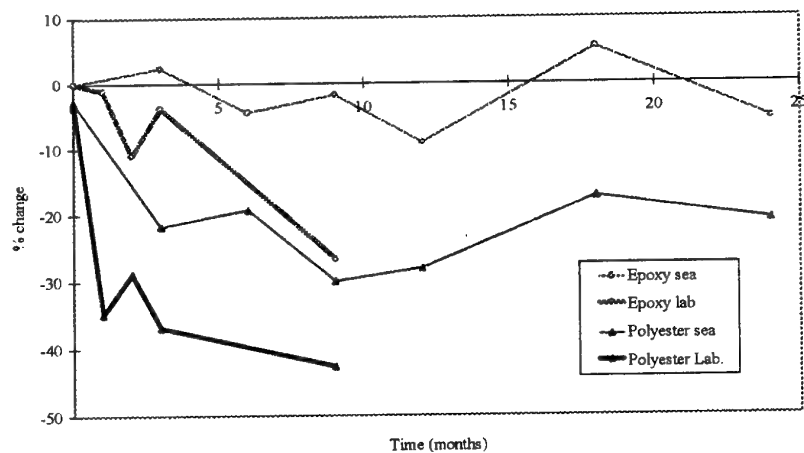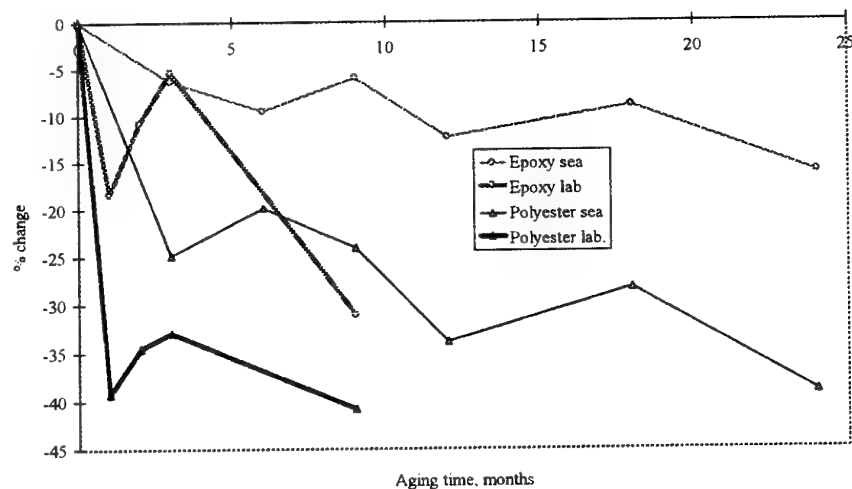Figure 4. Interlaminar shear strength

## Correlation between accelerated and natural aging of composites

These results suggest that the 50°C distilled water test is very severe in accelerating tensile and flexure strengths for both materials. Over the first year there seems to be a reasonable correlation between the forms of the changes in properties, with a decrease of around 20% and an accelerating factor in the laboratory of around four to five times (3 months in the laboratory corresponds to around a year at sea). However the results after 18 and 24 months then increase again and after two years the polyester tensile strength passes through a trough. The interlaminar shear results for polyester give a better quantitative correlation, but the 50°C acceleration is again very severe with respect to natural aging for the epoxy composite.

b) Joints

Examples of tensile loading curves of lap shear joints are shown in Figure 5. There is again a clear knee on the curve and this is caused by the appearance of a crack at the joint extremity in the composite. The force at which this appears, F_d, and the force at failure, F_r, are the two parameters which were used here to examine the correlation between laboratory aging and natural aging.

A large number of laboratory tests were performed in order to understand the mechanisms of degradation of these joints, and more data are available elsewhere [6].

Figure 5. Steel/composite lap shear in tension
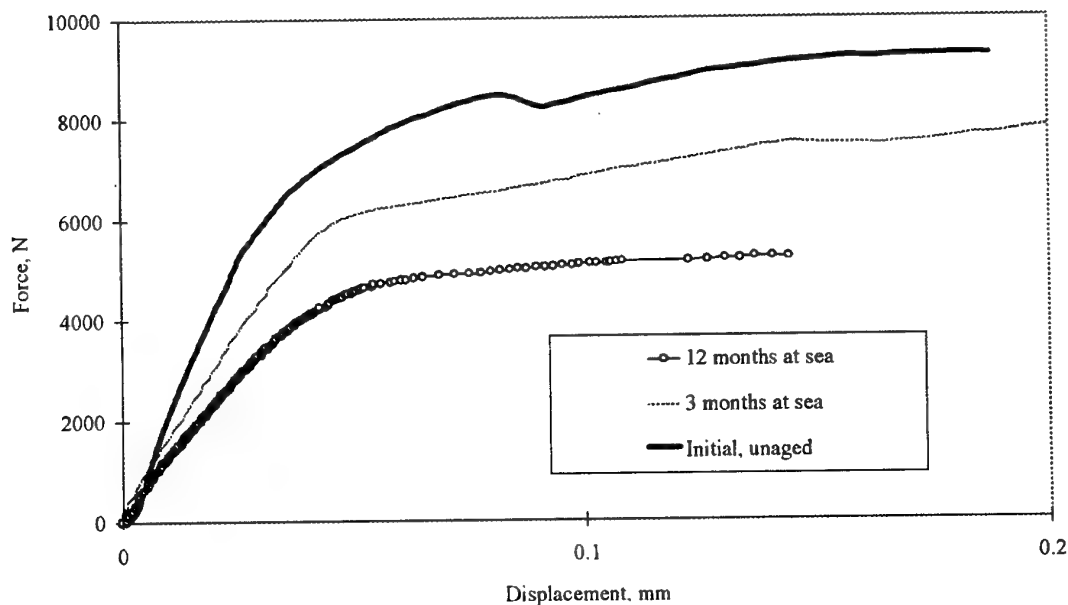
These curves clearly show the change in behaviour after aging. In order to simulate this in the laboratory several series of specimens were aged in natural sea water at 50°C, and in distilled water at 25°C and 40°C. Some results for F_r are shown in Figure 6 below.

Figure 6. Tensile behaviour of aged lap shear metal/composite
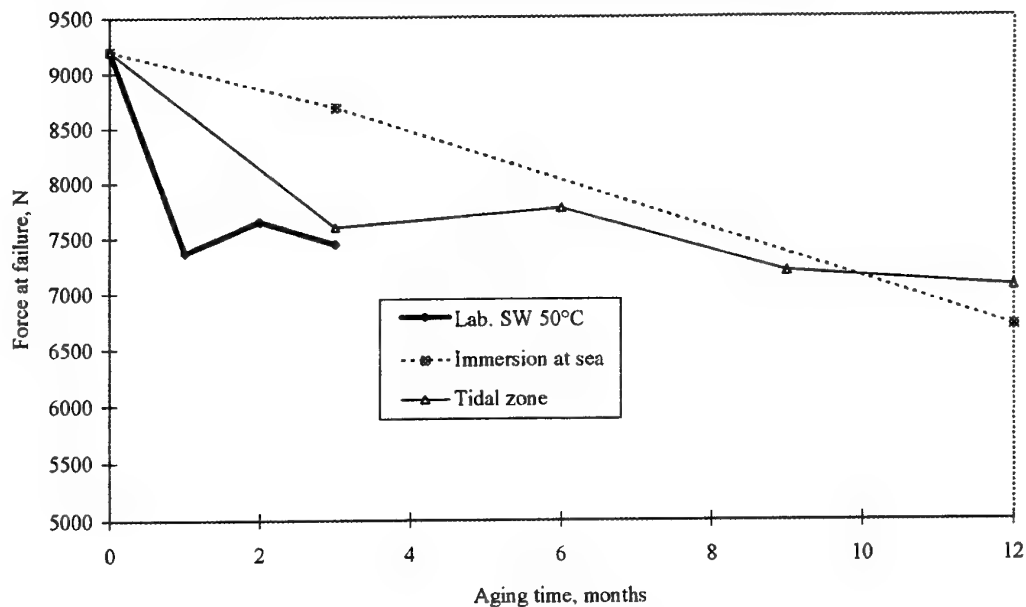
Conclusion

This abstract shows some of the results available after accelerated laboratory aging and tests at sea on composite and metal/composite specimens. While there is a reasonable correlation for the joints, provided sea water is used as the accelerated aging medium, there are significant differences for the composite strengths. These will be discussed in more detail in the full paper.

References

[1] Smith CS, 'Design of Marine Structures in Composite Materials', Elsevier, 1990.

[2] Davies P, in 'Durability analysis of structural composite systems', ed Cardon, 1996, p33.Balkema Publishers

[3] Shenoi RA, Wellicome JF, 'Composite Materials in Maritime Structures', Cambridge Ocean Technology series, 1993.

[4] Weitsman YJ, 'Effects of fluids on polymeric composites', Report MAES98-5.0-CM, University of Tennessee August 1998.

[5] Gutierrez J, LeLay F, Hoarau P, 'A study of aging of glass fibre-resin composites in a marine environment', Proc. 3rd IFREMER conference 'Nautical construction with composite materials', Paris 1992, IFREMER publication p338.

[6] Roy A, Gontcharova E, Davies P, Gacougnolle J-L, Hygrothermal effects on failure mechanisms of composite/steel bonded joints, Proc ASTM Symp. on Time dependent and Non-linear effects in polymers & Composites', May 1998

Reliability of Continuous Fiber-Reinforced Ceramic Composites under Stress-Rupture Conditions in Oxidizing Environments[1].

Edgar Lara-Curzio
Metals and Ceramics Division
Oak Ridge National Laboratory
Oak Ridge, TN 37831-6069

1. Introduction

The development of Continuous Fiber-reinforced Ceramic Composites (CFCCs) has been driven by the promise of substantial economic and environmental benefits if these materials are used in applications for the energy and chemical industries (e.g., combustor liners for gas turbine engines, filters in power plants, structural members in fusion reactors, etc.) [1]. In these applications CFCC components will be subjected to planned and accidental thermal and mechanical transients that will be superimposed on relatively constant stresses, at intermediate and elevated temperatures, over periods of time that are measured in thousands of hours. Therefore, the successful use of CFCCs in the aforementioned applications will depend on knowledge of their thermomechanical behavior over periods of time comparable to their expected service life, and on design methodologies to predict their reliability under the expected (planned and unplanned) service conditions.

In this paper a model is presented to estimate the reliability of a CFCC when subjected to stress-rupture conditions at stresses larger than the matrix cracking stress at high temperatures. The specific case of CG-Nicalon™/SiC CFCCs with a fiber coating that becomes fugitive upon oxidation (e.g., carbon) is considered.

2. Model of oxidation-assisted stress-rupture.

2.1 Micromechanics

Consider a unidirectional model composite of length h, that is reinforced with fibers of equal diameter $2r$ that occupy a fraction v_f of the composite volume (Figure 1). It is assumed that the fibers are coated with a dissimilar layer of finite thickness to impart composite behavior, that the tensile strength of the fibers are Weibull-distributed $\sigma(\sigma_o, m)$ and the fiber interfacial shear stress is τ. Let us consider the case when the model composite is subjected to a global tensile stress, σ_c, that is larger than the matrix cracking stress, σ_{mc}, so that a series of parallel and equally spaced cracks are formed in the matrix. At the plane of the matrix cracks the axial stress in the bridging fibers will increase to support the entire load applied to the composite. Away from the crack surfaces, the average fiber axial stress will decay linearly at a rate of $2\tau/r$ as the matrix picks up the complementary portion of the load. The axial stress distribution along the fiber will be given by

$$\sigma_z^f(z) = T - \frac{2\tau z}{r} \qquad\qquad 0 \leq l/2 \qquad\qquad (1)$$

where T is the axial stress in the fibers at the crack plane. Figure 1 also shows a diagram of the idealized fiber's axial stress profile. A balance of forces at the plane of the matrix cracks yields a

relationship between the maximum stress in the fiber, T, and the constant applied stress to the composite, σ_c, i.e.

$$\sigma_c = v_f \, T \, (1 - \Phi) + \frac{2\tau}{r} \lambda \Phi \tag{2}$$

where Φ is the fraction of failed fibers and λ is the average fiber pullout length [2]. By assuming global load sharing conditions, the maximum stress in the surviving fibers, T, will increase with progressive fiber failure as dictated by Equation 2, even though the value of the applied composite stress, σ_c, remains constant. The second term in the right hand side of Equation 2 accounts for the contribution of fibers that failed away from the matrix crack plane, to the load-bearing capacity of the CFCC.

2.2 Environmental effects

Matrix cracks serve as avenues for the ingress of the environment into the composite. When the environment is oxidizing, a sequence of events is triggered starting first with the oxidation of the fiber coating. As a result, both the axial stress distribution in the fibers and their probability of failure will change, because longer portions of the fibers will be subjected to the peak stress, T. (Figure 2). The fiber axial stress will change with the rate of oxidation of the fiber coating, and will be given by

$$\sigma_z^f(z,t) = T(t)\,[U(z)] - \frac{2\tau}{r}\,(z - \zeta(t))[U(z - \zeta(t))] \qquad 0 \; z \; l/2 \tag{3}$$

where ζ is the recession length of the fiber coating measured from the plane of the matrix crack, and $[U(z - z_o)]$ is Heaviside's unit function. The removal of the fiber coating will expose the fibers to the environment leading to the oxidation of the fibers and eventually to their loss of strength [3-4]. In the case of CG-Nicalon™, as with other SiC-based fibers, oxidation is controlled by diffusion of oxygen through the oxide layer. Therefore the oxide layer will grow on the fiber's surface according to:

$$\alpha = \sqrt{k_2 \, t} \tag{4}$$

where k_2 is the parabolic rate constant [5-6]. By assuming that the fracture toughness of the fibers remains constant and that the characteristic fiber strength, σ_o, is related to the mean oxide layer thickness, $\alpha(t)$, then the time-dependence of the fiber characteristic strength will be given by

$$\sigma_o(t) = \overline{\sigma}_o, \qquad t \leq \frac{1}{k_2}\left(\frac{K_{IC}}{Y\,\overline{\sigma}_o}\right)^4$$

$$\sigma_o(t) = \frac{K_{IC}}{Y\,\sqrt{\alpha(t)}}, \qquad t > \frac{1}{k_2}\left(\frac{K_{IC}}{Y\,\overline{\sigma}_o}\right)^4 \tag{5}$$

where K_{IC} is the fracture toughness, Y is a geometric parameter, and σ_o is the virgin characteristic strength [8-9]. Note that Equation 5 indicates the existence of an incubation period equal to the time required to grow an oxide layer as thick as the size of the average critical flaw in the virgin fibers and that afterwards the characteristic fiber strength changes with time as $t^{-1/4}$.

2

2.3 Reliability

The reliability of the model CFCC is obtained by discretizing the unit cell (Figure 1) into differential elements of length dz as illustrated in Figure 3. The product of the reliability of the differential elements yields [9-11]

$$\Re\,(t) = exp\left\{-\frac{2h}{l_c l_o}\left\{T^m \int_0^\zeta \frac{dz}{\left(\sigma_o(z,t)\right)^m} + \frac{1}{\overline{\sigma}_o^m}\int_\zeta^{l_c/2}\left(\sigma(z)\right)^m\,dz\right\}\right\} \quad 0 \le t \le \frac{l_c}{2\,k_1} \quad (10)$$

and once the carbonaceous fiber coating has been removed, i.e. when $\xi = l_c/2$, then the reliability of the model composite becomes

$$\Re\,(t) = exp\left\{-\frac{2h}{l_c l_o}\left\{T^m \int_0^{l_c/2}\frac{dz}{\left(\sigma_o(z,t)\right)^m}\right\}\right\} \quad t > \frac{l_c}{2\,k_1} \quad (12)$$

Note that at the end of the first stage, the analysis is reduced to that of a bundle of fibers in the Daniels sense [12] subjected to a non-uniform stress distribution that changes with time.

3. Results and Discussion.

Figure 4 shows predicted curves of stress versus time to failure for temperatures between 600°C and 950°C. The stress-rupture curves in Figure 4 exhibit three regimes: in regime I the composite fails at stresses close to its tensile strength but in a period of time that is less than the time required to consume all of the carbonaceous fiber coating. In this case, failure of the composite results from the inability of the fibers to bear the stress originally carried by the matrix and that is transferred to the fibers when the fiber coating becomes fugitive [10]. In regime II, composite failure occurs after all the carbonaceous fiber coating has been completely consumed and the rate of loss of strength for the composite is determined solely by the oxidation of the fibers. Note that the slope of the stress-rupture curves in regime II is equal to -1/4, which is consistent with the time-dependence of the decrease in the characteristic strength of the distribution of fiber strengths (Equation 5), and with experimental stress-rupture results at 600°C and 950°C for CG-Nicalon[TM]/Enhanced SiC [13-14]. Obviously no failure is expected at stresses below the matrix cracking stress (regime III).

4. Summary

A model was presented to predict the reliability and life of a CFCC subjected to stress-rupture conditions in an oxidizing environment. The model is based on the micromechanical analysis of a unidirectional composite and the consideration of a sequence of events that lead ultimately to the rupture of the composite. These events include: cracking of the matrix, ingress of the environment to the interior of the composite, oxidation of the fiber coating and oxidation of the fibers. The case of a composite containing fiber coatings that become fugitive after oxidation and fibers that lose strength due to oxidation was analyzed. It was shown that the oxidation of the fiber coating leads to changes in the stress distribution of fibers and exposure of the fibers to the environment. In turn oxidation of the fibers leads to fiber loss of strength and ultimately composite failure. The strain histories predicted by the model indicate that the compliance of the composite increases continuously, which is consistent with experimentally recorded strain histories under similar conditions. It is also found that the model predicts a rate of loss of composite strength proportional to $t^{-1/4}$ which is also consistent with experimental results.

3

5. References

1. M. A. Karnitz, D. F. Craig and S. L. Richlen, *Ceramic Bulletin*, **70**, (1991) pp. 430-5
2. A. Curtin, *J. Amer. Ceram. Soc.*, **74** [11] 2387-45 (1991)
3. G. Emig, and R. Wirth, *J. Mater. Sci.*, **30** (1995) pp. 5813-18
4. Y. G. Gogotsi, and M. Yoshimura, *J. Am. Ceram,. Soc.*, **78** [6] 1439-50 (1995)
5. T. Shimoo, H. Chen and K. Okamura,*J. Ceram. Soc. Japan*, **100**, 7 (1992) pp. 929-35
6. L. Filipuzzi and R. Naslain, in Advanced Structural Inorganic Composites, P. Vincenzini, Ed. Elsevier Science, (1991) pp. 35-46
7. T. Helmer, H. Peterlik, and K. Kromp, *J. Am. Ceram. Soc.*, **78** [1] pp. 133-36 (1995)
8. E. Lara-Curzio, *Journal of Engineering Materials and Technology* , vol. **120** April 1998, pp. 105-109
9. E. Lara-Curzio, *Composites Part A,* **30**, 4 (1999) pp. 549-554
10. E. Lara-Curzio, M. K. Ferber and P. F. Tortorelli, *Key Engineering Materials*, Vols. **127-131** (1997) pp. 1069-1082.
11. E. Lara-Curzio, P. F. Tortorelli and K. L. More, *Ceram. Eng. and Sci.*. **18,** (1997) pp. 209
12. H. E. Daniels, *Proc. R. Soc. London*, **A183**, pp. 405-35 (1944)
13. E. Lara-Curzio, *J. Am. Ceram. Soc.*, 80 [12] 3268-72 (1997)
14. M. J. Verrilli, A. M. Calomino, and D. N. Brewer, in Thermal and Mechanical Test Methods and Behavior of Continuous Fiber Ceramic Composites, ASTM STP 1309, M. G. Jenkins, S. T. Gonczy, E. Lara-Curzio, N. E. Ashbaugh and L. P. Zawada, Eds.. American Society for Testing and Materials, Conshohocken, PA (1997)
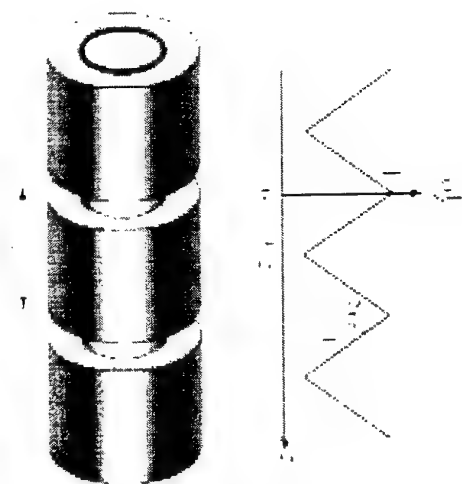15. L. Filipuzzi. and R. Naslain, *J. Amer. Ceram. Soc.*, **77** [2] 467-80 (1994)

Figure 1.- Schematic representation of model unidirectional composite and axial stress profile for fibers.
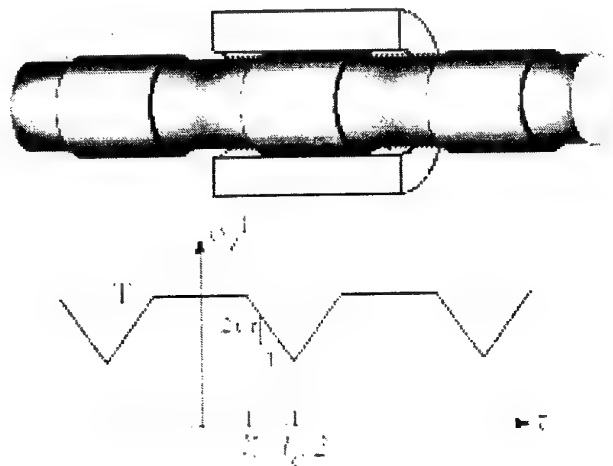

Figure 2.- Axial stress distribution in the fibers after partial removal of the carbonaceous fiber coating. Note that longer portions of the fiber are subjected to the peak fiber stress. *T*. in contrast to the stress distribution in Figure 1.
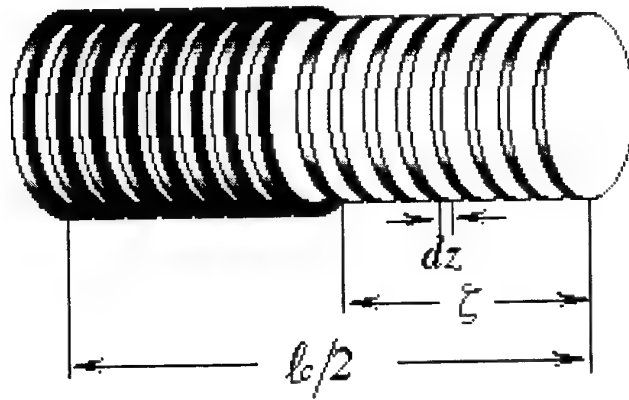
Figure 3.- Discretization of unit cell into differential elements. The reliability of the unit cell is given by the product of the reliabilities of the differential elements.
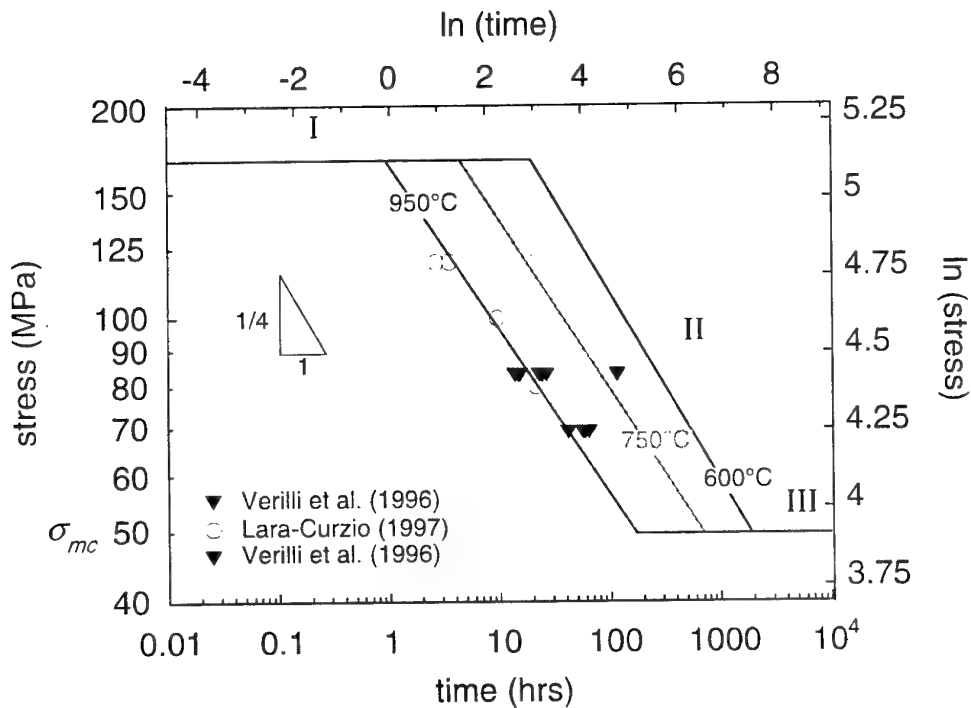

Figure 4.- Predicted strength versus time curves for model composite. Note that rupture curves have three well defined regimes. Also included are experimental stress-rupture results for CG-Nicalon[TM]/C/SiC.

THERMAL AGEING ON G$_{II}$ INTERLAMINAR FRACTURE MODE RESPONSE OF MULTIAXIAL 2D COMPOSITES

F. Segovia, V. Amigó, Mª D. Salvador, C. Bloem [*]

Departamento de Ingeniería Mecánica y Materiales
Escuela Técnica Superior de Ingenieros Industriales
Universidad Politécnica de Valencia
Cno. de Vera S/N 46022 VALENCIA
ESPAÑA
*Escuela de Ingeniería Mecánica, Facultad de Ingeniería.
Av. Tulio Febres Cordero 5101 Mérida, Edo. Mérida
VENEZUELA

INTRODUCTION.

The polyester glass fibre reinforced composites GFRP are getting more importance as a basic material in the elaboration of rust free equipment and facilities due to the advantages over metals. These equipments some times are exposed to environments which the temperatures are higher than atmospheric one's.

The increased use of GFRP and the newer technologies has been developed a special interest on the study of the environmental effect over the static mechanical properties [1,2] or impact [3,4], or fatigue behave [5,6]. Some works determine the effect on the fracture toughness due to a different kind of liquids exposition [7,8].

The Vinilester-Bisphenol is one of the most remarkable resins on the unsaturated polyester group. The knowledge of the thermal effect over the statical mechanical characteristics of this resin is really old and well-known [9]. No data is available on fracture toughness loss on Vinilester-Bisphenol composites due to the thermal ageing either the thermal ageing mathematical correlation is not found.

The aim of this work is to evaluate and perform a mathematical model of the interlaminar fracture toughness degradation due to elevated temperature exposition, and its relationship to the thermal cured treatment.

1. MATERIALS.

Glass fibre reinforced laminates were done employing a Vinilester-Bisphenol resin. The reinforcement were a multilayered equilibrated glass fibre E multiaxial 2D cloth of 440 g/m². The matrix was a Vinilester-Bisphenol A (Basf A430 VE/BA). The resin's mechanical and thermal characteristics such as axial, flexural, shear and impact stress and glass transition temperature are summarised on table 1.

The reinforcement configuration (0°-90°/±45°) were done with 8 alternately disposed sheets, where a ±45° sheet is placed over a 0°-90° sheet. Laminates were cured at environment temperature (20°C) and controlled temperature (50°C), the cured time in both cases was the same, 24 hours.

The end notched fracture samples ENF were done inserting between the 4th and 5th reinforcement ply a Teflon® sheet with a thickness of 50 μm.

Table 1. Vinilester-Bisphenol characteristics.

A(%)	MS (MPa)	T_G (°C)	ρ (J/cm^2)	E_F (MPa)	R_F (MPa)
6	83	130	4	4000	150

2. EXPERIMENTAL PROCEDURE

Polymer ageing.
The sample ageing process was developed employing a controlled temperature chamber. The chamber's temperature was of 100°C close to the heat distortion temperature, but lower to the glass transition temperature (130°C). The chamber's temperature was electronically controlled.

Interlaminar fracture mode II essay.
The essay was performed accordingly to Davis procedure [10]. The samples measures were of 25 mm in width, 150 mm in length. Teflon® inserts of 50 mm in length were employed to produce the precrack effect, on which 25 mm were the precrack length (**a**). The supports were positioned at the distance of (2L) 100 mm, so the relation between **a** and **L** (a/L) was 0.5. The fracture essay was developed at 2 mm/sec on an Instron 4202 universal testing machine.

The prior determination of the compliance (**C**) employing the equation (1) to different values of (**a**) was necessary to determinate the interlaminar fracture toughness **G$_{IIc}$** .

$$C = C_o + m\,a^3 \qquad\qquad (1)$$

Where:
C is the compliance: The relation between δ and the load **P.**
a is the crack length. And
m is the adjust constant.

The deformation energy release rate **G$_{IIC}$** were calculated applying the equation 2

$$G_{IIC} = \frac{3m P^2 a^2}{2w} \qquad\qquad (2)$$

Where:
W is the sample's width, and
P is the load on the following criteria:
  I) The point where the **P-δ** relationship loss its linearity (**NL**).
  II) A 5% lower slope than initial **P-δ** (**C5%**)

4.RESULTS AND DISCUSSION.

The flexural characteristics show a strong loss on strength **S$_f$** and Modulus **E$_f$** due to time see table 2.

If the cured temperature was of 20° C the losses reach up to 25% on modulus and 15% on strength, but if the cured temperature was of 50° C the losses on both characteristics are 22%. Samples cured at 50° C show better modulus up to 7% and strength of 3% compared with 20°C cured samples. After 5260 hours this difference becomes higher, up to 11% on modulus and 7% on strength.

Table 2. Flexural strength characteristics.

T (°C)	t (h)	E_F (GPa)	S_F (MPa)
20	0	13.0	357
	5260	9.7	304
50	0	13.9	368
	5260	10.8	325

Figure 1. G_{IIC} against time. **C5%** criteria.

This behaviour promotes the study on the interlaminar fracture toughness evolution due to long-term heat exposed samples. Figure 1 shows the 5%higher compliance criteria (**C5%**) of the energy release rate G_{IIC} against time.
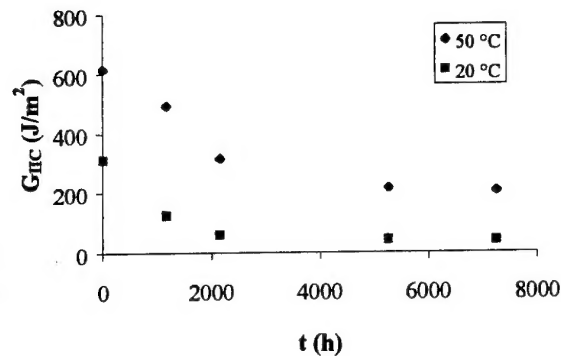
The strain energy release rate loss follows a damped exponential model against ageing time. The model could be mathematically expressed as equation (3)

$$G_{IIC} = A + B\,e^{-kt}$$

(3)

Where **A** represents the asymptotic value, **B** represents the difference between the initial value and the asymptotic one, **k** represents the extinction constant in hours^{-1} and t is the exposition time.
The adjusting parameters of the thermal ageing model are summarised on table 3

Table 3. Thermal ageing model's adjusting parameters.

Criteria	Cured temperature	A (J/m2)	B (J/m2)	A+B (J/m2)	k (10^{-4} h^{-1})	R^2
NL	20° C	14	77	91	9	0.98
	50° C	70	132	202	8	0.98
C5%	20 °C	39	241	280	10	0.99
	50 °C	210	425	635	6	0.95

Table 4. G_{IIC} percent Retention.

NL	A/(A+B) (%)	C5%	A/(A+B) (%)
20 °C	15	20 °C	14
50 °C	35	50 °C	33

Table 4 shows the material toughness degradability due to ageing time. Where a strong decay on the fracture toughness due to thermal effect could be observed.

The relation **A/(A+B)** exposes de accumulated loss beyond the asymptotic value **A**. The **A** corresponds the behaviour's value of a 7000 hours ageing. The **A+B** value predicts the model's value at 0 hours of ageing.

The residual toughness on 20°C cured samples are nearly 14~15% of the initial value. While on those samples cured at 50° C the residual toughness reach values up to 33%~35% approximately. The increase of cured temperature from 20° to 50°C decreases up to twice the material's degradability enhancing its durability.

Some aspects of micrographed fractures were analysed and discussed to invigorate this work. Observing figures 2 and 3 where the thermal ageing effect over the fracture morphology is distinguishable. Figure 2 shows a closed packed and deep curved morphology. While the aged sample (figure 3) shows a hackle packet reduction, an undeformed hackle morphology like facets and a lack of relief.
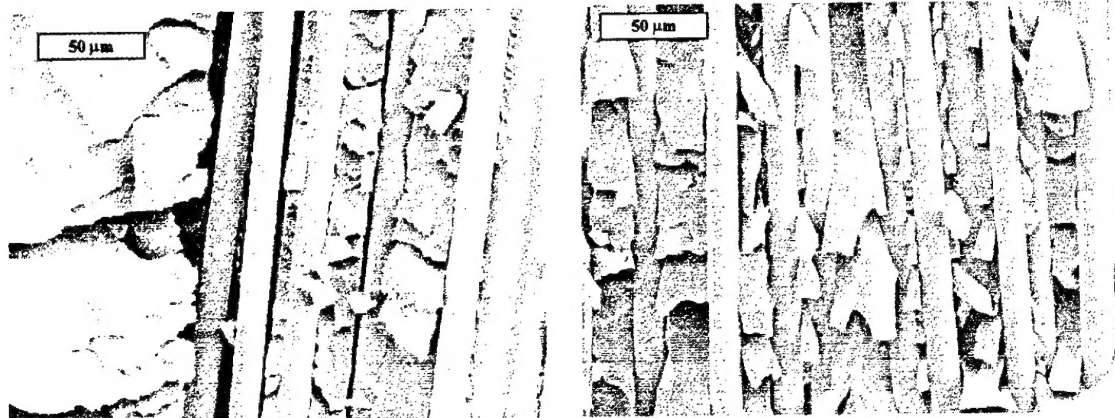

Figure 2. Non aged sample cured at 20 °C. X500.   Figure 3. Sample cured at 20°C, 2160 h aged. X500

5. CONCLUSIONS

The long-term exposition at high temperature (100°C) causes a high fracture toughness decrease on Vinilester glass fibre reinforced laminates.

The strain energy release rate **G$_{IIC}$** evolution due to ageing follows a damped decreasing exponential model.

The temperature of cured plays an important role over composite's toughness characteristics, a higher temperature of cured, higher initial toughness.

The degradability is cured temperature reverse dependent. The ageing effect is higher whiles lower is the cured temperature and vice versa. The adjusting parameters of the proposed model are temperature dependent too.

As a function of cured temperature the fracture interface shows dissimilar and particular features.

The fracture pattern is mainly mode II (Shear), but some type of mode I fracture could be distinguished too.

6. BIBLIOGRAPHY

[1]. Evans D., y Crook M.A. "Irradiation of plastics: damage and gas evolution". MRS Bulletin, 22 (4), pp 36-40 (1997).

[2]. Manrique F., Bonhome J. y Belzunce F.J. "Influence of enviromental aging on mechanical properties of single lap joints". Progress in Durability Analysis of Composite Systems, pp 311-316 Balkema Editors, Rotterdam (1996).

[3]. Boukhili R., Champoux L. Y Martin S. "Effect of water absortion on the low energy repeated impact of carbon/epoxy laminates". Durability Analysis of Composite Systems, pp 259-264, Balkema Editors, Rotterdam (1996).

[4]. Kasamori M., Funada Y., Awazu K., Watanabe Y., Nakada M. y Miyano Y. "Accelerated evaluation of mechanical degradation behavior of GFRP in hot water". Durability Analysis of Composite Systems, pp 273-277, Balkema Editors, Rotterdam (1996).

[5]. Chateauminois A. y Vauthier E. "Fatigue behaviour of aged glass-epoxy composites". Progress in Durability Analysis of Composite Systems, pp 159-165, Balkema Editors, Rotterdam (1996).

[6]. Lesko J.J., Hayes M.D., García K., McBagonluri D. y Verghese N. "Environmental-mechanical durability of glass/vinyl ester composites". DURACOSYS 97 proceedings, pp 4.10-4.13, Blacksburg, Virginia (1997).

[7]. R. Selzer, K. Friedrich. "Effects of water up-take on interlaminar fracture properties of various carbon fiber/epoxy composites". 9th ICCM proceedings vol 5 pp 875-881, Madrid (1993).

[8]. A.J. Russell, K.N. Street. "Moisture and temperature effects on the mixed-mode delamination fracture of unidirectional graphite/epoxy". Delamination and Debonding of Materials. ASTM STP 876, pp 349-370 (1985).

[9]. T.J. Reinhart. Composites. Engineered materials Handbook, vol. 1. ASM International, Metals Park, Oh (1.988).

[10]. Davis P. "Protocols for interlaminar fracture testing of composites", European Structural Integrity Society, Polymers & Composites Task Group (1993).